



**HAL**  
open science

# An evaluation of the behavior of the iron, chromium and copper during hydrothermal processes of serpentized peridotites from Tethyan ophiolites in Iran

Alireza Eslami

► **To cite this version:**

Alireza Eslami. An evaluation of the behavior of the iron, chromium and copper during hydrothermal processes of serpentized peridotites from Tethyan ophiolites in Iran. Applied geology. Université Grenoble Alpes [2020-..]; University of Teheran, 2022. English. NNT: 2022GRALU015 . tel-03775241

**HAL Id: tel-03775241**

**<https://theses.hal.science/tel-03775241>**

Submitted on 12 Sep 2022

**HAL** is a multi-disciplinary open access archive for the deposit and dissemination of scientific research documents, whether they are published or not. The documents may come from teaching and research institutions in France or abroad, or from public or private research centers.

L'archive ouverte pluridisciplinaire **HAL**, est destinée au dépôt et à la diffusion de documents scientifiques de niveau recherche, publiés ou non, émanant des établissements d'enseignement et de recherche français ou étrangers, des laboratoires publics ou privés.



University of  
TEHRAN



## THÈSE

Pour obtenir le grade de

**DOCTEUR DE L'UNIVERSITE GRENOBLE ALPES**

**préparée dans le cadre d'une cotutelle entre  
l'Université Grenoble Alpes et Université de  
Téhéran**

Spécialité : Terre, Univers, Environnement

Présentée par

**Alireza ESLAMI**

Thèse dirigée par **Benjamin MALVOISIN** et **Fabrice BRUNET**  
codirigée par **Ali KANANIAN**

préparée au sein des de l'Institut des Sciences de la Terre  
dans l'École doctorale Terre, Univers, Environnement

# **An evaluation of the behavior of the Fe, Cr and Cu during hydrothermal processes of serpentinized peridotites from the Tethyan ophiolites in Iran**

Thèse soutenue publiquement le 16 Mai 2022 devant le jury composé de :

**Isabelle MARTINEZ**

Associate Professor, Institute de Physique du Globe de Paris (Reviewer)

**Fernando BARRA**

Professor, Departamento de Geología, Universidad de Chile (Reviewer)

**Federica ZACCARINI**

Professor, Department of Applied Geosciences and Geophysics,  
Montanuniversität Leoben (Examiner)

**Andreas Michael BEINLICH**

Associate Professor, Department of Earth Science, University of Bergen  
(Examiner)

**Alexander SOBOLEV**

Professor, ISTerre, University of Grenoble Alpes (President)

**Fabrice BRUNET**

Director of Research, CNRS, ISTerre, University of Grenoble Alpes (Supervisor)

**Ali KANANIAN**

Professor, School of Geology, University of Tehran (Supervisor)

**Benjamin MALVOISIN**

Senior Researcher, CNRS, ISTerre, University of Grenoble Alpes (Co-Supervisor)



## Abstract

The main objective of this Ph.D. dissertation is to better understand mass transfer of Fe, Cr and Cu, three elements of economical interest, during serpentinization of ultramafic rocks. During the last decade, processes of formation of serpentinite-hosted metal deposits with mineable sizes has attracted attention as curiosities. One of the characteristics of the serpentinisation process is to generate highly reducing conditions in its early stages. Indeed, serpentinization of peridotite triggers the generation of substantial amounts of dihydrogen ( $H_2, aq$ ) which favors the stability of native metals in serpentinites. The study of the effect of these extreme RedOx conditions achieved during serpentinization, on the mobility of metals is at the heart of this PhD work.

To advance in this overall research goal, this Ph.D. thesis presents the results of two natural case studies of key processes of mass transfer and RedOx evolution during fluid-rock interaction: (i) serpentinite-hosted podiform magnetite ores in the Sabzevar ophiolite (NE Iran) and (ii) Cu-rich hydrothermally altered pyroxenites in the Cheshmeh-Bid ophiolitic massif (Southern Iran). These two occurrences have been selected since they provide a remarkable case study to better constrain Fe, Cr and Cu mobility during the hydrothermal evolution of peridotite-hosted hydrothermal systems. The systematic field observations together with textural observation at both  $\mu m$ - and  $nm$ -scales, geochemical signatures from whole-rock analyses and microanalysis and thermodynamic modelling were used to figure out the processes that promoted magnetite and copper formation in ophiolitic peridotites during serpentinization.

The studied magnetite deposits are remarkable because they arise from the hydrothermal alteration of chromitites. Strong iron and/or very limited chromium mobility is therefore involved. The magnetite deposits comprise a discontinuous trail of massive magnetite ore bodies in highly sheared serpentinites of the Late Cretaceous Sabzevar ophiolitic belt, northeastern of Iran. They show irregular and discontinuous shapes with variable sizes ranging from 30 to 60 cm. Chromian spinel grains are observed within both magnetite ores and host serpentinite. Magmatic chromian spinels, (Cr,Al)-spinel I, with compositions close to  $(Mg_{0.6}, Fe_{0.4})(Cr_{1.2}, Al_{0.75}, Fe^{3+}_{0.05})O_4$  are preserved in the host serpentinite where they display a porous alteration rim composed of Cr-bearing chlorite and three different spinel-structure minerals: Cr-spinel  $(Fe_{0.6}, Mg_{0.4})(Cr_{1.4}, Al_{0.4}, Fe^{3+}_{0.2})O_4$ , named Cr-spinel II (second generation), magnetite and ferritchromite, nominally  $FeCr_2O_4$ . In the magnetite ore body, no (Cr,Al)-spinel I is found and Cr-spinel II occurs as relict cores surrounded by ferritchromite and magnetite.

Detailed X-ray elemental mapping revealed that the 200  $\mu\text{m}$ -thick magnetite rim is composed of two magnetite types with different minor element compositions: the first rim found at the contact with ferritchromite is thin (20  $\mu\text{m}$ ; magnetite-I); the thicker outer rim contains numerous Fe-poor and Mg- and Si-rich silicate inclusions (magnetite-II). Observations at the nanoscale allows to identify ferritchromite which occurs as a micrometer-sized rim between Cr-spinel II and magnetite I. Thermodynamic modelling of the phase relationships in the studied Sabzevar serpentinite suggests that Cr-spinel II is produced along with chlorite during a first alteration stage at temperatures between 725 and 575  $^{\circ}\text{C}$  in the course of peridotite-water interactions. A second hydrothermal alteration stage producing ferritchromite and magnetite is inferred from the thermochemical modelling at temperatures  $< 400$   $^{\circ}\text{C}$  under high  $\text{H}_2$  fugacity. This latter stage corresponds to the serpentinization of the Sabzevar oceanic peridotite and associated podiform chromitite deposit. The two alteration stages are interpreted as the result of the interaction between seawater and oceanic mantle at two different depth ranges in the course of its exhumation. Our thermodynamic calculations and textural relationships revealed that Cr is immobile and Fe is the main element to be transferred to the magnetite ore during alteration processes. Fe possibly originated from direct transport of the  $\text{Fe}^{2+}$  produced during olivine dissolution or from the dissolution of nano-sized magnetite grains initially formed in the host serpentinite during early serpentinization. Mass balance calculation reveals significant iron transport at a scale  $> 10$  m during serpentinization.

Based on textural features and compositional maps, the Sabzevar serpentinite-hosted magnetite ores bears remarkable resemblance to the similar occurrences worldwide. Similar to the Sabzevar magnetite pods, analogous examples in the Nain (Central Iran), Skyros Island (Greece), Aniba (Oman) and Cogne (Italian Alps) ophiolite are hosted in intensely sheared and pervasively serpentinized peridotites. These shear zones which acted as high permeability pathways for hydrothermal fluids play a vital role for magnetite mineralization. The investigated magnetite ores from the Nain, Aniba and Skyros Island are heterogeneous in texture and consist of euhedral to anhedral magnetite crystals. The silicate mesostasis of the Nain and Skyros Island magnetite ores is mainly composed of fibrous serpentine, chlorite and andradite which is akin to those in the Sabzevar magnetite ores. Similar to the Sabzevar magnetite ores, euhedral to subhedral Cr-spinel relics are sporadically enclosed within large magnetite crystals of the Skyros Island, Nain and Aniba magnetite bodies. Similar to the Sabzevar occurrence, detailed X-ray elemental mapping on homogeneous Cr-spinel relicts rimmed by magnetite in the Skyros Island magnetite ore sample shows 200  $\mu\text{m}$ -thick magnetite rim comprising Si-poor and Si-rich magnetites. Si-rich magnetite can be attributed to presence

of tiny inclusions of silicate minerals. Laser-ablation inductively-coupled mass spectrometry (LA-ICPMS) studies of magnetite from Sabzevar serpentinite-hosted magnetite ores and analogous occurrences in the Nain, Oman, and Cogne ophiolites reveal typical hydrothermal compositions. These magnetite ore types have low V and Ti, as well as high Ni/Cr ratios, which are similar to magnetite found in hydrothermal deposits (i.e., skarn, IOCG). Magnetites from these serpentinite-hosted magnetite ore deposits formed at temperature  $<500\text{ }^{\circ}\text{C}$  which is compatible with serpentine stability field. Similarities observed between the different localities worldwide suggest that the mechanism described for the formation of Sabzevar serpentinite-hosted magnetite ore deposits may apply to magnetite ore formation at large scales in ophiolitic serpentinites.

In order to investigate factors controlling spinel alteration, textural and chemical changes were investigated in Cr-spinels in a representative set of chromitite-serpentinized dunite samples from the less altered chromitite deposits from the central sector of the Sabzevar ophiolite belt (NE Iran).

Two main alteration features were distinguished in spinels from both chromitite and serpentinized dunite samples: (i) Partly altered chromite corresponding to homogeneous spinel cores (Cr-spinel) either rimmed by or locally replaced by patches of porous chromite with pores filled with magnetite, serpentine and chlorite, or heterogeneous domain with little or no inclusions/pores (ii) Zoned chromite grains with a homogeneous core rimmed by a homogeneous corona of secondary spinel. Two chemical trends related to sub-solidus equilibration and hydrothermal alteration were observed in spinels from the Sabzevar chromitite-serpentinized dunite samples: (i) in the massive and semi-massive chromites, the trend consists in the progressive increase of Cr without  $\text{Fe}^{3+}$  incorporation; (ii) in serpentinized dunite containing disseminated chromite ( $< 50\%$  of the volume of the rock), the increase in Cr is smaller and associated with  $\text{Fe}^{3+}$  increase which is related to formation of Cr-spinel ( $\text{Fe}_{0.99}\text{Mg}_{0.37}\text{Cr}_{1.22}\text{Al}_{0.36}\text{Fe}^{3+}_{0.37}\text{O}_4$ ) with porous texture. Observation at the nanoscale shows that porous Cr-spinel contains intercalated platelets of magnetite and lizardite/chlorite. Automated crystal orientation mapping (ASTAR) reveals the epitaxial growth of porous Fe-Cr-spinel from primary Cr-spinel. Similar epitaxial relationship is observed between magnetite and porous Fe-Cr-spinel. A crystallographic relationship between lizardite/chlorite and Cr-spinel/magnetite shows that magnetite can occur as elongated plane in between phyllosilicate planes which confirms the contemporaneous formation of magnetite and phyllosilicates. TEM observation demonstrate that both secondary homogeneous and porous Fe-Cr-spinels have the same crystallographic orientation revealing their epitaxial replacement. A sequence of alteration

during cooling involving first chlorite at temperatures below  $\sim 700^{\circ}\text{C}$  and then serpentine formation is also predicted with thermodynamic modelling (Perple\_X with a new solid solution implemented for spinel). Aqueous Mg is also found to be at least two orders of magnitude more soluble than Fe and Si during alteration. The two different trends in composition between massive and disseminated chromites in a serpentinized dunite are reproduced with mass balance calculations by considering water to rock ratio  $>1$  and aqueous Mg formation. In this hydrothermal alteration process, chromium is found to be immobile even during serpentinization where  $f\text{O}_2$  is expected to be very low. Aluminum is transferred from the chromitite body to its host serpentinized dunite (chlorite formation) and, on the contrary, iron is transferred towards the chromitite to eventually form magnetite ores. Thus, early stages of Cr-spinel alteration are sought in other chromitite pods from the Sabzevar ophiolite, which did not reach the magnetite-ore transformation level.

The area that was studied to understand Cu mobility is located in the Cheshmeh-Bid district of the Khajeh-Jamali ophiolitic massifs (Southern Iran). Mantle peridotites are intruded by abundant pyroxenite dykes. A few of these dykes are remarkable for the occurrence of native copper associated with the development of a metasomatic reaction zone. The dykes are progressively reacted, from their margins towards the center, with an amphibole + antigorite selvage, followed by a centimeter-thick clinopyroxene + antigorite assemblage and, finally, by the native copper-bearing zone consisting of clinopyroxene + chlorite + antigorite. Native Cu occurs along cleavages and partially healed fractures in clinopyroxene, and as massive grains intergrown with antigorite. Copper isotope signatures and thermodynamic calculations show that the main driver for reaction zone formation is Ca-metasomatism. Native copper forms at the expense of chalcocite in the reaction zone. Such a reaction can only occur in reducing conditions, in agreement with the analysis of fluid inclusions composition displaying  $\text{H}_2$  and  $\text{CH}_4$ . Such fluids presumably originated from the hydration of mantle rocks. The observed reaction zone and native copper mineralization are thus interpreted as the result of Ca-metasomatism during hydrothermal alteration of the oceanic lithosphere. This is consistent with U/Pb dating of titanite, suggesting formation during the Albian when the dykes were exposed on the seafloor in a supra-subduction setting. The source for copper mineralization, as revealed by Cu isotopes, is probably mantle-like.

To conclude, the strongly reducing conditions associated with serpentinization of oceanic peridotites is considered to be a prerequisite for the formation of native copper and magnetite deposits in serpentinites. Under these low-T/high  $\text{H}_2$  activity conditions, Cr is almost immobile whereas Fe and Cu are elements to be transferred to mineralization sites during reaction. The

source of copper may be either desulfurization of primary Cu-sulfides or S-poor fluids during hydrothermal alteration for native copper formation. The source of iron necessary for magnetite ore formation is olivine breakdown and/or dissolution of nanoscale magnetite grains initially formed in the host serpentinite. Cumulative factors controlling the formation of ore deposits in serpentinites are fluid/rock ratio, silicate/spinel ratio, oxygen fugacity, permeable zone and initial composition of peridotites. Therefore, serpentinites in Tethyan ophiolites must be considered as a target for understanding the formation of the ores which helps for a future exploration.

## Résumé étendu

L'objectif principal de cette thèse de doctorat est de mieux comprendre le transfert de masse de trois éléments d'intérêt économique, le fer, le chrome et le cuivre, notamment pendant la serpentinisation des roches ultramafiques. Au cours de la dernière décennie, les processus de formation des gisements de métaux au sein de massifs de serpentine et de taille exploitable ont attiré l'attention des géologues. L'une des caractéristiques du processus de serpentinisation est de générer des conditions fortement réductrices, au moins dans ses premiers stades. En effet, la serpentinisation d'une péridotite produit des quantités substantielles de dihydrogène ( $H_2$ ) qui favorise la stabilité des métaux natifs. L'étude de l'effet de ces conditions extrêmes de RedOx pendant la serpentinisation, sur la mobilité des métaux est au cœur de ce travail de thèse.

Pour avancer dans cet objectif global de recherche, cette thèse de doctorat présente les résultats de deux études de cas naturels sur les processus clés du transfert de masse et de l'évolution du RedOx pendant l'interaction fluide hydrothermal – roche ultramafique : (i) les minerais de magnétite podiforme associés aux serpentinites dans l'ophiolite de Sabzevar (NE de l'Iran) et (ii) les pyroxénites riches en cuivre altérées par voie hydrothermale dans le massif ophiolitique de Cheshmeh-Bid (Sud de l'Iran). Les observations systématiques sur le terrain, ainsi que les observations texturales à l'échelle du  $\mu m$  et du nm, les signatures géochimiques provenant des analyses sur roche totale et de la microanalyse, et la modélisation thermodynamique ont été utilisées pour comprendre les processus qui ont conduit à la formation de magnétite et de cuivre natif dans les péridotites ophiolitiques, notamment au cours la serpentinisation.

Les gisements de magnétite étudiés sont remarquables car ils proviennent de l'altération hydrothermale de chromitites. Une forte mobilité du fer et une mobilité du chrome très limitée sont observées. Les gisements de magnétite se présente sous la forme d'alignements discontinus de corps minéralisés de magnétite massive dans des serpentinites fortement cisillées de la ceinture ophiolitique de Sabzevar du Crétacé supérieur. Ils présentent des formes irrégulières de taille variable allant de 30 à 60 cm. Les grains de spinelles chromifères sont observés à la fois dans les minerais de magnétite et dans la serpentine environnante. Des spinelles chromifères magmatiques, (Cr,Al)-spinelles I, avec des compositions proches de  $(Mg_{0.6}, Fe_{0.4})(Cr_{1.2}, Al_{0.75}, Fe^{3+}_{0.05})O_4$  sont préservés dans la serpentine hôte où ils présentent une bordure d'altération constituée de pores contenant de la chlorite chromifère. L'altération de ce

spinelles conduit à trois minéraux de structure spinelle de composition différente : un spinel chromifère enrichi en Fe ( $\text{Fe}_{0.6}, \text{Mg}_{0.4})(\text{Cr}_{1.4}, \text{Al}_{0.4}, \text{Fe}^{3+}_{0.2})\text{O}_4$ , nommé Cr-spinelle II (deuxième génération), de la magnétite et de la « ferritchromite », nominalement  $\text{FeCr}_2\text{O}_4$  très riche en chrome. Dans le corps minéralisé de magnétite, on ne trouve pas de (Cr,Al)-spinelles I et le Cr-spinelle II se présente sous la forme de reliques entourées de « ferritchromite » et de magnétite. La cartographie élémentaire détaillée a révélé un couronne de magnétite de 200  $\mu\text{m}$  d'épaisseur. Celle-ci est constituée de deux types de magnétite caractérisées par des compositions en éléments mineurs différentes. Une première couronne de magnétite, au contact de la ferritchromite, s'avère être relativement mince (20  $\mu\text{m}$  ; magnétite-I) ; une seconde couronne, externe, est plus épaisse et contient de nombreuses inclusions de silicate pauvres en Fe et riches en Mg (magnétite-II). Les observations à l'échelle nanométrique permettent d'identifier la « ferritchromite » qui se présente sous la forme d'une couronne de taille micrométrique entre le Cr-spinelle II et la magnétite I. La modélisation thermodynamique des relations de phases dans la serpentinite du Sabzevar suggère que le Cr-spinelle II est produit conjointement avec la chlorite au cours d'une première étape d'altération à des températures comprises entre 725 et 575 °C. Une deuxième étape d'altération hydrothermale produisant de la « ferritchromite » et de la magnétite est déduite de la modélisation thermochimique pour des températures < 400 °C sous une fugacité d' $\text{H}_2$  élevée. Cette dernière étape correspond à la serpentinitisation de la péridotite océanique du Sabzevar et du gisement de chromitite podiforme associé. Les deux stades d'altération sont interprétés comme le résultat de l'interaction entre l'eau de mer et le manteau océanique à des profondeurs différentes au cours de son exhumation. Nos calculs thermodynamiques et les relations texturales ont révélé que le Cr est immobile et que le Fe est le principal élément à être transféré pour former le minerai de magnétite pendant les processus d'altération. Le Fe peut provenir du transport direct du  $\text{Fe}^{2+}$  aqueux produit lors de la dissolution de l'olivine ou de la dissolution de grains de magnétite de taille nanométrique initialement formés dans la serpentinite hôte pendant la serpentinitisation précoce. Le calcul du bilan de masse révèle un transport significatif du fer à une échelle > 10 m pendant la serpentinitisation.

D'après les caractéristiques texturales et les cartes de composition chimique, les minerais de magnétite des serpentinites de Sabzevar présentent une ressemblance remarquable avec d'autres occurrences dans le monde entier. Tout comme les gisements podiformes de magnétite du Sabzevar, des exemples analogues dans l'ophiolite de Nain (Iran central), de l'île de Skyros (Grèce), d'Aniba (Oman) et de Cogne (Alpes italiennes) sont localisées dans des péridotites intensément cisailées et largement serpentinisées. Ces zones de cisaillement qui ont agi comme des voies de circulation préférentielle pour les fluides hydrothermaux jouent un rôle

crucial pour la minéralisation de la magnétite. Les minerais de magnétite étudiés provenant des îles de Nain, d'Aniba et de Skyros ont une texture hétérogène et sont constitués de cristaux de magnétite automorphes à xénomorphes. La matrice silicatée des minerais de magnétite de Nain et de l'île de Skyros est principalement composée de serpentine fibreuse, de chlorite et d'andradite, comme pour les minerais de magnétite de Sabzevar. De même, des reliques de spinelle chromifère sont sporadiquement englobées dans de gros cristaux de magnétite sur l'île Skyros, à Nain comme à Aniba. Comme dans le cas de l'occurrence du Sabzevar, les reliques de spinelle chromifère entourées de magnétite de l'île Skyros montre une couronne de magnétite de 200 µm d'épaisseur comprenant des magnétites pauvres en Si et d'autres plus riches en Si. La magnétite riche en Si peut être attribuée à la présence de minuscules inclusions de minéraux silicatés. Les études de spectrométrie de masse à couplage inductif par ablation laser (LA-ICPMS) de la magnétite des minerais de magnétite du Sabzevar et des occurrences analogues dans les ophiolites de Nain, Oman et Cogne révèlent des compositions typiques d'une origine hydrothermale. Ces types de minéralisation de magnétite ont une faible teneur en V et Ti, ainsi que des rapports Ni/Cr élevés, qui sont similaires à la magnétite trouvée dans les gisements hydrothermaux (c.-à-d., skarn, IOCG). Les magnétites de ces gisements de magnétite se sont formées à une température <500 °C, ce qui est compatible avec le champ de stabilité de la serpentine. Les similitudes observées entre les différentes localités du monde entier suggèrent que le mécanisme décrit pour la formation des gisements de minerai de magnétite du Sabzevar peut être généralisé à la formation de minerai de magnétite dans les serpentinites ophiolitiques.

Afin d'étudier les facteurs contrôlant l'altération des spinelles, les changements texturaux et chimiques ont été étudiés pour les spinelles chromifère d'un ensemble représentatif d'échantillons de chromitite – dunite serpentinisée provenant des gisements de chromitite les moins altérés du secteur central de la ceinture ophiolitique du Sabzevar (NE Iran).

Deux caractéristiques principales d'altération ont été distinguées dans les spinelles des échantillons de chromitite et de dunite serpentinisée: (i) chromite partiellement altérée correspondant à des coeurs de spinelle homogènes (Cr-spinelle-I) soit bordés par ou localement remplacés par a) des plages de chromite poreuse avec des pores parfois remplis de magnétite, de serpentine et de chlorite ou b) des zones de spinelle chimiquement hétérogènes avec peu ou pas d'inclusions/pores (ii) grains de chromite zonés avec un coeur chimiquement homogène bordé par une couronne, elle-même homogène, de spinelle secondaire. Deux tendances chimiques interprétées comme associées à un ré-équilibre sub-solidus et à l'altération hydrothermale ont été observées dans les spinelles des échantillons de chromitite – dunite serpentinisée de Sabzevar : (i) dans les chromites massives et semi-massives, la tendance

consiste en une augmentation progressive du chrome sans incorporation de  $\text{Fe}^{3+}$  ; (ii) dans les échantillons de dunite serpentinisée contenant des chromite disséminées (< 50 % du volume de la roche), l'augmentation du chrome est plus faible et associée à une augmentation du  $\text{Fe}^{3+}$  pour atteindre des compositions de type  $(\text{Fe}_{0.99}, \text{Mg}_{0.37})(\text{Cr}_{1.22}, \text{Al}_{0.36}, \text{Fe}^{3+}_{0.37})\text{O}_4$  ayant une texture poreuse (Fe-Cr-spinelle). L'observation à l'échelle nanométrique par diffraction électronique montre que les cristaux de magnétite et de lizardite/chlorite inclus dans les zones de spinelles poreux partagent des relations cristallographiques avec le spinelle hôte. La cartographie automatisée de l'orientation cristalline (ASTAR) révèle la croissance épitaxiale du Fe-Cr-spinel poreux à partir du cœur de spinelle original. Une relation épitaxiale similaire est observée entre la magnétite et le Fe-Cr-spinelle poreux. Les observations en microscopie électronique à transmission démontrent que les spinelles Fe-Cr secondaires, homogènes comme poreux ont la même orientation cristallographique que leur précurseur, révélant un remplacement isomorphe. Une séquence d'altération pendant le refroidissement impliquant d'abord la chlorite à des températures inférieures à  $\sim 700^\circ\text{C}$  et ensuite la formation de serpentine est également prédite par modélisation thermodynamique (Perple\_X avec une nouvelle solution solide implémentée pour le spinelle). La modélisation montre également que le Mg est au moins deux ordres de grandeur plus soluble que le Fe et le Si aux conditions de l'altération. Les deux tendances observées pour l'évolution de la composition chimique du spinelle chromifère entre les chromites massives et chromites disséminées dans une dunite serpentinisée sont reproduites par des calculs de bilan massique en considérant un rapport eau/roche  $>1$  et la solubilisation du Mg. Dans ce processus d'altération hydrothermale, on constate que le chrome est immobile même lors la serpentinisation alors que l'on s'attend à ce que la  $f\text{O}_2$  soit très faible et que le chrome soit divalent. L'aluminium est transféré de la chromite vers la dunite serpentinisée environnante (formation de chlorite) et, au contraire, le fer est transféré vers la chromite pour former des minerais de magnétite lors des stades ultimes de l'altération.

La zone qui a été étudiée pour comprendre la mobilité du Cu est située dans le district de Cheshmeh-Bid des massifs ophiolitiques de Khajeh-Jamali (Sud de l'Iran). Les péridotites du manteau sont recoupées par d'abondants dykes de pyroxénite. Quelques-uns de ces dykes sont remarquables par la présence de cuivre natif associé au développement d'une zone de réaction métasomatique. Les dykes réagissent progressivement, de leurs marges vers le centre, avec une lisière d'amphibole et d'antigorite, puis une zone constituée d'un assemblage de clinopyroxène et d'antigorite de quelques centimètres d'épaisseur et, enfin, de la zone cuprifère native constituée de clinopyroxène de chlorite et d'antigorite. Le cuivre natif est présent le long de clivages et de fractures partiellement cicatrisées dans le clinopyroxène, et sous forme de

grains massifs imbriqués dans l'antigorite. Les signatures isotopiques du cuivre et les calculs thermodynamiques montrent que le principal moteur de la formation de la zone de réaction est le métasomatisme calcique. Le cuivre natif se forme aux dépens de la chalcocite dans la zone de réaction. Une telle réaction ne peut se produire que sous des conditions réductrices, en accord avec l'analyse de la composition des inclusions fluides qui contiennent de l' $H_2$  et du  $CH_4$ . Ces fluides proviennent vraisemblablement de l'hydratation des roches du manteau. La zone de réaction observée et la minéralisation de cuivre natif sont donc interprétées comme le résultat du métasomatisme calcique pendant l'altération hydrothermale de la lithosphère océanique. Ceci est cohérent avec la datation U/Pb du sphène, suggérant une formation pendant l'Albien lorsque les dykes ont été exposés sur le plancher océanique dans un cadre de supra-subduction. La source de la minéralisation du cuivre, telle que révélée par les isotopes du cuivre, est probablement d'origine mantellique.

En conclusion, les conditions fortement réductrices associées à la serpentinisation des péridotites océaniques sont considérées comme une condition préalable à la formation de gisements de cuivre natif et de magnétite dans les serpentinites du Sabzevar. Dans ces conditions de faible température et de fugacité d' $H_2$  élevée, le chrome reste (quasi) immobile tandis que le Fe et le Cu sont des éléments qui sont transférés ( $> 10$  m) vers les sites de minéralisation au cours de la réaction. La source de cuivre peut être soit la désulfuration de sulfures de cuivre primaires, soit des fluides pauvres en S pendant l'altération hydrothermale pour la formation de cuivre natif. La source de fer nécessaire à la formation du minerai de magnétite est la décomposition de l'olivine et/ou la dissolution de grains de magnétite nanométriques initialement formés dans la serpentinite hôte. Les facteurs cumulatifs contrôlant la formation de gisements de minerai dans les serpentinites sont le rapport fluide/roche, le rapport silicate/spinelle, la fugacité d'oxygène, la zone perméable et la composition initiale des péridotites. Par conséquent, les serpentinites dans les ophiolites téthysiennes où ces paramètres peuvent amplement varier doivent être considérées comme une cible pour comprendre la formation des minerais, ce qui aide à une exploration future.

## Acknowledgments

I owe the completion of this thesis and the enjoyment of my time in Europe to a great many people. First and foremost, my sincere gratitude goes to my advisors Fabrice Brunet, Benjamin Malvoisin and Ali Kananian, for their healthy supervision and invaluable supports and for their hard work to get this PhD project off the ground.

Thank you, Fabrice, for nudging me in the right directions over the three years, and keeping me from getting carried away too much. I would especially like to thank you for your unrelenting patience when things got tough. You were always available to step in and help/answer all my questions. I appreciate the countless times you spent guiding me through field work, manuscript revisions, and several meetings. Your meticulous attention to detail inspired me to exceed my own expectations and abilities. I now find myself in a position where I believe I have accomplished something significant and created research that I am quite pleased of. Thank you for helping me to overcome all the obstacles that have been placed in my path due to coronavirus pandemic and funding issues.

Benjamin, I struggle to find the words to express how grateful I am for your guidance, invaluable support and friendship throughout my PhD researches. Without your eagerness and dedicated supervision, I would not have come this far and I cannot thank you enough. You're an inspiring scientist with an outstanding breadth of knowledge and experience in the field of thermochemical modelling and fluid-rock interactions. I was lucky enough to come in contact with you during a detailed core characterisation onboard the RV Chikyu (Japan). You are always brimming with impressive ideas and enthusiasm for my Ph.D. project. It is quite clear that I could not have done this project without your unwavering support. Thanks for introducing me to the Perplex, and for your amazingly sharp eye and critical mind. I am very grateful for all the support that you have extended to me during my time here at UGA.

I will forever be grateful to you Prof Kananian for your mentorship and for your continued support in Tehran. You fully respected as well as supported my scholarly pursuits, which led to Cotutelle and Sabbatical Leave Scholarship and INFS awards. I could not have dream of a better supervisor. My sincere gratitude to you for all you have done for my PhD.

Special thanks to Emilie Janots and Wolfgang Bach for their incisive comments on my PhD research which significantly improved this project.

This project has relied on the analytical facilities at universities of Grenoble-Alpes, Bremen, Milano, Milano-Bicocca and Eötvös Loránd. I am privileged to be coming to know such an amazing person like Giovanni Grieco from University of Milan. I have been working in collaboration with Giovanni for seven years, developing projects on chromite and copper ores in Iranian ophiolites. We had funny stories and great memories in several fieldworks in Iran and Italian Alps. He is not only a great professor, but he is also a faithful friend. He provided an enabling, supportive and friendly environment for me to succeed in my PhD study and research during my sabbatical leave in Milan. I am extremely lucky to have such a wonderful friend in my life. Thank to him and his exceptional wife, Katia, and his wonderful family. A massive thanks must goes to his colleagues in Italy: Alessandra Cavallo for his help with XRF analyses and Raman spectroscopy as well his kind invitation to chase the chromitites in serpentinite quarries in Valmalenco, Giulio Borghini and Alessandra Montanini for their scientific discussions on the Cheshmeh-Bid pyroxenites, Diego Gatta and Nicola Rotiroti for their help with single crystal XRD analyses. I am also, especially grateful to Wolfgang Bach for his great hospitality during my one-month stay in Bremen. His generous support for LA-ICPMS and EMP analyses is greatly appreciated. I also thanks Csaba Szabó for his kind invitation to visit Lithosphere Fluid Research Lab in Eötvös Loránd University. During my short stay in his lab, I could analyze a few nice fluid inclusions in my pyroxenite samples. It has been a pleasure to work with him and his wonderful students, especially László Előd Aradi. Gilles Renou (CMTC, Grenoble) is thanked for help with transmission electron microscopy. Without the help of Kavandegan Bana Company, the Sabzevar fieldwork would not have been possible; thanks are owed for providing access to their chromitite outcrops for sampling and their great hospitality during our visits to the Sabzevar ophiolite. Thank you to all the people I met during my stay in Sabzevar, especially to Eng. Mostafa Maldary for being the embodiment of Persian hospitality. I would like to also thank the Oman Drilling Project and IGCP649 for additional funding that allowed me to attend two fantastic conferences and workshops in Oman to present my work and meet so many amazing people. Many people made my time in Oman and Japan extremely memorable, however I'm particularly grateful to: Peter Kelemen for his kind invitation, my cabin mates (Ben and Wolf-Achim), Lotta, Clair, Samuel, Benoit, Beppe, Aida, Max, Joseph, Morishita, Yuji, Majid, Mohammad and Mahmoud for making life at sea seem easy and Marguerite Godard and Saebiyul Choe for making me work so hard. I would like to thank all those who helped me obtain valuable data at ISTerre, particularly the ever-lovely Nathaniel Findling for letting me loose on the SEM at all hours, the dignified Valentina Batanova and the ever-smiling Valerie Magnin, for their help with the extremely

laborious task of sample preparation and EMP analysis. I am also extremely grateful to the ever-kind Martin Lanson for her invaluable support and advice in use of the laboratories of the Geochemistry-Mineralogy platform in ISTerre. In addition, special big thanks to Marianna Corre for helping me handpick very nice magnetite crystals using a binocular microscope in ISTerre. I also thanks her for performing LA-ICPMS analysis on these crystals as well as magnetite (U-Th-Sm)/He thermochronometry. I would like to thank former office mates, Sonny Aribowo and Delgado Madera Gabino Fabrizio, for their company and friendships. And of course, thank you to the mineralogy team at ISTerre for being awesome.

A massive thanks goes to intimate friends Saeed, Mujtaba, Hanif, Sarvenaz, Sara and Hamed for reminding me there is a life outside of the PhD! You have been the best companions over the last two years and have made my time at Grenoble wonderful. Of course, I should include my other old and new friends. Thank you for being such lovely and prestigious friends during my academic life. Sorry, there are too many of you to quote but you know. Thanks! Merci! Grazie! Danke! Kösz! Terima kasih! Gracias! ありがとう! Ευχαριστώ! Спасибо! سپاس. Finally, heartfelt thanks to all the family (Mum and Dad, Hamid and Vahid) who have given me unfaltering support during my academic endeavours. Thank you from the bottom of my heart.

This work has been supported by a grant from LabEx OSUG@2020 (Investissements d'avenir – ANR10 LABX56) and supplemented by a further grant from the Iran National Science Foundation (INSF). I would like to thank the Embassy of France in Tehran, universities of Tehran and Grenoble-Alpes for their financial supports through the Cotutelle Scholarship Program between Iran and France.

Finally, I would like to dedicate this thesis to all the heroines and the heroes out there, who were at the heart of the fight against the recent coronavirus pandemic.

## Contents

### Part I Introduction, Research Goals and Dissertation Structure

1.	Introduction.....	2
1.1.	Geological settings for serpentinization.....	2
1.1.1.	Divergent margins: Mid-ocean ridges.....	2
1.1.2.	Convergent margins: Subduction zone.....	5
1.1.3.	On-land serpentinization: ophiolites.....	6
1.2.	Serpentinization reactions in the oceanic lithosphere.....	7
1.3.	RedOx conditions associated with serpentinization.....	8
1.4.	Stability of native metals during serpentinization.....	9
1.5.	Formation of magnetite upon serpentinization.....	12
2.	Motivation, Research Goals & Dissertation Structure.....	16
2.1.	Motivation.....	16
2.2.	Research goals.....	16
2.3.	Dissertation structure.....	18

### Part II Regional Geological Framework

3.	Regional Geological Framework.....	21
3.1.	Introduction.....	21
3.2.	Geotectonic realms of Iran.....	22
3.2.1.	Zagros Fold–Thrust Belt.....	23
3.2.2.	Sanandaj-Sirjan Zone.....	24
3.2.3.	Urumieh-Dokhtar Magmatic Arc.....	26
3.2.4.	Central-East Iranian Microcontinent.....	28
3.2.5.	Eastern Iranian Orogen.....	29
3.2.6.	Kopet Dagh Basin.....	31
3.2.7.	Makran Zone.....	33
3.3.	Ophiolite nappes in Iran.....	34
3.4.	Geological settings of study areas.....	37
3.4.1.	Northern Sabzevar Ophiolite Belt.....	37
3.4.2.	Neyriz ophiolite.....	44

### Part III Results

4.	Podiform magnetite ore (s) in the Sabzevar ophiolite (NE Iran): Oceanic hydrothermal alteration of a chromite deposit.....	52
4.1.	Introduction.....	52
4.2.	Geological setting and magnetite-ore occurrence.....	54
4.3.	Methods.....	55
4.3.2.	Bulk sample characterization.....	55

4.3.2	Micro- and nano-scale characterization.....	56
4.3.3	Thermodynamic modelling.....	57
4.4.	Mineralogical and textural characteristics.....	60
4.4.1.	Host serpentinite.....	60
4.4.2.	Magnetite ore.....	60
4.5.	Mineral chemistry.....	62
4.5.1.	Spinel.....	62
4.5.2.	Sulfides and alloys.....	65
4.5.3.	Andradite, chlorite and brucite.....	66
4.6.	Nanoscale characterization of the magnetite rims.....	67
4.7.	Thermodynamic modelling.....	71
4.8.	Discussion.....	76
4.8.1.	Two-stage spinel alteration process.....	76
4.8.2.	Conditions prevailing during the alteration stages.....	78
4.8.3.	Chromite microtexture formation and element mobility.....	80
4.8.4.	Iron mobility and magnetite ore formation.....	83
4.8.5.	Scenario of spinel alteration – magnetite formation.....	86
4.9.	Concluding remarks.....	87
5.	Comparison of the Sabzevar serpentinite-hosted magnetite ores with other occurrences worldwide.....	88
5.1.	Introduction.....	88
5.2.	Mode of occurrence and mineralogical features.....	89
5.2.1.	Nain.....	89
5.2.2.	Skyros Island.....	90
5.2.3.	Cogne.....	91
5.2.4.	Aniba.....	92
5.3.	Analytical methods.....	92
5.4.	Mineralogical and textural characteristics.....	93
5.5.	Trace element geochemistry of magnetite.....	95
5.6.	Discussion.....	97
5.6.1.	Style of deformation.....	97
5.6.2.	Factors controlling magnetite chemistry in serpentinite-hosted magnetite ores.....	98
5.7.	Conclusion.....	100
6.	Hydrothermal alteration of chromitite-dunite pairs from the Sabzevar ophiolite (NE Iran): Chemical and nano-textural evolution of chromite.....	102
6.1.	Introduction.....	102
6.2.	Geological outline and modes of occurrence.....	105
6.3.	Materials and methods.....	106
6.4.	Results.....	108
6.4.1.	Bulk-rock chemistry.....	108
6.4.2.	Mineral modes and temperature calculation.....	111
6.4.3.	Textural observation at the $\mu$ -scale.....	112
6.4.4.	Observations at the nano-scale.....	115

6.4.5. Mineral chemistry.....	117
6.4.5.1. Spinel.....	117
6.4.5.2. Serpentine and chlorite.....	120
6.4.6. Thermochemical modeling of the evolution of spinel composition: role of the silicate/chromite ratio.....	121
6.5. Discussion.....	122
6.5.1. Modelling the chromite chemical evolution during alteration.....	122
6.5.2. Chromite alteration, chromitite pods vs magnetite ores.....	130
6.5.3. Chromite alteration processes at the nano-scale.....	131
6.6. Conclusion.....	134
6.7. Supplementary Materials: Mass balance model of spinel composition evolution...	136
7. Native copper formation associated with serpentinization in the Cheshmeh-Bid ophiolite massif (Southern Iran).....	138
7.1. Introduction.....	138
7.2. Geological setting.....	139
7.3. Methods.....	139
7.3.1. Major and trace element analyses in minerals and whole-rocks.....	139
7.3.2. Copper isotope analysis.....	140
7.3.3. U-Pb LA-ICP-MS analysis of titanite.....	140
7.3.4. Raman Spectroscopy.....	141
7.3.5. Thermodynamic modelling.....	141
7.4. Results.....	142
7.4.1. Petrography of the host peridotites.....	143
7.4.2. Petrography and mineral chemistry of pyroxenite and reaction zones in contact with host peridotites.....	143
7.4.2.1. Orthopyroxenite.....	145
7.4.2.2. Zone I.....	148
7.4.2.3. Zone II.....	148
7.4.2.4. Zone III.....	148
7.4.3. Chemical changes across the reaction zone.....	151
7.4.4. Fluid inclusions in Zone II.....	151
7.4.5. U-Pb LA-ICP-MS dating of titanite.....	153
7.4.6. Copper isotope composition of native copper.....	154
7.4.7. Bulk-rock chemistry.....	156
7.4.8. Thermodynamic modelling of Ca-metasomatism.....	157
7.4.9. Stability of native copper.....	158
7.5. Discussion.....	160
7.5.1. Ca-metasomatism: the main driver for reaction zone formation.....	160
7.5.2. Reducing conditions during metasomatism.....	163
7.5.3. Model of native copper formation: Ca-metasomatism at the seafloor in a supra-subduction setting.....	165
7.5.3.1. Cu isotope constraints on the Cu provenance.....	165
7.5.3.2. Timing of copper formation.....	167
7.5.3.3. A model for copper formation.....	167
7.6. Concluding remarks.....	168

<b>Part IV Conclusions and Perspectives</b>	
8.1. Conclusions.....	171
8.2. Perspective.....	172
<b>Part V Supplementary Tables &amp; References</b>	
9.1. Supplementary Tables.....	176
9.2. References.....	260

# *Part I*

# Chapter 1. Introduction

---

Tectonic deformation leads to mantle rock exhumation near the surface. A complicated sequence of chemical reactions (i.e. serpentinization) can then occur leading to the hydration of ultramafic rocks at temperature below 500°C (e.g., Evans et al., 1976, Moody, 1976, Mével, 2003, O'Hanley, 1996). Serpentinization of ultramafic rocks significantly changes the rheological (e.g., Moore et al., 1997; Escartín et al., 1997; 2001), petrophysical (e.g., Christensen, 1972; Brown and Karson, 1988; Carlson and Miller, 1997; Dymant et al., 1997; Miller and Christensen, 1997) and chemical (e.g. Janecky and Seyfried, 1986) characteristics of the oceanic lithosphere. Furthermore, the microbial communities observed in serpentinized rocks may have profound implications for the origin of life on Earth and other planets (e.g. McCollom, 1999; Kelley et al. 2005; Martin et al. 2008; Russell et al. 2010).

## 1.1. Geological settings for serpentinization

Serpentinization is an ubiquitous process which have been discovered in a range of tectonic settings where the mantle peridotites are exposed to aqueous fluids. Serpentinization has been observed at divergent margins, mainly along slow to ultra-slow spreading mid-ocean ridges (Cannat et al., 1992; Cannat et al., 1993; Mével et al., 2003; Bach and Früh-Green, 2010), at convergent margins, along extensional faults and deep fractures formed in the bend of a subduction slab (e.g., Ranero et al., 2003; Ivandic et al., 2010), within the mantle wedge of subduction zones through the dehydration of subducting or underthrusting oceanic crust (Hyndman and Peacock, 2003; Scambelluri and Tonarini, 2012), or in ophiolites emplaced on the continent that are serpentinized during interaction with meteoric waters (e.g., Barnes et al., 1967; Barnes and O'Neil, 1969; Barnes et al., 1978; Miller et al., 2016), and greenstone belts (Kyser and Kerrich, 1991; O'Hanley et al., 1993). These different settings in which serpentinization occurs are described in the following.

### 1.1.1. Divergent margins: Mid-ocean ridges

There are two distinct hydrothermal circulation systems at mid-ocean ridges (Fig. 1.1; Schwarzenbach and Steele-MacInnis, 2020). (i) basalt-dominated systems which have been discovered along ridge segments with intermediate to fast-spreading rates, and are governed by subterranean magma lenses acting as the heat source (German and Seyfried, 2013). These

systems are marked by chimneys that vent hot fluids loaded mainly with Fe–S precipitates, forming black smokers. (ii) ultramafic-hosted systems which are frequently found on top of oceanic core complexes (e.g., Cannat, 1993; Kelley et al. 2001; Andreani et al., 2014). Magmatism is uncommon in these oceanic core complexes, with rare gabbroic intrusions or magmatic sills providing heat for high-temperature fluid circulation. A wide range of vent fluid types, from metal-rich, high-temperature fluids to alkaline and metal-poor, low-temperature fluids are generated through circulation of seawaters in ultramafic systems (Schwarzenbach and Steele-MacInnis, 2020). Based on fluid properties, three types of ultramafic-hosted hydrothermal sites can be distinguished at Mid Atlantic Ridge (Andreani et al., 2014): (i) intermediate-T hydrothermal sites with high-T (350–365°C) and low pH (<4) fluid flow venting from carbonate conduits, such as Rainbow (36°14' N), Logatchev (14°45' N) and Ashadze (12°58' N) systems (Charlou et al., 2010).; (ii) high-T hydrothermal sites with medium-T (up to 90°C) and high pH (>9) fluid flow venting from metal-rich sulfide chimneys, such as Lost City (30° N) (Kelley et al., 2001, 2005; Grimes et al., 2008) and (iii) low-T hydrothermal sites (<30°C) with unknown fluids venting through diffuse seepages, such as Saldanha (36°34' N) and Menez Hom (37°8' N) systems (Barriga et al., 1998).

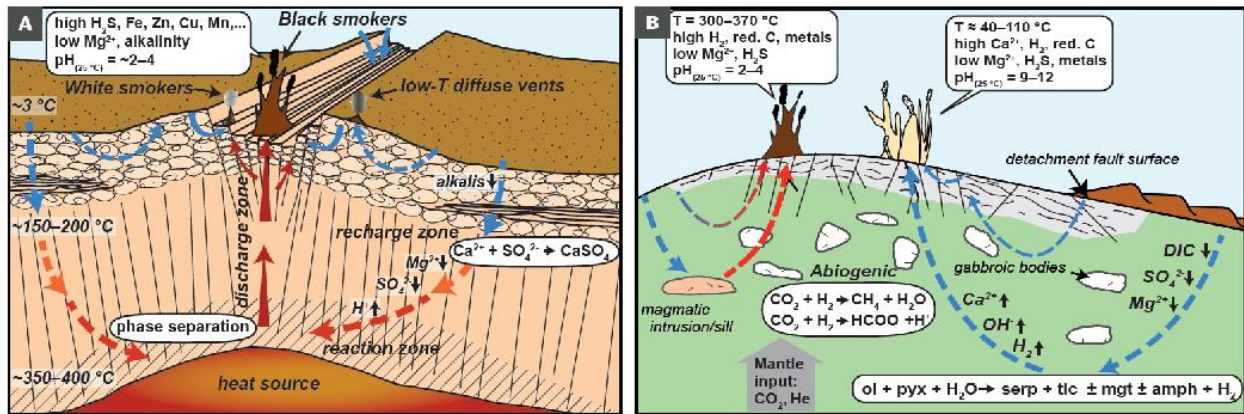


Fig. 1.1. (A) Schematic models of basalt-dominated hydrothermal systems and (B) ultramafic-hosted systems (Schwarzenbach et al., 2020). Abbreviations: red. C = reduced carbon; DIC = dissolved inorganic carbon; ol = olivine; pyx = pyroxene; serp = serpentine; tlc = talc; mgt = magnetite; amph = amphibole

At slow spreading mid-ocean ridges, mantle-derived rocks are tectonically exhumed at the seabed by large offset normal faults also called detachment faults (Karson, 1990; Cannat et al., 1997; Cann et al., 1997; Tucholke et al., 1998; Lavier et al., 1999; Escartín et al., 2003; Grimes et al., 2008; Sauter et al., 2013). These concave-downward detachment faults begin at steep

angles and gradually rotate to shallow dipping angles (de Martin et al., 2007; Escartín et al., 2003; Smith et al., 2006). The root depth of detachment faults is widely believed to be just above the brittle-ductile transition (Lavier et al., 2000; Olive et al., 2010). Axial detachment faults can act as conveyor belts for the exhumation of mantle-derived peridotites from the base of brittle lithosphere toward shallower depths where hydrothermal circulation and serpentinization occur (Fig. 1.2; Rouméjon and Cannat, 2014). During transition of mantle-derived peridotites from the ductile domain into the brittle domain, the combination of anisotropic thermal contraction and tectonic stresses results in widespread microfracturing (Rouméjon and Cannat, 2014). Fluid penetration along these microfractures trigger serpentinization and development of hierarchical microfractures at temperatures below 400°C (Rouméjon and Cannat, 2014). If the fluid supply is sufficient, the serpentine mesh texture can then be fully developed (Rouméjon and Cannat, 2014). At fast-spreading ridges, serpentinization can occur off-axis where the temperatures could be within the stability field of serpentine (Iyer, 2007).

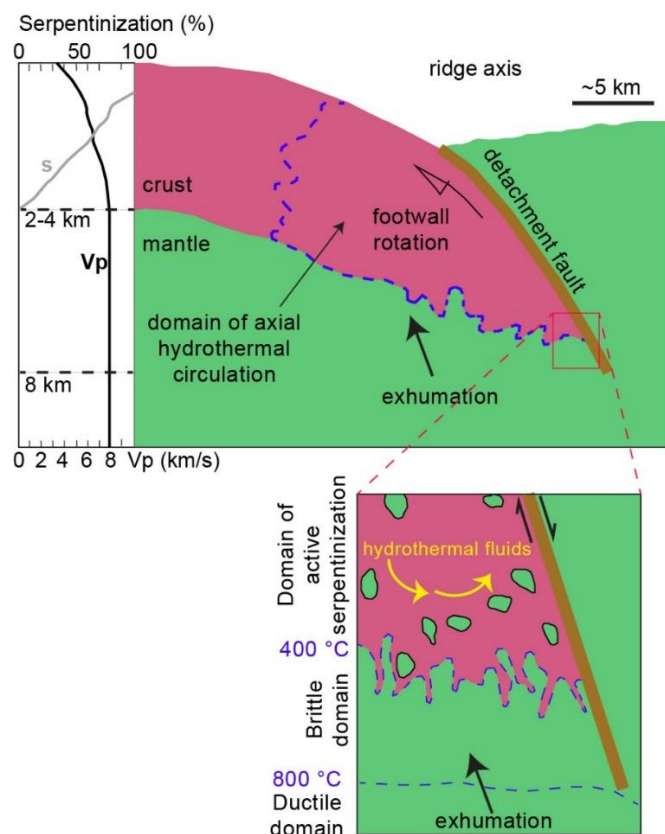


Fig. 1.2. Schematic cartoons of detachment faulting and serpentinization of mantle-derived peridotites at a slow spreading ridge (Cannat et al. 2010; Rouméjon and Cannat, 2014)

### 1.1.2. Convergent margins: Subduction zone

The portion of the mantle between the upper section of the subducting lithosphere and the lower half of the overriding plate is commonly referred to as the mantle wedge. Upward percolation of water released from the subducting slab may trigger the serpentinization of the mantle wedge at  $T < 700^{\circ}\text{C}$  (Bebout and Barton, 1989, Bostock et al., 2002, DeShon and Schwartz, 2004, Fryer et al., 1985, Gill, 1981, Guillot et al., 2000, Hattori and Guillot, 2003, Hyndman and Peacock, 2003, Kamiya and Kobayashi, 2000, Mottl et al., 2004, Peacock, 1987a, Peacock, 1987b, Peacock, 1993). Dehydration of the subducting slab has resulted in hydration of the overlying mantle wedge and protrusion of serpentinite diapirs at the seafloor. Such process can be seen in a huge zone of serpentinite seamounts along the trench axis in the Izu-Bonin and Mariana forearc. The seamounts are considered as mud volcanoes (<10 to 30 km wide) composed of serpentine fragments embedded in a serpentine mud (O'Hanley, 1996). Low-chlorinity fluids released from the slab vent from some of these seamounts (Mottl et al., 2003, Mottl et al., 2004). On the other hand, mantle wedge serpentinites are defined as a km-thick layer along the subduction plane and are found in the deepest and hottest portions of the supra-subduction mantle (Fig. 1.3; Deschamps et al., 2013; Guillot et al., 2009). The amount of serpentinization of the mantle wedge likely increases between 30 and 80 km depth as a result of fluid flux along warmer parts of the subducting slab (Hyndman and Peacock, 2003, Rüpke et al., 2004, Van Keken et al., 2011). The forearc region on nonaccretionary convergent margins such as the Puerto Rico, Tonga and Izu-Bonin/Mariana arc systems are well-known examples for serpentinization through fluids released by the subducting slab (Fryer, 2002). As a result of increased dehydration of the shallow slab, percentage serpentinization of the mantle wedge increases with increasing temperature of subduction (Reynard, 2013; Van Keken et al., 2011).

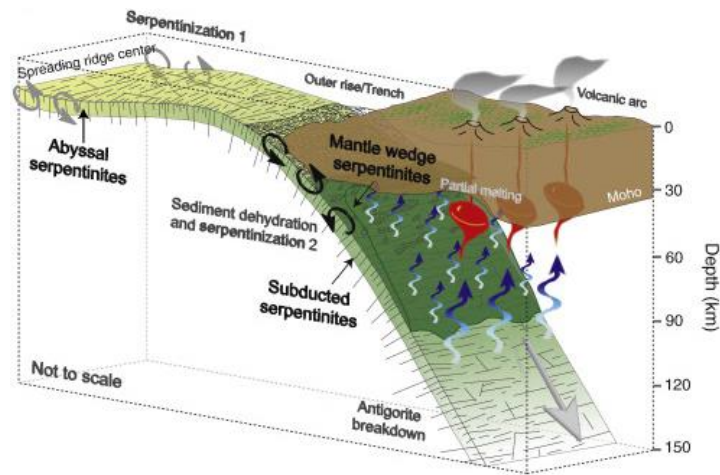


Fig. 1.3. Schematic sketch showing the geological setting during subduction-related serpentinization (Deschamps et al., 2013).

### 1.1.3. On-land serpentinization: ophiolites

Ophiolite complexes are oceanic lithosphere remnants generated at mid-oceanic ridges or in back arc conditions, then emplaced and exposed on land through a complex tectonic history. Ophiolite emplacement occurs (Wakabayashi and Dilek, 2004) (i) over passive continental margins or microcontinents as a result of collisional events (ii) over subduction complexes through accretionary processes; (iii) through spatial and temporal interaction between a spreading ridge and a subduction zone; (iv) with subaerial exposure due to a shift in plate boundary configuration along a mid-ocean ridge system. Recently, Porkoláb et al. (2021) suggested that buoyancy-driven extrusion of subducted crust is accountable for emplacement of far-travelled ophiolites. Mantle peridotites from ophiolites exhibit a wide variety of serpentinization degrees.

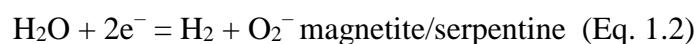
Serpentinization in ophiolites could have occurred in the paleo-oceanic setting, during thrust emplacement of the ophiolite over pelagic and continental margin sediments, during sub-aerial weathering and subsequent marine transgression (Früh-Green et al., 1990; Hanghj et al., 2010; Kelemen et al., 2011), and during ongoing water/rock reactions under subaerial conditions (Kelemen et al., 2011; Miller et al., 2016). Peridotites from the Oman ophiolite are locally undergoing low temperature serpentinization (<60 °C) (Barnes et al., 1978; Miller et al., 2016). The  $Mg^{2+}/HCO_3^-$ -rich fluids, and  $Ca^{2+}/OH^-$ -rich fluids are generated through infiltration and percolation of meteoric waters in the mantle rocks during ongoing water-rock reaction (Barnes et al., 1967, Barnes and O'Neil, 1969, Neal and Stanger, 1984, Neal and Stanger, 1985).

Modern day alteration of the ultramafic peridotite produces moderately alkaline (pH 8–9) (Barnes and O'Neill, 1969; Neal and Stanger, 1985) and hyperalkaline (pH 10–12) fluids rich

in H<sub>2</sub> and CH<sub>4</sub> (Barnes et al., 1978, Neal and Stanger, 1983, Neal and Stanger, 1985, Clark and Fontes, 1990, Kelemen and Matter, 2008, Kelemen et al., 2011). Therefore, presence of H<sub>2</sub> in the spring waters, active methane vents, presence of alkaline pH fluids and extensive carbonate deposits provide evidences for active serpentinization in ophiolites (e.g. Monnin et al., 2014; Sánchez-Murillo et al., 2014).

## 1.2. Serpentinization reactions in the oceanic lithosphere

During serpentinization, the oxidation of Fe<sup>2+</sup>, initially contained in olivine and pyroxene, oxidizes to form Fe<sup>3+</sup>. This oxidation reaction is coupled with water dissociation forming molecular hydrogen according to the two half reactions (Eqs. 1.1 and 1.2):



Ferric iron can be incorporated into magnetite, serpentine or brucite (e.g., Malvoisin et al., 2012; Andreani et al., 2013; Bach, 2016; Beard and Frost, 2016; Klein et al., 2009, 2014; Mayhew et al., 2013, 2018; McCollom and Bach, 2009; Marcaillou et al., 2011; Seyfried et al., 2007). However, the oxidation-reduction reaction is not complete since ferrous iron is still present in the serpentine and potentially in the brucite, which limits the production of hydrogen (Marcaillou et al., 2011; Malvoisin et al., 2012). Several parameters such as temperature, initial rock and fluid composition, water / rock ratio, oxygen fugacity and pH control the distribution of iron in the reaction products (Klein et al., 2009; Martin and Fyfe, 1970; Seyfried et al., 2007). Experiments and geochemical models have shown that magnetite is mainly formed above 200 °C (Seyfried et al., 2007 and Klein et al., 2009; Klein et al., 2014). Below 200 ° C, iron is mainly incorporated into serpentine and brucite. Without taking into account this incorporation of iron in serpentine and brucite, the serpentinization reaction for olivine (Fig. 1.4a) as the primary ingredient of peridotites (70 vol. percent), can be expressed as follows (Eq. 1.3).



For the pyroxene, the reaction does not produce brucite (Fig. 1.4b), and can release aqueous silica into the solution (Eq. 1.4):



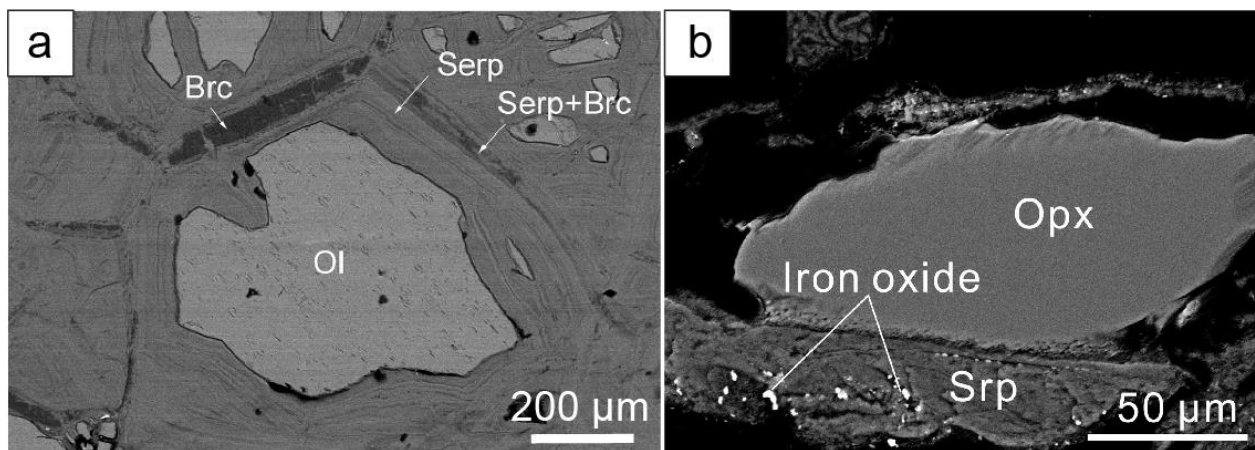


Fig. 1.4. Back-scattered electron image (BSE) of (a) Olivine replaced by serpentine and brucite (Wang et al., 2020); (b) Dehydration of orthopyroxene to serpentine and iron oxide (Huang et al., 2017).

Experimental studies revealed that pyroxene react faster than olivine at temperatures above 250°–300°C, while olivine reacts faster than pyroxene at temperatures below 250°–300°C (Martin and Fyfe, 1970; Janecky and Seyfried, 1986; Allen and Seyfried, 2003). Water supply, reaction-induced cracking, starting material composition, grain size distribution, temperature, intergranular diffusion and serpentine dissolution are factors controlling the rate of serpentinization (Martin and Fyfe, 1970; Wegner and Earnst, 1983; MacDonald and Fyfe, 1985. Malvoisin et al., 2012).

### 1.3. RedOx conditions associated with serpentinization

Low oxygen fugacity (Eckstrand, 1975), the lowest activities of dissolved silica ( $a_{\text{SiO}_2(\text{aq})}$ ) in terrestrial silicate (Frost and Beard, 2007) and a common high (e.g.  $13.1 \pm 0.1$  at 2.4 °C; Mottl, 2009) are notable characteristics of serpentinization. Low oxygen fugacity is associated with the ferrous iron contained in olivine and pyroxene leading to  $\text{H}_2$  generation during serpentinization.  $\text{H}_2$  generation during serpentinization varies as a function of protolith composition and temperature (Klein et al., 2013). Thermodynamic modelling indicates that  $\text{H}_2$  generation is at its peak around 200–315 °C and 350 bar pressure (McCollom and Bach, 2009). Compared to fluids interacting with orthopyroxene-rich lithologies, fluids interacting with olivine-rich lithologies are more reducing, have lower  $a_{\text{SiO}_2(\text{aq})}$ , and a higher pH at temperatures around 350 °C (Klein et al., 2013). It is crucial to note that hydrothermal alteration of basalt produces far less  $\text{H}_2$  than serpentinization of ultramafic rocks, despite the fact that

basalt has a significantly higher ferrous iron concentration (e.g. McCollom and Bach, 2009). Interaction between deep-sea hydrothermal fluids and ultramafic rocks (Fig. 1.5) generates  $H_2$  concentrations of 12–16 mmol kg<sup>-1</sup> (Charlou et al., 2002, Kelley et al., 2005).

At temperature < 400°C, serpentine-olivine-brucite-magnetite in metaserpentinites equilibrated with a oxygen fugacity 4 to 5 log units below the FMQ buffer (Frost, 1985).

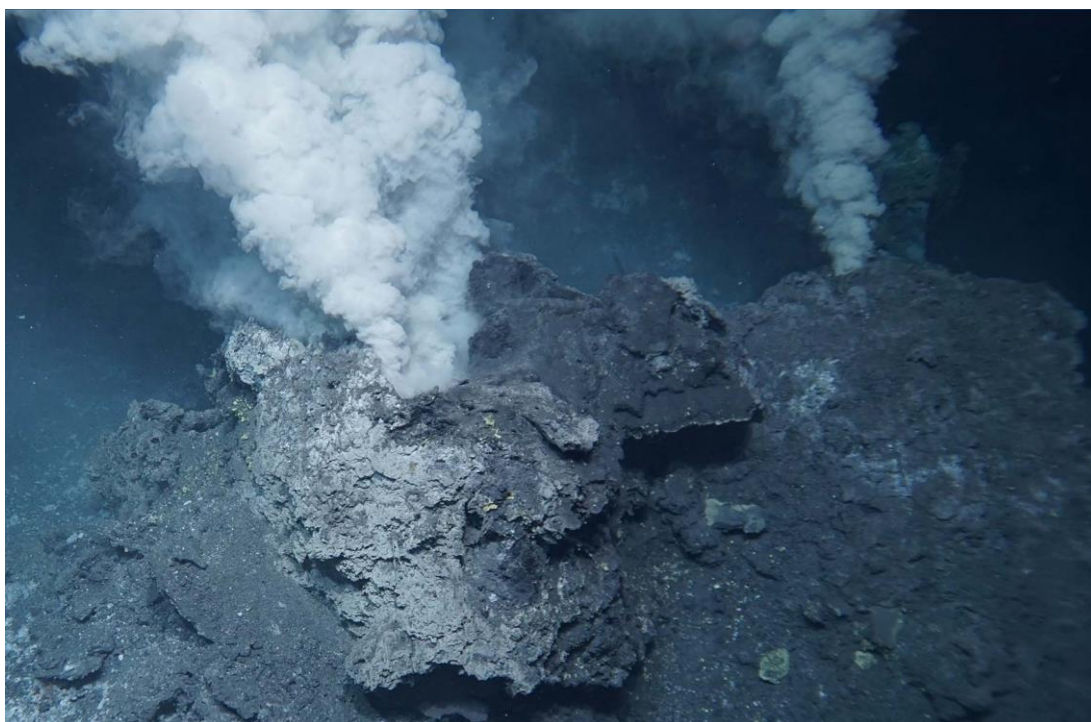


Fig. 1.5. A white smoker of the Kemp Caldera (from MARUM – Center for Marine Environmental Sciences, University of Bremen)

#### 1.4. Stability of native metals during serpentinization

In serpentinized peridotites, Fe, Cu and Ni commonly form fine-grained opaque minerals including oxides, sulphides and alloys. Study of these minerals can provide insight into oxygen and sulfur fugacities during serpentinization (e.g. Frost, 1985; Klein and Bach, 2009). Ore-forming elements in fresh peridotites are present primarily as divalent cations (e.g. Fe<sup>2+</sup>, Ni<sup>2+</sup>). Native metals form through reduction of these elements, which needs extremely reducing conditions. These highly conditions allow native metals, Fe–Ni alloys (e.g., awaruite, taenite), and other rare sulfides such as heazlewoodite or polydymite (Table 1.1) to be stable (Fig. 1.6, Frost 1985; Klein and Bach 2009).

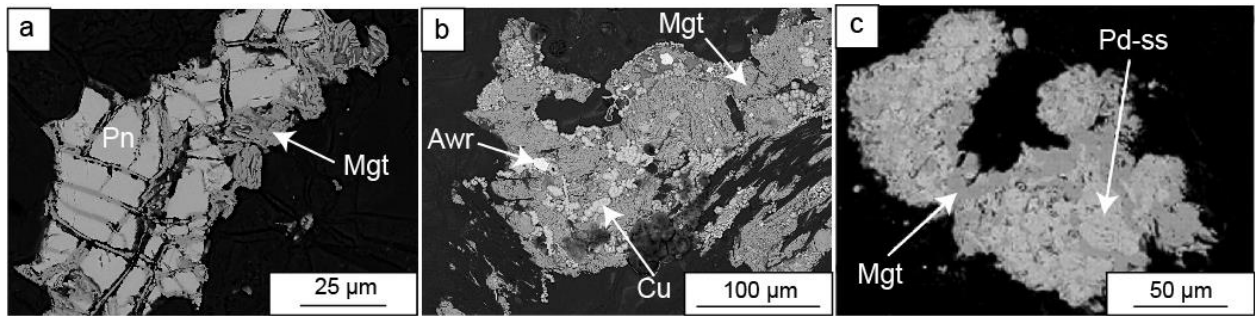


Fig. 1.6. Back-scattered electron (BSE) images: (a) Pentlandite rimmed by magnetite. (b) Association of native copper bubbles, awaruite and magnetite (Eslami et al., 2020) (c) Replacement of pentlandite by porous polydymites (Klein and Bach, 2009). Mineral abbreviations are, Pn: pentlandite, Mgt: magnetite, Awr: awaruite, Cu: native copper, Pd: polydymites.

The alteration system becomes fluid-dominated as the fluid/rock ratio increases, leading to more oxidizing conditions that generate opaque mineral assemblages associated with higher oxygen fugacity  $fO_2$  (e.g. Alt and Shanks, 1998; Schwarzenbach et al., 2012; Klein and Bach, 2009; de Obeso and Kelemen, 2020). Thermodynamic calculations suggested that co-occurrence of native metals and magnetite or some other  $Fe^{3+}$ -bearing phases in serpentinites is due to initial oxidation of  $Fe^{2+}$  which allows Fe reduction (McCullom and Bach, 2009).

Among ore-forming elements, native copper are rarely found in serpentinitized peridotites (Schwarzenbach et al., 2014). Formation of native copper and Cu–Fe sulfides in serpentinitized peridotite has been attributed to low S and  $O_2$  fugacities during serpentinitization (Eckstrand 1975; Frost 1985; Lorand 1987) or addition of Cu by a hydrothermal fluid in the basement of a peridotite-hosted hydrothermal field (Schwarzenbach et al., 2014). Abrajano and Pasteris (1989) report a primary magmatic assemblage comprising pyrrhotite, pentlandite, chalcopyrite, and magnetite, as well as a secondary assemblage of chalcocite, cubanite, digenite, bornite, and idaite and native copper in the Zambales ophiolite (Philippines) (Table 1.1).

Table 1.1. Mineral formulas

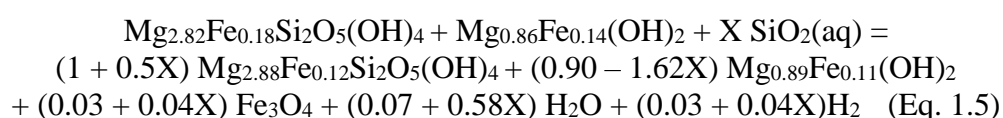
<b>Mineral name</b>	<b>Formula</b>
Awaruite	Ni <sub>2</sub> Fe to Ni <sub>3</sub> Fe
Bornite	Cu <sub>5</sub> FeS <sub>4</sub>
Chalcocite	Cu <sub>2</sub> S
Chalcopyrite	CuFeS <sub>2</sub>
Cubanite	CuFe <sub>2</sub> S <sub>3</sub>
Digenite	Cu <sub>9</sub> S <sub>5</sub>
Heazlewoodite	Ni <sub>3</sub> S <sub>2</sub>
Idaite	Cu <sub>5</sub> FeS <sub>6</sub>
Magnetite	Fe <sub>3</sub> O <sub>4</sub>
Pentlandite	(Fe,Ni) <sub>9</sub> S <sub>8</sub>
Pyrrhotite	FeS
Taenite	γ Fe–Ni alloy

They believe the secondary assemblage formed as a result of re-equilibration and modification of primary Cu-bearing sulfides at highly-reducing conditions during serpentinization. Lorand (1987) suggest that native copper in Iherzolites and harzburgites from the Bay of Islands Ophiolite (Newfoundland) formed through low temperature interaction of primary sulfides with highly reducing fluids during serpentinization. Schwarzenbach et al. (2014) proposed two hypotheses for the formation of Cu-bearing sulfides and native copper in partially serpentinized peridotites from Costa Rica: (i) desulfurization of primary sulfides during serpentinization due to highly reduced conditions, or (ii) interaction with a Cu-bearing, higher temperature fluid (350–400 °C) postdating serpentinization. Schwarzenbach et al. (2021) reported secondary sulfide assemblages including millerite, heazlewoodite, as well as Cu-bearing sulfides, native Cu, and awaruite in variably serpentinized peridotites from the methane-rich Chimaera hydrothermal field in Turkey. They suggested that the sulfide minerals with a mantle and mid-ocean ridge origin have been further altered by the first stage of partial serpentinization in which awaruite were formed. Subsequently, ongoing interaction of CH<sub>4</sub>- and H<sub>2</sub>-rich but highly sulfur-undersaturated fluids with serpentinized peridotite resulted in decomposition of sulfide decomposition and development of porosity. Discovery of native copper in the Ca-metasomatically altered pyroxenites from the Cheshmeh-Bid ophiolitic massif

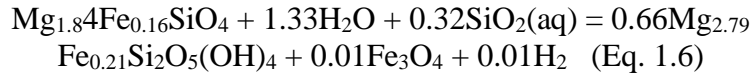
in the Khajeh-Jamali area, Southern Iran is of particular interest in understanding both the redox and the sulfur conditions during serpentinization.

## 1.5. Formation of magnetite upon serpentinization

Magnetite is found in most serpentinites. As previously stated, the ferric iron produced during serpentinization reaction is incorporated into the magnetite. However, natural serpentine can also incorporate significant amounts of ferric iron (Blaauw et al., 1979; O'Hanley and Dyar, 1993; Fuchs et al., 1998; Gonzalez-Mancera et al., 2003; Klein et al., 2009; Evans et al., 2012). Studies on serpentinites from the Mid-Atlantic Ridge 15°N suggest that magnetite is absent at the early stage of serpentinization when serpentine and Fe-rich brucite form through quasi-isochemical alteration of olivine, whereas it is produced at the late stage of serpentinization under open-system conditions through the breakdown of Fe-rich brucite (Bach et al., 2006). Very limited formation of iron oxide during early stage of peridotite serpentinization has been corroborated by several authors (e.g., Toft et al., 1990, Oufi et al., 2002, Bach et al., 2006, Marcaillou et al., 2011, Ogasawara et al., 2013; Huang et al., 2017). Frost et al. (2013) suggested that formation of magnetite is due to the extraction of iron from the early-formed serpentine and brucite. It is argued that silica has a strong influence on the generation of iron oxide during serpentinization because it modifies the composition and stability of Fe-bearing minerals (e.g., Bach et al., 2006, Frost and Beard, 2007, Klein et al., 2009). Frost and Beard (2007) believe that generation of magnetite is triggered by SiO<sub>2</sub> activity decrease or extraction of SiO<sub>2</sub> from iron-bearing serpentine or brucite. Miyoshi et al. (2014) argued that magnetite formation facilitated by addition of silica upon progress of serpentinization in natural harzburgite rocks. They believed that serpentinization of harzburgite from the Iwanaidake ultramafic body in Japan involves a two-staged episodes resulting in consecutive changes in textures, mineral chemistry, and magnetic susceptibility. During the first stage, a mesh-textured serpentine + brucite assemblage were formed by isochemical serpentinization of olivine (Eq. 1.5; Figs. 1.7a and 1.7b). Subsequently, a serpentine vein, brucite-magnetite veins at the center of the serpentine vein, and mesh-center serpentine and magnetite were formed during the second stage as follow (Eq. 1.6):



Serpentine + Brucite + Silica = Serpentine + Brucite + Magnetite + Water + Hydrogen.



Olivine + Water + Silica = Serpentine + Magnetite + Hydrogen.

The addition of aqueous silica produced by serpentinization of orthopyroxene aided these processes.

Katayama et al. (2010) suggested that magnetite is formed through a silica-depletion reaction during evolution of serpentinites from the Mineoka ophiolite, Japan. They argued that low abundance of serpentine in the magnetite-bearing veins and paucity of magnetite in pseudomorphs of orthopyroxene are evidence of low silica activity for hydrogen generation during serpentinization. However, Miyoshi et al. (2014) believed that these textural features (Fig. 1.7c) bears resemblance to their samples which dictates magnetites can also be considered to have generated through silica-addition reaction.

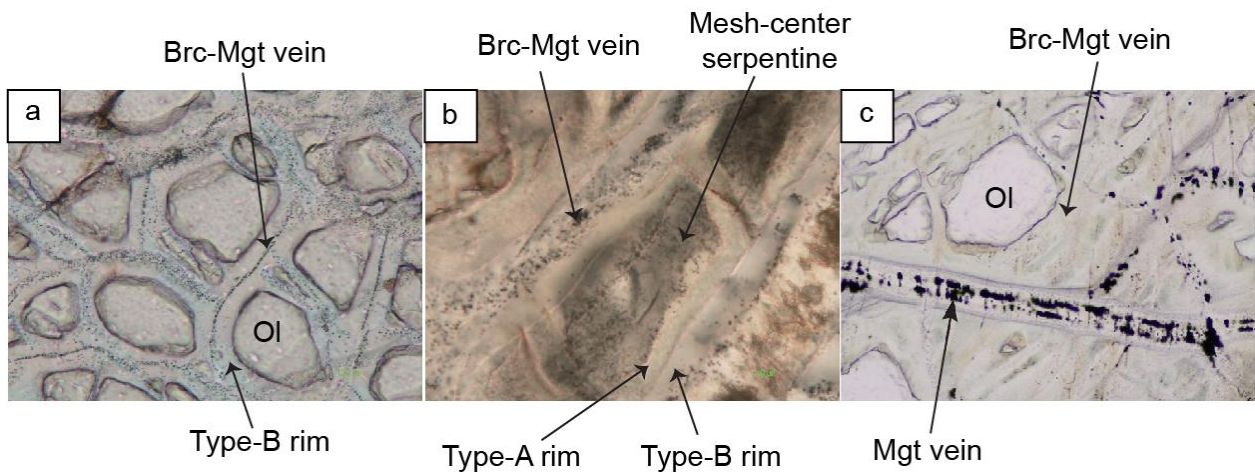


Fig. 1.7. Plane-polarized light (PPL) images of serpentinized peridotites. (a) mesh-textured serpentine with type-B rims. Brucite-magnetite veins are surrounded by type-B rims (Miyoshi et al., 2014). (b) Mesh-center serpentine surrounded by both type-A and type-B rims (Miyoshi et al., 2014). (c) Magnetite in the middle cut the mesh texture replacing olivine (Katayama et al., 2010). Mineral abbreviations are, Ol: olivine, Brc: brucite, Mgt: magnetite, Serp: serpentine.

Experimental investigation on natural ground orthopyroxene, olivine (with <5% pyroxene) and peridotite revealed that fluxes of aluminum and silica can have a significant impact on the generation of iron oxide during peridotite serpentinization (Huang et al., 2017). Aluminum may have a strong influence on the generation of iron oxide during the early stages of serpentinization, whereas silica has profound impact in late stage of serpentinization.

Experimental studies of peridotite serpentinization revealed that magnetite is not generated at 200 °C and 500 bar (Seyfried et al., 2007). Klein et al. (2014) suggested that there is a straightforward relationship between magnetite quantity, brucite Fe concentration, and serpentinization temperature. Their study revealed that magnetite-rich samples have Fe-poor brucite and were formed at temperatures of 200–300 °C, whereas magnetite-poor samples have Fe-rich brucite and were formed at temperatures of 200 °C.

As stated above, direct reaction of water with olivine and/or breakdown of early-formed Fe-bearing serpentine and brucite are main mechanism accountable for the formation of disseminated or semi-massive magnetites in serpentinites (e.g. Bach et al., 2006; Evans, 2008; Klein et al., 2014). Hydrothermal mobilization of iron through serpentinization may result in magnetite formation with mineable sizes. Magnetite as ore deposit have frequently been reported from the serpeninite in ophiolites (e.g., Gahlan et al., 2006; Toffolo et al., 2017; Eslami et al., 2018; Khedr et al., 2018; Kapsiotis et al., 2021), but their origin remains unclear. Several hypotheses have been put forward to explain their enigmatic genesis. Intriguingly, these magnetite deposits bear resemblance to the chromitite pods which are accumulation of Cr-spinel as podiform bodies usually enveloped by dunite in harzburgitic mantle section of ophiolites (e.g. Augé, 1987; Ceuleneer and Nicolas, 1985; Borisova et al., 2012; Gauthier et al., 1990; González-Jiménez et al., 2014; Lorand and Ceuleneer, 1989).

Their quite similar mode of occurrence and style of deformation open the possibility of **chromitite conversion to magnetite ores via multiple stages of metamorphism** (e.g., Rossetti et al., 2009). With regard to the magnetites from Northern Greece and Skyros Island, Paraskevopoulos and Economou (1980) suggested a gradual metasomatism of a pre-existing podiform chromitite during the tectonic events of the Alpine orogeny. The occasional discovery of Cr-spinel relicts dispersed within these magnetite bodies favors this scenario. According to Gervilla et al. (2012) precipitation of magnetite on the outermost boundaries of annealed and compositionally modified Cr-spinel crystals should give rise to the development of thick magnetite layers around them. However, the Cr-spinel “relicts” within some serpentinited-hosted magnetite ores do not commonly appear altered in petrographic examination, they do not display any typical dissolution textures and their relatively high Mg# suggests a lack in post-magmatic modification (Eslami et al., 2018). Kapsiotis et al. (2021) suggested that the Cr-spinel relicts from the Eretria magnetite in East Othris ophiolite (Greece) survived complete dissolution in the presence of magnetite-saturated fluids. In contrast, chromite relicts in Bou-Azzer magnetites revealed addition of magnetite component in Cr-spinel upon alteration (Gahlan et al., 2006). In some cases (e.g. Aniba, Oman), Cr-spinel relicts acted as a nucleus

for magnetite precipitation during low-T serpentinization (< 400 °C) (Khedr and Arai, 2018). These findings preclude the possibility that the magnetite bodies from the Nain, Bou-Azzer and Aniba originate from strongly metamorphosed (/metasomatized) chromitite proto-ores. Further evidence for this comes from the observation that a number of Cr-spinel relics host olivine inclusions. The composition of these inclusions in the Nain magnetites approximates that of olivine from mantle peridotites (Fo $\approx$  92 and NiO:  $\leq$  0.4 wt%; 1986; Arai, 1994) rather than that of olivine inclusions in Cr-spinel from chromitites (Fo up to 96-97; Arai, 1980). It is crucial to note that sometimes these magnetites (e.g. Nain, Cogne, Bou-Azzer and East Othrys) are hosted in intensely sheared and pervasively serpentinized peridotites. In such zones, the fluid/rock ratio increased significantly to permit a decrease of the fluid *P* that dropped the solubility of Fe and triggered magnetite precipitation (e.g., Hodel et al., 2017; Eslami et al., 2018). In the case of Nain, magnetite pods exposed along a semi-brittle shear zone between pervasively serpentinized harzburgites, upper one with higher-Cr# [=Cr/(Cr+Al), 0.6–0.7] spinel and lower one with lower Cr# (0.5) confirming the role of shear zones as permeability path enabling the localized passage of Fe-rich fluids. Co-precipitation of lizardite/chrysotile and rarely antigorite with magnetite indicates **100–300 °C serpentinization at high water-rock ratio** played a vital role for the formation of the Bou-Azzer magnetite ore deposit. **Multi-episodic serpentinization (~300–400 °C) at high water-rock ratio** during an advanced stage of ophiolite obduction was responsible for the genesis of Nain magnetites (Eslami et al. 2018).

Occurrence of magnetite ores in highly serpentinized peridotites does not necessarily reveal the role of serpentinization for their formation. Toffolo et al. (2017) used thermodynamic modelling of fluid-rock interactions and suggested that fluids produced by seawater–peridotite or seawater–Fe-gabbro are not sufficiently Fe-rich to account for the formation of the Cogne deposit. They believed that fractionation processes such as phase separation were efficient to form hydrothermal fluids capable to precipitate large amounts of magnetite in Cogne peridotites. However, there is sparsity of thermodynamic modelling data for other magnetite deposits. Toffolo et al. (2017) suggested that Cogne magnetites **precipitated from a high-temperature (~300–400 °C) fluid in a seafloor hydrothermal system**. Kapsiotis et al. (2021) suggested that Eretria serpentinite-hosted magnetite ores in East Othris ophiolite have been formed through mixing of Fe-rich hydrothermal fluids at temperatures ranging from ~460 °C to ~150–100 °C, in an old peridotite-hosted hydrothermal system.

## Chapter 2. Motivation, Research Goals & Dissertation Structure

---

### 2.1. Motivation

Sustained economic growth and stable standards of living in communities are closely tied to their metal and mineral resources. Therefore, detailed study of these resources in various geological settings is of paramount importance. Iran as main part of the Tethyan metallogenic belt is rich in natural resources, including numerous and diverse mineral deposits of iron, copper, chromium, gold, zinc, lead as well as industrial minerals, oil, and gas.

Iron mainly as magnetite has been found in various types of mineral deposits such as iron oxide-copper-gold (IOCG) and Kiruna type apatite–magnetite, Fe-Ti, porphyry and skarn deposits. This oxide mineral also form as a minor or trace phase in several deposit types, Ni-Cu-PGE magmatic massive sulfides, Cu-Zn-Pb VMS, Opemiska-type Cu veins and clastic-dominated Pb-Zn deposits (Leach et al., 2010). Rare occurrence of magnetite in forms of veins and/or lens can be found within serpentinized ultramafic rocks of ophiolites.

Copper is widely found in nature as sulfide and oxide minerals. Native copper, also known as zero-valance state copper, is a less common copper mineral that can be found in a variety of geological settings including mafic lavas, ultramafic intrusives, hypabyssal diabasic intrusives, clastic sedimentary rocks, and the oxidized zone of sulfide deposits (Cornwall, 1956). Occurrence of native copper has been previously reported in ophiolites which is attributed to very local reduction processes of pre-existing sulfide assemblages upon serpentinization in mafic or ultramafic rocks (e.g., Lorand, 1987).

During the last decade, processes of formation of serpentinite-hosted metal deposits with mineable sizes has attracted attention as curiosities. The motivation behind this PhD project is to make significant advances in the understanding of behavior of Fe, Cu and Cr during highly reducing process associated with serpentinization in peridotites from Tethyan ophiolites in Iran and highlight these new types of iron and copper ore deposits.

### 2.2. Research aims

The main objective of this Ph.D. dissertation is to improve our understanding of RedOx evolution and mass transfer during serpentinization. Serpentinite-hosted magnetite and copper ores are two examples of mass transfer and ore formation in relation with hydrothermal

alteration. The firstly reported Cu-rich hydrothermally altered pyroxenites in the Cheshmeh-Bid ophiolitic massif (Southern Iran) and serpentinite-hosted podiform magnetite ores in the Sabzevar ophiolite (NE Iran) are peculiar and unique examples of redox-controlled mineralization upon hydrothermal alteration of ultramafic rocks. These outcrops provide the unique opportunity to better constrain Fe, Cr and Cu mobility during the hydrothermal evolution of peridotite-hosted hydrothermal systems.

To contribute to this main research goal, the present PhD thesis aims at:

- i. Presenting a detailed mineralogical description of the new magnetite ore occurrence in the Sabzevar ophiolite with a particular emphasis on the micro- and nano-textural relationship between chromite and magnetite in both magnetite ore and host serpentinite.
- ii. Constraining the phase relationships in the host serpentinite of magnetite ores and thermodynamic modelling of fluid compositions
- iii. Figuring out the nature of the processes that promoted magnetite formation in the Sabzevar ophiolite which involves significant iron mass transfer from the serpentinite to the magnetite ore.
- iv. Understanding chemical factors controlling Fe and Cr mobility up to the kilometer scale
- v. Evaluating the source, timing and speciation of the copper assemblages upon serpentinitization in the Cheshmeh-Bid ophiolitic massif

To address the first three aims (i, ii and iii), I have carried out a detailed field, petrographic, mineral chemistry, thermodynamic and petrological study of a discontinuous trails of podiform magnetite ores and their host serpentinite from the central sector of the Sabzevar ophiolite. This part was the subject of an article in the *Journal of Contributions to Mineralogy and Petrology* published in 2021.

“Eslami, A., Malvoisin, B., Brunet, F., Kananian, A., Bach, W., Grieco, G., Cavallo, A., Gatta, D.G., 2021. Podiform magnetite ore(s) in the Sabzevar ophiolite (NE Iran): Oceanic hydrothermal alteration of a chromite deposit. *Contribution to Mineralogy and Petrology* 176, 43.”

To tackle the fourth aim (iv), I have investigated several chromitite ore deposits in the Kuh-Siah and Olangsir ultramafic massifs of the central sector of Sabzevar ophiolite belt. I studied their microtexture, and whole rock and mineral chemistry to track spinel alteration and formation of magnetite. Particular attention was paid to iron mass transfer between chromitite and host dunite. This study complements our current knowledge of Fe and Cr mobility during hydrothermal alteration. This part was the subject of an article submitted to *Lithos* in 2022.

“Eslami, A., Malvoisin, B., Brunet, F., 2022. Hydrothermal alteration of chromitite-dunite pairs from the Sabzevar ophiolite (NE Iran): Chemical and nano-textural evolution of chromite”

To accomplish the fifth aim (v), I conducted a detailed mineralogical, chronological and thermodynamic study on native copper-bearing pyroxenites from the Cheshmeh-Bid ophiolitic massif. I used a thermodynamic model for the origin of native copper and associated Ca-metasomatism. I also used copper isotopes to constrain the source of copper upon serpentinization. This part was the subject of an article in the *Lithos* published in 2021.

“Eslami, A., Malvoisin, B., Grieco, G., Aradi, L.E., Marchesi, C., Cavallo, A., Montanini, A., Borghini, G., Mathur, R., Ikehata, K., Davis, D.W., Li, C-H., Szabó, C., 2021. Native copper formation associated with serpentinization in the Cheshmeh-Bid ophiolite massif (Southern Iran). *Lithos* 382-383, 105953.”

## 2.3. Dissertation Structure

The dissertation is divided into five sections. **Part I** spells out the subject of study and makes the research hypotheses explicit. This part includes an introduction to the subject's background and state-of-knowledge (*Chapter 1*), the research goals, and an overview of the thesis structure (*Chapter 2*).

**Part II** presents an overview of the regional geology and geodynamic of Iran (*Chapter 3*). **Part III** depicts the main findings and outcomes of my thesis.

In *Chapter 4*, systematic field observations together with petrographic studies, microanalysis and thermodynamic modelling were used to figure out the nature of the processes that promoted magnetite formation in the peridotites of the Sabzevar ophiolite (NE Iran) during serpentinization.

*Chapter 5* highlights similarities and differences between the Sabzevar serpentinite-hosted magnetite ores and available case studies from the literature. The comparison is based on LA-ICPMS data from the Oman, Nain (Central Iran) and Cogne (Italian Alps) serpentinite-

hosted magnetite deposits and microtexture and composition variation maps from the Skyros (Greece) magnetite ores.

**Chapter 6** is a draft of a manuscript that addresses the second aim of this thesis, investigating the spinel alteration and formation of magnetite at a larger scale in several chromitite deposits in the central sector of the Sabzevar ophiolite belt, using thermodynamic modelling and mass-balance calculation.

In **Chapter 7**, field and petrographic observations combined with new geochronological and geochemical data were used to develop a conceptual model of native copper genesis within metasomatised pyroxenite dykes in the Neyriz ophiolite (Southern Iran).

**Part IV** presents the key outcomes of the three studies and outlines a more precise set of research questions (**Chapter 8**), followed by a supplementary tables and list of the references used throughout the thesis (**Part V**)

In addition to the publications mentioned above, the findings of this thesis have been presented at a number of international conferences and meetings, including 3<sup>rd</sup> European Mantle Workshop (Pavia, Italy, 2018), 2<sup>nd</sup> TRIGGER International Conference (Tehran, Iran, 2018), 5<sup>th</sup> IGCP-649 Diamonds and Recycled Mantle Workshop (Muscat, Oman, 2019), International Conference on Ophiolites and the Oceanic Lithosphere (Muscat, Oman, 2020), Goldschmidt2021 (Lyon, France, 2021), 3<sup>rd</sup> European Mineralogical Conference (Cracow, Poland, 2021), ISTERRE Mineralogy team seminar (Grenoble, France, 2021), a PhD Congress of ISTERRE (Chambéry, France, 2021) and Goldschmidt2022 (Hawai'i, USA, 2022).

## *Part II*

## Chapter 3. Regional Geological Framework

---

### 3.1. Introduction

Iran is a beacon of civilization which dates back to 7,000 BC. Geographically, Iran is surrounded on three sides by the Caspian Sea to the north, the Persian Gulf to the south, and the Gulf of Oman to the south (Fig. 3.1). It is also framed by two massive mountain ranges, the Zagros Mountains, a series of collateral craggy ridges in southwestern margin and the rugged Alborz chains in the northern margin. Alborz Mountains is stretched from west to east along the southern coast of the Caspian Sea. The Alborz Mountain Range separates the northern woodland environment from the southern dry plains of the country. The Alborz Mountains include the highest summits including Mount Damavand with elevation of 5670 meters above sea level. The Zagros Mountains stretches from the border territories of eastern Turkey and northern Iraq to the Strait of Hormuz. A large number of Zagros summits are higher than 3 km above sea level. Mount Dena, at 4409 meters, is the highest summit in the central portion of the Zagros chain.

Iranian Plateau covers an area of approximately 3,700,000 km<sup>2</sup>, and is made up of continental fragments accreted to the margin of Eurasia by the Late Cretaceous or early Tertiary (e.g., Sengör, 1990). These continental fragments, known as terranes, were separated by now-vanished Tethys Oceans (Prototethys, Palaeotethys, Neotethys) for most of the Phanerozoic, and their relicts - ophiolites and accretionary prisms - can be found all throughout the Iranian Plateau. Iran Plateau has a prominent position in the world, in terms of mineral resources and mineral production (copper, lead, zinc, iron, gold and chromite).

The geology of the Iran has been investigated for at least 70 years and a significant volume of published literature deals with its evolution. The geodynamic evolution of Iran during Phanerozoic time is the history of formation and destruction of a convergent plate margin. Despite the rising amount of geological data that has become available in the last two decades, geology of Iran is still exceedingly complex, and its fundamental features are still poorly understood. This chapter reviews the geological history of the Iran Plateau, with particular emphasis on the history of geotectonic domains preserved in this region. The geology of the Sabzevar and Neyriz ophiolite and its regional tectonic setting are reviewed.

### 3.2. Geotectonic realms of Iran

Earth's continental crust can be categorized into six tectonic provinces comprising shield, orogeny, platform, basin, big igneous province, and extended crust. Iran's crust is classified as orogeny by the US Geological Survey (USGS), which defines it as a "alinear or arcuate region that has been exposed to folding and other deformation during an orogenic cycle" (Neuendorf et al., 2011, p. 457). According to Bird (2003), Iran is also classified as an orogeny which is characterized as a complex region containing areas of dispersed deformation and uplift. A summary of the main geotectonic domains of Iran (Fig. 3.1) discussed in the following sections:

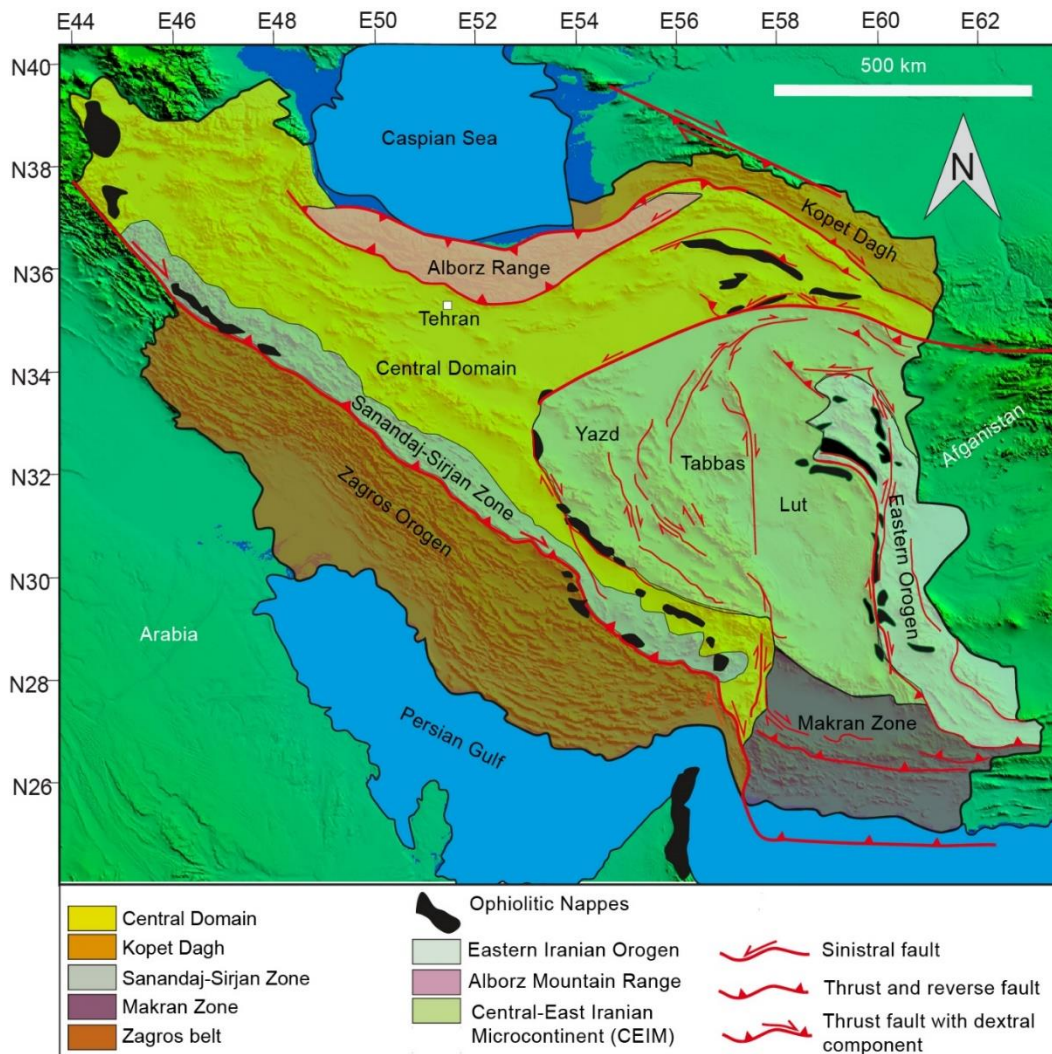


Fig. 3.1. Simplified tectonic map of Iran on the shaded-relief Shuttle Radar Topography Mission (SRTM) image, showing the main tectonic domains and the major strike-slip fault

systems (after Allen et al., 2004, 2011; Berberian, 1983; Berberian and King, 1981; Calzolari, et al., 2016; Morley et al., 2009; Nozaem et al., 2013; Stöcklin and Nabavi, 1973)

### 3.2.1. Zagros Fold–Thrust Belt

The Zagros Fold-and-Thrust Belt extends approximately 2,000 kilometers from southeastern Turkey to western and southern Iran. The Zagros Fold and Thrust belt reflects progressive shortening and off-scraping of Arabian plate sediments during protracted convergence history between Arabia and Eurasia (Farhoudi and Karig, 1977). Zagros orogen is shortening at a rate of 1 cm/yr (Regard et al., 2005). Mesopotamian Foredeep act as an oceanic trench filled with sediments as old as Neoproterozoic (Stern et al., 2021). The thickness of sediments ranges from 4500 meters on the Arabian plate to 1800 meters beside the Main Zagros Thrust (Edgell, 1996). Based on topography and structural data, this belt can be classified into two distinct zones extending from SW to NE (Fig. 3.2): (a) The Simply Folded Belt is situated in the neighbourhood of Persian Gulf with very uniform wavelength folds (Falcon, 1974; Sepehr and Cosgrove, 2004; Mouthereau et al., 2006). Simply Folded Belt is regarded as an active accretionary wedge with NW–SE oriented folds of the 13 km thick EO-Cambrian to Quaternary sedimentary cap (Blanc et al., 2003, Hessami et al., 2001, McQuarrie, 2004). (b) The High Zagros region (or Crush Zone) has greater height, a rapid rise in elevation, and kilometer-scale throws on main thrusts (Agard et al., 2011). The High Zagros is marked by imbricate tectonic slivers including Mesozoic limestones, radiolarites, obducted ophiolites and Eocene volcanic and flysch that thrust on the Zagros Folded belt (Agard et al., 2005). Main Zagros Thrust (MZT) dividing the aforementioned domains from the so-called internal zones (Braud and Ricou 1971) which might be considered to be part of the Zagros orogeny. Internal zones include Sanandaj-Sirjan Zone, Urumieh-Dokhtar mamatic belt and western parts of Central Iran.

Long-standing controversy remains over the timing of ultimate collision between the Afro-Arabian plate and Eurasia. These age estimates range from the Paleocene (Alavi, 1980), through the Eocene (Ghasemi and Talbot, 2006; Hafkenscheid et al., 2006; Allen and Armstrong, 2008; Horton et al., 2008; Allen, 2009; Dargahi et al., 2010; Mouthereau et al., 2012), Oligocene (Kargaranbafghi et al., 2012; Mohajjel and Fergusson, 2014), to the Miocene (Förster, 1978; Hassanzadeh, 1993; Allen et al., 2004; Ali et al., 2013) revealing the diachronous, multi-episode, and protracted nature of the collision (Richards and Sholeh 2016).

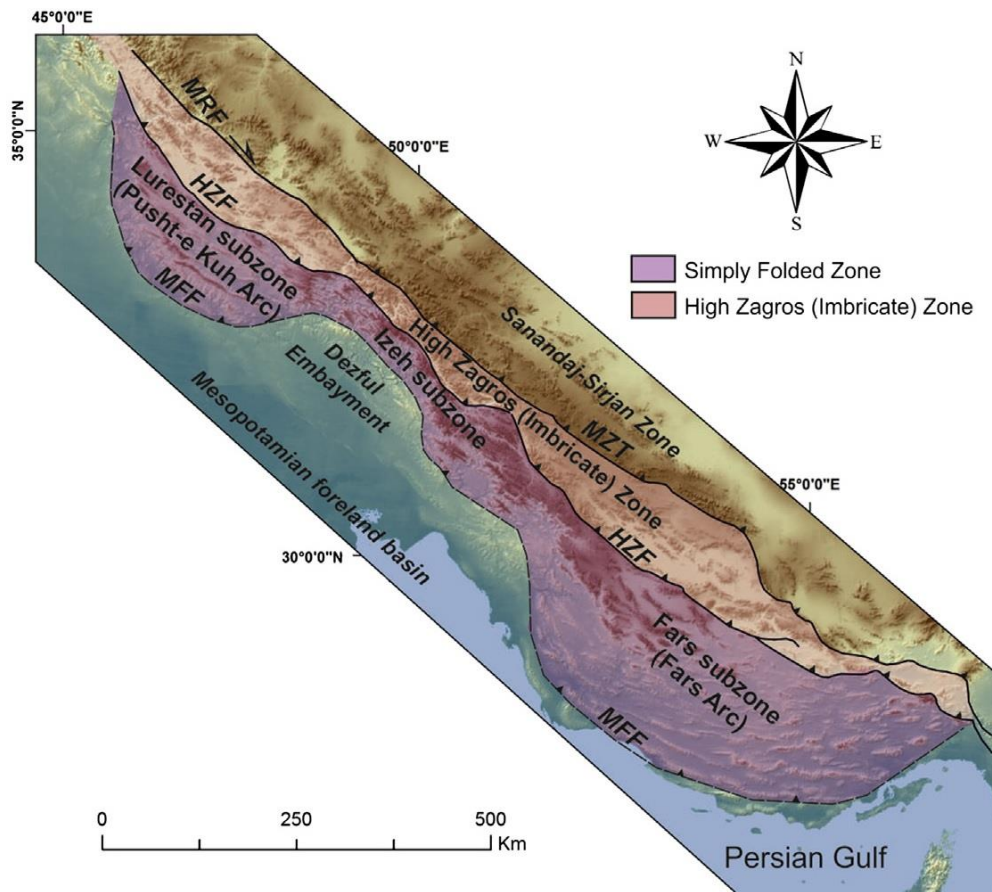


Fig. 3.2. Physiographic illustration of the Zagros Orogen (Gürbüz and Farzipour Saein, 2019). High Zagros fault; MFF, Mountain Front fault; MRF, Main Recent fault; MZT, Main Zagros thrust.

### 3.2.2. Sanandaj-Sirjan Zone

The Sanandaj-Sirjan zone stretches for roughly 1500 kilometers along strike from Sanandaj in the northwest to Sirjan in the southwest, with an average width of 150–200 kilometers (Mohajjel and Fergusson, 2000). Two schemes for classifying Sanandaj-Sirjan Zone have been proposed. Eftekharijad (1981) subdivided this zone into two subzones: (i) The southern subzone is dominantly marked by Middle to Late Triassic metamorphic suits; (ii) The northern subzone consists mainly of Late Cretaceous intrusive felsic rocks (such as the Alvand, Borojerd, Arak and Malayer plutons) as well as greenschist facies metamorphic assemblages. From north to south, this zone can also be split into three sectors (Fig. 3.3; Azizi and Stern, 2019): (i) The northern sector is made up of Cadomian (500–600 Ma) igneous and metamorphic rocks, Late Palaeozoic granite (Azizi et al., 2017), as well as basic to intermediate Cretaceous volcanic rocks with a calc-alkaline to alkaline affinity (Azizi and Jahangiri, 2008), interlayered with Mesozoic shale, limestone, and sandstone. These suits are crosscut by Late Cretaceous

granites and Palaeogene granites and volcanics (Abdulzahra, et al., 2018; Azizi et al., 2018; Azizi et al., 2019; Mazhari et al., 2009). (ii) The central sector is marked by three main tectonics: (a) Cadomian basement, mainly deformed amphibolite and Ediacaran (Upper Neoproterozoic) metagranitoids (Badr et al., 2018); (b) Early to Mid-Jurassic high-temperature metamorphic rocks (Baharifar et al., 2004). Submarine MORB and OIB-like volcanics have been considered to be protoliths of these assemblages (Azizi et al., 2018; Tavakoli et al., 2020); and (c) gabbro to granite intrusions of Jurassic age. Chronology of Jurassic igneous rocks in the Sanandaj-Sirjan implied that the shift in the locus of magmatism from ~175 Ma in the SE to ~145 Ma in the NW (Bayati et al., 2017). This progression is inconsistent with prolonged and sustained magmatism along a distinct magmatic front at a convergent plate margin (e.g. Azizi et al., 2018; Stern et al., 2021). (iii) The southern sector is made up of Palaeozoic metamorphic rocks overlain by unmetamorphosed Triassic and Jurassic sediments (Sheikholeslami, 2015).

The geodynamic setting of these Jurassic igneous rocks has been the subject of many frontline studies and remains a hotly debated topic with diverse and passionately defended hypotheses. The majority of investigations on Sanandaj-Sirjan Zone suggested that these Jurassic igneous rocks formed at an active margin as a result of convergence between the Afro-Arabian and Eurasian plates (e.g. Stöcklin and Nabavi, 1973; Berberian and Berberian, 1981; Mohajjel et al., 2003; Mohajjel and Fergusson, 2014; Moinevaziri et al., 2015; Nadimi and Konon, 2012; Ghasemi and Talbot, 2006; Davoudian et al., 2008; Mahmoudi et al., 2011; Azizi et al., 2011, 2013; Azizi and Asahara, 2013; Maanijou et al., 2013; Sepahi et al., 2018; Shahbazi et al., 2010; Agard et al., 2005; Hassanzadeh and Wernicke 2016). An alternative interpretation is that Jurassic igneous activity in this zone occurred in a continental rift, not an arc (Azizi and Stern 2019, Hunziker et al., 2015; Stern et al., 2021). The propagating continental rift model is further supported by thick Early Cretaceous limestone layers, most likely owing to thermal sinking of rifted continental lithosphere (Stern et al., 2021). Azizi and Stern (2019) suggested that the arc-like character of some Jurassic Sanandaj-Sirjan Zone igneous rocks can be attributed to the significant contamination of mafic melts by continental crust and sediments. Today, the SSZ is a rather rigid block migrating northward at 14 mm yr<sup>-1</sup> relative to Eurasia (Vernant et al., 2004).

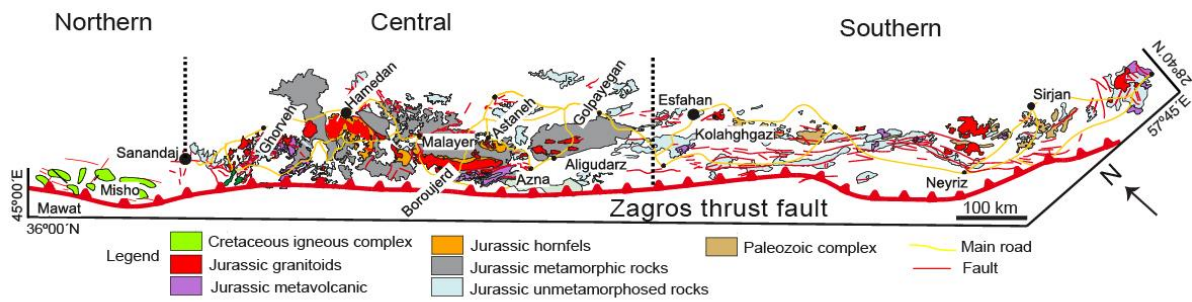


Fig. 3.3. Sanandaj-Sirjan Zone with Precambrian basement and granitoid bodies (Azizi and Stern, 2019)

### 3.2.3. Urumieh-Dokhtar Magmatic Arc

The Urumieh-Dokhtar Magmatic Arc is approximately 1000 km long and 50–80 km wide (Fig. 3.4). There is a common consensus that Urumieh-Dokhtar belt have developed over a subducting slab of the Neo-Tethyan oceanic lithosphere that was subducting beneath the Iranian Plate (Alavi, 1994). Concomitantly, as magmatism ceased in the Sanandaj-Sirjan zone in Late Cretaceous, arc volcanism flared up in the parallel Urumieh-Dokhtar magmatic arc (e.g. Hassanzadeh, 1993; Allen, 2009; Verdel et al., 2011; Castro et al., 2013; Nabatian et al., 2014; Richards, 2015; Richards and Sholeh, 2016). There is a long-standing and controversial debate about the relationship between the Sanandaj–Sirjan and Urumieh–Dokhtar arcs. It is argued that progressive flattening of the angle of subduction resulted in migration of NW–SE axis of magmatism in the Sanandaj-Sirjan to the northeast with formation of the Urumieh-Dokhtar arc in the Paleogene (Mohajjel and Fergusson, 2014; Whitechurch et al., 2013; Richards, 2015).

Magmatic activity initiated in Late Cretaceous (Hassanzadeh and Wernicke, 2016; Stern et al., 2021) or Early Eocene (Mohajjel et al., 2003; Verdal et al., 2011) with outpour of low-K tholeiitic and calc-alkaline magmas and evolved into a mature arc with adakite-like calc-alkaline magmatism in the Paleogene. This belt is made up of four igneous successions (i) The Eocene–Oligocene magmatic rocks with a geochemical characteristics of a continental arc under extension regime from ~55 Ma until ~37 Ma (e.g., Verdel et al., 2011), (ii) The Oligocene oceanic island basalt (OIB)-like magmatism, revealing a transition from arc-like to “OIB-like” (Sepidbar et al., 2019); (iii) the Late Oligocene–Miocene arc magmatism as a consequence of collision (e.g., Topuz et al., 2019); and (iv) the Late Miocene–Quaternary magmatism triggered by beginning of closure of the Tethys ocean. The Urumieh-Dokhtar belt is marked by its acme of magmatism in the Middle Eocene during a period of intense extension (Mohajjel et al., 2003; Verdal et al., 2011). The Urumieh-Dokhtar magmatic belt intrusive suits are Late Cretaceous

to the Miocene in age. The most ubiquitous intrusive rocks are Eocene–Oligocene to Miocene in age and exhibit calc-alkaline to high-K calc-alkaline characteristics (Babazadeh et al. 2017). Almost majority of these plutons are devoid of mineralization. It is argued that Oligocene to Miocene intrusive assemblages have been formed by melting of lithospheric or asthenospheric mantle (Asadi et al., 2014; Babazadeh et al., 2017; and/or subducted Arabian plate (Mirnejad et al. 2018) combined with contamination by Iran Cadomian crust to various extents. The volcanic succession of the Urumieh-Dokhtar magmatic belt comprises thick (4 km) layers of calc-alkaline, shoshonitic, and adakitic lavas and pyroclastic rocks (Stern et al., 2021). Stern et al. (2021) classified the Cenozoic arc of Iran into magmatic front (“called Urumieh Dokhtar magmatic belt”) and reararc magmatic belt in the north (called “the Alborz magmatic belt”) and northeast (Fig. 3.4). Paleogene rear-arc magmatism triggered by thinning of Iran continental crust associated with extension during the latest Cretaceous to Miocene (Sepidbar et al., 2021; Stern et al., 2021). Several transgression-regression cycles have also been observed in Cretaceous to Eocene reararc deposits (Ballato et al. 2011). Rear-arc plutonic pulses can be divided into three groups: (i) Late Cretaceous–Paleogene intrusive rocks in NE Iran with low-K tholeiitic to calc-alkaline characteristics. (ii) Eocene intrusive rocks range from calc-alkaline to adakitic in NE Iran and Na-rich alkaline intrusions in NW Iran (Ashrafi et al. 2018). (iii) Late Eocene–Oligocene to Miocene intrusive rocks in the NW Iran with high-K calc-alkaline to shoshonitic signatures (Castro et al. 2013).

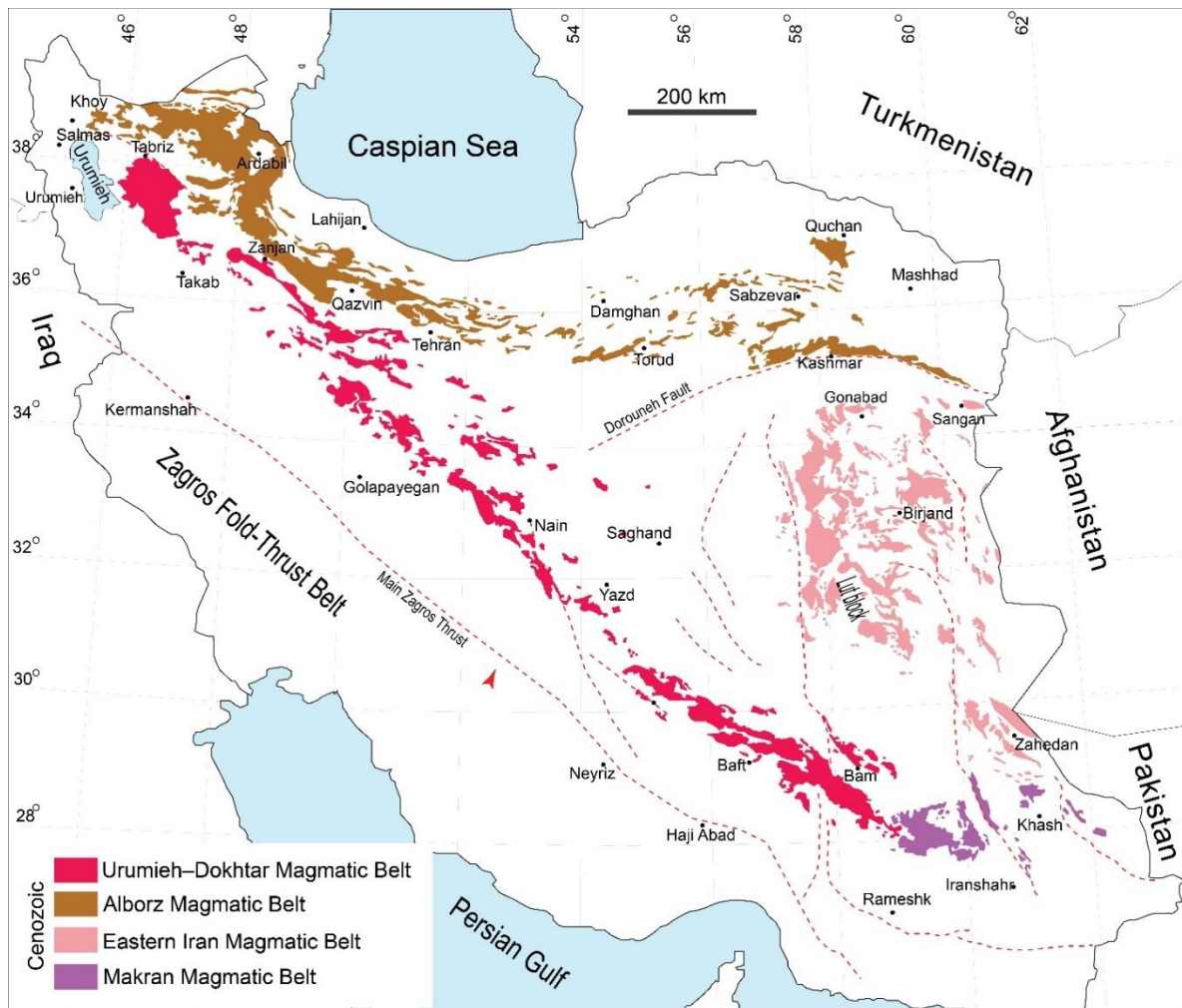


Fig. 3.4. Geological map of Iran showing distribution of the Cadomian basement rocks, Cenozoic magmatic belts including Urumieh-Dokhtar, Alborz, Eastern Iran and Makran (Sepidbar et al., 2018).

### 3.2.4. Central-East Iranian Microcontinent

Central-East Iranian Microcontinent is made up four Cadomian crustal tracts, comprising the Yazd, Tabas, Posht-Badam, and Lut blocks which are bordered by large strike-slip fault zones (Berberian, 1981). These faults allow northward migration of these blocks at a rate of 6–13 mm/yr with respect to the stable Afghan crust (Walpersdorf et al., 2014). These blocks are continental Cimmerian ribbons detached from Gondwana and were accreted to Eurasia during closure of Paleotethys in Triassic times (e.g., Stöcklin, 1968, Berberian and King, 1981, Şengör, 1984, Alavi, 1991, Ramezani and Tucker, 2003, Bagheri and Stampfli, 2008). According to Stern et al. (2021), these Cadomian tracts are considered as the most stable crust of Iran. Cadomian arc crust have been recorded in western (Golpayegan), northern (Lahijan granites), northeastern (Torud, Taknar), northwestern (Khoy-Salmas, Zanjan-Takab), and central Iran

(Saghand) (Hassanzadeh et al., 2008). Iran's Cadomian basement is marked by felsic igneous rocks – and their metamorphic counterparts – as well as detrital sedimentary successions (Shafaii Moghadam et al., 2016). Exhumation of Cadomian basement occurred during extensional events in Cenozoic time (Stockli 2004; Kargaranbafghi *et al.* 2015; Moghadam *et al.* 2016). The Ediacaran–early Cambrian ages (520–600 Ma) are attributed to the oldest igneous rocks (Ramezani and Tucker 2003). Late Cretaceous (Nain-Dehshir-Baft, Sabzevar) and Paleozoic (Jandagh-Anarak) are the major sutures of Central Iran (Shafaii Moghadam et al., 2015). Vast majority of Cadomian felsic rocks in Iran shows “volcanic arc granite” (VAG) geochemical signatures and within plate granites (WPG) are scarce (Badr et al., 2013; Balaghi Einalou et al., 2014; Rossetti et al., 2015). Cadomian within plate-like, alkaline felsic suits are uncommon and composed mainly of rhyolitic lavas (Sepidbar et al., 2020). These volcanic rocks and their plutonic counterparts occurred in northwest (Qare-Dash) and central Iran (Zarian-Narigan units), as well as exotic blocks within Ediacaran salt domes from southern Iran. Ediacaran salt diapirs are common in the south and south-eastern Zagros Fold-Thrust Belt. These salt diapirs are derived from a thick series of deeply buried Ediacaran-Cambrian (“Infracambrian”) evaporates known as the Hormuz salt (Husseini and Husseini, 1990, Smith, 2012).

### 3.2.5. Eastern Iranian Orogen

The Eastern Iranian range is an N-S-trending deformation belt with an average length of 900 km and width of 200 km. It is predominantly composed of preserved Mesozoic ophiolites (Saccani et al., 2010; Zarrinkoub et al., 2012), large-scale Cenozoic basins (Tirrul et al., 1983), abundant Cenozoic magmatism (Camp and Griffis, 1982; Pang et al., 2012, 2013), and diverse metamorphic rocks, including HP-LT relicts (Fotoohi Rad et al., 2005; Angiboust et al., 2013; Bröcker et al., 2013) extend between the Gondwana-derived blocks of Afghanistan in the east and Lut in the west. On a large map scale (Fig. 3.5), the Eastern Iranian Orogen appears as a curved belt, which is referred to as Eastern Iranian Orocline (Bagheri and Damani Gol, 2020). Tirrul et al. (1983) divided the Eastern Iranian Ranges into two distinct domains including the Neh-Ratuk complex (accretionary wedge “mélange”) to the west and the Sefidabeh fore-arc basin or the Sistan ocean zone. The Ratuk is a NW-trending ophiolitic complex which is dismembered and partially metamorphosed (Tirrul et al., 1983). Exposures of blueschist, amphibolite and eclogite were identified (Fotoohi Rad et al., 2005). Towards south-west, the Neh complex is made up of Senonian to Lower Eocene sedimentary rocks and ophiolitic

assemblages were partly metamorphosed in low-grade degrees (e.g., Tirrul et al., 1983; Bagheri and Damani Gol, 2020). The Sistan ocean zone including Maastrichtian to Eocene turbiditic or molassic deposits unconformably overlies the Ratuk and Neh complexes (e.g., Tirrul et al., 1983). Widespread ophiolitic outcrops in Eastern Iranian orogen revealed the presence of an early Cretaceous ocean between Afghan and Lut blocks, dated from the early Aptian (~120–115 Ma) to Albian (~110–100 Ma) (Babazadeh and de Wever, 2004), and early Albian (113–107 Ma) (Zarrinkoub et al., 2012). The Ratuk Complex records an early episode of ocean closure beneath the Afghan block due to E-directed subduction. The younger Neh complex records a later increment of E-directed subduction, after relocation of the subduction zone to a more westerly direction (Fotoohi Rad et al., 2009). There are some petrological and structural evidences supporting eastward subduction of the Sistan ocean under the Afghan block (Babazadeh, 2013; Camp and Griffis, 1982; Tirrul et al., 1983). Based on ubiquitous presence of Tertiary magmatic rocks in the Lut block, some studies have proposed westward-dipping (Beydokhti et al., 2015; Pang et al., 2013) or possibly double-vergent subduction (Beydokhti et al., 2015; Pang et al., 2013). (Arjmandzadeh et al., 2011). Sequences of clastic sediments together with episodes of carbonate deposition and calc-alkaline volcanism are recorded in the Sefidabeh deposits (Bagheri and Damani Gol, 2020). Since the Middle Eocene, the Sefidabeh basin has been influenced by folding and faulting. However, the most significant deformation phase that raised and dissected the basin occurred during the late Eocene-Oligocene period, which was contemporaneous with the commencement of collision (Tirrul et al., 1983). The Sefidabeh fore-arc deposits is covered by Eocene–Oligocene calc-alkaline to shoshonitic extrusive rocks (Stern et al., 2021). It is argued that westward subduction of the Sistan oceanic lithosphere beneath the Lut block resulted in Cretaceous and Cenozoic magmatic activity (Stern et al., 2021).

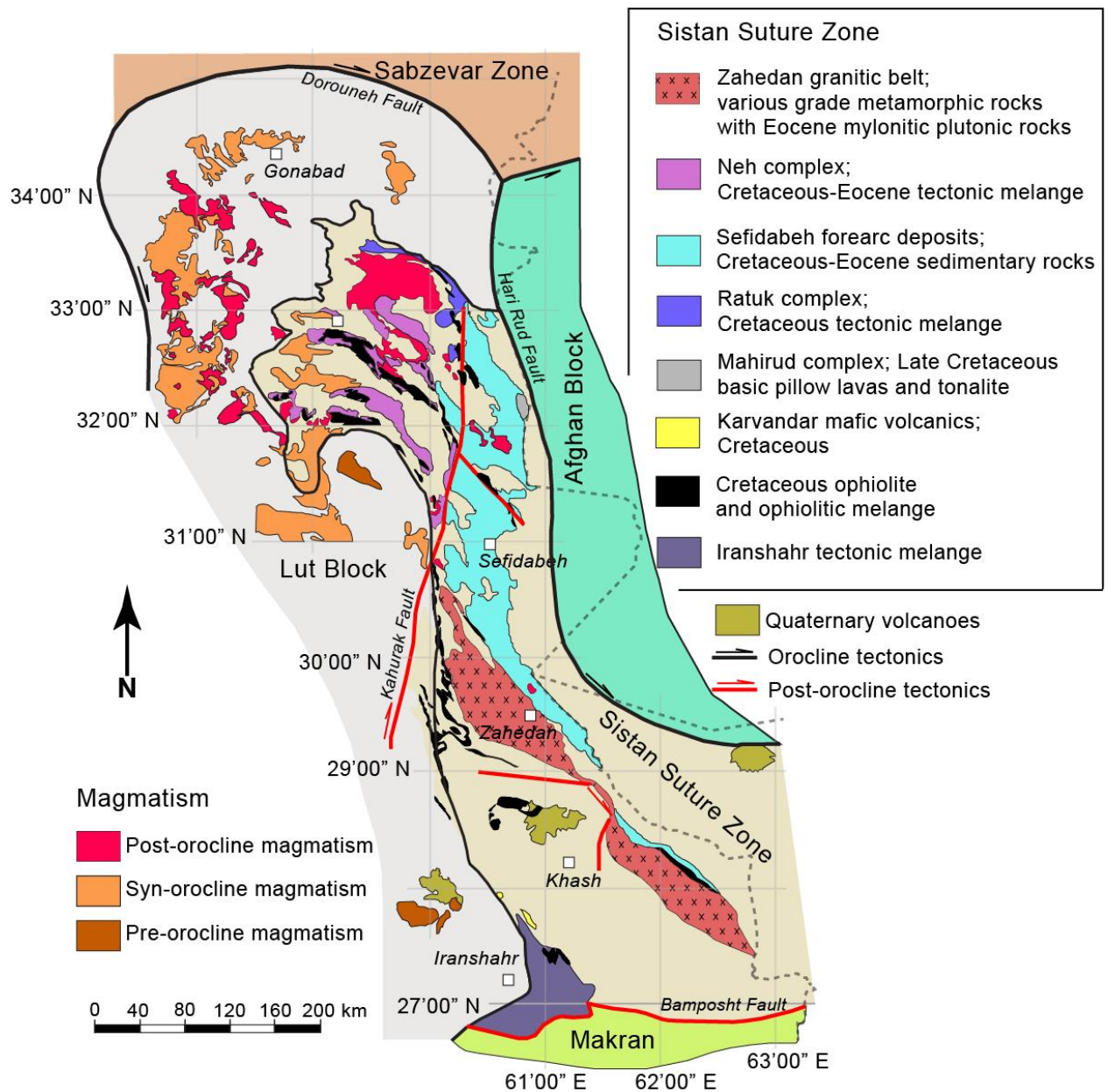


Fig. 3.5. Simplified geological map of the Eastern Iranian Orogen (modified from Bagheri and Damani Gol, 2020)

### 3.2.6. Kopet Dagh Basin

The Kopet Dagh Zone extends from the east of the Caspian Sea to northeast Iran, southern Turkmenistan, and northwest Afghanistan (Berberian and King, 1981; Afshar-Harb, 1994; Lyberis and Manby, 1999; Bretis, Grasmann, and Conradi, 2012). To the north, the Kopet Dagh Basin is bounded by the Main Kopet Dagh fault (Fig. 3.6). The Binalud Range which assumes as the Paleotethys suture zone limits the Eastern Kopet Dagh to the south. In the western section of the Kopet-Dagh Basin, obvious lateral facies and thickness fluctuations demonstrate the crucial function of basement faults in controlling the sedimentation (Afshar-

Harb, 1994). Many horst and graben formations are thought to have formed during the Late Cretaceous, resulting in facies differences and substantial hiatus/sedimentary discontinuity in various locations (Afshar-Harb, 1994). Eastern Kopet-Dagh Basin is marked by a marine succession, exceeding 6000 m, formed from Mid Jurassic through Miocene time (Afshar-Harb, 1979). The Kopeh Dagh Basin was formed after the Cimmerian orogeny (Garzanti and Gaetani, 2002). This basin was inverted during the Tertiary, due to the NE oriented convergence between Central Iranian blocks and the Eurasian plate (Robert et al., 2014). As a consequence of Palaeotethys closure, the Triassic sequences of the Aghdarband Group is unconformably sealed by syn-rift Middle Jurassic siliciclastics of the Kashafrud Fm (Taheri et al., 2009). Initial siliciclastic deposits were followed by marly carbonates and argillaceous limestones (Chaman Bid Formation) in the Middle Jurassic, presumably suggesting slower subsidence rates (Majidifard, 2003). The Mozduran Formation which is mostly made of coastal to shelf siliciclastics and few metre-thick carbonates overlies the Chaman Bid Formation (Adabi and Ager, 1997; Hadavi and Khodadadi, 2014; Hosseiniyoon et al., 2017; Schlagintweit et al., 2019). At the beginning of the Early Cretaceous, siliciclastic red beds deposited in fluvial to shallow-marine environments (Shurijeh Formation; Hosseinyar et al., 2019). The Kopet Dagh Basin is a highly productive oil and gas region with multiple massive gas fields (Ulmishek, 2004). Khangiran and the Gonbadli gas fields produce from the Upper Jurassic Mozduran Formation and the Lower Cretaceous Shurijeh Formation (Afshar-Harb, 1979; Aghanabati, 2004; Kavooosi et al., 2009).

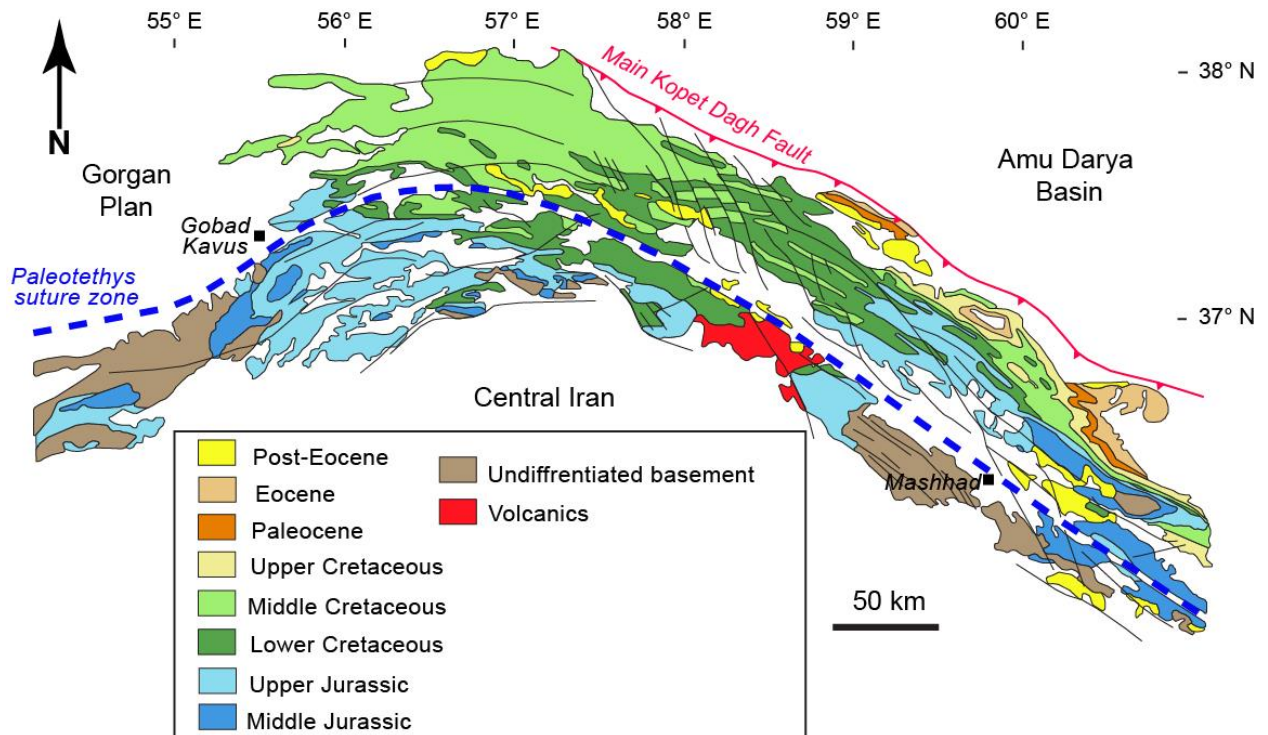


Fig. 3.6. Simplified geological map of the Kopet Dagh area (modified from Robert et al., 2014)

### 3.2.7. Makran Zone

The Makran Zone in southeastern Iran includes accretionary prism, Jaz Murian depression and Cenozoic magmatic belt. The Makran accretionary wedge with an E–W trend is surrounded by two major N–S trending strike-slip fault systems. It is bounded between the dextral Zendan–Minab faults system in the west and the sinistral Chaman–Ornach–Nal faults system in the east (Kopp et al., 2000; REGARD et al., 2010; Penney et al., 2015; Riaz et al., 2019). The Makran accretionary complex is divided into two sections including ophiolitic complexes and sedimentary segments comprising Eocene to Pliocene calcareous and turbiditic successions, mudstones, reef limestones, deltaic sandstone estuarine conglomerates (Fig. 3.7; Esmaili et al. 2021). Makran magmatic E–W trending belt is triggered by subduction of oceanic lithosphere beneath SE Iran. The belt host four large and young stratovolcanoes including Koh-i-Sultan in Pakistan and the Taftan, Kuh-e-Nadir, and Bazman volcanoes of Iran. North-dipping subduction of Arabian plate beneath the Central Iran and Afghan blocks is thought to have started during the Cretaceous (e.g. Alavi, 2007; Berberian et al., 1982; Ricou, 1994) and is still ongoing. The ophiolites of the late Cretaceous–Paleocene are the oldest rocks in this zone, which are overlain by a thick sandstone, shale, and marl sequence (about 5,000 m).

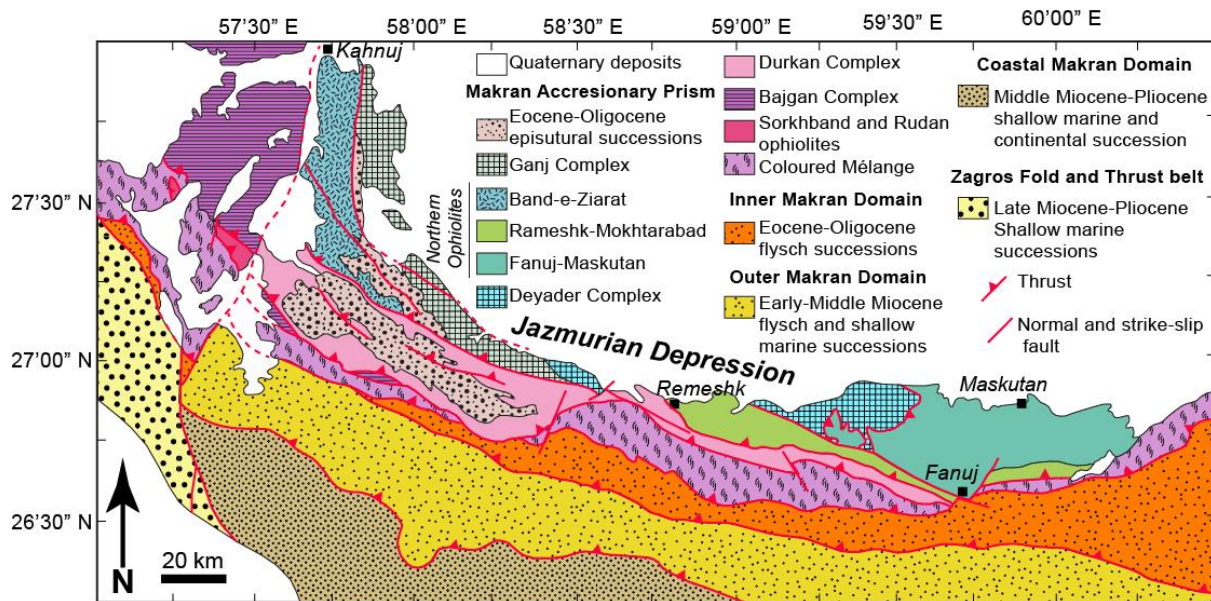


Fig. 3.7. Simplified geological-structural map of the North Makran Domain (modified from Barbero et al., 2021).

### 3.3. Ophiolite nappes in Iran

Ophiolites are pieces of oceanic lithosphere that have been thrust (obducted) onto the edge of continental plates. They delineate sutures between continental terranes and provide models for processes at mid-ocean ridges of oceanic lithosphere, but the tectonic setting that they form is often controversial.

Iran preserves two main great ophiolite belts types with different ages: less abundant Paleozoic Ophiolites (e.g. Weber-Diefenbach et al., 1986) and more abundant Mesozoic Ophiolites (e.g. Alavi, 1991; Arvin and Robinson, 1994). The first ones are distributed mostly in the north, where northward subduction of Paleo-Tethys and subsequent collision of the Central Iran plate (Cimmerian block) with Eurasia (Turan block) occurred. Paleozoic ophiolites are situated in two main zones in northern Iran (Fig. 3.8): Mashhad and Rasht in the north and Jandagh–Anarak and Takab ophiolites to the south. Paleozoic ophiolites from Iran show a progression from Devonian oceanic crust generation above a subduction zone to Permian accretionary convergence (Shafaii Moghadam and Stern, 2014). Almost all of Iranian Paleozoic ophiolites originated in backarc basins. They are associated with thick accretionary prisms, including Carboniferous flysch, Permian turbidites, along with segments of oceanic lithosphere associated with rare high-P metamorphic rocks (Shafaii Moghadam and Stern, 2014).

Neo-Tethys began its opening in Permian, accompanied by the drifting of the Cimmerian block (Iranian plate) northward to collide with Eurasia. These events brought to the closure of

Paleo-Tethys in Triassic time. Mesozoic ophiolites are more abundant, and depict the suture of Neo-Tethys Ocean, and related back-arc basins. This suture (Fig. 3.8) is expressed through the Late Cretaceous Ophiolite Belt of Southwest Asia (LCOBSWA). This is of great significance since it can support the reconstruction of the Neo-Tethyan Ocean from Permian rifting to final closure in Cenozoic time (Shafaii Moghadam and Stern, 2010). The LCOBSWA stretches for 3000 km from Cyprus to Oman through Iran (in the Zagros region where is less known). The Late Cretaceous Ophiolitic Belt is part of Maghrebian-Alpine-Himalayan belt, which extends to Morocco in the west, through the European Alps, the Anatolides, Zagros, Makran and the Himalayas in the east defining an orogenic belt 9000 km long (Furnes et al., 2014) which approximates the location of the Neo-Tethys seaway.

Stöcklin (1977) firstly divided Zagros Mesozoic ophiolites into an outer and an inner sub-belt. The outer sub-belt (Zagros outer belt ophiolites) is located immediately to the southwest of the Main Zagros Thrust Zone (MZT), and is interpreted as a remnant of the Neo-Tethys ocean that was obducted towards the Arabian plate along the MZT bounding the southern margin of Sanandaj-Sirjan Zone. This belt includes the Kermanshah and Neyriz ophiolites that extend into the Oman ophiolite (Babaie et al., 2001; Jannessary et al., 2012). The inner sub-belt (Zagros inner belt ophiolites) is located around the Central Iranian Microcontinent and the Sanandaj Sirjan Zone, represented by extensive Coloured Mèlange zones. It includes Nain-Baft (related to the Nain-Baft back-arc basin), Haji-Abad - Esfandagheh, Makran and Birjand ophiolites (Ahmadipour et al., 2003; Alavi-Therani, 1997; Arvin and Robinson, 1994; Desmonds and Beccaluva, 1983; Ghasemi et al., 2002; Jannessary et al., 2012; McCall, 1997). However, Haji-Abad – Esfandagheh has been recently considered as part of the outer sub-belt (Shafaii Moghadam and Stern, 2015; Najafzadeh and Ahmadipour, 2015). Other Mesozoic ophiolites include Khoy; Sabzevar, Birjand and Makran ophiolite. In their review on tectonic evolution of Mesozoic ophiolites, Shafaii Moghadam and Stern (2015) classified the Iranian Mesozoic ophiolites into five belts (Fig. 3.8), which include: (1) Zagros inner belt ophiolites, with Late Cretaceous ages, including Nain, Dehshir, Shahr-e-Babak and Balvard-Baft ophiolites, along the southern part of Central Iranian microplate; (2) Zagros outer belt ophiolites, with Late Cretaceous age along the Main Zagros Thrust, including Maku-Khoy-Salmas ophiolites in NW Iran, Neyriz, Kermanshah-Kurdistan and Esfandagheh (Haji-Abad) and Late Cretaceous-Eocene ophiolites along the Iraq-Iran border ophiolites; (3) Makran ophiolites, with Late Jurassic-Cretaceous ages in SE Iran, including Kahnuj ophiolites; (4) Late Cretaceous-Early Paleocene ophiolites, including Sabzevar-Torbat-e-Heydarieh ophiolites in NE of Iran and (5) Early to Late Cretaceous ophiolites, between Lut and Afghan blocks in

eastern Iran, including Birjand-Nehbandan-Tchehel-Kureh ophiolites. The majority of Mesozoic ophiolites in Iran have supra-subduction zone (SSZ) geochemical signatures reflecting a position of plate convergence in SW Asia during Late Mesozoic. There is also a considerable proportion with ocean-island basalt affinities, possibly indicating the presence of subcontinental lithospheric mantle (Shafaii Moghadam and Stern, 2015). Paleogene oceanic magmatic rocks along the Iran-Iraq border are distinguished by a thick pile (>1000m) of pillow lavas, pelagic sediments, and underlying plutonic rocks represents these rocks. These are sometimes thought to be Paleogene ophiolites, although no related mantle rocks have been found (Shafaii Moghadam et al., 2020). Shafaii Moghadam et al. (2020) believed that these rocks are more likely related to forearc rifting caused by extreme extension during the Late Paleogene period, which also triggered high-flux magmatism in the Urumieh-Dokhtar Magmatic Belt and exhumation of core complexes in Iran.

Prolonged SI-related extension during the Late Cretaceous resulted in continental rifting and back-arc opening across Iran, followed by formation of Neotethyan ophiolites (Shafaii Moghadam and Stern, 2021). The best examples may be found in the Northwest (Khoy-Maku ophiolite), the Northeast (Sabzevar-Torbat-e-Heydarieh ophiolite), and the East (Birjand-Nehbandan ophiolites) (Shafaii Moghadam and Stern, 2021).

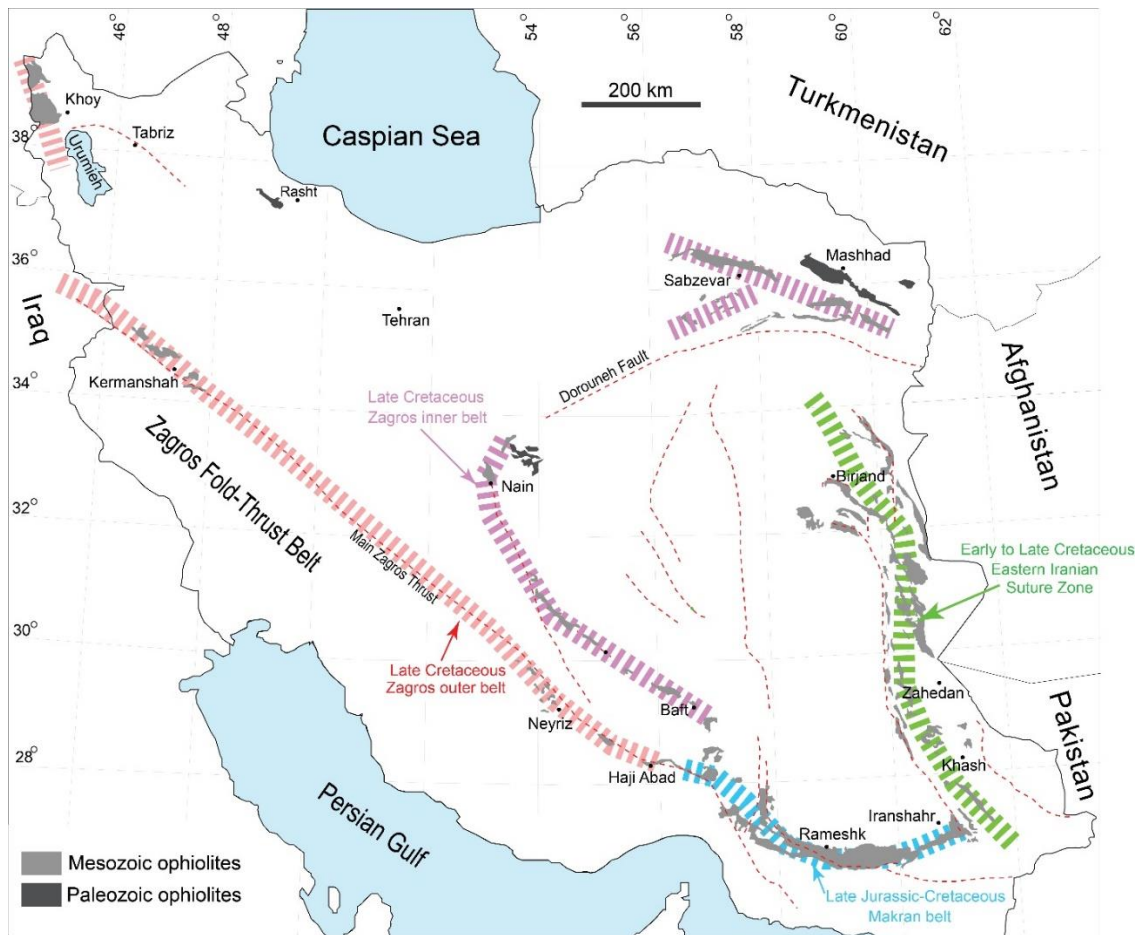


Fig. 3.8. Map of Iran showing the distribution of Paleozoic–Mesozoic ophiolites (modified after Shafaii Moghadam and Stern, 2015; Sepidbar et al., 2021). Main Mesozoic ophiolite belts are shown with thick dashed lines.

### 3.4. Geological settings of study areas

The following sections provide short overviews of the geological settings of the investigated case studies including Sabzevar and Neyriz ophiolites.

#### 3.4.1. Northern Sabzevar Ophiolite Belt

A series of Upper Cretaceous ophiolite nappes are scattered along five alignments in the NE Iran (Fig. 3.9). These ophiolite assemblages include: (i) northern Sabzevar ophiolite belt (NSOB); 2) southern Sabzevar ophiolite belt (SSOB); 3) Bardeskan/Torbat-e-Hedarieh ophiolite slivers; 4) Fariman ophiolite mélangé; and 5) Neyshabour ophiolite slices. These oceanic lithosphere fragments are bordered by two large-scale faults, the Dorouneh sinistral strike-slip fault in the south and the Sangbast–Shandiz dextral strike-slip fault to the north.

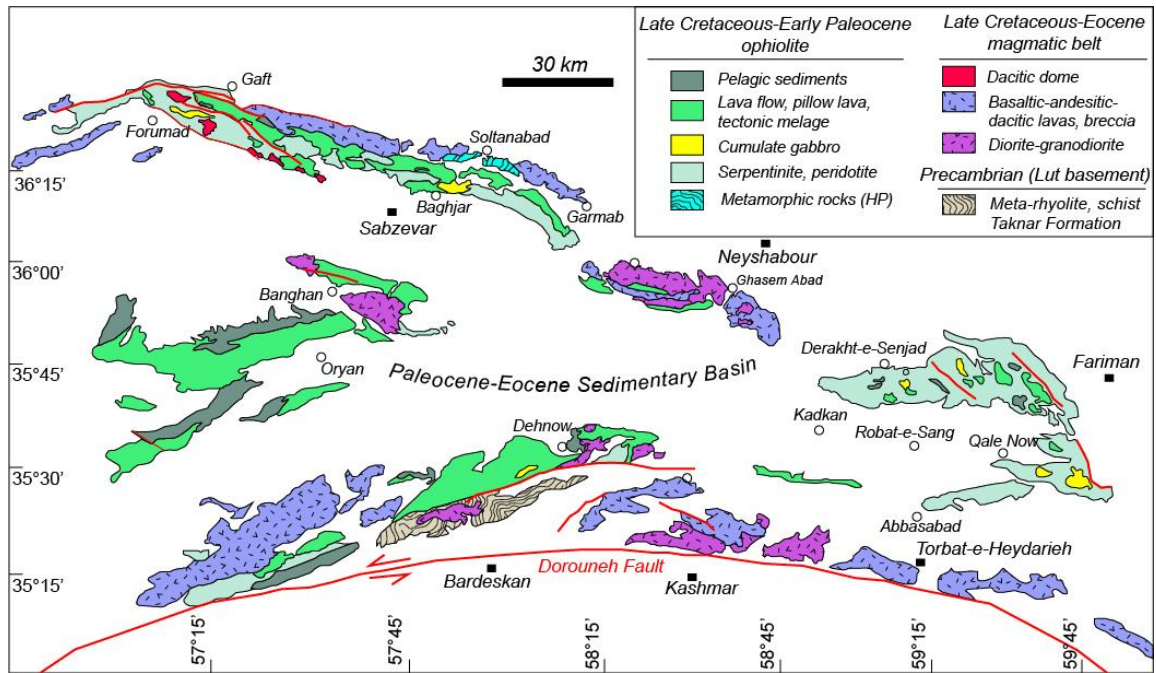


Fig. 3.9. Geological map of the Sabzevar–Torbat-e-Heydarieh region showing distribution of ophiolitic and arc-related rocks

NSOB occur as a SE-NW trending, continuous belt for about 150 km consisting of thrust-bounded blocks of Neotethyan oceanic lithosphere (Fig. 3.9 and 310). Sabzevar ophiolite suit have been considered as typical tectonic ophiolite mélange (Lensch, 1980, Noghreyan, 1982, Baroz et al., 1983, Shojaat et al., 2003) due to its high dismemberment. Sabzevar ophiolite contains all the main components of a typical ophiolite which shows a complete oceanic lithospheric section (Shafaii Moghadam and Stern, 2015 and references therein). The study areas belong to the central sector of this belt (Fig. 3.10). Central sector of NSOB is marked by a largest km-scale peridotite massifs, namely Kuh-Siah (Fig. 3.11a) and Olang-Sir (Fig. 3.11b). This massif covers rugged mountainous area of  $\sim 100 \text{ km}^2$  and is composed of the following lithologies of ophiolitic sequence (from bottom to top) (Fig. 3.12): (i) a nappe of depleted mantle harzburgites with discordant dunite lenses; (ii) layered, pegmatitic and isotropic gabbros; (iii) complex of sheeted dykes; (iv) association of marine sediments, radiolarian cherts, pelagic limestones and pillow lavas.

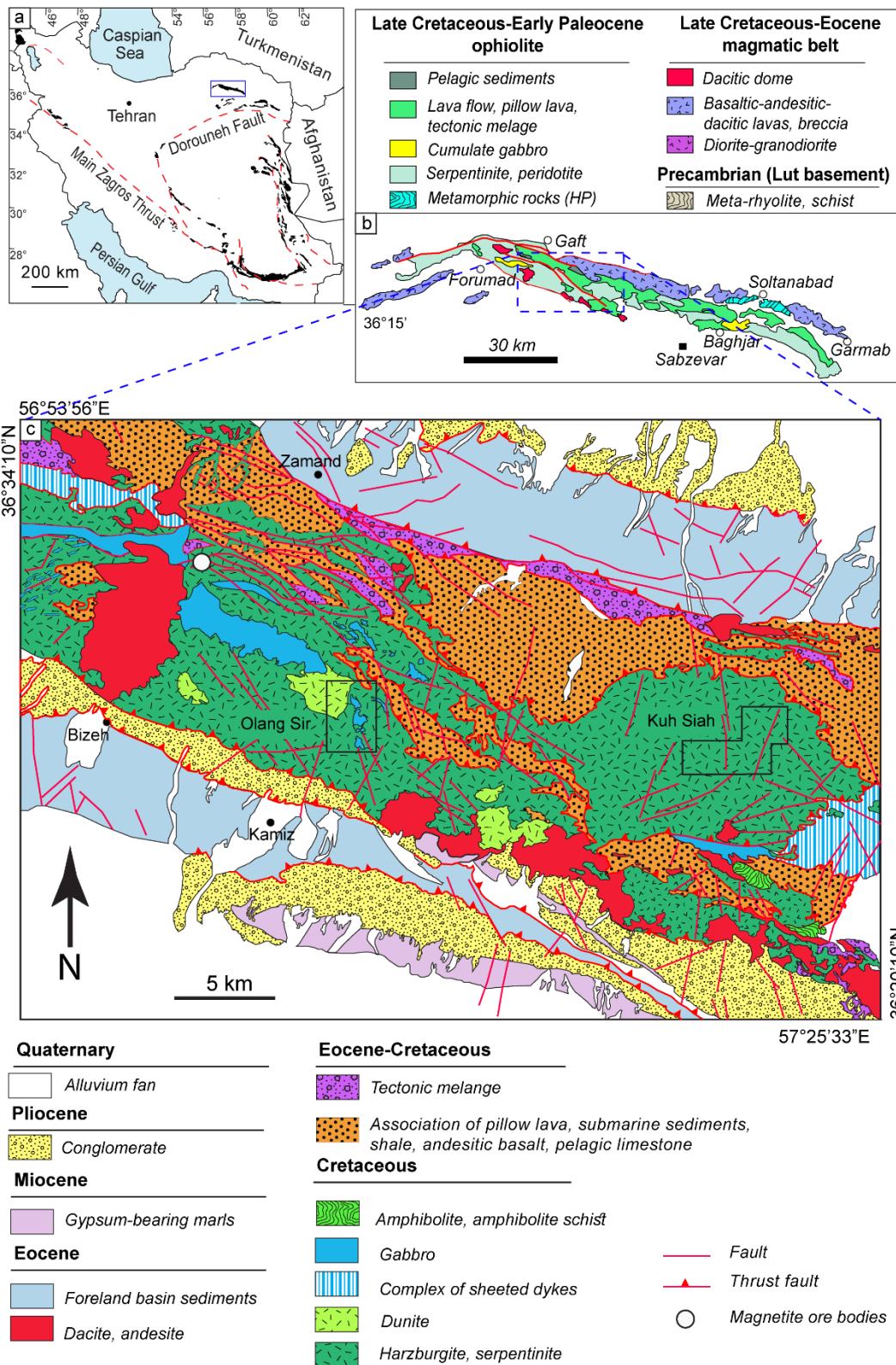


Fig. 3.10. (a) Outline map showing the distribution of Mesozoic ophiolites in Iran; (b) Simplified geological map of the Sabzevar ophiolite belt (modified after Shafaii Moghadam et al. 2014); (c) Simplified geological map of the study area in the central sector of Sabzevar ophiolite belt modified from the 1:100,000 geological quadrangle maps of Forumad (Bahruđi, 1999), Joghatay (Rahmati Ilkhchi, 1999), Bashtin (Bahruđi and Omrani, 1999) and Davarzan

(Radfar and Kohansal, 2001). Detailed geological maps with the study areas marked with black rectangles are shown in Figure 6.2.

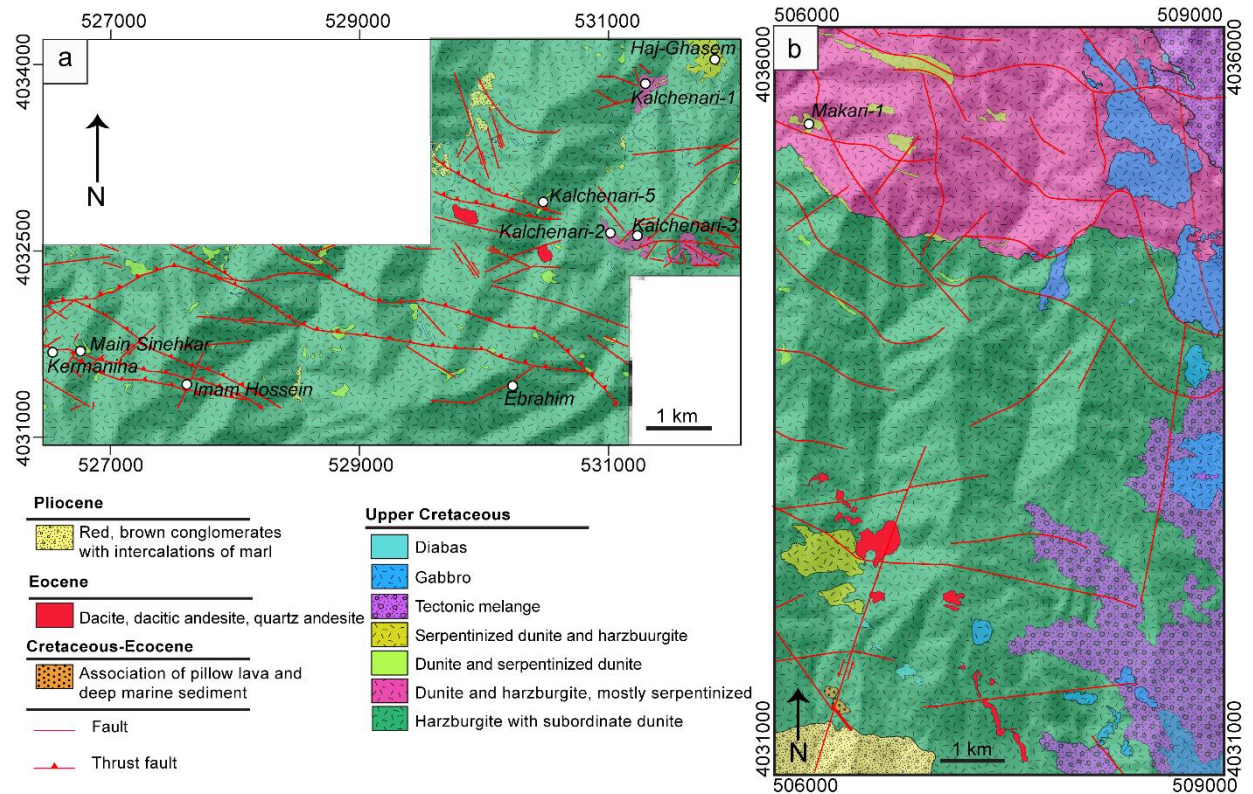


Fig. 3.11. Geological maps of the Kuh Siah (a) and Olang Sir (b) areas modified from the 1:25,000 geological maps of Cheshmeh Khan (KBC Exploration group, 2017) and Cheshmeh Palangan (Faramarzi et al., 2018) and Olang Sir (Alikhani et al., 2019). Location of the studied chromitite deposits are shown with white-filled circles.

The sedimentary cover of Sabzevar ophiolite consists of turbiditic and volcano-sedimentary rocks with interlayers of oceanic fossiliferous pelagic limestone and radiolarian chert. The Sabzevar crustal sequence is characterized by pillowed and massive lavas, sheeted dyke swarms, gabbroic rocks, plagiogranites and cumulate peridotites. The majority of pillow lavas are basaltic to dacitic in composition (Rezaei et al., 2018). Pelagic deposits cover and/or are interbedded within the pillow lava series stratigraphically. Occasionally, andesitic dikes (1–1.5 m thick) crosscut the pillow lavas. These pillow lavas are of the Oceanic Island Basalt (OIB) and supra-subduction zone (SSZ) varieties (Shafaii Moghadam et al., 2014). These two kinds of pillow lavas are geographically dispersed and have no clear links, however they are both overlain and/or intercalated with Late Cretaceous oceanic fossiliferous pink limestones.

The sheeted dyke complex is well-developed at top of the plutonic crustal sequences. The thickness of the dykes ranges from 25 cm to 4 m and their length can reach up to 2.5 km. Dykes are distinguished by an increase in grain size from the margins to the center, indicating fast cooling along the margins (Khalatbari Jafari et al., 2013). These dykes are mostly composed of basaltic andesite, andesite and porphyritic basalts (Rezaei et al., 2018). Dykes are affected by hydrothermal alteration under low-grade greenschist-facies condition. Faults primarily control the geometry of the magma chamber, its internal layering, and the structure of the overlying sheeted dykes (Ohnenstetter, 1980).

Cumulate rocks are typically found around the villages of Soleymanieh and Baghjar in the eastern portion of NSOB. The crustal sequence begins with cumulate peridotite and subsequently progresses to layered gabbro. The layered gabbro is made up of layers that range in thickness from 0.5 to 40 cm thick (Rahmani et al., 2020). Layered gabbros are marked by alternation of olivine-rich, melanocratic layers and plagioclase-rich, leucocratic layers. The layering of the gabbros fades at the top, and the gabbros become isotropic. The ultramafic cumulates are composed of wehrlite and olivine clinopyroxenite (Rahmani et al., 2020). The mafic cumulates include gabbro-norite, olivine gabbro-norite, amphibole gabbro-norite and quartz gabbro-norite. Rahmani et al. (2020) believed that these rocks formed through crystal accumulation from a primary tholeiitic melt within an intra-oceanic arc. Plagiogranite also occurs either as small veinlets and dykes, crosscutting diabasic dikes within mantle peridotites or as irregular masses of variable sizes within cumulate and coarse-grained gabbro. They also occurs as small pockets within the sheeted dikes. Occasionally, plagiogranites are injected into basaltic to andesitic lavas. These rocks could be fractionated products of (boninitic-like) melts produced by hydrous melting of mantle-depleted harzburgites (Shafaii Moghadam et al., 2011).

The most common rock types in mantle section of the Sabzevar ophiolite include lherzolite, clinopyroxen-bearing harzburgite, harzburgite, dunite, and serpentinite. Most lherzolites are late magmatic, formed by the migration and percolation of MORB- and/or SSZ-type basaltic melts through depleted mantle harzburgites (Shafaii Moghadam et al., 2013). The volumetrically dominant mantle peridotite is harzburgite, which contains discordant dunite lenses, pyroxenite layers, and veins (Rahmani, 2020). All lithologies in the mantle section are cut by abundant rodingitized diabase, pegmatitic gabbro, micro-gabbro, and amphibolite dikes.

A dismembered NW/SE-striking tectonic sliver of mafic granulites embedded within the ophiolitic mélangé is exposed in the central sector of the NSOB. In-situ U(-Th)-Pb geochronology of felsic melt segregation in these granulites show an Early Cretaceous (Albian) peak metamorphism before the Late Cretaceous opening of the Naïen and Sabzevar back-arc

oceans (Rossetti et al., 2009). It is argued that the Sabzevar granulites formed during subduction of a branch of the early formed, Late Jurassic–Early Cretaceous back-arc oceanic system, named Sistan oceanic system (Rossetti et al., 2009). In their model, Rossetti et al. (2009) suggested that a transition from a mature (Sistan) to nascent (Sabzevar) stage of oceanic subduction is the geodynamic scenario for genesis of the Sabzevar granulites. Main exposure of metamorphic rocks in the Sabzevar ophiolite complex is near the Soltan Abad village. These rock include blueschist, amphibolite and greenschist.

The post-orogenic Cenozoic magmatic rocks include volcanic (volcanoclastics), hypoabyssal and plutonic rocks. The Sabzevar volcanic suite is made up of both of mafic-to-acidic rocks and felsic extrusive domes (Jamshidi et al., 2015). Middle Eocene dacitic domes with adakite-like chemical characteristics are present to the south of these peridotite massifs. Volcanoclastic rocks and the Sabzevar ophiolitic sequences are intruded by felsic domes which are unconformably covered by Neogene-to-Quaternary deposits.

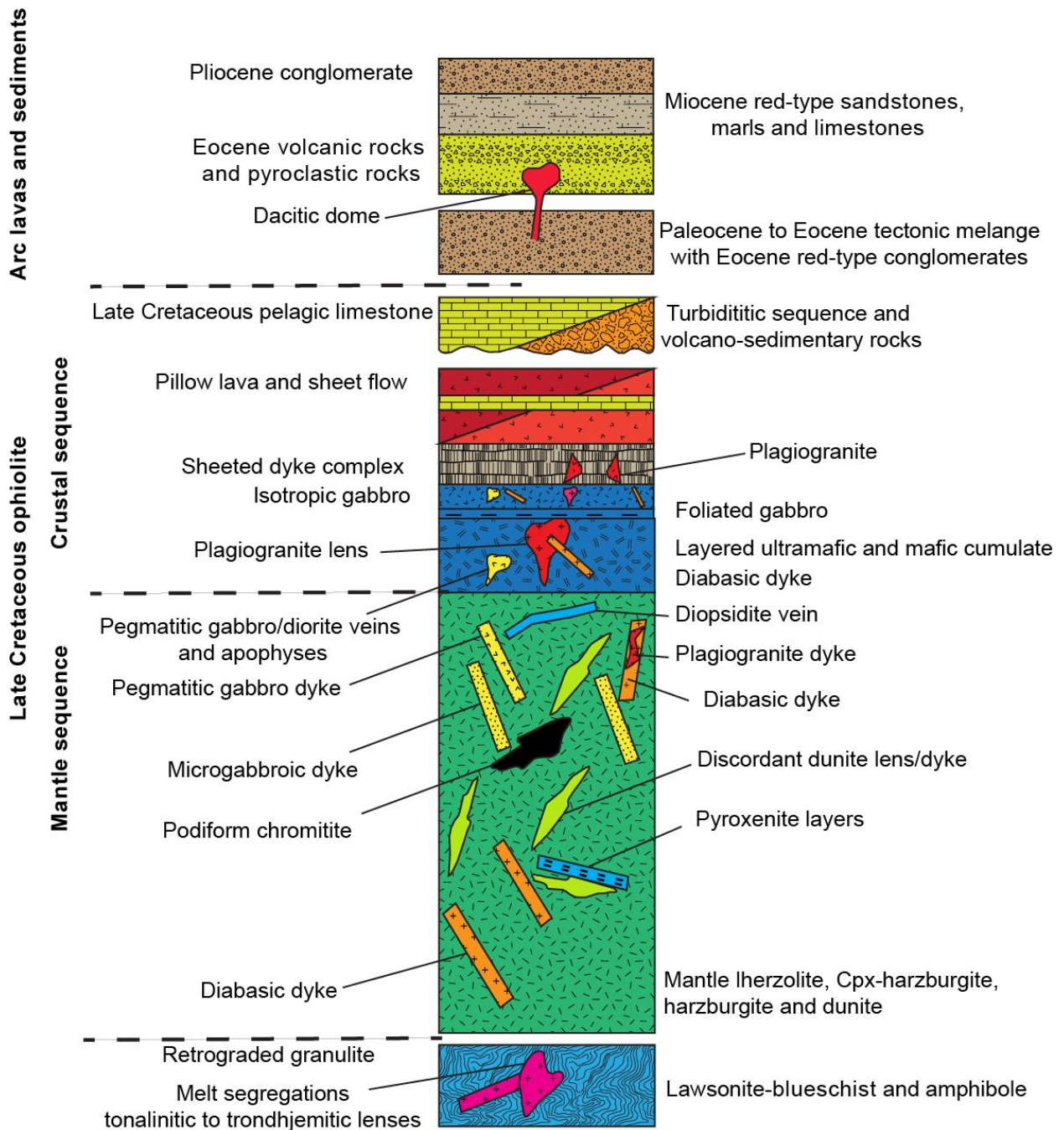


Fig. 3.12. Schematic stratigraphic column of the Sabzevar ophiolite (Rahmani et al., 2020)

Most research works on these ophiolites have been focused on the NSOB (so-called “Sabzevar ophiolite”). Several hypotheses have been put forward to explain the geotectonic settings of the NSOB. Noghreyan (1982) suggested that Sabzevar ophiolite was formed in a back-arc basin. Shojaat et al. (2003) argued that Sabzevar ophiolite was emplaced during NE-dipping subduction of the northern branch of a narrow Tethyan ocean. They reported three types of extrusive rocks in NSOB: 1) basalts and gabbros with N-MORB signature, 2) E-MORB type basalts and 3) basalts with an island arc affinity.

According to Shafaii Moghadam et al. (2014), Sabzevar ophiolites represent an embryonic, subduction-related oceanic basin that was opened between the Lut Block to the south and Turan block to the north since at least mid-Cretaceous time. They also argued that intraoceanic subduction began before the Albian (100-113Ma) was responsible for generating the SSZ-related magmas within the Sabzevar oceanic lithosphere. Omrani et al. (2018) suggested that mafic rocks in these ophiolites were formed in a suprasubduction zone setting within the Neotethys branch of the Sabzevar Ocean at the north of Central Iranian Micro-continent (CIM). They also believed that there are similarities in ophiolite age, lithology and mineralization between NSOB and ophiolites in southern parts (SSOB and Bardeskan/Torbate-Heydarieyh) and rotation or faulting of CIM during Eocene resulted in detachment of northern ophiolites from southern ones. The origin of NSOB remains disputable with manifold and well-defended hypotheses.

The K-Ar geochronology on amphiboles from the lavas and diabases provided formation ages of  $81.2 \pm 4.1$  Ma and  $76.8 \pm 3.8$  Ma, respectively (Lensch and Davoudzadeh, 1982). Shafaii-Moghadam et al. (2014) reported zircon TIMS U-Pb dates of 100, 90 and 78 Ma for three plagiogranites and faunal dates of  $\sim 75$ –68 Ma for pelagic limestones between pillows lavas throughout the NSOB, indicating a drawn-out period of formation of ophiolitic sequences. The U-Pb ages from zircon ( $107.4 \pm 2.4$  Ma) and titanite ( $105.9 \pm 2.3$  Ma) in felsic segregation of mafic granulitic bodies in central sector of NSOB have been interpreted to record peak metamorphism before the Late-Cretaceous Sabzevar back-arc basin development (Rossetti et al., 2010). It has also been argued that the formation of Sabzevar migmatitic granulites was an upshot of the subduction of early-formed Late Jurassic–Early Cretaceous back-arc oceanic system, followed by extension of Sabzevar back arc basin (Rossetti et al., 2010). Study of two chromitite varieties in three distinct peridotite massifs (i.e. Foroumad, Gaft, and Baghjar) throughout the NSOB (Shafaii Moghadam et al., 2015) indicated that the formation of podiform chromitites has been ascribed to melt-rock reaction. It is also suggested that low-Cr chromitites initially formed via MORB-like melts whereas subsequent arc-like or boninitic melts were accountable for high-Cr chromitites (Shafaii-Moghadam et al., 2015)

### **3.4.2. Neyriz ophiolite**

The Neyriz ophiolitic outcrops are distributed along the Main Zagros Thrust fault. Neyriz ophiolitic massifs occurred as intermittent exposures from the NW to SE, between the towns of Abadeh-e-Tashk and Neyriz. Lithological units in the north of the Neyriz city include three

imbricated sheets (Fig. 3.13; Ricou 1971, 1976; Ricou *et al.* 1977). From the bottom (southwest) to top (northeast), the sheets consist of (i) Pichakun radiolarite series; (ii) ophiolite and (iii) mélange units or Bakhtegan Beds of Hallam (1976), with carbonate blocks of Late Triassic age (Ricou, 1976).

The Pichakan radiolarite series stretches northwest of Bakhtegan Lake. The lower section of the Pichakun series consists of Upper Triassic megalodon limestone turbidites, dark marl, and serpentinite diapirs. Lower section progressively transforms into an alternating pattern of cherty radiolaritic thin-banks (5 cm) and medium to thick beds (up to 5 m) of detrital limestone, green siliceous shale, and finally a 500 m-thick radiolaritic sequence. Radiolarite in the upper section are younger than Middle Jurassic in age (Mehrnoosh and Hamdi, 1979; Tangestani *et al.*, 2011). Manganese mineralization occurs as individual ore interbeds with reddish radiolarites in the upper section of Pichakun series. The Pichakun series are similar to the Bisotun series of Kermanshah and Balambo Cretaceous carbonates and Qulqula deep-water radiolarites from the Iraqi Zagros ophiolites (Ali *et al.* 2012). The Neyriz ophiolite together with the Pichakun radiolarite series are overlain unconformably by shallow water marine reef limestones of the Late Cretaceous (Santonian) Tarbour Formation (Ricou, 1968a, Ricou, 1968b). The Neyriz ophiolite is thrust over the Pichakun formation during Turonian to Maastrichtian (e.g. Ricou *et al.* 1977; Alavi 1994; Babaie *et al.* 2006). Crustal sequences are tectonically scattered in the south-eastern and central parts of the Neyriz ophiolite. Basaltic to andesitic pillow and sheeted lava flows are situated in north of Abadeh Task and northwest of Neyriz. Occurrence of chert lenses intercalated with sheet lava flows as well as vesicles in pillows and sheeted lava flows reflect submarine volcanic activity (Monsef *et al.*, 2018). From the top of the ophiolitic pile to its base, the Neyriz ophiolitic massifs consist of the following lithospheric sections (Fig. 3.14): (1) clinopyroxene-poor and clinopyroxene-rich harzburgite cut by a series of mafic-ultramafic dikes (2) peridotite cumulate (3) layered gabbros cut by isotropic gabbros and plagiogranite bodies, (4) basaltic to andesitic pillow and sheet lava flows. Pillow lavas are severely fractured and their contact with pelagic sediments is occasionally retained.

The Neyriz ophiolite mantle sequence consists of depleted to highly impregnated harzburgite and lherzolite with patches of residual dunite and podiform chromitite. Harzburgites and lherzolites are marked by high-temperature foliation (Shafaii Moghadam *et al.*, 2014). The major mantle peridotites are harzburgite tectonites, which range from clinopyroxene (Cpx)-rich to Cpx-poor harzburgites. Dunites occur as discordant lenses within Cpx-poor harzburgites. Mantle peridotites are crosscut by abundant diabasic, gabbroic and pyroxenite dikes. Crustal

sequence is made up mostly of layered and isotropic gabbros, peridotite cumulates and plagiogranites which are tectonically scattered throughout the SE portion of Neyriz ophiolite belt. Peridotite cumulates at the base of crustal section are overlain by several meters of stunning layered gabbros. Plagiogranite bodies occurs as individual intrusions in the layered gabbros. The layered gabbros are cut by isotropic gabbros. Volcanic suits are mostly basaltic to andesitic pillow and sheet lava flows in faulted contact with gabbros (Monsef et al., 2018).

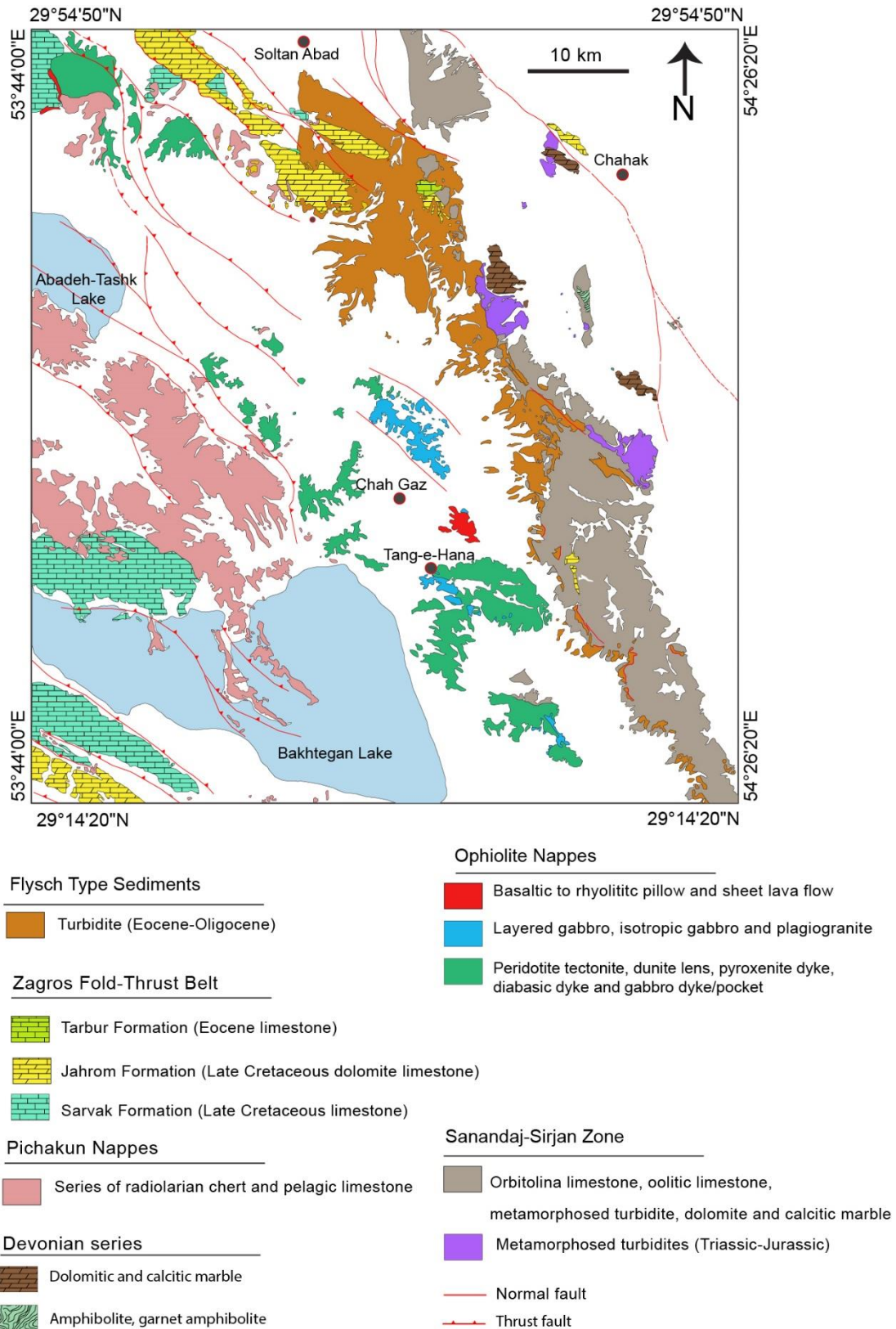


Fig. 3.13. Geologic map of the Neyriz area showing the distribution of the ophiolitic massifs

The Khajeh-Jamali ophiolites in the northwestern end of the Neyriz ophiolite belt, consist of four peridotite massifs belonging to ZOB in the Zagros Mountains (Southwestern Iran), and

outcrop about 20 km from the Main Zagros Thrust. These massifs are dominantly composed of mantle harzburgite-dunite tectonites and a Moho Transition Zone (MTZ) (Fig. 3.15; e.g. Rajabzadeh, 1998; Rajabzadeh and Nazari Dehkordi, 2013; Eslami et al., 2015). Mantle foliation strikes N20–35°W, dipping 35–44° to the southwest. Dunite occurs as small discordant lense or dyke in harzburgite. Several concordant or subconcordant orthopyroxenites and clinopyroxenites intrude both mantle tectonites and the MTZ. Boundaries between the pyroxenite intrusions and peridotite host rocks are generally sharp. The pyroxenite dykes/veins are usually coarse-grained and range from a few cm to 35 cm in thickness.

A typical cumulate sequence and a sheeted dyke complex are missing in the Khajeh-Jamali area. Peridotites are overlain by a very thin nappe of basaltic pillow lavas, reddish-purple radiolarian cherts and Late Cretaceous pelagic limestones (Rajabzadeh, 1998; Eslami et al., 2015). The ophiolitic assemblage is thrust onto the Cenomanian/Turonian shallow water deposits of the Sarvak Formation in the western portion of the Khajeh-Jamali area (Alavi, 1994). The Cheshmeh-Bid ophiolitic massif, as a largest peridotite massif, covers rugged mountainous area of ~25 km<sup>2</sup> in the northwest of the Khajeh-Jamali area. This massif hosts large economical concentrations of chromitites showing massive and high-grade disseminated texture (Rajabzadeh, 1998; Eslami et al., 2015).

## Neyriz ophiolite

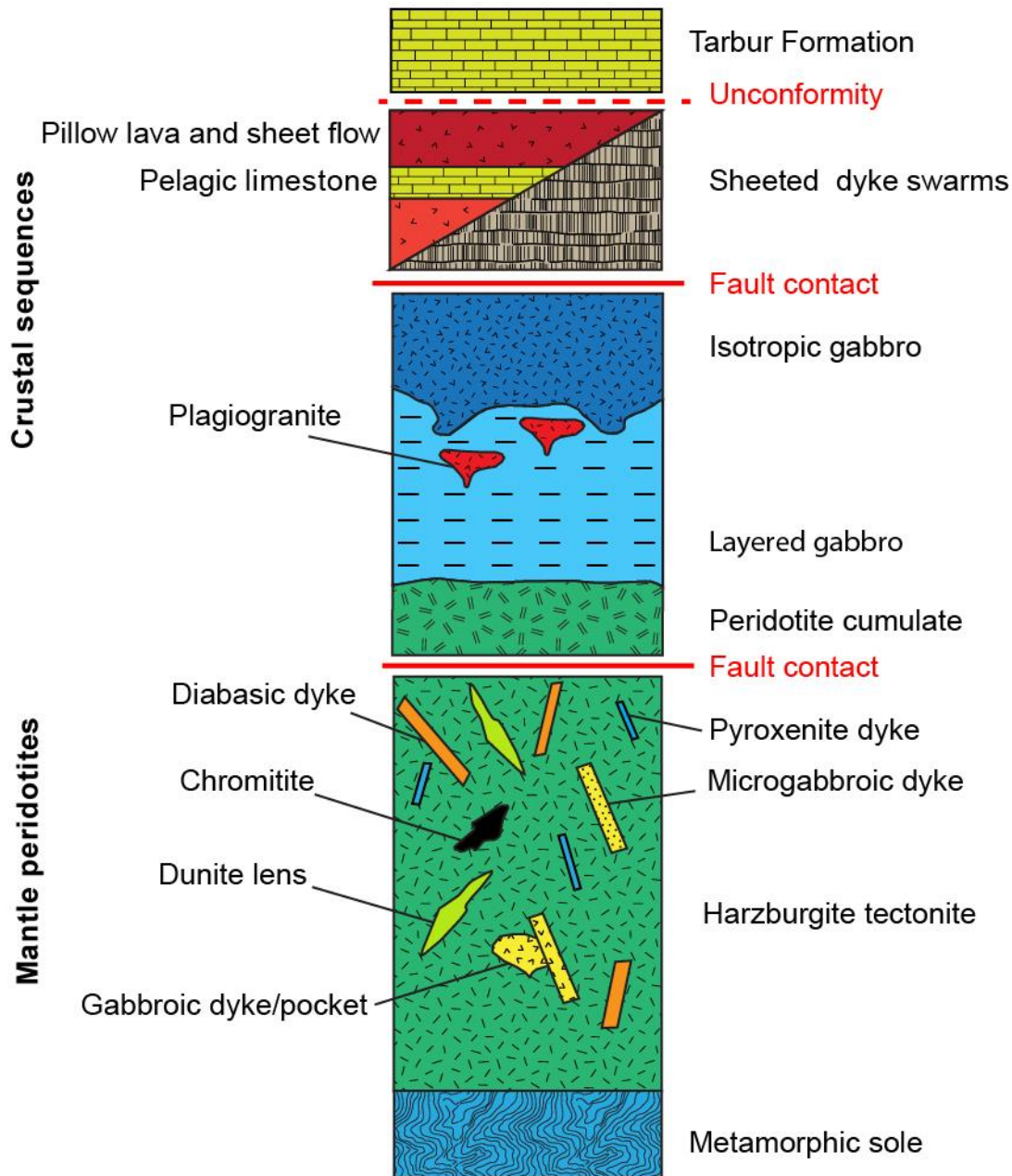


Fig. 3.14. Schematic stratigraphic column of the Neyriz ophiolite (modified after Shafaii Moghadam et al., 2014; Eslami, 2015; Monsef et al., 2018)

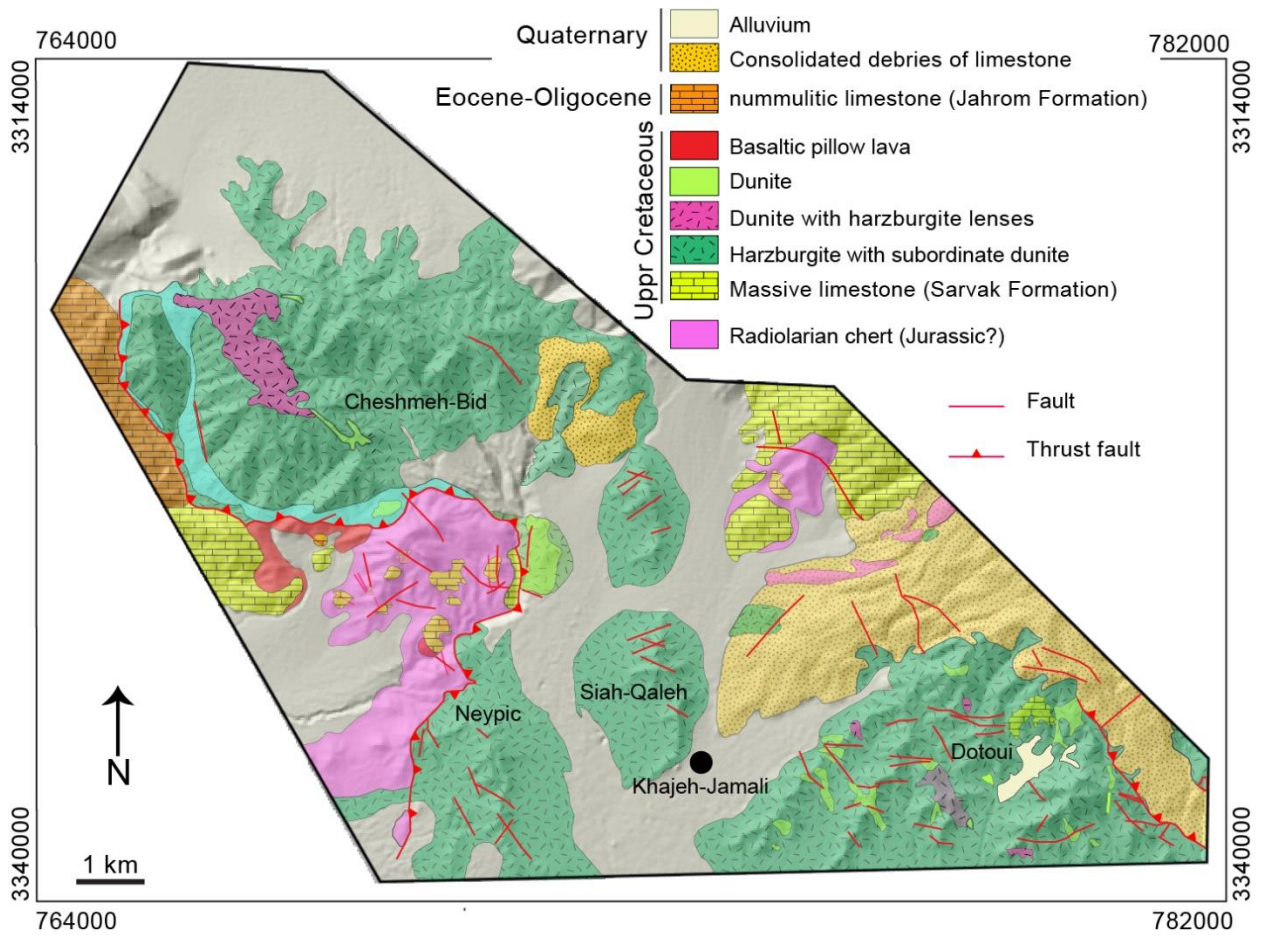


Fig. 3.15. Simplified geological map of Khajeh-Jamali area (modified after Rajabzadeh, 1998).

# *Part III*

## Chapter 4. Podiform magnetite ore (s) in the Sabzevar ophiolite (NE Iran): Oceanic hydrothermal alteration of a chromite deposit

---

### 4.1. Introduction

Magnetite ore bodies hosted by serpentinites have been described in several ophiolites worldwide, in Morocco (Bou-Azzer, e.g. Gahlan et al., 2006; Gahlan and Arai, 2007), in Greece (Olympus, Vermion, Edessa and Skyros Island; Paraskevopoulos and Economou, 1980), in central Iran (Nain; Eslami et al., 2018a), in the Bangong–Nujiang suture zone in Tibetan Plateau (Angwu, Cebojiyi, Beila, and Daru Co; Liu et al., 2020), in Southern Oman (Aniba; Khedr and Arai, 2018) and in the Western Alps (Southern Aosta Valley; Rossetti et al., 2009; Carbonin et al., 2015; Della Guista et al. 2011; Toffolo et al., 2017) among others. In all these occurrences, magnetite ores form massive, nodular and banded ores with an overall thickness that can vary from a few centimeters up to 50 m and with lengths typically between 2 and > 500 m. The processes involved in such a large iron segregation, and their driving forces remain poorly understood and the characterization at various scales of serpentinite-hosted magnetite ores is therefore needed.

Magnetite ore formation can also be associated with magmatic spinel alteration. Spinel composition is often used to determine the melting degree in residual peridotites (Dick and Bullen, 1984), along with mantle oxygen fugacity (O’Neil and Wall, 1987). The application of these two widely used proxies requires deciphering the modification of the original spinel composition by late magmatic processes, hydrothermal alteration and/or metamorphism.

It is well established that the hydrothermal alteration of peridotites at temperatures below 400 °C (i.e. serpentinization) induces the oxidation of the iron initially contained in olivine and pyroxene, leading to magnetite formation (e.g., Moody, 1976; Oufi et al., 2002). Magnetite is often found as disseminated grains in the serpentinite matrix or concentrated in mesh textures and in veins implying a certain extent of remobilization (Beard et al., 2009). A first possible view is that the formation of large ore bodies during serpentinization (or during a later metamorphic stage), implies iron mobilization at a large scale (e.g. Gahlan et al., 2006; Eslami et al., 2018a). Olivine and pyroxene serpentinization could then be the source of that iron (Prabhakar and Bhattacharya, 2013). The respective role of water/rock ratio, temperature,

oxygen fugacity and chemical potential gradients in driving this wide iron segregation still needs to be clarified.

In serpentinite-hosted magnetite ores, magmatic chromium spinels,  $(\text{Mg,Fe})(\text{Al,Cr,Fe})_2\text{O}_4$ , may also play a key role in magnetite formation (e.g. Kimball, 1990; Colas et al., 2019), as they are commonly found in the core of the magnetite grains (Michailidis, 1990; Barnes, 2000; Barra et al., 2014). However, the link between magnetite formation and Cr-spinel alteration is strongly debated.

Thermodynamic modelling predicts the formation of magnetite and ferritchromite ( $\text{FeCr}_2\text{O}_4$ ) at the expense of Cr-spinel at temperatures below  $\sim 550^\circ\text{C}$  (Sack and Ghiorso, 1991). Hence, the iron involved in magnetite formation at the Cr-spinel surface could be derived locally from Cr-spinel dissolution (Ulmer, 1974). The formation of magnetite and ferritchromite at the expense of Cr-spinel requires reactions in an open chemical system with Al and Cr removal or dilution. These two elements are often considered as largely immobile in geochemical processes. The solubility, and thus the mobility, of Cr depends on its oxidation state and on the presence of ligands, such as chlorine, which can complex chromium and enhance its solubility (Huang et al., 2019). Divalent and hexavalent chromium are actually orders of magnitude more soluble than trivalent chromium, Cr(III). The same type of solubility contrasts holds also true for Fe (II) and Fe(III), and therefore redox potential (or oxygen fugacity) has been logically identified as a key parameter in the formation of serpentinite-hosted magnetite ores. Indeed, redox conditions may vary considerably depending on whether the magnetite ore formed during serpentinization, which would produce  $\text{H}_2$  (Kimball, 1990), or during late stage fluid-rock interactions under more oxidizing conditions (Gervilla et al., 2012; Barra et al., 2014).

Here, for the first time, we report a distinct suite of m-scale pod-like bodies of massive-textured magnetite with a cataclastic fabric from the Late Cretaceous Sabzevar ophiolite in NE Iran. These magnetite ore bodies share striking resemblances to podiform chromitite deposits reported throughout the Sabzevar ophiolite belt by virtue of their common geological setting, analogous morphology and macroscopic characteristics. Serpentinized dunite encompasses the podiform magnetite and chromitite in the form of envelopes of variable thickness ( $\geq 0.5$  m). Chromium-rich spinel is occasionally found as relict core of magnetite grains inside the magnetite ore suggesting that the magnetite ores represent the transformation products of pre-existing semi-massive or weakly disseminated chromitite. Spinel in both magnetite ore and host serpentinite shows an intricacy of mineralogical, structural and geochemical fingerprints resulting from a multi-stage alteration history.

We present here a detailed mineralogical description of the new magnetite ore occurrence with a particular emphasis on the micro-nanotextural relationship between chromite and magnetite in both magnetite ore and host serpentinite. Both phase relationships in the host serpentinite and fluid compositions were modeled in order to interpret the micro- and nanoscale observation. A conceptual model for the genesis of magnetite ore in the Sabzevar ophiolite is eventually proposed that involves significant iron mass transfer from the serpentinite to the magnetite ore.

## 4.2. Geological setting and magnetite-ore occurrence

Geological setting of the study area is discussed in section 3.4.1. We observed several massive and rarely disseminated pod-like chromitite bodies ranging from a few centimeters to a few tens of meters in diameter. They are hosted in dismembered masses of harzburgite in a brittle shear zone. Irregular and discontinuous trails of podiform magnetite-ore bodies occurred within highly sheared serpentinite masses (Fig. 4.1a). These ores occur as a series of boudins and elongated lenses that can be tracked over a distance of a few tens of meters along a roadcut. The contacts between the magnetite ores and the host serpentinite are usually sharp (Fig. 4.1b). Small aggregated masses of octahedral magnetite crystals with variable sizes are barely visible to the naked eye on hand specimen (Fig. 4.1c).

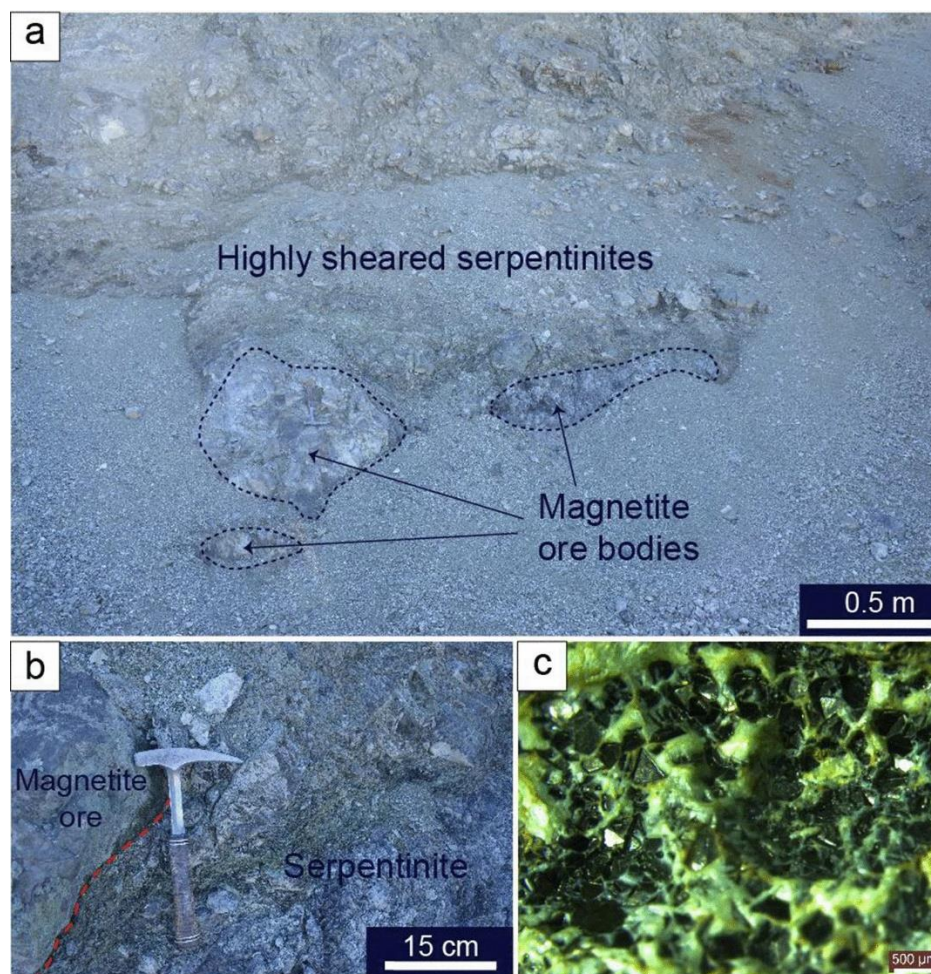


Fig. 4.1. (a) Boundins of magnetite ore-bodies hosted by highly sheared serpentinite in the Sabzevar ophiolite; (b) Sharp contact (red dashed line) between magnetite ore-body and sheared serpentinite; (c) Close-up view of aggregation of octahedral magnetite crystals embedded in pale-green serpentine

## 4.3. Methods

### 4.3.1. Bulk sample characterization

In total, nine specimens from individual magnetite pods and six samples from the host serpentinites were collected in the studied area (Fig. 4.1). Polished thin-sections of the corresponding samples were examined under transmitted and reflected light using a Leica optical microscope.

All collected rock samples were also crushed using a hydraulic press down to a grain size  $\leq 2$  mm. Subsequently, the granular material was milled with an agate ball mill for 15 minutes at 500 revolutions per minute. The obtained powders from each sample were mixed and quartered for the preliminary measurement of LOI (loss on ignition).

Major element concentrations and loss-on-ignition (LOI) of the host peridotite bulk samples (MG21, MG20 and MG16) were determined at the University of Milan Bicocca. Major element concentrations were measured by energy-dispersive X-ray fluorescence (EDXRF) on fused glass disks with a PANalytical Epsilon 3-XL spectrometer. The collected data were preliminary analyzed with the Malvern Panalytical Epsilon 3 software platform, using the Omnia - standardless model, which allows qualitative and quantitative chemical analysis of unknown materials without the construction of calibration lines. The quantitative analysis was then repeated in 6 different instrumental conditions, using the Panalytical WROXI® – synthetic, high quality Certified Reference Materials for calibration.

### 4.3.2. Micro- and nano-scale characterization

Quantitative chemical analyses of individual spinel and silicate minerals were collected using a JEOL JXA-8230 electron probe micro-analyzer (EPMA) equipped with five wavelength-dispersive spectrometers (WDS) and an energy-dispersive spectrometer (EDS) at the Institut des Sciences de la Terre, University Grenoble Alpes, France. Analyses were performed at 15 kV acceleration voltage, 100 nA beam current and a beam size with a diameter of ~1  $\mu\text{m}$ . The concentrations of minor and trace elements (Si, V, Ti, Ni, Co, Mn and Zn) and major elements (Fe, Cr, Al and Mg) were measured by WDS and EDS, respectively. Total counting times (peak plus background) were 440 s for Si  $K\alpha$ ; 240 s for V  $K\alpha$ , Ti  $K\alpha$ ; 360 s for Co  $K\alpha$ ; 180 s for Zn  $K\alpha$ ; 100 s for Ni  $K\alpha$  and Mn  $K\alpha$ . Natural minerals, pure metals and synthetic oxides were used as standards and the ZAF correction was applied. Spectral interference (V  $K\alpha$  vs Ti  $K\beta$ ) was corrected using the JEOL software-calculated correction factor. The detection limits varied between 0.005 and 0.02 wt%, using 3-sigma criterion (Batanova and al., 2018). Elemental distribution maps were collected using an accelerating voltage of 15 kV, a beam current of 200 nA and a dwell time of 700 ms,

Sulfide phases were analyzed using a four-WDS spectrometer CAMECA SX100 electron microprobe analyzer (EMPA) at Department of Geosciences, University of Bremen, Germany. Accelerating voltages of 20 kV and beam current of 20 nA were used. Peak counting times varied between 20 and 40 s per element. The reference materials included synthetic compounds (i.e., Co, ZnS, and FeS<sub>2</sub>) as well as mineral standards (As: arsenopyrite, Mn: ilmenite, Fe: pyrite, Co: native cobalt, Ni: native nickel, Cu: chalcopyrite, Zn: sphalerite, S: pyrite, Pb: galena, Sb: antimonite).

Chromite/magnetite contacts were characterized at the nanoscale in the magnetite ore by Transmission Electron Microscopy (TEM). A TEM lamella was first extracted from a petrographic thin section across a reaction zone surrounding chromite (sample MG15, location on Fig. 4.5) and thinned to < 100 nm with a Ga<sup>+</sup> focused ion beam using a Zeiss<sup>TM</sup>NVision 40 Crossbeam at the Interdisciplinary Center for Electron Microscopy (CIME<sup>-</sup>-EPFL, Lausanne, Switzerland). After attaching the TEM foil to a copper grid, we acquired high-angle annular dark-field images (HAADF) and high-resolution images (HRTEM) with a Tecnai<sup>TM</sup>Osiris microscope operated at 200 keV (CIME<sup>-</sup> - EPFL, Lausanne). The composition at the chromite/magnetite interfaces was determined by combining Scanning Transmission Electron Imaging (STEM) with Energy Dispersive Spectrometry (EDS) mapping using a Field Electron Gun JEOL<sup>TM</sup> 2100F TEM operated at 200 keV (CMTC, Grenoble, France). The maps were corrected for thickness variation by scaling the number of counts with the oxygen map. This latter instrument was also used in combination with an automatic crystallographic orientation tool (ASTAR<sup>TM</sup>; Rauch and Véron, 2014) to acquire crystal orientation maps at the nanoscale. A 1.5 nm-wide electron beam was scanned over the region of interest while acquiring diffraction patterns with a spacing of 4 nm on a 500 x 500 grid. The collected diffraction patterns were compared to pre-calculated templates generated for chromite and magnetite. The best-matching template was used for indexation at each pixel in order to determine crystallographic orientation. The crystallographic data of Santos et al. (2005) were used for generating the chromite templates. The magnetite templates were generated from a mineral structure determined on a magnetite collected in the magnetite ore with X-ray diffraction data collected with an Oxford<sup>TM</sup> Diffraction Xcalibur-1 diffractometer at the University of Milan.

Serpentine minerals were characterized using a Horiba Jobin Yvon LabRAM HR Evolution micro-Raman spectrometer at the University of Milan Bicocca. Spectra were collected using a green Nd 532-nm laser source at a maximum output power of 300 mW. For each thin section, serpentine mineral determination relied on the analysis of about hundred different serpentine areas.

### 4.3.3. Thermodynamic modelling

Temperature -  $fO_2$  stability diagrams were calculated with Perple\_X (version 6.9.0; Connolly, 2005) to investigate the influence of temperature and oxygen fugacity on Cr-spinel stability at 500 MPa. The calculation was performed using the mean composition of the serpentinites collected in Sabzevar (average on samples MG21, MG20 and MG16; Si 34.39

mol.%, Al 0.56 mol.%, Cr 0.26 mol.%, Fe 4.25 mol.%, Mg 60.45 mol.%, Ca 0.10 mol.%), and a water to rock ratio of  $\sim 1$ . The use of such compositions to compute pseudosections implicitly requires to assume thermodynamic equilibrium at the centimeter scale. Evans et al. (2013) have shown that the scale of equilibrium is probably smaller during metasomatic events. The calculations performed here have thus to be seen as predictions of the state towards which the rock should tend. The differences between the calculations and the observations will serve for discussing element mobility during reaction. We used the thermodynamic database for solid phases of Holland and Powell (2011) combined with the database of Sverjensky et al. (2014) for aqueous species (DEW19HP622ver\_elements.dat file). This database includes the dataset for chromium aqueous species from Huang et al. (2019). It was extended by including the Fe-chromite and Mg-chromite endmembers from Klemme et al. (2009). The fluid speciation was evaluated during the optimization with lagged forward-calculations (Galvez et al., 2015). The mineral solid solutions considered were olivine (O(HP); Holland and Powell, 1996, 1998), clinopyroxene (Cpx(HP); Holland and Powell, 1996, 1998), chlorite (Chl(HP); Holland and Powell, 1996, 1998), antigorite (Atg(PN); Padrón-Navarta et al., 2013), brucite (B) and garnet (Grt(JH); Jennings and Holland, 2015). An additional solid solution was built for Cr-bearing spinel by using a reciprocal model and the parameters for non-linearity in Gibbs energy from Sack and Ghiorso (1991). This solid solution predicts a critical temperature of  $\sim 550^\circ\text{C}$  for the  $\text{Fe}_3\text{O}_4\text{-FeCr}_2\text{O}_4$  solvus, which is consistent with the Sack and Ghiorso (1991)'s solid-solution model (Fig. 4.2). The fluid was modelled with the generic molecular fluid equation of state of Perple\_X considering  $\text{H}_2\text{O}$  and  $\text{H}_2$  as possible solvents. The thermodynamic database and solid solution model files used in this study are provided in the Supplementary Materials, in Eslami et al. (2021).

The determination of the spinel composition evolution during cooling requires to estimate the  $fO_2$ . All oxygen fugacities are given relative to the fayalite-magnetite-quartz buffer (FMQ) as  $\Delta\log_{10}fO_2$ . Frost (1985) proposed to calculate an internal  $fO_2$  buffer for ultramafic rocks by fixing the activities in Fe in the Fe-bearing phases (e.g. olivine, orthopyroxene and spinel). We used the same approach here but, as the calculation is performed for a fixed bulk rock composition, determining the  $fO_2$  only requires one additional constraint on the composition. In the stability field of olivine (430 to  $800^\circ\text{C}$ ), the  $fO_2$  is determined by using the  $\text{Mg}/(\text{Mg}+\text{Fe})$  ratio of olivine as the additional compositional constraint. This directly fixes the  $fO_2$  in the divariant fields. In the trivariant fields, two  $fO_2$  are calculated for a single  $\text{Mg}/(\text{Mg}+\text{Fe})$  ratio in olivine, one at  $\Delta\log_{10}fO_2 > -3$  and the other at  $\Delta\log_{10}fO_2 < -5$ . We selected the highest value of  $fO_2$  which is continuous with the values determined in the divariant fields, and provides values

consistent with the estimates of Frost (1985). The Mg/(Mg+Fe) ratio measured in olivine relicts found in the Sabzevar serpentinized dunite is ~ 0.92. This value is systematically higher than the range of ratios computed with the bulk rock composition of the Sabzevar serpentinite. To determine a bulk rock composition consistent with the Mg/(Mg+Fe) ratio measured in olivine, we performed several simulations with Fe contents higher than in the Sabzevar serpentinite. We selected the composition for which 1) the value of 0.92 is encompassed in the calculated Mg/(Mg+Fe) ratio in olivine, and 2) the spinel composition at 800°C is consistent with typical spinel composition from ophiolitic forearc peridotite ( $\text{Cr}^{3+} \sim \text{Al}^{3+}$ ;  $\text{Fe}^{3+} < \text{Cr}^{3+}/\text{Al}^{3+}$ ). The iron concentration in the selected bulk rock composition is by 20% higher than that of the analyzed Sabzevar serpentinite samples. This selected composition is further used to determine the variation of  $fO_2$  with temperature along the isopleth of Fo<sub>92</sub> olivine composition. At low temperature, where olivine is not stable, the additional compositional constraint used to fix the  $fO_2$  is the amount of oxygen in the system. It was considered to be equivalent to the amount of oxygen in an assemblage composed of pure water and a ferrous peridotite (FeO only in the bulk rock composition). Such an assemblage is expected to represent a mantle rock undergoing serpentinization. The  $fO_2$  determined with the two methods detailed above falls in the same range as the  $fO_2$  estimated by Frost (1985) in a cooling peridotite.

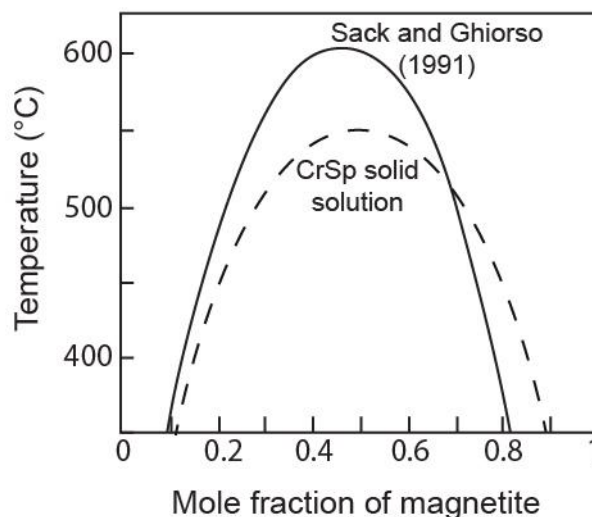


Fig. 4.2. Comparison of Sack and Ghiorso (1991)'s solid-solution model (solid line) with the model used here for Cr-spinel (CrSp solid solution; dashed line).

## 4.4. Mineralogical and textural characteristics

### 4.4.1. Host serpentinite

The host serpentinite displays a typical mesh texture, with olivine kernels of around 80  $\mu\text{m}$  in dimension, surrounded by serpentine and brucite. The scarcity of bastite suggests that the host protolith was a dunite. Magnetite is rare and occurs as euhedral grains with sizes up to 150  $\mu\text{m}$ . Raman spectroscopy shows that serpentinite is composed of abundant polygonal serpentine (peak at 3697  $\text{cm}^{-1}$  and a shoulder at 3689  $\text{cm}^{-1}$ ) and lizardite (two intense peaks at 3683 and 3703  $\text{cm}^{-1}$ ), with minor chrysotile (usually in veins, main peak at 3698  $\text{cm}^{-1}$  with a shoulder at 3691  $\text{cm}^{-1}$ ).

Spinel from the Sabzevar host serpentinite shows two main alteration features. We will call “*partly altered Al-spinel*”, the homogenous spinel single-crystals that are partly replaced along rim and cracks by a secondary spinel matrix containing voids filled with magnetite + Al-bearing hydrous silicate +/- brucite. This type of replacement texture is often called “porous” in the literature, due to the presence of (filled) voids. A second type of spinel alteration texture in the Sabzevar host serpentinite corresponds to entirely porous zones that lack any Al-spinel relict cores. This second type of texture will be called *porous Cr-spinel*, hereafter, since the dominant spinel in this textural type is Cr-rich. Porous Cr-spinel zones are strongly fractured and the average grain size is between 5 and 20  $\mu\text{m}$  (Figs. 4.3b and 4.3c). At the microscale, the porous Cr-spinel matrix seems to be replaced by patches of Fe-chromite and magnetite intergrowths (Fig. 4.3c), possibly indicative of a further alteration stage. Andradite occurs as skeletal masses surrounding porous Cr-spinel in serpentinites (Fig. 4.3d). Fe-Ni alloys are finely dispersed around spinel grains in the serpentine groundmass. Sulfide grains were not encountered in the studied serpentinite samples.

### 4.4.2. Magnetite ore

The studied Sabzevar magnetite ores are heterogeneous in texture and consist of euhedral to subhedral magnetite crystals with sizes from 5 to 500  $\mu\text{m}$  (Fig. 4.1c). The silicate matrix is composed of serpentine (70-80 vol.%), andradite (15-20 vol.%) and minor chlorite (< 5 vol.%). Relicts of spinel surrounded by polycrystalline magnetite were found within all investigated magnetite ore samples. The texture of these relict spinels can either be porous (Figs. 4.4e and 4.4f) as defined for serpentinite-hosted spinel or massive (Fig. 4.3g). Magnetite around porous chromite can either be small newly-formed grains (Fig. 4.3f) or form a thick polycrystalline rim with serpentine +/- brucite inclusions (Fig. 4.3e). Euhedral magnetite

crystals can also be found as inclusion in andradite crystals (Fig. 4.3h). In a few cases, individual andradite-rich veins cut through the magnetite ore. Sulfide minerals are sporadically dispersed in the Sabzevar magnetite ores. Pentlandite,  $(\text{Fe,Ni})_9\text{S}_8$ , with subordinate heazlewoodite,  $\text{Ni}_3\text{S}_2$ , and chalcopyrite are common sulfides. Pentlandite and heazlewoodite occur mainly as anhedral to subhedral inclusions with variable sizes and/or as large aggregation in magnetite crystals (Fig. 4.3i).

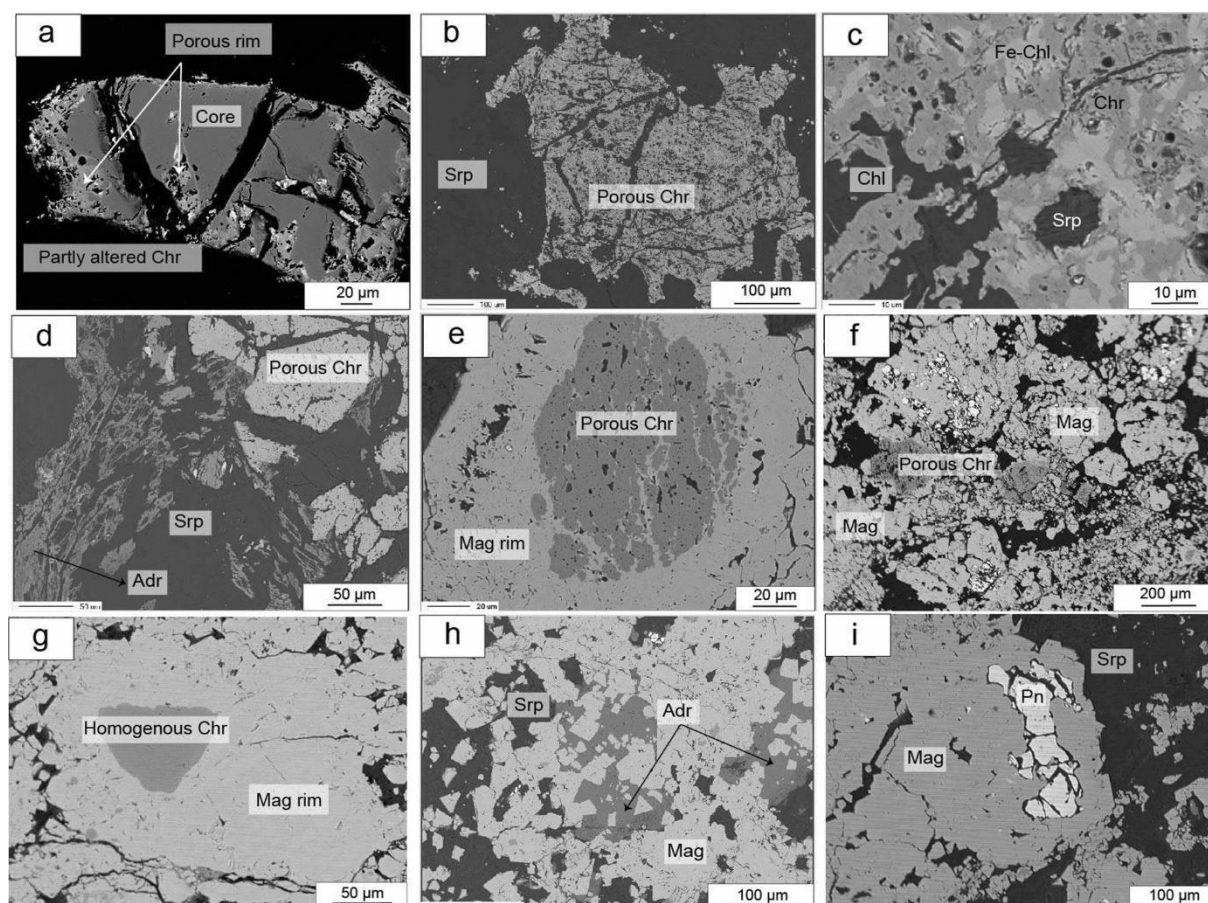


Fig. 4.3. Backscattered-electron images of the Sabzevar host serpentinite (a–d) and magnetite ore (e–i). a partly altered chromite; b anhedral porous chromite; c close-up of porous chromite with irregular patches of Fe-chromite and associated serpentine and chlorite inclusions; d Skeletal andradite surrounding chromian spinel; e Relict of porous chromian spinel with thick magnetite rim; f Porous chromite associated with mylonitized magnetite; g Homogenous chromite with thick magnetite rim; h Euhedral magnetite crystals associated with andradite; i Individual inclusion of pentlandite in magnetite crystals from magnetite ore. *Chr* chromian spinel, *Mag* magnetite, *Srp* serpentine, *Chl* chlorite, *Adr* andradite, *Pn* pentlandite

## 4.5. Mineral chemistry

### 4.5.1. Spinel

The composition of spinel from magnetite ores and from the host serpentinites have been plotted in a trivalent-cation ( $\text{Fe}^{3+}$ -Cr-Al) ternary plot as well as in binary  $X_{\text{Cr}} - X_{\text{Mg}}$  and  $\text{Fe}^{3+}/(\text{Fe}^{3+} + \text{Fe}^{2+}) - X_{\text{Mg}}$  diagrams (Fig. 4.4). The cores of partly altered Al-spinel have the lowest chromium number and the highest Al content. They display compositions that are typical for spinel from ophiolitic forearc peridotites (Fig. 4.4; Table 4.S1).

In the serpentinite samples, spinels from the porous rim of partly altered Al-spinel and from porous Cr-spinel matrix share strong chemical similarities and are most likely genetically related. They both plot in the same regions of the compositional diagrams shown in Fig. 4.4. They are relatively depleted in Al compared to the partly altered Al-spinel and enriched in chromium relatively. Patches of porous chromite formed by transformation of the Cr-spinel porous matrix have also been plotted in Fig. 4.4. The composition of porous and homogeneous chromite cores in the magnetite ores strongly resembles that of Cr-spinel from the serpentinite samples (Fig. 4.4).

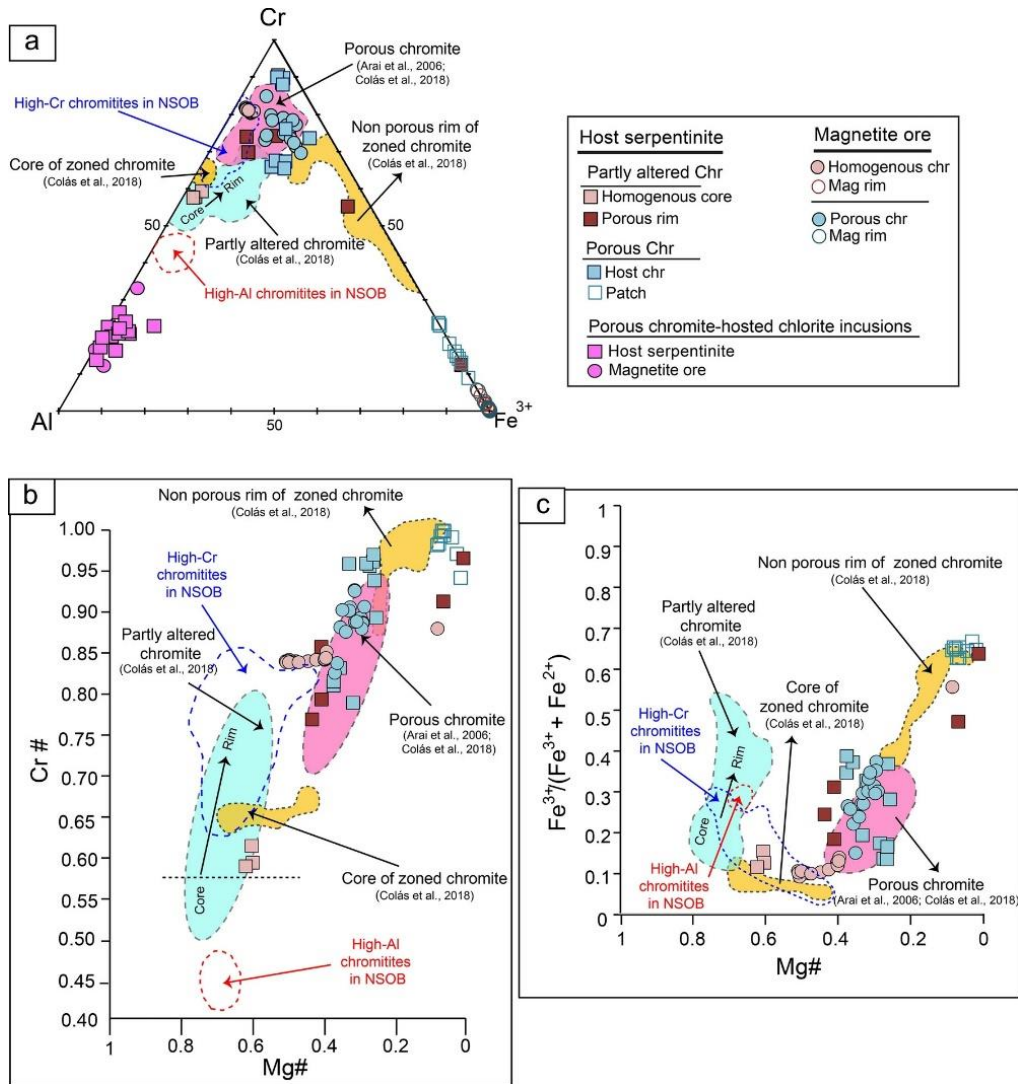


Fig. 4.4. Compositional plots of spinels on (a) ternary diagram Cr-Al-Fe<sup>3+</sup>; (b) a X<sub>Cr</sub> versus X<sub>Mg</sub> diagram; (c) Fe<sup>3+</sup>/(Fe<sup>3+</sup> + Fe<sup>2+</sup>) versus X<sub>Mg</sub>. Reference fields of podiform chromitites in the eastern sector of the Sabzevar ophiolite (Shafaii Moghadam et al. 2015; Eslami et al. 2018b, a; unpublished data from the first author) are shown for comparison.

X-ray elemental maps, along with point microanalyses, were collected using the EPMA on homogeneous and porous Cr-spinel relicts rimmed by magnetite (Figs. 4.5 and 4.6), from the magnetite ore samples. The various elemental maps obtained on homogeneous chromite confirms its chemical homogeneity at the minor elements level. On a chemical basis (Table 4.S2; Figs. 4.5 and 4.6), two generations of magnetite can be distinguished. A first magnetite rim is observed (called “magnetite-I rim”) from the Cr-spinel interface, which has a thickness of ~ 20  $\mu\text{m}$  and displays a  $\text{SiO}_2$  content <1 wt.%, a  $\text{Cr}_2\text{O}_3$  content of 2.70-3.69 wt.% and a  $\text{TiO}_2$  content > 1 wt.%. A second magnetite rim (called “magnetite-II rim”) has a variable thickness ranging from 40 to 200  $\mu\text{m}$ , and shows a different composition reflecting the presence of inclusions at the nanoscale. The  $\text{SiO}_2$  content is higher and ranges from 1.21 to 2.35 wt.%. The  $\text{MgO}$  and  $\text{Cr}_2\text{O}_3$  contents are variable in the 0.06-0.12 wt.% and 0.03-1.62 wt.% range, respectively. The  $\text{TiO}_2$  content is lower (< 0.47 wt.%). Titanium is heterogeneously distributed within the magnetite-I rim, with the highest concentration close to the chromite – magnetite-I boundary. On the elemental maps, the magnetite-I/II interface is sharp and seems to outline former crystal faces. Porous chromite shows higher Al, Mn, Ni and V in comparison with homogenous chromite relicts (Table 4.S2). Mg- and Al-rich spotty zones in porous chromite outline the numerous chlorite inclusions (Fig. 4.6).

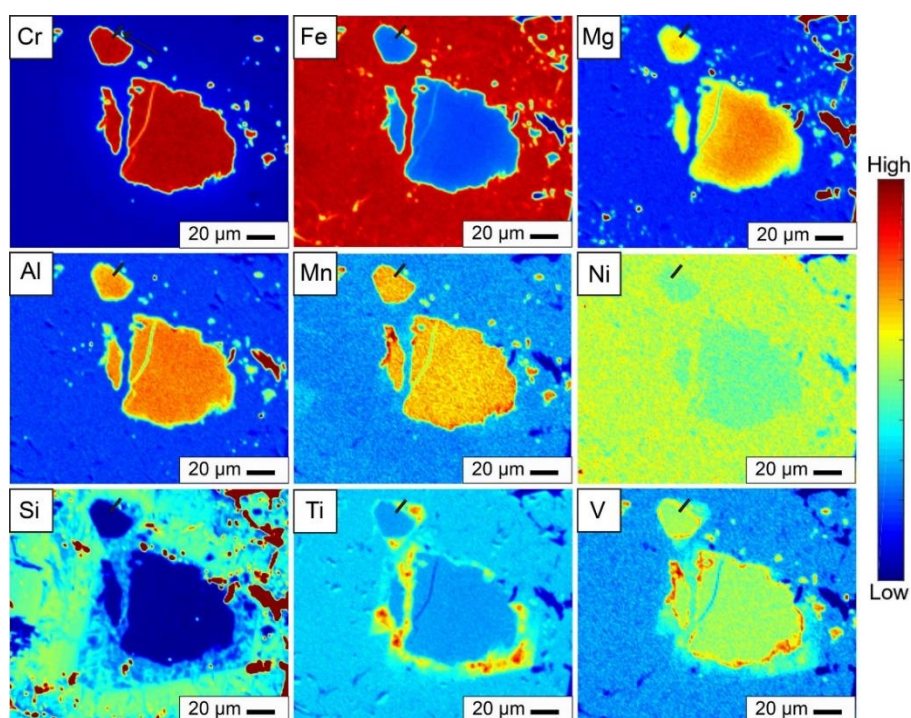


Fig. 4.5. Multi-element (WDS-EDS) mapping of homogeneous chromian spinel relict in magnetite ore (sample MG15)

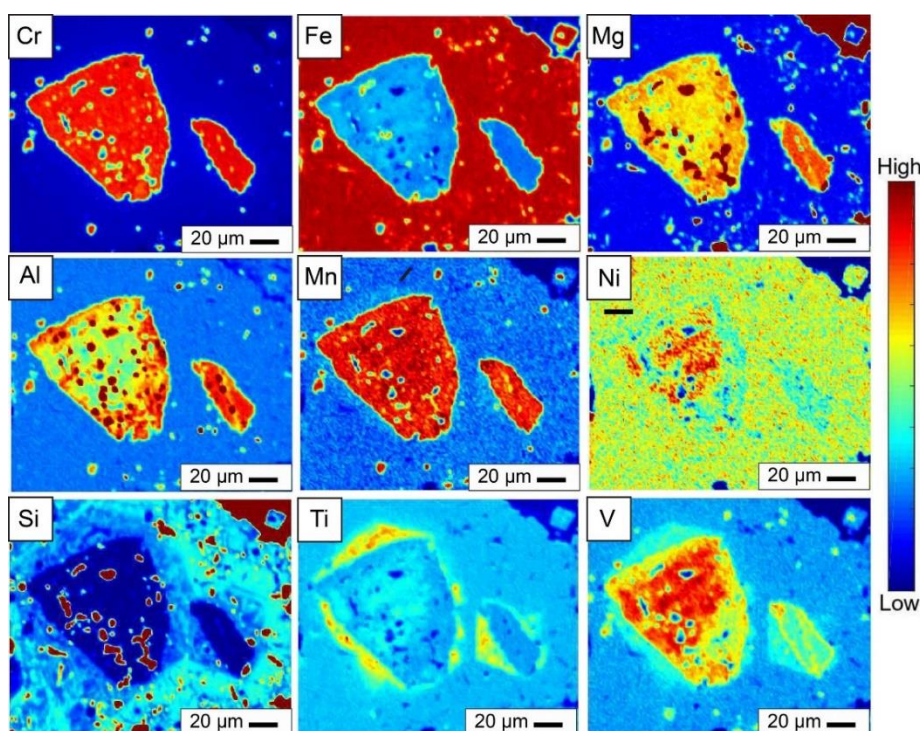


Fig. 4.6. Multi-element (WDS-EDS) mapping of a porous chromian spinel relict in magnetite ore (sample MG15)

#### 4.5.2. Sulfides and alloys

Chemical compositions of sulfides and alloys in the Sabzevar magnetite ores and associated serpentinites are given in Fig. 4.7 and Table 4.S3. Pentlandite displays a wide range of Co (7.53 - 27.12 wt.%), Ni (18.56 - 36.67 wt.%) and Fe (17.34 - 29.96 wt.%) contents. There is no obvious relationship between composition and textural position of pentlandite. Average composition of heazlewoodite shows Ni (74.03 wt.%), S (27.37 wt.%) and Co (0.17 wt.%). Fe–Ni alloys from the Sabzevar serpentinites show a large range of compositions from  $\text{Ni}_{73}\text{Fe}_{19}$  to  $\text{Ni}_{80}\text{Fe}_{26}$ , which can be classified as awaruite ( $\text{Ni}_3\text{Fe}$ ).

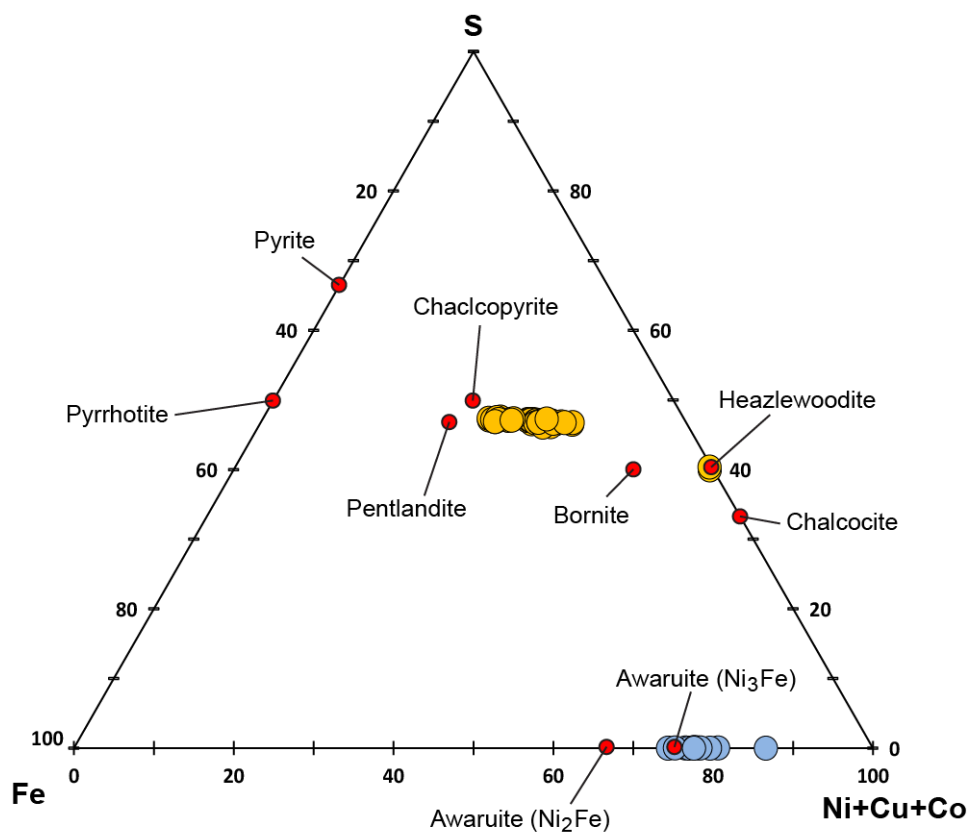


Fig. 4.7. Chemical composition of the analyzed sulfides of the studied magnetite ore and alloys in host serpentinite

### 4.5.3. Andradite, chlorite and brucite

Andradite in both magnetite ore and host serpentinite have similar chemical compositions (Table 4.S4). They are chemically homogeneous and characterized by TiO<sub>2</sub> content < 0.30 wt.%, Al<sub>2</sub>O<sub>3</sub> contents ranging between 0.40–1.15 wt.%, Cr<sub>2</sub>O<sub>3</sub> contents between 0.04 - 1.20 wt.% and Fe<sub>2</sub>O<sub>3</sub> contents between 28.76 - 30.24 wt.% (Table 4.S5). Chlorite inclusions in chromian spinels from the magnetite ores have higher FeO contents (2.55 - 5.52 wt.%) compared to those in chromian spinel from the host serpentinite (Table 4.S5). Chlorite inclusions in chromian spinel from both magnetite ore and host serpentinite display relatively high Cr<sub>2</sub>O<sub>3</sub> content (2.30 - 5.02 wt.%) and variable Al<sub>2</sub>O<sub>3</sub> content (6.66 - 14.74 wt.%) (Fig. 4.4a). Brucite in the Sabzevar host serpentinite has X<sub>Mg</sub> values ranging from 0.60 to 0.75.

## 4.6. Nanoscale characterization of the magnetite rims

A lamella was cut across the interface between Cr-spinel with homogeneous texture and magnetite from the magnetite ore (sample MG15; black arrow in Fig. 4.5) for TEM characterization to gain insight on the Cr-spinel alteration processes at the nanoscale. The contact between Cr-spinel with homogeneous texture and magnetite can be divided into four zones (Fig. 4.8).

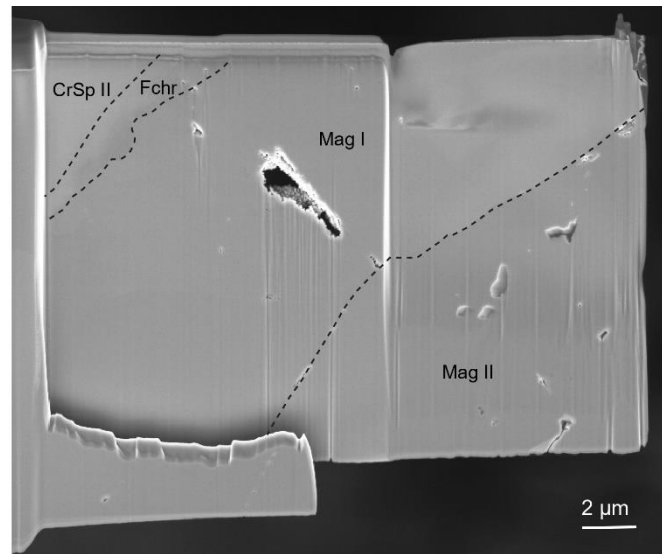


Fig. 4.8. BSE image of FIB section made across at the interface between magnetite and homogeneous Cr-spinel II

At the lamella scale, Cr-spinel is homogeneous in composition, Al-, Cr- and Mg-rich and relatively depleted in Fe (Table 4.S2; Fig. 4.9). This composition is consistent with EPMA analyses performed on the same grain (Fig. 4.4). It contains a few subgrain boundaries.

Automatic crystal orientation mapping reveals a homogeneous orientation in Cr-spinel with a misorientation of less than  $0.5^\circ$  over a distance of 1  $\mu\text{m}$ . STEM-EDS mapping indicates that Cr-spinel is separated from magnetite-I by a  $\sim 1 \mu\text{m}$  thick rim of a phase which could not be resolved with EPMA (Fig. 4.9a). This phase displays a Cr content similar to that of Cr-spinel but contains lower Al and Mg and higher Fe contents (Fig. 4.9b to 4.9g). Such a composition recalls the composition of ferritchromite from the host serpentinite. We therefore use in the following the same nomenclature as for the host serpentinite. The contact between ferritchromite and magnetite-I is sharp on STEM-EDS maps. Locally, the contact is marked with Ti-rich lenses with sizes below 50 nm (Fig. 4.9f) which indicate that Ti is segregated through the precipitation of a Ti-rich phase (e.g., rutile). Bright field and HAADF images do

not allow to locate the Cr-spinel – magnetite-I boundary as clearly as with STEM-EDS mapping (Fig. 4.9a).

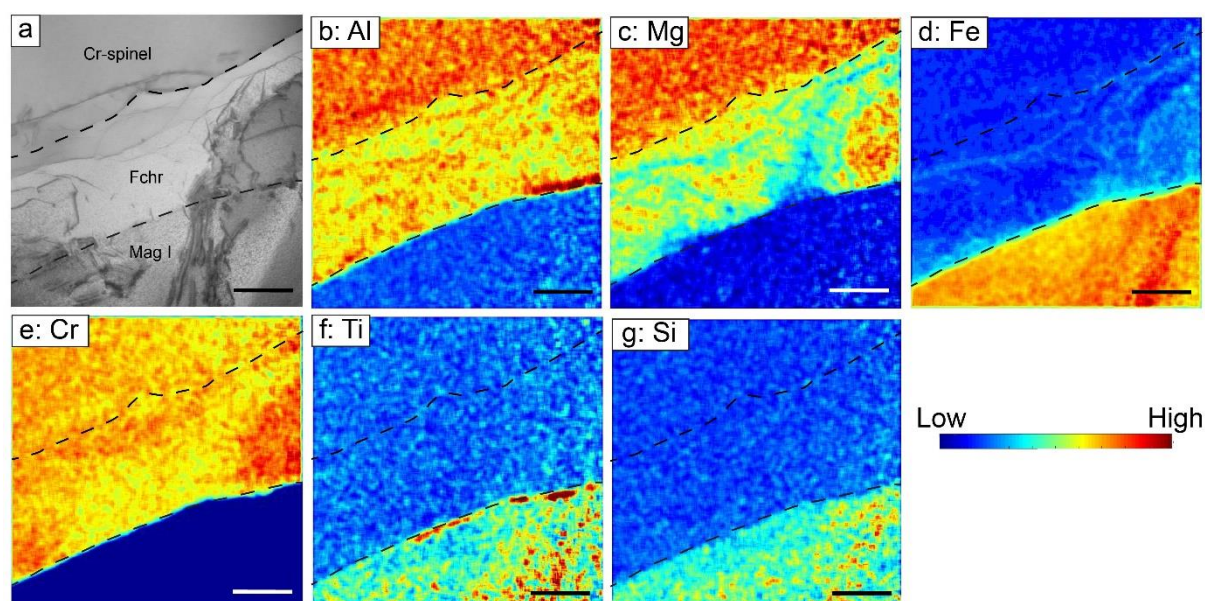


Fig. 4.9. Bright Field Image (a) and EDS-STEM element maps (b–g) of the Cr-spinel/magnetite I contact. The scale bar is 500 nm. *Fchr* ferritchromite, *Mag I* Magnetite I

The misorientation angles extracted from the orientation maps are of less than  $3^\circ$  and  $0.5^\circ$  at the Cr-spinel – ferritchromite and the ferritchromite – magnetite-I interfaces, respectively (Fig. 4.10a). The comparison of electron diffraction patterns (SAED) on both sides of the interface is in line with small misorientation angles. Cr-spinel and ferritchromite display coherent planes (Fig. 4.10b). The high resolution TEM images also show some continuous planes across the interface (Fig. 4.11a). The SAED patterns of ferritchromite and magnetite-I are identical, indicating perfect epitaxy (Fig. 4.10c).

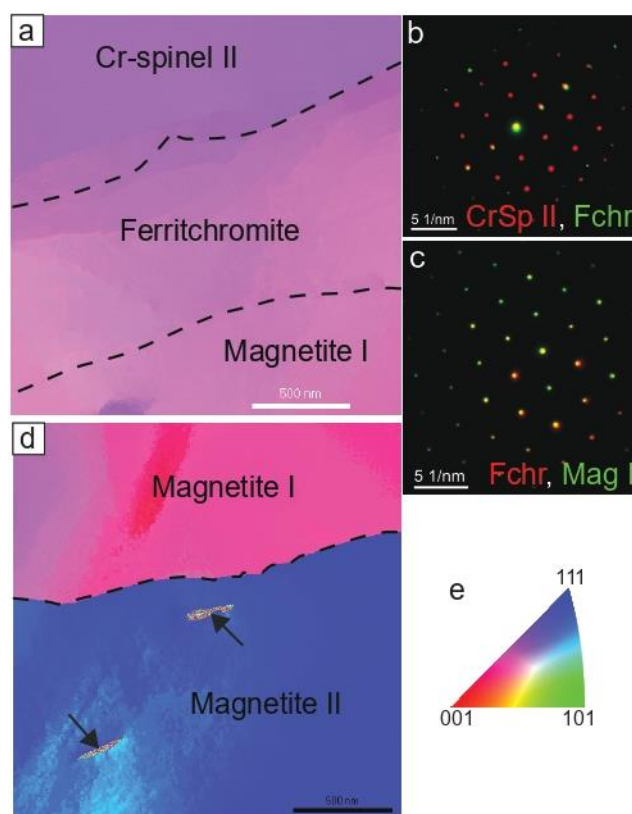


Fig. 4.10. Orientation maps and selected area electron diffraction (SAED) in the reaction zone around Cr-spinel. (a) orientation map in the same region as Fig. 4.10, in which the transition from Cr-spinel to magnetite I is observed. (b) superimposed SAEDs of Cr-spinel and ferritchromite. (c) superimposed SAEDs of ferritchromite and magnetite I. (d) orientation map in the same region as Fig. 4.10 at the magnetite I/magnetite II contact. e colour-coded inverse pole figure used for displaying orientation in a and d. The boundaries between the different phases were determined with the EDS-STEM maps. *CrSp* Cr-spinel, *Fchr* ferritchromite, *Mag I* magnetite I

Magnetite-I is ~ 10  $\mu\text{m}$  thick in the investigated region (Fig. 4.8). It is homogeneous in composition and enriched in Si and Ti compared to Cr-spinel and ferritchromite. The nanostructure of magnetite-I is complex with micrometer-wide grains surrounding regions composed of densely packed 20 nm-wide grains (Fig. 4.12).

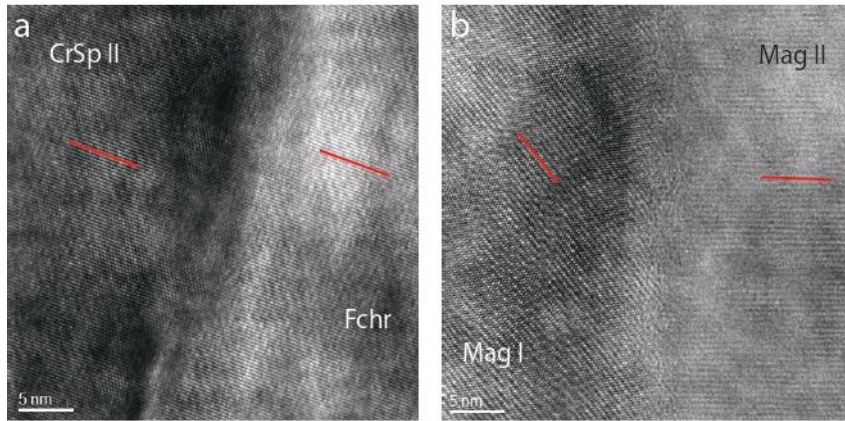


Fig. 4.11. High-resolution TEM images. (a) contact between Cr-spinel and ferritchromite. (b) contact between magnetite I and magnetite II. The red lines indicate the main orientation of the lattice planes. *CrSp* Cr-spinel, *Fchr* ferritchromite, *Mag I* magnetite I, *Mag II* magnetite II

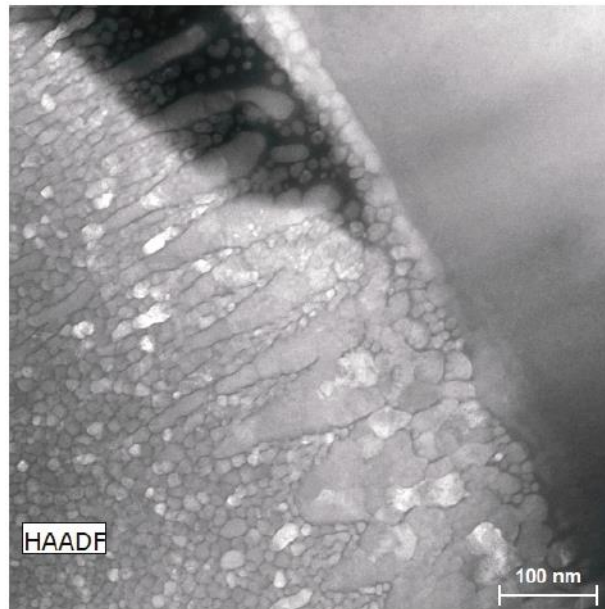


Fig. 4.12. HAADF image of magnetite I showing densely packed 20 nm-wide grains

The contact between magnetite-I and magnetite-II is sharp. The two magnetite types display similar composition (Fig. 4.13). Magnetite-II contains 100 nm-wide and 300 nm-long, Fe-poor and Mg- and Si-rich inclusions, probably made by serpentine. These inclusions are likely responsible for the high Si contents measured by EPMA (Figs. 4.5 and 4.6). The orientation of magnetite-I and magnetite-II is different with a misorientation angle between the two phases of  $35^\circ$  (Fig. 4.10d). This is confirmed on high-resolution images which show a steep angle between the lattice planes in magnetite-I and magnetite-II (Fig. 4.11b).

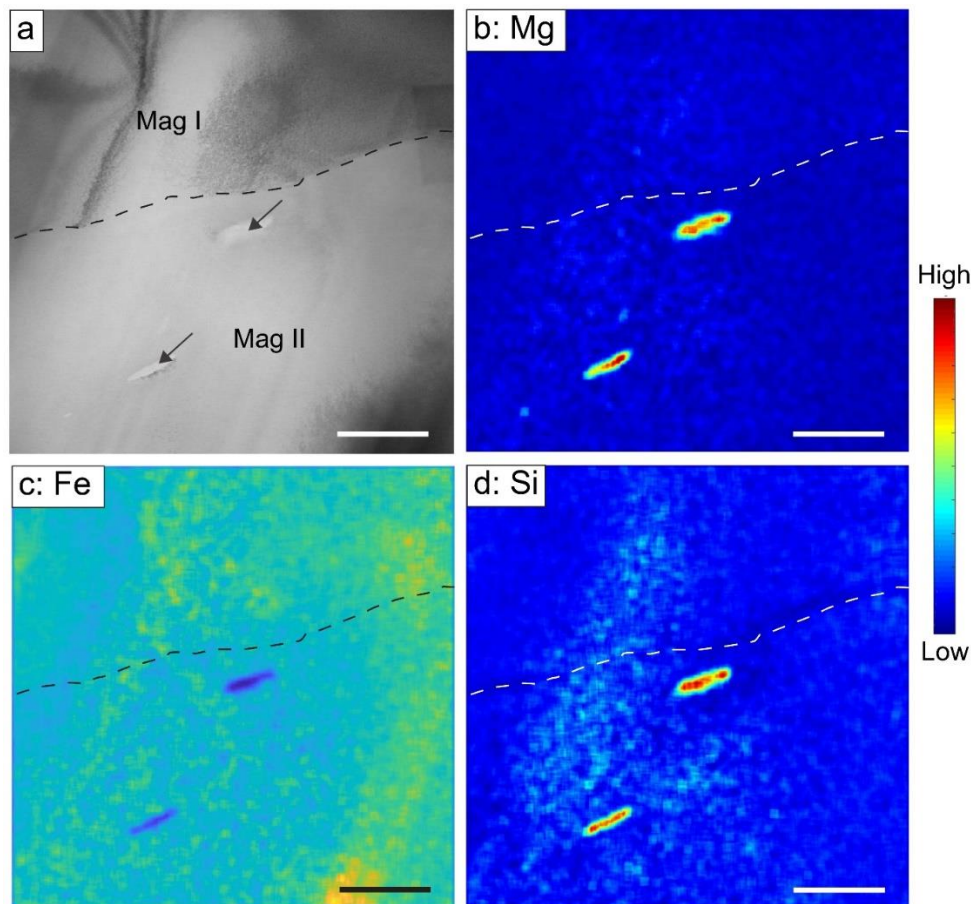


Fig. 4.13. Bright Field Image (a) and EDS-STEM element maps (b–d) of the magnetite I/magnetite II contact. The arrows indicate the location of silicate inclusions in magnetite II. The scale bar is 500 nm. *Mag I* magnetite I, *Mag II* magnetite II

#### 4.7. Thermodynamic modelling

Phase relationships have been calculated on the Sabzevar serpentinite composition at 500 MPa and plotted in a  $\Delta\log_{10}fO_2$ -T diagram (Fig. 4.14). Among the main features of this calculation, there is the composition of the spinel solid solution(s),  $(Mg,Fe)(Al,Fe,Cr)_2O_4$ , which contains two redox sensitive elements, Fe and Cr, and which is thus expected to be  $fO_2$  dependent. Furthermore, a solvus in the  $Fe(Fe,Cr)_2O_4$  spinel subsystem has been reported below ca. 550°C (Sack and Ghiorso, 1991), which is thus relevant to the temperature range investigated here. The incorporation of chromium in garnet is also accounted for by the garnet solid-solution considered here. Although chromium-bearing chlorite is also likely to share phase relationships with Cr-spinel and Cr-bearing garnet, no Cr-chlorite component has been considered in the chlorite solution used in the present calculation. Consequently, the stability field of chlorite might be larger than predicted here.

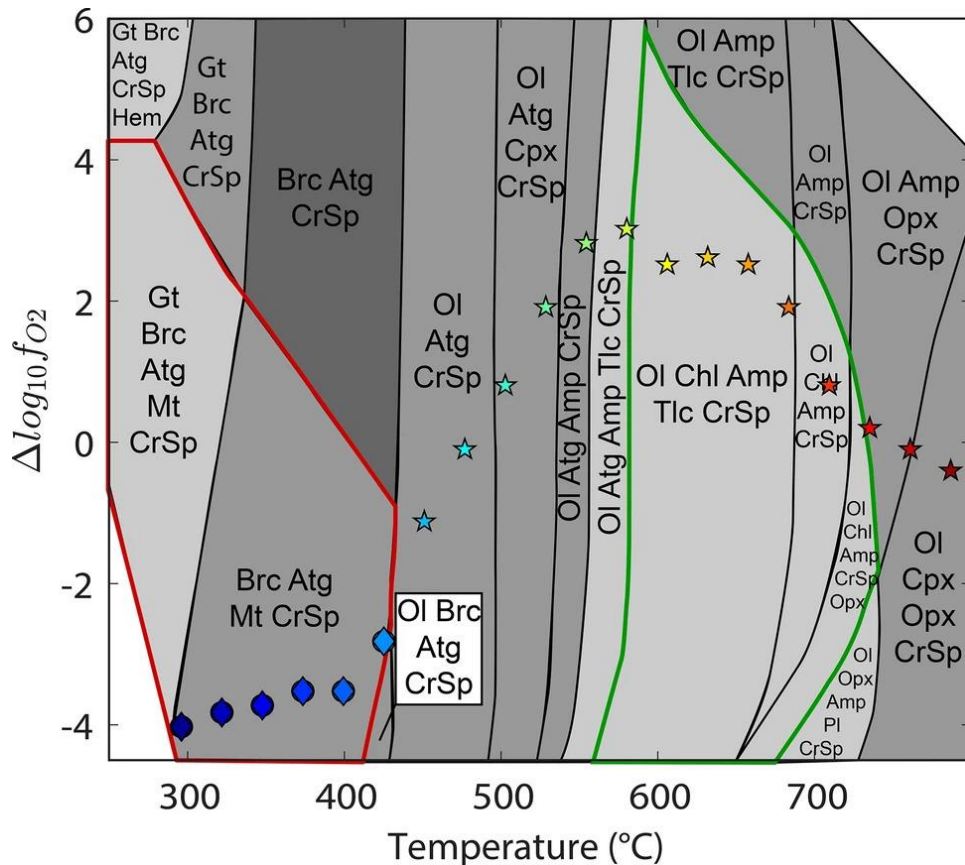


Fig. 4.14. T vs.  $\Delta\log_{10}f_{O_2}$  section for the Sabzevar serpentinite composition. The symbols indicate an expected evolution of  $\Delta\log_{10}f_{O_2}$  during cooling. They corresponds to an internally buffered oxygen fugacity (fixed by the olivine-Mg-silicate-spinel assemblage at  $T > 420$  °C and the peridotite + pure water assemblage at  $T < 420$  °C; see text for details). Stars are used as symbols when the calculation predicts the formation of a single phase. When two immiscible solid solutions are predicted to form, the composition is displayed with circles and diamonds for the Cr-rich and  $Fe^{3+}$ -rich solid solutions, respectively. The same symbols are used to display spinel composition in Fig. 4.15a. The red bold line separates the fields containing one (CrSp) and two (CrSp + Mt) spinels. The green bold line surrounds the chlorite stability field. *Gt* garnet, *Brc* brucite, *Atg* antigorite, *CrSp* Cr-bearing spinel, *Hem* hematite, *Ol* olivine, *Mt* magnetite, *Amp* amphibole, *Cpx* clinopyroxene, *Opx* orthopyroxene, *Tlc* talc, *Chl* chlorite

We computed the composition of the spinel solid solution(s) along a cooling path divided in two parts (Fig. 4.14). The oxygen fugacity in the high temperature part of the path (800 to 420°C) is internally buffered by the olivine – Mg-silicate – spinel assemblage (Frost, 1985). The low-temperature part of the path (420 to 300°C) considers a serpentization reaction in which the amount of oxygen is fixed. The bulk rock + fluid composition is assumed to be the one of a ferrous peridotite plus pure water. Such a path provides a first-order estimate

of the effect of temperature on spinel composition. At high temperature and high  $fO_2$  (800°C and  $\Delta\log_{10}fO_2 = 0$ , respectively), the single spinel solid-solution contains mainly Mg as divalent cation (Fig. 4.15b) and ~ 60 % of Al as trivalent cation (Fig. 4.15a), leading to simplified composition of  $Mg(Fe_{0.1},Cr_{0.3},Al_{0.6})_2O_4$ . At  $T < 730$  °C, the Al content of the spinel strongly decreases due to the formation of chlorite. As a result, the  $X_{Cr}$  of the spinel increases from 0.6 at ~730°C to > 0.95 at ~ 600°C and below. At  $T < 400$ °C, two spinels are predicted to form in association with brucite,  $(Mg,Fe)(OH)_2$ . The first type of spinel has a composition close to that of the high temperature spinel. Its  $Cr/(Cr+Fe^{3+})$  ratio progressively increases from ~ 85% at 400°C to 95 % at 350 °C leading to an  $Mg(Fe_{0.05},Cr_{0.95})_2O_4$  composition. The second type of spinel is close to the magnetite end-member since it contains mainly  $Fe^{3+}$  as trivalent cation and  $Fe^{2+}$  as divalent one. The formation of this near-endmember magnetite occurs at the expense of olivine through serpentinization reactions (Fig. 4.14). The amount of Mg among the divalent cations decreases from 70 down to 0 mol.% from 430 to 300 °C, respectively. Simultaneously, the molar fraction of brucite in the solid increases from 6 to 84 mol.% (0.1 to 5.9 wt.%; Fig. 4.16).

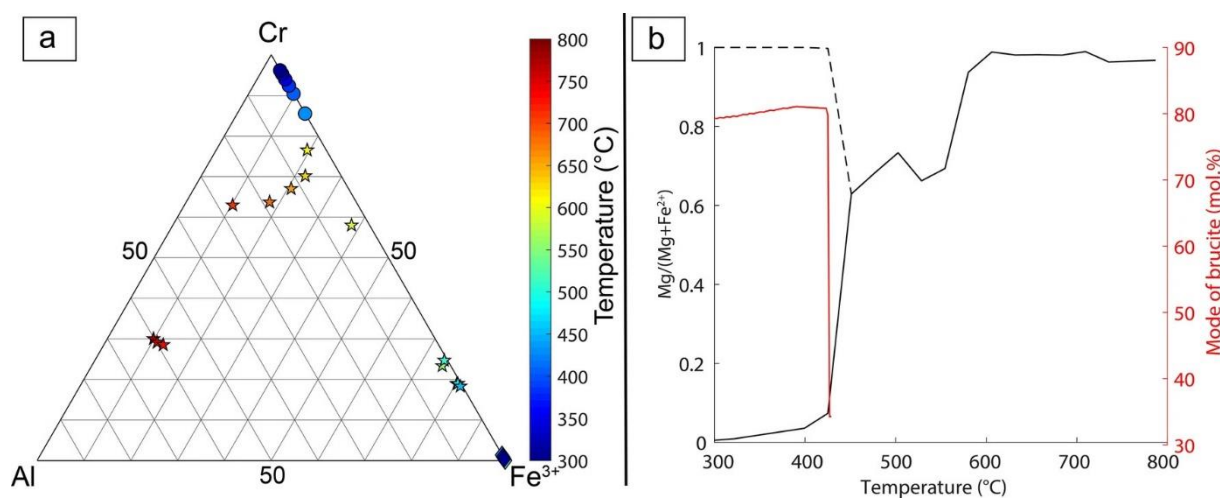


Fig. 4.15. Evolution of spinel composition during cooling and oxygen fugacity decrease. The composition is displayed along a typical peridotite cooling path. The temperature and  $\Delta\log_{10}fO_2$  conditions along this path are provided in Fig. 4.14 with the same symbols. **a** Calculated composition in the Cr–Al– $Fe^{3+}$  ternary diagram. Stars are used as symbols when the calculation predicts the formation of a single phase. When two immiscible solid solutions are predicted to form, the composition is displayed with circles and diamonds for the Cr- rich and  $Fe^{3+}$ -rich solid solutions, respectively. **b** Calculated  $Mg/(Mg + Fe^{2+})$  ratio and brucite molar fraction along the investigated path. The  $Mg/(Mg + Fe^{2+})$  ratios of the Cr-rich and  $Fe^{3+}$ -rich spinel solid solutions are displayed with dashed and plain lines, respectively.

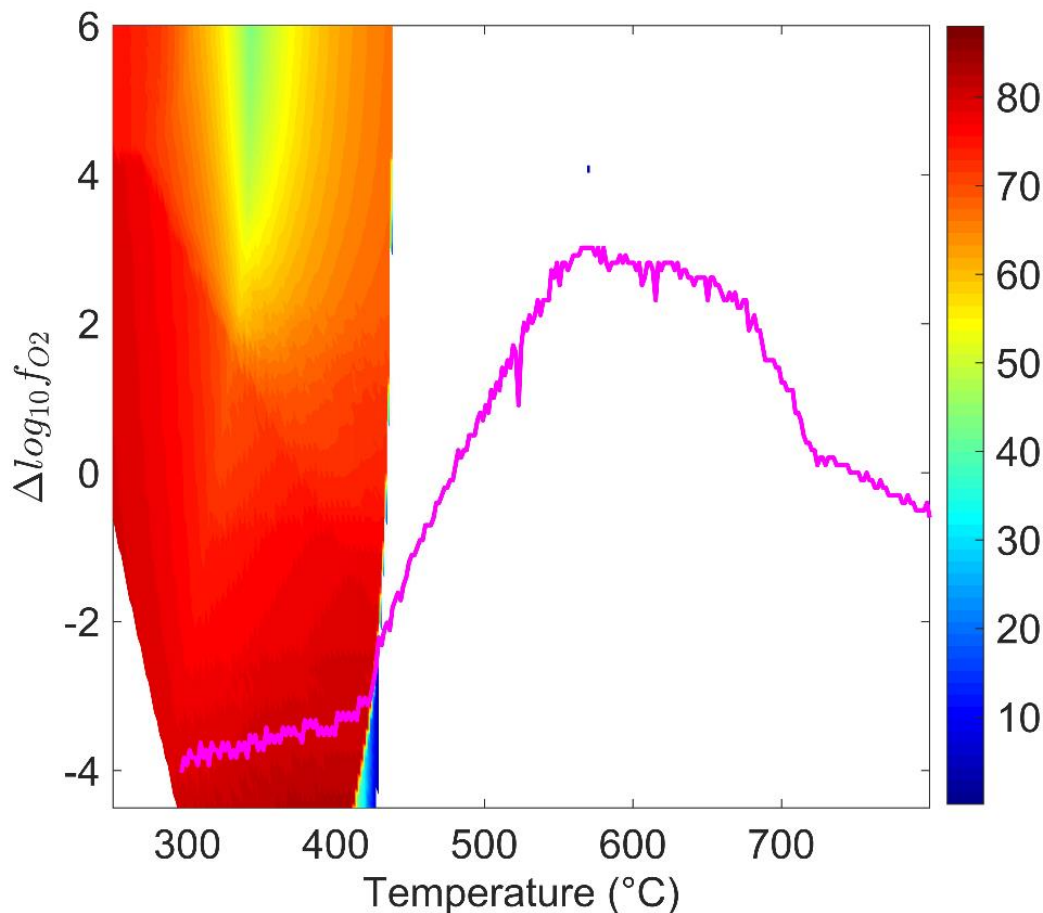


Fig. 4.16. Evolution of brucite composition as a function of temperature and  $\log_{10}f_{O_2}$ . The pink bold line corresponds to the cooling path used to computed spinel composition (see text for details).

The composition of the aqueous solution has also been calculated for the same bulk-rock composition and in the same  $\Delta\log_{10}f_{O_2} - T$  range. The pH is slightly alkaline at low temperatures, as expected for water interacting with an ultramafic lithology (Galvez et al., 2016). The pH decreases with temperature from 2.5 pH units above neutral at 250°C to 0.5 pH units above neutral at 800°C. The fraction of  $H_2$  in the solvent increases as the temperature increases and as the oxygen fugacity decreases. The concentration of dissolved iron is rather constant around  $10^{-3}$  mol/kg along the cooling path investigated here (Fig. 4.17a). The dominant iron-bearing aqueous species are ferrous iron species.  $HFeO^{2-}_{,aq}$  dominates at T below 500 °C whereas  $Fe(HSiO_3)^+$  dominates above 500 °C. Chromium solubility is between 7 and 8 orders of magnitude lower than iron solubility (Figs. 4.17b, 4.18 and 4.19). Therefore, Cr must be considered as an insoluble element in the conditions investigated here. The Cr aqueous species

are dominated by trivalent chromium species, Cr(III), at relatively low oxygen fugacity with  $\text{Cr(III)}/(\text{Cr(II)} + \text{Cr(III)} + \text{Cr(VI)}) > 99\%$  in most of the investigated  $\Delta\log_{10}f_{\text{O}_2} - T$  domain. Among the Cr(III) species,  $\text{Cr(OH)}_{4,\text{aq}}^-$  dominates. Cr solubility is approximately one order of magnitude higher at temperatures above 500 °C than at low temperature along the cooling path investigated here.

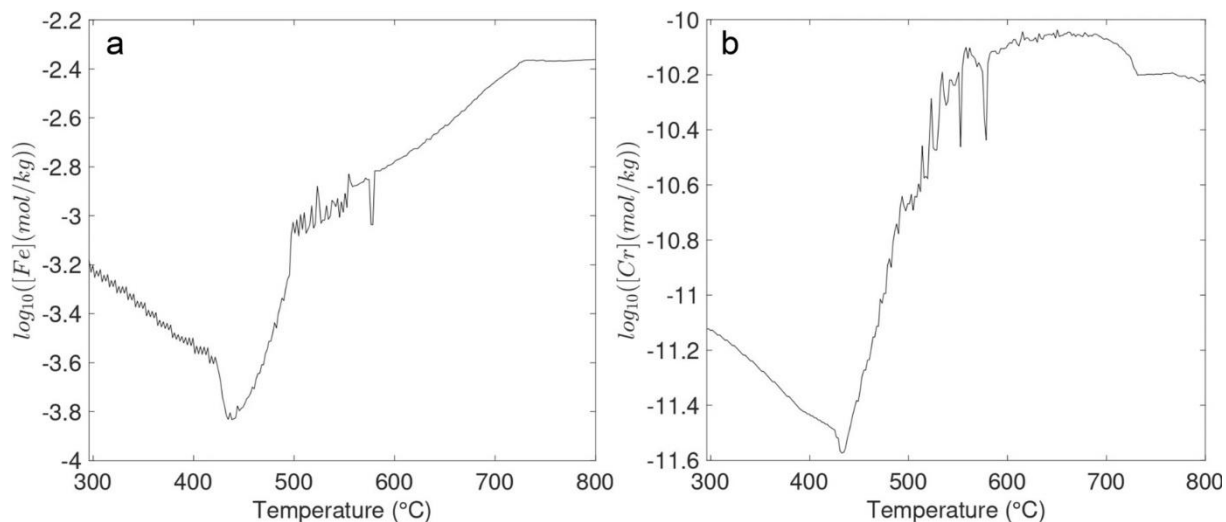


Fig. 4.17. Solubilities (mol/kg) as a function of temperature along the cooling path (see text and Fig. 4.14 for details about the path). (a) Fe solubility. (b) Cr solubility

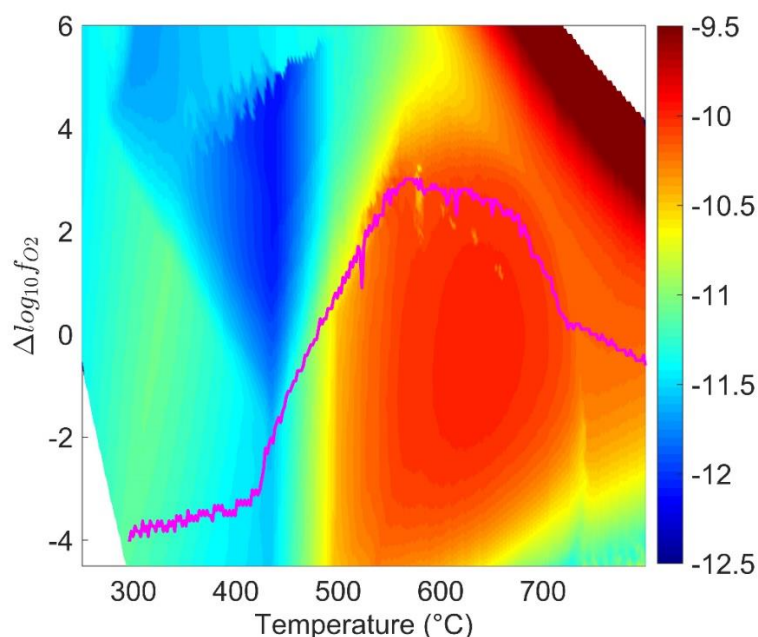


Fig. 4.18. Cr solubility as a function of temperature and  $\log_{10}f_{\text{O}_2}$ . The pink bold line corresponds to the cooling path used to computed spinel composition (see text for details).

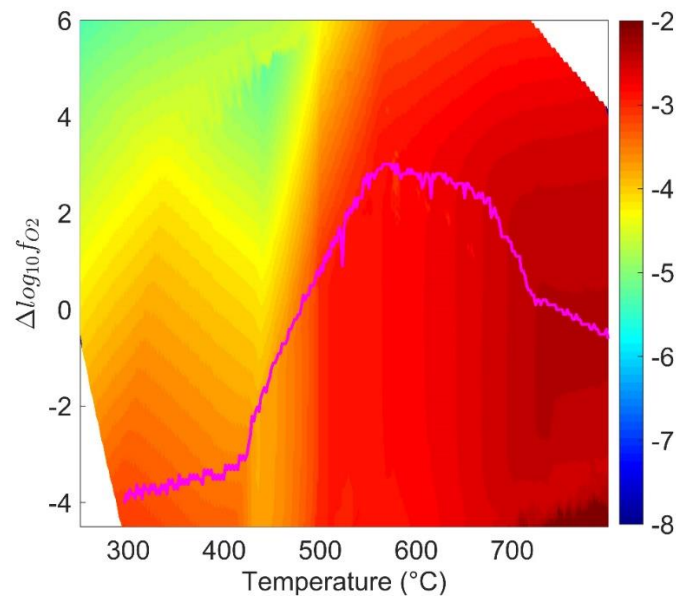


Fig. 4.19. Fe solubility as a function of temperature and  $\log_{10}f_{O_2}$ . The pink bold line corresponds to the cooling path used to computed spinel composition (see text for details).

## 4.8. Discussion

### 4.8.1. Two-stage spinel alteration process

Three types of spinel were identified based on their microtexture and composition in the serpentinite hosting the magnetite ores. We described the first type of microtexture as *partly altered spinel*, which consists in a *homogeneous* Al-Cr spinel core ( $X_{Cr}$  of 0.6). The Al-Cr spinel core composition falls at the end of the compositional range of magmatic spinels reported in the Sabzevar ophiolite podiform chromitite deposits (Fig. 4.4), which derived from island arc tholeiites with boninitic affinity (Shafaii Moghadam et al., 2015; Eslami et al. 2018b). Both textural relationships and composition suggest that the Al-Cr spinel core in the partly altered type is a relict of magmatic spinel that was possibly altered during magmatic processes. The magmatic part of the spinel history will however not be discussed here. We will consider that these residual cores correspond to a first generation of spinel and will thus be named (Cr,Al)-spinel-I in the following.

(Cr,Al)-spinel-I is partly replaced along rim and cracks by a *porous rim* composed of a secondary Cr-spinel, or Cr-spinel-II, matrix ( $X_{Cr}$  of= 0.8) containing voids partially stuffed with Al-bearing hydrous silicate +/- brucite. Besides the partly altered texture, other spinel-rich areas are found which are, texturally, entirely porous (i.e., with no homogeneous core). Cr-spinel-II of the porous rim of partly altered spinel and the spinel that composes the matrix of those fully

porous areas have also similar compositions. This suggests that these two spinel types are genetically related. The absence of a homogeneous core in that case is interpreted as the result of the complete replacement of (Cr,Al)-spinel-I leaving no relict behind in contrast to partly altered (Cr,Al)-spinel textures. Therefore, we did not distinguish between the secondary Cr-spinels (Cr-spinel-II) in both textural types.

At the micrometer scale, the chromite found in the magnetite ore displays two types of microtextures. They are either anhedral with a homogeneous composition (Fig. 4.5) or made by an aggregate of subgrains leading to a porous microtexture (Fig. 4.6). The homogenous spinel grains are surrounded by a magnetite rim, whereas such a rim is not systematically found around porous chromite in the magnetite ores. The regions where rims are not found are strongly deformed. This may indicate cataclasis, leading to a loss of the microtextural information necessary to link chromite and magnetite formations. All chromite grains have identical composition similar to Cr-spinel-II from the host serpentinite (Fig. 4.4). Moreover, some of them display a similar porous texture. Therefore, their formation probably originates from the reaction of the same type of magmatic spinels as in the serpentinite host. In that respect, we tentatively categorized them as Cr-spinel-II as well, even though, we did not find patches of magnetite and/or ferritchromite in the porous chromite found in the magnetite ores. Indeed, magnetite only occurs as a rim around the Cr-spinel-II core either homogeneous or porous. A  $\sim 1 \mu\text{m}$  thick spinel phase separates Cr-spinel-II from a first magnetite rim (magnetite-I). Its composition is consistent with the ferritchromite analyses collected in the serpentinite (Al, Mg and Fe contents intermediary between magnetite and Cr-spinel-II; Fig. 4.6). Ferritchromite and magnetite display a perfect epitaxial relationship, suggesting mutual growth during the same alteration stage at the expense of Cr-spinel-II. This type of pseudomorphic replacement of Cr-spinel-II can be considered as an indicator of replacement during a dissolution-precipitation process following Putnis (2002). The misorientation of only few degrees measured at the contact between Cr-spinel-II and ferritchromite is thus interpreted as evidence for replacement of Cr-spinel-II by an assemblage composed of magnetite and ferritchromite.

The microtextural and compositional information point thus towards spinel alteration sequence proceeding in two stages. The magmatic spinel, (Cr,Al)-spinel-I, is first replaced during alteration “Stage I” by a porous chromite, Cr-spinel-II, containing chlorite inclusions, which then reacted during alteration “Stage II” to form magnetite and ferritchromite. This alteration sequence occurred in both the host serpentinite and the magnetite ore. However, the spatial relationship (patches or reaction rims) and the fraction of ferritchromite (high or restricted to a thin layer) differ between the two lithologies. Thermodynamic modelling is used

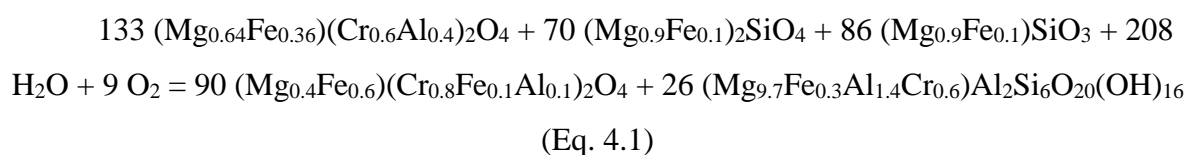
in the following to constrain the temperature and oxygen fugacity having prevailed during the two aforementioned stages of alteration.

#### 4.8.2. Conditions prevailing during the alteration stages

Thermodynamic modelling has been used in the past to predict the evolution of spinel composition as a function of temperature. Gervilla et al. (2012) were able to predict the evolution of the spinel  $X_{Cr}$  during alteration from the spinel solid solution model proposed by Klemme et al. (2009). Colas et al. (2019) calculated the evolution of the spinel  $X_{Mg}$  with another solid-solution model based on the ideal solid solution between Mg and  $Fe^{2+}$  on the tetrahedral site as proposed by Engi (1983). These solid solutions either ignore ferric end-members (magnetite,  $FeFe^{3+}_2O_4$ , and magnesioferrite,  $MgFe^{3+}_2O_4$ ) or they consider ideal mixing between end-members. This has only minor consequences on calculated high-temperature spinel compositions since spinel is  $Fe^{3+}$ -poor at high temperature. However, the consideration of ideal mixing precludes for instance the prediction of the immiscibility gap between magnetite and ferritchromite which is encountered towards low temperatures. We circumvented this problem by introducing the mixing parameters of Sack and Ghiorso (1991) in a reciprocal solid-solution model in *Perple\_X* (Supplementary Materials 1). Thermodynamic modelling with this latter solid-solution model in the Cr-CFMASH system with the composition of the Sabzevar serpentinite provides insights on the temperature –  $\Delta\log_{10}fO_2$  conditions prevailing during spinel alteration.

According to our thermochemical modelling, the composition of chromite is very sensitive to temperature and  $\Delta\log_{10}fO_2$ , as suggested by Evans and Frost (1976). Simulation of spinel composition during a cooling path from 800 down to 300 °C (500 MPa) associated with an increase from 0 to 2 followed by a decrease from 2 to -4 in  $\Delta\log_{10}fO_2$ , shows that the chromite composition drastically changes at ~ 700 and ~ 450 °C (Fig. 4.15). At temperature above ~ 700 °C, a magmatic spinel-like composition is obtained with an  $X_{Cr}$  of 0.4 slightly higher than in the natural samples and an  $X_{Mg}$  close to 1 (Fig. 4.15). Below ~ 700 °C,  $X_{Cr}$  rapidly increases due to the formation of chlorite which incorporates aluminum. The silica necessary to form chlorite is provided by olivine and orthopyroxene. This predicted evolution of the spinel composition is in good agreement with the evolution occurring in the course of alteration “Stage I” as observed in the Sabzevar samples where porous Cr-spinel-II containing chlorite inclusions has formed at the expense of (Cr,Al)-spinel-I. Thermodynamic modelling constrains the alteration “Stage I” to temperatures and  $\Delta\log_{10}fO_2$  comprised between 575 and 725 °C and 0

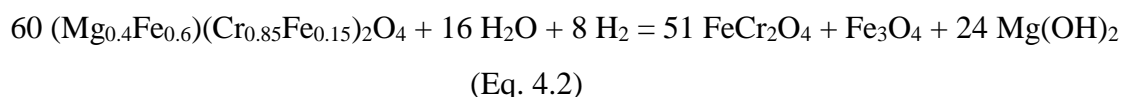
and 3, respectively. Based on thermodynamic modelling and the composition measured in the Sabzevar samples, the following reaction (Eq. 4.1) is proposed for “Stage I”:



Magmatic spinel + olivine + orthopyroxene + water + oxygen = Cr-spinel II + chlorite

The source of oxygen in the system is difficult to infer from the data and could be primary mineral reduction (pyroxene) or water dissociation. The reaction of one mole of magmatic spinel requires at least 1.2 times more moles of olivine and orthopyroxene to reach completion. Merlini et al. (2009) used image analysis on mineral assemblages having recorded a reaction similar to Reaction (Eq. 4.1). They found a correlation between the volume of silicates initially present and the extent of reaction. This observation indicates that reaction progress depends on silica availability rather than on kinetics. In the Sabzevar ophiolite, the olivine + orthopyroxene over magmatic spinel amount ratio is much higher in the serpentinite than in the magnetite ore. However, magmatic spinel is only preserved in the serpentinite, suggesting that silica availability does not control reaction progress alone. The silica source to form chlorite is derived from olivine and orthopyroxene in Reaction (Eq. 4.1) rather than antigorite as proposed by Merlini et al. (2009). This has fundamental implications for the inference of possible alteration scenarios. In the thermodynamic simulation provided here, the chlorite stability field can be entered either through cooling and olivine/orthopyroxene breakdown (retrograde metamorphism) or through heating and antigorite breakdown (prograde metamorphism). We found that the samples of the Sabzevar ophiolite experienced two alteration stages with first the production of Cr-spinel II at the expense of (Cr,Al)-spinel I and then the development of a reaction rim composed of Fe-chromite ( $\text{FeCr}_2\text{O}_4$ ) and magnetite ( $\text{Fe}_3\text{O}_4$ ) around Cr-spinel II. Thermodynamic modelling predicts that alteration Stage I occurs at approximately 650 °C and alteration Stage II below 430 °C (Figs. 4.14 and 4.15). The reaction sequence observed here thus proceeded upon cooling.

The thermodynamic simulation also predicts the formation of brucite during alteration “Stage II”, in agreement with the observations in the serpentinite from the Sabzevar ophiolite. Mg depletion from spinel is compensated through ferric iron reduction to form magnetite according to the following reaction (Eq. 4.2) based on the compositions measured in the Sabzevar samples (in which Al is not considered for simplicity):



Cr-Spinel II + water + dihydrogen = ferritchromite + magnetite + brucite end member

Reaction (Eq. 4.2) is  $f\text{O}_2$  dependent and is favored by reducing conditions, i.e., higher  $\text{H}_2$  partial pressures. This is consistent with the thermodynamic modelling which indicates that the serpentine + brucite + ferritchromite + magnetite assemblage is only stable at  $\Delta\log_{10}f\text{O}_2$  below 2. Serpentinization of olivine during mantle-rock alteration is known to produce  $\text{H}_2$  in the same temperature range as reaction (Eq. 4.2) (McCollom and Bach, 2009). It leads to extremely reducing conditions favoring the precipitation of Fe-Ni alloys (e.g., awaruite; Frost, 1985; Klein and Bach, 2009). We observed awaruite as tiny grains (<2  $\mu\text{m}$ ) close to Cr-spinel-II crystals in the serpentinites of the Sabzevar ophiolite, suggesting that the reducing conditions imposed by serpentinization promoted Reaction (Eq. 4.2) below  $\sim 400^\circ\text{C}$ .

Reaction (Eq. 4.2) produces a volume of ferritchromite which is 57 times larger than the volume of produced magnetite assuming isochemical conditions. This is not consistent with our observation of the magnetite ore where ferritchromite rims are approximately two orders of magnitude thinner than the magnetite rims. This implies that alteration “Stage II” is not isochemical in the magnetite ore and it should involve either Cr depletion or Fe addition. Alteration “Stage II” thus occurred under open system conditions with mass transfer at least over the size of the magnetite ore bodies (> 0.5 m). We use in the following the observed microtextures to provide additional constraints on the mobility of these two elements.

### 4.8.3. Chromite microtexture formation and element mobility

The formation of hydrous phases (chlorite, serpentine and brucite) during spinel alteration implies the presence of an aqueous fluid. Dissolution-precipitation occurring at the mineral interfaces is an efficient process to promote metamorphic reactions and mineral replacement reaction (Putnis and Austrheim, 2010). This type of process will be favored to interpret spinel alteration in the Sabzevar ophiolite.

Our dataset indicates that Cr-spinel-II either forms a porous texture or homogeneous grains. Based on the preservation of magmatic spinel cores rimmed by porous Cr-spinel-II, the development of Cr-spinel-II porous textures seems to imply the inward migration of the magmatic spinel – fluid boundary accompanied by the in-situ precipitation of the secondary

products (mainly Cr-spinel-II and chlorite) at constant Cr and Al content. Cr, which is present as Cr(III), and Al display both low concentration and low diffusivity, they are thus expected to be mostly immobile. Note that this general scheme does not apply if ligands that will complex Al and Cr are present (Huang et al., 2019). These aqueous species have not been considered in our thermochemical modelling. We do not see an indication for such complexation and suggest that the formation of porous textures is controlled by dissolution-precipitation reactions and the limited mobility of Cr and Al compared to that of aqueous Si, Fe and Mg.

The assumption of low Cr and Al mobility used to explain porous replacement textures is challenged by the fact that Cr-spinel-II can also be present as homogeneous area with a size up to 20  $\mu\text{m}$ , with no obvious co-precipitation features.

Owing to the large temperature range estimated for alteration “Stage II”, these larger Cr-spinel-II grains may have formed at the highest temperatures under which diffusive transport is more efficient. Cr and Al transport over larger distances (sub-cm scale) may have been enhanced locally by advection channels. Species transport may also depend on the initial microstructure of the (Al,Cr)-spinel-I which seems to be highly variable in podiform chromitites (Leblanc, 1980).

Alteration “Stage II” in the serpentinite preserves the patchy texture with small Fe-chromite and magnetite grains locally growing at the expense of Cr-spinel-II. In the magnetite ore, such a patchy texture is not encountered since Fe-chromite and magnetite are not found as isolated grains but rather as continuous rims surrounding the entire homogeneous or porous Cr-spinel II grains (Figs. 4.3, 4.5 and 4.6). Such a difference in microtexture may be inherited from the alteration “Stage I” during which homogeneous grains were more prone to form in the magnetite ore than in the serpentinite. The porous texture may favor fluid access and chemical exchange in the serpentinite in comparison to the less permeable homogeneous texture found in the magnetite ore. In the magnetite ore, the successive occurrence of Cr-spinel-II, Fe-chromite and magnetite from the grain center to the rim recalls previous observations in altered ultramafic rocks (Ulmer, 1974; Wylie et al., 1987; Michailidis, 1990; Prabhakar and Bhattacharya, 2013; Barra et al., 2014; Colas et al., 2019). Prabhakar and Bhattacharya (2013) interpreted the formation of ferritchromite as a result of intercrystalline diffusion between Cr-spinel-II and magnetite formed during serpentinization. The changes in composition observed here at the Cr-spinel-II – ferritchromite and ferritchromite – magnetite interfaces are sharp, even at the nanoscale, which is inconsistent with diffusion (Fig. 4.9). Ulmer (1974) observed a similar texture but with a larger ferritchromite rind and thus also ruled out a diffusion process based on the same textural argument. The interpretation of Prabhakar and Bhattacharya (2013)

was based on the fact that the magnetite outer rim does not mimic the Cr-spinel-II rim, as it would be expected for a replacement reaction (Putnis, 2002). We observed the same digitized outer rim of magnetite here. However, based on elemental X-ray maps (Figs. 4.5 and 4.6), collected on the magnetite rim, two distinct magnetite generations of different composition can be distinguished. The first type (magnetite-I) in contact with ferritchromite is Si-poor and Ti- and V-rich. Magnetite-I is surrounded by a second magnetite generation (magnetite-II). The interface between magnetite-I and magnetite-II is sharp and angular and mimics the shape of Cr-spinel-II. Pseudomorphic replacement is confirmed by the small misorientation between Cr-spinel-II and ferritchromite across their common interface. These observations indicate that ferritchromite and magnetite-I are formed through a replacement process (Wylie et al., 1987) during alteration Stage II. The spatial distribution of ferritchromite and magnetite suggests the presence of chemical potential gradients during precipitation. As for alteration “Stage I”, the calculated Cr solubility is low and the dissolved Cr species are trivalent during alteration “Stage I”. Fe is mainly divalent and several orders of magnitude more soluble than Cr. This promotes slow and fast Cr and Fe transports, respectively. As a result, a strong chemical potential gradient in Cr<sub>2</sub>O<sub>3</sub> is expected to develop during the alteration of the Cr-spinel-II whereas the chemical potential gradient in FeO, if any, is expected to be smooth. This generates a supersaturation in ferritchromite only in the vicinity of Cr-spinel-II. The small thickness of ~ 1 μm measured here for the ferritchromite indicates that Cr was almost immobile during the alteration and that the dissolution of Cr-spinel-II was extremely slow, in agreement with the low temperature inferred for alteration “Stage II”. In such conditions, the initial surface of the Cr-spinel-II grain is expected to be close from the actual position of the ferritchromite – magnetite contact. The presence of ferritchromite with a crystal structure and unit-cell parameters similar to magnetite can be used as a template for magnetite growth. Such an epitaxial growth of magnetite on ferritchromite is energetically favored since it circumvents the need for nucleation (Fig. 4.10). The observation of a second magnetite type (magnetite-II), with no orientation relationship with ferritchromite and magnetite-I suggests that magnetite could also precipitate in the serpentine/chlorite matrix during the alteration “Stage II” (Figs. 4.10 and 4.11). The differences in composition measured at the micrometer scale between magnetite-I and magnetite-II is no longer observed at the nanometer scale but Ti-rich and silicate inclusions have been found in magnetite-I and -II, respectively (Fig. 4.13; Deditius et al., 2018). Magnetite-I does not contain silicate inclusions but displays a silica content of ~ 1.23 wt.% (Figs. 4.5 and 4.14), indicating that Si is also incorporated in the magnetite structure. As a result, the micrometer-scale difference in composition between magnetite-I and magnetite-II does not necessary reflect a

difference in fluid composition or temperature during precipitation. It rather indicates different growth mechanisms (pseudomorphism or not) and different locus of precipitation (Cr-spinel II surface or silicate-rich matrix). Silican magnetite has been reported in a wide range of rocks including ultramafic rocks, igneous rocks and banded iron formations (Huberty et al., 2012 and references therein). Ciobanu et al. (2019) have recently reported pseudomorphic rutile inclusions and Mg-bearing silicate inclusions in magnetite, similar to the one reported here.

#### 4.8.4. Iron mobility and magnetite ore formation

Several genetic processes have been invoked for the genesis of serpentinite-hosted magnetite deposits: (i) precipitation from a high-temperature ( $\sim 300\text{--}400\text{ }^{\circ}\text{C}$ ) fluid in a hydrothermal system (e.g. Toffolo et al., 2017.; Khedr and Arai, 2018) ; (ii) low- $T$  ( $100\text{--}300\text{ }^{\circ}\text{C}$ ) serpentinization at high water-rock ratio (e.g. Gahlan et al., 2006; Eslami et al., 2018a); and (iii) metamorphic transformation of pre-existing chromitite with magmatic origin into magnetite (e.g. Paraskevopoulos and Economou, 1980; Rossetti et al., 2009).

The dataset presented here provides additional important constraints on the formation of magnetite ore bodies. Magnetite-I and magnetite-II are formed here during alteration “Stage II” at temperature below  $430\text{ }^{\circ}\text{C}$  and in reducing conditions (oxygen fugacity below the FMQ buffer). These conditions are compatible with serpentinization during which the iron initially contained in olivine and pyroxene is incorporated as  $\text{Fe}^{2+}$  in serpentine and brucite or oxidized and incorporated as  $\text{Fe}^{3+}$  in magnetite and serpentine (McCullom et al., 2009). The distribution of iron between the reaction products is mainly controlled by temperature, with magnetite being the main iron carrier at temperature above  $200\text{ }^{\circ}\text{C}$  (Klein et al., 2009; Malvoisin et al., 2012; Klein et al., 2014). The first magnetite grains formed in hydrothermal processes such as early serpentinization, are likely nano-sized and thus highly reactive (Brunet, 2019). Bach et al. (2006) and Beard et al. (2009) found in serpentinites from the Mid-Atlantic Ridge that iron first precipitates in brucite in the core of the meshes formed during olivine serpentinization. Also, submicrometer magnetite grains have been observed in similar mesh cores observed in natural samples (Rouméjon et al., 2018; Liu et al., 2019; Malvoisin et al., 2020). Iron is then re-mobilized during the dissolution of brucite or tiny magnetite grains and transported out of the center and towards the border of the meshes where magnetite precipitates. Maffione et al. (2014) used magnetic and petrographic data to show that nanograins of magnetite are formed in the incipient stages of serpentinization. The grain size then increases to reach several micrometers at higher serpentinization degrees. Malvoisin and Brunet (2014) reported the

formation of both submicrometer and tens of micrometer-wide magnetite grains during experiments of dunite serpentinization. Iron is thus transported at least at the hundreds of micrometer scale during serpentinization.

Alteration “Stage II” in the magnetite ore provides constraints on the extent of iron mobility during serpentinization. This stage should indeed produce a factor of 57 more ferritchromite than magnetite in volume if the reaction was occurring in a closed system according to Reaction (Eq. 4.2). This proportion is at odds with the observed 50 to 100  $\mu\text{m}$ -wide rim of magnetite-I + magnetite-II and 1  $\mu\text{m}$ -thick rind of ferritchromite at the Cr-spinel II surface. Such a phase proportion requires a pronounced mass transfer between the magnetite ore body and its surrounding, most likely the host serpentinite. We showed above that Cr is immobile and Fe is the main element to be transferred to the magnetite ore. Fe probably originated from direct transport of the  $\text{Fe}^{2+}$  produced during olivine dissolution or from the dissolution of nanosized magnetite grains initially formed in the host serpentinite during early serpentinization (Brunet, 2019). Thermodynamic modelling reveals that the iron content measured in the Sabzevar serpentinite is too low to reproduce the  $\text{Mg}/(\text{Mg}+\text{Fe})$  ratio measured in olivine relicts, suggesting that iron is lost in the peridotite during alteration. Iron transfer requires an iron chemical potential gradient between the host serpentinite and the magnetite ore. Such a gradient can be generated if the energetic barrier to overcome for magnetite precipitation is lower in the magnetite ore than in the serpentinite host. Three processes can contribute to reduce the energetic barrier at the spinel surface. As discussed above, the similarities in crystal structure first allow for an epitaxial growth of magnetite over Cr-spinel - II without a need for nucleation (Fig. 4.10). The growth of the tens of micrometer-wide spinel grains in the magnetite ore is also favored by their smaller interfacial energy compared to the nanograins of magnetite formed during serpentinization (Ostwald ripening). Magnetite formation during serpentinization also requires electron transfer from  $\text{Fe}^{2+}$  to water, leading to water splitting and  $\text{H}_2$  formation. Spinel-structure minerals have been proposed to catalyze this process (Mayhew et al., 2013) due to the high mobility of electrons in their structure (Hamilton, 1958; Skomurski et al., 2010) and to the possibility to sorb water at the spinel surface (Kendelewicz et al., 2000; Parkinson et al., 2011).

We aim in the following at calculating the amount of olivine necessary to form the magnetite ore bodies observed in the Sabzevar ophiolite. On the two-dimensional outcrop, magnetite ore bodies occur as boudins with a thickness of  $L_{\text{ore}} \sim 0.5$  m hosted in a serpentinite. We assume in the following that the thickness of the magnetite ore is also  $\sim 0.5$  m in the third direction, that the serpentinite was initially a dunite composed of olivine ( $\text{Fo}_{90}$ ) and that all the

iron initially contained in olivine has been transported up to the magnetite ore according to a simplified reaction:  $2(\text{Mg}_{0.9}, \text{Fe}_{0.1})_2\text{SiO}_4 + 2.2 \text{H}_2\text{O} + 0.8 \text{H}^+ \Rightarrow \text{Mg}_3\text{Si}_2\text{O}_5(\text{OH})_4 + 0.6 \text{Mg}(\text{OH})_2 + 0.4 \text{Fe}^{2+}_{\text{aq}}$ . This latter reaction implies that, in the host-serpentinite, no Fe is incorporated into lizardite and brucite and that no magnetite is formed. Under these assumptions, the minimum thickness of dunite necessary to form the ore bodies can be expressed as:

$$L_{\text{dun}} = \frac{3\nu \text{Lore} V_{\text{mol}}}{2X_{\text{Fe}} V_{\text{mmag}}} \quad (\text{Eq. 4.3})$$

where  $\nu$  is the volume fraction of magnetite in the ore bodies (90 vol. %) and  $V_{\text{mol}}$  and  $V_{\text{mmag}}$  are the molar volume of olivine and magnetite, respectively ( $V_{\text{mol}} = 44.73 \text{ cm}^3/\text{mol}$  and  $V_{\text{mmag}} = 44.56 \text{ cm}^3/\text{mol}$ ). Equation (Eq. 4.3) leads to an estimated dunite thickness of 6.8 m. This estimate is a minimum, as it is assumed that all iron is lost from the dunite. The bulk iron content measured in the Sabzevar serpentinite is around 20 % lower than the amount necessary to reproduce the measured olivine composition with our thermodynamic modelling. Considering such a Fe loss would lead to a dunite thickness of ~30 m. Iron transport at a scale > 10 m requires, in addition to the chemical potential gradient in iron, an efficient transport mechanism. We observe shear zones in the magnetite ore but not in the host serpentinite, suggesting that advection cannot explain alone iron transfer. The diffusivity of  $\text{Fe}^{2+}$  in a free fluid at 300°C and 100 MPa is  $D \sim 10^{-8} \text{ m}^2/\text{s}$  (Oelkers and Helgeson, 1988). It can be used to calculate a characteristic time for diffusion ( $\tau$ ) over a distance  $x = 10 \text{ m}$  of  $\tau = \frac{x^2}{D} = 300 \text{ yr}$ . This duration is a lower bound for diffusive iron transport as diffusion is slower at grain boundary than in a free fluid. Nevertheless, it indicates that diffusion is a possible mechanism for the observed segregation of iron.

The mechanism of magnetite ore formation proposed here involves limited chromium transport and chromite dissolution. As a result, the current amount of chromite in the magnetite ore is probably similar to the amount of chromite before alteration. Chromite now represents approximately 5 vol.% of the magnetite ore. This corresponds to a thickness of 2.5 cm for a pure chromitite layer. The chromitite was probably not exclusively composed of chromite but rather occurred as a disseminated chromitite.

#### 4.8.5. Scenario of spinel alteration – magnetite formation

Based on textural observation at micro- and nano-scales, as well as thermodynamic modelling, the Sabzevar magnetite ores and their host serpentinites are shown to have recorded two events of spinel alteration (Fig. 4.20). The presence of a non-metamorphic volcanogenic massive-sulfide (VMS) mineralization, and sea-floor alteration recorded in basaltic sequences of the Sabzevar ophiolite precludes the possibility of high-grade obduction-related metamorphism in the area. A first stage of alteration is ascribed to the formation of porous Cr-spinel II with chlorite inclusions at the expense of magmatic spinel. Temperatures and  $\Delta\log_{10}fO_2$  of alteration “Stage I” obtained using our new thermodynamic modelling range between 725 and 575 °C and between 0 and 3, respectively. These conditions are compatible with high-temperature hydrothermal circulation of seawater at mid-ocean ridges at depth, as suggested by Tao et al. (2020) and Hasenclever et al. (2014). A second stage of alteration is marked by the development of a reaction rim consisting of ferritchromite ( $FeCr_2O_4$ ), magnetite ( $Fe_3O_4$ ) and brucite at the expense of porous Cr-spinel-II at temperatures below 400 °C and  $\Delta\log_{10}fO_2 < -2$ . This reaction is  $fO_2$  dependent and favored by the presence of  $H_2$ . The second alteration stage is interpreted as the serpentinization of the Sabzevar oceanic peridotite during progressive exhumation of mantle peridotite and associated chromitite ore deposits. Therefore, unless additional geochemical data are collected to constrain with origin of the alteration aqueous fluid, we favor a simple geodynamic scenario of seawater/rock interaction during progressive exhumation of a mantle segment including chromitite bodies to account for the spinel alteration and the formation of the Sabzevar magnetite orebodies. Although there are no structural data on the study area, re-activation of oceanic faults can be expected for the remarkable hydrothermal alteration of chromitite bodies and associated peridotites in the study area. Low modal abundances of Cr-spinel relicts in the Sabzevar magnetite ore revealed that they may derive from disseminated chromitite protoliths during these two stages of spinel alteration.

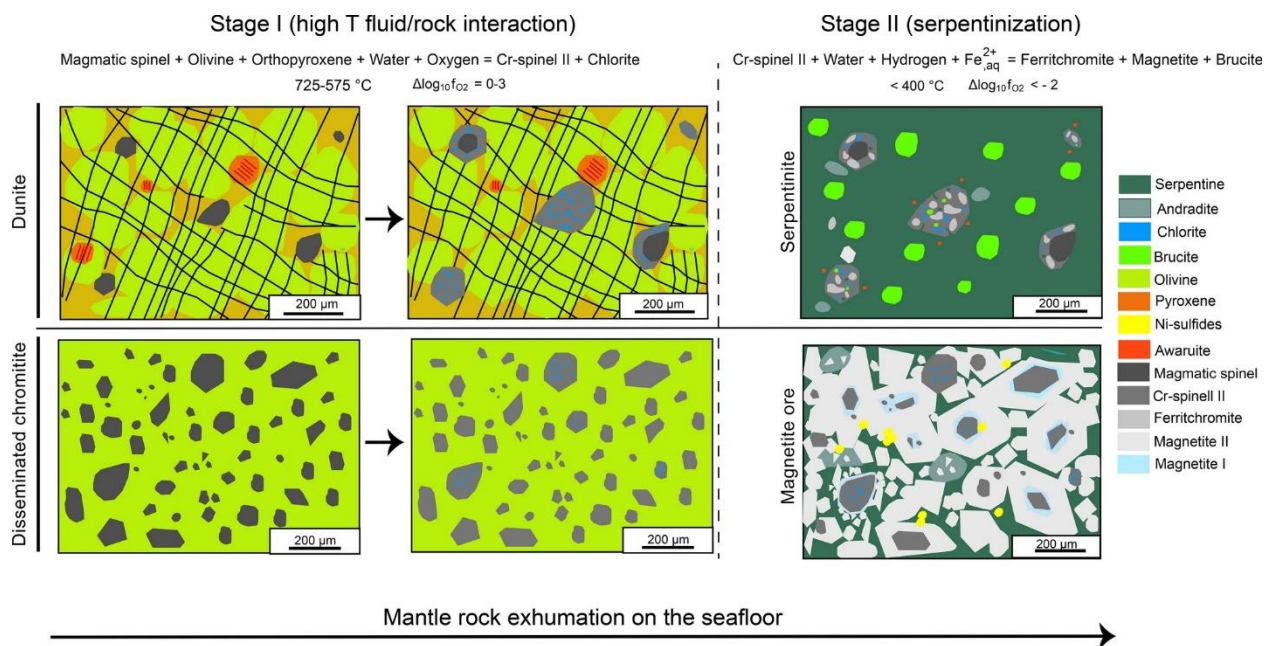


Fig. 4.20. Schematic evolution of spinel alteration in the Sabzevar serpentinite-hosted magnetite deposit and associated peridotites

## 4.9. Concluding remarks

Sabzevar magnetite ores and their host serpentinites recorded two events of spinel alteration. The first alteration stage occurred at temperatures between 725 and 575 °C and led to chlorite and Al-free Cr-spinel formation. The second alteration stage occurred during serpentinization at temperature < 400 °C and is associated with magnetite precipitation. The two alteration stages probably successively occurred during mantle-rock exhumation from depth at a mid-ocean ridge. During spinel alteration and magnetite ore formation, chromium mobility is extremely low and chromite dissolution is limited. Orientation mapping at the nanoscale reveals epitaxial growth of ferritchromite and magnetite on Cr-spinel II. This is interpreted as evidence for a coupled Cr-spinel II dissolution-ferritchromite + magnetite precipitation process. Olivine breakdown and/or dissolution of nanoscale magnetite grains initially formed in the host serpentinite provided the iron necessary for magnetite ore formation. Mass balance calculations indicate iron transport over distances beyond 10 meters during serpentinization.

## Chapter 5. Comparison of the Sabzevar serpentinite-hosted magnetite ores with other occurrences worldwide

---

### 5.1. Introduction

Recent years have seen an increased interest in the study of a peculiar occurrence of magnetite mineralization in the serpentinized peridotites from Tethyan ophiolites, which consists in magnetite veins, lenses and pods. Only a few examples of these magnetite enrichments are known from the Mesozoic ophiolites in Greece (Olympus, Vermion, Edessa and Skyros Island), Central Iran (Nain), Oman (Aniba) and Italy (southern Aosta Valley, Western Alps) as well as from the Late Proterozoic Bou-Azzer ophiolite in Morocco (Fig. 5.1). These deposits have diverse thickness (from a few centimeters up to 50 m) and length (2 to >500 m). Magnetite-mineralized rocks show variable microstructures, including massive, nodular and banded ores, veins, net and fine-grained disseminations in serpentinites.

In this chapter, I combine recent results from my own work and literature to highlight some of the key mechanisms involved in the formation of magnetite ore bodies in ophiolitic serpentinites from Tethyan ophiolites. Based on laser ablation inductively coupled plasma mass spectrometry (LA-ICP-MS) analyses, I have investigated the minor and trace element composition of magnetite from the Sabzevar, and then I have presented a comparison with Nain and Oman serpentinite-hosted magnetite ores. In addition, a comparison with Skyros serpentinite –hosted magnetite ores has been undertaken based on microtexture and composition variation maps.

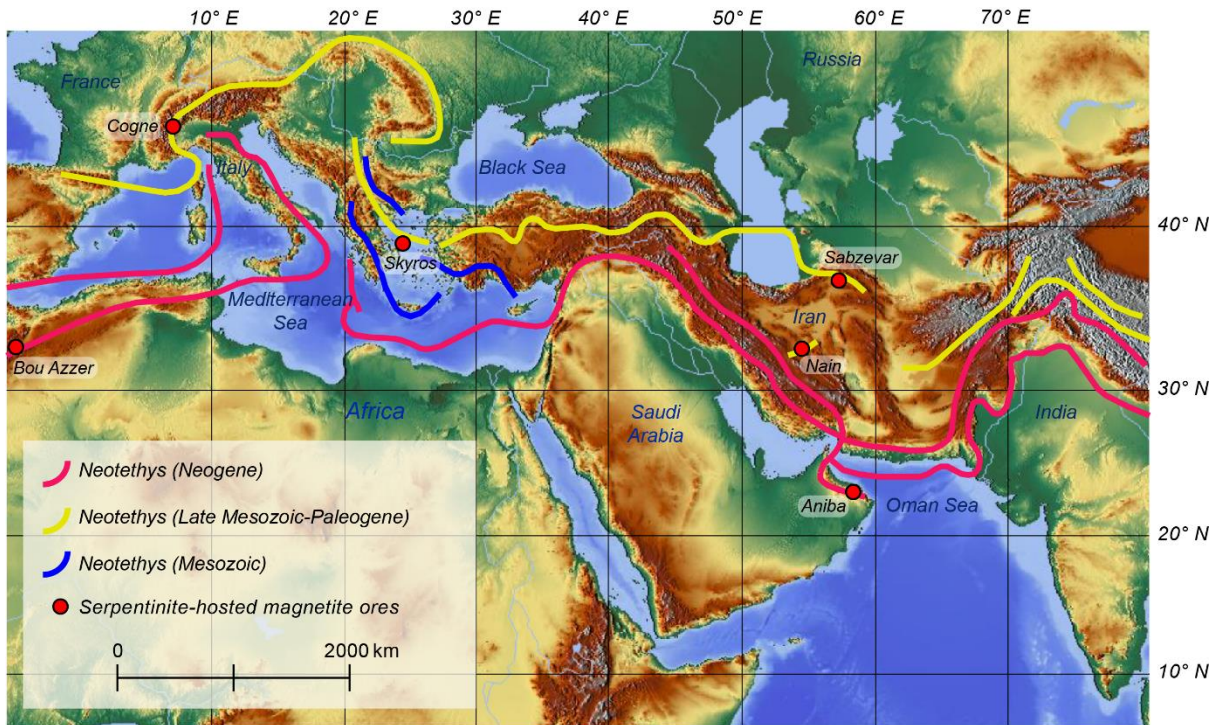


Fig. 5.1. Topographic relief map of the Alpine–Himalayan Tethyan orogenic belt showing serpentinite-hosted magnetite ores. The background topographic relief map is available from Maps-For-Free.com. Major Tethyan sutures are derived principally from Richards (2015).

## 5.2. Mode of occurrence and mineralogical features

Representative magnetite samples were collected from three serpentinite-hosted magnetite deposits including Nain (Central Iran), Skyros Island (Greece) and Aniba (Oman) during fieldwork studies in these areas and studied by means of optical microscopy and Scanning Electron Microscopy (SEM) in thin polished sections. Petrological and trace-element data of the Cogné magnetite deposits in the Piemonte ophiolite nappe, Italy are adapted from Toffolo et al., (2017) for comparison. A summary of general geology and field occurrence for each of the studied outcrops is given below.

### 5.2.1. Nain

An individual serpentinitized peridotite nappe hosts discontinuous trails of magnetite ore bodies from the Late Cretaceous Nain ophiolite mélangé (Central Iran). These ore deposits can be followed for almost 70 meters. A single fibrous-textured magnetite pod has been found along a striated fault plane near a tectonically attenuated serpentinitized dunite lens. The magnetite ores and the host peridotite have acute and sheared contacts that may be

distinguished. Nain magnetites were restricted to a shear zone that was semibrittle (5-10 m thick). On hand specimens, the magnetite is made up of monotonous aggregations of jet-black octahedral magnetite crystals that are usually matrixed by pale-green serpentine and chlorite.

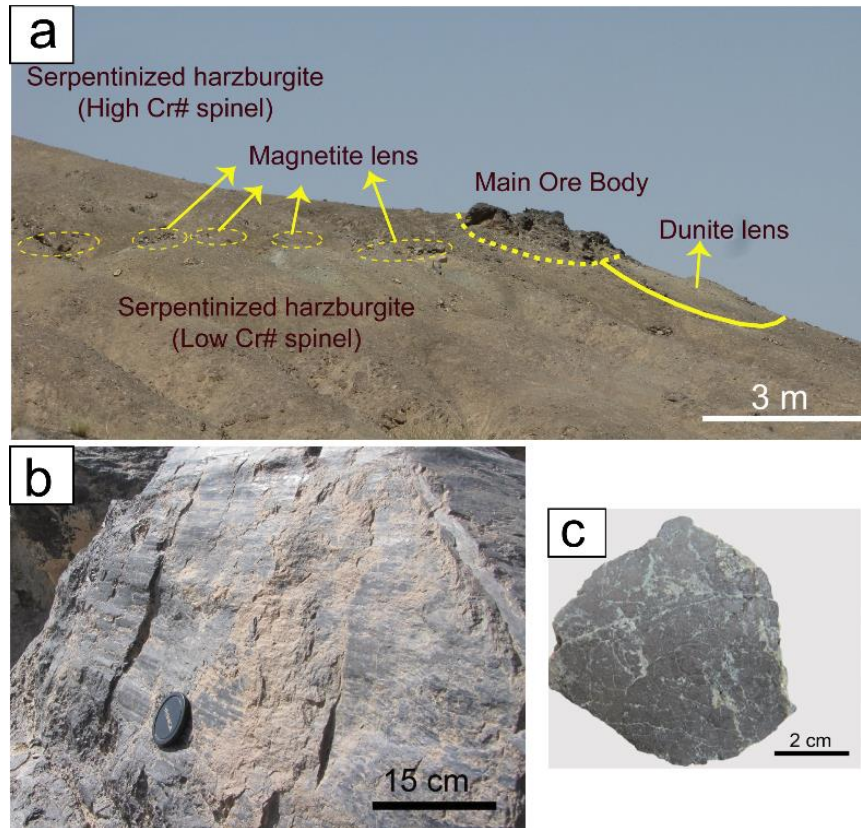


Fig. 5.2. (a) Field photo of magnetite ore bodies at the Nain ophiolite; (b) Magnetite body exhibiting a remarkable fibrous texture along a striated fault plane in the serpentized harzburgite. (c) Hand sample of magnetite sample and serpentine intergrowth. Photos adapted from Eslami et al. (2018).

### 5.2.2. Skyros Island

The Skyros Island is one of the Northern Sporades islands in the northwest of Aegean Sea. It is composed of three main paleo-tectonic domains including the Skyros Tectonic Unit (mainly marbles and breccia with basal flyschoid members), Pelagonian Zone (mostly metamorphosed sedimentary rocks), the Eohellenic Tectonic Nappe (dominantly marbles, schists, serpentinites and ophiolite *mélange*). The Skyros ophiolitic *mélange* covers mountainous area of  $\sim 4.5 \text{ km}^2$  in the north of Skyros Island. It is mainly composed of highly deformed serpentinites, massive gabbros, rodingitized and dolerites dykes, basaltic lavas and

ophicalcites. In a few places, magnetite ore bodies are distributed as boulders strewn across the serpentinites or lateritic zones (Fig. 5.3).

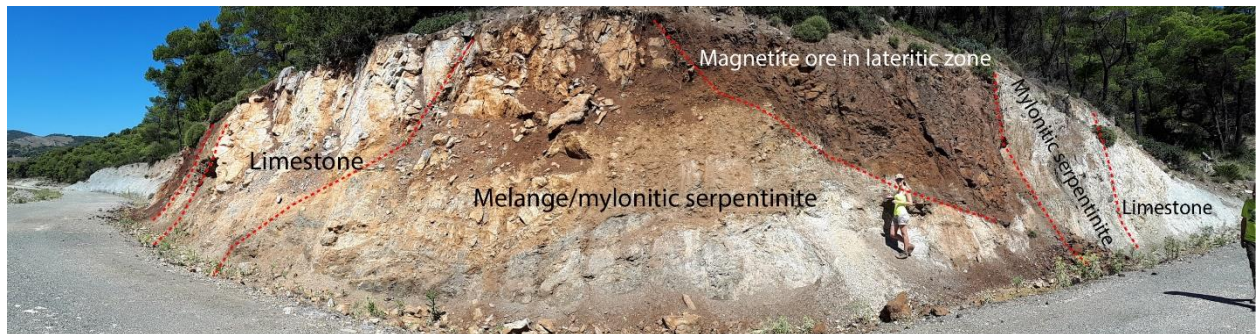


Fig. 5.3. Field photograph of magnetite ore bodies hosted by serpentinites in Skyros Island.

### 5.2.3. Cogne

The Cogne deposit is an apatite and sulphide-free serpentinite-hosted magnetite orebody which is situated in ophiolitic serpentinites (Fig. 5.4a) along the western Alpine collisional suture in Valle d'Aosta (Italy). These magnetites show a wide range of textures including fine-grained disseminated, vein and nodular (Fig. 5.4b). The Cogne magnetite ore bodies are characterized by <10m to 50-70m in thickness and 600m length.

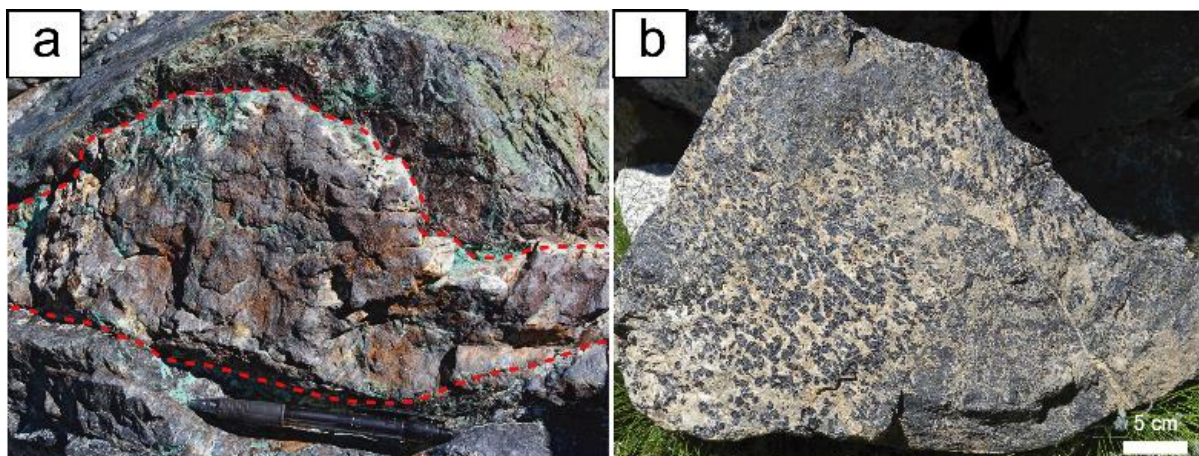


Fig. 5.4. Field photographs of the magnetite lens in serpentinized peridotite with Fe-oxyhydroxides and secondary copper minerals on the surface; (b) Nodular magnetite ore, showing leopard with the light serpentine matrix (+brucite + olivine). Photos adapted from Toffolo et al. (2017).

### 5.2.4. Aniba

The Oman ophiolites consist of a series of thrust-bounded massifs that widen in extent to ~500 km along the coast of Oman (Menzies and Allen, 1974; Menzies, 1976). The Aniba magnetite ore bodies (1 to 10 meters in width and up to 120 meters in length) of the Late Cretaceous Southern Oman ophiolite crop out in an arched boundary (nonconformity) between serpentinized peridotites and overlying limestone (Fig. 5.5a). Magnetite rocks were found as clasts within a ferruginous matrix composed of chlorite, serpentine, hematite and magnetite (Fig. 5.5b). These magnetite bodies which are discordant to sub-concordant with the overlying limestone foliation usually exhibit gradational contacts against the surrounding country rocks.

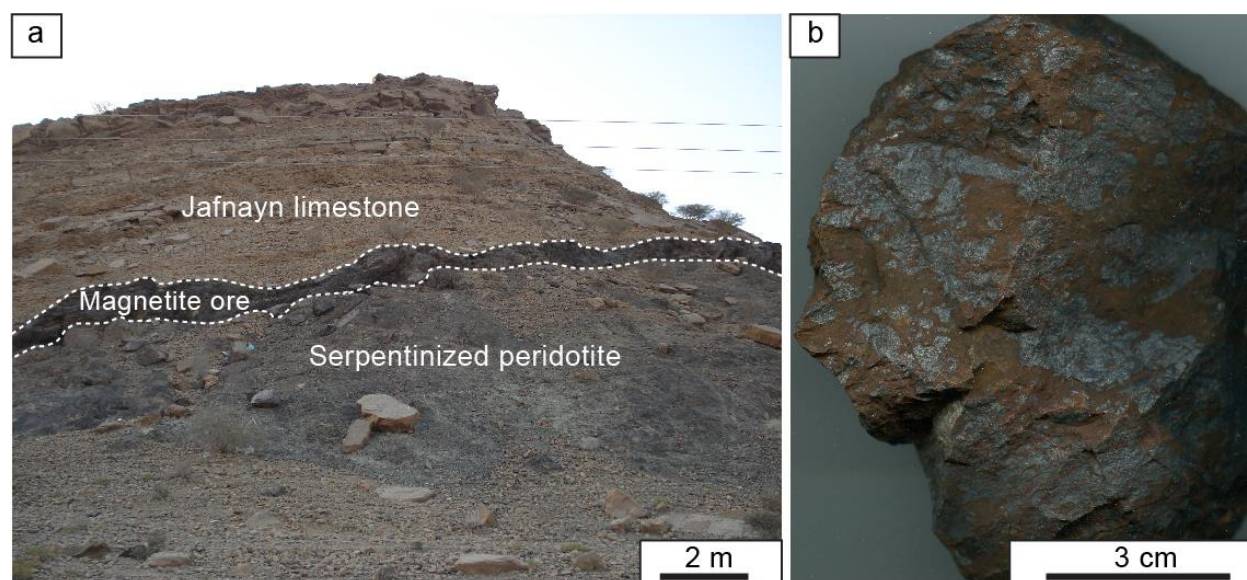


Fig. 5.5. (a) Field photo of the Aniba magnetite deposits between serpentinites and the overlying limestones; (b) specimen of brecciate magnetite deposits. Photos adopted from Khedr and Arai (2018).

### 5.3. Analytical methods

The minor and trace element compositions of magnetite were determined using a NewWave UP 193 laser system connected to a ThermoFinnigan Element2 ICP-MS in the Petrology of the Ocean Crust Laboratory, University of Bremen, Germany. The analyzed masses for chromite ( $^{51}\text{V}$ ,  $^{47}\text{Ti}$ ,  $^{55}\text{Mn}$ ,  $^{59}\text{Co}$ ,  $^{60}\text{Ni}$ ,  $^{71}\text{Ga}$  and  $^{66}\text{Zn}$ ), magnetite ( $^{43}\text{Ca}$ ,  $^{29}\text{Si}$ ,  $^{25}\text{Mg}$ ,  $^{53}\text{Cr}$ ,  $^{57}\text{Fe}$ ,  $^{47}\text{Ti}$ ,  $^{55}\text{Mn}$ ,  $^{59}\text{Co}$ ,  $^{60}\text{Ni}$ ,  $^{71}\text{Ga}$  and  $^{66}\text{Zn}$ ) and andradite (REEs: La, Ce, Pr, Nd, Sm, Eu,

Gd, Tb, Dy, Ho, Er, Yb and Lu) were measured using a ~10–35µm beam diameter, 5 Hz frequency, and 0.032–0.105 mJ/pulse power, during 60 s analysis. External standards (reference materials std610, BCR-2G and BHVO) were analysed under the same conditions as the samples every 6 to 12 analyses during the same session, in order to check the accuracy and precision of the analyses. The data obtained during ablation runs were processed using the GeoPro™ software (CETAC Technologies). Iron, aluminum and calcium values obtained by electron microprobe were used as the internal standards for magnetite, chromite and andradite, respectively. It is crucial to note that the BHVO2G were used as a calibration standard for the magnetites whereas chromite and andradite calibrated with std610. The results of LA–ICPMS analysis are presented in Table 5.S1.

Microanalyses of individual spinel and silicate minerals from the Skyros Island magnetite ore samples have been performed with a JEOL8200 electron microprobe equipped with a wavelength dispersive system (SEM-WDS) at the University of Milan. The analytical conditions were 15 kV accelerating voltage, 15 nA beam current, 2 µm beam diameter, and 20 s counting time, using WDS detectors. Synthetic as well as natural standards were used for calibration. Elemental distribution maps for the Skyros Island magnetite ore sample were collected at ISTerre using the same procedure explained in Chapter 4.

## 5.4. Mineralogical and textural characteristics

The investigated magnetite ores are heterogeneous in texture and consist of euhedral to anhedral magnetite crystals. The silicate mesostasis of the Nain and Skyros Island magnetite ores is mainly composed of fibrous serpentine, chlorite and andradite which is akin to those in the Sabzevar magnetite ores. Similar to the Sabzevar magnetite ores, euhedral to subhedral Cr-spinel relics are sporadically enclosed within large magnetite crystals of the Skyros, Nain and Aniba magnetite bodies (Fig. 5.6a-d). The texture of these relict spinels can either be homogenous or porous. Alteration is recorded in some individual chromite grains in the form of optical zoning (Fig. 5.6c). Altered Cr-spinel relicts contain pores filled with chlorite and serpentine. Magnetite ores from the Skyros Island is marked by ubiquitous presence of Fe-chlorite (Fig. 5.6a). Similar to the Sabzevar magnetite ore, Nain magnetites host a peculiar mineral inclusions that is mainly composed of pentlandite and chalcopyrite. In contrast, the investigated ore samples from the Aniba and Skyros Island lack base metal sulfides.

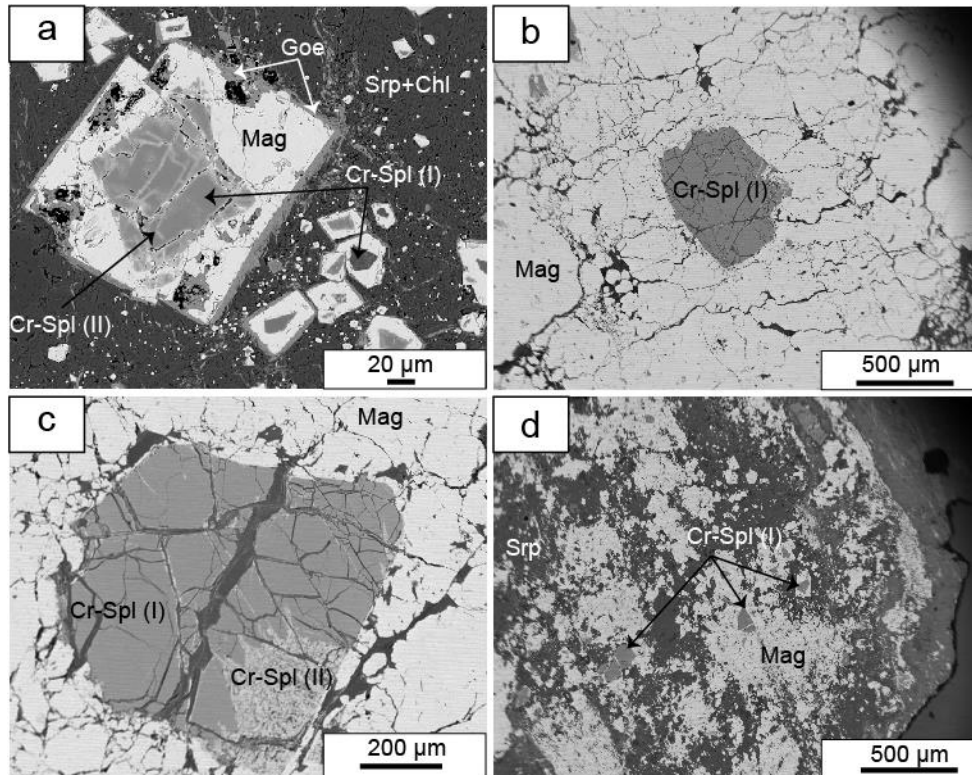


Fig. 5.6. Backscattered -electron images of the investigated magnetite ore. (a) Euhedral magmatic Cr-spinel (I) included in magnetite rimmed by goethite in the Skyros Island sample. Note the large inclusions of chlorite inside the magnetite. (b) homogeneous Cr-spinel relict inside the magnetite grain from the Nain magnetite ore. (c) close-up of Cr-spinel (I) partially altered by porous chromite or Cr-spinel from the Nain magnetite ore. (II); (d) Relict of homogenous chromian spinel sporadically distributed in the Aniba magnetite ore.

X-ray elemental maps, along with point microanalyses, were collected using the EPMA on homogeneous Cr-spinel relicts rimmed by magnetite in the Skyros Island magnetite ore sample (Fig. 5.7). Similar to the Sabzevar magnetite ores, two generations of magnetite can be distinguished. A first magnetite rim is observed (called “magnetite-I rim”) from the Cr-spinel interface, which has a thickness of  $\sim 10 \mu\text{m}$ . A second magnetite rim (called “magnetite-II rim”) has a variable thickness ranging from 5 to 200  $\mu\text{m}$ .

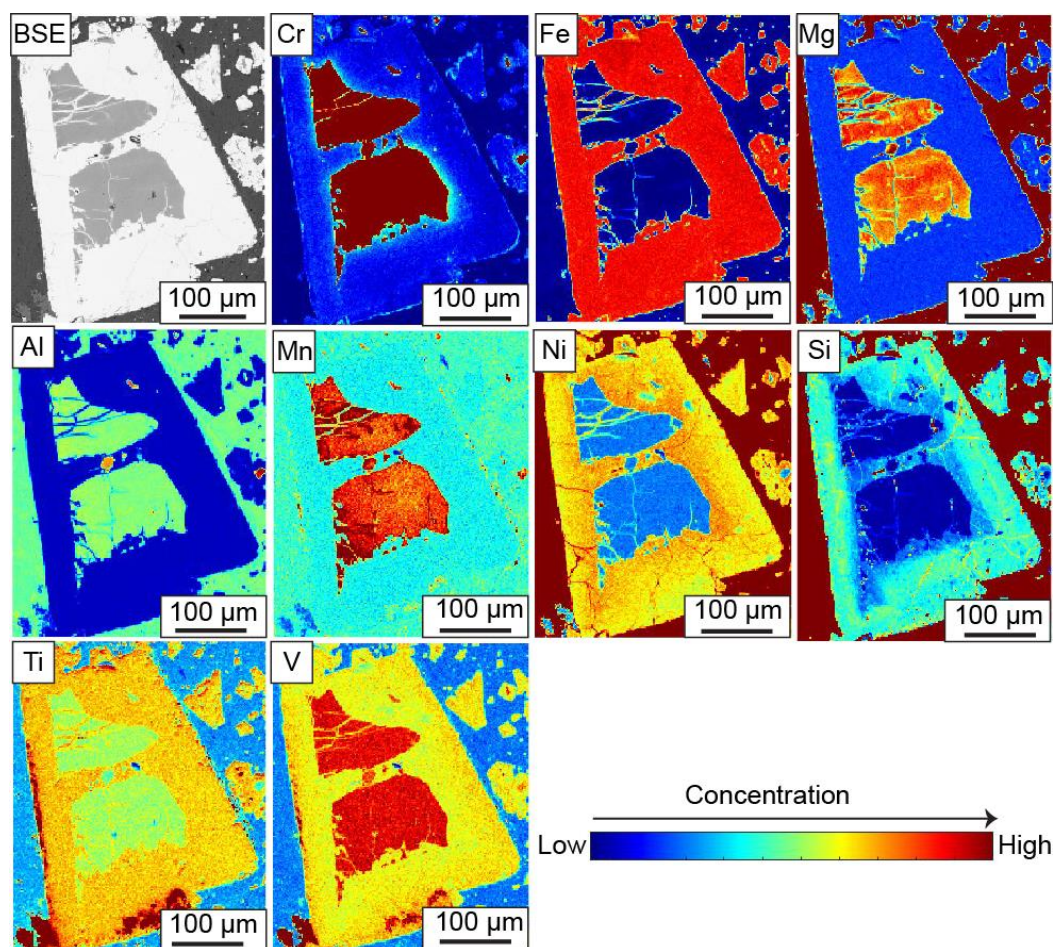


Fig. 5.7. Multi-element (WDS-EDS) mapping of homogeneous chromian spinel relicts in magnetite ore from the Skyros Island

## 5.5. Trace element geochemistry of magnetite

Magnetite grains from the Sabzevar deposit show variable contents of Mg (378–11096 ppm), Si (1850–26609), Cr (7–1545 ppm), Ti (4–1095 ppm), Mn (105–255 ppm), Co (58–440 ppm), Ni (14–397 ppm) and Zn (5–23 ppm) (Table. 5.S1).

Chemical composition of magnetite has been used to fingerprint several types of ore deposits

(Dupuis and Beaudoin, 2011; Dare et al., 2014; Boutroy et al., 2014; Makvandi et al., 2016, 2017). As previously indicated in Chapter 4, Sabzevar magnetite may contain Ti-rich and silicate nano-inclusions which could result in mixed analyses. Since the LA-ICP-MS data could be mixed analyses due to presence of nanoscale inclusions in magnetite, Ti, V and Ca contents of magnetite are still lower than those in magnetite from other types of ore deposits. Magnetite from Sabzevar and Nain deposits plot in undefined fields on discriminant diagram  $Ca + Al + Mn$  (wt%) vs.  $Ti + V$  (wt%) (Fig. 5.8a). In Fig. 5.8b, the Sabzevar and Nain magnetite analyses

from the present study plot in the field of skarn in the discriminant diagrams developed by Dupuis and Beaudoin (2011) and Nadoll et al. (2015). Magnetite from Sabzevar and Nain deposits plot in undefined fields on discriminant diagram Ca + Al + Mn (wt%) vs. Ti + V (wt%). The high Ni/Cr ratios of the Sabzevar magnetites are all similar to the magnetite of the typical hydrothermal deposits (i.e., skarn, IOCG) (Fig. 5.8c). Magnetite analyses from the Oman show two distinct group: (i) high Ti and low Ni/Cr with magmatic signature and (ii) low Ti and high Ni/Cr with hydrothermal signatures. Knipping et al. (2015) suggested an empirical discrimination diagram based on Ti and V (ppm) levels to distinguish magmatic and hydrothermal magnetite (Fig. 5.8d). In this diagram, the Sabzevar analyses show low V content (1-22 ppm) and plot in and below the defined discrimination field for hydrothermal magnetites. Similarly, a few magnetite analyses from the Oman deposit plot show low V content reflecting their hydrothermal whereas V content of other Oman magnetite grain ranges between 531 and 617 ppm plotting in the field of magmatic magnetites.

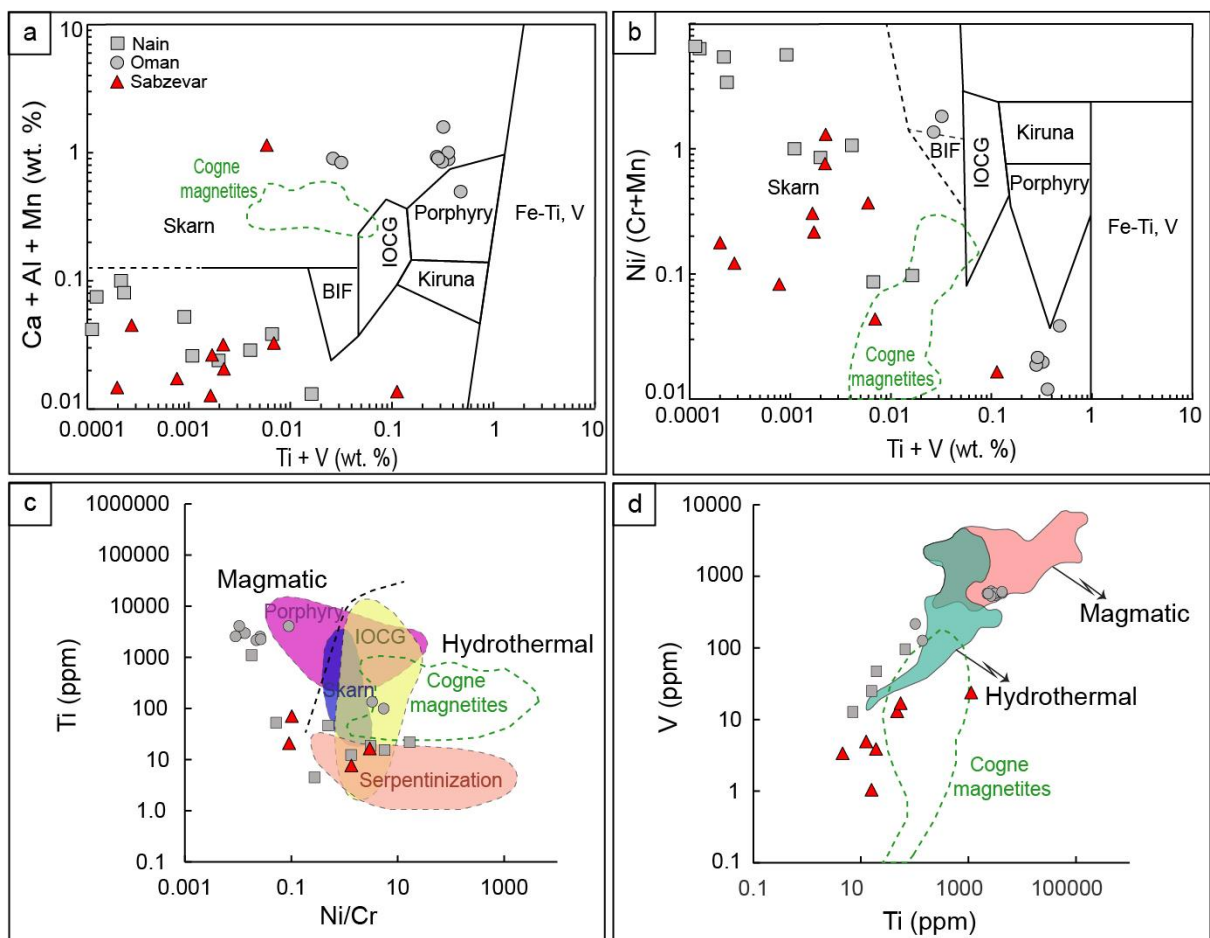


Fig. 5.8. Magnetite discrimination plots for various ore deposit types by Dupuis and Beaudoin (2011) with samples from the Sabzevar, Nain and Oman serpentinite-hosted magnetite ores

plotted. (a) Ca + Al + Mn (wt%) vs. Ti + V (wt%); (b) Ni/(Cr + Mn) vs. Ti + V (wt%); (c) Ti (ppm) vs. Ni/Cr; (d) V (ppm) vs. Ti (ppm). Hydrothermal vs magmatic discrimination diagrams in (c) and (d) proposed by Dare et al. (2014) and Knipping et al. (2015), respectively. Fields for Cogne magnetite deduced from Toffolo et al. (2017).

## 5.6. Discussion

### 5.6.1. Style of deformation

As mentioned in Chapter 4, the Sabzevar magnetite pods are hosted in intensely sheared and pervasively serpentinized peridotites. The lensoidal shape of the magnetite ores is a consequence of physical reorientation and relocation in shear zones. Cataclastic fragmentation of magnetite is visible in magnetite ore bodies leading to formation of micro-breccia zone. Similarly to the Sabzevar magnetite ore, in the Nain ophiolite (Central Iran), magnetite pods are exposed along a semi-brittle shear zone between serpentinized harzburgites with different magmatic Cr-spinel compositions. Distinguished conformability between deformation effects of the Nain magnetite ore and those recorded at a late stage of movement between the harzburgite nappes, reveal syn-kinematic emplacement of the ore bodies within the semi-brittle shear zone (Eslami et al., 2018). Indistinguishably, a few individual serpentinite-hosted magnetite pods and veins recorded in the Mesozoic ophiolites in Greece (Olympus, Vermion, Edessa and Skyros Island) show remarkable schistosity, similar to their host serpentinites (Paraskevopoulos and Economou, 1980). In southern Valle d'Aosta region (Western Alps), serpentinite-hosted magnetite ore bodies with variable sizes (<10 - 70 m thick and 10 - 600 meter long) were influenced by Alpine deformation, which resulted in detachment of some parts of magnetite ore deposits (Toffolo et al., 2017).

### 5.6.2. Factors controlling magnetite chemistry in serpentinite-hosted magnetite ores

Nadoll et al. (2014) suggested the chemistry of magnetite formed in hydrothermal and metamorphic conditions (200–650 °C) is controlled by several factors including temperature, melt/fluid composition, pressure, cooling rate, oxygen and sulfur fugacity, and silica activity. Specific element enrichments or depletions are typically difficult to relate to a single physicochemical factor.

Availability of elements in hydrothermal fluids are considered to be a first-order factor controlling the chemical composition of hydrothermal magnetite (Nadoll et al., 2014). If composition of magnetite is not affected by secondary factors such as host rock buffering, elements such as Mg, Mn, Co, and Zn that are regularly incorporated into magnetite at large amounts under hydrothermal conditions.

The vital role of oxygen fugacity ( $fO_2$ ) on the composition of magnetite has been studied in several studies (e.g. Toplis and Corgne, 2002; Toplis and Corgne, 2002; Dare et al., 2014; Nadoll et al., 2014). Substitution of cations generally occurs under lower oxygen fugacity (Lindsley, 1991; Buddington and Lindsley, 1964). Due to its 5+ oxidation state, vanadium is preferentially integrated into the magnetite structure at low oxygen fugacity and becomes incompatible at high oxygen fugacity (Bordage et al., 2011, Toplis and Carroll, 1995, Toplis and Corgne, 2002). Therefore, variations in V content of magnetite can be attributed to  $fO_2$  variances in the ore-forming fluid (e.g., Sun et al., 2017). In V-Ni diagram suggested by Li et al. (2018), Sabzevar and Nain magnetites show variable V concentration reflecting high to moderate oxygen fugacity. Compositional maps show increase of vanadium towards the margins of magnetite grains in the Sabzevar magnetite ore samples. Such spatial variation can be used as an indicator for the beginning of the spinel reaction in which magnetite formation initiates at lower oxygen fugacity and then, when the grain is progressively replaced, the V could decrease as the oxygen fugacity increases. Highly variable composition of magnetite from the Cogne deposit reflect  $fO_2$  differences in the ore-forming fluids. In contrast, very low oxygen fugacity can be deduced from high V concentration in the Oman magnetite samples.

Compared to V, Ti has only a 4+ oxidation state in hydrothermal fluids. As a result, magnetite formed from reduced fluids should have lower Ti/V ratios than magnetite formed from oxidized fluids (Wang et al., 2017). The Ti/V ratio of magnetite from the Sabzevar magnetite deposit ranges from 1.42 to 50.10 (Average 11.70). Such variation cannot simply be attributed to a relatively reduced depositional setting due to occurrence of Ti-rich and silicate nanoinclusions in the magnetite.

The concentrations of various elements in magnetite may be affected by temperature (Ilton and Eugster, 1989; Nielsen et al., 1994, Nadoll et al., 2014). Incorporation of elements such as Ti, Mg, and Al in magnetite is extensively controlled by temperature. These elements are rather immobile in low-temperature hydrothermal fluids (Van Baalen, 1993, Nielsen et al., 1994, Toplis and Carroll, 1995, Verlaquet et al., 2006). Experimental studies of Lindsley (1991) show that with an increase in temperature, Ti concentrations remarkably escalate in magnetite under oxygen fugacity conditions of Ni-NiO to fayalite-magnetite-quartz. This is

also corroborated by high solubility of Ti in high-temperature Cl- and F-bearing fluids (Rapp et al., 2010).

Nadoll et al. (2014) proposed a Ti + V vs. Al + Mn plot as a good classifier of magnetite formation temperatures. This diagram (Fig. 5.9) illustrates that high temperature magnetites plot at high Ti + V and Al + Mn, whereas low temperature magnetites plot at low Ti + V and Al + Mn contents. In this diagram, magnetites from the Sabzevar and Nain serpentinite-hosted magnetite ore deposits plot in the field of <300 °C. These temperatures are quite consistent with those estimated by pentlandite composition in the ternary system Fe<sub>9</sub>S<sub>8</sub>–Ni<sub>9</sub>S<sub>8</sub>–Co<sub>9</sub>S<sub>8</sub> proposed by Kaneda et al. (1986) (Fig. 5.10).

Conversely, magnetites from the Cogné deposit show higher temperature (300–500 °C) which is quite consistent with a high temperature (~300–400 °C) subseafloor hydrothermal origin for these magnetites (Toffolo et al., 2017). Magnetite from magnetite deposits hosted in Oman peridotites show set of compositions revealing different formation temperatures (300–500 °C and >500 °C). Although, a composite origin was suggested by Khedr and Arai (2018), they excluded magmatic origins for the magnetite deposits in the Oman ophiolite (Fig. 5.9).

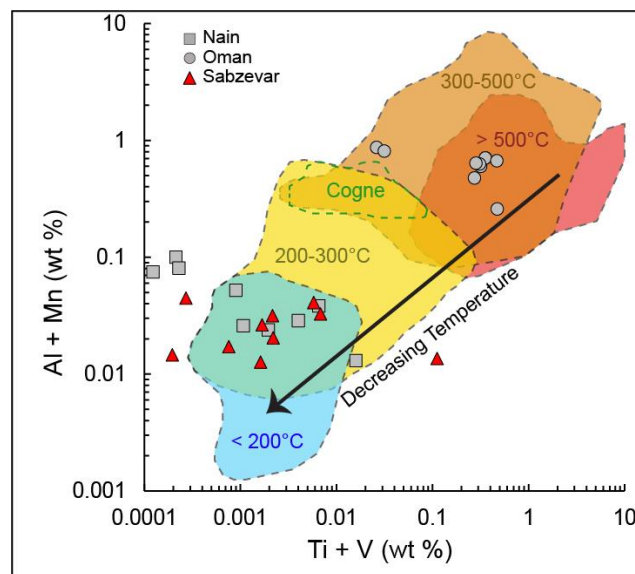


Fig. 5.9. Ti + V (wt %) vs. Al + Mn (wt%) plot showing formation temperatures of magnetite from the Sabzevar, Nain and Oman ophiolites. Temperature fields deduced from Nadoll et al. (2014)

In addition, strong partition of foreign cations into coexisting mineral phases, such as sulfides and silicates, under specific  $T$ – $fO_2$ – $fS_2$  conditions, may cause depletion of minor and trace element concentrations in the corresponding magnetite (Nadoll et al., 2014). Sulfide inclusions in the magnetite preferably incorporate chalcophile and siderophile elements

whereas silicate inclusions are preferentially partitioned by lithophile elements (Toplis and Corgne, 2002, Zhou et al., 2017). Presence of micro-sized inclusions of Ni-sulfides and nano-sized inclusions of silicate phases in the Sabzevar magnetite could be responsible for depleted concentrations of chalcophile elements (i.e. Co and Ni) and lithophile elements (i.e. Ca, Mg and Al) in the magnetite, although magnetite grain devoid of micron-sized sulfide inclusions were selected for LA-ICPMS.

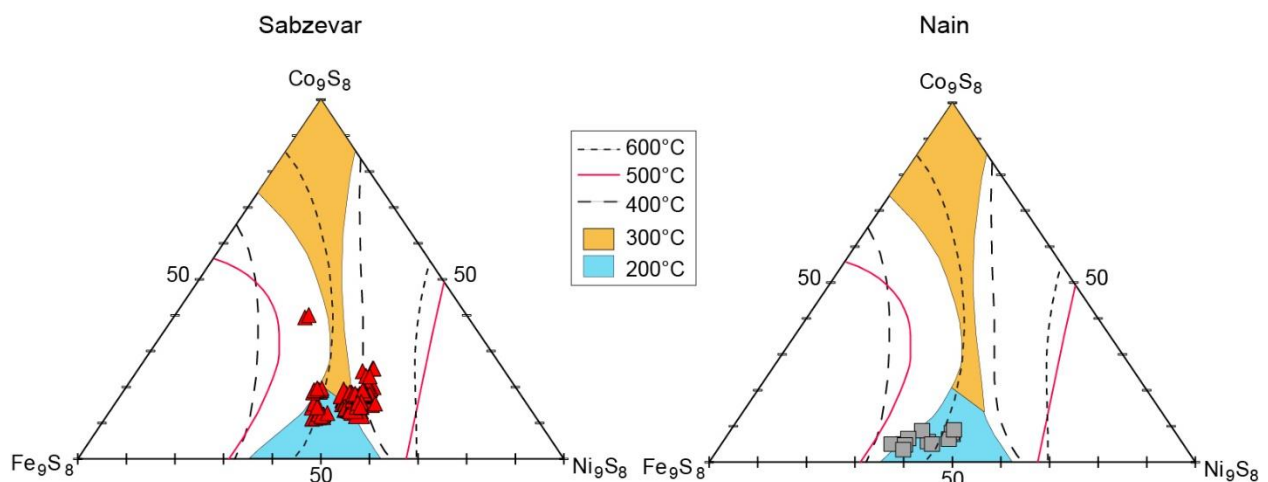


Fig. 5.10. Ternary system  $\text{Fe}_9\text{S}_8$ – $\text{Ni}_9\text{S}_8$ – $\text{Co}_9\text{S}_8$  showing temperature of pentlandite from the Sabzevar (left) and Nain (right) magnetite ores (after Kaneda et al. 1986).

## 5.7. Conclusion

Based on textural features and compositional maps, the Sabzevar serpentinite-hosted magnetite ores bears remarkable resemblance to the similar occurrences worldwide. Similar to the Sabzevar magnetite pods, analogous examples in the Nain (Central Iran), Skyros Island (Greece), Aniba (Oman) and Cogne (Italian Alps) ophiolite are hosted in intensely sheared and pervasively serpentinized peridotites. These shear zones which acted as high permeability pathways for hydrothermal fluids play a vital role for magnetite mineralization. The investigated magnetite ores from the Nain, Aniba and Skyros Island are heterogeneous in texture and consist of euhedral to anhedral magnetite crystals. The silicate mesostasis of the Nain and Skyros Island magnetite ores is mainly composed of fibrous serpentine, chlorite and andradite which is akin to those in the Sabzevar magnetite ores. Similar to the Sabzevar magnetite ores, euhedral to subhedral Cr-spinel relics are sporadically enclosed within large

magnetite crystals of the Skyros Island, Nain and Aniba magnetite bodies strengthen the possibility that these magnetite ores are transformation products of pre-existing chromitites. Similar to the Sabzevar occurrence, detailed X-ray elemental mapping on homogeneous Cr-spinel relicts rimmed by magnetite in the Skyros Island magnetite ore sample shows 200  $\mu\text{m}$ -thick magnetite rim comprising Si-poor and Si-rich magnetites. Si-rich magnetite can be attributed to presence of tiny inclusions of silicate minerals. Trace element analyses of magnetite from the Sabzevar serpentinite-hosted magnetite ores and similar occurrences in the Nain, Oman and Cogne ophiolites by laser-ablation inductively-coupled mass spectrometry reveal typical hydrothermal compositions. The low V and Ti and high Ni/Cr ratios of these magnetite ore types are all similar to the magnetite of the typical hydrothermal deposits (i.e., skarn, IOCG). Magnetites from these serpentinite-hosted magnetite ore deposits formed at temperature  $<500\text{ }^{\circ}\text{C}$  which is consistent with serpentine stability field. In the Oman magnetite ores, a few grains with magmatic origins are characterized by high Ti, V and low Ni/Cr ratio. The discriminant diagrams presented in this chapter can be used to identify a new magnetite deposit type according to magnetite composition. The results show that magnetite composition is very powerful in establishing the origin of serpentinite-hosted magnetite deposits.

## Chapter 6. Hydrothermal alteration of chromitite-dunite pairs from the Sabzevar ophiolite (NE Iran): Chemical and nano-textural evolution of chromite

---

### 6.1. Introduction

Chromian spinel (Cr-spinel) is a common accessory mineral in igneous mafic and ultramafic rocks. Mantle section of ophiolite may host accumulation of Cr-spinel as podiform and/or stratiform bodies (*e.g.*, Augé, 1987; Ceuleneer and Nicolas, 1985; Borisova et al., 2012; Gauthier et al., 1990; González-Jiménez et al., 2014; Lorand and Ceuleneer, 1989). These bodies are usually separated from the host harzburgite by a dunite aureole of variable thickness from a few centimeters to several meters. Accumulation of Cr-spinels in mantle peridotites displays massive, banded, disseminated and nodular textures. Spinel is often highly resistant and non-reactive mineral which tend to retain its initial magmatic composition (*e.g.*, Burkhard, 1993; Barnes, 2000; Barnes and Roeder, 2001; Oze et al., 2004). However, hydrothermal alteration and/or metamorphism may lead to changes in spinel composition which evolves towards an increase of iron ( $\text{Fe}^{2+}$  and/or  $\text{Fe}^{3+}$ ) and  $\text{Cr}^{3+}$  and a decrease of magnesium and aluminum contents. Therefore, the spinel composition shifts towards the chromite end-member ( $\text{FeCr}_2\text{O}_4$ ) and/or towards ferrian chromite compositions ( $\text{Cr}^{3+} > \text{Fe}^{3+} > \text{Al}^{3+}$ ). Ferrian chromite compositions with  $\text{Fe}^{2+} \gg \text{Mg}^{2+}$  and  $\text{Fe}^{3+} \gg \text{Al}^{3+}$  are often termed “ferritchromit” in the literature. The conditions and processes of Cr-spinel alteration were widely discussed in the 1970s.

Ferrian chromite often occurs as rim around Cr-spinel, which evolves chemically towards pure magnetite. In altered chromitites from the Stillwater complex (Montana, USA), Beeson and Jackson (1969) proposed a volume-to-volume replacement of the original Cr-spinel by ferrian chromite at constant chromium and with Al and Mg being incorporated into chlorite. The prominent role of chlorite production on Mg and Al depletion in ferrian chromite with respect to the original Cr-spinel was also outlined in the Twin Sisters dunite (Washington, USA) by Onyeagocha (1974) who, in addition, invoked an oxidation process. Furthermore, Haslam et al. (1976) described chlorite – ferrian chromite intergrowths in the serpentinized Chimwadzulu Hill peridotite (Malawi). They

proposed the simplified  $\text{MgAl}_2\text{O}_4$  (spinel ss) + enstatite + forsterite  $\Rightarrow$  Mg-chlorite reaction to account for Mg and Al removal from magmatic spinel. In the Pennsylvania-Maryland district, Ulmer (1974) interpreted ferrian chromite rinds around the original spinel core as a secondary overgrowth fed in chromium by the serpentinization fluid. Bliss and McLean (1975) argued that, in central Manitoba, ferrian chromite rims were produced through a metamorphic reaction between Cr-spinel core and a magnetite rim which developed during serpentinization prior to the metamorphic event. Prabhakar and Bhattacharya (2013) also interpreted ferrian chromite formation as a result of inter-crystalline diffusion between magnetite and Cr-spinel core. On the contrary, Wylie et al. (1987) ruled out the possibility of ferrian chromite rinds as a reaction zone between Cr-spinel and magnetite in the case of altered spinels from the Maryland Piedmont. The authors rather favored a dissolution – crystallization process under hydrothermal conditions.

Spinel alteration has often been characterized in serpentinized ultramafic which were submitted to subsequent metamorphism (*e.g.*, Evans and Frost, 1975; Pinsent and Hirst, 1977; Burkhard, 1993). However, there is now a large number of studies which show that Cr-spinel alteration can already occur at the serpentinization stage (Spandenberg, 1943, Ulmer, 1974; Ashley, 1975; Burkhard, 1993; Khalil & El-Makky, 2009; Mukherjee et al., 2010; Barra et al., 2014; Eslami et al., 2021). At the P-T conditions of serpentinization, a miscibility gap occurs in ferrian chromite ( $T < 600^\circ\text{C}$ , Sack and Ghiorso, 1991) which is thus expected to exsolve magnetite and ferrian chromite,  $(\text{Fe}^{2+}, \text{Mg})\text{Cr}_2\text{O}_4$ . Actually, Mitra et al. (1992) pointed out the absence of exsolution relationship between ferrian chromite and its spinel host in samples from the Sukinda and Nuggihalli belts (India). They propose that “ferritchromitization” is actually an oxidation process with Mg and Al being expelled from the spinel to release lattice strain.

Over the years, a general scheme which is supported by thermochemical modelling, has emerged that considers the alteration of magmatic spinel under retrograde conditions to be a two-stage process (Gervilla et al., 2012; Barra et al., 2014; Colás et al., 2014; Colás et al., 2017; Eslami et al., 2021). A first step produces  $\text{Fe}^{3+}$ -poor chromite, sometimes termed ferrous chromite, through chlorite formation, possibly under reducing condition and high silica activity (Colás et al., 2017). Mass transfer from spinel to chlorite is believed to be responsible for the formation of porous spinel textures (*e.g.*, Gervilla et al., 2012;

Gervilla et al., 2019). A second step, at lower temperature, involves ferrian chromite moving to Fe<sup>3+</sup>-rich composition which has been ascribed to an oxidizing hydrothermal event (e.g., Gervilla et al., 2012, Colás et al., 2017). This two-step chemical trend follows a typical clockwise path in the typical Al-Cr<sup>3+</sup>-Fe<sup>3+</sup> ternary plot.

While most inferences about the processes of Cr-spinel alteration are based on alteration textures combined with EPMA data, some studies clearly show that nanoscale information can also be highly relevant. For example, Shen et al. (1988) showed using TEM that “ferritchromite” is not a stoichiometric spinel but is rather composed of a toptaxial intergrowth of an RO phase (iron-rich rock salt) and an R<sub>3</sub>O<sub>4</sub> phase (spinel structure). Reducing conditions prevailing during serpentinization may account for the presence of the FeO-rich oxide (RO). Shen et al. (1988) were also able to show that “ferritchromite” is associated with phyllosilicates, composed of interleaving chlorite and serpentine layers which are the likely hosts for the Al and Mg released by the original spinel to form “ferritchromite”. Mellini et al. (2005) characterized, using transmission electron microscopy (TEM), the contact between altered spinel rims and mesh-textured lizardite. They showed that the so-called “ferritchromite” rim consists of Cr-magnetite and chlorite/lizardite layers sharing clear epitaxial orientations. Again, phase relationships between ferrian Cr-spinel and chlorite/serpentine formation is emphasized.

In order to gain insight into hydrothermal Cr-spinel alteration under retrograde conditions (lithospheric mantle exhumation and cooling), the Sabzevar ophiolite (NE Iran) is remarkable since it host magnetite ores that formed at the expense of Cr-spinel (Eslami et al., 2021). The magnetite ore is now embedded in a serpentinized dunite aureole. Magnetite proportion can reach more than 50%. Surprisingly, ferrian chromite was not initially observed and TEM inspection was needed to identify a thin Fe-chromite rim (ca. 1 μm) in between the spinel core and its magnetite rim ranging from 70 to 220 μm in thickness. Despite reducing conditions associated with serpentinization, chromium was found to be mostly immobile. On the contrary, iron which was likely supplied by the alteration of olivine from the surrounding dunite at the early stages of serpentinization, was transported over distances of more than 10 m during serpentinization.

The Sabzevar ophiolite also hosts chromitite pods containing spinel that is much less altered. Nine such chromitite deposits from the central sector of the Sabzevar ophiolite belt (NE Iran) containing accessory magnetite were investigated. A set of chromitite -

dunite pairs were collected, which refers to samples from both the chromitite and its serpentinized dunite aureole. Chemical and textural evolution of altered spinel was characterized down to the nanoscale using EPMA and Transmission Electron Microscopy (TEM) in combination with an automatic crystallographic orientation tool (ASTAR™; Rauch and Véron 2014) for the acquisition of crystal orientation maps. Changes in spinel composition and texture are interpreted in the frame of fluid - rock interactions and spinel - silicate ratio using thermochemical modeling with a spinel solid-solution that accounts for the presence of Fe<sup>3+</sup> (Eslami et al., 2021).

## 6.2. Geological outline and modes of occurrence

Geological setting of the study area is discussed in section 3.4.1. Several chromitite bodies in the form of pods are hosted by serpentinized dunites in the Kuh-Siah and Olang-Sir massifs in the central sector of the NSOB (Figs. 3.11a and 3.11b). The deposits possess a range of morphologies occurring either as a single chromitite pod or as a series of discrete bodies. The diameter of the chromitite bodies ranges from a few centimeters to a few tens of meters. They are concordant to sub-discordant with the host peridotite foliation. A variety of chromitite textures grading from low-grade disseminated to nodular (Fig. 6.1a) and massive (Fig. 6.1b) is observed in the studied chromitite deposits. Most of the studied chromitite bodies are clustered along the NW-SE trending thrust fault system. Numerous NW-SE trending strike-slip faults often displace and terminate the chromite ore bodies. The investigated ore bodies in the locus of thrust fault zone(s) show strong shearing deformation. These ore bodies are intensively folded and show mylonitic structure. In the Olang-Sir deposit, a few magnetite ore veins with massive texture are embedded in serpentinized dunite (Fig. 6.1c). The thickness of the ore veins vary between 2 to 5 centimeters.

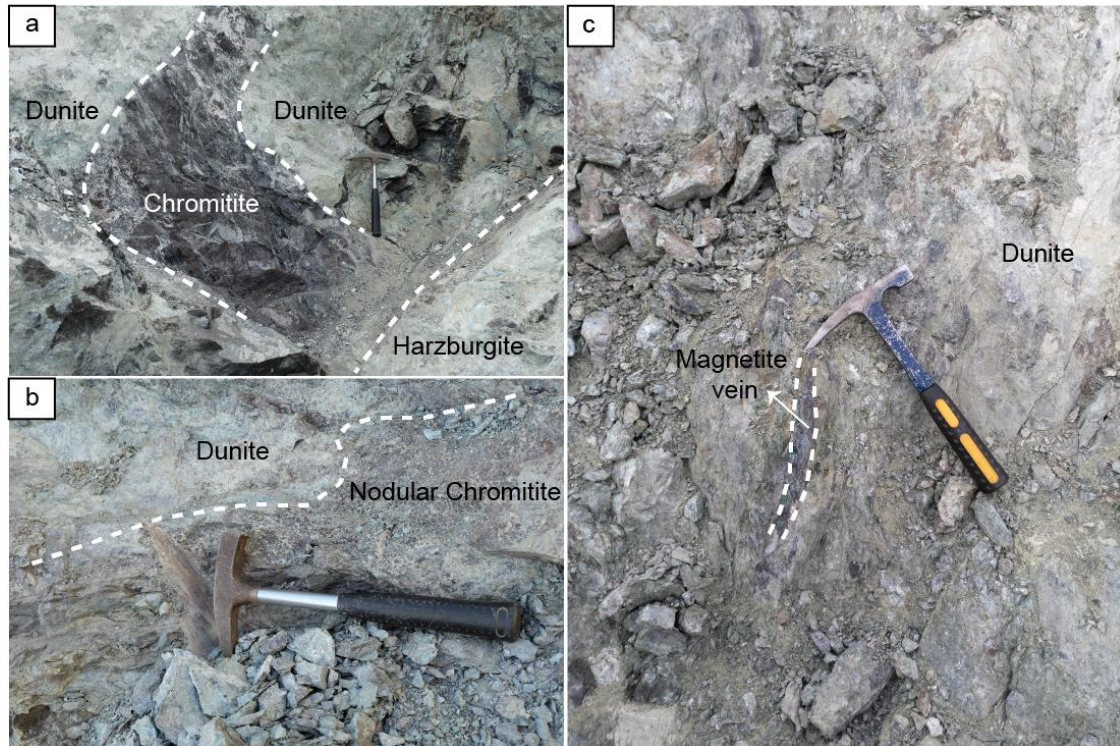


Fig. 6.1. Field photographs showing the different chromitite textures in the Sabzevar ophiolite. (a) Deformed massive chromitite pod; (b) Nodular chromitite embedded dunite; (c) magnetite ore vein hosted by serpentinized dunite (sample O1).

### 6.3. Materials and methods

Thirteen chromitite specimens from individual chromitite pods and nine samples from the host dunite were collected from nine chromitite mines in the studied area (Fig. 3.11).

Bulk-rock analyses were carried out in the Service d'Analyse des Roches et des Minéraux (SARM) at the Centre de Recherches Pétrographiques et Géochimiques (Nancy, France). Major element analyses were performed using an inductively coupled-plasma optical emission spectrometer (ICP OES iCap 6500, from ThermoFisher) and trace element compositions were measured using an inductively coupled-plasma mass-spectrometer (ICP-MS iCapQ from ThermoFisher). The samples were prepared for the analyses by fusion with  $\text{LiBO}_2$  and dissolution with  $\text{HNO}_3$ . Analytical uncertainty ( $1\sigma$ ) is 5 – 25% for major elements and 5 – 20% for minor and trace elements.

Quantitative chemical analyses of individual spinel and silicate minerals were carried out using a JEOL JXA-8230 electron probe micro-analyzer (EPMA) equipped with five wavelength-dispersive spectrometers (WDS) and an energy-dispersive spectrometer (EDS) at the Institut des Sciences de la Terre, University Grenoble Alpes, France. The beam was set at an accelerating potential of 15 kV and a probe current of 100 nA and ~1  $\mu\text{m}$  beam diameter. The concentrations of minor and trace elements (Si, V, Ti, Ni, Co, Mn and Zn) and major elements (Fe, Cr, Al and Mg) were measured by WDS and EDS, respectively. Total counting times (peak plus background) were 440 s for Si  $K\alpha$ ; 240 s for V  $K\alpha$ , Ti  $K\alpha$ ; 360 s for Co  $K\alpha$ ; 180 s for Zn  $K\alpha$ ; 100 s for Ni  $K\alpha$  and Mn  $K\alpha$ . Natural minerals, pure metals and synthetic oxides were used as standards and the ZAF correction was applied. Spectral interference (V  $K\alpha$  vs Ti  $K\beta$ ) was corrected using the JEOL software-calculated correction factor. The detection limits varied between 0.005 and 0.02 wt%, using 3-sigma criterion (Batanova and al., 2018). Elemental distribution maps were collected using an accelerating voltage of 15 kV, a beam current of 200 nA and a dwell time of 700 ms.

Interfaces between spinels with different microstructures and compositions were examined at the nanoscale in a dunite sample (sample O26) by Transmission Electron Microscopy (TEM). Three TEM lamellae were first extracted from a petrographic thin section across a marginal portions of Cr-spinels (sample O26, location on Fig. 6.3) and thinned to < 100 nm using the focused ion beam (FIB) technique at the Institut d'Electronique, de Microélectronique et de Nanotechnologie of Lille (France). The composition at the interfaces of spinels were determined by combining Scanning Transmission Electron Imaging (STEM) with Energy Dispersive Spectrometry (EDS) mapping using a Field Electron Gun JEOL™ 2100F TEM operated at 200 keV (CMTC, Grenoble, France). The oxygen maps were used to scale the number of counts and thus correct for thickness variation. Electron diffraction patterns were also acquired with an automatic crystallographic orientation tool (ASTARTM; Rauch and Véron, 2014) with a spacing ranging from 6 to 10 nm on ~ 600 x 600 grids. A comparison of the acquired patterns with templates pre-calculated with X-ray diffraction data for lizardite, chlorite, chromite and magnetite allowed to determine the nature of each phase and its orientation.

Perple\_X software (Connolly, 2005) was used to investigate the influence of the silicate/chromite ratio on the evolution of the chemical composition of chromite during alteration in the 500 - 800°C temperature range. For simplicity, pressure was set to 500 MPa based on the hydrothermal alteration climax deduced by Eslami et al. (2021). Computation was performed using three distinct bulk-rock compositions corresponding to chromite/(olivine + chromite) fractions ( $X_{\text{Chr}}$ ) of 5, 50 and 99 mol.%. The compositions of olivine and chromite were set to  $(\text{Mg}_{0.92}\text{Fe}_{0.08})_2\text{SiO}_4$  and  $(\text{Mg}_{0.95}\text{Fe}_{0.05})(\text{Cr}_{1.31}\text{Al}_{0.61}\text{Fe}_{0.08})\text{O}_4$ , respectively, and a water to rock ratio of  $\sim 1$  was used. The thermodynamic database of Holland and Powell (2011) was used for the solid phases. A generic molecular fluid equation of state for a  $\text{H}_2\text{O}/\text{H}_2$  mixture allowed to model the fluid. Aqueous speciation was calculated with the database of Sverjensky et al. (2014) and optimization with lagged forward calculations (Galvez et al., 2015). The considered solid solutions are: olivine, orthopyroxene, clinopyroxene and chlorite from Holland and Powell (1996, 1998); antigorite from Padron-Navarta et al. (2013); garnet from Jennings and Holland (2015); Cr-spinel from Eslami et al. (2021). The spinel composition evolution was determined as in Eslami et al. (2021) along a  $f\text{O}_2$  - temperature path calculated for  $X_{\text{Chr}} = 5$  mol.% with a fixed olivine composition corresponding to an  $\text{Mg}/(\text{Mg}+\text{Fe})$  ratio of 0.92.

## 6.4. Results

### 6.4.1. Bulk-rock chemistry

Whole-rock geochemical analyses from the collected chromitite – host serpentinite pairs are listed in Table 6.S1 along with those of three serpentinites hosting magnetite ores from Eslami et al. (2021) for comparison. The LOI values in serpentinitized dunite samples are very high ranging from 15 to 19 wt.%, indicating pervasive and complete serpentinitization. As described in the next section, these bulk-rock compositions can be accounted for by a biminerale assemblage composed of olivine ( $x_{\text{Mg}} = 0.92 - 0.93$ ) and Cr-spinel along with 15-19 wt.% of water. Therefore, the serpentinitized ultramafic rocks which host the studied chromitites can be considered as former dunites.

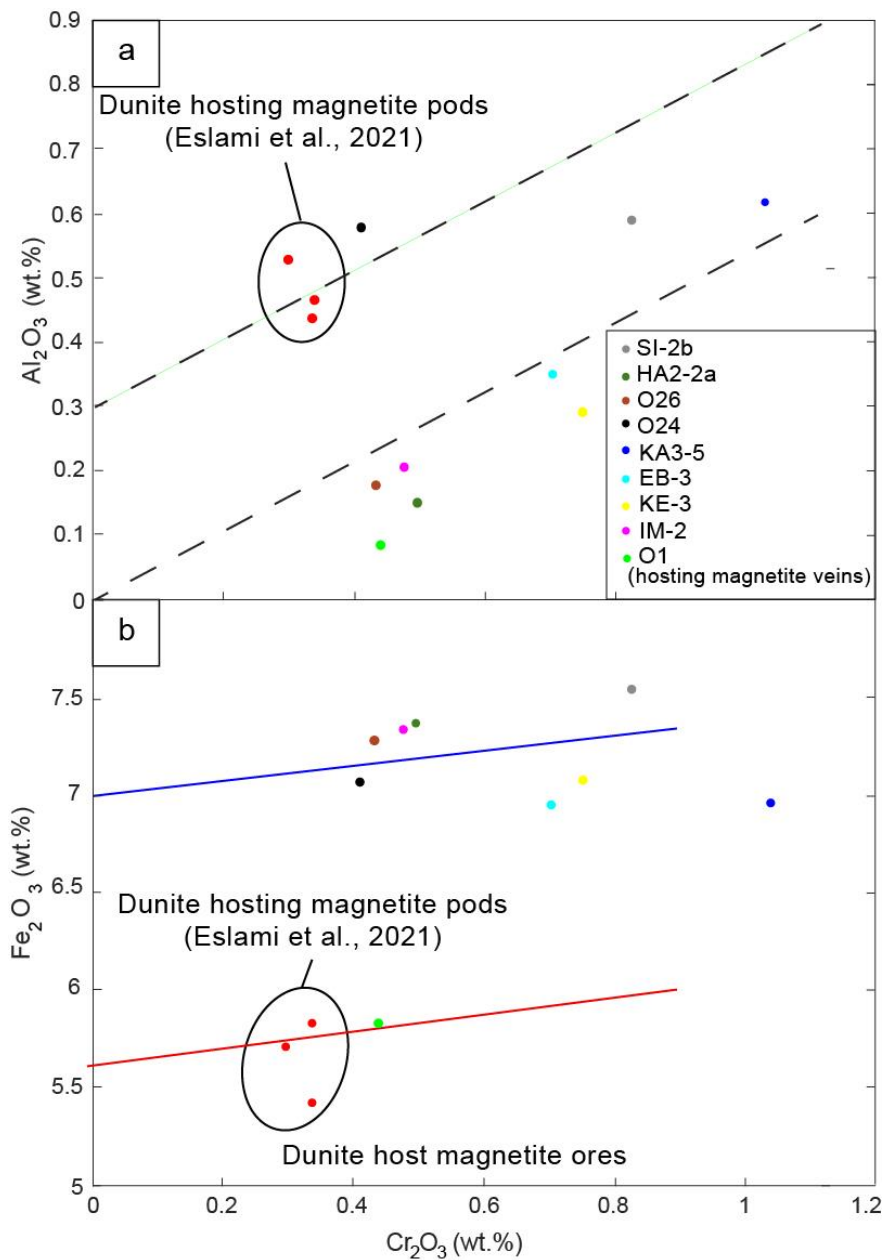


Fig. 6.2. Bulk rock analyses of the serpentinized dunite aureole around the studied chromitite pods and serpentinized dunite hosting magnetite ores plotted in a  $Al_2O_3 - Cr_2O_3$  (a) and  $Fe_2O_3 - Cr_2O_3$  (b) diagrams. Colored lines are calculated compositional trends assuming isochemical hydration of a bimineralic dunite (serpentinization) composed of olivine with  $Mg\# = 0.922$  (blue line) and  $0.938$  (red line) and Cr-spinel with a  $Al_2O_3/Cr_2O_3$

mass ratio of 0.65 as deduced from EPMA. Dashed lines are calculated considering a Cr-spinel with a  $\text{Al}_2\text{O}_3/\text{Cr}_2\text{O}_3$  ratio of 0.53 deduced from EMPA on spinel cores.

The  $\text{Cr}_2\text{O}_3$  content of the serpentinized dunite varies between 0.3 and 1.1 wt.% which is interpreted as reflecting variable amount spinel in the original dunite. Based on this assumption,  $\text{Al}_2\text{O}_3$  and  $\text{Fe}_2\text{O}_3$  contents should also be affected by the amount of spinel. The expected variations are plotted in  $\text{Al}_2\text{O}_3$  vs.  $\text{Cr}_2\text{O}_3$  and  $\text{Fe}_2\text{O}_3$  vs.  $\text{Cr}_2\text{O}_3$  diagrams (Fig. 6.2) based on representative  $\text{Al}_2\text{O}_3/\text{Cr}_2\text{O}_3$  and  $\text{Fe}_2\text{O}_3/\text{Cr}_2\text{O}_3$  ratio of spinel present in the studied serpentinized dunite samples. In the  $\text{Al}_2\text{O}_3$  vs.  $\text{Cr}_2\text{O}_3$  diagram (Fig. 6.2a), the  $\text{Al}_2\text{O}_3$  content of the serpentinized dunite samples which host the chromitites is found to follow the expected trend which, when extrapolated down to  $\text{Cr}_2\text{O}_3$  free composition, indicates that chromite was the only Al-bearing phase in the original dunite. Serpentinized dunite which host magnetite ores follows the same trend but about 0.3 wt.% of the bulk  $\text{Al}_2\text{O}_3$  must be hosted by another phase. Eslami et al. (2021) reported the presence of chlorite in these serpentinized dunite, which is the likely  $\text{Al}_2\text{O}_3$  host together with spinel. This additional  $\text{Al}_2\text{O}_3$  may either reflect the former presence of Al-bearing orthopyroxene or Al-mass transfer, possibly from the magnetitized chromitite due to intensive fluid-rock interaction (Eslami et al., 2021). In the  $\text{Fe}_2\text{O}_3$  vs.  $\text{Cr}_2\text{O}_3$  diagram, again, serpentinized dunite hosting chromitites plot on a same trend which is consistent with a dunite composed of olivine ( $x_{\text{Mg}} = 0.92$ ) and variable amount of Cr-spinel. Serpentinized dunite hosting magnetite ores (samples MG16, MG20 and MG21) are rather consistent with a former dunite composed of Fo94. As described by Eslami et al. (2021), this apparent enrichment in Mg reflects the transfer of iron from the ultramafic host-rock towards magnetite ores during fluid-rock interactions. It must be noted that sample O1 which was collected near a magnetite vein (Fig. 6.1c) also display a relative MgO enrichment (Fig. 6.2b) again iron mobility can be invoked.

Bulk chromite chemistry was also measured on thirteen chromitite samples. There are characterized by  $\text{SiO}_2$  contents which vary from below detection in massive chromitite to up to 22 wt.% in a serpentinized dunite with disseminated chromite grains. LOI and Ni-content ( $< 0.25$  wt.%) are correlated to  $\text{SiO}_2$  indicating that the Ni-bearing silicate matrix is hydrated.  $\text{TiO}_2$  is close to 0.15 wt.% and relatively constant whatever the chromitite

texture. Among trace and minor elements which are hosted by Cr-spinel, Ga < 25 ppm, As < 500 ppm, V < 900 ppm, Zn < 1500 ppm and Mn < 2700 ppm.

#### 6.4.2. Mineral modes and temperature calculation

Assuming that prior to serpentinisation, the dunite was exclusively composed of olivine and chromite, the respective modes of chromite, fayalite and forsterite prior to serpentinization were retrieved by least squares regression (LSQ) through the bulk composition of the serpentinized dunite samples (Table 6.1). The chromite composition used in the regression is based on the electron microprobe data. Variations in chromite composition observed with the electron microprobe (Fig. 6.6) have little effect on the calculated modes due to the low spinel content which is close to 1 wt. %. Recalculation of the bulk oxide content from these modes leads to deviation below 1.5 wt.% on each oxides, except for sample SI-2b whose deviation can be up to 3 wt.%.

Table 6.1. Dunite mineral modes (wt.%) and  $X_{Mg}$  of olivine were retrieved from least-square (LSQ) regression through the bulk dunite composition

Sample No.	Deposit name	$X_{Mg}$ Ol	Chr (wt.%)	Srp (wt. %)
KA3-5	Kalchenari-3	92.9	1.8	78.3
HA2-2a	Haj-Ghasem	90.5	1.5	80.4
SI-2b	Main Sinerkar	89.5	0.2	81.5
O1	Olang-Sir	93.8	0.9	80
EB-3	Ebrahim	90.5	1.6	78.7
KE-3	Kermaniha Tunnel	92.3	1.2	79.5
IM-2	Imam Hossein	91.7	0.7	80.3
O24	Olang-Sir	88.1	0.5	82.9
O26	Olang-Sir	91.8	0.7	80.9

Olivine Mg# is found to cluster around 0.92 (Fig. 6.2b, Table 6.1) with a few samples corresponding to dunite around magnetite and the O1 sample which display a higher value, around 0.94 (Fig. 6.2b).

Owing to the small chromite content, olivine – chromite Fe-Mg exchange upon cooling does not affect the olivine composition. Therefore, reconstructed olivine compositions were tentatively used to infer equilibration temperature with spinel using the thermometer calibrated by Ballhaus et al. (1991). Temperature in the 500-750°C range were obtained which likely reflect the blocking temperature of the Fe-Mg exchange

(Bussolesi et al., 2022). This temperature may be hampered by the formation of Mg-chlorite which is expected to form at  $T < 700$  °C according to our thermochemical modelling.

Mineral mode calculation (Table 6.2) was also performed on semi-massive and a serpentinized dunite with disseminated chromite grains assuming again olivine and spinel as the only rock-forming minerals. The bulk SiO<sub>2</sub> content in massive chromitites is below 3 wt.%. Therefore four samples (KA3-1c, KA5-1a, KE-2, KA1-1b) were considered as composed of chromite only and modes were not calculated. For the other chromitite samples, recalculation of the bulk composition with the retrieved modes led to deviations below 1.5 wt. % from the analyzed oxide content. The approximation of isochemical serpentinization of an initial dunitic matrix is thus supported. In the chromitites, Fe-Mg exchange between chromite and olivine upon cooling is expected to strongly affect the olivine Mg# (Engi, 1983) which is a minor component in these samples. The Mg# of the initial olivine could be reliably retrieved for samples with SiO<sub>2</sub> content above 5 wt.% and was found to range between 0.92 and 0.94. From these Mg#'s and chromite core compositions, temperature comprised between 900 and 1080°C could be derived with the Ballhaus et al. (1991) thermometer.

Table 6.2. Chromitite mineral modes (wt.%) retrieved from LSQ regression through the chromitite bulk rock composition

Sample No.	Deposit name	Texture	X <sub>Mg</sub> Ol	Spinel (wt.%)
SI-2c	Sineh-Kar	Semi-massive	-	80.3
KA3-1c	Kalchenari-3	Semi-massive	93.8	70.9
HA2-1	Haj-Ghasem	Semi-massive	-	86.8
KA1-1b	Kalchenari-1	Semi-massive	93.8	68.5
KE-2	Kermaniha Tunnel	Semi-massive	92.5	67.8
KA5-1a	Kalchenari-5	Disseminated	93.4	53.7

### 6.4.3. Textural observation at the $\mu$ -scale

The Sabzevar chromitite samples are made up of massive chromitite (> 90 vol% chromite), semi-massive chromitite (corresponding to serpentinized olivine chromitite as

defined in Greenbaum, 1977). A single sample (KA5-1a) is a serpentinite containing disseminated chromite grains (corresponding to serpentized chromitiferous dunite as defined by Greenbaum, 1977) (Table 6.2). Chromites from both chromitite and serpentized dunite samples show two main alteration microtextures that can be described as follows on the basis of SEM images. A first textural type is encountered which corresponds to homogeneous spinel cores either rimmed by (or locally replaced by) heterogeneous domains composed of spinel grains with little or no inclusions / pores (Fig. 6.3a) or patches of porous chromite (Fig 6.3b-c). This textural type is mostly visible in the massive and semi-massive chromitites. Rims of porous chromite have thicknesses ranging from 15 to 250  $\mu\text{m}$ . The pore size ranges from 2 to 15  $\mu\text{m}$ . The pores are either empty or filled with magnetite, serpentine or chlorite (Fig. 6.3c); Following the nomenclature used by Gervilla et al. (2012) and Eslami et al. (2021), this type of texture will be called *partly altered*. In addition to partly altered textural feature, in highly deformed chromitite sample (SI-2c), magnetite veinlets cut through Cr-spinel grains encompassed by a matrix of andradite, carbonate and serpentine (Fig. 6.3d) and/or crystallized at the chromite surface.

The last textural type is composed of zoned chromite grains with a homogeneous core (spinel -I) that is rimmed by a homogeneous corona of secondary spinel having a thickness of 5 to 30  $\mu\text{m}$  (Fig. 6.3e-f). The contact between spinel core and its alteration rim is sharp (Fig. 6.3g). Following Gervilla et al. (2012) this type of texture will be called zoned chromite. It is only found in serpentized dunite sample (sample O26). It must be noted that zoned chromite texture can also display a partly altered texture with patches of pores that form at the interface between spinel core and homogeneous rim (Fig. 6.3h-i). The chronology between these two coexisting types of alteration textures cannot be inferred from the SEM observation. The porous chromite areas are marked by globular or elongated pores.

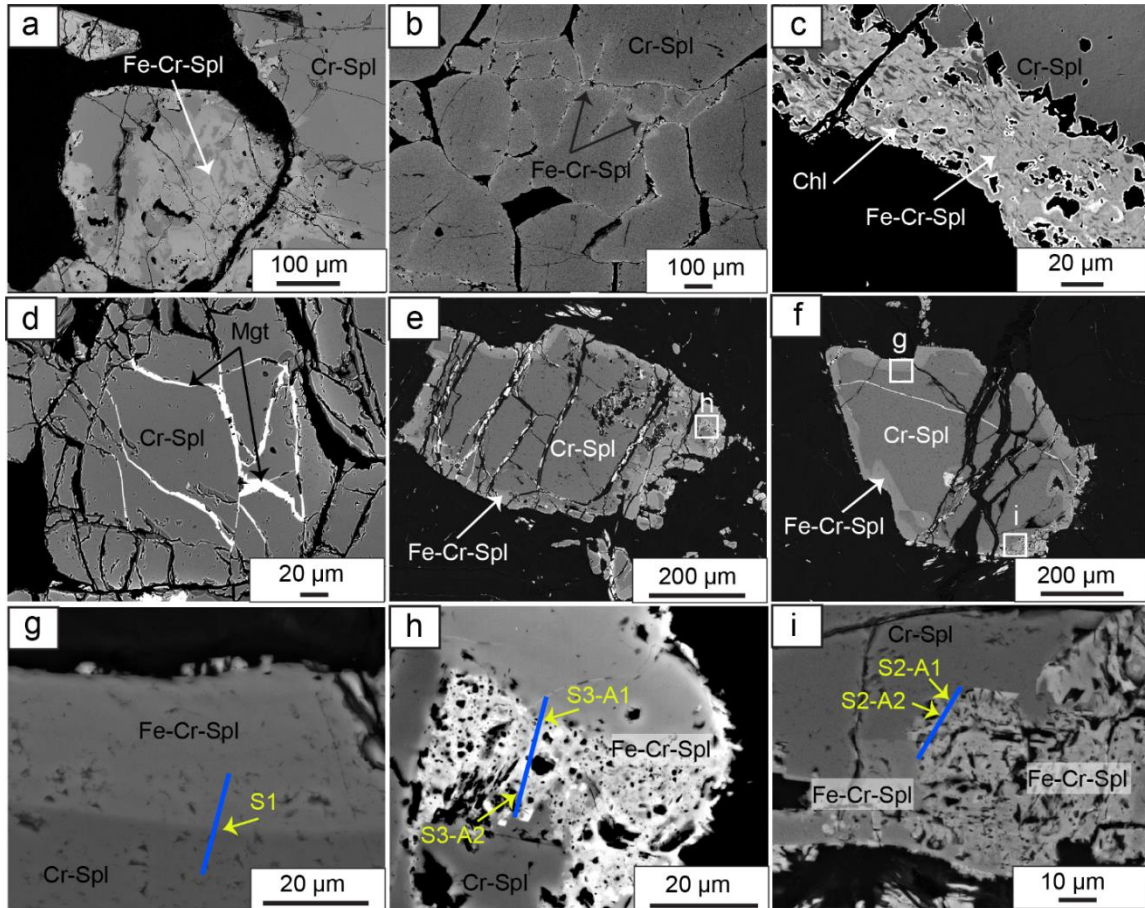


Fig. 6.3. Backscattered-electron images of slightly to mildly altered occurrences in the Sabzevar ophiolite. (a) Heterogeneous chromite (Fe-Cr-Spl) domains around homogeneous chromite (Cr-Spl) (sample EB-4). (b) Heterogeneous chromite (Fe-Cr-Spl) along the cracks and boundaries of homogeneous chromite (Cr-Spl) (sample O27). (c) Porous chromite (Fe-Cr-Spl) with serpentine and chlorite inclusions at marginal parts of homogeneous chromite core (sample IM-1b); (d) Magnetite (Mgt) veinlets rumbling through the homogeneous chromite (sample SI-2c); (e-f) Zoned chromite with homogeneous chromite core (Cr-Spl) surrounded by homogeneous chromite rim (Fe-Cr-Spl) (sample O26). (g) Sharp contact between homogeneous chromites. (h) Porous chromite with tiny globular silicate inclusions; (i) Porous chromite with sheet silicate inclusions; Blue lines indicate the location TEM lamella.

#### 6.4.4. Observations at the nano-scale

In order to resolve spinel alteration and replacement processes at the nanoscale from TEM observation, three FIB lamellae were cut across the interface between homogeneous Spinel-I cores and their alteration rims in a dunite sample (sample O26; blue thick lines in Fig. 6.3).

Three compositional maps (S2-A1, S2-A2 and S3-A2) were collected at the interface between homogeneous Cr-spinel and a secondary porous Fe-Cr-spinel zone (Fig. 6.4). The maps show that chromite in the porous zone is chemically distinct from Cr-spinel. It is characterized by higher Cr and Fe as well as lower Al contents as expected according to the chemical effect of alteration deduced from EPMA data at the microscale (Fig. 6.4). Whereas Cr-spinel is devoid of mineral inclusions, Fe-Cr-spinel in the porous zone contains pores filled with intercalated platelets of magnetite and silicates (S2-A1 and S3-A2). The silicates display fine cleavage planes consistent with layered silicates. Based on the Fe-poor and Mg- and Si-rich composition and on the presence of Al, these silicates could either consist in lizardite or chlorite with platy shapes and perfect cleavage along the (001) plane. Electron diffraction pattern matching indicates the co-existence of these two phases (Fig. 6.5). However, the phase identification reliability is low, which does not allow to unequivocally conclude on the nature of the silicate inclusions. At the nanometer scale, remnants of pristine  $\sim 1 \mu\text{m}$ -wide Cr-spinel are observed as irregular selvages in porous Fe-Cr-spinel. Automated crystal orientation mapping (Fig. 6.5a-c) shows epitaxial growth of porous Fe-Cr-spinel from Cr-spinel. Similar epitaxial relationship is observed between magnetite and porous chromite. A crystallographic relationship between lizardite/chlorite and chromite/magnetite is also observed with the (001) phyllosilicate plane being parallel to the (111) chromite/magnetite plane (Fig. 6.5e). Magnetite can occur as elongated plane in between (001) phyllosilicate planes (reference to S3-A2).

Another elemental map (S3-A1) has been collected at the interface between the rim of a zoned chlorite and the porous chromite area described above (Fig. 6.4). The pores have a rounded shape (below  $1 \mu\text{m}$  across) and are distinct from the elongated pores filled with phyllosilicate. Both chromite homogeneous rim and porous area result from the alteration/replacement of Cr-spinel but it cannot be deduced from SEM images which one formed first. At the nanometer scale, the homogeneity of the alteration rim (zoned chromite texture) is confirmed since it is devoid of pores and voids filled with silicate

phases. In the porous zone, the pores seem to play a role in promoting the chemical exchange (e.g., Al and Mg removal, Fig. 6.4 section S3-A1) involved in the Cr-spinel alteration.

Chromite in the porous zone and homogeneous alteration rim (zoned chromite) are characterized by higher Fe and Cr and lower Al than the Cr-spinel core in agreement with the chemical alteration trend outlined on Fig. 6.6 based on EPMA data. The homogeneous chromite rim contains however lower Cr and Fe and higher Al contents than ferrian chromite in the porous area what would either suggest that porous alteration occurred at a later stage or that it was more efficient in modifying the original spinel composition. Despite the slight chemical differences between these spinel textural types, they plot in the same region in ternary diagram Cr-Al-Fe<sup>3+</sup> (Fig. 6.6b). Again, both types of secondary spinel share similar crystallographic orientation which is inherited from Cr-spinel, indicating topotaxial replacement.

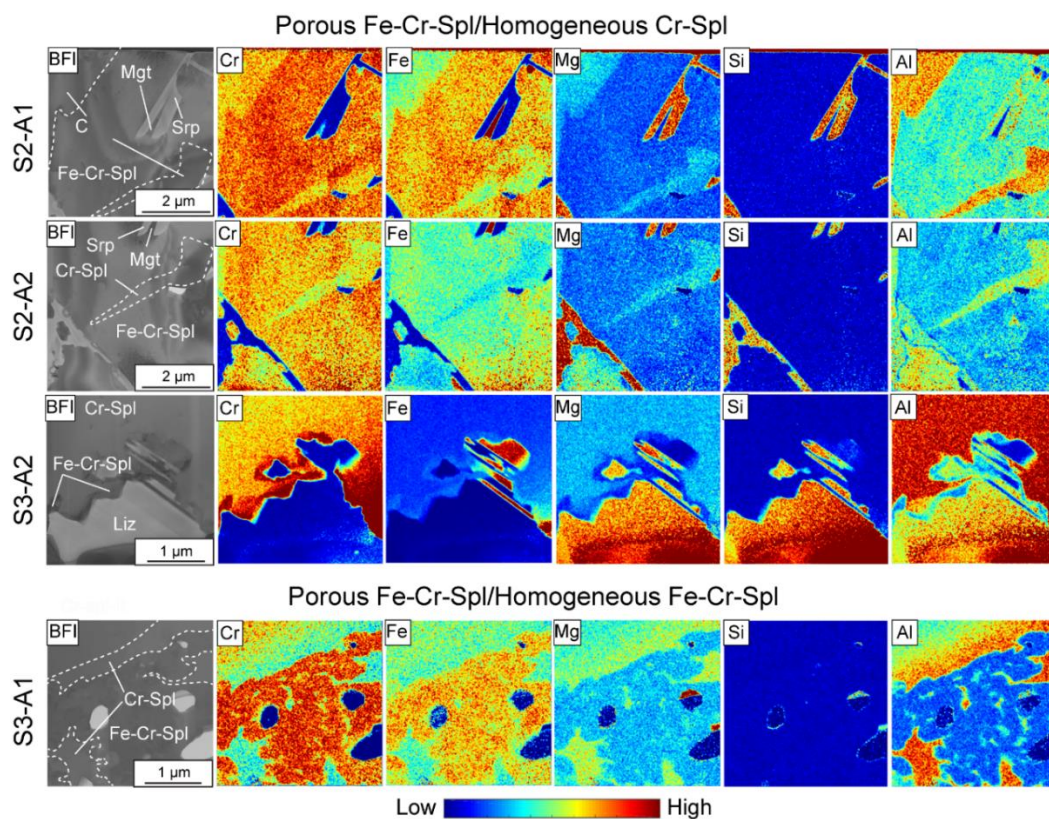


Fig. 6.4. Bright Field Image and EDS-STEM element maps of the porous Fe-Cr-spinel/homogeneous Cr-spinel and porous Fe-Cr-spinel /homogeneous Fe-Cr-spinel. Abbreviation: Srp (serpentine), Mgt (magnetite), Cr-spl (Cr-spinel), Liz (Lizardite).

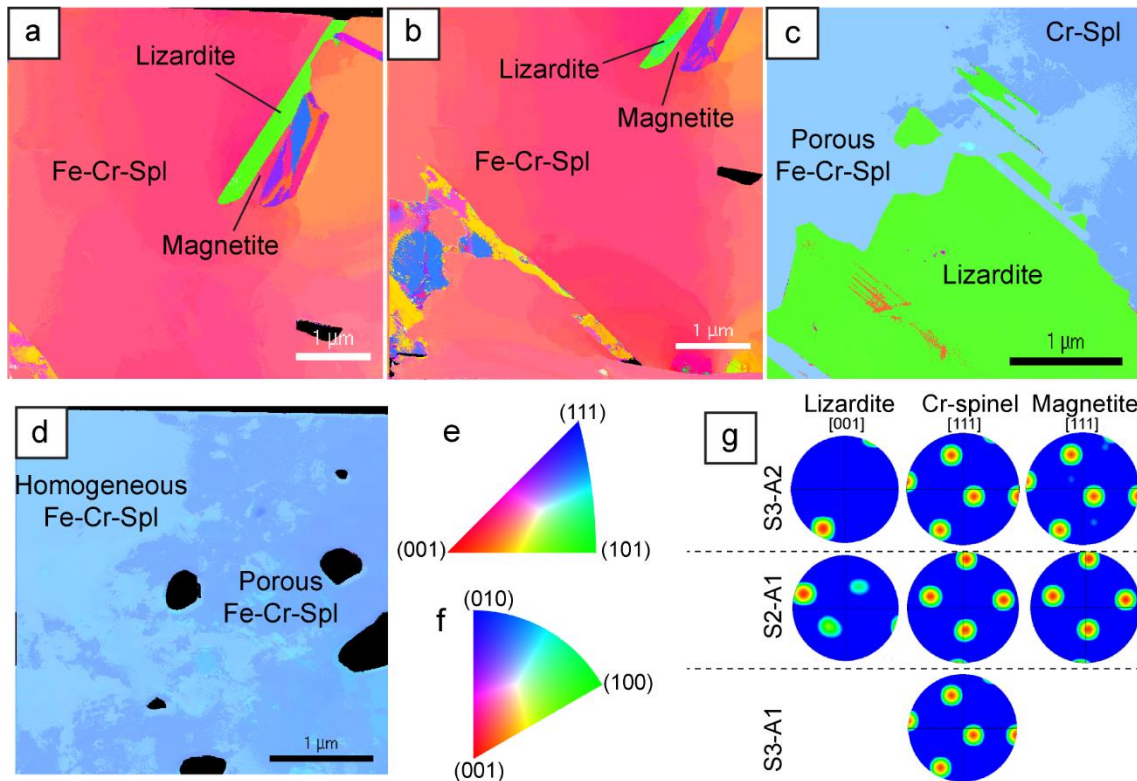


Fig. 6.5. Orientation maps (a-d) of spinels and associated silicate inclusions in the same region as Fig. 4 (a: S2-A1; b: S2-A2; c: S3-A2 and d: S3-A1). (e-f) Colour-coded inverse pole figures used for displaying Cr-spinel/magnetite (e) and lizardite (f) orientation in (a-d). (g) pole figures of lizardite and spinels in (a-d).

## 6.4.5. Mineral chemistry

### 6.4.5.1. Spinel

The composition of spinel from chromitite and associated dunite is plotted in a ( $\text{Fe}^{3+}$ -Cr-Al) ternary plot (Fig. 6.6a). All these compositions correspond either to chromite or magnesiochromite according to the spinel classification proposed by Bosi et al. (2019). The composition of homogeneous spinel cores in the investigated chromitites corresponds to magnesiochromite, it is characterized by a Cr#,  $(\text{Cr}/\text{Cr} + \text{Al}) \times 100$ , ranging between 60 and 74 and an Mg#,  $(\text{Mg}/\text{Mg} + \text{Fe}^{2+}) \times 100$ , ranging between 61 and 71 (Table 6.S2). Minor oxide content in these homogeneous cores is typically below 0.35 wt.% ( $\text{TiO}_2 \leq 0.31$  wt. %;  $\text{MnO} \leq 0.19$  wt. % and  $\text{NiO} = 0.08 - 0.18$  wt. %; Table 6.S2) and generally

analogous to those measured in the spinels from the serpentinized dunite envelope (Table 6.S3). These compositions might depart from original magmatic compositions since they have been likely modified by sub-solidus equilibration with olivine (e.g., Bussolesi et al., 2021). However, they will be called Cr-spinel in the following since they represent the earliest stage that is preserved. The composition of chromites formed after Cr-spinel when plotted as a function of their trivalent cation content in a ternary Al-Cr-Fe diagram, seems to follow two distinct chemical trends. (Fig. 6.6a): (i) A “Trend 1” in the ternary plot (closer to the Cr apex), in which Cr progressively increases from the primary composition. This trend is discernible in semi-massive and massive chromitites. (ii) A “Trend 2” in which there is an increase in Cr associated with increase in total iron compared to the “Trend 1” (Fig. 6.6b). This latter trend is related to Cr-spinel ( $\text{Fe}_{0.65}, \text{Mg}_{0.35})(\text{Cr}_{1.06}, \text{Al}_{0.32}, \text{Fe}^{3+}_{0.59})\text{O}_4$  with porous texture in a serpentinized dunite with disseminated chromite grains and serpentinized dunite samples. In both trends, total iron (Fig. 6.6c) is increasing whereas Mg# (Fig. 6.6d) is decreasing through spinel alteration. These two distinct trends are distinguishable in Figures 6.7a and 6.7b. In serpentinized dunites, NiO is remarkable increasing with increase of alteration which may be ascribed to presence of olivine as a main repository of Ni (Fig. 6.7c).

The composition of homogeneous rim around Cr-spinel in zoned chromite plots in the same area ascribed to porous Cr-spinel-II in the Sabzevar highly altered occurrence(s) (Eslami et al. 2021) and is marked by an Mg# between 37 and 44 and a Cr# between 63 and 73. Heterogeneous portions of Cr-spinel in a serpentinized dunite with disseminated chromite grains and massive chromitites plot in the areas assigned to porous Fe-Cr-spinel and homogeneous Fe-Cr-spinel, respectively (Fig. 6.6b). They have Cr# values ranging from 62 to 100, and Mg# from 12 to 70. In the serpentinized dunite sample where we cut three FIB sections, the structural formula of homogeneous corona surrounded primary Cr-spinel is  $(\text{Fe}_{0.55}, \text{Mg}_{0.44})(\text{Cr}_{1.3}, \text{Al}_{0.57}, \text{Fe}^{3+}_{0.12})\text{O}_4$  which plots in the field of porous Fe-Cr-spinel (Fig. 6b).

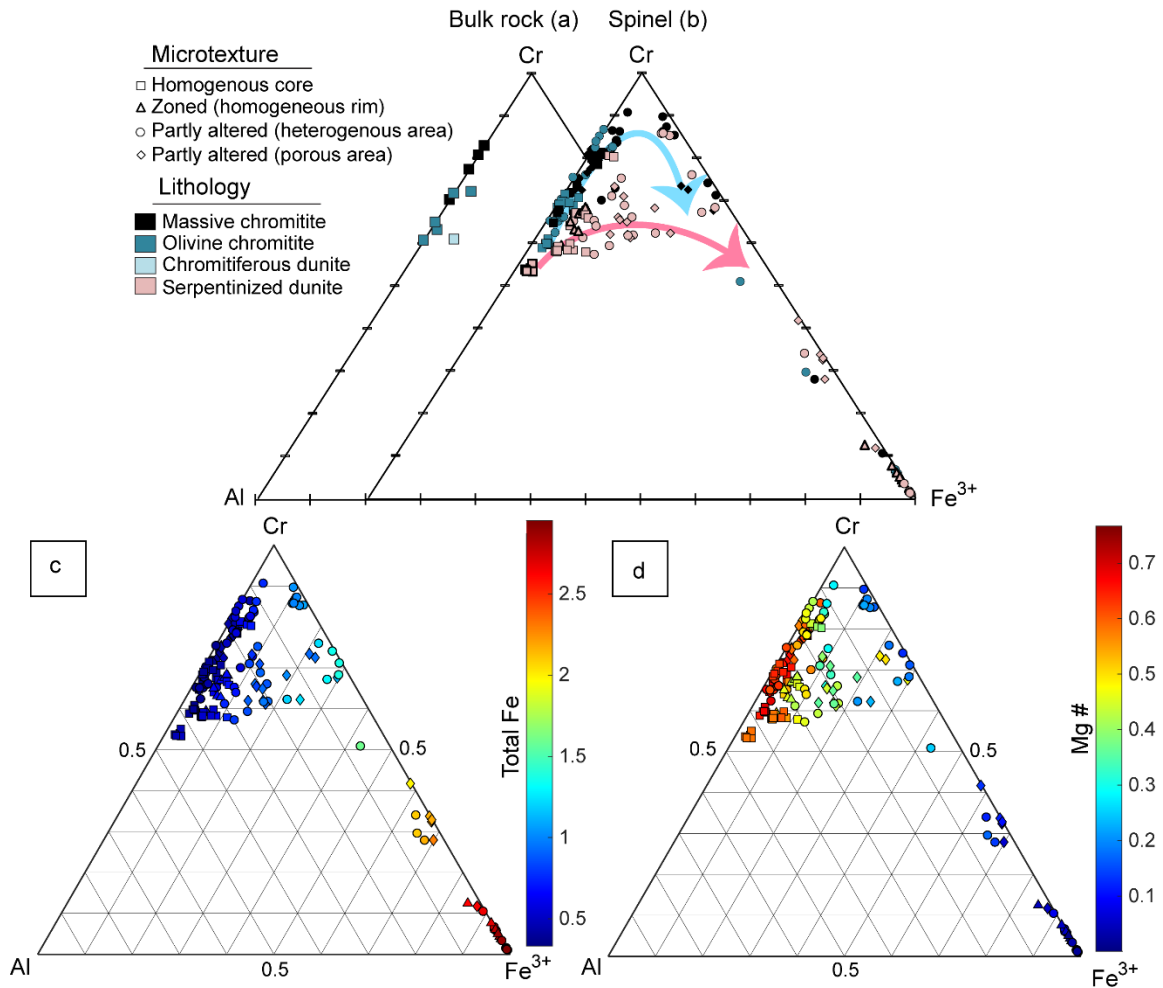


Fig. 6.6. Compositional plot of chromitites (a) and spinels (b) on a ternary diagram Cr-Al-Fe<sup>3+</sup> showing two distinct compositional trends (c), total iron (apfu on a 4 oxygen basis) (d) and Mg# variations through alteration processes.

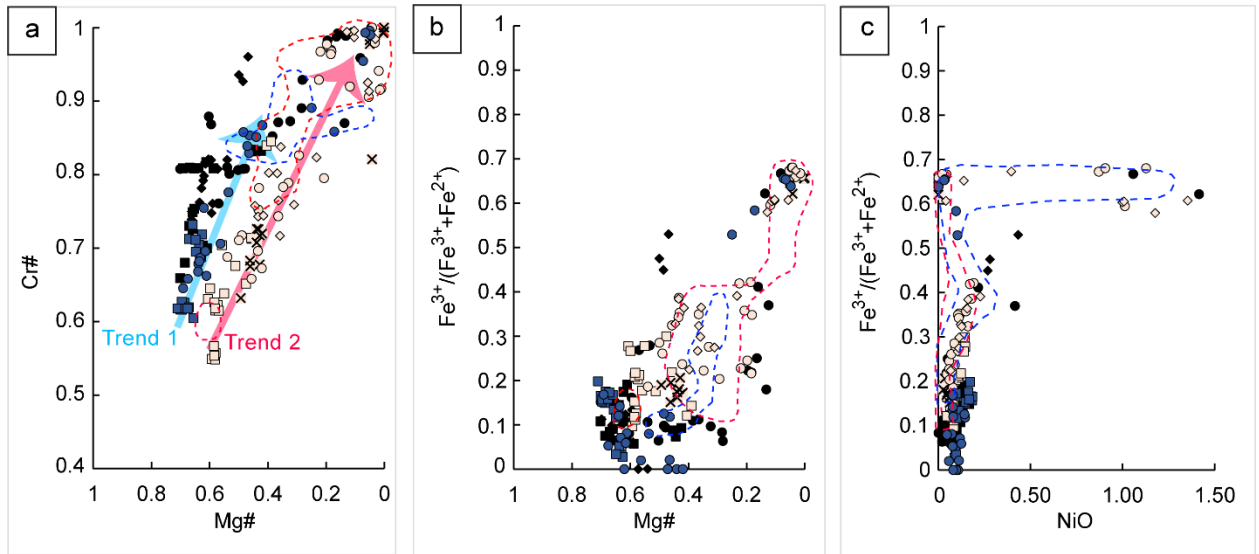


Fig. 6.7. Compositional variations of Cr-spinel grains from the Sabzevar ophiolite, in terms of Cr#, Mg#,  $\text{Fe}^{3+}/(\text{Fe}^{3+} + \text{Fe}^{2+})$  and NiO (wt. %). Fields for the Sabzevar magnetite ore (blue dashed line) and its host dunite (red dashed line) are given for comparison (Eslami et al., 2021).

#### 6.4.5.2. Serpentine and chlorite

Representative microprobe analyses of serpentine and spinel-hosted chlorite inclusions from the Sabzevar chromitite ore deposits are given in Tables 6.S4 and 6.S5, respectively. Serpentine from massive and semi-massive chromitite samples shows lower FeO content (1.13 - 4.61 wt. %) and higher Mg# (0.94 - 0.99) than serpentine from a serpentinized dunite with disseminated chromites (3.04 - 3.85 wt.% and 0.95 - 0.96, respectively) and serpentinized dunite samples (3.48 - 12.47 wt.% and 0.84 - 0.96, respectively).

Chlorite inclusions in spinel are categorized as clinochlore following the classification of Bailey (1980). Their Mg# ranges from 0.88 to 0.99,  $\text{Al}_2\text{O}_3$  is comprised between 11.1 and 19.9 wt.%. They are characterized by the presence of chromium with  $\text{Cr}_2\text{O}_3$ -content up to 4.0 wt.%.

#### 6.4.6. Thermochemical modeling of the evolution of spinel composition: role of the silicate/chromite ratio

The evolution of spinel composition upon cooling from 800 down to 500°C has been calculated for three chromite molar proportions,  $X_{\text{Chr}}$ , of 5, 50 and 99 mol.% and a mass water to rock ratio of  $\sim 0.5$  (Fig. 6.S1). When the chromite fraction is high ( $X_{\text{Chr}} = 99$  mol.%), the spinel composition is close from  $(\text{Mg}_{0.95}\text{Fe}_{0.05})(\text{Cr}_{1.31}\text{Al}_{0.61}\text{Fe}_{0.08})\text{O}_4$ , that is from the composition used to compute the bulk rock composition. The  $\text{Fe}^{3+}$ -content at high temperature (800°C) slightly increases as  $X_{\text{Chr}}$  decreases. This is due to the presence of orthopyroxene in the calculated stable assemblage. The presence of orthopyroxene instead of the olivine considered to determine the bulk rock composition implies that less Mg and Fe are incorporated in the silicates. Orthopyroxene indeed has a  $(\text{Mg} + \text{Fe})/\text{Si}$  ratio of 1 whereas this ratio is of 2 in olivine. Excess Mg and Fe are found in spinel through the combined incorporation of  $\text{Mg}^{2+}$  and  $\text{Fe}^{3+}$ , responsible for the increase in iron in the Cr-Al- $\text{Fe}^{3+}$  diagram at 800°C (Fig. 6.S1).

The Al fraction in chromite decreases with temperature. This trend is more pronounced for  $X_{\text{Chr}} = 5$  mol.% and 50 mol.% than for  $X_{\text{Chr}} = 99$  mol.%. It corresponds to the formation of chlorite at temperature below 725°C. The amount of available silica is not sufficient at  $X_{\text{Chr}} = 99$  mol.% to allow for a significant change in composition. For  $X_{\text{Chr}} = 5$  mol.% and 50 mol.%, chlorite formation during spinel reaction leads to the complete removal of Al from spinel. The bulk Al/Si molar ratio is of 0.61 at  $X_{\text{Chr}} = 50$  mol.%. This value is close from the Al/Si molar ratio of 2/3 computed for chlorite composition. As a result, silica is entirely consumed by chlorite formation at  $X_{\text{Chr}} = 50$  mol.%. This is not the case at  $X_{\text{Chr}} = 5$  mol.%, leading to an additional trend at temperature below 600°C with the progressive increase of the spinel  $\text{Fe}^{3+}$  content towards the magnetite end member (Fig. 6.S1). This latter trend is associated with the formation of serpentine. As the  $\text{Mg}/(\text{Mg}+\text{Fe})$  ratio is lower than 2 mol.% in serpentine, the iron released during olivine reaction as temperature decreases is incorporated into Cr-spinel and the  $\text{Fe}^{3+}$  content increases.

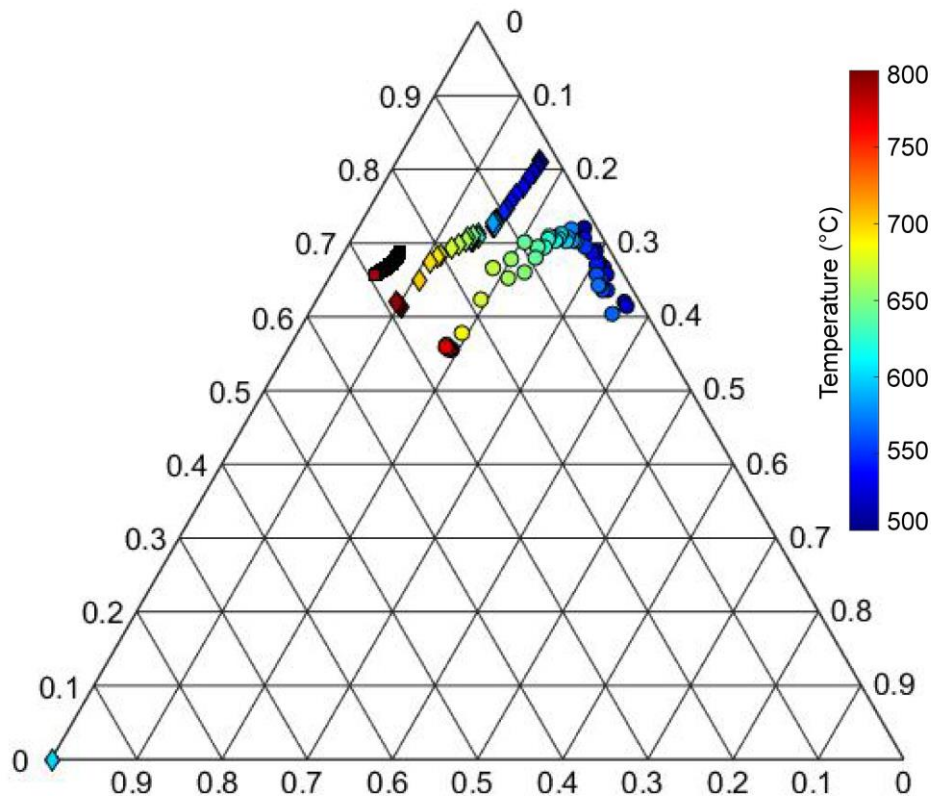


Fig. 6.S1. Evolution of Cr-spinel composition in a Al-Cr-Fe<sup>3+</sup> diagram. The evolution of composition is displayed for three different rock composition corresponding to a fraction of chromite ( $X_{Chr}$ ) of 5 mol.% (circles), 50 mol.% (diamonds) and 99 mol.% (squares). The color corresponds to the temperature at which the composition at the equilibrium is displayed.

## 6.5. Discussion

### 6.5.1. Modelling the chromite chemical evolution during alteration

Two types of spinel chemical evolution are observed in samples from the Sabzevar ophiolite. The first trend (Trend 1) is measured in massive and semi-massive chromitites. Actually both bulk chromitite and chromite grain compositions follow Trend 1. This trend is mainly characterized by a progressive decrease in aluminum displacing spinel composition towards the (Mg,Fe)Cr<sub>2</sub>O<sub>4</sub> end-member. The second trend (Trend 2) is measured in a serpentinized dunite with disseminated chromite grains as well as in the serpentinized dunite aureole around massive and semi-massive chromitites. It also

involves aluminum removal but this removal occurs concurrently with  $\text{Fe}^{3+}$  incorporation in spinel. The final part of the two trends is similar. It involves the formation of two different spinels, one is close to the  $\text{FeCr}_2\text{O}_4$  end-member and the other close to magnetite,  $\text{Fe}_3\text{O}_4$ . The two trends involve a decrease in the Mg #. However, the value of the Mg# for a given Cr # is systematically lower in a serpentized dunite with disseminated chromites/serpentized dunitites than in massive chromitites, leading to two parallel trends in Cr# vs. Mg# diagram (Fig. 6.7a). These two trends may be also observed in previous studies (Gonzalez-Jimenez et al., 2009; Barra et al., 2014). However, the influence of lithology (a serpentized dunite with disseminated chromites/serpentized dunitites versus massive chromites) was not considered in the previous studies as a main parameter influencing the trends.

The regional geology indicates that the Sabzevar ophiolite was progressively exhumed and obducted (e.g. Kazemi et al., 2019). These two trends could thus be the results of retrograde metamorphism (Eslami et al., 2021). Thermodynamic modelling indicates that during cooling chromite composition evolves due first to chlorite formation at temperatures below  $\sim 725^\circ\text{C}$  and then to serpentine formation at temperatures below  $550^\circ\text{C}$ , in good agreement with previous studies (Mellini et al., 2005; Grieco and Merlini, 2011; Gervilla et al., 2012; Eslami et al., 2021). This alteration in two steps induces first  $\text{Fe}^{2+}$ -rich and Al-poor chromite formation and then  $\text{Fe}^{3+}$ -rich incorporation in to spinel. Even though thermodynamic modelling reproduces the general trend observed for spinel composition evolution (Fig. 6.S1), it does not allow to understand why two trends can be formed during spinel alteration upon cooling.

This is due to the fact that the initial composition of the spinel depends on  $X_{\text{Chr}}$  in the thermodynamic model (different location of spinel composition at  $800^\circ\text{C}$ ), preventing a simple comparison of the predicted trends. Moreover, the considered chlorite solid solution does not include Cr which plays a key role regarding spinel evolution composition. In addition, the spinel solid solution used in thermodynamic modelling predicts  $\text{Mg}/(\text{Mg} + \text{Fe}^{2+})$  systematically higher than the measured values. Last but not least, the model assumes equilibrium at the bulk-rock scale which is obviously not the case in the studied samples where chromite reaction is limited and did not reach equilibrium. To circumvent these issues and determine the factors responsible for the two observed trends, we built a mass balance model based on the two successive reactions predicted by

thermodynamic modelling. This model is detailed in the Appendix 6.7. Its main constitutive equation is recalled here.

Based on thermodynamic modelling, the retrograde reaction of a chromite + olivine + orthopyroxene assemblage is expected to form chlorite and then serpentine as the temperature decreases. In addition to these phases, brucite,  $(\text{Mg}, \text{Fe})(\text{OH})_2$ , and aqueous species have been proposed to be involved in similar reactions (e.g., Gervilla et al., 2012; Barra et al., 2014; Colas et al., 2017). The formation of brucite occurs at temperatures below  $400^\circ\text{C}$  for which magnetite and Cr-bearing spinels are immiscible (Sack and Ghiorso, 1991; Eslami et al., 2021). The spinel compositions measured in Sabzevar spinels fall in the miscible region, suggesting that alteration occurred at  $T > 400^\circ\text{C}$ , i.e., outside the stability field of brucite. This latter phase is thus not considered in the model.

For the three thermodynamic models with different  $X_{\text{Chr}}$ , the aqueous species concentrations are comprised between  $\sim 10^{-4}$  and  $10^{-1}$  mol/kg for silica,  $10^{-5}$  and  $10^{-2}$  mol/kg for iron and  $10^{-2}$  and  $10^{0.5}$  mol/kg for magnesium (Fig. 6.S2). The model thus predicts that Mg is several orders of magnitude more soluble than Fe and Si during ultramafic rocks alteration in the  $500 - 800^\circ\text{C}$  temperature range. We therefore considered aqueous Mg as a potential reaction product in the spinel alteration reaction. The solubility of Mg was fixed to  $10^{-0.5}$  mol/kg and the total amount of aqueous Mg ( $\text{Mg}^{2+}_{\text{aq}}$ ) thus depends on the water to rock ratio (w/r ratio).

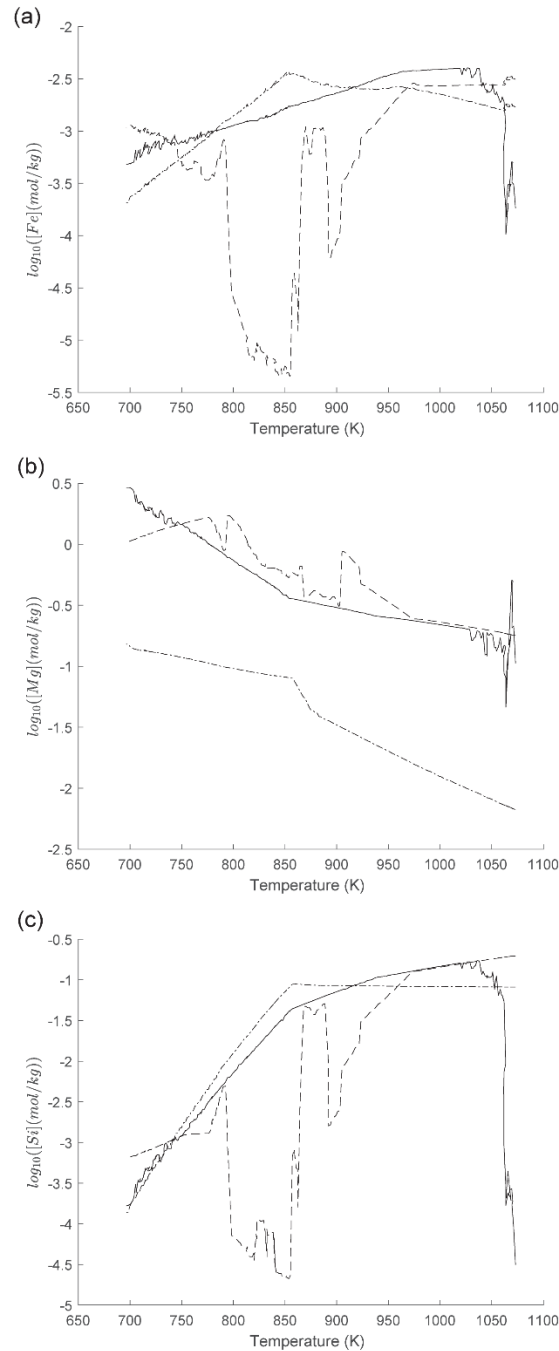
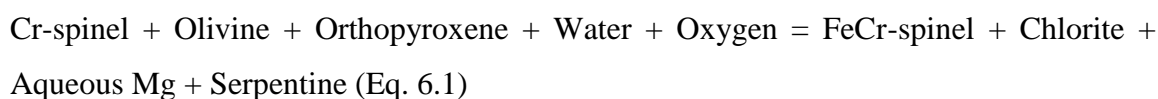
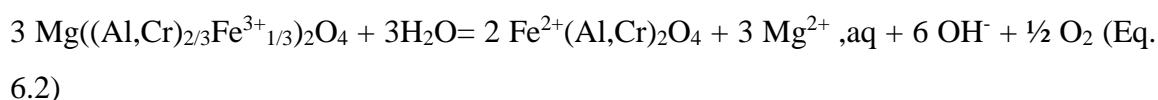


Fig. 6.S2. Solubility as a function of temperature along the cooling path (the oxygen fugacity along this path is calculated by assuming the olivine composition is fixed to Fo92; see text for details). a. Fe solubility. b: Mg solubility. c: Si solubility. The plain, dashed and dash-dotted lines correspond to models with bulk compositions calculated for molar fractions in chromite (chromite/(chromite+olivine)) of 5, 50 and 99%, respectively.

Considering olivine and orthopyroxene as possible reactants and the possibility for  $Mg^{2+}_{aq}$  formation, the spinel alteration reaction to form chlorite and serpentine can be written as:



Chlorite formation in Eq. 6.1 occurs at higher temperature than serpentine formation (Eslami et al., 2021). The formation of serpentine in the mass balance model is thus only allowed if silica is left after chlorite formation. The effect of three parameters on spinel composition evolution is investigated: (1) the molar fraction of olivine among the silicates ( $X_{ol} = n_{ol} / (n_{ol} + n_{opx})$  where  $n_{ol}$  is the number of moles of olivine and  $n_{opx}$  is the number of moles of orthopyroxene in the reactants); (2) the chromite fraction in the rock ( $X_{chr} = n_{chr} / (n_{chr} + n_{ol} + n_{opx})$  where  $n_{chr}$  is the number of moles of Cr-spinel in the reactants); (3) the water to rock ratio (w/r ratio) which fixes the amount of aqueous Mg in the reaction products of Eq. 6.1. The model considers spinel composition evolution for different reaction progresses ( $\xi$ ).  $\xi$  is defined as the amount of silicates having reacted with spinel ( $n_{olr} + n_{opxr}$ ) relative to the total amount of silicates ( $\xi = (n_{olr} + n_{opxr}) / (n_{ol} + n_{opx})$ ). The fluid is considered as associated with the silicates and its amount is thus set as proportional to  $\xi$ . The mass balance model produces a decrease in Al content in spinel accompanied by an increase in  $Fe^{3+}$  content leading to a horizontal trend (Trend 2) in the Al-Cr<sup>3+</sup>-Fe<sup>3+</sup> diagram for  $X_{ol} = 1$  and a low water to rock ratio ( $<1$ ; Fig. 6.8). The trend measured in the samples from the Sabzevar for massive chromitites with a decrease in Al without increase in  $Fe^{3+}$  (Trend 1) can be reproduced with the mass balance model by independently varying three parameters: (1) decreasing  $X_{ol}$  (Fig. 6.8a); (2) increasing the w/r ratio (Fig. 6.8b); decreasing  $X_{chr}$  with a fixed high water to rock ratio (Fig. 6.8c). The decrease in  $Fe^{3+}$  in the spinel occurs in parallel with a decrease of the  $Mg / (Mg + Fe^{2+})$  ratio (Fig. 6.S1). Iron is indeed the only major element in spinel with two valences. It is thus able to accommodate release/uptake of magnesium in spinel through the following reaction:



Equation 6.2 indicates that the fate of magnesium during alteration controls the  $\text{Fe}^{3+}$  content in spinel. Modifying  $X_{\text{ol}}$ ,  $X_{\text{Chr}}$  and  $w_r$  are three different ways to modify Mg distribution during alteration in the mass balance model (Fig. 6.8). The  $(\text{Mg}+\text{Fe})/\text{Si}$  ratio in olivine and orthopyroxene is of 2 and 1, respectively. The  $(\text{Mg}+\text{Fe})/\text{Si}$  ratio in the reactants of Equation 6.1 thus increases with  $X_{\text{ol}}$ . At high  $X_{\text{ol}}$ , this ratio can be higher than in chlorite and serpentine ( $5/3$  and  $3/2$ , respectively), triggering reaction 6.2 from right to left. At low  $X_{\text{ol}}$ , the opposite trend is predicted with a decrease of the  $\text{Fe}^{3+}$  content in spinel through reaction 6.2 from left to right. Figure 6.8a indicates that  $X_{\text{ol}} < 0.6$  is required to reproduce Trend 2.

Another way of triggering reaction 6.2 from left to right is to favor aqueous magnesium formation by increasing the water to rock ratio. Figure 6.8b shows that water to rock ratios above 1 can lead to Trend 1.

For a fixed water to rock ratio above 1 and  $X_{\text{ol}} = 1$ , reproducing Trend 1 is also possible by increasing the amount of spinel in the reactant ( $X_{\text{Chr}}$ ; Fig. 6.8c). Aqueous Mg formation according to reaction 6.1 either originates from spinel reaction through reaction 6.2 from left to right, or from olivine reaction releasing excess Mg while forming chlorite and serpentine as discussed above. As a result, high  $X_{\text{Chr}}$  in the rock promotes changes in spinel composition during Mg release and  $\text{Fe}^{3+}$  decrease. However, at low  $X_{\text{Chr}}$ , aqueous Mg formation is controlled by olivine reaction involving less changes in spinel composition during reaction and thus a less pronounced Trend 1.

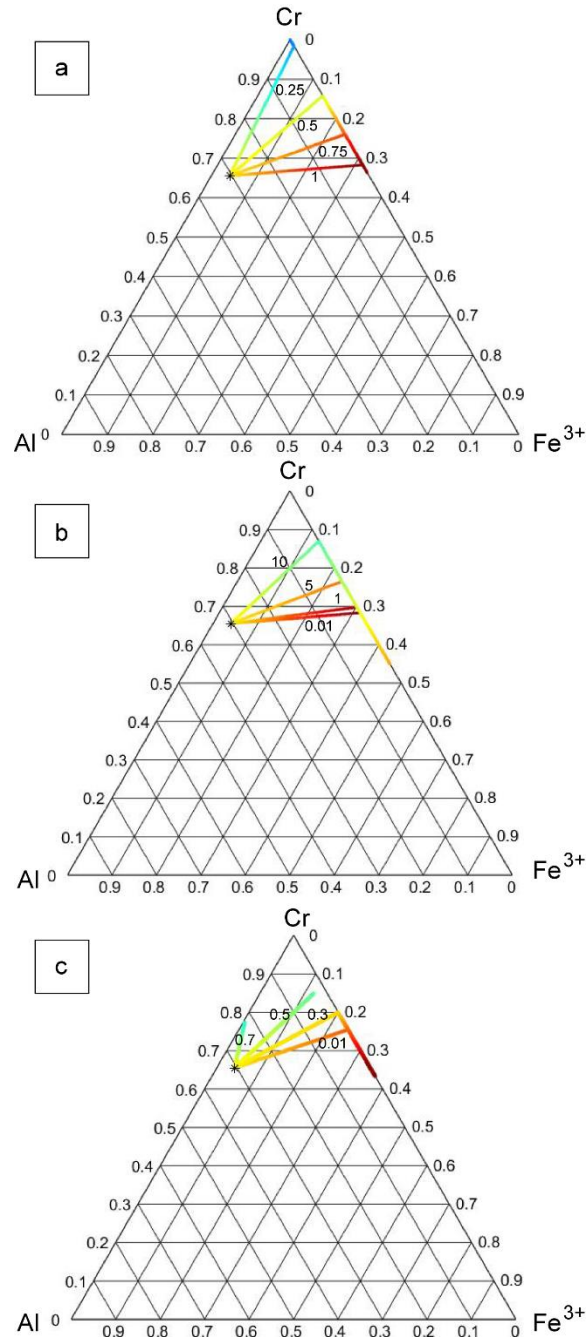


Fig. 6.8. Evolution of spinel composition in the mass balance model. The stars represents the initial spinel composition which evolves during chlorite and serpentine formation. The color corresponds to the  $Mg/(Mg + Fe^{2+})$  ratio in spinel. a: model results for olivine molar fraction in the silicates ( $X_{Ol}$ ) of 0.25, 0.5, 0.75 and 1. The molar fraction of Cr-spinel in the rock ( $X_{Chr}$ ) is fixed to 0.1 and the water to rock ratio to 0.01. b: model results for water to rock ratio of 0.01, 1, 5 and 10.  $X_{Chr} = 0.1$  and  $X_{Ol} = 1$ . c: model results for  $X_{Chr}$  of 0.01, 0.3, 0.5 and 0.7.  $X_{Ol} = 1$  and the water to rock ratio is fixed to 5.

According to the mass balance model, the observation of both chemical Trend 1 and Trend 2 in the samples from Sabzevar could be explained by either 1)  $X_{ol}$  variation from 1 up to values of less than 0.6, 2) water to rock ratio variation over several orders of magnitude or 3)  $X_{chr}$  variation in the presence of fluid (high w/r ratio). Regarding 1), low  $X_{ol}$  values are not consistent with the observation of dunite in Sabzevar with no evidence for the presence of a Si-rich mineral presence. 2) would imply water to rock ratio variation at the meter scale, which is not supported by observations since no preferential fluid pathways are observed in massive chromitites. 3) is compatible with the observation of Trend 2 in the dunite (low  $X_{chr}$ ) and of Trend 1 in the massive chromites from Sabzevar (high  $X_{chr}$ ). As a result, the variation of chromite / silicate ratio appears to be the main factor controlling spinel composition evolution during alteration. This is only effective if significant amount of aqueous Mg can be formed during the alteration, that is at high water to rock ratio ( $> 1$ ). Barra et al. (2014) have shown that  $X_{chr}$  also modifies the temperature of chlorite formation during alteration.

The mass balance model reproduces the two trends depicted in the Al – Cr<sup>3+</sup> – Fe<sup>3+</sup> ternary diagram (Fig. 6.7a). We show that  $X_{chr}$  controls the evolution of the spinel composition in water-bearing systems where hydrous silicates can form. However, the mass balance model does not explain the systematic difference in Mg# at a given Cr # observed in Figure 6.8a at the onset of the two trends. Thus, alteration alone with chlorite and serpentine formation cannot account for this difference. Actually,  $X_{chr}$  has been pointed out as a main parameter that controls chromite – spinel re-equilibration upon cooling in dry systems (*e.g.*, Engi, 1983, Grieco et al., 2018). Therefore, we have modeled the evolution with temperature of both olivine and spinel Mg# for samples IM-2 (serpentinized dunite, Table 1) and KE-2 (chromitite, Table 2) of contrasted  $X_{chr}$ . For this calculation,  $X_{chr}$  was deduced from mineral modes retrieved by LSQ regression. The composition of spinel cores obtained with EPMA were used for the computation and Cr# was set as constant. The evolution of the Mg# of both spinel and olivine with temperature was calculated using Ballhaus et al. (1991). In the 1100 – 700 °C range, spinel Mg# is calculated to decrease from 0.69 down to 0.65 for the KE-2 sample (chromitite) whereas it decreases from 0.69 down to 0.55 for the IM-2 (serpentinized dunite). Therefore, the shift in Mg# of +1 unit at the onset of Trend 2 with respect to Trend 1 (Fig. 6.8a) can be

explained by the effect of sub-solidus re-equilibration for rocks of contrasted  $X_{chr}$  (i.e., chromite vs dunite, respectively).

### 6.5.2. Chromite alteration, chromitite pods vs magnetite ores

In comparison to the magnetite ores found in the same area (Eslami et al., 2021), the studied chromitite samples show much less alteration. In particular, magnetite is an accessory phase in the studied chromitites which mostly occurs as fillings in micrometer-sized cracks.

In terms of bulk rock composition whereas the magnetite ores would plot close to the magnetite end-member, the bulk chromitite minus silicate for either massive, semi-massive or serpentinized dunite with disseminated chromites plots close to the Al-Cr<sup>3+</sup> composition line (Fig. 6.6a). They thus contain little or no Fe<sup>3+</sup> which is a good proxy for spinel alteration. The alignment of bulk chromite minus olivine compositions along the Al-Cr<sup>3+</sup> tie line may result either from early magmatic processes or from alteration at the sample scale which would involve chemical exchange/heterogeneity at the tenth of centimeters scale.

The lesser extent of alteration led to textures which significantly differ from those encountered in chromites in the magnetite ores and their serpentinized dunite aureole. In particular although the two types of occurrences show partly altered textures with porous zones, spinels in serpentinized dunite in the vicinity of magnetite ores are more extensively replaced leading, in some instances, to fully porous chromite grains where the original spinel is no longer visible.

Therefore if the chromite in the studied chromitite samples are obviously much less transformed than those from the magnetite ores where the original spinel is almost fully altered into magnetite (and ferric chromite), the chromite grains in the serpentinized dunite aureole are also much less altered.

This is not only evidenced by the chromite alteration textures but also by the composition of the serpentinized dunite aureole. We have showed (Eslami et al., 2021) that iron was transferred from the dunite to the chromitite in order to form the magnetite ore. No such iron transfer can be inferred here from the iron content of the serpentinized dunite around the chromitite pods (Fig. 6.4b). Furthermore, we show here that aluminum must have been transferred from the initial chromitite and its dunite envelope in order to

produce the magnetite ores (Fig. 6.2b). Such Al transfer does not seem to have been significant in the case of the studied chromitites (Fig. 6.2a). It could be argued that Al transfer occurred upon sub-solidus dunite – chromite re-equilibration at temperature higher than that of chlorite formation ( $> 700$  °C). However, (1) Al (and Cr) have been showed to be retained in spinel during such HT sub-solidus re-equilibration (Rassios and Kostopoulos, 1990) and (2) Al is here transferred to the silicate component (Fig. 6.2b) which was, at high-temperature, composed of olivine which barely contains more than 1000 ppm  $\text{Al}_2\text{O}_3$  (Sobolev et al., 2007; Coogan et al., 2014). Al content in serpentinized dunites hosting magnetite pods is higher than in the serpentinized dunites associated with the chromites studied here. This high content does not correlate with  $\text{Cr}_2\text{O}_3$  content as it is observed in the serpentinized dunites associated with chromitites (Fig. 6.2a). This suggests that chromite is not the only Al-bearing mineral in the serpentinized dunites hosting magnetite pods. This is consistent with the observation of chlorite in these rocks (Eslami et al., 2021). Figure 6.2a allows to subtract the contribution of chromite to Al content in the serpentinized dunites to estimate that chlorite formation corresponds to a gain of 0.3 wt.% of  $\text{Al}_2\text{O}_3$  ( $C_{dun}$ ). This mass transfer probably occurred during chromitite reaction to form magnetite. The magnetite pods are  $\sim 0.5$  m thick ( $L_{ore}$ ) and the  $\text{Al}_2\text{O}_3$  concentration measured here in slightly altered massive chromitite is of  $\sim 12$  wt.% ( $C_{chr}$ ). Assuming that the volume of the chromitite leading to magnetite formation is similar to the volume of the ore, the distance of Al transport in serpentinized dunite from the chromitite ( $L_{dun}$ ) can be calculated as:  $L_{dun} = \frac{\rho_{chr}L_{ore}C_{chr}}{\rho_{dun}C_{dun}}$  where  $\rho_{chr}$  and  $\rho_{dun}$  are the densities of the chromite and the serpentinized dunite, respectively (4800 and 2700  $\text{kg/m}^3$ , respectively).  $L_{dun}$  value calculated with the values given above is of  $\sim 40$  m. This value is close to the value of  $\sim 30$  m calculated in Eslami et al. (2021) for Fe transfer from the serpentinized dunite to the magnetite pods. This suggests mass transfer promoted by an efficient transport mechanism during alteration. At the scale of chromitite pods and its dunite envelope, alteration has been much less efficient than in the localities where magnetite ores were formed. Since alteration involves the formation of hydrous phases (chlorite and serpentine) and thus, hydrothermal conditions, differences in water rock ratio, deformation and access to the fluid, fluid composition or alteration temperatures can be invoked to account for the contrasted level of chromite alteration. The presence higher density of shear and fracture

zones near the magnetite ore than near the chromite pods may explain the observed difference in mass transfer (Fig. 3.10c).

### 6.5.3. Chromite alteration processes at the nano-scale

Nanoscale observation using TEM provides valuable information on the alteration processes thanks, in particular, to the crystallographic information provided by electron diffraction. In particular, it has been showed that spinel alteration into ferrian chromite and magnetite can involve topotactic intergrowth (Shen et al., 1988) or epitaxial replacement (Eslami et al., 2021). Fleet et al. (1993) and Mellini et al. (2005) showed that even layered silicates involved in ferrian chromite and Cr-magnetite formation from spinel share crystallographic relationships with their ferrian chromite or Cr-magnetite host. Actually, they reported that the layers with the closest-packed anions in chlorite / lizardite, (001) planes, and in ferrian chromite and Cr-magnetite, (111) planes, are parallel. The same crystallographic relationship has been found here between layered silicates (Liz/Chl) and chromite in porous zones (Fig. 6.5e). Actually, the nanotextures that have been characterized here with the TEM all converge towards epitaxial growth of secondary phases (oxides and silicates) upon spinel alteration.

The spinel rim in zoned chromite shows a perfect crystallographical continuity with the chromite core (Fig. 6.5). The rim is enriched in  $\text{Fe}^{2+}$  and  $\text{Cr}^{3+}$  and contains little  $\text{Fe}^{3+}$  ( $\text{Fe}^{3+}/\text{Fe}_{\text{tot}} < 0.18$ ). This compositional evolution is typical for high-temperature chlorite formation (Stage 1 described in Gervilla et al., 2012, Barra et al., 2014, Eslami et al., 2021). The rim is devoid of pores and inclusions although the chlorite-forming stage is believed to create porosity (Gervilla et al., 2012) – Homogeneous core of zoned chromite has higher Cr# (63 - 73) and lower Mg# (42 - 49), compared to homogeneous rim (Cr#: 55 - 57; Mg#: 58 - 59). At the nanoscale (Fig. 6.S3), the transition from core to rim is smooth chemically. Al and Cr diffusion at temperature below 700°C is supposed to be ineffective, at least under dry condition (calculate from Suzuki et al., 2008). A dissolution – crystallization process is more likely with epitaxial growth of secondary spinel. Volume reduction is not accommodated by pores in the secondary chromite rim. A second replacement process, Stage 2, involves the production of a network of a nano to submicrometer-sized pores that are either empty or filled with secondary silicate products which, however, share crystallographic relationships with the host spinel matrix. Chemical

maps at the nanoscale highlights the role of the porosity for elemental transfer in and out the alteration zone. The presence of chlorite + serpentine + magnetite as reaction products indicates that partly altered textures, involving pores, form at serpentinization temperature, i.e., below 550°C according to our thermochemical modelling. Again, Al diffusion is negligible at such low temperatures (Suzuki et al., 2008) and dissolution – recrystallization processes assisted by a porous network connects the alteration zone to the external silicate matrix (e.g., Putnis et al., 2005; Raufaste et al., 2011). Compared to the higher temperature Stage 1, equilibration distance in Stage 2 are shorter and heterogeneity are preserved at the submicrometer scale (Fig 6.4, S3-A1). Reliable EPMA analyses of porous zones is difficult to obtain since the excitation volume is larger than chemical heterogeneity.

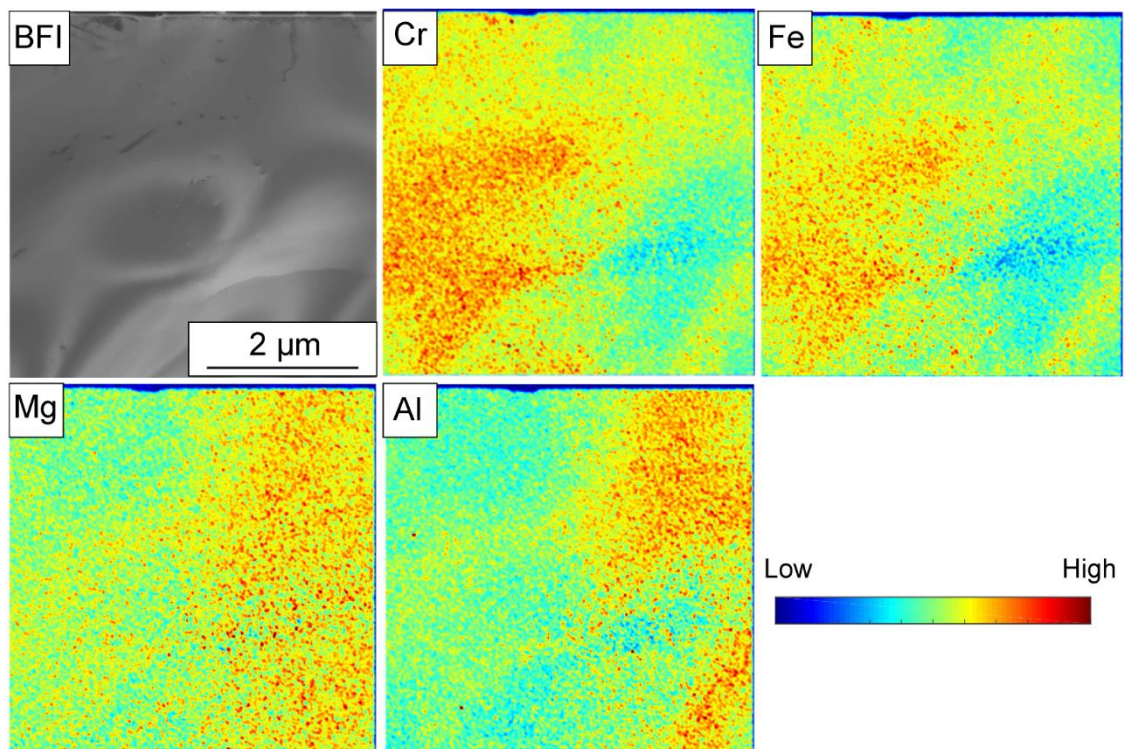


Fig. 6.S3. Bright Field Image and EDS-STEM element maps of the Fe-Cr-spinels (FIB section S1 in Fig. 6.3g)

The development of porous zones is considered as the way to reach the ferric chromite + magnetite stage which is not attained in the studied samples which are only partly altered. Aqueous fluid was present in sufficient amount to achieve full serpentinization of the host dunite. However, as outlined from the bulk rock dataset, the extent of fluid-rock interaction seems to have been somehow limited. Pervasive

hydration of the dunite host is clearly not sufficient to reach the Cr-spinel-III stage described for chromite in the magnetite ores and their host dunite (Eslami et al., 2021). Additional fluid rock interaction in shear zones where, in addition, spinel alteration can be promoted by deformation (*e.g.*, Kapsiotis, 2015; Satsukawa et al. 2015; Qiu and Zhu, 2018; Gervilla et al., 2019) is required to reach Cr-spinel-III stage and ultimately magnetite ores. This is rather consistent with our field observation showing serpentinite-hosted magnetite ores occurred in a locus of fault system (Fig. 3.10c).

## 6.6. Concluding remarks

The following conclusions are drawn based on our observations, chemical and mineralogical measurements and thermodynamic and mass balance calculations:

- Early stages of Cr-spinel alteration are observed in chromitite pods from the Sabzevar ophiolite. Cr-spinel is only partly altered in chromitite and their dunite envelopes. It is thus rather resistant to hydrothermal alteration. Nevertheless, this is not always the case, especially in the Sabzevar ophiolite where extensive fluid-rock interaction can lead to magnetite ore formation.

- Massive and semi-massive chromitites display a chemical trend different from serpentinitized dunite in ternary Al-Cr-Fe<sup>3+</sup> diagram. The alteration trend includes progressive increase of Cr in both lithologies but it is associated with Fe<sup>3+</sup> incorporation for serpentinitized peridotites whereas chromites in massive and semi-massive chromitites are almost Fe<sup>3+</sup>-free during the alteration process. These two trends can be explained using mass balance calculations by the difference in the chromite/(chromite + silicate) ratio in these lithologies. They indicate high water to rock ratio and significant Mg solubility during hydrothermal alteration. The chromite/(chromite + silicate) ratio also controls spinel composition evolution during sub-solidus equilibration at temperature above 700°C.

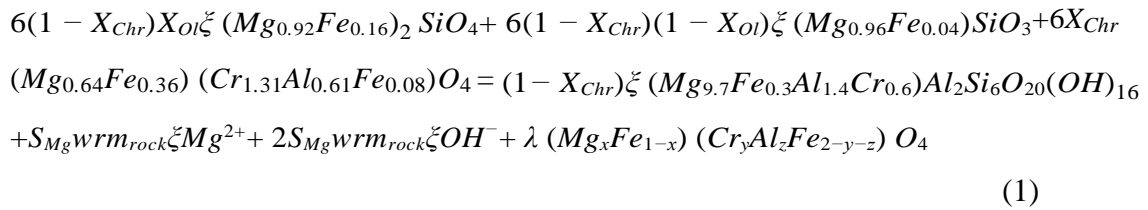
- The early alteration texture is characterized by the formation of a zoned chromite. Serpentine and chlorite filling pores developed during the serpentinitization stage. These pores may have been acted as pathways for SiO<sub>2</sub>-bearing fluids. Porous texture development is rather restricted which might be related to fluid availability.

- Identical crystallographic orientation of lizardite/chlorite and Cr-spinel/magnetite reveals contemporaneous formation of magnetite and phyllosilicates as alteration phases.

- Limited chemical exchange between chromitites and their host (serpentinized) dunite resulted in lack of magnetite ore formation. In contrast, localities in the Sabzevar ophiolite belt where magnetite ores are present do show a significant mass transport of Fe and Al at a scale of a few tenths of meters. The difference in alteration extent may be related to differences in deformation degree and in efficiency of hydrothermal fluid drainage.

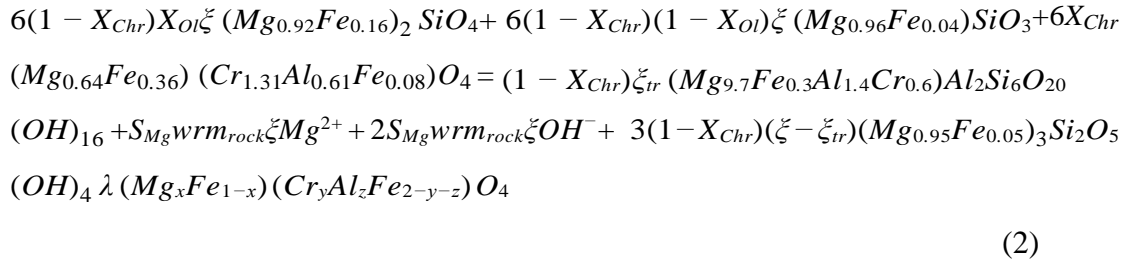
## 6.7. Mass balance model of spinel composition evolution

Based on thermodynamic modelling, two successive reactions are identified during the retrograde reaction of a chromite + olivine + orthopyroxene assemblage. They consist in the formation of chlorite at high temperature followed by serpentine precipitation. We used three parameters in the model: the fraction of olivine in the silicates ( $X_{Ol} = \frac{n_{ol}}{n_{ol}+n_{opx}}$ ) with  $n_{ol} + n_{opx}$  and  $n_{opx}$  the number of moles of olivine and orthopyroxene in the reacting rock); the fraction of Cr-spinel in the reacting rock ( $X_{Chr} = \frac{n_{Chr}}{n_{ol}+n_{opx}+n_{Chr}}$ ) with  $n_{Chr}$  the number of moles of Cr-spinel in the reacting rock); the water to rock ratio ( $w_r$ ) defined as the mass of fluid over the mass of reacting rock. The model considers the progressive addition of silicates and fluid to a fixed amount of Cr-spinel. The extent of interaction between spinel and the silicate + fluid assemblage is defined with  $\zeta$ , the reaction progress. The compositions of olivine, orthopyroxene, chlorite, serpentine and fluid are fixed in the model. They are determined through the measurements of mineral compositions performed here for spinel (the composition of Cr-spinel I is used) and in Eslami et al. (2021) for chlorite and serpentine. The solubility of magnesium in the fluid ( $S_{Mg}$ ) is fixed to  $10^{-0.5} mol/kg$  based on the calculations performed here with Perple X at thermodynamic equilibrium. The first reaction to occur when the temperature decreases is the formation of chlorite:



Where  $m_{rock}$  is the mass of  $6(1 - X_{Chr})X_{Ol}$  moles of olivine +  $6(1 - X_{Chr})(1 - X_{Chr})$  moles of orthopyroxene +  $6X_{Chr}$  moles of Cr-spinel I.

As spinel/silicates interaction continues, Al initially contained in Cr-spinel I can be completely consumed by reaction 1. The reaction is then assumed to continue according to the following equation producing serpentine:



where  $\zeta_{tr} = \frac{3.66X_{Chr}}{3.4(1-X_{Chr})}$  is the reaction progress for which all Al has been consumed for chlorite production.

The model solves for mass balance in equation 1 and 2 while respecting spinel stoichiometry to determine  $\lambda$ ,  $x$ ,  $y$ ,  $z$  as a function of  $\zeta$ ,  $X_{Ol}$ ,  $X_{Chr}$  and  $wr$ .  $H_2O$  and  $O$  necessary to equilibrate equations 1 and 2 are not considered here for simplicity.

# Chapter 7. Native copper formation associated with serpentinization in the Cheshmeh-Bid ophiolite massif (Southern Iran)

---

## 7.1. Introduction

Native copper has been documented in ultramafic and mafic rocks from ophiolitic and orogenic massifs. It was observed in partially serpentinized peridotites of Costa Rica (Schwarzenbach et al., 2014), pillow basalts from la Désirade, Lesser Antilles island arc (Nagle et al., 1973), rodingitized gabbro in serpentinites of the Braszowice-Brzeznica Massif, Poland (Gunia, 1986), basal cumulate sequence of the massif from the Zambales ophiolite, Philippines (Abrajano and Pasteris, 1989), plagioclase lherzolites from the Horoman peridotite complex, Hokkaido, northern Japan (Ikehata and Hirata, 2012) and websterite from the Totalp ultramafic massif, Swiss Alps (Van Acken et al., 2007). Three hypotheses have been put forward to explain the genesis of native copper in peridotites and basalts: ((i) crystallization in equilibrium with a mafic magma (e.g. Cabral and Beaudoin, 2007; Ikehata and Hirata, 2012); (ii) low-temperature in situ alteration of magmatic or hydrothermal Cu-sulfides at highly reducing conditions (e.g. Lorand and Grégoire, 2006; Schwarzenbach et al., 2014); (iii) precipitation from low-temperature hydrothermal fluids (e.g. Dekov et al., 2013; Ikehata et al., 2016).

Thermodynamic calculations show that hypothesis (ii) requires reducing conditions for native copper to precipitate in hydrothermal environments (Schwarzenbach et al., 2014). The observation of Fe-Ni alloys and native metals in serpentinized peridotites (e.g. Klein and Bach, 2009; Schwarzenbach et al., 2014) shows that highly reducing conditions prevail during serpentinization. This is consistent with vent fluid compositions measured in ultramafic-hosted hydrothermal fields (Charlou et al., 2002) and gas seep compositions analyzed in ophiolites (e.g. Abrajano et al., 1988). During serpentinization, hydrogen production relates to water reduction coupled with iron oxidation during replacement of primary olivine and pyroxene by secondary magnetite and serpentine (McCullom and Bach, 2009; Malvoisin et al., 2012). Water-rock interaction is also intimately associated with Ca-metasomatism of mafic rocks in which the removal of silica (SiO<sub>2</sub>) and addition of Ca are the main mass transfers (Coleman 1967).

In this contribution, we report a new occurrence of native copper mineralization within Ca-metasomatically altered pyroxenites from the Cheshmeh-Bid ophiolitic massif in the

Khajeh-Jamali area, Southern Iran. Based on field and petrographic observations combined with new geochronological and geochemical data we aim to: (1) define the paragenetic sequence of the ore and silicate minerals; (2) produce a thermodynamic model for the origin of Ca-metasomatism and native copper; (3) determine the sources of Cu in the mineralization system; (4) constrain the timing of the copper mineralization and, finally, (5) develop a conceptual model of native copper genesis within metasomatised pyroxenite veins.

## 7.2. Geological setting

Geological setting of the study area is discussed in section 3.4.2. In the Cheshmeh-Bid chromitite mine, a few pyroxenite dykes and veins crosscutting massive chromitite and serpentinized dunite are partially (Figs. 7.1a and 7.1b) or completely (Fig. 7.1c) metasomatised with remarkable native copper mineralization.

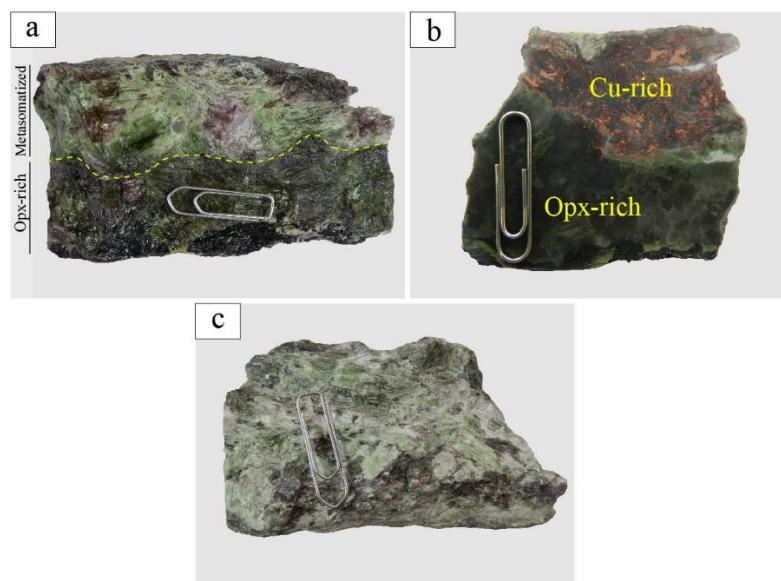


Fig. 7.1. Hand samples of: a-b: partly metasomatised pyroxenite with native copper mineralization; c: highly metasomatised and deformed pyroxenite containing native copper mineralization. Scale of clips is 2 cm in length. Opx-rich zone is composed of orthopyroxene and minor clinopyroxene.

## 7.3. Analytical methods

Analytical work has been focused on five representative samples of metasomatically altered pyroxenite veins (KJPX04, KJPX05, KJPX06, KJPX11 and KJPX12) and two fresh pyroxenites (KJPX01 and KJPX20). Polished thin sections of both fresh and altered

pyroxenites were examined under transmitted light using a Leica optical microscope at University of Milan. Samples KJPX04, KJPX05 and KJPX06 were selected for petrography observation because they show typical metasomatic zoning on the micrometer scale.

### 7.3.1. Major and trace element analyses in minerals and whole-rocks

Quantitative chemical analyses of silicate minerals (except chlorite) were obtained using a JEOL JXA-8230 electron probe micro-analyzer (EPMA) equipped with five wavelength-dispersive spectrometers (WDS) at the Institut des Sciences de la Terre, Université Grenoble Alpes, France. Analytical conditions were: 15 kV acceleration voltage, 12nA beam current, 3µm beam size. Natural minerals, pure metal and synthetic oxides were used as standards and ZAF correction was applied. Spectral interference (V K $\alpha$  vs Ti k $\beta$ ) was corrected using the software-calculated correction factor. Elemental distribution maps were done at an accelerating voltage of 15kV, a beam current of 100 nA and a dwell time of 200 ms. Major element composition of chlorites, sulfides and spinels were analyzed using a JEOL JXA 8200 Superprobe equipped with five wavelength-dispersive (WDS) spectrometers, an energy dispersive (EDS) spectrometer, and a cathodoluminescence detector (accelerating potential 15 kV, beam current 15 nA), at the Dipartimento di Scienze della Terra “Ardito Desio”, University of Milano (Italy).

Major elements and Cr and Ni in whole-rock samples were analysed by X-ray Fluorescence (XRF) with a BRUKER S4-Pioneer instrument at the Instituto Andaluz de Ciencias de la Tierra (IACT, Granada, Spain), using standard sample preparation and analytical procedures. The accuracy of analyses was assessed by repeated analyses of international reference material JP-1 (peridotite) handled as unknown, which show good agreement with accepted values for this standard (Govindaraju, 1994). Whole-rock trace elements (REE, Ba, Th, Pb, Nb, Ta, Sr, Y and Sc) were analyzed by an Agilent 8800 QQQ ICP–MS (Inductively Coupled Plasma–Mass Spectrometer) at the IACT. Sample digestion was performed following the HF/HClO<sub>4</sub> dissolution procedure described in detail by Ionov et al. (1992), and element concentrations were determined by external calibration using aqueous solutions. Accuracy of the ICP–MS analyses has been assessed analyzing the BIR-1 basalt standard as an unknown, which show good agreement with reference concentrations of Jochum et al. (2016).

### 7.3.2. Copper isotope analysis

Grains of native copper were separated through crushing and hand picking. Samples were processed similar to the techniques in previous studies, namely Bornhorst and Mathur (2017), Mathur et al. (2009a) and Wall et al. (2011). The native copper samples were dissolved in Teflon beakers with 8 mL of ultrapure aquaregia at 140°C for 24 hours or until complete dissolution occurred. Samples were diluted to 100 ng/g for Cu isotope analysis with a Neptune MC-ICP-MS at Pennsylvania State University. Copper isotope compositions are reported in the traditional per mil format compared to the NIST 976 international standard. Mass bias was corrected for using standard-sample-standard bracketing. All samples matched the intensities of the standards within 25 %. An internal copper metal standard (USA 1838 Cent, reported in Mathur et al. 2009b) was measured 4 times during the session and produced a  $\delta^{65}\text{Cu} = 0.04 \pm 0.05$  per mil value. This value is identical to accepted  $\delta^{65}\text{Cu}$  of the standard ( $-0.02$  per mil  $\pm 0.08$ ).

### 7.3.3. U-Pb LA-ICP-MS analysis of titanite

Titanite grains were ablated in thin section using a 213 nm laser beam with diameter of 25  $\mu\text{m}$  at 5 Hz and 40 % power (NWA ablation system). ICP-MS analyses were carried out using a Plasmaquad instrument. Data were collected on  $^{206}\text{Pb}$ ,  $^{207}\text{Pb}$ , and  $^{238}\text{U}$ . Immediately prior to each analysis, the spot was briefly pre-ablated over a larger area than the beam diameter to clean the surface. Following a 10 s period of baseline accumulation the laser sampling beam was turned on and data were collected for 25 s followed by a 50 s washout period. About 150 measurement cycles per sample were produced and ablation pits are about 15  $\mu\text{m}$  deep. Data were edited and reduced using custom VBA software (UTILLAZ program) written by the author.  $^{206}\text{Pb}/^{238}\text{U}$  show only slight fractionation caused by hole depth through the run and most of the  $^{207}\text{Pb}/^{206}\text{Pb}$  and  $^{206}\text{Pb}/^{238}\text{U}$  data can be averaged. Pb-204 was not measured since this peak is relatively small and would require a large amount of measurement time as well as being subject to interference from  $^{204}\text{Hg}$  in the Ar. Ages are determined by projecting data along a common Pb mixing line to the concordia curve (see Results below). Titanite from a quartz diorite sample in northwest Ontario, DD81-29, previously dated at  $2700 \pm 2$  Ma (Davis and Edwards, 1986) was used as a standard.

### 7.3.4. Raman Spectroscopy

Raman spectroscopic analyses were carried out at the Research and Industrial Relations Center of the Faculty of Science at the Eötvös University, Budapest. Analyses were carried out with a Horiba LabRAM HR800 spectrometer, using a 532 nm (green) laser with a maximum laser energy of 130 mW (~25 mW on the sample surface). A 100  $\mu\text{m}$  confocal pinhole and an optical grating with 1800 grooves/mm were used. The spectral resolution of the measurements was 0.8  $\text{cm}^{-1}$  at 1707.9  $\text{cm}^{-1}$  (defined as the measured full width at half maximum values of neon atomic emission lines). During the measurements an objective with 100 $\times$  magnification was used (NA=0.9). Analyses ran with 2 to 5 repetitions for an accumulated 200-500 seconds.

### 7.3.5. Thermodynamic modelling

We used thermodynamic modelling to determine (1) the conditions prevailing during native copper formation, and (2) the factors controlling metasomatism. The calculations were performed differently for these two objectives. We therefore constructed phase diagrams in the Fe-Ni-Cu-O-S system with SUPCRT92 (Johnson et al., 1992) for (1). We used the thermodynamic database provided in Klein and Bach (2009) in which the SUPCRT92 database is extended by including thermodynamic data for Fe-Ni sulfides. The diagrams are computed as a function of the activities of  $\text{H}_{2,\text{aq}}$  ( $a_{\text{H}_{2,\text{aq}}}$ ) and  $\text{H}_{2\text{S},\text{aq}}$  ( $a_{\text{H}_{2\text{S},\text{aq}}}$ ) at  $a_{\text{H}_2\text{O}} = 1$  and 50 MPa. This latter pressure is used to compute equilibrium constants in Klein and Bach (2009), and is relevant for serpentinization on the seafloor.

We used Gibbs energy minimization with Perple\_X (Connolly, 2005) for (2) because it provides solid solutions for the phases observed here. This ensures accurate modelling of the distribution of major elements during metasomatism. The equilibrium assemblages were determined for the composition of the orthopyroxenite (sample IRKJPX20; Table 7.S11) as a function of the chemical potential of CaO and temperature at 50 MPa. We did not include components with a concentration below 0.5 wt.% in the calculation. The chemical potential of CaO was also computed as a function of temperature for three metasomatised samples (IRKJPX04, IRKJPX11 and IRKJPX12). We used the thermodynamic database of Holland and Powell (1998a) and the solid solution models of Holland and Powell (1996) for orthopyroxene and clinopyroxene, Holland and Powell (1998a) for olivine, spinel and staurolite, Holland and Powell (1998b) for chlorite, Diener et al. (2007) for amphibole, Padrón-Navarta et al. (2013) for antigorite and White et al. (2000) for garnet. The solid solutions for talc and brucite were considered as ideal.  $\text{H}_2\text{O}$  was added in excess and modelled with the CORK equation of state

(Holland and Powell, 1998). This explains why the orthopyroxenite is not composed of orthopyroxene in the calculations but rather of its hydration products (talc and antigorite). We did not consider here the kinetic effects that led to orthopyroxene preservation.

Copper, and iron-nickel sulfides are not all available in *Perple\_X*. We therefore constructed phase diagrams in the Fe-Ni-Cu-O-S system with SUPCRT92 (Johnson et al., 1992) for (2). We used the thermodynamic database provided in Klein and Bach (2009) at 50 MPa in which the SUPCRT92 database is extended by including thermodynamic data for Fe-Ni sulfides. The diagrams are computed as a function of the activities in  $H_{2,aq}$  ( $a_{H_2,aq}$ ) and  $H_{2S,aq}$  ( $a_{H_2S,aq}$ ) at  $a_{H_2O} = 1$  and at the pressure at which the thermodynamic data are available (50 MPa).

## 7.4. Results

### 7.4.1. Petrography of the host peridotites

Petrography of the Cheshmeh-Bid host peridotites and chromitites has been discussed in detail by previous authors (e.g. Rajabzadeh, 1998; Eslami, 2015). The scarcity of bastite suggests that the host peridotites of the studied pyroxenites was originally a dunite. The host dunites consist of >95 % mesh-textured serpentine, cut by serpentine veins, plus 1–3 % spinel minerals. The Cheshmeh-Bid harzburgites are composed of 70-85 modal% olivine and 10-20 modal% orthopyroxene. The minor phases are fine-grained anhedral clinopyroxene (3–5 modal%) and subhedral spinel (0.5–3 modal%). Pervasive alteration in harzburgite includes the formation of serpentine minerals after olivine and orthopyroxene. In the Cheshmeh-Bid peridotites, Fe, Cu and Ni commonly form fine-grained opaque minerals including oxides (magnetite), sulfides (pentlandite, heazlwoodite) and alloys (awaruite) that occur together with (accessory) platinum-group minerals (PGM). Base metal sulfide inclusions inside alloys show desulfurization effects in the matrix of the Cheshmeh-Bid chromitite and host dunite and harzburgite (Eslami, 2015).

### 7.4.2. Petrography and mineral chemistry of pyroxenite and reaction zones in contact with host peridotites

Along the interface with the peridotite host rock, orthopyroxenite veins developed three mineralogically and chemically distinct alteration zones. These are described below. The transition between least altered and altered zones can either be sharp or progressive.

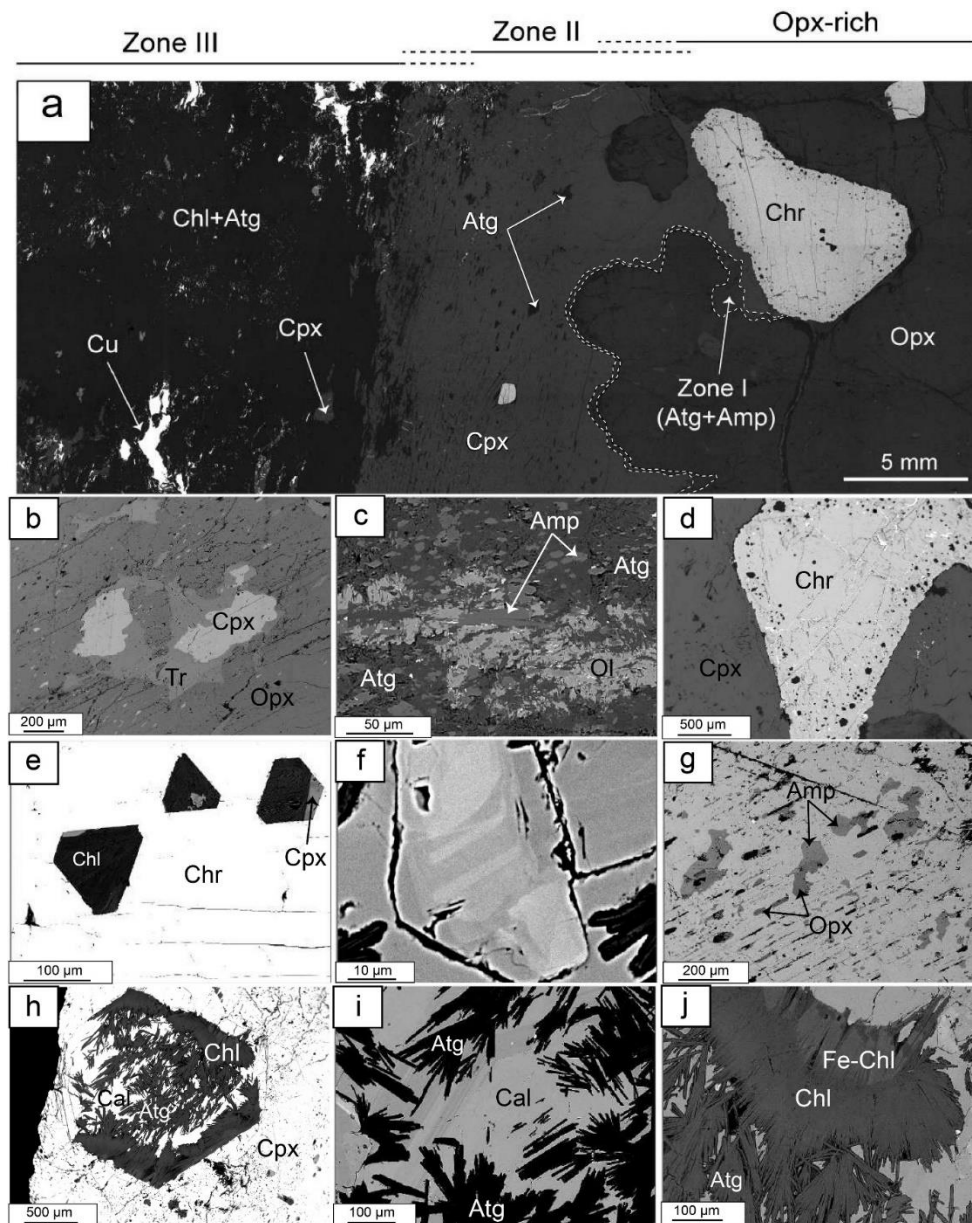


Fig. 7.2. Back-scatter-electron (BSE) images of the Cheshmeh-Bid Cu-rich pyroxenites. (a) Whole profile from Opx-rich portion and metasomatic zones (I) amphibole (Amp) + antigorite (Atg), (II) clinopyroxene (Cpx) + antigorite and (III) clinopyroxene + chlorite (Chl) + antigorite. Zone I (antigorite+amphibole) is characterized by small narrow selvage of amphibole and antigorite; (b) Ovoid and lamellae inclusions of clinopyroxene in orthopyroxene; (c) Spinifex-like textured olivine (Ol) in the middle of antigorite; (d) Sieve-textured chromite (Chr) included in orthopyroxene (Opx); (e) Euhedral inclusions of chlorite and clinopyroxene in chromite; (f) Zoned clinopyroxene in Zone II; (g) Inclusions of amphibole and orthopyroxene in metasomatic clinopyroxene; (h) Pseudomorph of clinopyroxene replaced by antigorite, chlorite and calcite; (i) Replacement of orthopyroxene by calcite (Cal); (j) Fe-poor (dark grey) and Fe-rich (light grey) chlorite.

### 7.4.2.1. Orthopyroxenite

The least altered mineral assemblage of the pyroxenite vein comprises orthopyroxene and chromian spinel. It occurs in a zone with an average thickness of 1.5 cm (hereafter Opx-rich zone; Fig. 7.2a). Clinopyroxene, olivine and antigorite are secondary minerals in this zone. This zone displays a porphyroclastic texture with 1 to 3 mm large pyroxene grains surrounded by antigorite. The composition of orthopyroxene in this zone is mostly enstatitic (Fig. 7.S1), with Mg# [ $Mg/(Mg+Fe_{tot})$ ] of 0.90–0.93. Orthopyroxene has  $Cr_2O_3$ ,  $Al_2O_3$  and  $TiO_2$  contents of 0.12–0.46 wt.%, 0.40–1.38 wt.% and  $<0.05$  wt.%, respectively (Table 7.S1). The orthopyroxene crystals contain numerous ovoid and lamellar exolutions of clinopyroxene (Fig. 7.2b). Clinopyroxene exolutions in the Opx-rich zone have high CaO contents ranging between 21.02–23.62 wt.% (with average of 22.94 wt.%), low  $Al_2O_3$  contents of 0.50–2.20 wt.% (with average of 1.33 wt.%) and  $Cr_2O_3$  contents of 0.26 to 0.94 wt.% with average of 0.63 wt.% (Table 7.S2). The Mg# of clinopyroxene exolutions, observed in large orthopyroxenes, range from 0.91 to 0.99. Clinopyroxene from pyroxenites are mostly diopside (Fig. 7.S1).

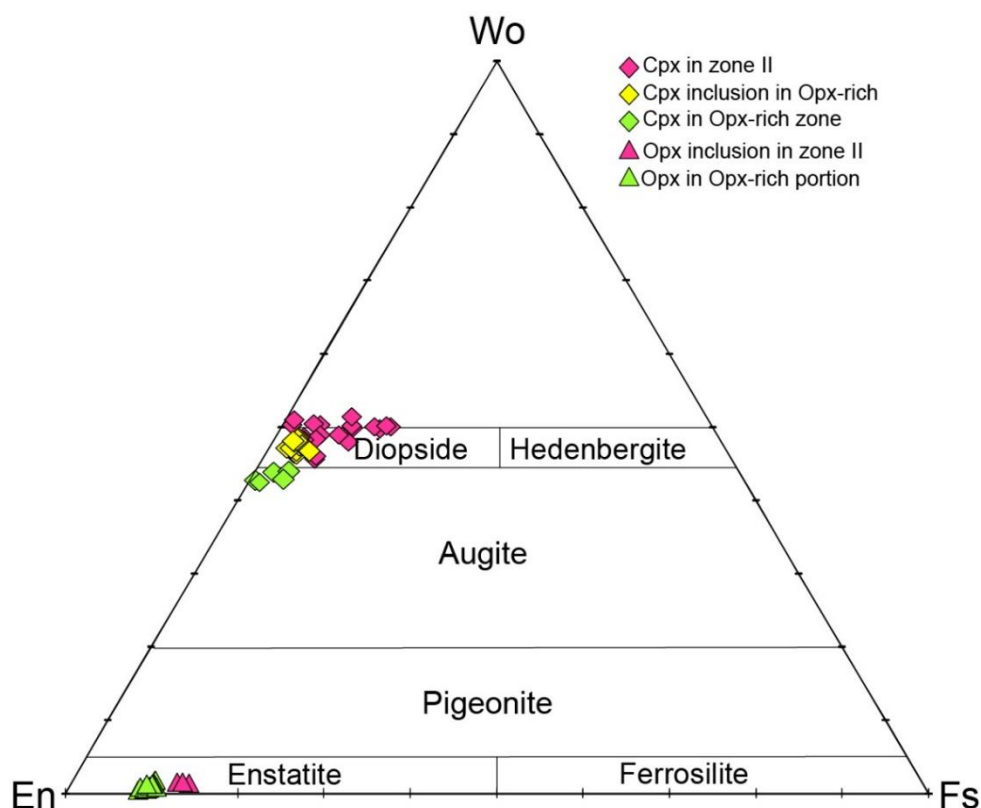


Fig. 7.S1. Pyroxene ternary diagram showing clinopyroxene and orthopyroxene compositions from the Cheshmeh-Bid Cu-rich pyroxenites.

In Opx-rich zone of Cu-rich pyroxenites, secondary olivine occurred as vein-like texture in the middle of antigorite around the orthopyroxene porphyroclasts (Fig. 7.2c). Representative analyses of olivine with vein-like texture from the Cu-bearing pyroxenites are given in Table 7.S3. Olivine has low forsterite contents comprised between 75 and 83 mol.%. Compared to the vein-like textured olivine in Cu-bearing pyroxenites, primary olivines found in dunite and harzburgite of the studied area have considerably higher Fo content (91-95 mol %) (Fig. 7.3; Rajabzadeh and Nazari-Dehkordi, 2013). MnO contents for vein-like textured olivines vary from 0.34 to 0.82 wt.% whereas they are lower than 0.21 wt.% for olivine in associated harzburgite and dunite (Fig. 7.4a). NiO contents for vein-like textured olivines are homogeneous in all samples and lower (0.08 to 0.16 wt.%) compared to those in associated dunite and harzburgite (0.27-0.66 wt.%) (Fig. 7.3b). MnO contents and Mg# are negatively correlated for vein-like textured olivines whereas there is a broad positive correlation between NiO contents and Mg# for olivines from associated harzburgite and dunites.

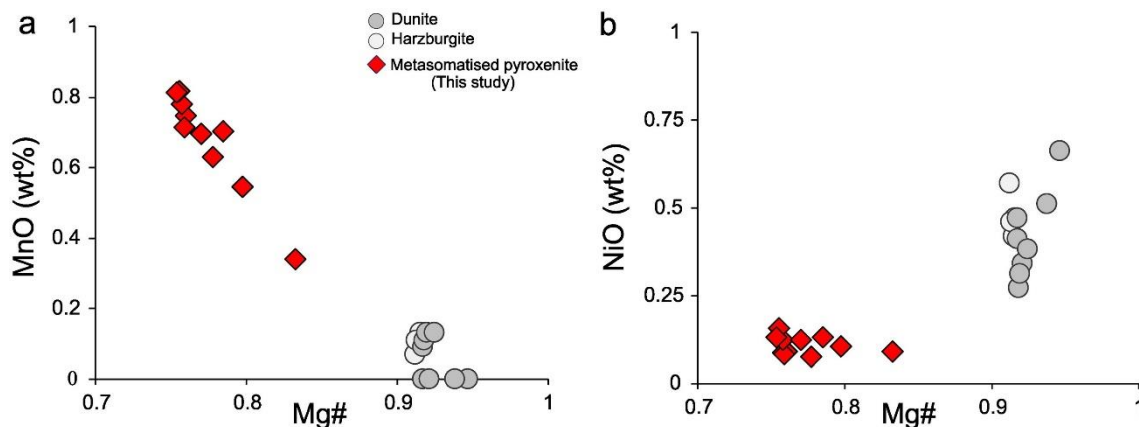


Fig. 7.3. Chemical compositions of olivines from the Cheshmeh-Bid peridotites. a Mg# vs. MnO (wt%); b. Mg# vs. NiO (wt%). The olivine compositions from the Cheshmeh-Bid dunites and harzburgites (Rajabzadeh and Nazari-Dehkordi, 2013) are included for comparison.

Euhedral or subhedral chromian spinel (50  $\mu\text{m}$  to 2.5 mm in diameter) is interstitial or included in orthopyroxene grains (Fig. 7.2d). Chromian spinel grains show alteration to ferrian chromite across their cracks and fractures. Rarely, spongy reaction rims developed around homogeneous chromian spinel grains. Sieve-textured rims of chromian spinel results from the occurrence of several euhedral to anhedral inclusions of chlorite and clinopyroxenes (Fig. 7.2e). Inclusion sizes range from 5 to 100  $\mu\text{m}$ . Fresh cores of spinel show Cr# [Cr/(Cr + Al)]

ranging from 0.65 to 0.73 (average of 0.70) and Mg# [ $\text{Mg}/(\text{Mg} + \text{Fe}^{2+})$ ] from 0.49 to 0.59 (average of 0.55) (Table 7.S4; Fig. 7.4). These high-Cr# spinels are characterized by low  $\text{TiO}_2$  content  $< 0.18$  wt.%, MnO contents of 0.04-0.24 wt.%, FeO contents of 18.29-25.21 wt.%,  $\text{Al}_2\text{O}_3$  contents of 13.38–20.29 wt.% (Fig. 7.4).

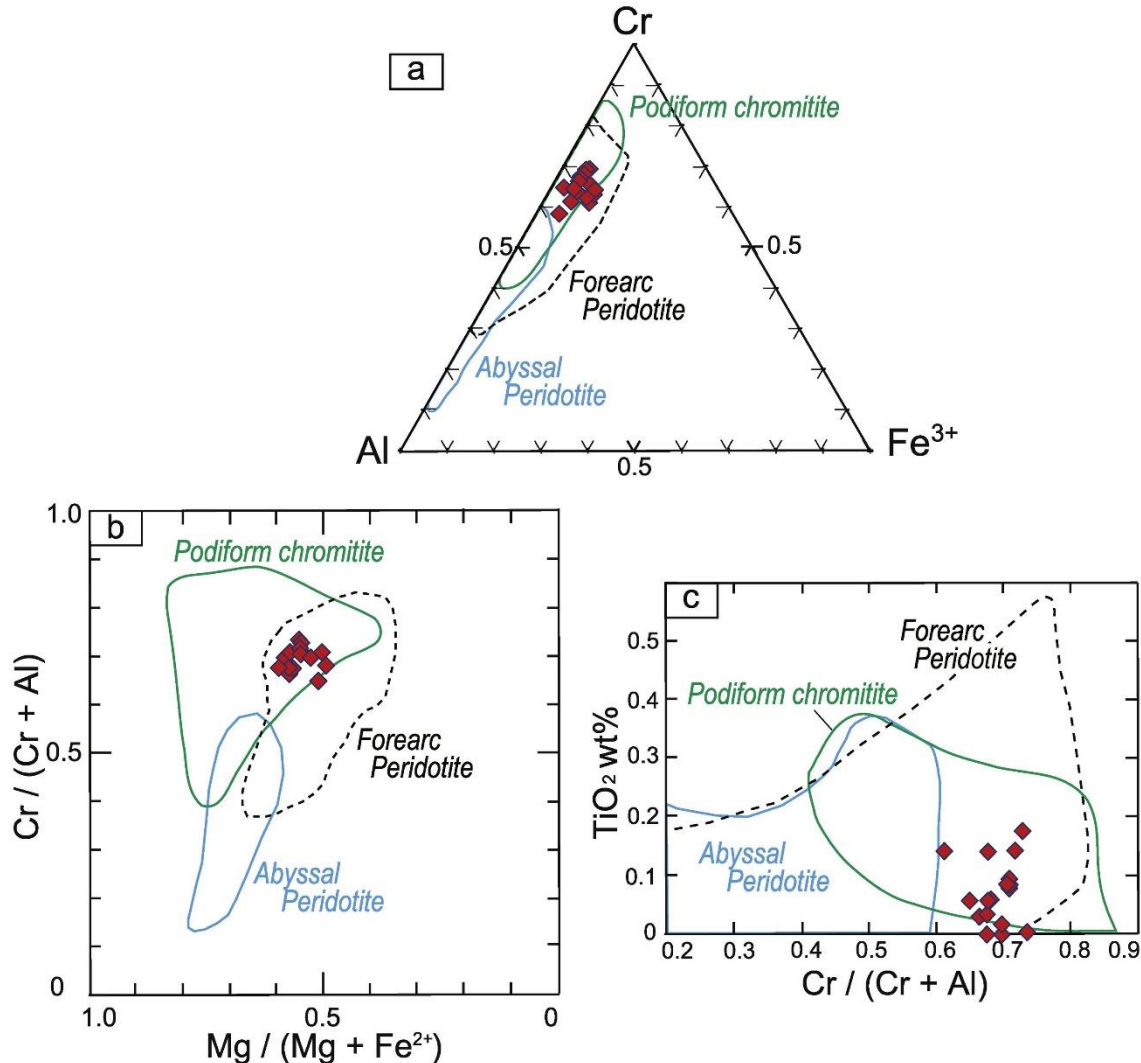


Fig. 7.4. Composition of Cr-spinels from the Cheshmeh-Bid orthopyroxenites. (a) Compositional plot of Cr-spinels on the Cr-Al- $\text{Fe}^{3+}$  ternary diagram (b)  $\text{Cr}/(\text{Cr} + \text{Al})$  vs.  $\text{Mg}/(\text{Mg} + \text{Fe}^{2+})$  (c)  $\text{Cr}/(\text{Cr} + \text{Al})$  vs.  $\text{TiO}_2$  (wt%). Compositional fields of Cr-spinel from abyssal peridotites, forearc peridotites and podiform chromitites (Miura and Arai, 2014) are shown for comparison.

The products of three successive reactions overprinted the Opx-rich zone. We distinguished three reaction zones from inner to outer portions of the orthopyroxenite dykes:

#### 7.4.2.2. Zone I

Zone I is characterized by a narrow selvage of amphibole with subordinate antigorite between Opx-rich zone and Zone II. The thickness of this zone is 50  $\mu\text{m}$  to 100  $\mu\text{m}$  (Fig. 7.2a). The chemical composition of amphibole from the Cheshmeh-Bid pyroxenites is given in Table 7.S5. Based on the nomenclature of Leake et al. (1997), amphiboles show a wide range of compositions from tremolite to magnesio-hornblende and edenite. They are characterized by Mg# between 0.92 and 0.98,  $\text{TiO}_2 < 0.07$  wt.%,  $\text{Cr}_2\text{O}_3$  contents are between 0.12 and 2.50 wt.% and  $\text{Al}_2\text{O}_3$  contents between 0.26-10.30 wt.%.

#### 7.4.2.3. Zone II

Zone II is composed of clinopyroxene megacrysts with subordinate antigorite and very rare orthopyroxene. The thickness of this zone is from 1 cm to 1.5 cm (Fig. 7.2a). Clinopyroxenes in Zone II show a wide range of Mg# (0.75-0.98) and are characterized by CaO contents of 21.95–26.1 wt.% with average of 23.25 wt.%,  $\text{Al}_2\text{O}_3$  and  $\text{Cr}_2\text{O}_3$  contents lower than 2.23 wt.% and 1.56 wt.%, respectively (Table 7.S2; Fig. 7.S1). Light grey bands on zoned clinopyroxenes in Zone II have lower Mg# values (0.76-0.80) and higher  $\text{Cr}_2\text{O}_3$  contents compared to dark grey zones (Fig. 7.2f). Sporadic inclusions of amphiboles are discernible along the cleavage of clinopyroxenes (Fig. 7.2g). Amphibole inclusions in Zone II are magnesio-hornblende to edenite. They are characterized by Mg# between 0.90 and 0.97 and  $\text{TiO}_2$  contents  $< 0.23$  wt.%,  $\text{Cr}_2\text{O}_3$  contents of 0.80-2.53 wt.% and  $\text{Al}_2\text{O}_3$  contents of 4.14-9.71 wt.% (Table 7.S5). Orthopyroxene inclusions in diopside megacrysts of Zone II show lower Mg# ( $\sim 0.87$ ). These inclusions have average  $\text{Al}_2\text{O}_3 = 1.5$  wt.% and  $\text{Cr}_2\text{O}_3 = 0.51$  wt.%. Clinopyroxene is locally replaced by calcite with perfect rhombohedral cleavage (Figs. 7.2h and 7.2i).

#### 7.4.2.4. Zone III

Zone III is the mineralized zone consisting dominantly of clinopyroxene, chlorite, antigorite and native copper. Zone III range from 0.5 cm to 1.5 cm in width and is typically massive in texture (Fig. 7.2a). Antigorite forms well-shaped tablets or laths that penetrate deeply into the clinopyroxenes. Chlorite forms patches or more commonly occurs interstitially in between the antigorite plates (Fig. 7.2j). It shows chemical variations (dominantly clinochlore) in each set of samples (Table 7.S6). Generally, chlorites in Zone III from the studied pyroxenites display low FeO ( $< 5.08$  wt.%), high MgO (28.46-33.26 wt.%) and variable  $\text{Cr}_2\text{O}_3$  contents (0.17-3.84 wt.%). Chlorites are mainly clinochlore with subordinate pennine

(Fig. 7.S2). In backscattered electron images, the Fe-rich chlorites and Fe poor have the same texture (Fig. 7.2i). Rarely, apatite is interstitial with respect to chlorite and antigorite.

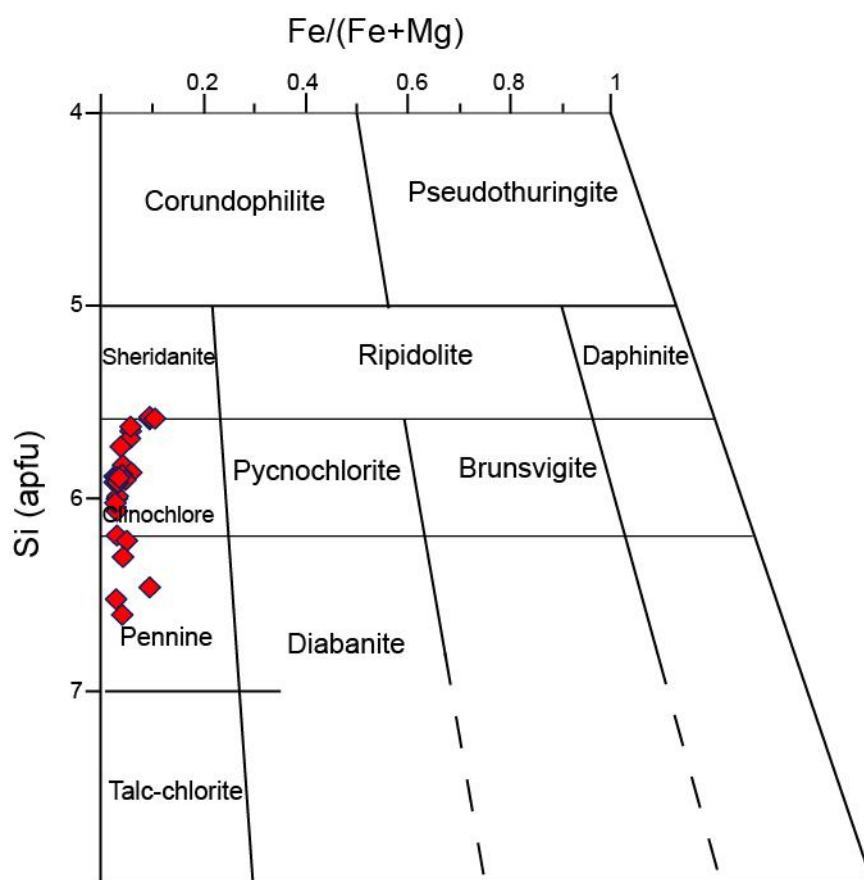


Fig. 7.S2. Plot of the analyzed chlorites on their classification diagram (after Hey, 1954).

Native Cu with pure composition occurs as flames intergrown with antigorite (Figs. 7.5a and 7.5b; Table 7.S7), along cleavage planes and along partially healed fractures cutting clinopyroxene (Fig. 7.5c). Occasionally, native copper occurs in fractures of chromian spinel as well as along chromian spinel grain boundaries (Fig. 7.5d). Occasionally, individual titanite grains are closely associated with native copper and chlorite (Fig. 7.5e) in zone III. Rare Cu-Au alloy is found in Zone III (Fig. 7.5e). Small inclusions of chalcocite ( $\text{Cu}_2\text{S}$ ) are fully embedded within native copper (Fig. 7.5f). Chalcocites hosted by native copper as vein and inclusion shows a relatively narrow range of Cu (76.69-80.92 wt.%) and S (20.05-21.71 wt.%) (Table 7.S7). Occasionally, cadmium sulfides (Greenockite) occur as inclusions in native copper and have Cu (3.87-6.78 wt.%) and Cd contents (76.5-78.1 wt.%) (Table 7.S7).

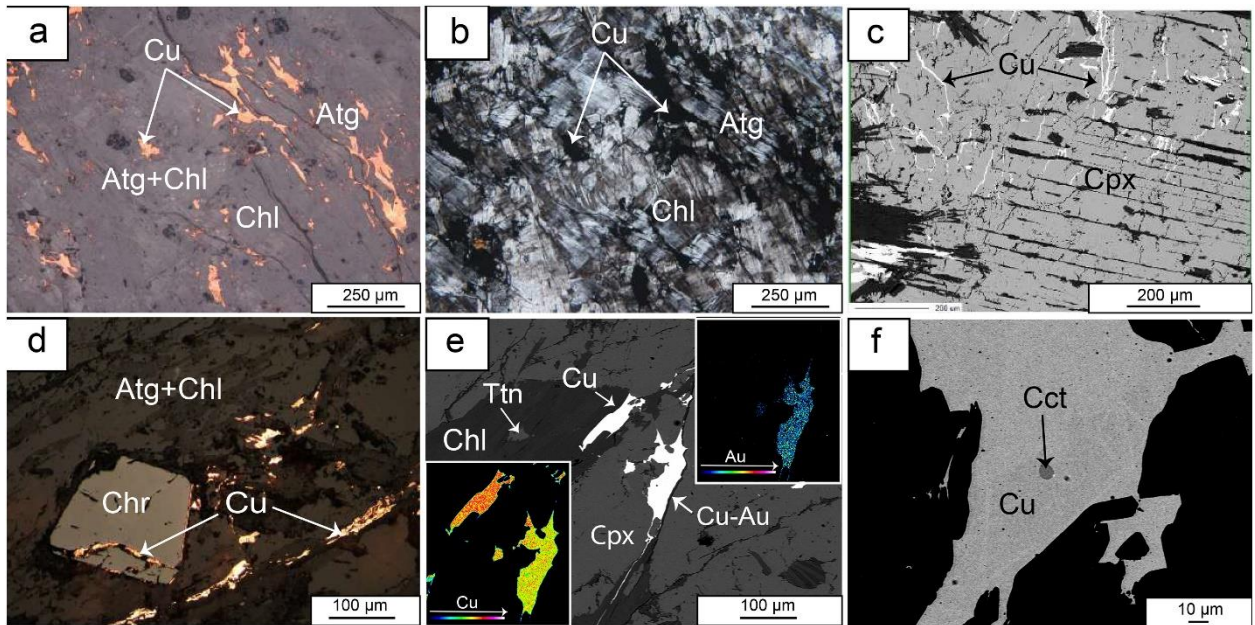


Fig. 7.5. Photomicrograph and back-scatter-electron (BSE) images of copper assemblage (zone III): (a-b) Reflected light (a) and cross polarized (b) images of native copper (Cu) intergrown with antigorite (Atg); (c) Native Cu along cleavage planes and along partially healed fractures cutting clinopyroxene (Cpx); (d) native copper filling fracture of chromian spinel (Chr); (e) association of Cu, Cu–Au alloy and titanite (Ttn) in metasomatic clinopyroxene. Cu and Au maps are shown as small insets; (f) chalcocite (Cct) inclusions in native copper.

### 7.4.3. Chemical changes across the reaction zone

X-ray element mapping shows that the contact between Opx-rich and metasomatic zones (I and II) of Cu-rich pyroxenite samples is sharp (Fig. 7.6). The formation of amphiboles in Zone I is associated with increase in Ca, Na and Al. Sporadic high concentrations of these elements also occur in Zone II where they correspond to amphibole inclusions. Aluminium transfer may have also a significant role in the formation of chlorite in zone III. The high volumetric proportion of clinopyroxene in zone II is responsible for an increase in Ca.

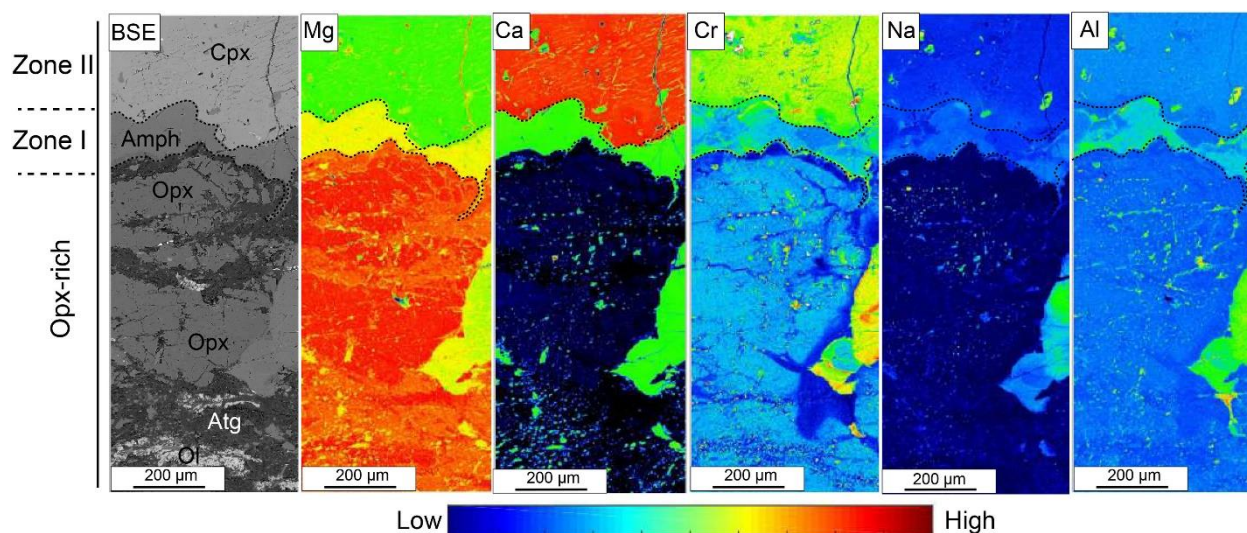


Fig. 7.6. Back-scattered electron (BSE) imaging and multi-element wavelength-dispersive spectroscopy (WDS) mapping of sharp contact between orthopyroxene-rich and metasomatised portion of Cu-rich pyroxenite sample.

### 7.4.4. Fluid inclusions in Zone II

A study of fluid inclusions (FIs) in clinopyroxene from zone II was carried out for the sample PX05 (Fig. 7.7a). FIs appear in cloudy clinopyroxenes either oriented randomly or along cleavage planes and healed cracks. The FIs mainly range in size from 3 to 10  $\mu\text{m}$  and display various shapes (Fig. 7.7a). The inclusions are often partially or fully decrepitated and whiskers may occur (Fig. 7.7a). At room temperature two phases (liquid + vapor) can be observed (Fig. 7.7a). The FIs were discriminated based on their petrographic position following Roedder (1984) and Van den Kerkhof and Hein (2001). The FIs are considered to have a secondary origin, since they mostly occur along healed fractures and cleavage planes, indicating that they were captured after the formation of the host clinopyroxenes.

We determined the nature of the phases in the FIs using Raman microspectroscopy. The molar proportion of the fluid components (shown in Table 7.S8) in the fluid (vapor + liquid) at room temperature was calculated based on 1) the integrated band area of their characteristic

Raman bands and 2) Raman cross-sections following the method of Dubessy et al. (1989). In all studied FIs we identified CH<sub>4</sub> and H<sub>2</sub> based on their highest intensity bands (at ~2918; ~588 and ~4156 cm<sup>-1</sup>, respectively) (Fig. 7.7b). The fraction of H<sub>2</sub> widely varies in the FIs from 20 to 98 vol.%.

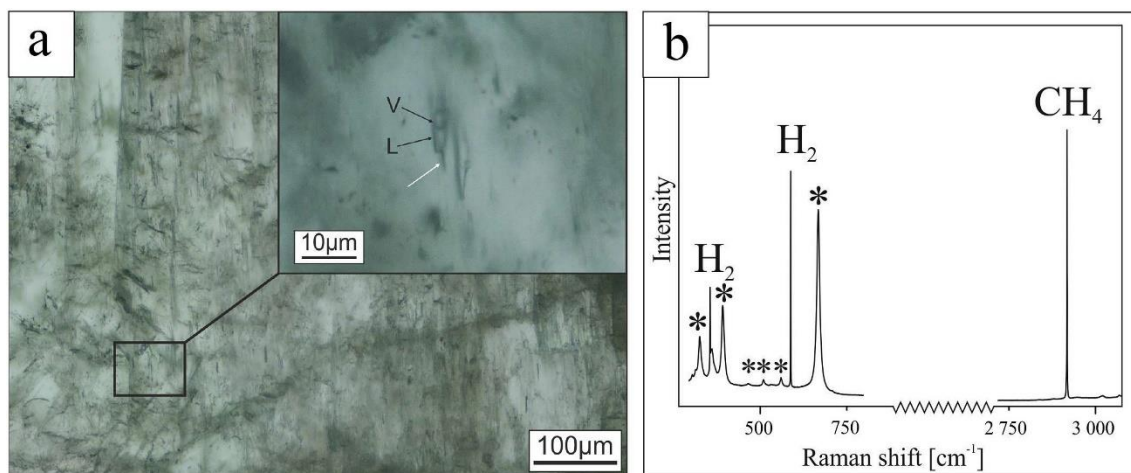


Fig. 7.7. (a) Fluid inclusions in the cloudy clinopyroxene of sample X05. In the zoomed area, the fluid inclusions appear in healed fractures and along the cleavage planes of the clinopyroxene. The white arrow shows a whisker, suggesting decrepitation of the FI. Abbreviations: L - liquid phase; V - vapor phase. (b) Main Raman bands of the components (CH<sub>4</sub> and H<sub>2</sub>) of the FIs. The stars note the Raman bands of the host clinopyroxene.

Table 7.S8. Composition of the fluid phase (liquid+vapor) in studied clinopyroxene-hosted fluid inclusions from the PX05 sample.

Inclusion	CH <sub>4</sub> (mol.%)	H <sub>2</sub> (mol.%)
F10_A	65.4	34.6
F10_B	8.3	91.7
F10_C	78	22
F10_D	74	26
F10_E	46.6	53.4
F11_A	11.3	88.7
F11_B	33.6	66.4
F11_C	24.5	75.5
F11_D	9.2	90.8
F11_E	14	86
F12_A	62.4	37.6
F12_B	65.1	34.9
F12_C	72.3	27.7
F13_A	22.9	77.1
F13_B	32.3	67.7
F13_C	14.8	85.2
F4_A	1.7	98.3

#### 7.4.5. U-Pb LA-ICP-MS dating of titanite

Laser ablation ICP-MS U-Pb analyses including U and Pb contents, isotopic ratios and ages of seven titanite grains from the Cheshmeh-Bid Cu-rich pyroxenite are given in Table 7.S9. All titanite grains contain some U ranging from 5 to 38 µg/g as well as some initial Pb. Concordia plots of titanite U–Pb isotopic results are shown in Figure 7.8. All titanite grains contain significant initial common Pb and therefore lie on a mixing line between the <sup>207</sup>Pb/<sup>206</sup>Pb ratio of the common Pb component and the age of the radiogenic component as defined by the lower concordia intercept (Fig. 7.8). Regressing data from the titanite grains using Isoplot (Ludwig, 2003) gives a line that projects to an age of 101±22 Ma. The MSWD of 3.8 indicates scatter outside of measurement error, probably because of excess variations in the Pb/U ratio. To some extent the 95% confidence error takes account of this since it scales as the square root of the MSWD (Ludwig, 2003).

Table 7.S9. Laser ablation ICP-MS U-Pb analyses including U and Pb contents, isotopic ratios and ages of seven titanite grains from the Cheshmeh-Bid Cu-bearing pyroxenites

Spot	U (ppm)	Pb <sup>206</sup> (ppm)	$\frac{^{207}\text{Pb}}{^{235}\text{U}}$	1 Sig	$\frac{^{206}\text{Pb}}{^{238}\text{U}}$	1 Sig	Err. Correl.	$\frac{^{207}\text{Pb}}{^{235}\text{U}}$	1 Sig	$\frac{^{206}\text{Pb}}{^{238}\text{U}}$	1 Sig
								Age (Ma)	Age (Ma)		
<b>Titanite</b>											
SmallTit-4.2	4.8	0.1	1.833	0.156	0.0284	0.0012	0.5093	1057	55	180	8
LargeTit-5.1	5.7	0.3	3.898	0.250	0.0481	0.0017	0.5503	1613	51	303	10
LargeTit-5.2	21.1	0.5	0.844	0.053	0.0224	0.0007	0.5068	621	29	143	5
LargeTit-5.3	16.2	0.4	0.959	0.095	0.0221	0.0009	0.4058	683	48	141	6
BladeTit-3.1	37.9	1.1	1.289	0.068	0.0287	0.0008	0.5482	841	30	182	5
SmallTit-4.1	8.6	0.4	3.677	0.184	0.0490	0.0014	0.5597	1566	39	308	8
IrregTit-2.1	9.6	0.2	1.309	0.135	0.0258	0.0016	0.5860	850	58	164	10

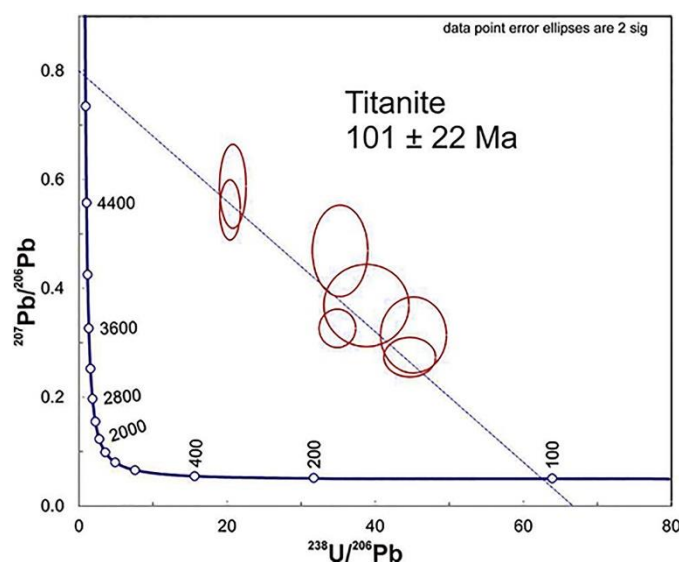


Fig. 7.8. Concordia plots of titanite U–Pb isotopic results.

#### 7.4.6. Copper isotope composition of native copper

Copper isotopic results of eight native copper grains from the Cheshmeh-Bid Cu-rich pyroxenite are given in Table 7.S10. The eight native copper grains have Cu isotope compositions ranging from  $\delta^{65}\text{Cu} = -0.20$  to  $+0.28\%$  (Fig. 7.9). Errors for all the analyses are  $\pm 0.08\%$ . An average  $\delta^{65}\text{Cu}$  Bulk Silicate Earth (BSE) value of  $+0.07 \pm 0.10\%$  (2SD) (Savage et al., 2015) was used to examine and characterize the Cu isotope composition of Cheshmeh-Bid native copper. The copper isotope values for the studied native copper lie within the previously reported copper isotope range for bulk mantle rocks (Fig. 7.9; Ben Othman et al., 2006; Ikehata and Hirata, 2012; Liu et al., 2015; Zou et al., 2019). Native copper grains from the Cheshmeh-Bid pyroxenites display significant isotope fractionation compared to primary

native copper in Horoman peridotite complex but there is significant isotope fractionation for Cheshmeh-Bid native copper.

Table 7.S10. Copper isotopic results of eight native copper grains from the Cheshmeh-Bid Cu-bearing pyroxenite

	$d^{65}\text{Cu}$ (per mil)	Errors
CHNC-02	-0.2	0.08 2 sigma
CHNC-07	0.07	0.08 2 sigma
CHNC-01	0.12	0.08 2 sigma
CHNC-04	0.28	0.08 2 sigma
CHNC-03	0.04	0.08 2 sigma
CHNC-05	-0.07	0.08 2 sigma
CHNCC11	0.11	0.08 2 sigma
CHNC-08	0.12	0.08 2 sigma

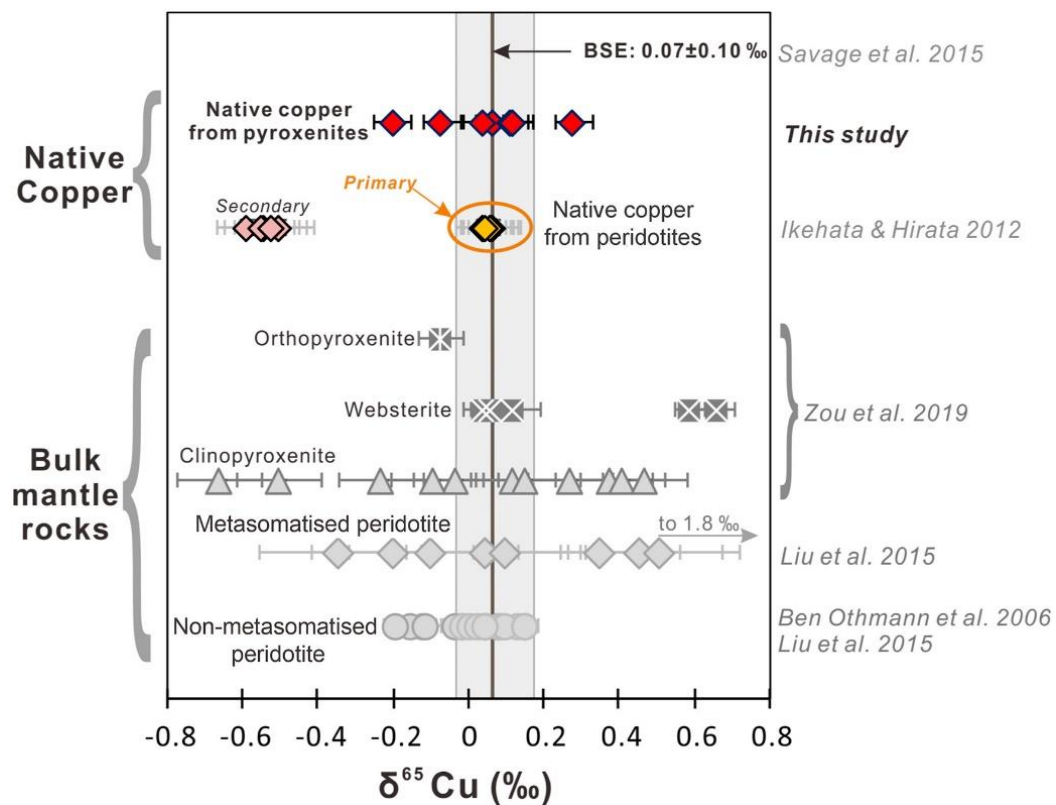


Fig. 7.9. Variations of  $\delta^{65}\text{Cu}$  values in the Cheshmeh-Bid Cu-rich pyroxenites. Data of peridotites from previous studies are also shown for comparison. The grey rectangle represents the estimated  $\delta^{65}\text{Cu}$  value of the Bulk Silicate Earth (BSE:  $0.07 \pm 0.10\%$ , Savage et al., 2015).

### 7.4.7. Bulk-rock chemistry

Whole rock geochemical data of the Cheshmeh-Bid pyroxenite samples are shown in Table 7.S11. Compared to fresh pyroxenite samples (PX01 and PX20), matasomatized pyroxenites show slightly higher Mg# values (0.91-0.96), lower SiO<sub>2</sub> (46.37-51.76 wt.%), higher Al<sub>2</sub>O<sub>3</sub> (2.60-8.84 wt.%), CaO (5.18-18.96 wt.%) and TiO<sub>2</sub> contents (0.07-0.17 wt.%) (Table 7.S11). The Cheshmeh-Bid metasomatised pyroxenites have high REE concentrations (3.79-15.64 µg/g).

We use in the following an isocon diagram of Grant (2005) to estimate element mobility associated with metasomatism in the Cheshmeh-Bid pyroxenites (Fig. 7.10). We used average composition of the Cheshmeh-Bid fresh orthopyroxenites (samples IRKJPX01 and IRKJPX20) and metasomatic pyroxenite samples (samples IRKJPX04, IRKJPX05, IRKJPX06, IRKJPX11 and IRKJPX12). The isocon diagrams allow to quantify the loss and gain of elements during the alteration of fresh samples by using TiO<sub>2</sub> and Sc to define the isocon (Fig. 7.10). These elements are commonly considered as relatively immobile during alteration (Van Baalen, 1993; Grant, 2005; Beinlich et al., 2010). The elements plotting above the isocon were gained during metasomatism, whereas those plotting below were lost. Concentration of Al<sub>2</sub>O<sub>3</sub>, CaO and REE increased during the metasomatism of the Cheshmeh-Bid orthopyroxenites, whereas MgO, FeO, SiO<sub>2</sub>, MnO, K<sub>2</sub>O and Ba decreased (Fig. 7.10). The slope of the constant composition line in the isocon diagram is 1.9. This indicates that the total mass and the total volume decreased of 47 % and 61 % during the alteration, respectively. This is consistent with the observation that most major elements were lost during metasomatism.

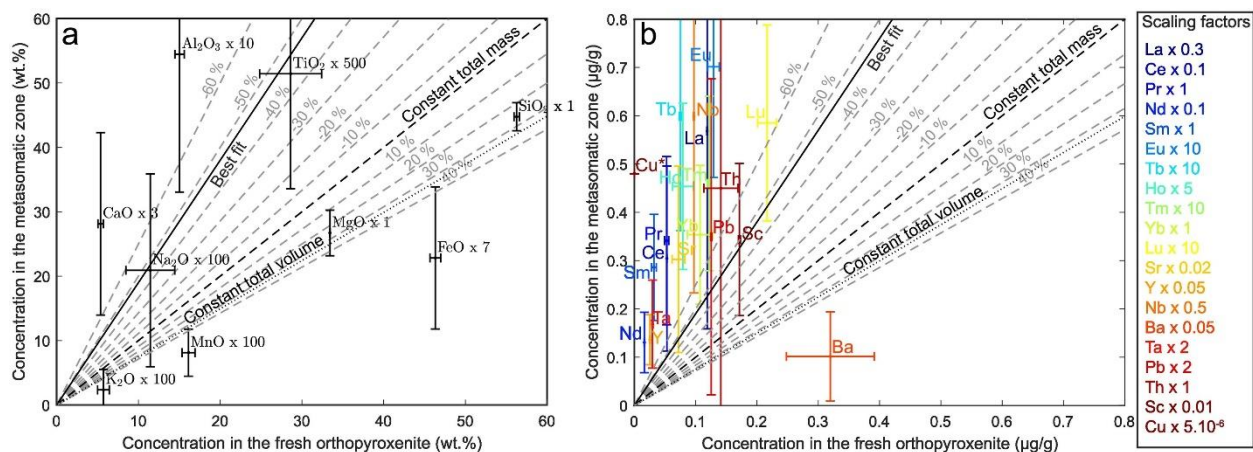


Fig. 7.10. Isocon diagram for major (a), and trace and rare earth elements (b) using the method of Grant (2005) comparing average composition of Cheshmeh-Bid fresh orthopyroxenites and average composition of five metasomatised samples. The error bars correspond to  $\pm$  one standard deviation. Scaling factors have been used to display a better dispersion of the elements. Scaling factors are shown on isocon diagrams. The lines for constant total mass (black dashed

line), constant total volume (black dotted line) and the best fit of the composition in immobile elements (isocon assuming Sc and TiO<sub>2</sub> as immobile; black plain line) are displayed. No change in composition is assumed along the isocon. The grey dashed lines correspond to compositions calculated for different mass gain(+)/loss(-). The densities used for constant volume and volume change calculations are 2896 kg/m<sup>3</sup> for the fresh orthopyroxenites and 3870 kg/m<sup>3</sup> for the Cu-bearing metasomatised samples. They are retrieved with image analysis of the modal composition in the fresh orthopyroxenite and in zone III. \*: estimated based on image analysis.

#### 7.4.8. Thermodynamic modelling of Ca-metasomatism

Thermodynamic modelling of phase equilibria indicates that the talc + antigorite + amphibole assemblage is stable in the presence of fluid at temperatures below ~ 420°C and at the lowest chemical potential of CaO investigated here ( $\mu_{\text{CaO}}$ ; Fig. 7.11). This assemblage is replaced at higher  $\mu_{\text{CaO}}$  by amphibole + antigorite (I), then by clinopyroxene + antigorite (II) and finally by clinopyroxene + antigorite + chlorite (III). The samples having experienced Ca metasomatism are predicted to be composed of one of these three mineralogical assemblages (assemblage I for IRKJPX04 and assemblage III for IRKJPX11 and IRKJPX12). At the highest  $\mu_{\text{CaO}}$  investigated in the simulation, phases such as brucite, wollastonite and vesuvianite are stable. These latter phases are not observed in the natural samples. The olivine-antigorite transition occurs at a higher temperature at low  $\mu_{\text{CaO}}$  (450°C at -730 kJ/mol) than at high  $\mu_{\text{CaO}}$  (250°C at -675 kJ/mol).

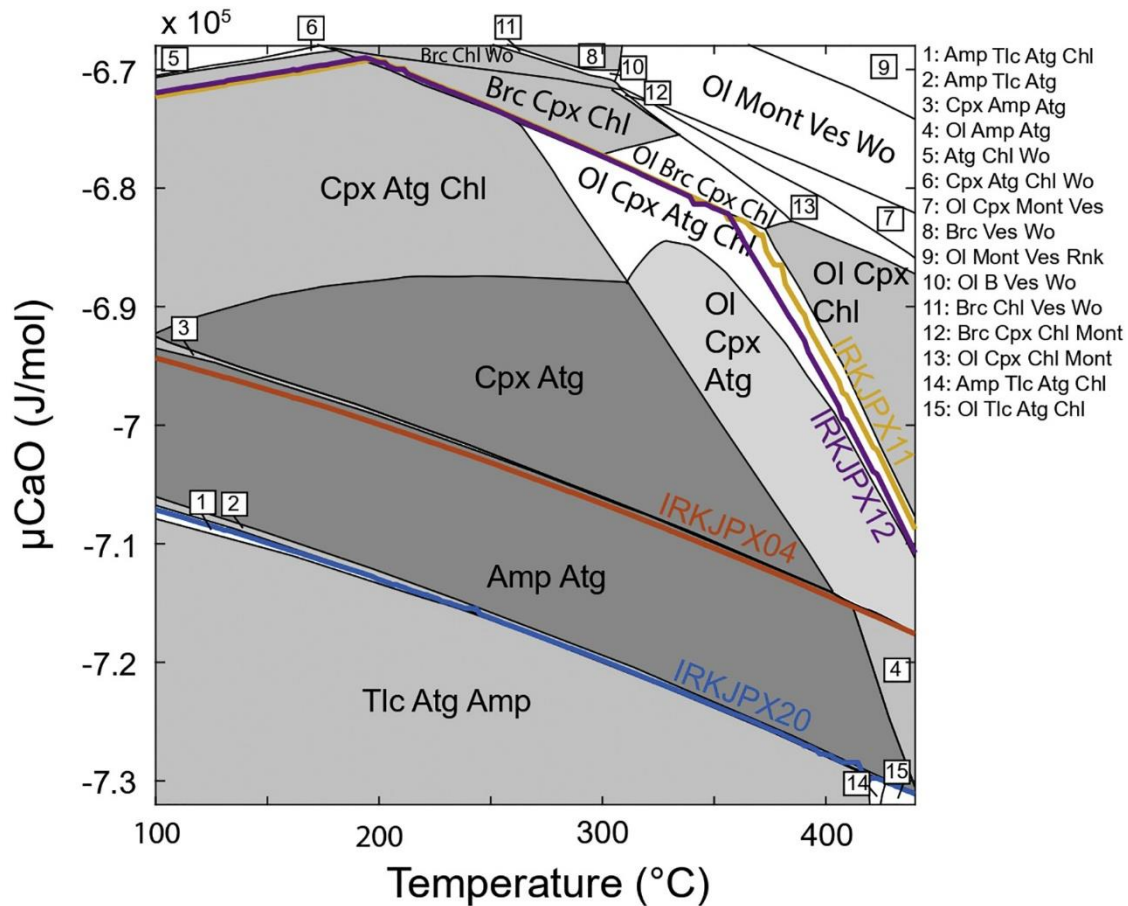


Fig. 7.11. Temperature- $\mu\text{CaO}$  pseudosection for the composition of sample IRKJPX20 (orthopyroxenite) at 50 MPa.  $\mu\text{CaO}$  calculated as a function of temperature is displayed for the orthopyroxenite and three samples affected by Ca-metasomatism (IRKJPX04, IRKJPX11 and IRKJPX12). Tlc: talc; Atg: antigorite; Amp: amphibole; Cpx: clinopyroxene; Chl: chlorite; Ol: olivine; Brc: brucite; Wo: wollastonite; Mont: monticellite; Ves: vesuvianite; Rnk: rankinite.

#### 7.4.9. Stability of native copper

The Cu-Fe-Ni-O-S phase relations are displayed in Figure 7.12 as a function of the activities in  $\text{H}_{2,\text{aq}}$  and  $\text{H}_{2\text{S},\text{aq}}$  at 50 MPa and 200 °C, 300 °C and 400 °C. In the Fe-Ni-O-S system, the stability fields are identical to the ones calculated in Klein and Bach (2009). Native copper is stable at  $a_{\text{H}_{2,\text{aq}}} > 10^{-3}$  and  $a_{\text{H}_{2\text{S},\text{aq}}} < 10^{-3}$  together with awaruite or heazlewoodite in the Cu-Fe-Ni-O-S system. Its stability field is bound by chalcocite ( $\text{Cu}_2\text{S}$ ) at low  $a_{\text{H}_{2\text{S},\text{aq}}}$  and bornite ( $\text{Cu}_5\text{FeS}_4$ ) at higher  $a_{\text{H}_{2\text{S},\text{aq}}}$ . The stability field of bornite is bound by chalcopyrite ( $\text{CuFeS}_2$ ) at  $a_{\text{H}_{2\text{S},\text{aq}}} > 10^{-3}$  at 200°C and at  $a_{\text{H}_{2\text{S},\text{aq}}} > 10^{-2}$  at 400°C. In the Cu-O-S system, the stability field of native copper extends towards higher  $a_{\text{H}_{2\text{S},\text{aq}}}$  and is entirely bound by chalcocite.

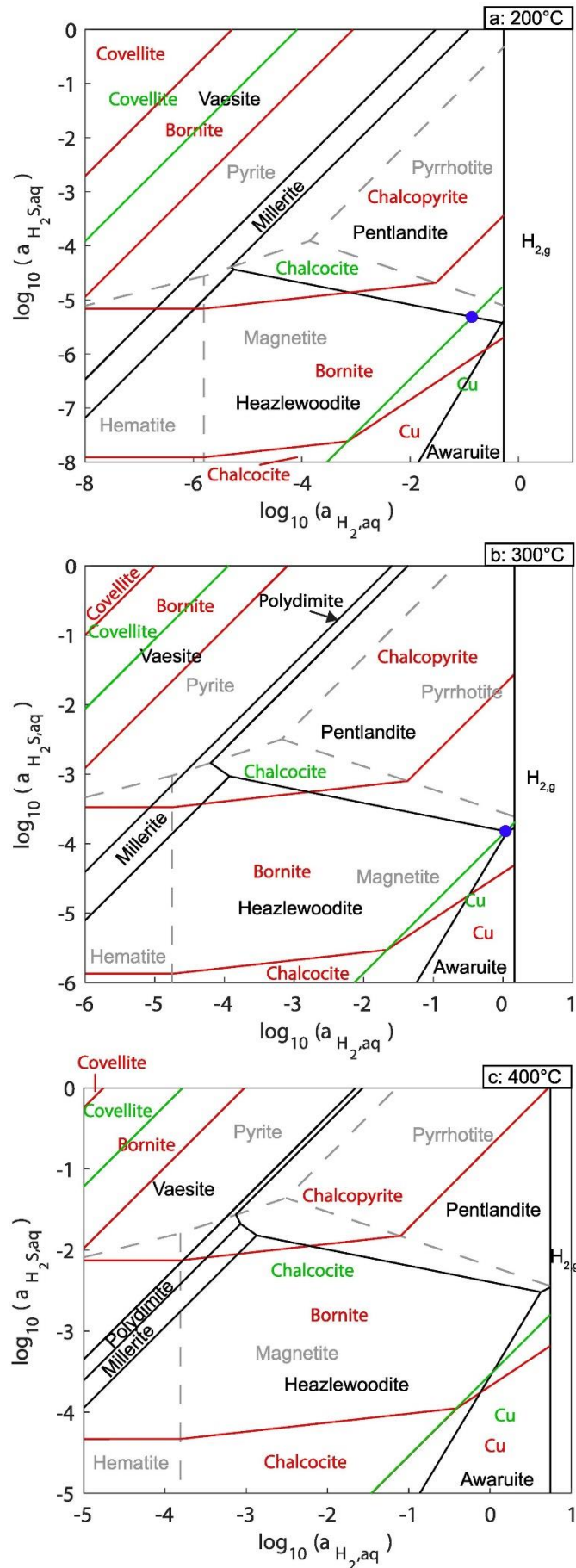


Fig. 7.12. Sulfide and oxide stabilities as a function of  $a_{H_2, aq}$  and  $a_{H_2S, aq}$  in the Cu-Fe-Ni-O-S system. The phase diagrams are computed at 50 MPa,  $a_{H_2O} = 1$  and 200 °C (a), 300 °C (b) and 400 °C (c). The boundaries in the Fe-O-S, Cu-O-S, Fe-Ni-O-S, and Cu-Fe-O-S systems are

displayed with grey dashed lines, green plain lines, black plain lines and red plain lines, respectively. The blue spot corresponds to the intersection of the pentlandite/hezlewoodite and the chalcocite/Cu boundaries. This intersection is used to determine the stability of native copper in a system where  $a_{\text{H}_2,\text{aq}}$  and  $a_{\text{H}_2\text{S},\text{aq}}$  are buffered by the pentlandite/hezlewoodite equilibrium. (For interpretation of the references to colour in this figure legend, the reader is referred to the web version of this article.)

## 7.5. Discussion

### 7.5.1. Ca-metasomatism: the main driver for reaction zone formation

Thermodynamic calculations predict the progressive replacement of orthopyroxene by amphibole, clinopyroxene and chlorite as  $\mu\text{CaO}$  increases (Fig. 7.11). This mineralogical sequence is exactly the one observed in the reaction zone where amphibole, clinopyroxene and clinopyroxene + chlorite are the main components of zones I, II and III, respectively (Fig. 7.2a). This suggests that calcium input is the main driver for metasomatism. Clinopyroxene crystals in zone II show a wide range of Mg# (0.76-0.98) due to almost unity Mg-Fe partition coefficient between clinopyroxene and associated antigorite and chlorites. Clinopyroxenes cogenetic with chlorites, antigorite and/or tremolite have metasomatic origin. Aluminum transfer may also play a role for the formation of zone III in which significant amounts of chlorite are observed. The chromian spinel of the orthopyroxenite appears to react during metasomatism and may provide the Al needed to form chlorite. Chromian spinel alteration may also explain the high Cr content measured in chlorite (up to 3.41 wt.%). The presence of chlorite inclusions and ferrian chromite in porous textured chromian spinel can be attributed to metamorphism or hydrothermal events (e.g. Beinlich et al 2020). Gervilla et al. (2012) suggested that during the early stage of chromite alteration, pristine chromite may react with olivine in the presence of reducing fluids to form chlorite and secondary high Cr-chromite with porous texture. Textural evidence (Fig. 7.2d) suggests the possibility that chromite grains from the Cheshmeh-Bid pyroxenites also reacted with percolating  $\text{Ca}^{2+}$ - $\text{H}_2$ -rich fluids during metasomatism. Possible support for this scenario arises from the abundant large inclusions of chlorite and metasomatic clinopyroxene in porous chromian spinel rims.

Ca-metasomatism is thought to occur by interaction between the pristine orthopyroxenite and Ca-OH fluids derived from serpentinization of ultramafic rocks. The observation of secondary/metamorphic olivine may also strengthen the interpretation of reaction zone formation by Ca-metasomatism. The mode of occurrence and mineral chemistry of olivine (Mg# = 0.75-0.83) in Opx-rich zone of Cu-rich pyroxenites is indeed in agreement with a secondary origin. It is interesting to note that the Mg# of olivine is also controlled by the phases

in equilibrium (i.e. antigorite) and low-Mg# olivine is quite ordinary in low-T metaperidotites (Arai and Oyama, 1981).

Several hypotheses have been proposed to explain the dehydration of serpentine producing olivine: (i) injection of magma into meta-peridotites or -serpentinites (e.g. Vance and Dungan, 1977); (ii) Barrovian-type metamorphism (e.g. Evans, 1977). (iii) de-serpentinization in deep portion of subducting slab that has been linked to intermediate-depth intraslab earthquake (e.g. Hacker *et al.*, 2003; Plümper *et al.*, 2017); (iv) in-situ dehydration of serpentinized mantle within oceanic lithosphere prior to subduction and/or obduction processes (Iyer *et al.*, 2010). Figure 7.11 shows that serpentine breakdown occurs at temperatures above 400°C at 50 MPa at low  $\mu\text{CaO}$  (-730 kJ/mol). This is in agreement with experimental constraints in the Mg-Si-O-H system (Ulmer and Trommsdorff, 1999; Padrón-Navarta *et al.*, 2010). Furthermore, the addition of CaO significantly shifts the antigorite-olivine equilibrium towards lower temperature (250°C at  $\mu\text{CaO} = -675$  kJ/mol; Fig. 7.11). The evolution of the modes of the rock-forming minerals (Fig. 7.S2) indicates that the reaction of olivine formation at high  $\mu\text{CaO}$  can be written in the Mg-Si-Ca-O-H system as (Eq. 7.1):

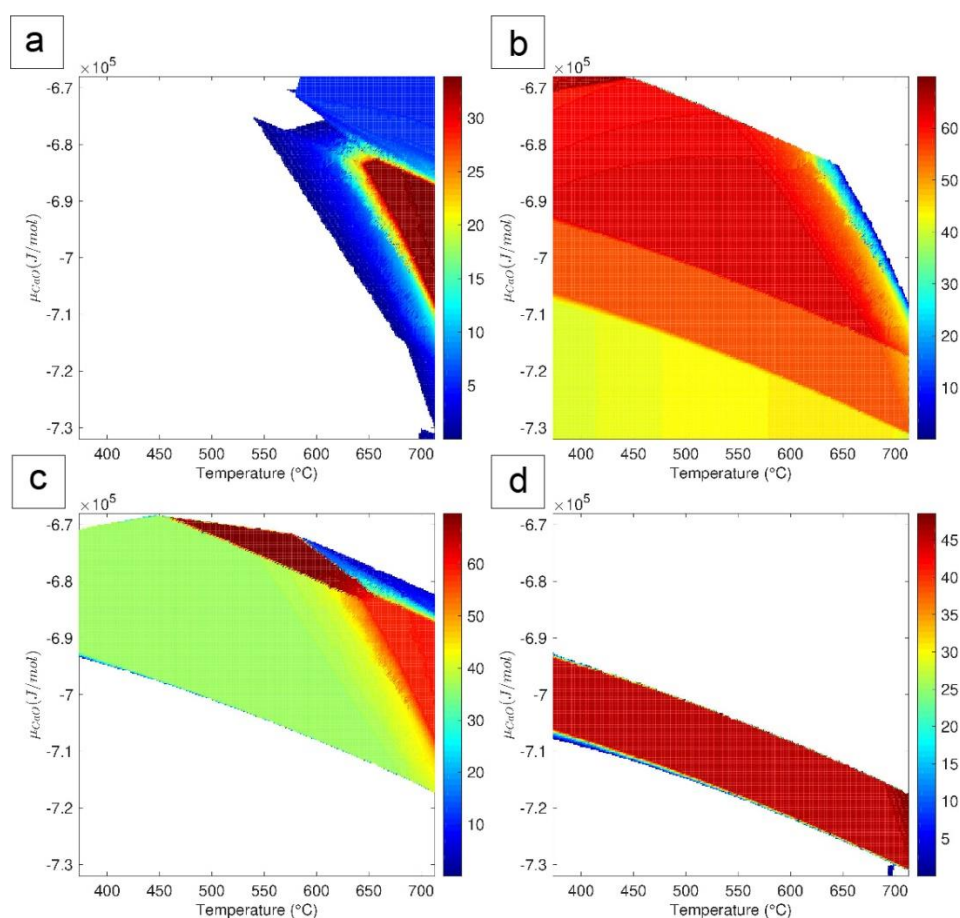


Fig. 7.S3. Modes (vol.%) of the phases as a function of temperature and chemical potential in CaO for the pseudosection calculated with the composition of sample IRKJPX20 at 50 MPa. (a) Olivine. (b) Antigorite. (c) Clinopyroxene. (d) Amphibole.

There is no evidence for high-pressure metamorphism in the studied pyroxenites. This suggests that serpentine breakdown and olivine formation are the result of Ca-metasomatism rather than heating at high-pressure in the Cheshmeh-Bid pyroxenites.

Fluids originated during serpentinization, usually referred as “serpentinization-buffered fluids”, are Si-undersaturated and Ca-rich (e.g. Bach and Klein, 2009). The source of Ca is still a matter of debate and two ultimate sources have been suggested: (i) breakdown of pyroxenes during serpentinization, which may release  $\text{Ca}^{2+}$  into aqueous fluids (e.g. Coleman, 1967; Allen and Seyfried, 2003). Bach and Klein (2009) proposed that addition of  $\text{Ca}^{2+}$  from serpentinizing peridotite is likely driven by diffusive mass transfer in the form of hydroxo species ( $\text{CaOH}^+$ ); (ii) external hydrothermal solutions (e.g. Hatzipanagiotou and Tsikouras, 2001). The isocon diagram (Fig. 7.10) confirms mobility of major elements and REE (La-Lu) during metasomatism. Significant increase of CaO and decrease of  $\text{SiO}_2$  reflect the Ca-metasomatism reaction during alteration of the Cheshmeh-Bid orthopyroxenites. Although REEs are generally regarded as immobile elements during fluid-rock reaction, they can be mobilized during metasomatic process and hydrothermal alteration (e.g., Salvioli-Mariani et al., 2020). Composition of fluid(s), pH conditions of the fluid phase, availability of ligands in the aqueous fluids and water/rock ratio are key factors controlling the pronounced REE mobilization during hydrothermal alteration and/or metasomatic processes. The formation of calcite and apatite during Ca-metasomatism of the Cheshmeh-Bid pyroxenites is likely related to high activities in  $\text{CO}_3^{2-}$  and  $\text{PO}_4^{3-}$ , respectively. Complexation of LREE may be triggered by carbonate ions (e.g. Gimeno-Serrano et al., 2000). High concentration of LREE with respect to the HREE can be explained by preferential complexation of carbonates with LREE. High pH and relatively basic conditions are favourable for the REE-carbonate complexation (e.g. Haas et al., 1995), which is consistent with alkaline nature of fluids during serpentinization of peridotites (e.g. Barnes and O'Neil, 1969).

The Ca-metasomatism observed in the case of Cheshmeh-Bid Cu-rich pyroxenites leads to the formation of a reaction zone. The dykes are surrounded by harzburgites and dunites having experienced extensive serpentinization, suggesting that clinopyroxene breakdown in the ultramafic rocks during hydration may play a key role for the Ca-metasomatism described here. In the following, we further investigate the links between Ca-metasomatism and serpentinization by looking at evidence for reducing conditions during fluid/rock interaction.

## 7.5. 2. Reducing conditions during metasomatism

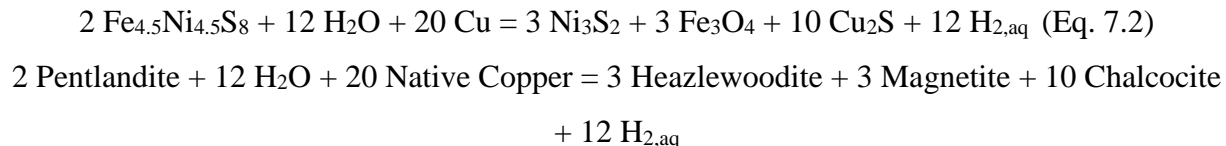
Serpentinization leads to reducing conditions due to the coupled reduction of water to form  $H_2$  and the oxidation of the ferrous iron initially contained in the primary minerals (mostly olivine) to form ferric minerals (e.g. magnetite) (McCollom and Bach, 2009; Malvoisin et al., 2012).

$H_2$  (e.g. Barnes et al., 1967) is commonly observed in fluids associated with serpentinized peridotites and Ni-Fe alloys (e.g. Ramdohr, 1950) have been described in serpentinized peridotites. Methane is also found in serpentinizing environments; it is generated through reduction of  $CO_2$  or CO by  $H_2$  (e.g. Charlou et al., 2002; McCollom, 2016). The observation of  $H_2$ - $CH_4$ -bearing fluid inclusions in metasomatic diopside from the Cheshmeh-Bid pyroxenites indicates that Ca-metasomatism occurred under reducing conditions, most likely associated with the serpentinization of the surrounding rocks.

The source of copper may be either desulfurization of primary Cu-sulfides of the pyroxenite during the hydrothermal overprint or transportation of Cu in a S-poor fluid from the surrounding harzburgites-dunitites into the orthopyroxenite dike during hydrothermal alteration. Thermodynamic modelling indicates that native copper can be stable at high  $H_2$  activity and/or at a low  $H_2S$  activity (Fig. 7.12). The fluid inclusions data reveal the presence of  $H_2$  during metasomatism (Figs. 7.7a and 7.7b), suggesting that a high activity in  $H_2$  prevailed during native copper formation in the Cheshmeh-Bid pyroxenites.  $H_2S$  activity during alteration is probably relatively low (Fig. 7.12) and thus difficult to constrain. Some mineral equilibria allow  $H_2S$  activity to be retrieved from  $H_2$  activity. Seyfried et al. (2004) proposed that  $a_{H_2}$  and  $a_{H_2S}$  may be buffered by the equilibrium magnetite + bornite + chalcocite in serpentinized peridotites. Klein and Bach (2009) used mineralogical observations in serpentinized peridotites collected on the seafloor and measurements of  $H_2S$  and  $H_2$  concentrations in fluids venting at peridotite-hosted hydrothermal fields (Rainbow and Logatchev, Charlou et al., 2002) to determine that the heazlewoodite/pentlandite equilibrium buffers  $a_{H_2S}$  where serpentinization occurs (HP buffer). The sulfide mineralogy in the serpentinized peridotites surrounding the orthopyroxenites described here is dominated by pentlandite and heazlewoodite suggesting that the HP buffer may fix  $a_{H_2}$  and  $a_{H_2S}$  during native Cu formation. This would imply fast  $H_2$  and  $H_2S$  transport between the serpentinized peridotites and the orthopyroxenites.  $H_2$  is known to diffuse rapidly in water (Kallikragas et al., 2014). Figure 7.12 shows that native copper is not stable at  $a_{H_2}$  and  $a_{H_2S}$  fixed by the HP buffer in the Cu-Fe-Ni-O-S system. Bornite ( $Cu_5FeS_4$ ) is indeed the stable Cu-bearing mineral along the HP buffer under reducing conditions. Bornite and other iron-bearing sulfides have not been observed in the samples from the Cheshmeh-Bid Ophiolite. This may be interpreted as evidence for i)  $a_{H_2S}$  below the one fixed by the HP buffer

or ii) a low iron availability preventing Fe-bearing sulfide formation in zone III during metasomatism (Fig. 7.12). It is difficult to select one of these two options since the mobility of H<sub>2</sub>S and the availability of iron are poorly constrained in the studied system. The isocon diagram (Fig. 7.10) indicates that Fe is lost during metasomatism but the concentration in Fe is still sufficient to form bornite instead of native copper in zone III. The thermodynamic calculations performed here in the Cu-Fe-Ni-O-S system assume the presence of Fe in excess and thus do not allow for Fe distribution to be investigated. Thermodynamic calculation of iron distribution in a Cu-bearing system is theoretically possible, for example, with Gibbs energy minimization. However, it cannot be currently performed due to the lack of a thermodynamic database containing Cu-sulfides and realistic silicate solid solutions.

The scarcity of chalcocite in the studied samples and its occurrence as inclusions in native copper (Fig. 7.5f) suggest that native copper is formed at the expense of chalcocite during alteration. If  $a_{\text{H}_2\text{S}}$  is below the HP buffer (i), native copper formation can be explained by desulfurization induced by an increase in H<sub>2</sub> activity associated with serpentinization in the surrounding peridotites. If a low iron availability is assumed and bornite formation is excluded from thermodynamic calculations (ii), native Cu can be stable at the activities in H<sub>2, aq</sub> and H<sub>2S, aq</sub> fixed by the HP buffer (Fig. 7.12), allowing the following equation to be written (Eq. 7.2):



This equilibrium can be used to estimate the minimum  $a_{\text{H}_2}$  achieved during native copper formation (see Fig. 7.12 and 7.13). Klein and Bach (2009) estimated that H<sub>2</sub> gas could be produced after saturation in the liquid during serpentinization providing an estimate for  $a_{\text{H}_2}$  variation with temperature (Fig. 7.13). If  $a_{\text{H}_2}$  is fixed on the gas saturation line, native Cu is stable at temperature below ~ 325 °C, whereas chalcocite is stable at higher temperature. Native Cu may thus be formed through chalcocite desulfurization associated with a decrease in temperature.

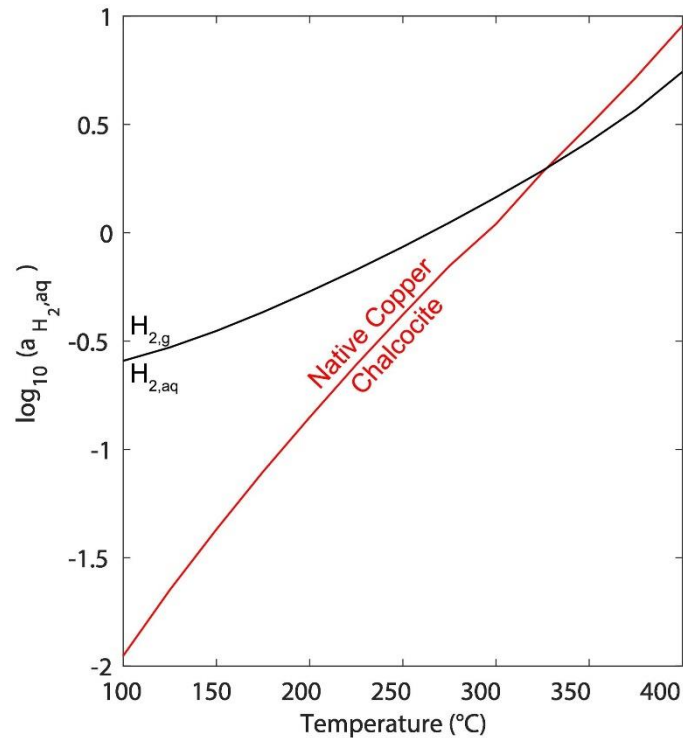


Fig. 7.13.  $a_{H_2}$  as a function of temperature for the  $H_{2,aq} = H_{2,g}$  equilibrium (black line) and the 2 Pentlandite + 12  $H_2O$  + 20 Native Copper = 3 Heazlewoodite + 3 Magnetite + 10 Chalcocite + 12  $H_{2,aq}$  equilibrium (red line). This latter equilibrium allows to determine the activity in hydrogen at which the transition from chalcocite to native copper occurs in the rock. Hydrogen partial pressure and hydrostatic pressure are assumed to be equal (50 MPa).

### 7.5.3. Model of native copper formation: Ca-metasomatism at the seafloor in a supra-subduction setting

#### 7.5.3.1. Cu isotope constraints on the Cu provenance

The copper isotope values for the studied native copper are similar to those reported for bulk mantle rocks (Fig. 7.9; Ben Othman et al., 2006; Ikehata and Hirata, 2012; Liu et al., 2015; Zou et al., 2019). As discussed above, native Cu formation in the Cheshmeh-Bid pyroxenites can be related to addition of external Cu or desulfurization of pre-existing Cu sulfides. These two hypotheses can be assessed by copper isotopes of other mafic-ultramafic lithologies. Copper sourced from the surrounding mafic ophiolitic rocks provides the most straightforward interpretation of the data. The study by Dekov et al. (2013) augments this interpretation. In their study of native copper associated with modern oceanic crust, they proposed that Cu was mobilized within the basalts with no significant copper fractionation, whereas highly fractionated copper derived from seawater was found in the sedimentary sections of the drilled cores. Ikehata and Hirata (2012) also showed copper isotope value of primary native copper in peridotite was same as that of the host rock and demonstrated that there was no significant copper isotope fractionation during high-temperature magmatic processes.

In-situ alteration of the copper sulfides by metamorphic fluid certainly occurred and could have impacted the copper isotope values in the native copper. How metamorphic fluids could alter the copper isotope composition in this tectonic environment are not well studied, however, Höhn et al. (2017) demonstrated that the metamorphic processes associated with sulfide deposition generated a relatively tight range of copper isotope value from -0.3 to +0.4 ‰. Equally interesting and related to the formation of native copper in association with basalts, the Michigan native copper associated with secondary mobilization of copper also display a relatively tight range of copper isotope values that overlap the values reported here (Bornhorst and Mathur, 2017; Larson et al., 2003; Mathur et al., 2014). Therefore, significant copper isotope fractionation could not have occurred during secondary alteration by metamorphic fluids. This interpretation is in agreement with the textural and thermodynamic evidence discussed.

Most certainly, the copper isotope values seen in the native copper samples are not related to secondary supergene processes or high temperature magmatic processes. Baggio et al. (2017) demonstrated that copper sourced from local basalts was later redistributed through supergene process that causes the 2 ‰ variation measured. Mathur et al. (2005) and Mathur et al. (2009a) clearly show that highly fractionated copper isotope values in supergene minerals resulted from low temperature oxidation. Ikehata et al. (2011) found that copper isotope values of supergene native copper (from +1.4 to +1.7 ‰) were significantly higher than those of primary chalcopyrite (from -0.3 to -0.1 ‰) from the same deposit.

Due to textural equilibrium of the Cheshmeh-Bid native copper with antigorite and chlorite, high temperature magmatic processes suggested by Ikehata and Hirata (2012) for the primary native copper in the peridotite are unlikely for its formation. Zou et al. (2019) suggested that remarkable copper isotope heterogeneity for Balmuccia pyroxenites is due to variable extent of sulfide segregation as well as melt-peridotite reaction. The absence of any main sulfide phases (e.g. pentlandite, chalcopyrite and pyrrhotite) in the Cheshmeh-Bid pyroxenites precludes the possibility of magmatic sulfide segregation and/or melt-peridotite reaction. Unfortunately, we could not obtain the copper isotope values of the magmatic chalcocite grains because they are very small (Fig. 7.5f). However, the chalcocites probably has the same  $\delta^{65}\text{Cu}$  values to bulk mantle rocks. Previous studies of copper isotope values of sulfide minerals from igneous-hosted ore deposits are tightly clustered around 0 ‰ (-0.6 to 0.4 ‰) (e.g. Larson et al., 2003).

Our petrographic and geochemical results show that metasomatic fluids were involved for the formation of the Cheshmeh-Bid native copper. Copper isotope variations of native copper grains from the Cheshmeh-Bid pyroxenites are slightly large in comparison with those of non-metasomatised peridotite (Fig. 9; Ben Othman et al., 2006; Ikehata and Hirata, 2012;

Liu et al., 2015), probably due to Cu isotope heterogeneity of the magmatic chalcocite grains and isotope fractionations during desulfurization of the sulfides. Our study also indicates that Cu isotopes can be a powerful tool to trace the source of copper in ophiolitic rocks.

### 7.5.3.2. Timing of copper formation

Based on  $^{40}\text{Ar}/^{39}\text{Ar}$  dating on hornblendes from plagiogranites and diabase, the genesis of Neyriz ophiolite in the southeast of Neyriz/Khajeh-Jamali ophiolite belt was constrained to Late Cretaceous (range between  $83.6 \pm 8.4$  Ma and  $93.19 \pm 2.48$  Ma) (Lanphere and Pamić, 1983; Babaie et al., 2006). U-Pb zircon dating of plagiogranite and gabbro intrusions provided formation ages of  $100.1 \pm 2.3$  to  $93.4 \pm 1.3$  Ma for the Neyriz ophiolite (Monsef et al., 2018). The nature and formation age of Khajeh-Jamali ophiolitic massifs in the northwest of Neyriz/Khajeh-Jamali ophiolite belt remains currently debated. The uncertainty of geochronological data for the Khajeh-Jamali ophiolitic massifs made it difficult to understand the formation age of these massifs. Uranium–lead dating carried out in this study on titanite grains in association with native copper yield an age of  $101 \pm 22$  Ma (Fig. 7.8) which may be thus considered as the age of copper mineralization. If the previously reported age interval ( $83.6 \pm 8.4$  Ma– $100.1 \pm 2.3$  Ma) could be attributed to the Khajeh-Jamali ophiolitic massifs, our U-Pb geochronological data on titanite indicates seafloor serpentinization, Ca-metasomatism and native copper precipitation during formation of an intra-oceanic forearc setting.

### 7.5.3.3. A model for copper formation

Considering all available data, a genetic model is proposed for the formation of native Cu occurrence during Ca-metasomatism affecting orthopyroxenites (Fig. 7.14). High Cr-spinels of the studied pyroxenites bear remarkable chemical resemblance to the peridotites and mantle-hosted chromitites from the studied area (Fig. 7.4). High Cr#, low  $\text{TiO}_2$  content of the Cheshmeh-Bid pyroxenites are consistent with crystallization from arc-related magmas such as high-Mg andesite or boninite. At the first stage, orthopyroxenite dykes formed by magmatic segregation from Mg-andesite or boninite melts within a supra-subduction mantle at oceanic-arc system.

At the second stage, the associated mantle peridotites underwent sub-sea floor hydrothermal alteration. Mantle exhumation was possibly enhanced by the trench-slab roll-back system (e.g. Barth et al., 2008). In such a scenario,  $\text{Ca}^{2+}$  and  $\text{H}_2$  released from the serpentinizing peridotite metasomatised ultramafic lithologies (here pyroxenite dykes). Circulation of hydrothermal fluids formed reaction zones I (amphibole + antigorite), II (clinopyroxene + antigorite) and III (clinopyroxene + chlorite + antigorite), respectively. During late stage of sea-

floor serpentinization, native copper was likely formed by low-temperature alteration of Cu-sulfides in the pyroxenites at highly reducing conditions.

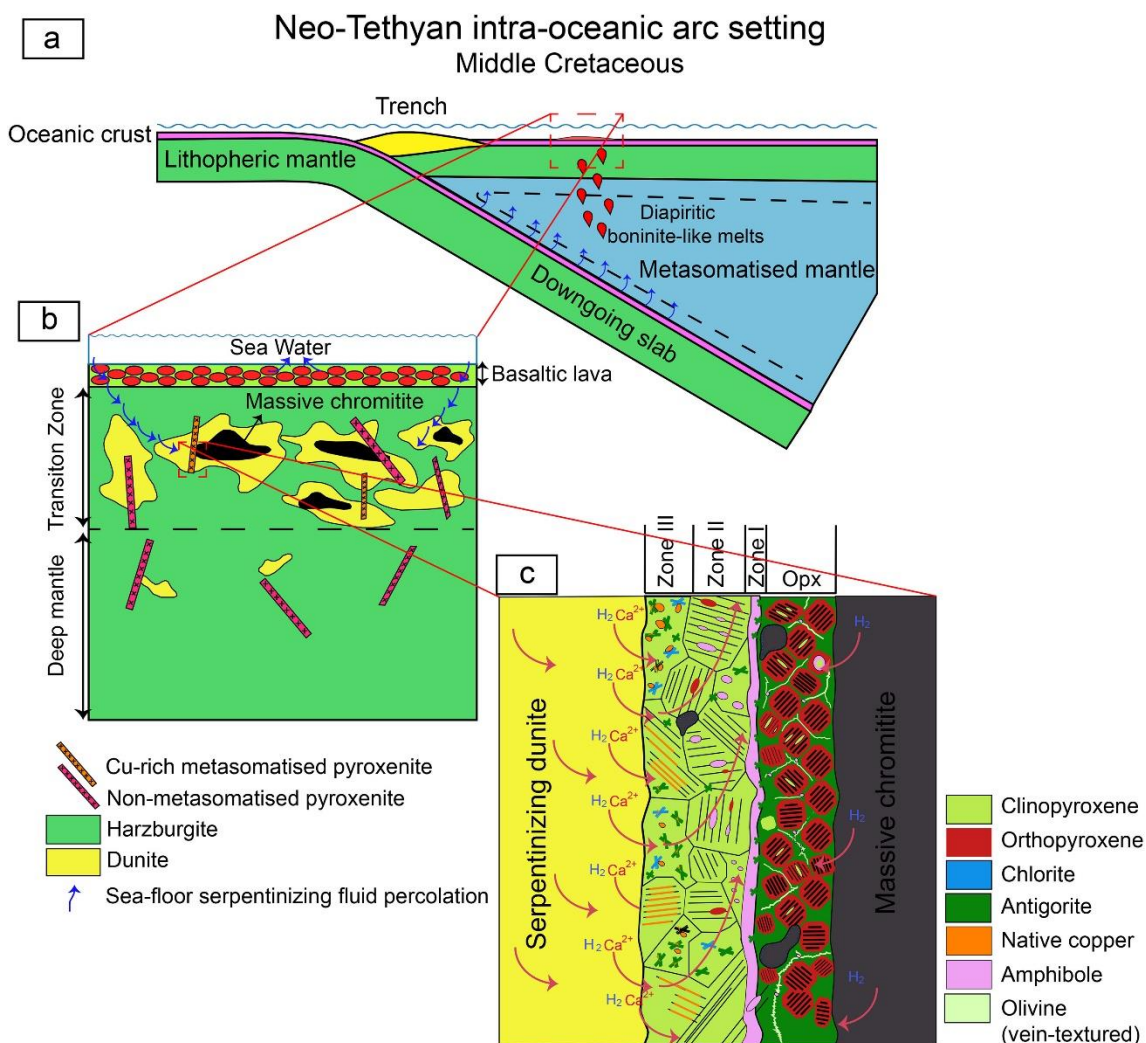


Fig. 7.14. Schematic model for the genesis of Cu-rich pyroxenite from the Cheshmeh-Bid massif. Figures (a) and (b) are presented as meso-scale.

## 7.6. Concluding remarks

Alteration of pyroxenites from the Cheshmeh-Bid massif led to the formation of a reaction zone composed of three distinct metasomatic mineral assemblages (i) amphibole + antigorite (ii) clinopyroxene + antigorite and (iii) clinopyroxene + chlorite + antigorite (III). Metasomatism was driven by calcium transport and low  $a_{\text{SiO}_2}$  fluids which could be related to interaction with Ca-rich fluids formed during clinopyroxene breakdown in the surrounding serpentinized peridotites. The fluid inclusions data reveal the presence of  $\text{H}_2$  inclusions along the cleavage planes and healed cracks of clinopyroxenes in Zone II, revealing that a high activity in  $\text{H}_2$  prevailed during native copper formation in the Cheshmeh-Bid pyroxenites. These observations are consistent with thermodynamic calculations showing that native copper can be stable at high  $\text{H}_2$  activity. The reducing conditions associated with serpentinization allowed for native copper formation under decreasing T conditions. Tightly clustered copper

isotope values of native copper also indicate secondary alteration by metamorphic fluids. According to the Cu isotope composition, a mantle origin can be inferred for copper. Serpentinization and Ca-metasomatism likely occurred in an intra-oceanic forearc setting during Albian.

# *Part IV*

## Chapter 8. Conclusions & Perspectives

---

### 8.1. Conclusions

This thesis provides new insights on the mobility of ore-forming elements including Fe, Cr and Cu, with aiming at understanding the formation of ore deposits in serpentinites. For this point, two natural case studies including: (i) serpentinite-hosted podiform magnetite ores in the Sabzevar ophiolite (NE Iran) and (ii) Cu-rich hydrothermally altered pyroxenites in the Cheshmeh-Bid ophiolitic massif (Southern Iran) were investigated to figure out processes of mass transfer and RedOx evolution during fluid-rock interaction.

Textural and compositional data indicate that the Cr-spinels from the Sabzevar magnetite ores and their host serpentinitized peridotites record two stages of alteration. During the initial alteration stage, Al-free Cr-spinel and chlorite are first formed after magmatic spinel at temperatures between 575 and 725 °C. In later stage which is ascribed to serpentinitization, ferritchromite and magnetite are predicted to form at a lower temperature ( $T < 400^{\circ}\text{C}$ ) under a high  $\text{H}_2$  fugacity. The two successive alteration episodes are interpreted as the consequences of seawater/mantle rock interaction during exhumation on the seafloor. During spinel alteration and formation of magnetite ore, chromium is relatively immobile element. Epitaxial growth of ferritchromite and magnetite on Cr-spinel II is interpreted as evidence for a coupled Cr-spinel II dissolution-ferritchromite + magnetite precipitation process. Dissolution of nanoscale magnetite grains initially formed in the host serpentinite and olivine breakdown are considered as potential sources for the magnetite ore formation. Mass balance calculations reveals iron transport at a scale  $> 10$  m during serpentinitization.

Early stages of Cr-spinel alteration are sought in other chromitite pods from the Sabzevar ophiolite, which did not reach the magnetite-ore transformation level. This confirms that Cr-spinel is rather resistant phase to hydrothermal alteration. Massive and semi-massive chromitite shows a chemical trend different from serpentinite dunite. Presence of Cr-spinel with partly altered zones reveals the incomplete modification of Cr-spinel in chromitite and their dunite envelopes. The early alteration texture is associated with formation of a zoned chromite along with chlorite filling pores during serpentinitization stage. These pores may have been acted as pathways for  $\text{SiO}_2$ -bearing fluids in the hydrothermal system. Porous texture development is rather restricted which might be related to fluid availability. Identical crystallographic orientation of lizardite/chlorite and Cr-spinel/magnetite reveals contemporaneous formation of magnetite and phyllosilicates. Chemical evolution of spinel both under dry sub-solidus equilibration ( $T > 700^{\circ}\text{C}$ ) and hydrothermal alteration is controlled by chromite/silicate ratio. During chemical modification of spinel, a fraction of Mg become soluble. Aqueous Mg is also

found to be at least two orders of magnitude more soluble than Fe and Si during alteration. Limited chemical exchange between chromitites and their host dunite resulted in lack of magnetite ore formation. Localities in the Sabzevar ophiolite belt where magnetite ores are present do show a significant mass transport of Fe and Al at a scale of a few tenths of meters.

Based on textural features and compositional maps, the Sabzevar serpentinite-hosted magnetite ores share significant similarities to analogous occurrences worldwide. Laser-ablation inductively-coupled mass spectrometry studies of magnetite from Sabzevar serpentinite-hosted magnetite ores and analogous occurrences in the Nain, Oman, and Cogne ophiolites reveal typical hydrothermal compositions. Magnetites from these serpentinite-hosted magnetite ore deposits formed at temperature  $<500$  °C which is consistent with serpentine stability field. Based on magnetite composition, the discriminant diagrams described in this thesis can be utilized to identify a new magnetite deposit type.

In addition to Fe, Cr and Al, I also investigated the transfer of Cu during ultramafic rocks alteration. Copper isotope signatures and thermodynamic calculations show that development of reaction zone in the Cheshmeh-Bid pyroxenite is triggered by Ca-metasomatism. In the reaction zone, native copper forms through desulfurization of chalcocite induced by an increase in  $H_2$  activity associated with serpentinization in the surrounding peridotites. The source for copper mineralization, as revealed by Cu isotopes, is probably mantle-like. Serpentinization and associated Ca-metasomatism most likely occurred in an intra-oceanic forearc setting during Albian.

To sum up, the strongly reducing conditions associated with serpentinization of oceanic peridotites are thought to be required for the production of native copper and magnetite deposits in serpentinites. Cr is largely immobile under these low-T/high- $H_2$  activity conditions, whereas Fe and Cu are the major elements that are transported to mineralization sites throughout the reaction. Desulfurization of initial Cu-sulfides or S-poor fluids during hydrothermal alteration could be the source of copper. The olivine breakdown and/or dissolution of nanoscale magnetite grains generated in the host serpentinite provide the iron required for magnetite ore production. Fluid/rock ratio, silicate/spinel ratio, oxygen fugacity, permeable zone, and initial composition of peridotites are all elements that influence the genesis of ore deposits in serpentinites. As a result, serpentinites in Tethyan ophiolites should be viewed as a prospective target for future exploration and extraction

## 8.2. Perspectives

The output of this Ph.D. thesis contribute to our understanding of RedOx evolution and mass transfer during serpentinization as well as their implications for mobility of Cu, Fe and Cr through serpentinization reactions. The findings of the thesis also highlight unresolved

questions that merit further investigation. Sparsity of mineralogical, geochemical and structural data in similar occurrences worldwide made it difficult to accurately constrain the genesis of serpentinite-hosted ore mineralization. Global production of iron and copper is principally derived from porphyry, sediment-hosted copper, iron-oxide copper gold deposits, skarn and volcanogenic massive sulfide (VMS) deposits but serpentinite-hosted ore deposits are less known. The results of this PhD will contribute significantly to the knowledge about favorable and optimum conditions for the formation of iron and copper at ore levels in serpentinitized peridotites of Tethyan ophiolites which help to assess serpentinites as a promising target for a future exploration and exploitation.

Particularly, the interplay between chemical reactions, deformation, fluid pathways, and the role of oxygen and sulfur fugacities for the transfer of Fe, Cu and Cr through hydrothermal alteration of peridotites remain subjects to future investigations. In addition to geological, mineralogical and geochemical investigation on the serpentinite-hosted magnetite ore occurrences, magnetic anomaly map surveying can allow to determine the amount of magnetite at the meter scale and to track iron mobility up to a hundred of meters scale. Moreover, magnetic properties of spinel alteration products are still poorly understood. Magnetic susceptibility measurements coupled with mineral chemistry of spinel alteration products and exploring magnetic signatures may help to better understand the processes from which they form and reconstruct the alteration history associated with formation of magnetite in serpentinite. Among the investigated serpentinite-hosted magnetite deposits, Aniba area in the Oman ophiolite will be a suitable asset for magnetic measurements because magnetite orebody is least disturbed by faulting and its dimensions can be easily estimated. On the other hand, extent of serpentinitization is decreasing away from main magnetite ore body resulted in a clear zonation which helps to track systematically iron mobility.

As it is mentioned earlier, the Sabzevar magnetite ores and similar occurrences worldwide are limited to shear zones. These deformation zones provide high-permeability pathways for fluid circulation and mineral precipitation. In order to evaluate the role of deformation in spinel alteration as well as magnetite formation in ophiolitic nappes, macroscopic-, mesoscopic-, and microscopic-scale analyses of a wide-spectrum of ductile and brittle deformation structures must be carried out. In addition, understanding the timing of deformation with respect to serpentinite/magnetite ore chemical interaction will provide valuable information on the role of deformation in spinel alteration and magnetite ore formation.

As previously stated, serpentinitization of peridotites from the oceanic lithosphere can occur in a variety of geodynamic environments, ranging from the ridge axis to both passive and active continental margins. Understanding the relationship between tectonic setting of

serpentinization and metallogeny of ophiolitic peridotites will improve our understanding for formation of metals in these rock types. The timing of magnetite formation is still a subject of debate and could possibly be resolved by magnetite (U-Th-Sm)/He dating method. This method provides geochronological constraints on serpentinization episodes.

Geochemistry of trace elements in serpentinite-hosted magnetites provides a useful tool to help understand the processes that control partitioning of these elements in magnetite as well as its genesis. In the Chapter 5 of this thesis, a new field for this style of mineralization has been proposed in discriminant diagrams. Trace element analyses of magnetite from similar serpentinite-hosted magnetite ores by laser-ablation inductively-coupled mass spectrometry is useful tool to constrain their single or composite origin. Composite origin for the Oman serpentinite-hosted magnetite ores revealed by trace element composition show two different generation of magnetite grains in these ore samples. The textural relationship between these two generations must be taken into further investigation.

Mass balance calculations is missing in chapter 7 as Cu isotope were not measured in different potential places including basaltic lavas, host peridotites and overlying sedimentary sequences that constrain the sources of Cu and processes that produced native copper. Therefore, understanding copper isotope composition of all existing lithologies in the Cheshmeh-Bid ophiolitic massif may provide more insights into the fluid provenance and potential sources of copper.

# *Part V*

## Chapter 9.

### 1. Supplementary Tables

Table 4.S1. Representative analyses of spinels from the Sabzevar host serpentinite

Sample No.	MG17															
Analysis No.	A-01	A-02	A-03	A-04	CH-2	CH-3	CH-4	CH-5	CH-6	CH-7	CH-8	CH-9	CH-10	CH-11	CH-12	CH-13
	P. Chr			P. Chr			P. Chr		P. Chr		P. Chr		P. Chr			
	Chr-III		Chr-II	Chr-III		Chr-III	Chr-II									
SiO <sub>2</sub>	0.01	0	0	0.01	0.02	0.02	0.01	0.02	0.15	0.01	0.16	0.03	0.01	0	0.01	0.01
TiO <sub>2</sub>	0.17	0.09	0.13	0.1	0.11	0.12	0.08	0.13	0.17	0.11	0.01	0.1	0.04	0.11	0.03	0.12
V <sub>2</sub> O <sub>3</sub>	0.14	0.08	0.3	0.28	0.3	0.12	0.08	0.2	0.21	0.29	0.01	0.24	0.04	0.29	0.05	0.23
Al <sub>2</sub> O <sub>3</sub>	0.17	0.03	1.66	1.77	1.85	0.13	0.04	0.07	4.39	2.02	0.02	2.33	0.05	1.39	0.07	8.71
Cr <sub>2</sub> O <sub>3</sub>	12.18	15.86	62.56	63.16	61.93	10.04	15.51	10.83	53.83	63.48	0.93	51.5	8.74	62.8	9.47	48.48
FeO*	79.51	77.1	29.5	27.96	28.67	82.08	77.55	81.46	34.88	27.95	90.37	38.45	83.16	29.11	83.67	34.93
MnO	0.13	0.67	0.28	0.29	0.27	0.07	0.66	0.1	0.32	0.29	0.11	0.23	0.1	0.27	0.46	0.27
MgO	1.4	1.08	4.82	4.81	5.18	1.33	1.07	1.24	4.77	5.04	0.46	4.74	1.08	4.8	0.7	6.15
ZnO	0.01	0.02	0.09	0.09	0.09	0	0.03	0.01	0.11	0.09	0.02	0.08	0.02	0.08	0.02	0.1
CoO	0.03	0.07	0.1	0.1	0.1	0.02	0.05	0.03	0.1	0.1	0.04	0.09	0.04	0.1	0.04	0.09
NiO	1.16	0.43	0.05	0.02	0.03	1.14	0.4	1.14	0.05	0.03	0.09	0.26	0.58	0.04	0.09	0.15
Total	94.91	95.43	99.5	98.58	98.55	95.08	95.48	95.22	98.96	99.41	92.22	98.06	93.85	98.99	94.6	99.24
Si	0.000	0.000	0.000	0.000	0.001	0.001	0.000	0.001	0.005	0.000	0.006	0.001	0.000	0.000	0.000	0.000
Ti	0.005	0.003	0.003	0.003	0.003	0.003	0.002	0.004	0.005	0.003	0.000	0.003	0.001	0.003	0.001	0.003
V	0.004	0.002	0.009	0.008	0.009	0.004	0.002	0.006	0.006	0.008	0.000	0.007	0.001	0.008	0.002	0.006
Al	0.008	0.001	0.070	0.075	0.078	0.006	0.002	0.003	0.183	0.085	0.001	0.099	0.002	0.059	0.003	0.351
Cr	0.362	0.471	1.766	1.799	1.757	0.298	0.461	0.321	1.503	1.788	0.028	1.463	0.263	1.784	0.284	1.310

Fe2+	0.886	0.905	0.732	0.730	0.712	0.892	0.907	0.896	0.742	0.721	0.972	0.731	0.917	0.732	0.942	0.673
Fe3+	1.616	1.520	0.149	0.112	0.148	1.684	1.530	1.661	0.288	0.112	1.957	0.424	1.730	0.143	1.709	0.326
Mn	0.004	0.021	0.008	0.009	0.008	0.002	0.021	0.003	0.010	0.009	0.004	0.007	0.003	0.008	0.015	0.008
Mg	0.079	0.061	0.257	0.258	0.277	0.074	0.060	0.069	0.251	0.268	0.027	0.254	0.061	0.257	0.040	0.313
Zn	0.000	0.001	0.002	0.002	0.002	0.000	0.001	0.000	0.003	0.002	0.001	0.002	0.001	0.002	0.001	0.003
Co	0.001	0.002	0.003	0.003	0.003	0.001	0.002	0.001	0.003	0.003	0.001	0.003	0.001	0.003	0.001	0.002
Ni	0.035	0.013	0.001	0.001	0.001	0.034	0.012	0.034	0.001	0.001	0.003	0.008	0.018	0.001	0.003	0.004
Scat	3.000	3.000	3.000	3.000	3.000	3.000	3.000	3.000	3.000	3.000	3.000	3.000	3.000	3.000	3.000	3.000
Sox	4.000	4.000	4.000	4.000	4.000	4.000	4.000	4.000	4.000	4.000	4.000	4.000	4.000	4.000	4.000	4.000
Mg#	0.08	0.06	0.26	0.26	0.28	0.08	0.06	0.07	0.25	0.27	0.03	0.26	0.06	0.26	0.04	0.32
Cr#	0.98	1.00	0.96	0.96	0.96	0.98	1.00	0.99	0.89	0.95	0.97	0.94	0.99	0.97	0.99	0.79
Fe3+/(Fe3++Fe2+)	0.65	0.63	0.17	0.13	0.17	0.65	0.63	0.65	0.28	0.13	0.67	0.37	0.65	0.16	0.64	0.33
Fe3+/(Fe3++Al+Cr)	0.81	0.76	0.08	0.06	0.07	0.85	0.77	0.84	0.15	0.06	0.99	0.21	0.87	0.07	0.86	0.16
Sum	1.985	1.992	1.984	1.986	1.984	1.988	1.992	1.985	1.974	1.985	1.987	1.986	1.996	1.986	1.996	1.987
Al	0.380	0.067	3.519	3.784	3.944	0.289	0.089	0.156	9.256	4.273	0.046	4.968	0.112	2.964	0.157	17.662
Cr	18.248	23.664	88.976	90.569	88.575	14.987	23.127	16.188	76.135	90.079	1.434	73.659	13.182	89.828	14.214	65.949
Fe3+	81.373	76.270	7.505	5.647	7.481	84.723	76.784	83.656	14.609	5.648	98.520	21.373	86.706	7.208	85.630	16.389

Table 4.S1 (Continued)

MG21				MG20										
CH-14	CH-15	CH-16	CH-17	CH-18	CH-19	CH-20	CH-21	CH-22	CH-24	CH-25	CH-26	CH-27	CH-28	
P. Chr		P. Chr		P. Chr		Partly altered chromite			Partly altered chromite			Partly altered chromite		
Chr-II	Chr-III	Chr-II		Chr-II	Chr-III	Chr-I	Chr-III	Chr-II	Chr-I	Chr-III	Chr-II	Chr-I	Chr-II	
						Core	Porous rim		Core	Porous rim		Core	Porous rim	
0.03	0.03	0.01	0.01	0.01	0.02	0.02	0.08	0.02	0.02	0.01	0.03	0.02	0.03	
0.1	0.01	0.1	0.09	0.11	0.1	0.05	0.01	0.04	0.05	0.04	0.11	0.05	0.05	
0.29	0.03	0.3	0.29	0.3	0.11	0.21	0.04	0.24	0.22	0.14	0.3	0.22	0.23	
7.83	0.26	6.71	7.36	1.89	0.03	22.01	0.21	9.72	21.74	2.41	6.1	20.23	10.73	
49.63	6.08	49.15	48.25	62.69	15.97	47.39	8.33	55.46	47.67	36.99	54.35	48.28	53.16	
33.22	88.53	35.18	35.39	27.79	76.74	16.7	85.34	25.57	17.77	53.04	29.74	18	26.85	
0.23	0.1	0.28	0.28	0.32	0.17	0.15	0.25	0.23	0.16	1.36	0.23	0.15	0.22	
7.23	0.28	6.82	7.21	6.16	1.17	13.42	0.15	8.02	13.04	1.09	7.88	12.93	8.68	
0.07	0	0.1	0.09	0.12	0.01	0.13	0.01	0.1	0.15	0.23	0.09	0.14	0.1	
0.07	0.01	0.06	0.06	0.09	0.03	0.07	0	0.08	0.07	0.13	0.06	0.06	0.08	
0.13	0.01	0.15	0.17	0.05	1.09	0.05	0.02	0.04	0.04	0.1	0.08	0.06	0.06	
98.84	95.35	98.85	99.19	99.53	95.44	100.19	94.44	99.51	100.91	95.54	98.97	100.13	100.18	
0.001	0.001	0.000	0.000	0.000	0.001	0.001	0.003	0.001	0.001	0.000	0.001	0.001	0.001	
0.003	0.000	0.003	0.002	0.003	0.003	0.001	0.000	0.001	0.001	0.001	0.003	0.001	0.001	
0.008	0.001	0.008	0.008	0.008	0.003	0.005	0.001	0.006	0.005	0.004	0.008	0.005	0.006	
0.315	0.012	0.272	0.296	0.079	0.001	0.795	0.009	0.385	0.783	0.107	0.246	0.738	0.418	
1.341	0.181	1.337	1.301	1.749	0.475	1.148	0.251	1.474	1.152	1.100	1.473	1.182	1.390	

0.621	0.982	0.636	0.619	0.663	0.898	0.379	0.986	0.588	0.398	0.884	0.588	0.395	0.562
0.328	1.804	0.376	0.390	0.158	1.514	0.049	1.732	0.131	0.057	0.785	0.264	0.071	0.181
0.007	0.003	0.008	0.008	0.010	0.005	0.004	0.008	0.007	0.004	0.043	0.007	0.004	0.006
0.368	0.016	0.350	0.367	0.324	0.066	0.613	0.009	0.402	0.594	0.061	0.403	0.597	0.428
0.002	0.000	0.003	0.002	0.003	0.000	0.003	0.000	0.002	0.003	0.006	0.002	0.003	0.002
0.002	0.000	0.002	0.002	0.003	0.001	0.002	0.000	0.002	0.002	0.004	0.002	0.001	0.002
0.004	0.000	0.004	0.005	0.001	0.033	0.001	0.001	0.001	0.001	0.003	0.002	0.001	0.002
3.000	3.000	3.000	3.000	3.000	3.000	3.000	3.000	3.000	3.000	3.000	3.000	3.000	3.000
4.000	4.000	4.000	4.000	4.000	4.000	4.000	4.000	4.000	4.000	4.000	4.000	4.000	4.000
0.37	0.02	0.35	0.37	0.33	0.07	0.62	0.01	0.41	0.60	0.06	0.41	0.60	0.43
0.81	0.94	0.83	0.81	0.96	1.00	0.59	0.96	0.79	0.60	0.91	0.86	0.62	0.77
0.35	0.65	0.37	0.39	0.19	0.63	0.11	0.64	0.18	0.12	0.47	0.31	0.15	0.24
0.17	0.90	0.19	0.20	0.08	0.76	0.02	0.87	0.07	0.03	0.39	0.13	0.04	0.09
1.985	1.996	1.986	1.987	1.985	1.990	1.991	1.992	1.990	1.991	1.993	1.984	1.991	1.989
15.891	0.578	13.706	14.889	3.960	0.067	39.907	0.473	19.348	39.320	5.363	12.423	37.073	21.026
67.567	9.060	67.349	65.481	88.105	23.852	57.641	12.588	74.055	57.837	55.221	74.250	59.353	69.880
16.542	90.363	18.945	19.630	7.936	76.082	2.452	86.938	6.597	2.843	39.416	13.328	3.574	9.094

Table 4.S2. Representative analyses of spinels from the Sabzevar magnetite ore. Homogeneous Cr-spinel relict (grain B) from the sample MG15 were selected for TEM.

Sample No. Analysis No.	MG05														MG15															
	chr-1a		mgt-1a		chr-1b		mgt-1b		chr-2a		mgt-2a		chr-3a		mgt-3a		chr-3b		mgt-3b		chr-4a		mgt-4a		chr-4b		mgt-4b		B-1-11-1	B-1-11-2
	Core	Rim	Core	Rim	Core	Rim	Core	Rim	Core	Rim	Core	Rim	Core	Rim	Core	Rim	Core	Rim	Core	Rim	Core	Rim	Core	Rim	Core	Rim	Core	Rim		
	P. Chr	Mgt -II	P. Chr	Mgt-II	P. Chr	Mgt-II	P. Chr	Mgt-I	P. Chr	Mgt-II	P. Chr	Mgt-II	P. Chr	Mgt-II	P. Chr	Mgt-I	P. Chr	Mgt-I	H. Chr											
SiO <sub>2</sub>	0.04	1.79	0.01	1.9	0.01	1.81	0.02	1.32	0.02	2.09	0.02	1.92	0.02	1.21	0.04	0.01														
TiO <sub>2</sub>	0.35	0	0.24	0	0.47	0	0.25	0	0.23	0	0.22	0.01	0.24	0	0.11	0.1														
V <sub>2</sub> O <sub>3</sub>	0.33	0	0.27	0	0.33	0	0.33	0	0.32	0	0.29	0.01	0.31	0	0.16	0.15														
Al <sub>2</sub> O <sub>3</sub>	4.32	0.03	4.44	0.03	4.26	0.04	3.84	0.03	4.99	0.02	4.51	0.02	4.43	0	7.04	7.84														
Cr <sub>2</sub> O <sub>3</sub>	52.86	0.36	50.94	0.18	49.25	0.48	54.52	0.21	53.78	0.03	52.58	1.37	51.89	0.16	59.79	60.96														
FeO*	34.67	90.58	36.82	90.43	38.34	90.39	34.52	91.04	34.14	90.56	34.82	90.05	35.97	90.94	24.59	21.88														
MnO	0.27	0	0.27	0.02	0.28	0.01	0.26	0.02	0.27	0.02	0.25	0.02	0.26	0.02	0.22	0.21														
MgO	5.61	0.08	5.5	0.09	5.51	0.07	5.43	0.08	5.61	0.1	5.92	0.09	5.86	0.08	7.67	8.79														
ZnO	0.09	0	0.08	0	0.07	0	0.07	0	0.07	0	0.09	0	0.07	0	0.1	0.11														
CoO	0.07	0	0.08	0	0.07	0	0.08	0	0.08	0.01	0.07	0	0.07	0.01	0.08	0.07														
NiO	0.11	0	0.14	0	0.17	0	0.08	0	0.09	0	0.13	0	0.14	0.02	0.02	0.02														
Total	98.72	92.83	98.79	92.65	98.77	92.8	99.4	92.7	99.6	92.84	98.9	93.49	99.24	92.43	99.82	100.14														
Si	0.001	0.069	0.000	0.073	0.000	0.070	0.001	0.051	0.001	0.080	0.001	0.073	0.001	0.047	0.001	0.000														
Ti	0.009	0.000	0.006	0.000	0.012	0.000	0.007	0.000	0.006	0.000	0.006	0.000	0.006	0.000	0.003	0.003														
V	0.009	0.000	0.008	0.000	0.009	0.000	0.009	0.000	0.009	0.000	0.008	0.000	0.009	0.000	0.004	0.004														
Al	0.179	0.001	0.184	0.001	0.176	0.002	0.159	0.001	0.205	0.001	0.186	0.001	0.182	0.000	0.282	0.310														
Cr	1.471	0.011	1.415	0.005	1.369	0.015	1.513	0.006	1.480	0.001	1.455	0.041	1.432	0.005	1.609	1.618														

Fe <sup>2+</sup>	0.701	1.064	0.702	1.067	0.707	1.065	0.709	1.046	0.701	1.074	0.682	1.068	0.687	1.041	0.603	0.552
Fe <sup>3+</sup>	0.320	1.850	0.380	1.847	0.420	1.844	0.304	1.890	0.293	1.838	0.337	1.810	0.363	1.901	0.096	0.062
Mn	0.008	0.000	0.008	0.001	0.008	0.000	0.008	0.001	0.008	0.001	0.007	0.001	0.008	0.001	0.006	0.006
Mg	0.294	0.005	0.288	0.005	0.289	0.004	0.284	0.005	0.291	0.006	0.309	0.005	0.305	0.005	0.389	0.440
Zn	0.002	0.000	0.002	0.000	0.002	0.000	0.002	0.000	0.002	0.000	0.002	0.000	0.002	0.000	0.003	0.003
Co	0.002	0.000	0.002	0.000	0.002	0.000	0.002	0.000	0.002	0.000	0.002	0.000	0.002	0.000	0.002	0.002
Ni	0.003	0.000	0.004	0.000	0.005	0.000	0.002	0.000	0.003	0.000	0.004	0.000	0.004	0.001	0.001	0.001
Scat	3.000	3.000	3.000	3.000	3.000	3.000	3.000	3.000	3.000	3.000	3.000	3.000	3.000	3.000	3.000	3.000
Sox	4.000	4.000	4.000	4.000	4.000	4.000	4.000	4.000	4.000	4.000	4.000	4.000	4.000	4.000	4.000	4.000
Mg#	0.30	0.00	0.29	0.00	0.29	0.00	0.29	0.00	0.29	0.01	0.31	0.00	0.31	0.00	0.39	0.44
Cr#	0.89	0.89	0.89	0.80	0.89	0.89	0.90	0.82	0.88	0.50	0.89	0.98	0.89	1.00	0.85	0.84
Fe <sup>3+</sup> /(Fe <sup>3+</sup> +Fe <sup>2+</sup> )	0.31	0.63	0.35	0.63	0.37	0.63	0.30	0.64	0.29	0.63	0.33	0.63	0.35	0.65	0.14	0.10
Fe <sup>3+</sup> /(Fe <sup>3+</sup> +Al+Cr)	0.16	0.99	0.19	1.00	0.21	0.99	0.15	1.00	0.15	1.00	0.17	0.98	0.18	1.00	0.05	0.03
Sum	1.969	1.862	1.979	1.854	1.965	1.861	1.976	1.898	1.978	1.839	1.979	1.852	1.977	1.906	1.987	1.990
Al	9.098	0.073	9.292	0.073	8.980	0.098	8.039	0.072	10.352	0.049	9.404	0.049	9.216	0.000	14.207	15.583
Cr	74.678	0.588	71.513	0.296	69.647	0.785	76.564	0.337	74.841	0.050	73.546	2.234	72.413	0.257	80.944	81.283
Fe3+	16.224	99.339	19.196	99.631	21.373	99.117	15.398	99.591	14.808	99.901	17.050	97.717	18.371	99.743	4.849	3.133

Table 4.S2 (Continued)

Sample No.	MG15																
Analysis No.	B-1-11-3	B-1-11-4	B-1-11-5	B-1-11-6	B-1-11-7	B-1-11-8	B-1-11-9	B-1-11-10	B-1-11-11	B-1-11-12	B-1-11-13	B-1-11-14	B-1-11-15	B-M-L1-1	B-M-L1-2	B-M-L1-3	
	Core													Rim			
	H. Chr													Mgt-II	Mgt-I	Mgt-I	
SiO <sub>2</sub>	0.02	0.02	0.02	0.02	0.02	0.02	0.02	0.02	0.02	0.02	0.02	0.02	0.02	0.56	1.89	1.46	1.5
TiO <sub>2</sub>	0.1	0.1	0.09	0.09	0.09	0.09	0.09	0.09	0.09	0.09	0.09	0.09	0.09	0.53	0.02	0.01	0
V <sub>2</sub> O <sub>3</sub>	0.15	0.16	0.15	0.15	0.16	0.16	0.15	0.15	0.15	0.15	0.15	0.15	0.09	0.01	0	0	
Al <sub>2</sub> O <sub>3</sub>	7.89	7.87	7.94	7.82	7.93	7.92	7.94	7.95	8.02	7.99	7.94	7.67	2.05	0.01	0.01	0	
Cr <sub>2</sub> O <sub>3</sub>	61.35	61.46	61.51	61.56	61.7	61.63	61.71	61.93	61.76	61.55	61.21	60.38	22.1	1.62	0.65	0.43	
FeO*	20.56	20.11	19.9	19.95	19.92	19.79	19.69	19.55	19.69	20.02	20.82	22.74	68.08	90.06	90.98	90.3	
MnO	0.2	0.2	0.2	0.21	0.19	0.2	0.21	0.2	0.2	0.2	0.2	0.21	0.18	0.03	0.02	0.03	
MgO	9.53	9.82	9.9	9.91	9.95	9.97	10.13	10.03	10.11	9.94	9.34	8.29	1.49	0.09	0.07	0.08	
ZnO	0.09	0.11	0.11	0.11	0.1	0.11	0.1	0.1	0.09	0.1	0.1	0.1	0.04	0.01	0	0	
CoO	0.07	0.06	0.07	0.06	0.06	0.07	0.07	0.06	0.06	0.06	0.07	0.07	0.05	0.01	0.01	0.01	
NiO	0.02	0.04	0.04	0.03	0.02	0.04	0.02	0.03	0.03	0.04	0.04	0.02	0.01	0.01	0	0.01	
Total	99.98	99.94	99.94	99.91	100.14	99.98	100.13	100.12	100.23	100.16	99.98	99.75	95.17	93.75	93.2	92.37	
Si	0.001	0.001	0.001	0.001	0.001	0.001	0.001	0.001	0.001	0.001	0.001	0.001	0.021	0.072	0.056	0.058	
Ti	0.003	0.003	0.002	0.002	0.002	0.002	0.002	0.002	0.002	0.002	0.002	0.002	0.015	0.001	0.000	0.000	
V	0.004	0.004	0.004	0.004	0.004	0.004	0.004	0.004	0.004	0.004	0.004	0.004	0.003	0.000	0.000	0.000	
Al	0.311	0.310	0.312	0.308	0.311	0.311	0.311	0.312	0.314	0.313	0.313	0.306	0.090	0.000	0.000	0.000	
Cr	1.622	1.622	1.622	1.624	1.624	1.624	1.622	1.629	1.622	1.619	1.620	1.615	0.653	0.049	0.020	0.013	

Fe <sup>2+</sup>	0.518	0.503	0.499	0.499	0.499	0.496	0.490	0.495	0.492	0.499	0.526	0.574	0.944	1.066	1.051	1.052
Fe <sup>3+</sup>	0.057	0.058	0.056	0.058	0.055	0.055	0.057	0.049	0.055	0.058	0.057	0.069	1.183	1.805	1.867	1.871
Mn	0.006	0.006	0.006	0.006	0.005	0.006	0.006	0.006	0.006	0.006	0.006	0.006	0.006	0.001	0.001	0.001
Mg	0.475	0.489	0.492	0.493	0.494	0.495	0.502	0.498	0.501	0.493	0.466	0.418	0.083	0.005	0.004	0.005
Zn	0.002	0.003	0.003	0.003	0.002	0.003	0.002	0.002	0.002	0.002	0.002	0.002	0.001	0.000	0.000	0.000
Co	0.002	0.002	0.002	0.002	0.002	0.002	0.002	0.002	0.002	0.002	0.002	0.002	0.001	0.000	0.000	0.000
Ni	0.001	0.001	0.001	0.001	0.001	0.001	0.001	0.001	0.001	0.001	0.001	0.001	0.000	0.000	0.000	0.000
Scat	3.000	3.000	3.000	3.000	3.000	3.000	3.000	3.000	3.000	3.000	3.000	3.000	3.000	3.000	3.000	3.000
Sox	4.000	4.000	4.000	4.000	4.000	4.000	4.000	4.000	4.000	4.000	4.000	4.000	4.000	4.000	4.000	4.000
Mg#	0.48	0.49	0.50	0.50	0.50	0.50	0.51	0.50	0.50	0.50	0.47	0.42	0.08	0.00	0.00	0.00
Cr#	0.84	0.84	0.84	0.84	0.84	0.84	0.84	0.84	0.84	0.84	0.84	0.84	0.88	0.99	0.98	1.00
Fe <sup>3+</sup> /(Fe <sup>3+</sup> +Fe <sup>2+</sup> )	0.10	0.10	0.10	0.10	0.10	0.10	0.10	0.09	0.10	0.10	0.10	0.11	0.56	0.63	0.64	0.64
Fe <sup>3+</sup> /(Fe <sup>3+</sup> +Al+Cr)	0.03	0.03	0.03	0.03	0.03	0.03	0.03	0.02	0.03	0.03	0.03	0.03	0.61	0.97	0.99	0.99
Sum	1.990	1.989	1.990	1.990	1.990	1.990	1.990	1.990	1.990	1.990	1.990	1.990	1.926	1.854	1.887	1.884
Al	15.626	15.562	15.684	15.456	15.632	15.631	15.630	15.665	15.772	15.742	15.739	15.366	4.687	0.024	0.024	0.000
Cr	81.507	81.527	81.509	81.623	81.591	81.595	81.491	81.863	81.477	81.348	81.393	81.146	33.895	2.632	1.044	0.698
Fe3+	2.867	2.911	2.807	2.921	2.777	2.774	2.879	2.472	2.751	2.910	2.868	3.488	61.419	97.343	98.932	99.302

Table 4.S2 (Continued)

Sample No.	MG15															
Analysis No.	B-M-L1-5	B-M-L2-1	B-M-L2-4	B-M-L2-5	B-M-L2-6	B-M-L2-7	B-M-L2-8	B-16-a-2	B-M-2	B-16-a-3	B-M-3	B-16-a-4	B-M-4	A-L1-1	A-L1-2	A-L1-3
								Core	Rim	Core	Rim	Core	Rim			
	Mgt-II	Mgt-I	Mgt-II	Mgt-II	Mgt-II	Mgt-II	Mgt-II	H. Chr	Mgt-I	H. Chr	Mgt-II	H. Chr	Mgt-II			P. Chr
SiO <sub>2</sub>	2.26	0.88	1.85	2.03	2.16	2.35	2.34	0.02	1.05	0.02	2.05	0.02	2.15	0.36	0.03	0.01
TiO <sub>2</sub>	0	1.33	0.03	0.01	0.01	0.01	0	0.11	0.77	0.11	0.01	0.11	0	0.2	0.41	0.44
V <sub>2</sub> O <sub>3</sub>	0	0	0	0	0	0	0	0.14	0	0.15	0	0.15	0	0.2	0.34	0.32
Al <sub>2</sub> O <sub>3</sub>	0.01	0.02	0.02	0.02	0.01	0.01	0	7.58	0.04	7.56	0.01	7.47	0	5.23	4.11	3.99
Cr <sub>2</sub> O <sub>3</sub>	0.22	3.4	0.59	0.39	0.29	0.2	0.15	59.7	2.7	59.85	0.69	59.8	0.3	57.24	56.12	56.2
FeO*	89.91	89.11	90.48	90.29	90.43	90.21	90.32	24.12	89.69	23.94	90.37	24.37	90.21	28.85	31.22	31.38
MnO	0.02	0.04	0.01	0.01	0.02	0.01	0.02	0.21	0.01	0.21	0.02	0.21	0.02	0.22	0.22	0.24
MgO	0.12	0.09	0.06	0.08	0.09	0.1	0.11	7.8	0.08	7.78	0.07	7.73	0.09	6.9	6.35	6.23
ZnO	0	0	0	0	0	0	0	0.12	0.01	0.11	0	0.11	0	0.08	0.08	0.1
CoO	0.01	0	0.01	0.01	0.01	0	0	0.08	0	0.07	0.01	0.09	0.01	0.08	0.07	0.08
NiO	0.01	0.01	0	0	0.01	0	0	0.02	0.01	0.02	0	0.03	0.02	0.04	0.08	0.1
Total	92.56	94.89	93.06	92.84	93.02	92.88	92.94	99.89	94.37	99.83	93.23	100.09	92.8	99.39	99.03	99.07
Si	0.087	0.033	0.071	0.078	0.083	0.090	0.090	0.001	0.040	0.001	0.079	0.001	0.083	0.012	0.001	0.000
Ti	0.000	0.038	0.001	0.000	0.000	0.000	0.000	0.003	0.022	0.003	0.000	0.003	0.000	0.005	0.011	0.012
V	0.000	0.000	0.000	0.000	0.000	0.000	0.000	0.004	0.000	0.004	0.000	0.004	0.000	0.006	0.010	0.009
Al	0.000	0.001	0.001	0.001	0.000	0.000	0.000	0.303	0.002	0.302	0.000	0.298	0.000	0.213	0.169	0.165

Cr	0.007	0.102	0.018	0.012	0.009	0.006	0.005	1.600	0.081	1.606	0.021	1.601	0.009	1.563	1.552	1.556
Fe <sup>2+</sup>	1.079	1.064	1.068	1.073	1.077	1.084	1.083	0.598	1.056	0.599	1.074	0.601	1.076	0.650	0.668	0.672
Fe <sup>3+</sup>	1.819	1.755	1.837	1.831	1.824	1.812	1.816	0.086	1.793	0.081	1.821	0.089	1.826	0.183	0.245	0.247
Mn	0.001	0.001	0.000	0.000	0.001	0.000	0.001	0.006	0.000	0.006	0.001	0.006	0.001	0.006	0.007	0.007
Mg	0.007	0.005	0.003	0.005	0.005	0.006	0.006	0.394	0.005	0.394	0.004	0.390	0.005	0.355	0.331	0.325
Zn	0.000	0.000	0.000	0.000	0.000	0.000	0.000	0.003	0.000	0.003	0.000	0.003	0.000	0.002	0.002	0.003
Co	0.000	0.000	0.000	0.000	0.000	0.000	0.000	0.002	0.000	0.002	0.000	0.002	0.000	0.002	0.002	0.002
Ni	0.000	0.000	0.000	0.000	0.000	0.000	0.000	0.001	0.000	0.001	0.000	0.001	0.001	0.001	0.002	0.003
Scat	3.000	3.000	3.000	3.000	3.000	3.000	3.000	3.000	3.000	3.000	3.000	3.000	3.000	3.000	3.000	3.000
Sox	4.000	4.000	4.000	4.000	4.000	4.000	4.000	4.000	4.000	4.000	4.000	4.000	4.000	4.000	4.000	4.000
Mg#	0.01	0.00	0.00	0.00	0.00	0.01	0.01	0.40	0.00	0.40	0.00	0.39	0.00	0.35	0.33	0.33
Cr#	0.94	0.99	0.95	0.93	0.95	0.93	1.00	0.84	0.98	0.84	0.98	0.84	1.00	0.88	0.90	0.90
Fe <sup>3+</sup> /(Fe <sup>3+</sup> +Fe <sup>2+</sup> )	0.63	0.62	0.63	0.63	0.63	0.63	0.63	0.13	0.63	0.12	0.63	0.13	0.63	0.22	0.27	0.27
Fe <sup>3+</sup> /(Fe <sup>3+</sup> +Al+Cr)	1.00	0.94	0.99	0.99	0.99	1.00	1.00	0.04	0.96	0.04	0.99	0.04	1.00	0.09	0.12	0.13
Sum	1.826	1.858	1.856	1.843	1.834	1.819	1.820	1.989	1.876	1.989	1.842	1.989	1.835	1.959	1.967	1.967
Al	0.025	0.048	0.049	0.049	0.025	0.025	0.000	15.224	0.095	15.202	0.025	14.993	0.000	10.868	8.615	8.369
Cr	0.367	5.474	0.965	0.643	0.480	0.334	0.250	80.436	4.322	80.734	1.134	80.517	0.497	79.791	78.908	79.081
Fe3+	99.608	94.477	98.986	99.308	99.496	99.641	99.750	4.340	95.582	4.064	98.841	4.490	99.503	9.341	12.477	12.549

Table 4.S2 (Continued)

Sample No.	MG15												
Analysis No.	A-L1-4	A-L1-5	A-L1-6	A-L1-7	A-L1-8	A-L1-9	A-L1-10	A-M-L1-1	A-M-L1-2	A-M-L1-3	A-M-L1-4	A-M-L1-5	A-M-L1-6
	Core							Rim					
	Pchr							Mgt-I	Mgt-II	Mgt-I	Mgt-II	Mgt-II	Mgt-II
SiO <sub>2</sub>	0.03	0.01	0.01	0.02	0.01	0.01	0.05	0.96	1.71	1.47	2.15	2.21	1.65
TiO <sub>2</sub>	0.51	0.63	0.49	0.23	0.2	0.17	0.19	1.07	0.47	0.08	0	0	0
V <sub>2</sub> O <sub>3</sub>	0.33	0.32	0.29	0.2	0.2	0.32	0.23	0.01	0	0	0	0	0
Al <sub>2</sub> O <sub>3</sub>	4.05	2.94	3.05	5.46	7.61	4.51	7.1	0.08	0.05	0.05	0.04	0.03	0.03
Cr <sub>2</sub> O <sub>3</sub>	54.48	54.2	55.41	56.88	53.49	61.28	54.32	3.69	1.17	0.62	0.33	0.2	0.16
FeO*	32.46	34.2	33.3	29.85	29.66	26.17	29.7	89.06	89.97	90.71	90.35	90.15	90.51
MnO	0.24	0.25	0.25	0.24	0.21	0.23	0.22	0.04	0.01	0.02	0	0.01	0.02
MgO	6.27	5.97	5.95	6.51	7.16	6.66	7.03	0.11	0.07	0.06	0.07	0.1	0.08
ZnO	0.07	0.07	0.07	0.09	0.1	0.09	0.09	0	0	0.01	0	0	0.02
CoO	0.07	0.07	0.07	0.07	0.07	0.09	0.09	0	0	0.01	0.01	0.02	0.02
NiO	0.11	0.12	0.12	0.06	0.07	0.03	0.05	0	0	0.01	0	0.01	0
Total	98.61	98.79	99.02	99.6	98.79	99.56	99.05	95.03	93.45	93.03	92.95	92.73	92.48
Si	0.001	0.000	0.000	0.001	0.000	0.000	0.002	0.036	0.065	0.056	0.083	0.085	0.064
Ti	0.013	0.017	0.013	0.006	0.005	0.004	0.005	0.030	0.014	0.002	0.000	0.000	0.000
V	0.009	0.009	0.008	0.006	0.006	0.009	0.006	0.000	0.000	0.000	0.000	0.000	0.000
Al	0.168	0.122	0.127	0.222	0.308	0.185	0.287	0.004	0.002	0.002	0.002	0.001	0.001
Cr	1.513	1.513	1.543	1.554	1.451	1.684	1.475	0.110	0.035	0.019	0.010	0.006	0.005

Fe <sup>2+</sup>	0.672	0.688	0.686	0.658	0.627	0.647	0.634	1.059	1.075	1.054	1.078	1.078	1.057
Fe <sup>3+</sup>	0.281	0.322	0.295	0.205	0.225	0.113	0.219	1.753	1.804	1.861	1.823	1.823	1.866
Mn	0.007	0.007	0.007	0.007	0.006	0.007	0.006	0.001	0.000	0.001	0.000	0.000	0.001
Mg	0.328	0.314	0.313	0.335	0.366	0.345	0.360	0.006	0.004	0.003	0.004	0.006	0.005
Zn	0.002	0.002	0.002	0.002	0.003	0.002	0.002	0.000	0.000	0.000	0.000	0.000	0.001
Co	0.002	0.002	0.002	0.002	0.002	0.003	0.002	0.000	0.000	0.000	0.000	0.001	0.001
Ni	0.003	0.003	0.003	0.002	0.002	0.001	0.001	0.000	0.000	0.000	0.000	0.000	0.000
Scat	3.000	3.000	3.000	3.000	3.000	3.000	3.000	3.000	3.000	3.000	3.000	3.000	3.000
Sox	4.000	4.000	4.000	4.000	4.000	4.000	4.000	4.000	4.000	4.000	4.000	4.000	4.000
Mg#	0.33	0.31	0.31	0.34	0.37	0.35	0.36	0.01	0.00	0.00	0.00	0.01	0.00
Cr#	0.90	0.93	0.92	0.87	0.83	0.90	0.84	0.97	0.94	0.89	0.85	0.82	0.78
Fe <sup>3+</sup> /(Fe <sup>3+</sup> +Fe <sup>2+</sup> )	0.29	0.32	0.30	0.24	0.26	0.15	0.26	0.62	0.63	0.64	0.63	0.63	0.64
Fe <sup>3+</sup> /(Fe <sup>3+</sup> +Al+Cr)	0.14	0.16	0.15	0.10	0.11	0.06	0.11	0.94	0.98	0.99	0.99	1.00	1.00
Sum	1.962	1.957	1.965	1.981	1.983	1.982	1.980	1.866	1.842	1.882	1.835	1.830	1.873
Al	8.546	6.251	6.445	11.226	15.517	9.321	14.507	0.191	0.122	0.120	0.099	0.074	0.073
Cr	77.116	77.312	78.541	78.451	73.164	84.964	74.455	5.901	1.921	1.001	0.546	0.332	0.261
Fe3+	14.338	16.437	15.015	10.323	11.320	5.714	11.038	93.908	97.956	98.879	99.355	99.593	99.666

Table. 4.S3. Representative analyses of sulfides and alloys in the Sabzevar magnetite ore and host serpentinite

Sample No.	MG01														
	Hzi		Pn												
Analysis No.	D_01	D_02	K_01	K_02	K_03	K_05	K_07	I_01	I_03	I_05	J_01	J_03	C_01	C_04	C_05
Fe	0.51	0.31	23.89	23.69	24.03	23.53	23.84	23.01	23.43	24.05	24.38	23.85	23.03	23.67	23.37
Ni	73.93	74.12	31.96	31.98	31.87	31.02	32.61	33.89	33.09	33.49	33.05	32.73	33.94	33.69	35.20
Co	0.22	0.12	11.91	11.91	10.97	12.53	11.17	10.14	10.45	9.97	9.98	10.19	10.28	10.01	8.80
Cu	0.00	0.01	0.01	0.03	0.03	0.00	0.03	0.00	0.00	0.00	0.00	0.03	0.01	0.00	0.01
Zn	0.04	0.02	0.00	0.01	0.02	0.00	0.02	0.00	0.00	0.00	0.00	0.00	0.00	0.02	0.00
S	27.16	27.57	33.27	33.13	33.28	33.30	33.21	33.27	33.23	33.51	33.33	33.11	33.22	33.43	33.33
Mn	0.00	0.02	0.01	0.01	0.00	0.00	0.01	0.00	0.00	0.01	0.00	0.02	0.01	0.00	0.02
As	0.07	0.00	0.05	0.04	0.09	0.14	0.06	0.07	0.12	0.05	0.03	0.05	0.00	0.01	0.08
Pb	0.08	0.00	0.02	0.14	0.10	0.05	0.25	0.08	0.14	0.19	0.11	0.01	0.02	0.11	0.04
Sb	0.01	0.00	0.00	0.00	0.03	0.00	0.01	0.02	0.00	0.00	0.00	0.02	0.00	0.00	0.01
Total	102.02	102.16	101.12	100.94	100.42	100.57	101.20	100.48	100.45	101.28	100.88	100.01	100.49	100.93	100.85

Table 4.S3 (Continued)

Sample No.	MG05																
	Pn																
Analysis No.	L_01	L_03	L_04	M_01	M_02	R_01	R_02	R_03	R_04	R_05	Q_01	Q_02	Q_03	Q_05	Q_06	O_01	O_02
Fe	18.72	20.24	21.40	22.12	22.80	22.47	22.91	22.88	22.13	22.99	20.29	19.95	20.92	20.42	19.69	22.04	20.66
Ni	34.19	33.90	33.23	34.44	33.67	32.08	32.07	33.32	34.64	32.83	34.79	34.75	34.26	34.44	33.86	33.76	34.65
Co	13.41	13.63	12.33	9.73	9.76	12.65	11.95	10.90	10.81	11.17	12.44	13.14	11.99	12.19	13.77	11.44	12.24
Cu	0.00	0.00	0.04	0.00	0.00	0.00	0.03	0.01	0.00	0.00	0.00	0.01	0.00	0.00	0.00	0.00	0.01
Zn	0.00	0.00	0.00	0.03	0.00	0.03	0.00	0.00	0.00	0.00	0.02	0.00	0.04	0.00	0.04	0.01	0.03
S	32.40	32.76	32.37	32.70	32.53	32.82	32.89	33.10	32.79	32.66	32.58	32.86	32.85	32.96	32.77	32.80	32.46
Mn	0.00	0.01	0.01	0.00	0.01	0.01	0.00	0.00	0.01	0.00	0.00	0.01	0.01	0.00	0.01	0.00	0.03
As	0.00	0.02	0.00	0.10	0.08	0.05	0.08	0.06	0.04	0.03	0.02	0.02	0.02	0.04	0.04	0.05	0.03
Pb	0.17	0.19	0.10	0.14	0.01	0.04	0.08	0.16	0.06	0.11	0.17	0.17	0.09	0.11	0.07	0.09	0.07
Sb	0.00	0.00	0.00	0.02	0.00	0.00	0.00	0.00	0.00	0.03	0.03	0.00	0.01	0.02	0.02	0.01	0.01
Total	98.89	100.75	99.47	99.28	98.87	100.14	100.01	100.43	100.47	99.82	100.33	100.93	100.19	100.16	100.26	100.19	100.19

Table 4.S3 (Continued)

Sample No.	MG05															
	Pn															
Analysis No.	O_03	O_05	O_07	O_08	N_01	N_02	N_04	N_05	N_06	J_01	J_02	J_03	J_04	K_01	K_02	K_04
Fe	22.16	21.33	20.80	20.86	22.54	21.97	22.22	22.11	20.83	22.03	22.48	22.68	20.41	17.60	17.34	18.61
Ni	32.81	34.05	34.33	34.10	32.61	33.36	33.80	32.74	33.51	34.39	33.79	34.85	36.67	33.05	32.95	33.19
Co	11.80	12.40	12.62	12.45	12.32	12.01	11.43	12.39	13.03	10.82	10.64	9.97	10.56	17.34	17.19	15.74
Cu	0.00	0.00	0.02	0.00	0.00	0.03	0.00	0.02	0.00	0.02	0.00	0.00	0.00	0.02	0.00	0.02
Zn	0.00	0.02	0.01	0.00	0.01	0.00	0.02	0.03	0.01	0.00	0.02	0.00	0.02	0.00	0.03	0.03
S	32.81	32.78	32.70	32.82	32.90	32.46	32.89	32.50	32.03	31.92	32.72	32.96	32.78	32.70	32.76	32.81
Mn	0.01	0.00	0.00	0.00	0.01	0.00	0.00	0.00	0.00	0.01	0.02	0.01	0.00	0.01	0.01	0.00
As	0.02	0.04	0.02	0.06	0.07	0.05	0.04	0.02	0.02	0.07	0.02	0.03	0.01	0.05	0.02	0.04
Pb	0.14	0.05	0.21	0.08	0.05	0.10	0.12	0.13	0.14	0.19	0.00	0.05	0.11	0.11	0.07	0.20
Sb	0.00	0.00	0.01	0.00	0.00	0.01	0.00	0.03	0.00	0.02	0.00	0.03	0.00	0.00	0.01	0.01
Total	99.74	100.65	100.71	100.36	100.51	99.99	100.52	99.94	99.58	99.46	99.69	100.57	100.56	100.88	100.38	100.64

Table 4.S3 (Continued)

Sample No.	MG12															
	Pn															
Analysis No.	N_03	M_01	M_02	M_03	M_04	M_05	M_06	M_08	l_01	L_02	L_03	P_01	P_04	P_05	Q_01	O_01
Fe	20.97	29.96	29.79	29.05	28.01	28.87	28.22	27.54	26.91	26.29	26.91	29.35	28.25	28.21	29.45	25.81
Ni	18.56	28.94	28.70	29.55	29.63	29.79	29.13	29.33	26.71	27.22	26.86	29.22	28.82	29.61	28.18	27.12
Co	27.12	7.59	7.53	7.96	7.96	7.86	8.21	8.16	12.71	12.59	12.87	7.68	8.37	8.05	9.83	12.79
Cu	0.00	0.00	0.01	0.01	0.05	0.01	0.04	0.00	0.00	0.01	0.00	0.00	0.03	0.04	0.05	0.03
Zn	0.00	0.00	0.00	0.00	0.00	0.01	0.01	0.00	0.03	0.00	0.04	0.02	0.01	0.00	0.02	0.03
S	33.13	33.10	33.23	32.83	32.67	33.36	32.55	32.86	32.92	32.90	33.00	33.06	33.02	32.88	33.29	32.88
Mn	0.00	0.00	0.00	0.02	0.03	0.03	0.01	0.00	0.00	0.00	0.00	0.00	0.01	0.01	0.00	0.02
As	0.02	0.02	0.00	0.04	0.12	0.07	0.00	0.03	0.03	0.02	0.02	0.06	0.04	0.07	0.02	0.00
Pb	0.04	0.10	0.16	0.00	0.13	0.18	0.22	0.18	0.14	0.09	0.03	0.00	0.19	0.00	0.13	0.17
Sb	0.00	0.00	0.00	0.00	0.03	0.00	0.00	0.00	0.00	0.00	0.00	0.01	0.00	0.00	0.00	0.00
Total	99.83	99.72	99.43	99.44	98.61	100.18	98.40	98.09	99.46	99.12	99.72	99.41	98.72	98.86	100.96	98.83

Table 4.S3 (Continued)

Alloys										
Aw										
Sample No.	MG17									
Analysis No.	awa-1	awa-2	awa-3	awa-4	awa-5	awa-7	awa-8	awa-9	awa-10	awa-11
Fe	20.27	23.97	17.98	22.01	21.65	19.77	20.61	20.24	23.56	20.99
Ni	75	71.32	77.96	73.43	74.37	80.52	73.87	75.06	73.53	75.02
Co	0.89	1.76	0.79	2.04	1.68	0.65	1.41	2.19	1.73	1.31
Cu	0	0	0	0	0	0	0.02	0.04	0	0.17
Zn	-	-	-	-	-	-	-	-	-	-
S	0.02	0	0.03	0.02	0	0	0.05	0.01	0.01	0
Mn	0	0	0.02	0.02	0.01	0.01	0	0	0.01	0.02
As	-	-	-	-	-	-	-	-	-	-
Pb	-	-	-	-	-	-	-	-	-	-
Sb	-	-	-	-	-	-	-	-	-	-
Total	96.21	97.08	96.81	97.52	97.76	100.97	96.02	97.6	98.86	97.54

Table 4.S4. Representative analyses of andradite from the Sabzevar magnetite ore and host serpentinite

Sample No.	Host serpentinite								Magnetite ore									
	MG21								MG05									
	Analysis No.	andr-1	andr-2	andr-3	andr-4	andr-5	andr-6	andr-14	andr-15	andr-1	andr-2	andr-3	andr-4	andr-5	andr-6	andr-7	andr-8	andr-9
SiO <sub>2</sub>	34.03	34.42	34.65	35.29	34.72	34.78	30.88	32.2	34.09	35.46	35.46	35.53	34.74	35.82	36.02	35.55	35.65	35.76
TiO <sub>2</sub>	bdl	bdl	bdl	bdl	0.04	bdl	bdl	0.03	0.03	0.15	0.18	0.18	0.3	bdl	bdl	bdl	bdl	bdl
Al <sub>2</sub> O <sub>3</sub>	1.06	0.4	1.13	0.52	0.52	0.73	0.75	0.85	0.94	1.06	0.83	0.92	1.03	0.84	1.05	0.77	1.15	0.92
FeO	25.94	27.05	25.88	26.95	26.73	27.21	27.18	26.47	26.67	26.35	26.81	26.5	26.12	25.99	26.58	26.99	26.33	26.92
Fe <sub>2</sub> O <sub>3</sub>	28.83	30.06	28.76	29.95	29.71	30.24	30.21	29.41	29.64	29.28	29.8	29.45	29.03	28.88	29.54	29.99	29.27	29.91
MnO	bdl	bdl	bdl	bdl	bdl	bdl	bdl	bdl	bdl	bdl	bdl	bdl	bdl	bdl	bdl	bdl	bdl	bdl
MgO	0.38	0.15	0.38	0.31	0.33	0.11	0.39	0.63	0.1	0.07	0.06	0.12	0.1	0.07	0.07	0.05	0.23	0.21
CaO	33.04	32.73	33.19	32.64	32.81	32.94	33.21	32.82	33.24	33.09	32.88	33.14	33.15	33.03	33.14	33.05	32.9	32.93
Na <sub>2</sub> O	bdl	bdl	bdl	bdl	bdl	bdl	bdl	bdl	bdl	0.05	bdl							
K <sub>2</sub> O	bdl	bdl	bdl	bdl	bdl	bdl	bdl	bdl	bdl	0.03	bdl							
Cr <sub>2</sub> O <sub>3</sub>	0.59	0.72	0.41	0.31	0.28	0.25	0.25	0.12	0.04	0.12	0.06	bdl	0.08	1.2	bdl	0.22	bdl	bdl
Total	97.93	98.48	98.51	99.01	98.41	99.05	95.69	96.07	98.07	99.31	99.27	99.34	98.43	99.84	99.81	99.62	99.2	99.73
Si	2.914	2.949	2.946	2.999	2.967	2.958	2.718	2.813	2.923	2.997	3.006	3.004	2.964	3.017	3.03	3.003	3.014	3.012
Ti	0	0	0	0	0.003	0	0	0.002	0.002	0.009	0.012	0.011	0.019	0	0	0	0	0
Al	0.107	0.04	0.113	0.052	0.053	0.073	0.078	0.087	0.095	0.106	0.083	0.092	0.104	0.083	0.104	0.076	0.115	0.091
Fe	1.858	1.938	1.84	1.916	1.911	1.936	2.001	1.934	1.912	1.863	1.901	1.874	1.864	1.831	1.87	1.907	1.862	1.897
Mn	0	0	0	0	0	0	0	0	0	0	0	0	0	0	0	0	0	0
Mg		0.019	0.049	0.039	0.042	0.014	0.052	0.083	0.012	0.009	0.008	0.016	0.013	0.009	0.008	0.006	0.029	0.027
Ca	3.032	3.005	3.024	2.973	3.005	3.002	3.133	3.073	3.053	2.997	2.987	3.003	3.031	2.98	2.987	2.992	2.981	2.973
Na	0	0	0	0	0	0	0	0	0	0.009	0	0	0	0	0	0	0	0
K	0	0	0	0	0	0	0	0	0	0.003	0	0	0	0	0	0	0	0
Cr	0.04	0.049	0.027	0.021	0.019	0.017	0.017	0.008	0.002	0.008	0.004	0	0.005	0.08	0	0.015	0	0
Total	7.951	8	8	8	8	8	8	8	8	8	8	8	8	8	8	8	8	8

Table 4.S5. Representative analyses of chlorite inclusions in chromites from the Sabzevar magnetite ore and host serpentinites.

Sample No.	Host serpentinite													Magnetite ore		
	MG17													Mg05		
Analysis No.	chl1	chl2	chl3	chl4	chl5	chl9	chl10	chl11	chl13	chl14	chl16	chl17	chl19	chl-1	chl-9	chl-10
SiO <sub>2</sub>	31.88	33.31	32.49	33.62	33.25	34.15	37.46	35.33	35.39	36.11	35.34	35	34.79	35.23	35.08	30.96
TiO <sub>2</sub>	0.02	0.03	0	0	0	0.03	0.04	0.05	0.04	0.04	0.06	0.02	0.04	0.03	0.04	0.03
Al <sub>2</sub> O <sub>3</sub>	14.74	10.43	13.09	10.85	11.7	12.56	7.24	9.18	9.98	9.57	7.76	9.26	8.73	6.66	10.61	13.78
Cr <sub>2</sub> O <sub>3</sub>	3.55	4.56	4.08	4.17	4.29	3.87	3.72	3.88	4.1	4.19	4.22	4.58	3.86	5.02	2.3	4.07
Fe <sub>2</sub> O <sub>3</sub>	0.47	0	0.22	0.44	0	1.22	1.81	1.14	0.68	1.08	0.09	0.66	0.51	0.25	0.82	0
FeO	1.33	2.76	1.55	1.24	1.83	1.19	1.41	1.42	1.58	1.33	2.51	1.97	2.12	3.94	5.52	2.55
MnO	0.01	0.03	0	0.01	0.02	0	0	0.01	0.01	0.01	0.01	0.01	0.01	0.02	0.07	0.02
MgO	33.64	35.88	34.44	34.78	35.46	33.94	34.71	34.46	35.68	35.56	36.05	35.05	34.89	34.63	32.35	33.44
CaO	0.04	0.06	0.04	0.03	0.03	0	0.01	0	0.02	0.01	0.04	0.02	0.03	0.02	0.29	0.03
Na <sub>2</sub> O	0	0.02	0	0	0	0	0	0.02	0.01	0.01	0	0	0	0	0.05	0
K <sub>2</sub> O	0	0	0	0	0	0	0.01	0.01	0.01	0	0	0	0	0.01	0.01	0
Total	98.15	99.61	98.39	97.53	99.14	99.62	98.97	97.91	100.19	100.68	98.54	99.09	97.32	98.09	99.63	97.15
Si	6.118	6.346	6.236	6.501	6.342	6.456	7.125	6.801	6.665	6.76	6.801	6.689	6.761	6.874	6.729	6.045
Al iv	1.882	1.654	1.764	1.499	1.658	1.544	0.875	1.199	1.335	1.24	1.199	1.311	1.239	1.126	1.271	1.955
Al vi	1.457	0.698	1.2	0.977	0.974	1.263	0.756	0.889	0.885	0.879	0.562	0.78	0.764	0.407	1.134	1.222
Ti	0.003	0.004	0	0	0	0.004	0.006	0.008	0.005	0.005	0.009	0.002	0.006	0.005	0.006	0.005
Cr	0.539	0.688	0.619	0.637	0.647	0.578	0.56	0.59	0.61	0.62	0.643	0.692	0.594	0.775	0.349	0.629
Fe <sup>3+</sup>	0.067	0	0.031	0.064	0	0.173	0.26	0.166	0.096	0.152	0.013	0.094	0.075	0.037	0.118	0
Fe <sup>2+</sup>	0.213	0.546	0.248	0.2	0.307	0.188	0.225	0.229	0.248	0.209	0.404	0.315	0.345	0.643	0.886	0.454
Mn	0.002	0.004	0	0.001	0.003	0	0	0.002	0.001	0.002	0.002	0.001	0.002	0.004	0.011	0.003
Mg	9.624	10.189	9.854	10.026	10.083	9.565	9.844	9.887	10.018	9.926	10.343	9.986	10.109	10.074	9.249	9.734
Ca	0.007	0.011	0.007	0.007	0.007	0.001	0.001	0	0.005	0.002	0.008	0.005	0.007	0.004	0.061	0.007
Na	0	0.011	0	0.003	0	0	0	0.013	0.004	0.009	0	0	0	0	0.04	0
K	0.001	0	0	0.001	0	0	0.003	0.003	0.004	0	0.001	0	0	0.003	0.006	0
Total	35.913	36.15	35.959	35.917	36.021	35.774	35.656	35.787	35.877	35.803	35.983	35.875	35.901	35.952	35.861	36.054

Table 5.S1. Trace element composition (LA-ICPMS) of magnetite from the investigated occurrences

Locality	Sabzevar										Nain							
Sample No.	MG01						MG15				IRNAM01							
Analysis No.	G-5	G-6	B-3	C-6	C-7	G-10	G-3	E-9	E-8	D-4	Q-2	A-3	A-5	A-4	E-3	C-2	K-4	N-2
Si <sup>29</sup>	8618	9365	9894	11534	11433	26609	10468	10099	8391	7874	1052	1575	1480	1764	6558	1060	8290	8781
Ca <sup>43</sup>	nd	nd	BDL	nd	BDL	11106	nd	BDL	nd	BDL	BDL	BDL	BDL	BDL	BDL	BDL	BDL	BDL
Mg <sup>25</sup>	542	916	2364	1796	3282	11096	890	692	588	662	957	1197	1162	1288	1916	940	2225	3556
Ti <sup>47</sup>	12	1095	53	4	19	46	4	4	22	15	15	BDL	BDL	BDL	7	4	65	19
V <sup>51</sup>	5	22	16	3	4	12	3	2	BDL	1	25	1	1	1	13	11	95	47
Cr <sup>53</sup>	31	1545	804	91	115	810	52	14	7	7	107	BDL	BDL	BDL	234	15	3198	3683
Mn <sup>55</sup>	156	106	130	189	154	255	116	127	151	129	185	274	251	260	136	209	132	123
Co <sup>59</sup>	132	89	114	172	405	230	104	119	440	165	315	265	261	201	363	269	307	340
Ni <sup>60</sup>	41	28	41	35	353	397	14	25	121	42	312	104	89	93	317	226	327	333
Zn <sup>66</sup>	7	7	7	8	11	23	5	7	8	11	9	12	11	12	26	9	10	12
Mo <sup>98</sup>	BDL	BDL	nd	BDL	nd	BDL	BDL	BDL	BDL	nd	BDL	BDL	0.7	BDL	BDL	BDL	BDL	BDL

Table 5.S1 (Continued)

											Aniba (Oman)								
	MS1			MS2						TV196						TV209			
	A-3	B-3	H-2	A-2	A-5	A-6	C-2	B-2	D-2	B-4-K	B-1	C-6	C-7	C-10	A-1	A-4	A-6	B-4-a	B-5-a
Si <sup>29</sup>	4076	3704	3332	3297	4961	2915	1092	640	1059	5017	8505	5696	5584	5067	4318	5454	5600	3171	3201
Ca <sup>43</sup>	BDL	BDL	BDL	BDL	BDL	nd	BDL	nd	BDL	1849	10004	3014	4584	2250	2406	2683	119776	387	319
Mg <sup>25</sup>	357	604	350	913	550	402	1131	1099	429	54	797	219	90	196	58	113	447	539	440
Ti <sup>47</sup>	BDL	3011	2548	2975	2166	2565	4122	2253	4065	136	100								
V <sup>51</sup>	2	2	0.5	9	1	1	0.5	0.3	1	543	617	577	573	531	587	572	609	127	216
Cr <sup>53</sup>	BDL	95	nd	46	9	BDL	nd	BDL	BDL	5110	10241	14687	8421	22257	21245	15376	2023	2128	1237
Mn <sup>55</sup>	110	128	121	105	104	121	277	215	158	2864	2874	1360	1354	2962	2290	3260	2579	2961	2418
Co <sup>59</sup>	166	175	140	146	135	123	223	210	127	2	5	9	5	22	12	9	3	774	852
Ni <sup>60</sup>	598	760	626	855	501	765	392	381	1043	59	263	195	186	198	223	408	179	6953	6669
Zn <sup>66</sup>	9	10	8	10	7	9	17	12	8	16	20	14	19	24	24	46	7	236	154
Mo <sup>98</sup>	1.0	1.0	0.7	0.6	BDL	0.6	BDL	BDL	BDL	2.0	9.7	2.5	2.5	3.4	1.4	6.5	5.0	1.2	5.5

Table 6.S1. Representative bulk-rock analyses of the Sabzevar samples.

	Harzburgite			Dunite						
	KA3-3	SI-2 a	O2	KA3-5	EB-3	SI-2 b	KE-3	IM-2	HA2-2 a	O1
SiO2	39.03	39.46	35.56	32.61	31.80	36.98	33.02	33.24	31.82	32.90
Al2O3	0.65	0.64	0.58	0.62	0.35	0.59	0.29	0.21	0.15	0.08
Fe2O3	7.49	7.59	6.31	6.90	6.96	7.56	7.09	7.35	7.38	5.83
MnO	0.11	0.11	0.09	0.10	0.09	0.11	0.09	0.10	0.11	0.08
MgO	38.46	40.26	39.81	40.37	41.21	37.09	40.61	40.60	42.59	42.17
CaO	0.90	0.60	0.20	0.09	0.11	0.55	0.14	0.25	0.13	0.08
Na2O	<L.D.	<L.D.	<L.D.	<L.D.	<L.D.	<L.D.	<L.D.	<L.D.	<L.D.	<L.D.
K2O	<L.D.	<L.D.	<L.D.	<L.D.	<L.D.	<L.D.	<L.D.	<L.D.	<L.D.	<L.D.
TiO2	<L.D.	<L.D.	<L.D.	<L.D.	<L.D.	<L.D.	<L.D.	<L.D.	<L.D.	<L.D.
P2O5	<L.D.	<L.D.	<L.D.	<L.D.	<L.D.	<L.D.	<L.D.	<L.D.	<L.D.	<L.D.
PF	12.78	11.19	16.80	17.93	18.25	16.07	18.69	18.03	17.70	17.94
Total	99.43	99.84	99.35	98.62	98.77	98.95	99.94	99.77	99.88	99.08
µg/g										
As	<L.D.	<L.D.	1	<L.D.	<L.D.	2	<L.D.	<L.D.	<L.D.	1
Ba	<L.D.	14	<L.D.	<L.D.	<L.D.	<L.D.	<L.D.	<L.D.	<L.D.	<L.D.
Be	<L.D.	<L.D.	<L.D.	<L.D.	<L.D.	<L.D.	<L.D.	<L.D.	<L.D.	<L.D.
Bi	<L.D.	<L.D.	0	<L.D.	<L.D.	<L.D.	<L.D.	<L.D.	<L.D.	<L.D.
Cd	0	0	0	0	0	0	0	0	0	0
Co	99	100	94	101	96	95	106	103	107	93
Cr	3192	2946	2824	7045	4820	5649	5145	3268	3395	3008
Cs	<L.D.	0	<L.D.	<L.D.	<L.D.	<L.D.	<L.D.	<L.D.	<L.D.	<L.D.
Cu	15	6	<L.D.	15	6	9	2	2	13	<L.D.
Ga	1	1	0	1	1	1	1	0	0	0
Ge	1	1	1	1	1	1	1	1	1	1
Hf	<L.D.	<L.D.	<L.D.	<L.D.	<L.D.	<L.D.	<L.D.	<L.D.	<L.D.	0
In	<L.D.	<L.D.	<L.D.	<L.D.	<L.D.	<L.D.	<L.D.	<L.D.	<L.D.	<L.D.
Mo	<L.D.	1	<L.D.	1	1	<L.D.	2	2	<L.D.	<L.D.
Nb	0	0	<L.D.	0	0	1	<L.D.	0	0	0
Ni	2031	2060	2082	2631	2799	2607	2441	2348	2434	2885
Pb	1	3	1	1	105	8	42	4	2	1
Rb	<L.D.	<L.D.	<L.D.	<L.D.	<L.D.	<L.D.	<L.D.	<L.D.	<L.D.	<L.D.
Sb	0	0	0	0	5	0	8	10	0	0
Sc	10	10	6	4	4	4	3	4	3	2
Sn	<L.D.	<L.D.	0	<L.D.	<L.D.	<L.D.	<L.D.	<L.D.	1	1
Sr	1	2	<L.D.	1	1	19	1	7	1	<L.D.
Ta	0	<L.D.	<L.D.	0	0	<L.D.	0	0	<L.D.	0
Th	<L.D.	<L.D.	0	<L.D.	0	<L.D.	0	0	0	0
U	<L.D.	<L.D.	<L.D.	<L.D.	0	<L.D.	<L.D.	<L.D.	<L.D.	0
V	38	28	23	19	13	19	11	12	8	5
W	<L.D.	<L.D.	<L.D.	<L.D.	<L.D.	<L.D.	<L.D.	<L.D.	<L.D.	<L.D.
Y	0	0	0	0	0	0	0	0	0	0
Zn	70	46	31	55	36	29	37	46	43	33
Zr	<L.D.	<L.D.	<L.D.	<L.D.	<L.D.	<L.D.	<L.D.	<L.D.	<L.D.	9
La	<L.D.	<L.D.	0	<L.D.	0	0	0	0	0	0
Ce	<L.D.	0	0	<L.D.	0	0	0	0	0	0
Pr	<L.D.	<L.D.	0	<L.D.	0	<L.D.	0	0	0	0
Nd	<L.D.	<L.D.	<L.D.	<L.D.	0	<L.D.	0	0	0	0
Sm	<L.D.	<L.D.	<L.D.	<L.D.	0	<L.D.	0	<L.D.	<L.D.	<L.D.
Eu	<L.D.	<L.D.	<L.D.	<L.D.	<L.D.	<L.D.	<L.D.	<L.D.	<L.D.	<L.D.

Gd	<L.D.	<L.D.	<L.D.	<L.D.	<L.D.	<L.D.	0	0	0	<L.D.
Tb	<L.D.	<L.D.	<L.D.	<L.D.	<L.D.	<L.D.	0	<L.D.	<L.D.	<L.D.
Dy	0	0	0	0	<L.D.	<L.D.	0	0	<L.D.	<L.D.
Ho	0	0	0	0	0	0	0	0	0	0
Er	0	0	0	0	0	0	0	0	0	0
Tm	0	0	0	0	0	<L.D.	0	0	0	<L.D.
Yb	0	0	0	0	0	0	0	0	0	0
Lu	0	0	0	0	0	0	0	0	0	0

Table 6.S1 (Continued)

	Dunite		Disseminated	Semi-massive						
	O24	O26	KA5-1 a	KA1-1 a	KE-2	KA1-1 b	KA1-2	HA2-1	KA3-1 c	SI-2 c
SiO <sub>2</sub>	36.90	33.75	15.70	25.90	12.35	12.50	22.35	4.94	9.80	4.95
Al <sub>2</sub> O <sub>3</sub>	0.58	0.18	9.76	2.72	10.08	12.53	5.88	11.18	13.29	17.60
Fe <sub>2</sub> O <sub>3</sub>	7.08	7.29	11.92	8.60	13.30	13.12	9.90	13.80	13.08	15.81
MnO	0.11	0.10	0.11	0.11	0.11	0.10	0.10	0.13	0.11	0.13
MgO	39.24	40.74	28.31	38.29	22.10	24.45	33.64	18.56	21.64	16.17
CaO	0.31	0.08	<L.D.	0.10	<L.D.	<L.D.	<L.D.	0.07	<L.D.	0.91
Na <sub>2</sub> O	0.03	<L.D.	<L.D.	<L.D.	<L.D.	<L.D.	<L.D.	<L.D.	<L.D.	<L.D.
K <sub>2</sub> O	<L.D.	<L.D.	<L.D.	<L.D.	<L.D.	<L.D.	<L.D.	<L.D.	<L.D.	<L.D.
TiO <sub>2</sub>	<L.D.	<L.D.	0.13	0.02	0.14	0.13	<L.D.	0.12	0.16	<L.D.
P <sub>2</sub> O <sub>5</sub>	<L.D.	<L.D.	<L.D.	<L.D.	<L.D.	<L.D.	<L.D.	<L.D.	<L.D.	<L.D.
PF	14.89	17.19	8.43	16.36	4.97	6.44	12.29	1.90	3.67	1.41
Total	99.12	99.34	74.35	92.11	63.05	69.26	84.16	50.68	61.75	56.97
µg/g										
As	<L.D.	<L.D.	2	<L.D.	2	2	3	1	3	3
Ba	<L.D.	<L.D.	<L.D.	<L.D.	<L.D.	<L.D.	<L.D.	<L.D.	<L.D.	<L.D.
Be	<L.D.	<L.D.	<L.D.	<L.D.	<L.D.	<L.D.	<L.D.	<L.D.	<L.D.	<L.D.
Bi	<L.D.	<L.D.	<L.D.	<L.D.	<L.D.	<L.D.	<L.D.	<L.D.	<L.D.	<L.D.
Cd	<L.D.	0	<L.D.	0	<L.D.	0	<L.D.	0	<L.D.	<L.D.
Co	98	105	145	107	155	158	130	159	157	180
Cr	2812	2970	181527	44419	261954	227597	103006	333247	253821	306561
Cs	0	<L.D.	<L.D.	<L.D.	<L.D.	<L.D.	<L.D.	<L.D.	<L.D.	<L.D.
Cu	3	3	13	8	23	36	<L.D.	11	38	29
Ga	0	0	18	5	21	23	10	21	22	29
Ge	1	1	1	1	1	1	1	1	1	1
Hf	<L.D.	<L.D.	<L.D.	<L.D.	<L.D.	<L.D.	<L.D.	<L.D.	<L.D.	<L.D.
In	<L.D.	<L.D.	<L.D.	<L.D.	<L.D.	<L.D.	<L.D.	<L.D.	<L.D.	<L.D.
Mo	1	1	<L.D.	1	<L.D.	<L.D.	<L.D.	3	<L.D.	<L.D.
Nb	0	0	0	0	0	0	0	0	0	0
Ni	1982	2082	1919	2354	1682	1682	1996	1317	1562	1275
Pb	13	25	4	17	7	11	6	4	4	4
Rb	0	<L.D.	<L.D.	<L.D.	<L.D.	<L.D.	<L.D.	<L.D.	<L.D.	<L.D.
Sb	5	5	1	6	2	1	1	9	1	1
Sc	6	3	2	4	4	4	3	5	6	6
Sn	0	1	<L.D.	<L.D.	1	<L.D.	<L.D.	<L.D.	<L.D.	<L.D.
Sr	1	<L.D.	<L.D.	1	<L.D.	<L.D.	<L.D.	<L.D.	<L.D.	8
Ta	0	0	0	0	0	0	<L.D.	0	0	<L.D.
Th	0	0	0	0	0	0	<L.D.	0	<L.D.	0
U	0	<L.D.	<L.D.	0	<L.D.	<L.D.	<L.D.	<L.D.	<L.D.	<L.D.
V	23	10	320	87	379	375	185	412	450	839
W	<L.D.	<L.D.	<L.D.	<L.D.	<L.D.	<L.D.	<L.D.	<L.D.	<L.D.	<L.D.
Y	0	0	0	0	<L.D.	0	<L.D.	0	<L.D.	0
Zn	36	42	203	81	241	270	146	268	260	338
Zr	<L.D.	<L.D.	<L.D.	<L.D.	<L.D.	<L.D.	<L.D.	<L.D.	<L.D.	<L.D.
La	0	0	<L.D.	0	<L.D.	0	<L.D.	0	0	<L.D.
Ce	0	0	0	0	0	0	0	1	<L.D.	0
Pr	0	0	0	0	0	0	<L.D.	0	<L.D.	0
Nd	0	0	0	0	<L.D.	0	<L.D.	0	<L.D.	<L.D.
Sm	0	0	<L.D.	0	<L.D.	0	<L.D.	0	<L.D.	<L.D.
Eu	0	<L.D.	<L.D.	<L.D.	<L.D.	0	<L.D.	<L.D.	<L.D.	<L.D.
Gd	0	0	<L.D.	<L.D.	<L.D.	0	<L.D.	0	<L.D.	0

Tb	0	0	<L.D.	0	0	0	<L.D.	<L.D.	0	<L.D.
Dy	0	0	<L.D.	0	<L.D.	0	<L.D.	0	<L.D.	0
Ho	0	0	0	0	0	0	<L.D.	0	0	0
Er	0	0	0	0	0	0	0	0	0	0
Tm	0	<L.D.	<L.D.	0	<L.D.	0	<L.D.	<L.D.	<L.D.	0
Yb	0	0	0	0	0	0	0	0	0	0
Lu	0	0	0	0	0	0	<L.D.	<L.D.	0	0

Table 6.S1 (Continued)

	Semi-massive		Massive chromitite		
	O21	IM-1 b	O3	O27	EB-4 (fragments)
SiO2	2.45	< L.D.	< L.D.	1.15	< L.D.
Al2O3	7.69	10.93	9.43	7.66	14.28
Fe2O3	24.35	14.32	18.53	24.62	19.69
MnO	0.33	0.13	0.20	0.34	0.15
MgO	10.45	16.15	13.46	9.85	14.51
CaO	< L.D.	0.34	< L.D.	< L.D.	< L.D.
Na2O	< L.D.	< L.D.	< L.D.	< L.D.	< L.D.
K2O	< L.D.	< L.D.	< L.D.	< L.D.	< L.D.
TiO2	0.09	0.12	0.11	0.10	0.14
P2O5	< L.D.	< L.D.	< L.D.	< L.D.	< L.D.
PF	0.30	1.45	-0.86	-0.88	0.03
Total	45.65	43.44	40.86	42.84	48.80
µg/g					
As	4	3	10	6	3
Ba	< L.D.	< L.D.	< L.D.	< L.D.	< L.D.
Be	< L.D.	< L.D.	< L.D.	< L.D.	< L.D.
Bi	< L.D.	< L.D.	< L.D.	< L.D.	< L.D.
Cd	< L.D.	< L.D.	0	< L.D.	< L.D.
Co	449	179	249	458	316
Cr	358493	382950	405732	382162	345259
Cs	< L.D.	< L.D.	< L.D.	< L.D.	< L.D.
Cu	31	19	34	< L.D.	12
Ga	12	21	17	12	26
Ge	1	1	0	1	1
Hf	< L.D.	< L.D.	< L.D.	< L.D.	< L.D.
In	< L.D.	< L.D.	< L.D.	< L.D.	< L.D.
Mo	< L.D.	< L.D.	< L.D.	< L.D.	< L.D.
Nb	1	0	0	0	0
Ni	322	1077	839	338	987
Pb	17	7	13	18	18
Rb	1	1	1	1	< L.D.
Sb	2	1	2	1	1
Sc	< L.D.	5	4	< L.D.	5
Sn	< L.D.	< L.D.	< L.D.	< L.D.	< L.D.
Sr	< L.D.	< L.D.	< L.D.	< L.D.	< L.D.
Ta	< L.D.	< L.D.	0	0	0
Th	< L.D.	< L.D.	< L.D.	0	< L.D.
U	< L.D.	< L.D.	< L.D.	< L.D.	< L.D.
V	424	578	393	411	678
W	< L.D.	< L.D.	< L.D.	< L.D.	< L.D.
Y	< L.D.	0	< L.D.	< L.D.	< L.D.
Zn	1305	298	576	1311	443
Zr	< L.D.	< L.D.	6	< L.D.	< L.D.
La	0	0	0	0	< L.D.
Ce	2	0	1	1	0
Pr	0	0	0	< L.D.	0
Nd	< L.D.	< L.D.	< L.D.	0	< L.D.
Sm	< L.D.	< L.D.	< L.D.	< L.D.	< L.D.
Eu	< L.D.	< L.D.	< L.D.	< L.D.	< L.D.
Gd	< L.D.	0	< L.D.	0	< L.D.

Tb	<L.D.	0	<L.D.	0	<L.D.
Dy	<L.D.	0	<L.D.	<L.D.	<L.D.
Ho	<L.D.	0	<L.D.	<L.D.	<L.D.
Er	<L.D.	0	<L.D.	<L.D.	<L.D.
Tm	<L.D.	0	<L.D.	<L.D.	<L.D.
Yb	0	0	0	0	0
Lu	<L.D.	0	<L.D.	<L.D.	<L.D.

Table 6.S2. Representative analyses of spinels from the studied chromitites in the Sabzevar ophiolite

Sample No.	SI-2C																	
Analysis No.	A3	A4	C3	C4	D1	E1	H3	I1	I3	E2	E3	F1	F2	F3	H4	I2	JJ2	JJ3
	Homogeneous core									Heterogeneous rim								
SiO <sub>2</sub>	0.01	0.01	0.01	0.03	0.03	0.02	0.02	0.01	0.01	0.02	0.02	0.01	0.01	0.01	0.02	0.01	0.72	0.03
TiO <sub>2</sub>	0.07	0.07	0.07	0.07	0.07	0.08	0.07	0.07	0.07	0.07	0.06	0.07	0.07	0.07	0.06	0.06	0.07	0.06
V <sub>2</sub> O <sub>3</sub>	0.16	0.16	0.16	0.16	0.16	0.16	0.16	0.15	0.16	0.16	0.15	0.16	0.15	0.16	0.16	0.15	0.16	0.18
Cr <sub>2</sub> O <sub>3</sub>	49.98	50.21	49.29	49.29	49.18	48.54	49.45	49.40	49.41	52.20	55.16	54.43	54.96	53.37	53.45	52.64	51.81	53.18
MgO	14.91	15.16	15.26	15.15	15.52	14.31	14.64	14.95	14.72	12.94	11.67	13.44	12.98	14.60	13.69	13.66	15.82	13.51
Al <sub>2</sub> O <sub>3</sub>	20.08	20.08	20.59	20.61	20.41	21.33	20.39	20.49	20.53	17.87	15.42	16.67	16.13	18.61	16.99	17.56	19.12	16.65
Mno	0.16	0.14	0.13	0.14	0.13	0.18	0.16	0.15	0.16	0.22	0.25	0.16	0.19	0.17	0.20	0.19	0.19	0.21
FeO	14.26	13.93	13.95	14.01	14.06	15.47	15.31	14.94	14.97	15.99	16.48	14.98	15.40	13.26	15.94	15.59	15.15	16.10
CoO	0.03	0.02	0.03	0.02	0.02	0.03	0.02	0.02	0.03	0.03	0.04	0.02	0.03	0.03	0.03	0.03	0.03	0.03
NiO	0.15	0.15	0.18	0.18	0.17	0.11	0.18	0.16	0.17	0.07	0.06	0.12	0.12	0.08	0.07	0.08	0.08	0.08
ZnO	0.04	0.04	0.05	0.04	0.04	0.05	0.04	0.04	0.05	0.08	0.07	0.05	0.06	0.06	0.07	0.06	0.06	0.07
Total	99.84	99.98	99.71	99.68	99.79	100.30	100.45	100.40	100.27	99.65	99.36	100.11	100.09	100.42	100.68	100.03	103.22	100.10
Si	0.000	0.000	0.000	0.001	0.001	0.001	0.001	0.000	0.000	0.001	0.001	0.000	0.000	0.000	0.001	0.000	0.021	0.001
Ti	0.002	0.002	0.002	0.002	0.002	0.002	0.002	0.002	0.002	0.002	0.001	0.002	0.002	0.002	0.001	0.002	0.001	0.001
Al	0.726	0.724	0.742	0.743	0.734	0.767	0.733	0.736	0.739	0.661	0.583	0.616	0.599	0.675	0.622	0.645	0.670	0.614
Cr	1.212	1.214	1.191	1.192	1.186	1.171	1.193	1.190	1.193	1.296	1.400	1.349	1.369	1.299	1.314	1.298	1.217	1.316
Fe <sup>3+</sup>	0.055	0.054	0.059	0.056	0.071	0.053	0.065	0.067	0.061	0.034	0.009	0.028	0.024	0.018	0.056	0.049	0.063	0.060
Fe <sup>2+</sup>	0.311	0.302	0.297	0.302	0.288	0.342	0.326	0.314	0.322	0.386	0.433	0.365	0.382	0.323	0.358	0.358	0.313	0.362
Mn	0.004	0.004	0.003	0.004	0.003	0.005	0.004	0.004	0.004	0.006	0.007	0.004	0.005	0.005	0.005	0.005	0.005	0.006
Mg	0.682	0.691	0.695	0.691	0.706	0.651	0.666	0.679	0.670	0.606	0.558	0.628	0.610	0.670	0.634	0.635	0.701	0.631
V	0.004	0.004	0.004	0.004	0.004	0.004	0.004	0.004	0.004	0.004	0.004	0.004	0.004	0.004	0.004	0.004	0.004	0.004
Co	0.001	0.001	0.001	0.001	0.000	0.001	0.000	0.001	0.001	0.001	0.001	0.001	0.001	0.001	0.001	0.001	0.001	0.001
Ni	0.004	0.004	0.004	0.004	0.004	0.003	0.005	0.004	0.004	0.002	0.001	0.003	0.003	0.002	0.002	0.002	0.002	0.002
Zn	0.001	0.001	0.001	0.001	0.001	0.001	0.001	0.001	0.001	0.002	0.002	0.001	0.001	0.001	0.002	0.001	0.001	0.002
Total	3.000	3.000	3.000	3.000	3.000	3.000	3.000	3.000	3.000	3.000	3.000	3.000	3.000	3.000	3.000	3.000	3.000	3.000

Cr/(Cr+Al)	0.625	0.626	0.616	0.616	0.618	0.604	0.619	0.618	0.618	0.662	0.706	0.686	0.696	0.658	0.679	0.668	0.645	0.682
Fe <sup>3+</sup> /(Fe <sup>3+</sup> +Cr+Al)	0.149	0.153	0.166	0.157	0.198	0.134	0.166	0.176	0.159	0.081	0.020	0.071	0.059	0.054	0.135	0.120	0.168	0.142
Mg/(Mg+Fe <sup>2+</sup> )	0.687	0.696	0.700	0.696	0.710	0.656	0.671	0.684	0.676	0.611	0.563	0.633	0.615	0.675	0.639	0.640	0.691	0.636

Table 6.S2 (Continued)

Sample No.	SI-2C			KE2															
Analysis No.	H1	H2	JJ1	C2	D1	A3	E1	E4	H3	I4	H1	H2	A1	A2	C1	D2	E2	E3	
	Heterogeneous rim			Homogeneous core							Heterogeneous rim								
SiO <sub>2</sub>	1.61	1.88	0.11	0.01	0.01	0.01	0.02	0.02	0.02	0.02	0.94	0.92	0.02	0.02	0.01	0.04	0.39	1.71	
TiO <sub>2</sub>	0.00	0.00	0.09	0.18	0.21	0.19	0.17	0.19	0.20	0.20	0.02	0.02	0.27	0.28	0.23	0.41	0.09	0.07	
V <sub>2</sub> O <sub>3</sub>	0.01	0.01	0.18	0.09	0.11	0.10	0.10	0.10	0.09	0.10	0.00	0.01	0.10	0.10	0.10	0.13	0.04	0.03	
Cr <sub>2</sub> O <sub>3</sub>	4.21	3.54	58.82	56.14	54.69	54.77	56.44	55.15	54.87	55.03	3.90	4.28	59.24	59.40	60.71	62.41	34.22	18.61	
MgO	0.94	0.88	11.02	13.92	13.39	14.22	13.14	13.40	13.64	13.74	1.32	1.18	8.90	9.29	9.10	8.42	4.53	3.24	
Al <sub>2</sub> O <sub>3</sub>	0.01	0.02	11.40	13.82	16.60	14.85	14.84	15.52	14.95	16.22	0.12	0.02	6.83	6.61	8.40	7.33	2.81	2.06	
Mno	0.89	0.87	0.29	0.17	0.16	0.15	0.16	0.15	0.15	0.15	0.39	0.36	0.19	0.19	0.20	0.22	0.34	0.28	
FeO	86.35	86.03	18.51	15.42	14.55	15.02	14.41	14.38	14.92	13.80	86.21	86.37	20.82	20.19	19.13	19.10	51.52	66.74	
CoO	0.03	0.03	0.03	0.03	0.03	0.03	0.03	0.02	0.03	0.03	0.02	0.03	0.03	0.03	0.02	0.03	0.12	0.03	
NiO	0.00	0.00	0.05	0.09	0.09	0.10	0.09	0.09	0.10	0.10	0.04	0.03	0.14	0.14	0.11	0.10	0.10	0.10	
ZnO	0.03	0.04	0.04	0.03	0.05	0.03	0.04	0.04	0.03	0.04	0.00	0.00	0.04	0.03	0.04	0.05	0.00	0.00	
Total	94.07	93.31	100.53	99.91	99.90	99.46	99.42	99.06	99.00	99.42	92.93	93.21	96.59	96.29	98.04	98.25	94.18	92.87	
Si	0.061	0.072	0.004	0.000	0.000	0.000	0.001	0.001	0.001	0.001	0.036	0.035	0.001	0.001	0.000	0.001	0.014	0.064	
Ti	0.000	0.000	0.002	0.004	0.005	0.004	0.004	0.005	0.005	0.005	0.001	0.000	0.007	0.007	0.006	0.011	0.003	0.002	
Al	0.001	0.001	0.436	0.515	0.615	0.552	0.557	0.581	0.561	0.603	0.006	0.001	0.280	0.271	0.337	0.296	0.123	0.091	
Cr	0.126	0.107	1.508	1.405	1.359	1.367	1.421	1.386	1.380	1.372	0.118	0.129	1.630	1.636	1.636	1.692	1.000	0.552	
Fe <sup>3+</sup>	1.752	1.749	0.040	0.069	0.013	0.069	0.011	0.020	0.046	0.012	1.804	1.799	0.071	0.074	0.011	0.000	0.842	1.223	
Fe <sup>2+</sup>	0.978	0.992	0.462	0.340	0.370	0.328	0.373	0.362	0.351	0.351	0.947	0.955	0.534	0.514	0.534	0.548	0.750	0.873	
Mn	0.028	0.028	0.008	0.005	0.004	0.004	0.004	0.004	0.004	0.004	0.012	0.012	0.006	0.006	0.006	0.006	0.011	0.009	
Mg	0.053	0.050	0.533	0.657	0.627	0.669	0.623	0.635	0.647	0.646	0.075	0.067	0.462	0.483	0.462	0.430	0.250	0.181	
V	0.000	0.000	0.005	0.002	0.003	0.002	0.002	0.002	0.002	0.003	0.000	0.000	0.003	0.003	0.003	0.004	0.001	0.001	
Co	0.001	0.001	0.001	0.001	0.001	0.001	0.001	0.001	0.001	0.001	0.000	0.001	0.001	0.001	0.001	0.001	0.004	0.001	
Ni	0.000	0.000	0.001	0.002	0.002	0.002	0.002	0.002	0.003	0.002	0.001	0.001	0.004	0.004	0.003	0.003	0.003	0.003	
Zn	0.001	0.001	0.001	0.001	0.001	0.001	0.001	0.001	0.001	0.001	0.000	0.000	0.001	0.001	0.001	0.001	0.000	0.000	

Total	3.000	3.000	3.000	3.000	3.000	3.000	3.000	3.000	3.000	3.000	3.000	3.000	3.000	3.000	3.000	2.992	3.000	3.000
Cr/(Cr+Al)	0.996	0.990	0.776	0.732	0.688	0.712	0.718	0.704	0.711	0.695	0.955	0.993	0.853	0.858	0.829	0.851	0.891	0.858
Fe <sup>3+</sup> /(Fe <sup>3+</sup> +Cr+Al)	0.642	0.638	0.080	0.168	0.034	0.173	0.027	0.052	0.117	0.034	0.656	0.653	0.118	0.125	0.021	0.000	0.529	0.584
Mg/(Mg+Fe <sup>2+</sup> )	0.051	0.048	0.536	0.659	0.629	0.671	0.626	0.637	0.648	0.648	0.073	0.065	0.464	0.484	0.464	0.440	0.250	0.172

Table 6.S2 (Continued)

Sample No.	KE2			IM-1B															
Analysis No.	I1	I2	I3	A7	A8	E3	A1	A2	A3	A4	A5	A9	B1	B2	B3	B5	B6	E1	
	Heterogeneous rim			Homogeneous core			Heterogeneous rim												
SiO <sub>2</sub>	0.02	0.02	0.02	0.01	0.01	0.03	0.01	0.01	0.01	0.01	0.00	0.01	0.00	0.01	0.01	0.01	0.01	0.01	0.02
TiO <sub>2</sub>	0.32	0.24	0.17	0.27	0.31	0.24	0.29	0.28	0.29	0.26	0.30	0.30	0.31	0.33	0.17	0.14	0.31	0.24	
V <sub>2</sub> O <sub>3</sub>	0.13	0.11	0.09	0.13	0.14	0.14	0.15	0.15	0.16	0.14	0.15	0.15	0.15	0.16	0.12	0.12	0.14	0.14	
Cr <sub>2</sub> O <sub>3</sub>	61.96	63.03	58.81	54.19	52.65	54.47	58.56	59.91	59.05	61.60	61.50	61.09	61.09	61.03	57.62	58.14	52.38	57.09	
MgO	8.84	7.74	12.48	14.76	15.24	13.57	13.16	12.83	12.93	12.53	10.81	11.51	12.29	12.63	13.98	13.82	15.12	12.44	
Al <sub>2</sub> O <sub>3</sub>	7.99	6.48	12.83	17.11	18.29	16.67	12.25	10.57	11.08	9.40	9.05	9.77	8.96	9.19	13.66	13.02	18.23	12.93	
Mno	0.21	0.24	0.17	0.16	0.16	0.19	0.19	0.21	0.20	0.20	0.22	0.19	0.21	0.21	0.18	0.20	0.16	0.23	
FeO	17.73	19.13	13.66	13.05	12.97	14.95	14.39	15.49	15.19	14.84	16.43	15.35	16.05	16.04	14.07	13.94	13.15	17.52	
CoO	0.03	0.03	0.03	0.03	0.03	0.03	0.03	0.03	0.03	0.03	0.03	0.03	0.03	0.03	0.03	0.03	0.03	0.04	
NiO	0.11	0.10	0.08	0.09	0.12	0.09	0.09	0.10	0.10	0.08	0.09	0.10	0.10	0.10	0.07	0.08	0.12	0.08	
ZnO	0.04	0.03	0.04	0.07	0.08	0.11	0.08	0.06	0.08	0.08	0.06	0.07	0.06	0.07	0.07	0.07	0.08	0.13	
Total	97.37	97.14	98.39	99.87	99.99	100.50	99.21	99.63	99.11	99.17	98.64	98.57	99.26	99.79	99.99	99.56	99.72	100.87	
Si	0.001	0.001	0.001	0.000	0.000	0.001	0.000	0.000	0.000	0.000	0.000	0.000	0.000	0.000	0.000	0.000	0.000	0.001	
Ti	0.008	0.006	0.004	0.006	0.007	0.006	0.007	0.007	0.007	0.006	0.008	0.008	0.008	0.008	0.004	0.003	0.007	0.006	
Al	0.323	0.267	0.491	0.627	0.664	0.613	0.466	0.404	0.424	0.363	0.356	0.381	0.347	0.353	0.510	0.489	0.664	0.485	
Cr	1.680	1.739	1.510	1.331	1.282	1.344	1.493	1.535	1.516	1.597	1.624	1.601	1.587	1.573	1.442	1.466	1.280	1.436	
Fe <sup>3+</sup>	0.000	0.000	0.000	0.026	0.036	0.025	0.024	0.043	0.042	0.023	0.000	0.000	0.046	0.054	0.037	0.035	0.038	0.062	
Fe <sup>2+</sup>	0.509	0.558	0.371	0.314	0.298	0.365	0.364	0.377	0.371	0.384	0.459	0.425	0.395	0.383	0.336	0.337	0.301	0.404	
Mn	0.006	0.007	0.005	0.004	0.004	0.005	0.005	0.006	0.005	0.006	0.006	0.005	0.006	0.006	0.005	0.005	0.004	0.006	
Mg	0.452	0.403	0.605	0.684	0.700	0.631	0.633	0.620	0.626	0.613	0.538	0.569	0.602	0.614	0.660	0.657	0.697	0.590	
V	0.004	0.003	0.002	0.003	0.003	0.003	0.004	0.004	0.004	0.004	0.004	0.004	0.004	0.004	0.003	0.003	0.003	0.004	
Co	0.001	0.001	0.001	0.001	0.001	0.001	0.001	0.001	0.001	0.001	0.001	0.001	0.001	0.001	0.001	0.001	0.001	0.001	
Ni	0.003	0.003	0.002	0.002	0.003	0.002	0.002	0.003	0.003	0.002	0.003	0.003	0.003	0.003	0.002	0.002	0.003	0.002	
Zn	0.001	0.001	0.001	0.002	0.002	0.002	0.002	0.001	0.002	0.002	0.001	0.002	0.001	0.002	0.002	0.002	0.002	0.003	
Total	2.988	2.988	2.993	3.000	3.000	3.000	3.000	3.000	3.000	3.000	3.000	2.999	3.000	3.000	3.000	3.000	3.000	3.000	

Cr/(Cr+Al)	0.839	0.867	0.755	0.680	0.659	0.687	0.762	0.792	0.781	0.815	0.820	0.808	0.821	0.817	0.739	0.750	0.658	0.748
Fe <sup>3+</sup> /(Fe <sup>3+</sup> +Cr+Al)	0.000	0.000	0.000	0.075	0.108	0.065	0.061	0.103	0.101	0.057	0.001	0.000	0.104	0.123	0.099	0.093	0.113	0.133
Mg/(Mg+Fe <sup>2+</sup> )	0.471	0.419	0.620	0.686	0.701	0.634	0.634	0.622	0.628	0.615	0.540	0.572	0.604	0.616	0.663	0.661	0.698	0.594

Table 6.S2 (Continued)

Sample No.	IM-1B									O3							
Analysis No.	E2	F1	F2	B4	A6	D1	D2	D3	F3	A3	A4	B3	B4	A1	A2	B1	B2
	Heterogeneous rim			Homogeneous Core (spl II)						Homogeneous core				Heterogeneous rim			
SiO <sub>2</sub>	0.02	0.01	0.01	0.01	0.01	0.02	0.01	0.02	0.01	0.02	0.02	0.01	0.01	0.02	0.01	0.02	0.01
TiO <sub>2</sub>	0.20	0.30	0.34	0.14	0.15	0.24	0.30	0.20	0.28	0.11	0.11	0.11	0.11	0.10	0.10	0.11	0.11
V <sub>2</sub> O <sub>3</sub>	0.12	0.15	0.15	0.12	0.12	0.14	0.15	0.12	0.12	0.07	0.07	0.06	0.07	0.07	0.07	0.07	0.07
Cr <sub>2</sub> O <sub>3</sub>	58.75	61.24	60.10	58.17	58.59	61.69	60.88	57.15	56.85	60.79	61.08	60.45	60.79	59.18	59.80	59.61	59.22
MgO	12.27	12.02	12.78	13.81	13.65	12.50	11.97	14.17	13.95	13.40	14.24	12.98	13.65	9.47	9.98	10.76	9.59
Al <sub>2</sub> O <sub>3</sub>	12.42	9.03	10.18	13.10	12.87	9.28	9.68	14.17	14.42	9.70	9.72	9.60	9.61	9.45	9.65	9.39	9.47
Mno	0.23	0.20	0.19	0.19	0.17	0.17	0.19	0.18	0.17	0.21	0.17	0.21	0.18	0.33	0.30	0.27	0.32
FeO	16.17	15.48	15.83	14.01	13.79	15.11	15.90	13.58	13.74	14.79	13.54	15.36	14.25	20.31	18.84	18.31	20.22
CoO	0.04	0.03	0.03	0.03	0.03	0.03	0.03	0.03	0.02	0.03	0.03	0.03	0.02	0.05	0.05	0.04	0.05
NiO	0.05	0.08	0.11	0.08	0.08	0.09	0.10	0.10	0.10	0.17	0.16	0.13	0.16	0.03	0.03	0.12	0.05
ZnO	0.11	0.06	0.06	0.06	0.06	0.06	0.08	0.06	0.08	0.05	0.04	0.06	0.05	0.17	0.16	0.10	0.18
Total	100.39	98.61	99.78	99.73	99.52	99.32	99.28	99.77	99.74	99.33	99.17	99.00	98.91	99.18	98.99	98.79	99.28
Si	0.001	0.000	0.000	0.000	0.000	0.001	0.000	0.001	0.000	0.001	0.001	0.000	0.000	0.001	0.000	0.001	0.000
Ti	0.005	0.007	0.008	0.003	0.003	0.006	0.008	0.005	0.007	0.003	0.003	0.003	0.003	0.003	0.003	0.003	0.003
Al	0.470	0.353	0.389	0.492	0.485	0.358	0.375	0.528	0.538	0.371	0.370	0.370	0.369	0.373	0.380	0.368	0.373
Cr	1.490	1.603	1.541	1.464	1.480	1.598	1.580	1.428	1.422	1.561	1.562	1.562	1.565	1.566	1.579	1.569	1.564
Fe <sup>3+</sup>	0.026	0.025	0.049	0.034	0.024	0.027	0.025	0.030	0.024	0.060	0.060	0.061	0.059	0.053	0.034	0.054	0.055
Fe <sup>2+</sup>	0.407	0.404	0.380	0.339	0.345	0.387	0.411	0.329	0.340	0.342	0.306	0.359	0.329	0.515	0.492	0.455	0.509
Mn	0.006	0.006	0.005	0.005	0.005	0.005	0.005	0.005	0.005	0.006	0.005	0.006	0.005	0.009	0.009	0.008	0.009
Mg	0.587	0.594	0.618	0.655	0.651	0.610	0.586	0.668	0.658	0.649	0.687	0.633	0.663	0.472	0.496	0.534	0.477
V	0.003	0.004	0.004	0.003	0.003	0.004	0.004	0.003	0.003	0.002	0.002	0.002	0.002	0.002	0.002	0.002	0.002
Co	0.001	0.001	0.001	0.001	0.001	0.001	0.001	0.001	0.001	0.001	0.001	0.001	0.001	0.001	0.001	0.001	0.001
Ni	0.001	0.002	0.003	0.002	0.002	0.002	0.003	0.002	0.002	0.004	0.004	0.003	0.004	0.001	0.001	0.003	0.001
Zn	0.003	0.002	0.002	0.001	0.001	0.002	0.002	0.001	0.002	0.001	0.001	0.001	0.001	0.004	0.004	0.002	0.005
Total	3.000	3.000	3.000	3.000	3.000	3.000	3.000	3.000	3.000	3.000	3.000	3.000	3.000	3.000	3.000	3.000	3.000

Cr/(Cr+Al)	0.760	0.820	0.798	0.749	0.753	0.817	0.808	0.730	0.726	0.808	0.808	0.809	0.809	0.808	0.806	0.810	0.808
Fe <sup>3+</sup> /(Fe <sup>3+</sup> +Cr+Al)	0.061	0.057	0.114	0.091	0.065	0.065	0.058	0.085	0.065	0.149	0.164	0.145	0.152	0.094	0.064	0.106	0.098
Mg/(Mg+Fe <sup>2+</sup> )	0.590	0.595	0.619	0.659	0.654	0.612	0.588	0.670	0.659	0.655	0.692	0.638	0.668	0.478	0.502	0.540	0.484

Table 6.S2 (Continued)

Sample No.	O3			O27																
Analysis No.	B5	B6	B7	A1	A6	A7	D2	A2	A3	A4	A5	A8	A9	A10	C1	C2	C3	C4	C5	
	Heterogeneous rim			Homogeneous core				Heterogeneous rim												
SiO <sub>2</sub>	0.00	0.01	0.02	0.02	0.01	0.01	0.03	0.01	0.00	0.02	0.08	0.00	0.01	0.17	0.02	0.02	0.37	0.02	0.02	
TiO <sub>2</sub>	0.07	0.08	0.11	0.12	0.12	0.12	0.12	0.07	0.05	0.10	0.01	0.06	0.05	0.02	0.06	0.05	0.05	0.05	0.03	
V <sub>2</sub> O <sub>3</sub>	0.05	0.05	0.07	0.07	0.07	0.07	0.07	0.08	0.13	0.07	0.03	0.08	0.13	0.04	0.14	0.13	0.09	0.08	0.08	
Cr <sub>2</sub> O <sub>3</sub>	64.82	63.63	61.12	60.51	60.53	60.11	60.14	61.06	58.23	60.21	7.13	47.77	59.26	19.01	60.24	60.24	47.70	61.16	61.96	
MgO	11.86	11.94	14.43	8.84	8.88	8.30	8.63	6.96	2.90	7.41	1.43	2.74	3.25	2.37	2.30	3.48	2.09	6.13	5.32	
Al <sub>2</sub> O <sub>3</sub>	5.99	6.48	9.77	8.10	8.13	8.14	8.17	6.06	0.49	7.00	0.21	0.25	1.25	1.91	0.47	0.72	0.25	5.98	5.12	
Mno	0.37	0.27	0.16	0.32	0.31	0.34	0.32	0.41	0.68	0.38	0.17	0.84	0.67	0.31	0.62	0.75	0.80	0.42	0.46	
FeO	15.12	17.27	12.90	20.99	21.00	22.13	20.88	24.35	35.00	23.71	85.58	43.58	33.04	70.45	32.78	32.80	41.67	25.35	26.01	
CoO	0.05	0.04	0.02	0.06	0.05	0.06	0.06	0.07	0.07	0.06	0.04	0.08	0.07	0.06	0.08	0.08	0.09	0.07	0.07	
NiO	0.02	0.04	0.17	0.03	0.04	0.03	0.05	0.02	0.05	0.03	1.06	0.22	0.04	1.41	0.05	0.05	0.42	0.02	0.00	
ZnO	0.15	0.12	0.04	0.15	0.15	0.18	0.16	0.19	0.24	0.18	0.00	0.20	0.26	0.08	0.25	0.26	0.20	0.22	0.27	
Total	98.49	99.93	98.81	99.21	99.29	99.48	98.63	99.28	97.82	99.18	95.73	95.81	98.03	95.84	96.99	98.58	93.72	99.51	99.36	
Si	0.000	0.000	0.001	0.001	0.000	0.000	0.001	0.000	0.000	0.001	0.003	0.000	0.000	0.006	0.001	0.001	0.014	0.001	0.001	
Ti	0.002	0.002	0.003	0.003	0.003	0.003	0.003	0.002	0.001	0.003	0.000	0.002	0.001	0.001	0.002	0.001	0.001	0.001	0.001	
Al	0.237	0.253	0.373	0.323	0.324	0.325	0.328	0.247	0.021	0.283	0.009	0.011	0.054	0.083	0.021	0.031	0.012	0.245	0.212	
Cr	1.724	1.664	1.565	1.617	1.616	1.608	1.618	1.668	1.701	1.634	0.209	1.420	1.718	0.554	1.786	1.738	1.456	1.678	1.720	
Fe <sup>3+</sup>	0.034	0.077	0.053	0.051	0.052	0.058	0.044	0.079	0.271	0.074	1.774	0.563	0.221	1.349	0.185	0.223	0.498	0.071	0.063	
Fe <sup>2+</sup>	0.391	0.400	0.297	0.542	0.541	0.568	0.550	0.624	0.811	0.606	0.885	0.807	0.793	0.821	0.843	0.779	0.848	0.664	0.700	
Mn	0.011	0.008	0.004	0.009	0.009	0.010	0.009	0.012	0.021	0.011	0.005	0.027	0.021	0.010	0.020	0.023	0.026	0.012	0.014	
Mg	0.594	0.589	0.697	0.446	0.447	0.419	0.438	0.358	0.159	0.379	0.079	0.154	0.178	0.130	0.128	0.189	0.120	0.317	0.278	
V	0.001	0.001	0.002	0.002	0.002	0.002	0.002	0.002	0.004	0.002	0.001	0.002	0.004	0.001	0.004	0.004	0.003	0.002	0.002	
Co	0.001	0.001	0.000	0.002	0.001	0.002	0.002	0.002	0.002	0.002	0.001	0.002	0.002	0.002	0.003	0.002	0.003	0.002	0.002	
Ni	0.001	0.001	0.004	0.001	0.001	0.001	0.001	0.001	0.001	0.001	0.032	0.007	0.001	0.042	0.001	0.002	0.013	0.001	0.000	
Zn	0.004	0.003	0.001	0.004	0.004	0.005	0.004	0.005	0.006	0.004	0.000	0.006	0.007	0.002	0.007	0.007	0.006	0.006	0.007	
Total	3.000	3.000	3.000	3.000	3.000	3.000	3.000	3.000	3.000	3.000	3.000	3.000	3.000	3.000	3.000	3.000	3.000	3.000	3.000	

Cr/(Cr+Al)	0.879	0.868	0.808	0.834	0.833	0.832	0.832	0.871	0.988	0.852	0.959	0.992	0.970	0.870	0.989	0.983	0.992	0.873	0.890
Fe <sup>3+</sup> /(Fe <sup>3+</sup> +Cr+Al)	0.081	0.162	0.152	0.086	0.088	0.093	0.074	0.112	0.251	0.109	0.667	0.411	0.218	0.622	0.180	0.222	0.370	0.097	0.083
Mg/(Mg+Fe <sup>2+</sup> )	0.603	0.595	0.701	0.451	0.452	0.424	0.443	0.365	0.164	0.385	0.082	0.160	0.183	0.137	0.132	0.196	0.124	0.323	0.285

Table 6.S2 (Continued)

Sample No.	HA2-1														KA3-1C			
Analysis No.	A1	A5	B1	C4	C6	A2	A3	A4	B2	B3	C1	C2	C3	C5	A1	A3	B1	A2
	Homogeneous core					Heterogeneous rim									Homogeneous core			Heter rim
SiO <sub>2</sub>	0.02	0.02	0.03	0.02	0.09	0.08	0.25	0.07	0.02	0.01	0.01	0.01	0.01	0.01	0.03	0.04	0.02	0.03
TiO <sub>2</sub>	0.16	0.16	0.16	0.16	0.16	0.18	0.18	0.16	0.17	0.20	0.17	0.20	0.22	0.18	0.20	0.16	0.21	0.23
V <sub>2</sub> O <sub>3</sub>	0.08	0.08	0.08	0.08	0.08	0.09	0.08	0.08	0.09	0.08	0.08	0.09	0.09	0.08	0.09	0.09	0.09	0.10
Cr <sub>2</sub> O <sub>3</sub>	55.96	56.04	55.80	56.25	55.98	59.63	56.92	58.05	58.09	57.82	57.08	56.07	55.65	57.92	52.79	56.26	52.58	56.64
MgO	14.88	14.69	14.43	14.45	14.50	13.07	12.11	13.17	12.42	12.58	11.36	11.64	11.86	11.68	14.83	14.13	14.58	11.79
Al <sub>2</sub> O <sub>3</sub>	13.33	13.24	13.58	13.39	13.38	4.68	4.00	4.96	5.63	5.59	4.16	4.39	4.09	4.48	17.78	15.49	17.33	5.93
Mno	0.15	0.14	0.15	0.15	0.15	0.28	0.31	0.19	0.21	0.20	0.24	0.25	0.24	0.22	0.17	0.17	0.16	0.28
FeO	14.59	14.80	15.07	15.04	15.27	20.02	22.69	21.39	21.72	21.96	25.56	25.81	26.19	23.77	14.42	14.06	14.92	24.18
CoO	0.03	0.02	0.03	0.03	0.02	0.04	0.03	0.03	0.03	0.03	0.03	0.03	0.03	0.03	0.02	0.03	0.03	0.03
NiO	0.12	0.12	0.10	0.10	0.10	0.15	0.20	0.19	0.12	0.17	0.15	0.21	0.30	0.15	0.11	0.08	0.12	0.21
ZnO	0.03	0.04	0.05	0.05	0.05	0.05	0.05	0.06	0.06	0.05	0.04	0.05	0.06	0.05	0.04	0.04	0.03	0.04
Total	99.35	99.36	99.48	99.72	99.79	98.27	96.82	98.35	98.57	98.67	98.87	98.74	98.73	98.56	100.50	100.54	100.07	99.45
Si	0.001	0.001	0.001	0.001	0.003	0.003	0.009	0.002	0.001	0.000	0.000	0.000	0.000	0.000	0.001	0.001	0.001	0.001
Ti	0.004	0.004	0.004	0.004	0.004	0.005	0.005	0.004	0.004	0.005	0.004	0.005	0.005	0.005	0.005	0.004	0.005	0.006
Al	0.497	0.495	0.507	0.499	0.498	0.185	0.161	0.195	0.222	0.220	0.165	0.174	0.162	0.178	0.646	0.570	0.633	0.232
Cr	1.400	1.404	1.397	1.407	1.398	1.578	1.540	1.532	1.534	1.524	1.523	1.492	1.480	1.545	1.285	1.389	1.289	1.488
Fe <sup>3+</sup>	0.092	0.090	0.084	0.083	0.088	0.220	0.270	0.259	0.232	0.244	0.300	0.320	0.344	0.265	0.055	0.028	0.064	0.264
Fe <sup>2+</sup>	0.294	0.302	0.315	0.315	0.315	0.340	0.379	0.338	0.375	0.368	0.421	0.406	0.393	0.406	0.316	0.339	0.323	0.408
Mn	0.004	0.004	0.004	0.004	0.004	0.008	0.009	0.005	0.006	0.006	0.007	0.007	0.007	0.006	0.004	0.004	0.004	0.008
Mg	0.702	0.694	0.681	0.681	0.683	0.653	0.618	0.655	0.618	0.625	0.571	0.584	0.595	0.587	0.681	0.658	0.674	0.584
V	0.002	0.002	0.002	0.002	0.002	0.002	0.002	0.002	0.002	0.002	0.002	0.002	0.002	0.002	0.002	0.002	0.002	0.003
Co	0.001	0.001	0.001	0.001	0.001	0.001	0.001	0.001	0.001	0.001	0.001	0.001	0.001	0.001	0.001	0.001	0.001	0.001
Ni	0.003	0.003	0.003	0.003	0.003	0.004	0.005	0.005	0.003	0.004	0.004	0.006	0.008	0.004	0.003	0.002	0.003	0.005
Zn	0.001	0.001	0.001	0.001	0.001	0.001	0.001	0.002	0.002	0.001	0.001	0.001	0.002	0.001	0.001	0.001	0.001	0.001
Total	3.000	3.000	3.000	3.000	3.000	3.000	3.000	3.000	3.000	3.000	3.000	3.000	3.000	3.000	3.000	3.000	3.000	3.000

Cr/(Cr+Al)	0.738	0.740	0.734	0.738	0.737	0.895	0.905	0.887	0.874	0.874	0.902	0.895	0.901	0.897	0.666	0.709	0.671	0.865
Fe <sup>3+</sup> /(Fe <sup>3+</sup> +Cr+Al)	0.239	0.230	0.211	0.209	0.219	0.393	0.416	0.433	0.382	0.398	0.416	0.441	0.466	0.395	0.149	0.077	0.166	0.393
Mg/(Mg+Fe <sup>2+</sup> )	0.705	0.697	0.684	0.684	0.684	0.657	0.620	0.659	0.622	0.629	0.576	0.590	0.602	0.591	0.683	0.660	0.676	0.589

Table 6.S2 (Continued)

Sample No. Analysis No.	KA3-1C		EB-4						
	B2	B3	B7	C4	B6	B8	C3	C1	C2
			Homogeneous core		Porous rim				
SiO <sub>2</sub>	0.07	0.03	0.02	0.02	0.02	0.01	0.00	0.00	0.00
TiO <sub>2</sub>	0.27	0.28	0.15	0.14	0.18	0.15	0.17	0.15	0.17
V <sub>2</sub> O <sub>3</sub>	0.10	0.11	0.12	0.12	0.12	0.11	0.12	0.13	0.12
Cr <sub>2</sub> O <sub>3</sub>	57.50	59.93	53.24	53.67	53.03	48.71	53.36	54.22	55.61
MgO	12.42	12.18	12.91	13.13	9.62	8.82	9.29	11.66	10.77
Al <sub>2</sub> O <sub>3</sub>	6.70	9.70	15.35	15.18	2.45	1.35	2.82	11.45	9.27
Mno	0.22	0.22	0.16	0.15	0.26	0.28	0.27	0.19	0.22
FeO	21.59	17.19	18.19	17.14	32.77	38.03	31.85	21.55	23.35
CoO	0.03	0.03	0.04	0.04	0.05	0.05	0.06	0.05	0.04
NiO	0.07	0.07	0.12	0.14	0.28	0.43	0.27	0.12	0.13
ZnO	0.03	0.04	0.05	0.05	0.07	0.06	0.06	0.05	0.06
Total	99.00	99.76	100.36	99.78	98.86	97.99	98.26	99.58	99.74
Si	0.002	0.001	0.001	0.000	0.001	0.000	0.000	0.000	0.000
Ti	0.007	0.007	0.003	0.003	0.005	0.004	0.004	0.004	0.004
Al	0.262	0.373	0.570	0.566	0.099	0.055	0.115	0.439	0.360
Cr	1.506	1.546	1.327	1.343	1.440	1.344	1.459	1.393	1.448
Fe <sup>3+</sup>	0.212	0.063	0.092	0.079	0.447	0.589	0.414	0.157	0.180
Fe <sup>2+</sup>	0.386	0.406	0.388	0.375	0.494	0.522	0.507	0.428	0.464
Mn	0.006	0.006	0.004	0.004	0.008	0.008	0.008	0.005	0.006
Mg	0.613	0.592	0.607	0.620	0.493	0.459	0.479	0.565	0.529
V	0.003	0.003	0.003	0.003	0.003	0.003	0.003	0.003	0.003
Co	0.001	0.001	0.001	0.001	0.001	0.001	0.002	0.001	0.001
Ni	0.002	0.002	0.003	0.004	0.008	0.012	0.007	0.003	0.003
Zn	0.001	0.001	0.001	0.001	0.002	0.001	0.002	0.001	0.001
Total	3.000	3.000	3.000	3.000	3.000	3.000	3.000	3.000	3.000

Cr/(Cr+Al)	0.852	0.806	0.699	0.703	0.935	0.960	0.927	0.761	0.801
Fe <sup>3+</sup> /(Fe <sup>3+</sup> +Cr+Al)	0.354	0.134	0.191	0.175	0.475	0.530	0.450	0.269	0.279
Mg/(Mg+Fe <sup>2+</sup> )	0.614	0.593	0.610	0.623	0.499	0.468	0.486	0.569	0.533

Table 6.S3. Representative analyses of spinels from the studied serpentized dunite aureoles in the Sabzevar ophiolite

Sample No.	IM-2												O26				
Analysis No.	A2	2A-A2	B1I	A3	A4	A5	2A-B1I	A1	B1	B2	B3	2A-A1	2A-A3	2A-C1	2A-C2	A1	A2
	Homogeneous core			Porous				Heterogeneous rim								Homogeneous core	
SiO <sub>2</sub>	0.05	0.02	0.01	0.14	0.09	0.09	0.01	32.88	0.58	0.05	0.06	0.04	0.03	0.02	0.06	0.02	0.02
TiO <sub>2</sub>	0.10	0.14	0.14	0.03	0.11	0.13	0.29	0.01	0.06	0.12	0.09	0.36	0.18	0.14	0.31	0.04	0.04
V <sub>2</sub> O <sub>3</sub>	0.16	0.12	0.12	0.03	0.18	0.20	0.13	0.02	0.02	0.21	0.15	0.24	0.19	0.13	0.21	0.19	0.19
Cr <sub>2</sub> O <sub>3</sub>	44.85	52.61	50.15	7.87	46.30	47.26	44.09	1.84	0.95	47.41	44.01	45.87	51.75	51.36	46.52	44.52	44.32
MgO	9.71	11.60	10.58	0.91	7.05	5.85	4.34	28.32	0.92	8.60	9.24	3.30	3.22	11.24	4.09	12.93	12.71
Al <sub>2</sub> O <sub>3</sub>	16.10	14.84	16.16	0.50	12.28	10.07	6.34	12.17	0.07	15.51	15.34	0.96	1.16	15.65	2.39	24.54	24.53
Mno	0.27	0.21	0.23	0.78	0.41	0.44	0.45	0.01	0.28	0.36	0.27	0.65	0.74	0.24	0.74	0.22	0.22
FeO	27.28	19.89	21.84	84.76	32.07	31.97	41.88	3.43	88.43	27.62	29.04	44.48	39.68	21.03	43.25	17.53	18.31
CoO	0.05	0.04	0.05	0.07	0.07	0.06	0.07	0.00	0.05	0.06	0.06	0.07	0.08	0.05	0.08	0.06	0.06
NiO	0.14	0.08	0.08	0.14	0.11	0.11	0.23	0.19	0.87	0.09	0.16	0.19	0.11	0.08	0.17	0.08	0.08
ZnO	0.14	0.09	0.15	0.02	0.21	0.17	0.13	0.00	0.00	0.15	0.12	0.10	0.15	0.12	0.14	0.20	0.20
Total	98.84	99.64	99.52	95.24	98.90	96.36	97.96	78.87	92.22	100.17	98.52	96.28	97.28	100.05	97.96	100.32	100.67
Si	0.002	0.001	0.000	0.005	0.003	0.003	0.000	0.976	0.022	0.002	0.002	0.002	0.001	0.001	0.002	0.001	0.001
Ti	0.002	0.003	0.003	0.001	0.003	0.003	0.008	0.000	0.002	0.003	0.002	0.010	0.005	0.003	0.008	0.001	0.001
Al	0.616	0.561	0.612	0.022	0.486	0.416	0.264	0.426	0.003	0.593	0.592	0.042	0.050	0.589	0.101	0.879	0.877
Cr	1.150	1.333	1.274	0.233	1.229	1.308	1.232	0.043	0.029	1.215	1.139	1.346	1.507	1.296	1.325	1.070	1.063
Fe <sup>3+</sup>	0.222	0.095	0.103	1.732	0.269	0.257	0.484	0.000	1.919	0.177	0.258	0.582	0.425	0.104	0.546	0.043	0.052
Fe <sup>2+</sup>	0.519	0.439	0.484	0.924	0.631	0.679	0.754	0.085	0.933	0.572	0.537	0.798	0.797	0.457	0.757	0.402	0.413
Mn	0.007	0.006	0.006	0.025	0.012	0.013	0.013	0.000	0.009	0.010	0.007	0.020	0.023	0.006	0.022	0.006	0.006
Mg	0.470	0.554	0.507	0.051	0.353	0.305	0.229	1.253	0.053	0.416	0.451	0.183	0.177	0.535	0.220	0.586	0.575
V	0.004	0.003	0.003	0.001	0.005	0.006	0.004	0.001	0.001	0.006	0.004	0.007	0.006	0.003	0.006	0.005	0.005
Co	0.001	0.001	0.001	0.002	0.002	0.002	0.002	0.000	0.002	0.002	0.001	0.002	0.002	0.001	0.002	0.001	0.001
Ni	0.004	0.002	0.002	0.004	0.003	0.003	0.006	0.004	0.027	0.002	0.004	0.006	0.003	0.002	0.005	0.002	0.002
Zn	0.003	0.002	0.004	0.001	0.005	0.004	0.003	0.000	0.000	0.003	0.003	0.003	0.004	0.003	0.004	0.004	0.004
Total	3.000	3.000	3.000	3.000	3.000	3.000	3.000	2.789	3.000	3.000	3.000	3.000	3.000	3.000	3.000	3.000	3.000

Cr/(Cr+Al)	0.651	0.704	0.676	0.913	0.717	0.759	0.823	0.092	0.906	0.672	0.658	0.970	0.968	0.688	0.929	0.549	0.548
Fe <sup>3+</sup> /(Fe <sup>3+</sup> +Cr+Al)	0.299	0.177	0.176	0.652	0.299	0.275	0.391	0.000	0.673	0.237	0.324	0.422	0.348	0.186	0.419	0.097	0.112
Mg/(Mg+Fe <sup>2+</sup> )	0.475	0.558	0.512	0.052	0.358	0.310	0.233	0.936	0.054	0.421	0.456	0.186	0.182	0.539	0.225	0.593	0.582

Table 6.S3 (Continued)

Sample No.	O26																	O1	
Analysis No.	B2	C1	A3	A4	A5	A6	B3	B4	B5	C2	C3	C4	B6	B7	C5	C6	D12	A1	B1
	Homogeneous core		Homogeneous rim															Homogeneous core (spl II)	
SiO <sub>2</sub>	0.03	0.01	0.01	0.00	1.43	1.03	0.01	0.01	0.01	0.01	0.02	0.02	0.02	0.03	0.86	0.03	0.03	0.02	0.01
TiO <sub>2</sub>	0.05	0.02	0.04	0.03	0.00	0.00	0.03	0.03	0.03	0.04	0.02	0.03	0.00	0.00	0.00	0.00	0.03	0.12	0.12
V <sub>2</sub> O <sub>3</sub>	0.19	0.17	0.17	0.16	0.02	0.03	0.16	0.14	0.14	0.17	0.14	0.14	0.01	0.01	0.01	0.01	0.16	0.08	0.09
Cr <sub>2</sub> O <sub>3</sub>	44.99	43.69	50.90	49.41	4.78	7.98	51.06	51.35	51.32	46.95	52.02	52.21	2.47	2.86	3.83	3.27	48.41	59.56	58.85
MgO	12.59	12.59	9.47	9.43	0.89	0.78	8.76	8.32	8.49	10.21	8.64	8.76	0.01	0.01	0.91	0.05	8.64	7.86	7.49
Al <sub>2</sub> O <sub>3</sub>	23.10	23.65	15.87	15.96	0.07	1.17	14.17	13.42	13.59	18.36	13.19	13.23	0.01	0.00	0.05	0.02	15.45	7.65	7.23
Mno	0.23	0.22	0.31	0.32	1.26	0.05	0.32	0.35	0.34	0.29	0.34	0.33	0.03	0.03	0.04	0.03	0.37	0.37	0.38
FeO	18.02	18.80	23.20	24.44	84.86	82.70	23.84	24.81	24.39	23.11	24.73	24.25	90.51	90.39	87.53	89.38	25.92	23.45	24.42
CoO	0.06	0.06	0.07	0.06	0.07	0.00	0.06	0.06	0.07	0.06	0.06	0.07	0.00	0.00	0.00	0.00	0.07	0.06	0.07
NiO	0.07	0.07	0.06	0.07	0.00	0.00	0.06	0.05	0.04	0.06	0.03	0.05	0.00	0.00	0.00	0.00	0.03	0.05	0.06
ZnO	0.20	0.20	0.20	0.21	0.05	0.00	0.19	0.21	0.22	0.20	0.20	0.19	0.00	0.00	0.00	0.02	0.22	0.16	0.18
Total	99.52	99.50	100.30	100.11	93.44	93.74	98.67	98.77	98.64	99.47	99.39	99.27	93.05	93.33	93.22	92.80	99.32	99.38	98.89
Si	0.001	0.000	0.000	0.000	0.055	0.039	0.000	0.000	0.000	0.000	0.001	0.001	0.001	0.001	0.033	0.001	0.001	0.001	0.000
Ti	0.001	0.001	0.001	0.001	0.000	0.000	0.001	0.001	0.001	0.001	0.001	0.001	0.000	0.000	0.000	0.000	0.001	0.003	0.003
Al	0.840	0.857	0.602	0.606	0.003	0.052	0.552	0.526	0.532	0.691	0.513	0.515	0.000	0.000	0.002	0.001	0.595	0.307	0.293
Cr	1.097	1.063	1.296	1.259	0.144	0.239	1.335	1.349	1.348	1.185	1.358	1.363	0.075	0.087	0.116	0.100	1.251	1.603	1.598
Fe <sup>3+</sup>	0.055	0.074	0.095	0.129	1.743	1.629	0.107	0.119	0.114	0.117	0.123	0.116	1.923	1.911	1.816	1.897	0.146	0.081	0.100
Fe <sup>2+</sup>	0.410	0.410	0.530	0.530	0.960	0.994	0.552	0.570	0.563	0.500	0.559	0.553	0.999	1.000	0.980	0.996	0.562	0.587	0.601
Mn	0.006	0.006	0.008	0.009	0.041	0.002	0.009	0.010	0.009	0.008	0.010	0.009	0.001	0.001	0.001	0.001	0.010	0.011	0.011
Mg	0.579	0.578	0.455	0.453	0.050	0.044	0.432	0.412	0.420	0.486	0.425	0.431	0.001	0.001	0.052	0.003	0.421	0.399	0.383
V	0.005	0.004	0.004	0.004	0.001	0.001	0.004	0.004	0.004	0.004	0.004	0.004	0.000	0.000	0.000	0.000	0.004	0.002	0.002
Co	0.001	0.001	0.002	0.002	0.002	0.000	0.002	0.002	0.002	0.002	0.002	0.002	0.000	0.000	0.000	0.000	0.002	0.002	0.002
Ni	0.002	0.002	0.002	0.002	0.000	0.000	0.001	0.001	0.001	0.002	0.001	0.001	0.000	0.000	0.000	0.000	0.001	0.001	0.002
Zn	0.005	0.005	0.005	0.005	0.001	0.000	0.005	0.005	0.005	0.005	0.005	0.005	0.000	0.000	0.000	0.001	0.005	0.004	0.005
Total	3.000	3.000	3.000	3.000	3.000	3.000	3.000	3.000	3.000	3.000	3.000	3.000	3.000	3.000	3.000	3.000	3.000	3.000	3.000

Cr/(Cr+Al)	0.566	0.553	0.683	0.675	0.977	0.821	0.707	0.720	0.717	0.632	0.726	0.726	0.995	1.000	0.983	0.992	0.678	0.839	0.845
Fe <sup>3+</sup> /(Fe <sup>3+</sup> +Cr+Al)	0.118	0.153	0.151	0.195	0.645	0.621	0.162	0.173	0.169	0.190	0.181	0.174	0.658	0.657	0.650	0.656	0.206	0.121	0.143
Mg/(Mg+Fe <sup>2+</sup> )	0.585	0.585	0.462	0.461	0.050	0.042	0.439	0.420	0.428	0.493	0.432	0.438	0.001	0.001	0.050	0.003	0.428	0.405	0.389

Table 6.S3 (Continued)

Sample No.	O1						KE-3					EB-5A								
Analysis No.	B4	B5	A2	A3	B2	B3	A1	B1	A2	A3	A4	A6	B1	B7	C3	D3	A1	A2	A3	
	Heterogeneous rim						Homogeneous core		Heterogeneous rim			Homogeneous core					Heterogeneous rim			
SiO <sub>2</sub>	0.11	3.63	0.03	0.03	0.02	0.03	0.02	0.02	0.02	0.02	0.02	0.03	0.02	0.03	0.03	0.02	0.02	0.02	0.02	0.02
TiO <sub>2</sub>	0.00	0.00	0.15	0.01	0.11	0.13	0.18	0.18	0.29	0.25	0.29	0.17	0.17	0.17	0.17	0.16	0.07	0.07	0.17	
V <sub>2</sub> O <sub>3</sub>	0.00	0.00	0.13	0.00	0.12	0.12	0.11	0.11	0.15	0.14	0.16	0.12	0.12	0.12	0.12	0.13	0.17	0.18	0.14	
Cr <sub>2</sub> O <sub>3</sub>	1.02	0.80	58.27	0.66	58.98	58.30	50.92	51.61	50.33	54.75	52.10	46.59	47.21	47.44	46.52	46.52	50.15	49.51	49.17	
MgO	0.74	15.54	3.52	0.70	3.28	3.91	9.31	9.38	6.38	5.63	6.74	12.35	12.18	12.43	12.10	12.32	9.91	10.19	8.48	
Al <sub>2</sub> O <sub>3</sub>	0.00	0.02	0.91	0.00	1.48	1.32	13.79	13.89	9.05	7.73	9.68	19.58	19.21	19.02	19.57	19.30	13.28	13.54	9.21	
Mno	0.10	0.11	0.64	0.08	0.66	0.54	0.29	0.28	0.44	0.46	0.41	0.19	0.18	0.17	0.20	0.18	0.24	0.22	0.25	
FeO	87.82	64.56	33.76	88.82	33.10	31.93	25.36	24.73	31.88	30.33	29.06	20.05	20.31	19.93	20.77	20.19	24.96	25.47	30.86	
CoO	0.04	0.03	0.07	0.03	0.07	0.06	0.06	0.05	0.07	0.07	0.07	0.05	0.06	0.05	0.07	0.06	0.07	0.07	0.07	
NiO	1.13	0.91	0.06	0.90	0.05	0.06	0.10	0.09	0.09	0.06	0.07	0.10	0.10	0.11	0.11	0.12	0.07	0.09	0.11	
ZnO	0.00	0.00	0.23	0.00	0.24	0.24	0.13	0.13	0.18	0.20	0.17	0.08	0.08	0.07	0.10	0.08	0.10	0.10	0.08	
Total	90.95	85.60	97.76	91.25	98.11	96.64	100.27	100.48	98.88	99.63	98.77	99.33	99.64	99.55	99.74	99.07	99.03	99.45	98.55	
Si	0.004	0.132	0.001	0.001	0.001	0.001	0.001	0.001	0.001	0.001	0.001	0.001	0.001	0.001	0.001	0.001	0.000	0.001	0.001	
Ti	0.000	0.000	0.004	0.000	0.003	0.004	0.004	0.004	0.008	0.006	0.007	0.004	0.004	0.004	0.004	0.004	0.002	0.002	0.004	
Al	0.000	0.001	0.039	0.000	0.064	0.057	0.528	0.531	0.365	0.314	0.389	0.724	0.710	0.703	0.722	0.716	0.513	0.519	0.367	
Cr	0.032	0.023	1.692	0.021	1.706	1.704	1.308	1.323	1.362	1.491	1.406	1.155	1.170	1.176	1.151	1.157	1.300	1.274	1.313	
Fe <sup>3+</sup>	1.960	1.711	0.254	1.977	0.219	0.225	0.151	0.133	0.252	0.178	0.184	0.109	0.108	0.109	0.115	0.116	0.179	0.198	0.307	
Fe <sup>2+</sup>	0.921	0.257	0.783	0.928	0.794	0.763	0.538	0.537	0.661	0.696	0.645	0.417	0.425	0.414	0.428	0.416	0.506	0.495	0.564	
Mn	0.003	0.003	0.020	0.003	0.020	0.017	0.008	0.008	0.013	0.013	0.012	0.005	0.005	0.004	0.005	0.005	0.007	0.006	0.007	
Mg	0.043	0.844	0.193	0.041	0.179	0.215	0.451	0.453	0.325	0.289	0.343	0.577	0.569	0.581	0.564	0.578	0.484	0.494	0.427	
V	0.000	0.000	0.004	0.000	0.003	0.004	0.003	0.003	0.004	0.004	0.004	0.003	0.003	0.003	0.003	0.003	0.005	0.005	0.004	
Co	0.001	0.001	0.002	0.001	0.002	0.002	0.002	0.001	0.002	0.002	0.002	0.001	0.002	0.001	0.002	0.001	0.002	0.002	0.002	
Ni	0.036	0.027	0.002	0.028	0.001	0.002	0.003	0.002	0.003	0.002	0.002	0.003	0.002	0.003	0.003	0.003	0.002	0.002	0.003	
Zn	0.000	0.000	0.006	0.000	0.007	0.006	0.003	0.003	0.005	0.005	0.004	0.002	0.002	0.002	0.002	0.002	0.002	0.002	0.002	
Total	3.000	3.000	3.000	3.000	3.000	3.000	3.000	3.000	3.000	3.000	3.000	3.000	3.000	3.000	3.000	3.000	3.000	3.000	3.000	

Cr/(Cr+Al)	1.000	0.966	0.977	1.000	0.964	0.967	0.712	0.714	0.789	0.826	0.783	0.615	0.622	0.626	0.615	0.618	0.717	0.710	0.782
Fe <sup>3+</sup> /(Fe <sup>3+</sup> +Cr+Al)	0.680	0.869	0.245	0.680	0.216	0.228	0.219	0.199	0.276	0.203	0.222	0.207	0.203	0.208	0.212	0.218	0.261	0.285	0.353
Mg/(Mg+Fe <sup>2+</sup> )	0.045	0.767	0.197	0.042	0.184	0.220	0.456	0.457	0.330	0.293	0.347	0.581	0.573	0.584	0.569	0.582	0.489	0.499	0.431

Table 6.S3 (Continued)

Sample No.	EB-5A															KA3-5		
Analysis No.	A4	A5	B2	B3	B4	B5	B6	C1	C2	D1	D2	D4	D5	D6	E1	A1	B2	C1
	Heterogeneous rim		Porous													Homogeneous core		
SiO <sub>2</sub>	0.02	0.03	0.02	0.03	0.06	0.02	0.02	0.02	0.02	0.01	0.02	0.07	0.02	0.02	0.04	0.02	0.04	0.03
TiO <sub>2</sub>	0.19	0.16	0.30	0.24	0.20	0.35	0.23	0.05	0.18	0.27	0.24	0.01	0.22	0.12	0.15	0.13	0.13	0.13
V <sub>2</sub> O <sub>3</sub>	0.26	0.08	0.09	0.08	0.19	0.20	0.20	0.04	0.21	0.06	0.06	0.00	0.19	0.18	0.16	0.15	0.17	0.15
Cr <sub>2</sub> O <sub>3</sub>	46.05	22.59	22.29	21.29	50.91	49.15	48.79	18.55	45.69	21.75	27.67	0.78	46.21	54.33	47.84	47.01	46.25	48.18
MgO	8.53	2.03	1.96	1.76	7.03	6.85	8.81	0.96	8.57	1.76	2.19	0.53	8.21	7.78	7.08	12.93	11.54	12.77
Al <sub>2</sub> O <sub>3</sub>	10.18	1.32	0.09	0.19	8.44	6.39	10.49	1.01	10.61	0.06	0.11	0.01	10.66	8.97	9.87	18.47	17.59	17.80
Mno	0.26	0.21	0.26	0.25	0.26	0.27	0.21	1.21	0.24	0.25	0.34	0.09	0.24	0.24	0.29	0.21	0.23	0.20
FeO	32.51	66.50	68.42	68.87	29.32	34.77	29.22	72.29	32.40	69.03	62.82	89.62	32.42	27.20	32.67	20.74	23.30	20.80
CoO	0.06	0.05	0.05	0.05	0.06	0.06	0.07	0.10	0.06	0.05	0.06	0.05	0.07	0.07	0.08	0.04	0.05	0.04
NiO	0.18	1.01	1.00	1.01	0.10	0.15	0.12	0.04	0.16	1.35	1.18	0.40	0.16	0.07	0.13	0.13	0.14	0.14
ZnO	0.08	0.02	0.02	0.02	0.09	0.07	0.08	0.09	0.09	0.00	0.02	0.00	0.08	0.08	0.08	0.09	0.11	0.09
Total	98.33	94.01	94.50	93.78	96.68	98.27	98.25	94.35	98.22	94.58	94.70	91.55	98.47	99.06	98.40	99.93	99.56	100.32
Si	0.001	0.001	0.001	0.001	0.002	0.001	0.001	0.001	0.001	0.000	0.001	0.003	0.001	0.001	0.002	0.001	0.001	0.001
Ti	0.005	0.005	0.009	0.007	0.005	0.009	0.006	0.001	0.004	0.008	0.007	0.000	0.006	0.003	0.004	0.003	0.003	0.003
Al	0.404	0.059	0.004	0.008	0.347	0.261	0.415	0.045	0.420	0.003	0.005	0.000	0.422	0.358	0.396	0.679	0.657	0.655
Cr	1.225	0.676	0.667	0.642	1.404	1.347	1.297	0.557	1.214	0.651	0.827	0.024	1.228	1.456	1.288	1.159	1.158	1.189
Fe <sup>3+</sup>	0.354	1.252	1.308	1.331	0.228	0.368	0.269	1.393	0.350	1.328	1.151	1.969	0.332	0.173	0.301	0.150	0.172	0.145
Fe <sup>2+</sup>	0.561	0.852	0.858	0.867	0.627	0.640	0.552	0.902	0.561	0.858	0.835	0.956	0.580	0.598	0.630	0.391	0.446	0.398
Mn	0.008	0.007	0.008	0.008	0.008	0.008	0.006	0.039	0.007	0.008	0.011	0.003	0.007	0.007	0.008	0.005	0.006	0.005
Mg	0.428	0.115	0.110	0.100	0.365	0.354	0.442	0.054	0.429	0.099	0.123	0.031	0.411	0.393	0.360	0.601	0.545	0.594
V	0.007	0.002	0.003	0.002	0.005	0.006	0.005	0.001	0.006	0.002	0.002	0.000	0.005	0.005	0.004	0.004	0.004	0.004
Co	0.002	0.002	0.002	0.001	0.002	0.002	0.002	0.003	0.002	0.001	0.002	0.001	0.002	0.002	0.002	0.001	0.001	0.001
Ni	0.005	0.031	0.030	0.031	0.003	0.004	0.003	0.001	0.004	0.041	0.036	0.012	0.004	0.002	0.003	0.003	0.004	0.003
Zn	0.002	0.001	0.001	0.001	0.002	0.002	0.002	0.003	0.002	0.000	0.001	0.000	0.002	0.002	0.002	0.002	0.003	0.002
Total	3.000	3.000	3.000	3.000	3.000	3.000	3.000	3.000	3.000	3.000	3.000	3.000	3.000	3.000	3.000	3.000	3.000	3.000

Cr/(Cr+Al)	0.752	0.920	0.994	0.987	0.802	0.838	0.757	0.925	0.743	0.996	0.994	0.984	0.744	0.802	0.765	0.631	0.638	0.645
Fe <sup>3+</sup> /(Fe <sup>3+</sup> +Cr+Al)	0.386	0.595	0.604	0.606	0.267	0.365	0.328	0.607	0.384	0.608	0.580	0.673	0.364	0.225	0.323	0.277	0.278	0.267
Mg/(Mg+Fe <sup>2+</sup> )	0.433	0.119	0.114	0.104	0.368	0.356	0.444	0.057	0.434	0.104	0.129	0.031	0.415	0.397	0.364	0.606	0.550	0.599

Table 6.S3 (Continued)

Sample No.	KA3-5						
Analysis No.	A2	A3	B1	B3	B4	C2	C3
Heterogeneous rim							
SiO <sub>2</sub>	0.37	0.08	0.05	0.06	0.51	0.04	0.25
TiO <sub>2</sub>	0.00	0.12	0.14	0.19	0.00	0.03	0.16
V <sub>2</sub> O <sub>3</sub>	0.00	0.02	0.18	0.26	0.01	0.00	0.16
Cr <sub>2</sub> O <sub>3</sub>	0.75	0.79	46.04	44.99	2.18	0.77	43.21
MgO	0.18	0.34	7.14	8.71	0.58	0.28	3.73
Al <sub>2</sub> O <sub>3</sub>	0.05	0.03	10.67	13.18	0.03	0.05	7.47
Mno	0.11	0.11	0.44	0.33	0.14	0.12	1.02
FeO	90.52	90.72	34.19	30.83	89.91	91.34	39.68
CoO	0.00	0.02	0.05	0.07	0.00	0.01	0.11
NiO	0.02	0.04	0.10	0.11	0.00	0.02	0.15
ZnO	0.00	0.00	0.17	0.17	0.00	0.00	0.36
Total	92.01	92.27	99.19	98.90	93.36	92.65	96.29
Si	0.015	0.003	0.002	0.002	0.020	0.002	0.009
Ti	0.000	0.003	0.004	0.005	0.000	0.001	0.004
Al	0.002	0.002	0.423	0.513	0.001	0.002	0.316
Cr	0.023	0.024	1.225	1.175	0.066	0.023	1.227
Fe <sup>3+</sup>	1.946	1.960	0.336	0.292	1.893	1.970	0.426
Fe <sup>2+</sup>	1.000	0.982	0.626	0.560	0.982	0.982	0.765
Mn	0.004	0.004	0.013	0.009	0.005	0.004	0.031
Mg	0.010	0.019	0.358	0.429	0.033	0.016	0.200
V	0.000	0.001	0.005	0.007	0.000	0.000	0.005
Co	0.000	0.000	0.001	0.002	0.000	0.000	0.003
Ni	0.001	0.001	0.003	0.003	0.000	0.001	0.004
Zn	0.000	0.000	0.004	0.004	0.000	0.000	0.010

Total	3.000	3.000	3.000	3.000	3.000	3.000	3.000
Cr/(Cr+Al)	0.917	0.941	0.743	0.696	0.979	0.915	0.795
Fe <sup>3+</sup> /(Fe <sup>3+</sup> +Cr+Al)	0.661	0.666	0.350	0.342	0.658	0.667	0.358
Mg/(Mg+Fe <sup>2+</sup> )	0.010	0.019	0.364	0.434	0.033	0.016	0.207

Table. 6.S4. Representative analyses of serpentine in the studied chromitite and dunite samples from the Sabzevar ophiolite

Texture	Massive								Semi massive									
	Sample No.	IM-1B		O27		O3				SI-2C			HA2-1					KA3-1C
		Analysis No.	C1	C2	C12	C14	D1	D2	D3	D4	A5	B1	B2	D1	D4	D5	D6	D7
	SiO <sub>2</sub>	41.38	40.81	41.22	42.57	42.18	37.44	42.22	39.10	38.30	41.38	40.87	43.05	42.40	42.01	41.96	41.83	37.56
	TiO <sub>2</sub>	0.00	0.00	0.00	0.00	0.00	0.00	0.00	0.00	0.00	0.00	0.00	0.00	0.00	0.00	0.00	0.00	0.00
	Al <sub>2</sub> O <sub>3</sub>	0.67	0.89	0.02	1.90	0.52	0.18	0.23	0.23	0.69	0.86	0.94	0.04	0.06	0.09	0.06	0.09	0.50
	Cr <sub>2</sub> O <sub>3</sub>	0.54	0.55	0.10	1.26	0.00	0.68	0.21	0.15	1.19	0.73	0.93	0.04	0.16	0.42	0.24	0.19	1.18
	FeO*	2.12	2.04	2.60	2.14	1.91	2.65	1.13	2.60	4.61	2.41	3.39	1.90	1.90	1.52	1.93	1.87	3.49
	MnO	0.04	0.03	0.00	0.00	0.00	0.05	0.00	0.00	0.00	0.03	0.00	0.00	0.00	0.04	0.00	0.00	0.01
	MgO	41.25	41.31	41.28	40.28	40.29	37.44	42.45	38.85	38.91	41.25	40.87	41.96	43.45	43.54	43.13	43.02	36.98
	CaO	0.04	0.04	0.06	0.00	0.03	0.04	0.02	0.07	0.14	0.05	0.06	0.05	0.03	0.03	0.04	0.04	0.03
	Na <sub>2</sub> O	0.00	0.00	0.00	0.00	0.00	0.00	0.00	0.00	0.00	0.00	0.00	0.00	0.00	0.00	0.00	0.00	0.01
	K <sub>2</sub> O	0.00	0.00	0.00	0.00	0.00	0.00	0.00	0.00	0.00	0.00	0.00	0.00	0.00	0.00	0.00	0.00	0.00
	NiO	0.57	0.50	0.41	0.16	0.23	0.47	0.24	0.38	0.25	0.46	0.29	0.54	0.50	0.00	0.44	0.46	0.08
	Total	86.61	86.18	85.69	88.31	85.17	78.94	86.51	81.39	84.10	87.18	87.34	87.59	88.50	87.64	87.80	87.51	79.84
	Si	3.905	3.872	3.935	3.923	4.014	3.899	3.954	3.932	3.792	3.887	3.853	3.997	3.909	3.898	3.901	3.901	3.880
	Ti	0.000	0.000	0.000	0.000	0.000	0.000	0.000	0.000	0.000	0.000	0.000	0.000	0.000	0.000	0.000	0.000	0.000
	Al	0.075	0.100	0.003	0.207	0.059	0.022	0.026	0.027	0.080	0.095	0.104	0.005	0.007	0.010	0.007	0.010	0.060
	Cr	0.040	0.041	0.007	0.092	0.000	0.056	0.016	0.012	0.093	0.054	0.069	0.003	0.012	0.030	0.017	0.014	0.096
	Fe*	0.167	0.162	0.207	0.165	0.152	0.230	0.088	0.219	0.382	0.189	0.267	0.148	0.147	0.118	0.150	0.146	0.301
	Mn	0.003	0.002	0.000	0.000	0.000	0.004	0.000	0.000	0.000	0.002	0.000	0.000	0.000	0.003	0.000	0.000	0.000
	Mg	5.799	5.838	5.870	5.530	5.711	5.807	5.921	5.820	5.739	5.771	5.739	5.802	5.967	6.018	5.974	5.977	5.691
	Ca	0.004	0.004	0.006	0.000	0.004	0.004	0.002	0.008	0.015	0.005	0.006	0.005	0.003	0.003	0.004	0.004	0.004
	Na	0.000	0.000	0.000	0.000	0.000	0.000	0.000	0.000	0.000	0.000	0.000	0.000	0.000	0.000	0.000	0.000	0.003
	K	0.000	0.000	0.000	0.000	0.000	0.000	0.000	0.000	0.000	0.000	0.000	0.000	0.000	0.000	0.000	0.000	0.000
	Ni	0.044	0.038	0.031	0.012	0.018	0.039	0.018	0.030	0.020	0.035	0.022	0.040	0.037	0.000	0.033	0.035	0.007
	Total	10.037	10.058	10.060	9.928	9.957	10.062	10.026	10.048	10.121	10.039	10.061	10.000	10.081	10.081	10.086	10.087	10.043
	Si/Mg	0.673	0.663	0.670	0.709	0.703	0.671	0.668	0.676	0.661	0.673	0.671	0.689	0.655	0.648	0.653	0.653	0.682
	Mg#	0.972	0.973	0.966	0.971	0.974	0.962	0.985	0.964	0.938	0.968	0.955	0.975	0.976	0.981	0.976	0.976	0.950

Table 6.S4 (Continued)

Texture			Disseminated					Dunite											
Sample No.			KE-2					O26					KE-3			EB-5A			
Analysis No.	A2	A3	B2	F1	F2	F3	F4	C9	D6	D7	D8	D9	D10	C3	C4	C6	A20	D22	D23
SiO <sub>2</sub>	38.76	41.49	42.43	43.09	42.98	43.51	43.21	36.71	34.95	38.74	44.46	44.72	38.48	32.44	36.86	30.58	35.36	40.69	41.58
TiO <sub>2</sub>	0.00	0.01	0.00	0.00	0.00	0.00	0.00	0.00	0.00	0.00	0.00	0.00	0.00	0.00	0.00	0.00	0.00	0.00	0.00
Al <sub>2</sub> O <sub>3</sub>	0.74	1.65	0.28	0.35	0.28	0.23	0.21	0.06	0.04	0.00	0.17	0.16	0.06	0.16	0.07	0.35	0.00	0.00	0.05
Cr <sub>2</sub> O <sub>3</sub>	1.10	1.10	0.06	0.45	0.23	0.10	0.30	0.25	0.00	0.00	0.15	0.13	0.00	0.00	0.03	0.00	0.11	1.01	0.69
FeO*	2.76	4.50	3.06	3.85	3.40	3.04	3.04	4.93	6.68	5.74	4.23	4.22	5.22	7.85	5.65	9.48	5.76	5.04	4.97
MnO	0.06	0.01	0.00	0.00	0.00	0.00	0.03	0.06	0.10	0.13	0.09	0.09	0.08	0.11	0.00	0.14	0.10	0.05	0.06
MgO	37.62	40.20	40.41	39.70	40.59	41.18	41.04	37.67	42.53	40.12	39.60	40.00	39.85	40.93	41.45	41.78	44.49	40.94	39.79
CaO	0.09	0.02	0.05	0.07	0.07	0.05	0.04	0.06	0.05	0.06	0.00	0.00	0.09	0.05	0.05	0.07	0.10	0.06	0.02
Na <sub>2</sub> O	0.00	0.01	0.05	0.00	0.00	0.00	0.00	0.00	0.00	0.00	0.00	0.00	0.00	0.00	0.00	0.00	0.07	0.00	0.00
K <sub>2</sub> O	0.02	0.00	0.00	0.00	0.00	0.00	0.00	0.00	0.00	0.00	0.00	0.00	0.00	0.00	0.00	0.00	0.00	0.00	0.00
NiO	0.20	0.04	0.61	0.60	0.50	0.49	0.32	0.24	0.25	0.30	0.11	0.13	0.20	0.64	0.35	0.80	0.33	0.00	0.00
Total	81.35	89.02	86.97	88.11	88.05	88.60	88.20	79.99	84.59	85.09	88.79	89.43	83.99	82.18	84.46	83.21	86.32	87.79	87.15
Si	3.910	3.849	3.992	4.015	3.998	4.011	4.002	3.825	3.514	3.807	4.093	4.088	3.818	3.406	3.668	3.224	3.475	3.853	3.945
Ti	0.000	0.001	0.000	0.000	0.000	0.000	0.000	0.000	0.000	0.000	0.000	0.000	0.000	0.000	0.000	0.000	0.000	0.000	0.000
Al	0.088	0.180	0.032	0.039	0.031	0.024	0.023	0.007	0.005	0.000	0.018	0.017	0.007	0.020	0.008	0.043	0.000	0.000	0.005
Cr	0.088	0.080	0.005	0.033	0.017	0.008	0.022	0.021	0.000	0.000	0.011	0.009	0.000	0.000	0.003	0.000	0.009	0.076	0.051
Fe*	0.233	0.349	0.241	0.300	0.265	0.235	0.236	0.430	0.561	0.472	0.325	0.322	0.433	0.689	0.470	0.836	0.473	0.399	0.394
Mn	0.005	0.001	0.000	0.000	0.000	0.000	0.003	0.005	0.008	0.011	0.007	0.007	0.007	0.010	0.000	0.012	0.008	0.004	0.005
Mg	5.652	5.555	5.664	5.511	5.624	5.654	5.662	5.847	6.370	5.873	5.431	5.447	5.888	6.400	6.144	6.562	6.512	5.773	5.624
Ca	0.010	0.002	0.005	0.007	0.007	0.005	0.004	0.007	0.005	0.006	0.000	0.000	0.010	0.006	0.005	0.008	0.011	0.006	0.002
Na	0.000	0.002	0.009	0.000	0.000	0.000	0.000	0.000	0.000	0.000	0.000	0.000	0.000	0.000	0.000	0.000	0.013	0.000	0.000
K	0.002	0.000	0.000	0.000	0.000	0.000	0.000	0.000	0.000	0.000	0.000	0.000	0.000	0.000	0.000	0.000	0.000	0.000	0.000
Ni	0.016	0.003	0.046	0.045	0.037	0.036	0.024	0.020	0.020	0.024	0.008	0.009	0.016	0.054	0.028	0.068	0.026	0.000	0.000
Total	10.004	10.021	9.994	9.949	9.978	9.973	9.975	10.161	10.483	10.193	9.893	9.899	10.179	10.584	10.326	10.754	10.527	10.110	10.027
Si/Mg	0.692	0.693	0.705	0.729	0.711	0.709	0.707	0.654	0.552	0.648	0.754	0.751	0.648	0.532	0.597	0.491	0.534	0.667	0.702
Mg#	0.960	0.941	0.959	0.948	0.955	0.960	0.960	0.932	0.919	0.926	0.943	0.944	0.932	0.903	0.929	0.887	0.932	0.935	0.935

Table 6.S4 (Continued)

Texture		Dunite	
Sample No.	KA3-5	IM-2A	
Analysis No.	B15	G1	G2
SiO <sub>2</sub>	40.34	37.63	37.31
TiO <sub>2</sub>	0.00	0.00	0.00
Al <sub>2</sub> O <sub>3</sub>	0.34	0.00	0.00
Cr <sub>2</sub> O <sub>3</sub>	0.00	0.00	0.00
FeO*	3.48	9.77	12.47
MnO	0.04	0.07	0.11
MgO	42.66	38.68	37.43
CaO	0.07	0.03	0.06
Na <sub>2</sub> O	0.00	0.00	0.00
K <sub>2</sub> O	0.00	0.00	0.00
NiO	0.55	0.54	0.34
Total	87.49	86.73	87.72
Si	3.808	3.721	3.699
Ti	0.000	0.000	0.000
Al	0.038	0.000	0.000
Cr	0.000	0.000	0.000
Fe*	0.275	0.808	1.034
Mn	0.003	0.006	0.009
Mg	5.999	5.697	5.527
Ca	0.007	0.003	0.006
Na	0.000	0.000	0.000
K	0.000	0.000	0.000
Ni	0.042	0.043	0.027
Total	10.173	10.279	10.301
Si/Mg	0.635	0.653	0.669
Mg#	0.956	0.876	0.842

Table 6.S5. Representative analyses of chlorite from the studied chromitite and dunite samples in the Sabzevar ophiolite

Texture		Massive																
Sample No.		EB4					IM-1B											
Analysis No.	A5	A6	A7	A8	A9	D11	B8	B9	B10	B11	F5	F7	A10	A11	B11	C3	E5	B12
SiO <sub>2</sub>	33.73	34.06	33.07	34.09	33.57	31.58	31.90	31.12	33.65	31.65	34.60	28.18	31.20	32.54	31.45	32.12	32.99	31.04
TiO <sub>2</sub>	0.00	0.00	0.00	0.00	0.00	0.00	0.12	0.09	0.10	0.08	0.10	0.11	0.09	0.11	0.11	0.10	0.09	0.11
Al <sub>2</sub> O <sub>3</sub>	14.02	13.95	15.75	12.29	14.55	19.82	15.62	15.97	16.66	15.29	17.28	14.62	15.40	16.31	16.29	17.09	16.95	14.68
Cr <sub>2</sub> O <sub>3</sub>	2.79	2.82	2.65	2.67	3.21	1.90	2.98	3.42	3.05	3.30	4.09	12.52	3.77	3.26	3.25	2.37	2.80	3.21
FeO*	1.45	1.56	1.40	1.42	1.31	1.76	1.09	1.10	1.20	0.90	1.28	3.16	1.18	1.04	1.02	0.98	1.36	1.07
MnO	0.00	0.00	0.00	0.00	0.00	0.00	0.00	0.01	0.02	0.01	0.01	0.01	0.03	0.01	0.02	0.00	0.00	0.02
MgO	36.44	36.84	33.34	37.49	35.89	34.09	33.68	33.11	35.68	35.49	33.18	32.69	33.24	34.51	34.27	34.75	34.95	32.33
CaO	0.05	0.04	0.03	0.00	0.00	0.02	0.01	0.00	0.01	0.01	0.08	0.10	0.00	0.00	0.02	0.00	0.04	0.02
Na <sub>2</sub> O	0.00	0.06	0.00	0.00	0.00	0.00	0.02	0.00	0.02	0.00	0.00	0.03	0.01	0.01	0.00	0.00	0.00	0.00
K <sub>2</sub> O	0.00	0.00	0.00	0.00	0.00	0.00	0.00	0.00	0.01	0.00	0.01	0.01	0.00	0.01	0.00	0.00	0.02	0.00
Total	88.48	89.33	86.24	87.96	88.53	89.18	85.42	84.83	90.38	86.73	90.63	91.43	84.91	87.80	86.43	87.41	89.21	82.49
Si	6.251	6.258	6.257	6.360	6.216	5.790	6.109	6.013	6.090	5.988	6.238	5.306	6.035	6.065	5.964	5.996	6.051	6.159
Ti	0.000	0.000	0.000	0.000	0.000	0.000	0.017	0.014	0.013	0.011	0.013	0.015	0.013	0.015	0.015	0.014	0.012	0.017
Al	3.060	3.019	3.512	2.701	3.174	4.281	3.523	3.636	3.553	3.409	3.670	3.245	3.509	3.582	3.640	3.759	3.664	3.433
Cr	0.409	0.409	0.396	0.393	0.470	0.275	0.452	0.522	0.436	0.493	0.583	1.863	0.576	0.480	0.488	0.350	0.405	0.504
Fe*	0.224	0.240	0.221	0.222	0.203	0.270	0.174	0.178	0.181	0.143	0.194	0.497	0.191	0.161	0.162	0.154	0.209	0.177
Mn	0.000	0.000	0.000	0.000	0.000	0.000	0.000	0.002	0.004	0.002	0.001	0.002	0.004	0.002	0.003	0.000	0.000	0.003
Mg	10.059	10.082	9.397	10.417	9.899	9.311	9.606	9.529	9.620	10.002	8.909	9.169	9.578	9.581	9.681	9.663	9.550	9.558
Ca	0.011	0.008	0.006	0.000	0.000	0.005	0.002	0.001	0.002	0.003	0.014	0.020	0.000	0.001	0.003	0.000	0.009	0.004
Na	0.000	0.022	0.000	0.000	0.000	0.000	0.008	0.000	0.006	0.000	0.000	0.012	0.005	0.004	0.000	0.000	0.000	0.001
K	0.000	0.000	0.000	0.000	0.000	0.000	0.000	0.001	0.002	0.001	0.003	0.001	0.001	0.002	0.001	0.000	0.006	0.001
Total	20.014	20.039	19.789	20.093	19.962	19.932	19.892	19.895	19.906	20.051	19.624	20.132	19.912	19.892	19.957	19.935	19.905	19.857
Mg#	0.978	0.977	0.977	0.979	0.980	0.972	0.982	0.982	0.982	0.986	0.979	0.949	0.980	0.983	0.983	0.984	0.979	0.982

Table 6.S5 (Continued)

Texture	Disseminated		Dunite				
Sample No.	KE-2		EB-5A				
Analysis No.	I8	I9	E8	E9	D10	C10	B11
SiO <sub>2</sub>	32.32	27.04	32.19	31.38	30.29	32.36	32.51
TiO <sub>2</sub>	0.02	0.07	0.00	0.02	0.03	0.02	0.00
Al <sub>2</sub> O <sub>3</sub>	14.93	11.06	16.65	15.71	18.81	15.61	15.06
Cr <sub>2</sub> O <sub>3</sub>	3.30	15.05	2.49	2.66	2.47	2.41	2.56
FeO*	1.25	4.89	2.31	2.34	2.11	2.15	2.26
MnO	0.01	0.02	0.00	0.01	0.01	0.00	0.01
MgO	34.45	30.33	34.65	32.86	32.44	33.77	34.63
CaO	0.04	0.03	0.01	0.01	0.02	0.00	0.01
Na <sub>2</sub> O	0.05	0.02	0.01	0.06	0.03	0.02	0.00
K <sub>2</sub> O	0.00	0.00	0.01	0.00	0.00	0.00	0.00
Total	86.37	88.53	88.32	85.05	86.22	86.35	87.04
Si	6.139	5.373	5.996	6.073	5.772	6.151	6.143
Ti	0.002	0.011	0.001	0.003	0.005	0.002	0.000
Al	3.341	2.589	3.654	3.582	4.224	3.495	3.354
Cr	0.496	2.363	0.366	0.406	0.371	0.362	0.383
Fe*	0.199	0.813	0.360	0.379	0.336	0.342	0.357
Mn	0.002	0.003	0.000	0.001	0.002	0.000	0.002
Mg	9.745	8.978	9.613	9.473	9.206	9.559	9.749
Ca	0.007	0.006	0.002	0.002	0.004	0.000	0.001
Na	0.017	0.007	0.003	0.023	0.012	0.008	0.001
K	0.000	0.001	0.002	0.000	0.000	0.001	0.000
Total	19.949	20.144	19.996	19.942	19.932	19.922	19.989
Mg#	0.980	0.917	0.964	0.962	0.965	0.965	0.965

Table 7.S1. Representative analyses of orthopyroxenes from the Cheshmeh-Bid Cu-bearing pyroxenites

Sample No.	Opx in Opx-rich portion															
	PX6a					PX04			PX05							
	Analysis No.	31	32	33	34	35	1	19	20	O-16	O-17	O-18	O-19	O-7	O-8	O-34
SiO <sub>2</sub>	58.34	57.61	57.78	58.37	58.6	57.65	57.95	58.21	57.55	57.68	57.72	58.07	57.95	57.99	57.92	57.79
TiO <sub>2</sub>	0.02	0.05	0	0	0	0.03	0	0	0.02	0	0.02	0.02	0.01	0.04	0.02	0.03
Al <sub>2</sub> O <sub>3</sub>	0.4	1.23	1.2	0.47	0.52	1.16	0.82	1.03	1.23	1.38	1.01	1	0.9	1.03	1	0.93
Cr <sub>2</sub> O <sub>3</sub>	0.12	0.41	0.43	0.18	0.18	0.46	0.33	0.33	0.42	0.43	0.46	0.44	0.43	0.45	0.4	0.37
FeO	4.51	5.01	4.93	4.44	4.62	5.75	5.29	5.23	6.53	6.42	6.77	6.68	6.65	6.36	6.32	6.48
MnO	0.09	0.1	0.13	0.14	0.1	0.11	0.13	0.19	0.18	0.15	0.19	0.17	0.16	0.17	0.15	0.15
MgO	35.61	35	34.75	35.18	35.48	34.4	35.02	35.05	34.17	34.16	34.33	34.77	34.44	34.55	34.57	34.73
CaO	0.21	0.44	0.38	0.28	0.28	0.39	0.38	0.38	0.86	0.91	0.62	0.53	0.44	0.62	0.66	0.65
Na <sub>2</sub> O	0.01	0.03	0	0.01	0.01	0.03	0.02	0	0.01	0.03	0.02	0.04	0.03	0.04	0.01	0.02
K <sub>2</sub> O	0.01	0	0	0.01	0.01	0.01	0	0	0	0.01	0.02	0	0.01	0	0	0
NiO	0.13	0.05	0.1	0.14	0.03	0.11	0.08	0.17								
Total	99.46	99.92	99.7	99.22	99.85	100.09	100.01	100.59	100.97	101.18	101.16	101.71	101.04	101.25	101.07	101.16
Si	2.002	1.976	1.984	2.007	2.003	1.98	1.987	1.985	1.97	1.969	1.973	1.973	1.98	1.976	1.977	1.973
Al <sup>(iv)</sup>	-0.002	0.024	0.016	-0.007	-0.003	0.02	0.013	0.015	0.03	0.031	0.027	0.027	0.02	0.024	0.023	0.027
Al <sup>(vi)</sup>	0.018	0.025	0.033	0.026	0.024	0.027	0.02	0.026	0.019	0.025	0.014	0.013	0.017	0.018	0.017	0.01
Fe <sup>3+</sup>	0	0	0	0	0	0	0	0	0	0	0.002	0.006	0	0	0	0.01
Fe <sup>total</sup>	0.129	0.144	0.142	0.128	0.132	0.165	0.152	0.149	0.187	0.183	0.194	0.19	0.19	0.181	0.181	0.185
Cr	0.003	0.011	0.012	0.005	0.005	0.012	0.009	0.009	0.011	0.012	0.012	0.012	0.012	0.012	0.011	0.01
Ti	0.001	0.001	0	0	0	0.001	0	0	0.001	0	0	0.001	0	0.001	0.001	0.001
Fe <sup>2+</sup>	0.165	0.164	0.185	0.184	0.179	0.195	0.175	0.179	0.188	0.189	0.192	0.183	0.2	0.189	0.188	0.175
Mn	0.003	0.003	0.004	0.004	0.003	0.003	0.004	0.006	0.005	0.004	0.005	0.005	0.005	0.005	0.004	0.004
Mg	1.822	1.79	1.779	1.803	1.808	1.762	1.79	1.782	1.744	1.739	1.75	1.761	1.754	1.755	1.759	1.767

Ca	0.008	0.016	0.014	0.01	0.01	0.014	0.014	0.014	0.032	0.033	0.023	0.019	0.016	0.022	0.024	0.024
Na	0.001	0.002	0	0.001	0.001	0.002	0.001	0	0.001	0.002	0.001	0.003	0.002	0.003	0.001	0.001
K	0	0	0	0	0	0	0	0	0	0	0.001	0	0.001	0	0	0
Ni	0.004	0.002	0.003	0.004	0.001	0.003	0.002	0.005	0	0	0	0	0	0	0	0
Co	0	0	0	0	0	0	0	0	0	0	0	0	0	0	0	0
Total	4.024	4.014	4.029	4.038	4.032	4.02	4.015	4.02	4.001	4.003	4.001	4.002	4.007	4.005	4.005	4.003
Mg/(Mg+Fe <sup>2+</sup> )	0.92	0.92	0.91	0.91	0.91	0.9	0.91	0.91	0.9	0.9	0.9	0.91	0.9	0.9	0.9	0.91
Mg/(Mg+Fe <sup>total</sup> )	0.93	0.93	0.93	0.93	0.93	0.91	0.92	0.92	0.9	0.9	0.9	0.9	0.9	0.91	0.91	0.91
En	0.91	0.91	0.9	0.9	0.91	0.89	0.9	0.9	0.89	0.89	0.89	0.9	0.89	0.89	0.89	0.9
Fs	0.08	0.08	0.09	0.09	0.09	0.1	0.09	0.09	0.1	0.1	0.1	0.09	0.1	0.1	0.1	0.09
Wo	0	0.01	0.01	0.01	0.01	0.01	0.01	0.01	0.02	0.02	0.01	0.01	0.01	0.01	0.01	0.01

Table 7.S1 (Continued)

Opx inclusions in metasomatic Cpx			
Sample No.	PX05		
Analysis No.	A-8C	A-8D	A-8E
SiO <sub>2</sub>	57.02	56.95	57.21
TiO <sub>2</sub>	0.02	0.02	0.01
Al <sub>2</sub> O <sub>3</sub>	1.64	1.53	1.33
Cr <sub>2</sub> O <sub>3</sub>	0.52	0.5	0.5
FeO	8.81	8.36	8.4
MnO	0.19	0.21	0.19
MgO	32.41	32.83	32.76
CaO	0.69	0.76	0.75
Na <sub>2</sub> O	0	0.01	0.02
K <sub>2</sub> O	0	0.02	0
NiO			
Total	101.31	101.17	101.17
Si	1.964	1.962	1.97
Al <sup>(iv)</sup>	0.036	0.038	0.03
Al <sup>(vi)</sup>	0.031	0.024	0.024
Fe <sup>3+</sup>	0	0.001	0
Fe <sup>total</sup>	0.254	0.241	0.242
Cr	0.014	0.014	0.014
Ti	0.001	0	0
Fe <sup>2+</sup>	0.269	0.24	0.252
Mn	0.006	0.006	0.006

Mg	1.665	1.686	1.682
Ca	0.025	0.028	0.028
Na	0	0.001	0.001
K	0	0.001	0
Ni	0	0	0
Co	0	0	0
Total	4.01	4	4.007
Mg/(Mg+Fe <sup>2+</sup> )	0.86	0.88	0.87
Mg/(Mg+Fe <sup>total</sup> )	0.87	0.87	0.87
En	0.85	0.86	0.86
Fs	0.14	0.12	0.13
Wo	0.01	0.01	0.01

Table 7.S2. Representative analyses of clinopyroxenes from the Cheshmeh-Bid Cu-bearing pyroxenites

Clinopyroxene inclusion in Opx-rich portion																	
Sample No.	PX05																
Analysis No.	a-E1	a-E3	a-C4	a-C1	a-D1	a-B1	a-B3	a-B4	a-C1 2	a-A15	a-A16	a-A2	a-A3	a-A5	a-A6	a-A7	a-A8
SiO <sub>2</sub>	55.42	54.77	54.25	55.05	54.74	54.72	54.76	55.22	55.05	55.02	54.94	55.36	53.61	53.47	55.16	55.87	55.55
TiO <sub>2</sub>	0.02	0.01	0.04	0.02	0.02	0.02	0.01	0.04	0.02	0.03	0.03	0.03	0.03	0.02	0.03	0.03	0.01
Al <sub>2</sub> O <sub>3</sub>	1.05	1.29	1.61	1.02	0.91	1.66	1.37	1.43	1.02	1.62	1.65	1.64	1.89	2.2	0.94	0.5	0.67
Cr <sub>2</sub> O <sub>3</sub>	0.53	0.8	0.87	0.37	0.33	0.91	0.85	0.82	0.37	0.94	0.91	0.84	0.43	0.26	0.39	0.36	0.44
FeO	2.21	2.27	2.62	1.99	2.08	2.52	2.33	2.38	1.99	2.27	2.26	2.07	1.61	1.5	1.31	1.31	1.4
MnO	0.07	0.07	0.06	0.06	0.08	0.08	0.08	0.07	0.06	0.1	0.05	0.1	0.01	0.04	0.01	0.03	0.06
MgO	18.06	17.8	17.55	18	18.05	17.08	17	17.25	18	17.15	16.97	17.08	19.95	20	19.65	19.33	19.59
CaO	23.26	22.98	22.97	23.55	23.38	23.24	23.62	23.25	23.55	23.2	23.41	23.53	21.02	21.04	22.27	22.75	21.99
Na <sub>2</sub> O	0.44	0.42	0.42	0.4	0.41	0.7	0.68	0.7	0.4	0.83	0.8	0.79	0.17	0.18	0.19	0.12	0.16
K <sub>2</sub> O	0.01	0	0	0	0	0	0	0.01	0	0	0.01	0	0.02	0.03	0.02	0.02	0.02
NiO																	
Total	101.05	100.41	100.4	100.46	100	100.93	100.7	101.17	100.46	101.16	101.03	101.44	98.75	98.74	99.98	100.31	99.88
Si	1.985	1.976	1.962	1.983	1.982	1.97	1.976	1.98	1.983	1.973	1.974	1.978	1.95	1.944	1.982	2.001	1.996
Al <sup>(iv)</sup>	0.015	0.024	0.038	0.017	0.018	0.03	0.024	0.02	0.017	0.027	0.026	0.022	0.05	0.056	0.018	-0.001	0.004
Al <sup>(vi)</sup>	0.029	0.031	0.031	0.026	0.021	0.04	0.034	0.04	0.026	0.042	0.043	0.047	0.031	0.039	0.022	0.022	0.025
Fe <sup>3+</sup>	0.001	0	0.014	0.01	0.022	0.019	0.019	0.006	0.01	0.021	0.016	0.006	0.025	0.033	0	0	0
Fe <sup>total</sup>	0.066	0.069	0.079	0.06	0.063	0.076	0.07	0.071	0.06	0.068	0.068	0.062	0.049	0.046	0.039	0.039	0.042
Cr	0.015	0.023	0.025	0.011	0.009	0.026	0.024	0.023	0.011	0.027	0.026	0.024	0.012	0.008	0.011	0.01	0.012
Ti	0	0	0.001	0.001	0.001	0.001	0	0.001	0.001	0.001	0.001	0.001	0.001	0.001	0.001	0.001	0
Fe <sup>2+</sup>	0.065	0.07	0.065	0.05	0.041	0.057	0.051	0.065	0.05	0.047	0.051	0.056	0.024	0.012	0.044	0.078	0.075
Mn	0.002	0.002	0.002	0.002	0.003	0.002	0.003	0.002	0.002	0.003	0.002	0.003	0	0.001	0	0.001	0.002
Mg	0.964	0.957	0.946	0.967	0.975	0.916	0.915	0.922	0.967	0.917	0.909	0.91	1.082	1.084	1.053	1.032	1.049
Ca	0.893	0.888	0.89	0.909	0.907	0.896	0.913	0.893	0.909	0.891	0.901	0.901	0.819	0.82	0.857	0.873	0.847
Na	0.03	0.029	0.03	0.028	0.029	0.049	0.047	0.049	0.028	0.058	0.055	0.055	0.012	0.012	0.013	0.008	0.011

K	0	0	0	0	0	0	0	0	0	0	0	0	0.001	0.001	0.001	0.001	0.001
Ni	0	0	0	0	0	0	0	0	0	0	0	0	0	0	0	0	0
Co	0	0	0	0	0	0	0	0	0	0	0	0	0	0	0	0	0
Total	4	4.001	4.005	4.003	4.007	4.006	4.006	4.002	4.003	4.007	4.005	4.002	4.008	4.011	4.003	4.026	4.022
Mg/(Mg+Fe <sup>2+</sup> )	0.94	0.93	0.94	0.95	0.96	0.94	0.95	0.93	0.95	0.95	0.95	0.94	0.98	0.99	0.96	0.93	0.93
Mg/(Mg+Fe <sup>total</sup> )	0.94	0.93	0.92	0.94	0.94	0.92	0.93	0.93	0.94	0.93	0.93	0.94	0.96	0.96	0.96	0.96	0.96
En	0.5	0.5	0.5	0.5	0.51	0.49	0.49	0.49	0.5	0.49	0.49	0.49	0.56	0.57	0.54	0.52	0.53
Fs	0.03	0.04	0.03	0.03	0.02	0.03	0.03	0.03	0.03	0.03	0.03	0.03	0.01	0.01	0.02	0.04	0.04
Wo	0.46	0.46	0.47	0.47	0.47	0.48	0.49	0.47	0.47	0.48	0.48	0.48	0.43	0.43	0.44	0.44	0.43

Table 7.S2 (Continued)

Sample No.	Clinopyroxene in zone II															
	PX06		PX04		PX05											
	18	19	14	13	a-A17	a-A18	A-9I	A-9J	A-8J	A-9I 4	A-9J 5	A-10B	A-11C	O-25	O-26	O-32
SiO <sub>2</sub>	53.08	54.09	54.17	54.07	55.61	55.55	55.15	54.47	54.63	55.15	54.47	55.4	54.98	55.44	55.42	54.96
TiO <sub>2</sub>	0	0	0.03	0.01	0	0	0.01	0.05	0.03	0.01	0.05	0.1	0.03	0	0.03	0.04
Al <sub>2</sub> O <sub>3</sub>	1.4	1.27	1.35	1.46	1.02	1.16	1.23	1.69	1.2	1.23	1.69	0.52	0.71	0.44	1.09	1.17
Cr <sub>2</sub> O <sub>3</sub>	0.53	0.37	0.81	0.81	0.44	0.48	0.83	0.77	0.63	0.83	0.77	0.26	0.53	0.44	0.74	0.75
FeO	2.78	2.65	2	2.41	2.11	2	2.23	2.65	2.97	2.23	2.65	0.72	2.22	2.44	2.62	2.74
MnO	0.02	0.05	0.1	0.07	0.07	0.09	0.08	0.06	0.12	0.08	0.06	0	0.07	0.1	0.11	0.11
MgO	17.14	17.11	17.12	16.91	18.12	17.56	17.94	17.38	17.39	17.94	17.38	18.03	17.29	17.3	17.42	17.56
CaO	23.19	23.07	23.28	22.75	23.5	23.54	23.04	23.33	23.63	23.04	23.33	25.98	24.42	23.99	23.29	23.23
Na <sub>2</sub> O	0.35	0.33	0.43	0.47	0.45	0.64	0.5	0.4	0.23	0.5	0.4	0.03	0.3	0.55	0.49	0.45
K <sub>2</sub> O	0.01	0	0	0	0	0.01	0	0.01	0.02	0	0.01	0	0.02	0.01	0.01	0
NiO	0	0.05	0.11	0.03												
Total	98.51	98.98	99.4	98.98	101.31	101.04	101.02	100.81	100.85	101.02	100.81	101.06	100.58	100.7	101.21	101.01
Si	1.962	1.983	1.976	1.98	1.986	1.99	1.977	1.963	1.972	1.977	1.963	1.984	1.987	2	1.987	1.977
Al <sup>(iv)</sup>	0.038	0.017	0.024	0.02	0.014	0.01	0.023	0.037	0.028	0.023	0.037	0.016	0.013	0	0.013	0.023
Al <sup>(vi)</sup>	0.023	0.037	0.034	0.043	0.029	0.039	0.029	0.035	0.023	0.029	0.035	0.006	0.017	0.018	0.033	0.026
Fe <sup>3+</sup>	0.039	0	0	0	0.005	0.004	0.006	0.009	0.005	0.006	0.009	0	0.002	0.012	0	0.009
Fe <sup>total</sup>	0.086	0.081	0.061	0.074	0.063	0.06	0.067	0.08	0.09	0.067	0.08	0.021	0.067	0.074	0.079	0.083
Cr	0.015	0.011	0.023	0.023	0.012	0.014	0.023	0.022	0.018	0.023	0.022	0.007	0.015	0.012	0.021	0.021
Ti	0	0	0.001	0	0	0	0	0.001	0.001	0	0.001	0.003	0.001	0	0.001	0.001
Fe <sup>2+</sup>	0.046	0.092	0.068	0.095	0.058	0.055	0.06	0.071	0.085	0.06	0.071	0.022	0.065	0.061	0.089	0.074
Mn	0.001	0.001	0.003	0.002	0.002	0.003	0.002	0.002	0.004	0.002	0.002	0	0.002	0.003	0.003	0.003
Mg	0.944	0.935	0.931	0.923	0.965	0.938	0.959	0.934	0.936	0.959	0.934	0.963	0.932	0.93	0.931	0.942
Ca	0.918	0.906	0.91	0.893	0.899	0.904	0.885	0.901	0.914	0.885	0.901	0.997	0.945	0.927	0.895	0.895
Na	0.025	0.023	0.031	0.034	0.031	0.045	0.035	0.028	0.016	0.035	0.028	0.002	0.021	0.039	0.034	0.032

K	0.001	0	0	0	0	0	0	0	0	0.001	0	0	0	0.001	0	0	0
Ni	0	0.001	0.003	0.001	0	0	0	0	0	0	0	0	0	0	0	0	0
Co	0	0	0	0	0	0	0	0	0	0	0	0	0	0	0	0	0
Total	4.013	4.007	4.005	4.014	4.002	4.001	4.002	4.003	4.002	4.002	4.003	4	4.001	4.004	4.007	4.003	
Mg/(Mg+Fe <sup>2+</sup> )	0.95	0.91	0.93	0.91	0.94	0.94	0.94	0.93	0.92	0.94	0.93	0.98	0.93	0.94	0.91	0.93	
Mg/(Mg+Fe <sup>total</sup> )	0.92	0.92	0.94	0.93	0.94	0.94	0.93	0.92	0.91	0.93	0.92	0.98	0.93	0.93	0.92	0.92	
En	0.49	0.48	0.49	0.48	0.5	0.49	0.5	0.49	0.48	0.5	0.49	0.49	0.48	0.48	0.49	0.49	
Fs	0.02	0.05	0.04	0.05	0.03	0.03	0.03	0.04	0.04	0.03	0.04	0.01	0.03	0.03	0.05	0.04	
Wo	0.48	0.47	0.48	0.47	0.47	0.48	0.46	0.47	0.47	0.46	0.47	0.5	0.49	0.48	0.47	0.47	

Table 7.S2 (Continued)

Sample No.	PX05										PX06				
	Analysis No.	O-33	A-4A	A-4B	A-4C	A-4D	A-4H	A-4I	A-5	A-6	A-7	a-8	a-18	a-22	a-27
SiO <sub>2</sub>	54.87	54.48	55.09	54.78	54.84	56.35	55.28	53.83	55.18	54.96	53.9	54.94	53.23	55.02	53.71
TiO <sub>2</sub>	0.02	0.14	0	0.09	0.02	0.09	0.09	0.03	0	0.02	0.04	0.08	0.07	0.02	0.05
Al <sub>2</sub> O <sub>3</sub>	0.69	0.08	0.04	0.1	0.05	0.21	0.11	0	0.1	0.28	1.18	0.44	2.23	0.06	1.89
Cr <sub>2</sub> O <sub>3</sub>	0.16	0.11	1.56	0.25	1.25	0.14	0.06	0.5	0.51	0.9	0.66	0.75	0.02	0	0.88
FeO	5.09	7.55	4.56	6.52	4.56	2.72	2.92	5.8	0.91	2.46	3.15	2.19	2	1.02	2.57
MnO	0.25	0.14	0.06	0.11	0.09	0.05	0	0.1	0	0.09	0.12	0.08	0.02	0.07	0.06
MgO	15.53	13.55	14.69	14.07	14.87	16.39	16.64	14.64	17.63	16.42	16.65	17.06	16.31	17.21	16.75
CaO	24.07	25.32	24.53	25.25	24.93	25.56	25.76	25.55	26.1	25.13	21.95	22.88	24.18	24.8	23.32
Na <sub>2</sub> O	0.25	0.06	0.63	0.11	0.42	0.14	0.12	0.16	0.1	0.4	0.57	0.44	0.08	0	0.47
K <sub>2</sub> O	0.01	0	0	0	0	0	0.01	0	0	0	0.04	0.01	0	0.03	0
NiO											0.04	0.02	0.06	0.06	0.1
Total	100.93	101.44	101.17	101.29	101.05	101.63	101	100.61	100.54	100.66	98.29	98.9	98.2	98.29	99.8
Si	1.997	2.002	2.006	2.006	2.001	2.017	1.999	1.986	1.991	1.993	1.991	2.01	1.965	2.02	1.958
Al <sup>(iv)</sup>	0.003	-0.002	-0.006	-0.006	-0.001	-0.017	0.001	0	0.004	0.007	0.009	-0.01	0.035	-0.02	0.042
Al <sup>(vi)</sup>	0.027	0.006	0.008	0.01	0.003	0.026	0.004	0	0	0.005	0.043	0.029	0.062	0.023	0.039
Fe <sup>3+</sup>	0	0	0	0	0	0	0	0.033	0.008	0.005	0	0	0	0	0.012
Fe <sup>total</sup>	0.155	0.232	0.139	0.2	0.139	0.081	0.088	0.179	0.028	0.075	0.097	0.067	0.062	0.031	0.078
Cr	0.005	0.003	0.045	0.007	0.036	0.004	0.002	0.015	0.014	0.026	0.019	0.022	0	0	0.025
Ti	0.001	0.004	0	0.002	0.001	0.002	0.002	0.001	0	0	0.001	0.002	0.002	0.001	0.001
Fe <sup>2+</sup>	0.173	0.253	0.161	0.23	0.156	0.145	0.088	0.145	0.019	0.07	0.117	0.118	0.099	0.097	0.066
Mn	0.008	0.004	0.002	0.003	0.003	0.001	0	0.003	0	0.003	0.004	0.002	0.001	0.002	0.002
Mg	0.843	0.743	0.798	0.768	0.809	0.875	0.897	0.805	0.948	0.888	0.917	0.931	0.897	0.942	0.91
Ca	0.939	0.997	0.957	0.991	0.974	0.98	0.998	1.01	1.009	0.976	0.869	0.897	0.956	0.976	0.911
Na	0.017	0.005	0.045	0.008	0.03	0.009	0.009	0.011	0.007	0.028	0.041	0.031	0.006	0	0.034

K	0.001	0	0	0	0	0	0	0	0	0	0.002	0.001	0	0.001	0
Ni	0	0	0	0	0	0	0	0	0	0	0.001	0.001	0.002	0.002	0.003
Co	0	0	0	0	0	0	0	0	0	0	0	0	0	0	0
Total	4.012	4.014	4.015	4.021	4.011	4.042	4	4.011	4.003	4.002	4.013	4.034	4.025	4.044	4.004
Mg/(Mg+Fe <sup>2+</sup> )	0.83	0.75	0.83	0.77	0.84	0.86	0.91	0.85	0.98	0.93	0.89	0.89	0.9	0.91	0.93
Mg/(Mg+Fe <sup>total</sup> )	0.85	0.76	0.85	0.79	0.85	0.92	0.91	0.82	0.97	0.92	0.9	0.93	0.94	0.97	0.92
En	0.43	0.37	0.42	0.39	0.42	0.44	0.45	0.41	0.48	0.46	0.48	0.48	0.46	0.47	0.48
Fs	0.09	0.13	0.08	0.12	0.08	0.07	0.04	0.07	0.01	0.04	0.06	0.06	0.05	0.05	0.04
Wo	0.48	0.5	0.5	0.5	0.5	0.49	0.5	0.52	0.51	0.5	0.46	0.46	0.49	0.48	0.48

Table 7.S3. Representative analyses of olivine with vein-like texture from the Cu-bearing pyroxenites

Sample No.	PX05										
Analysis No.	9	10	11	12	O-1	O-2	O-3	O-13	O-14	O-15	O-16
SiO <sub>2</sub>	38.01	38.36	37.26	38.53	38.68	42.09	39.07	38.6	38.56	38.47	38.51
TiO <sub>2</sub>	0	0.02	0.04	0.04	0.02	0.03	0	0	0.02	0	0
Al <sub>2</sub> O <sub>3</sub>	0.01	0	0.03	0.01	0.33	0.25	0.15	0	0.01	0	0
Cr <sub>2</sub> O <sub>3</sub>	0.03	0.03	0.06	0.02	0.28	0.43	0.09	0.03	0.27	0.03	0.03
FeO*	20.77	16.03	20.14	19.19	21.56	19.32	21.85	22.19	21.27	22.34	22.43
MnO	0.63	0.34	0.7	0.55	0.75	0.78	0.71	0.78	0.7	0.82	0.81
MgO	40.78	44.65	41.32	42.35	38.41	33.92	38.69	38.98	40.1	38.82	38.6
CaO	0.03	0.04	0.03	0.02	0.03	1.84	0.03	0.03	0.04	0.04	0.03
Na <sub>2</sub> O	0	0.02	0	0.04							
K <sub>2</sub> O	0	0.01	0	0							
NiO	0.08	0.09	0.13	0.1	0.09	0.09	0.08	0.12	0.13	0.16	0.13
Total	100.34	99.59	99.71	100.85	100.15	98.74	100.67	100.74	101.09	100.67	100.56
Si	0.982	0.977	0.969	0.982	1.003	1.089	1.008	0.998	0.99	0.997	0.999
Ti	0	0	0.001	0.001	0	0.001	0	0	0	0	0
Al	0	0	0.001	0	0.01	0.008	0.004	0	0	0	0
Cr	0.001	0.001	0.001	0	0.006	0.009	0.002	0.001	0.005	0.001	0.001
Fe*	0.449	0.341	0.438	0.409	0.467	0.418	0.471	0.48	0.457	0.484	0.487
Mn	0.014	0.007	0.015	0.012	0.016	0.017	0.016	0.017	0.015	0.018	0.018
Mg	1.569	1.693	1.601	1.608	1.483	1.308	1.486	1.502	1.534	1.499	1.492
Ca	0.001	0.001	0.001	0	0.001	0.051	0.001	0.001	0.001	0.001	0.001
Na	0	0.001	0	0.002	0	0	0	0	0	0	0
K	0	0	0	0	0	0	0	0	0	0	0
Ni	0.002	0.002	0.003	0.002	0.002	0.002	0.002	0.003	0.003	0.003	0.003

Total	3.017	3.023	3.029	3.017	2.989	2.902	2.989	3.001	3.006	3.003	3
Mg#	0.78	0.83	0.79	0.8	0.76	0.76	0.76	0.76	0.77	0.76	0.75

---

Table 7.S4. Representative analyses of chromian spinel in the Cheshmeh-Bid Cu-bearing pyroxenite

Sample No.	PX06												PX05		
	Analysis No.	5	6	11	12	13	14	32	33	3a	38a	40a	42a	1	2
SiO <sub>2</sub>	0	0.04	0.05	0.04	0.02	0.05	0.05	0.05	0	0	0	0.05	0.03	0.03	0.05
TiO <sub>2</sub>	0	0.02	0	0.05	0.08	0	0.08	0.09	0.06	0.09	0.12	0.09	0.18	0.18	0.03
Al <sub>2</sub> O <sub>3</sub>	15.68	5.65	14.5	5.4	14.71	13.38	14.19	13.82	15.36	12.38	12.53	12.65	13.67	13.67	17.82
Cr <sub>2</sub> O <sub>3</sub>	48.54	62.88	49.9	62.41	53.2	55.24	51.58	50.05	48.9	57.04	57.16	57.09	54.54	54.54	52.51
FeO*	23.13	21.8	22.83	23.99	20.51	20.99	21.59	25.21	24.91	17.45	16.64	16.61	20.86	20.86	18.29
MnO	0.12	0.1	0.04	0.32	0.06	0.13	0.09	0.21	0.24	0.1	0.06	0.08	0.1	0.1	0.09
MgO	12.13	9.11	12.22	7.17	11.43	11.64	11.88	10.38	10.27	13.03	12.85	13.15	11.43	11.43	12.29
CaO	0.01	0.03	0.01	0.03	0.02	0	0	0.03	0	0	0	0.03	0	0	0.02
Na <sub>2</sub> O	0.02	0	0	0	0.01	0	0	0.04	0	0	0	0.02	0	0	0.01
K <sub>2</sub> O	0.01	0.01	0.01	0	0	0	0.01	0	0	0.01	0.02	0	0	0	0
NiO	0.11	0.01	0.18	0.06	0.03	0.11	0.19	0.16	0.17	0.2	0.09	0.13	0.08	0.08	0.1
Total	99.75	99.66	99.75	99.47	100.06	101.55	99.66	100.04	99.92	100.31	99.47	99.9	100.88	100.88	101.21
Si	0	0.001	0.002	0.002	0.001	0.002	0.002	0.002	0	0	0	0.002	0.001	0.001	0.001
Ti	0	0.001	0	0.001	0.002	0	0.002	0.002	0.001	0.002	0.003	0.002	0.004	0.004	0.001
Al	0.602	0.228	0.559	0.222	0.561	0.507	0.546	0.539	0.595	0.471	0.479	0.481	0.521	0.521	0.658
Cr	1.249	1.705	1.289	1.719	1.362	1.405	1.332	1.309	1.27	1.456	1.466	1.456	1.393	1.393	1.3
Fe <sup>2+</sup>	0.436	0.543	0.428	0.634	0.458	0.455	0.437	0.508	0.516	0.381	0.383	0.373	0.457	0.457	0.43
Fe <sup>3+</sup>	0.197	0.084	0.198	0.072	0.095	0.113	0.152	0.191	0.173	0.089	0.064	0.073	0.101	0.101	0.05
Mn	0.003	0.003	0.001	0.009	0.002	0.004	0.003	0.006	0.007	0.003	0.002	0.002	0.003	0.003	0.002
Mg	0.588	0.466	0.595	0.372	0.552	0.558	0.578	0.512	0.503	0.627	0.621	0.632	0.55	0.55	0.574
Ca	0	0.001	0	0.001	0.001	0	0	0.001	0	0	0	0.001	0	0	0.001
Na	0.001	0	0	0	0	0	0	0.002	0	0	0	0.001	0	0	0.001
K	0.001	0	0	0	0	0	0	0	0	0.001	0.001	0	0	0	0
Ni	0.002	0	0.004	0.001	0.001	0.002	0.004	0.004	0.004	0.004	0.002	0.003	0.002	0.002	0.002

total	3.709	3.659	3.7	3.732	3.589	3.61	3.646	3.772	3.754	3.504	3.472	3.474	3.596	3.596	3.499
$\text{Fe}^{2+}/(\text{Fe}^{2+} + \text{Mg})$	0.43	0.54	0.42	0.63	0.45	0.45	0.43	0.5	0.51	0.38	0.38	0.37	0.45	0.45	0.43
$\text{Fe}^{3+}/(\text{Fe}^{3+} + \text{Al} + \text{Cr})$	0.1	0.04	0.1	0.04	0.05	0.06	0.07	0.09	0.08	0.04	0.03	0.04	0.05	0.05	0.02
Mg#	0.57	0.46	0.58	0.37	0.55	0.55	0.57	0.5	0.49	0.62	0.62	0.63	0.55	0.55	0.57
Cr#	0.67	0.88	0.7	0.89	0.71	0.73	0.71	0.71	0.68	0.76	0.75	0.75	0.73	0.73	0.66

Table 7.S4 (Continued)

Sample No.	PX04										
Analysis No.	4	5	6	7	3	4	6	12	15	16	162
SiO <sub>2</sub>	0.07	0.04	0.04	0.05	0.03	0.04	0.05	0.07	0.02	0.08	0.08
TiO <sub>2</sub>	0.14	0.09	0.03	0.06	0.02	0.07	0.06	0.14	0.14	0.01	0.01
Al <sub>2</sub> O <sub>3</sub>	14.23	14.94	16.58	17.68	15.21	13.68	16.21	20.29	16.46	13.81	13.81
Cr <sub>2</sub> O <sub>3</sub>	53.76	53.16	51.34	48.91	52.25	54.12	50.54	47.65	51.42	52.46	52.46
FeO*	20.89	20.38	20.6	22.91	21.27	23.06	20.43	18.4	19.03	25.32	25.32
MnO	0.11	0.15	0.13	0.1	0.11	0.28	0.07	0.09	0.12	0.28	0.28
MgO	11.51	11.49	12.03	10.8	10.99	9.25	12.05	13.49	12.57	8.43	8.43
CaO	0	0	0	0.01	0.04	0.03	0.08	0	0	0.05	0.05
Na <sub>2</sub> O	0	0.04	0.01	0.01	0	0.03	0.05	0	0	0	0
K <sub>2</sub> O	0	0.01	0	0	0	0	0	0	0.01	0.01	0.01
NiO	0.15	0.16	0.13	0.07	0.05	0.01	0.11	0.15	0.15	0.05	0.05
Total	100.87	100.45	100.9	100.59	99.96	100.57	99.64	100.28	99.92	100.49	100.49
Si	0.002	0.001	0.001	0.002	0.001	0.001	0.002	0.002	0.001	0.003	
Ti	0.003	0.002	0.001	0.001	0	0.002	0.001	0.003	0.003	0	0.003
Al	0.541	0.568	0.622	0.668	0.582	0.529	0.616	0.745	0.62	0.539	0
Cr	1.37	1.354	1.292	1.239	1.34	1.404	1.288	1.173	1.299	1.372	0.539
Fe <sup>2+</sup>	0.455	0.456	0.441	0.496	0.48	0.555	0.432	0.38	0.409	0.596	0.701
Fe <sup>3+</sup>	0.105	0.093	0.109	0.117	0.1	0.082	0.118	0.095	0.096	0.112	0.596
Mn	0.003	0.004	0.004	0.003	0.003	0.008	0.002	0.002	0.003	0.008	0.112
Mg	0.553	0.552	0.571	0.516	0.531	0.452	0.579	0.626	0.599	0.416	0.008
Ca	0	0	0	0	0.001	0.001	0.003	0	0	0.002	0.416
Na	0	0.002	0.001	0	0	0.002	0.003	0	0	0	0.002
K	0	0	0	0	0	0	0	0	0	0	0
Ni	0.003	0.003	0.003	0.001	0.001	0	0.002	0.003	0.003	0.001	0

total	3.598	3.586	3.592	3.658	3.617	3.669	3.596	3.511	3.542	3.75	0.001
											3.75
Fe <sup>2+</sup> /(Fe <sup>2+</sup> +Mg)	0.45	0.45	0.44	0.49	0.47	0.55	0.43	0.38	0.41	0.59	
Fe <sup>3+</sup> /(Fe <sup>3+</sup> +Al+Cr)	0.05	0.05	0.05	0.06	0.05	0.04	0.06	0.05	0.05	0.06	0.59
Mg#	0.55	0.55	0.56	0.51	0.53	0.45	0.57	0.62	0.59	0.41	0.06
Cr#	0.72	0.7	0.67	0.65	0.7	0.73	0.68	0.61	0.68	0.72	0.41

Table 7.S5. Representative analyses of amphiboles from the Cheshmeh-Bid Cu-bearing pyroxenites

Analysis No.	Amp in zone II											Amp selvage around Cpx			
	PX05										PX06	PX05			
	O-27	O-28	O-29	O-30	O-31	A-8A	A-8B	A-8F	A-8G	A-11A	A-11B	1	O-6	O-9	O-10
SiO <sub>2</sub>	50.75	54.11	53.65	51.02	49.23	50.87	49.17	53.52	51.56	50.81	51.7	45.61	55.77	52.97	57.23
TiO <sub>2</sub>	0.18	0.09	0.09	0.12	0.18	0.12	0.14	0.07	0.09	0.23	0.1	0.17	0.02	0.06	0
Al <sub>2</sub> O <sub>3</sub>	6.42	4.14	4.85	7.4	8.11	7.16	9.71	5.04	6.67	7.26	6.54	9.61	3.55	6.14	0.98
Cr <sub>2</sub> O <sub>3</sub>	2.23	0.8	0.98	0.93	1.64	1.98	0.83	0.99	1.19	1.93	2.02	2.53	0.46	0.96	0.36
MnO	0.03	0.07	0.06	0.08	0.07	0.07	0.09	0.04	0.07	0.05	0.04	0.04	0.06	0.04	0.12
FeO	3.83	3.39	3.36	4.47	3.82	4.09	4.48	3.59	4.34	3.35	3.23	3.64	2.81	3.06	3.47
NiO	-	-	-	-	-	-	-	-	-	-	-	0.15	-	-	-
MgO	20.17	21.41	20.72	19.45	19.7	19.69	19.05	21.02	20.06	20.11	20.18	18.64	22.4	21.17	24.44
CaO	12.39	12.66	12.42	12.47	12.36	12.17	12.39	12.66	12.78	12.53	12.68	11.47	12.03	11.82	11.28
Na <sub>2</sub> O	1.82	1.05	1.43	1.66	2.03	1.38	1.42	0.82	1.17	1.41	1.36	2.26	0.68	1.28	0.14
K <sub>2</sub> O	0.02	0.25	0.19	0.5	0.53	0.19	0.71	0.11	0.41	0.26	0.04	0.64	0.13	0.17	0.01
Cl	0.02	0.01	0.03	0.06	0.04	0.04	0.05	0.03	0.04	0.03	0.02		0.01	0.02	0.01
Total	97.86	97.97	97.77	98.14	97.69	97.74	98.03	97.88	98.35	97.95	97.91	94.75	97.92	97.69	98.05
T (ideally 8 apfu)															
Si	7.084	7.49	7.434	7.119	6.924	7.075	6.874	7.37	7.155	7.062	7.177	6.636	7.608	7.292	7.78
Al	0.916	0.51	0.566	0.881	1.076	0.925	1.126	0.63	0.845	0.938	0.823	1.364	0.392	0.708	0.157
Ti															
Fe <sup>3+</sup>															0.062
T subtotal	8	8	8	8	8	8	8	8	8	8	8	8	8	8	7.999
C (ideally 5 apfu)															
Ti	0.019	0.009	0.01	0.012	0.019	0.012	0.015	0.007	0.009	0.024	0.011	0.018	0.002	0.006	
Al	0.141	0.164	0.226	0.336	0.268	0.248	0.473	0.187	0.245	0.251	0.247	0.283	0.178	0.288	0
Cr	0.246	0.087	0.107	0.103	0.182	0.217	0.091	0.108	0.131	0.212	0.222	0.291	0.049	0.105	0.039

Fe <sup>3+</sup>	0.185		0.067	0.096	0.1	0.317	0.145	0.272	0.172	0.172	0.119	0.223	0.218	0.237	0.178
Ni												0.017			
Mn <sup>2+</sup>															
Fe <sup>2+</sup>	0.214	0.321	0.31	0.407	0.3	0.123	0.307	0.11	0.293	0.174	0.226	0.125		0.018	
Mg	4.196	4.419	4.281	4.045	4.131	4.082	3.969	4.315	4.15	4.166	4.176	4.043	4.553	4.346	4.783
C subtotal	5.001	5	5.001	4.999	5	4.999	5	4.999	5	4.999	5.001	5	5	5	5
B (ideally 2 apfu)															
Mn <sup>2+</sup>	0.004	0.008	0.007	0.009	0.008	0.008	0.011	0.005	0.008	0.006	0.004	0.005	0.007	0.005	0.014
Fe <sup>2+</sup>	0.049	0.072	0.012	0.018	0.049	0.036	0.072	0.031	0.039	0.043	0.03	0.095	0.102	0.097	0.154
Mg													0.003		0.17
Ca	1.852	1.877	1.845	1.864	1.862	1.814	1.856	1.868	1.9	1.865	1.886	1.788	1.758	1.744	1.644
Na	0.095	0.043	0.136	0.109	0.081	0.143	0.061	0.096	0.053	0.086	0.08	0.112	0.13	0.154	0.019
B subtotal	2	2	2	2	2	2.001	2	2	2	2	2	2	2	2	2.001
A (from 0 to 1 apfu)															
Ca															
Na	0.398	0.239	0.249	0.341	0.474	0.228	0.323	0.124	0.26	0.294	0.287	0.525	0.05	0.188	0.019
K	0.004	0.044	0.034	0.09	0.094	0.033	0.126	0.02	0.072	0.045	0.008	0.118	0.023	0.031	0.002
A subtotal	0.402	0.283	0.283	0.431	0.568	0.261	0.449	0.144	0.332	0.339	0.295	0.643	0.073	0.219	0.021
OH	1.994	1.997	1.993	1.986	1.989	1.991	1.987	1.994	1.991	1.994	1.995	2	1.997	1.995	1.999
Cl	0.006	0.003	0.007	0.014	0.011	0.009	0.013	0.006	0.009	0.006	0.005		0.003	0.005	0.001
Sum T,C,B,A	15.403	15.283	15.284	15.43	15.568	15.261	15.449	15.143	15.332	15.338	15.296	15.643	15.073	15.219	15.021
Mg/(Mg+Fe <sup>2+</sup> )	0.94	0.92	0.93	0.9	0.92	0.96	0.91	0.97	0.93	0.95	0.94	0.95	0.98	0.97	0.97

Table 7.S5 (Continued)

Sample No.	PX05														PX06a
Analysis No.	O-11	O-12	a-C2	a-C3	a-C5	a-D2	a-E2	a-E4	a-E5	a-E6	a-A9	a-A10	a-A11	a-A12	5
SiO <sub>2</sub>	57.85	57.96	50.65	50.79	49.94	50.43	53.23	54.16	51.66	48.56	52.42	52.77	52.24	52.22	52.05
TiO <sub>2</sub>	0.02	0.01	0.08	0.08	0.1	0.08	0.05	0.02	0.05	0.15	0.06	0.05	0.06	0.07	0.05
Al <sub>2</sub> O <sub>3</sub>	0.28	0.71	8.05	7.47	8.23	7.75	5.45	4.4	7.3	9.99	6.52	6.13	6.6	6.56	5.08
Cr <sub>2</sub> O <sub>3</sub>	0.23	0.12	0.85	1.26	1.38	1.15	0.9	0.74	0.99	1.72	0.86	0.72	1.15	1.01	0.49
MnO	0.18	0.14	0.04	0.07	0.07	0.03	0.05	0.06	0.06	0.04	0.07	0.03	0.05	0.06	0.08
FeO	3.68	2.92	2.85	2.96	3.01	2.84	2.78	2.61	3.03	3.46	2.61	2.76	2.78	2.81	3.36
NiO	-	-	-	-	-	-	-	-	-	-	-	-	-	-	0.12
MgO	22.88	23.32	20.58	20.54	20.19	20.6	21.56	21.87	21	19.58	21.44	21.35	20.86	21.02	20.83
CaO	12.5	12.56	12.16	11.86	11.92	11.86	11.81	11.99	11.96	11.73	11.9	11.91	12.02	12	10.6
Na <sub>2</sub> O	0.03	0.07	2.08	2.25	2.29	2.34	1.83	1.46	2.13	2.68	1.88	1.91	1.91	1.95	1.16
K <sub>2</sub> O	0.02	0.01	0.4	0.34	0.41	0.29	0.22	0.17	0.26	0.43	0.22	0.2	0.21	0.2	0.19
Cl	0	0.01	0.01	0.04	0.03	0.02	0.02	0.01	0.03	0.03	0.02	0.01	0.02	0.02	
Total	97.66	97.83	97.74	97.66	97.56	97.39	97.88	97.49	98.46	98.35	98.01	97.84	97.92	97.89	94.01
T (ideally 8 apfu)															
Si	7.951	7.922	7.033	7.067	6.971	7.033	48.97	7.461	7.112	6.756	7.213	7.269	7.207	7.204	7.421
Al	0.046	0.078	0.967	0.933	1.029	0.967	0.673	0.539	0.888	1.244	0.787	0.731	0.793	0.796	0.579
Ti	0.002														
Fe <sup>3+</sup>	0.001														
T subtotal	8	8	8	8	8	8	49.643	8	8	8	8	8	8	8	8
C (ideally 5 apfu)															
Ti		0.002	0.008	0.009	0.01	0.008	0.005	0.002	0.005	0.016	0.006	0.005	0.006	0.008	0.005
Al	0	0.035	0.351	0.292	0.325	0.308	0.211	0.176	0.297	0.394	0.27	0.264	0.28	0.27	0.274
Cr	0.025	0.012	0.093	0.139	0.152	0.127	0.098	0.08	0.108	0.189	0.094	0.078	0.126	0.11	0.055

Fe <sup>3+</sup>	0.019	0.028	0.166	0.176	0.176	0.167	0.217	0.205	0.177	0.202	0.206	0.214	0.214	0.22	0.273
Ni															0.014
Mn <sup>2+</sup>															
Fe <sup>2+</sup>	0.268	0.172	0.123	0.125	0.135	0.108	0.046	0.045	0.103	0.139	0.026	0.055	0.085	0.07	
Mg	4.688	4.751	4.259	4.26	4.201	4.283	4.424	4.492	4.31	4.06	4.398	4.385	4.29	4.322	4.379
C subtotal	5	5	5	5.001	4.999	5.001	5.001	5	5	5	5	5.001	5.001	5	5
B (ideally 2 apfu)															
Mn <sup>2+</sup>	0.021	0.016	0.004	0.008	0.008	0.003	0.006	0.007	0.007	0.004	0.009	0.003	0.006	0.007	0.01
Fe <sup>2+</sup>	0.135	0.134	0.042	0.044	0.04	0.057	0.058	0.051	0.069	0.061	0.069	0.05	0.023	0.034	0.128
Mg															0.049
Ca	1.841	1.839	1.809	1.769	1.782	1.772	1.742	1.77	1.765	1.748	1.754	1.758	1.777	1.773	1.619
Na	0.004	0.01	0.144	0.179	0.169	0.168	0.195	0.172	0.159	0.186	0.168	0.19	0.194	0.187	0.195
B subtotal	2.001	1.999	1.999	2	1.999	2	2.001	2	2	1.999	2	2.001	2	2.001	2.001
A (from 0 to 1 apfu)															
Ca															
Na	0.004	0.009	0.414	0.427	0.452	0.466	0.293	0.217	0.41	0.538	0.334	0.32	0.318	0.334	0.126
K	0.003	0.001	0.071	0.061	0.073	0.051	0.039	0.029	0.045	0.076	0.039	0.035	0.038	0.034	0.034
A subtotal	0.007	0.01	0.485	0.488	0.525	0.517	0.332	0.246	0.455	0.614	0.373	0.355	0.356	0.368	0.16
OH	2	1.998	1.997	1.992	1.993	1.995	1.994	1.997	1.993	1.992	1.996	1.997	1.996	1.996	2
Cl		0.002	0.003	0.008	0.007	0.005	0.006	0.003	0.007	0.008	0.004	0.003	0.004	0.004	
Sum T,C,B,A	15.008	15.009	15.484	15.489	15.523	15.518	56.977	15.246	15.455	15.613	15.373	15.357	15.357	15.369	15.161
Mg/(Mg+Fe <sup>2+</sup> )	0.92	0.94	0.96	0.96	0.96	0.96	0.98	0.98	0.96	0.95	0.98	0.98	0.98	0.98	0.97

Table 7.S5 (Continued)

Analysis No.	PX06a						Amp in zone I	
	PX05						O-23	O-24
	12	17	19	21	17	20		
SiO <sub>2</sub>	52.38	58.19	57.72	52.85	46.6	46.44	56.9	57.23
TiO <sub>2</sub>	0.07	0	0.04	0.13	0.22	0.24	0.02	0.02
Al <sub>2</sub> O <sub>3</sub>	5.53	0.26	0.36	4.92	9.83	10.3	2.43	1.73
Cr <sub>2</sub> O <sub>3</sub>	0.51	0.41	0.42	1.19	2.5	2.11	0.31	0.49
MnO	0.05	0.02	0.06	0.09	0.05	0.04	0.09	0.04
FeO	3.48	2.34	2.36	2.57	3.43	3.94	2.83	2.81
NiO	0.14	0	0.06	0.11	0.12	0.18	-	-
MgO	21.23	21.97	22.41	20.91	18.98	18.33	22.65	22.49
CaO	10.82	12.27	12.58	11.62	11.42	11.59	12.18	12.71
Na <sub>2</sub> O	1.11	0.01	0.05	1.13	1.94	1.86	0.51	0.36
K <sub>2</sub> O	0.22	0	0.05	0.14	0.39	0.63	0.06	0.06
Cl							0.02	0.01
Total	95.54	95.47	96.1	95.66	95.48	95.66	98	0
T (ideally 8 apfu)								
Si	7.357	8.101	8.014	7.418	6.688	6.667	7.758	7.822
Al	0.643			0.582	1.312	1.333	0.242	0.178
Ti								
Fe <sup>3+</sup>								
T subtotal	8	8.101	8.014	8	8	8	8	8
C (ideally 5 apfu)								
Ti	0.008		0.004	0.014	0.024	0.026	0.002	0.002
Al	0.272	0.043	0.058	0.232	0.35	0.41	0.149	0.1
Cr	0.057	0.045	0.046	0.132	0.284	0.24	0.033	0.053

Fe <sup>3+</sup>	0.275			0.208	0.208	0.237	0.109	0.065
Ni	0.016		0.007	0.013	0.013	0.021		
Mn <sup>2+</sup>		0.002						
Fe <sup>2+</sup>		0.272	0.247	0.027	0.06	0.143	0.103	0.198
Mg	4.372	4.56	4.638	4.375	4.061	3.923	4.605	4.582
C subtotal	5	4.922	5	5.001	5	5	5.001	5
B (ideally 2 apfu)								
Mn <sup>2+</sup>	0.006		0.007	0.011	0.006	0.004	0.011	0.005
Fe <sup>2+</sup>	0.133		0.027	0.067	0.144	0.093	0.112	0.059
Mg	0.074							
Ca	1.628	1.83	1.871	1.747	1.756	1.783	1.779	1.861
Na	0.159	0.003	0.012	0.175	0.094	0.12	0.099	0.075
B subtotal	2	1.833	1.917	2	2	2	2.001	2
A (from 0 to 1 apfu)								
Ca								
Na	0.143			0.133	0.445	0.398	0.036	0.021
K	0.04		0.009	0.025	0.072	0.115	0.011	0.01
A subtotal	0.183	0	0.009	0.158	0.517	0.513	0.047	0.031
OH	2	2	2	2	2	2	1.996	1.997
Cl							0.004	0.003
Sum T,C,B,A	15.183	14.856	14.94	15.159	15.517	15.513	15.049	15.031
Mg/(Mg+Fe <sup>2+</sup> )	0.97	0.94	0.94	0.98	0.95	0.94	0.96	0.95

Table 7.S6. Representative analyses of chlorites in Zone III from the Cu-bearing pyroxenites

Sample No.	PX05														PX6a	
	Analysis No.	A-2A	A-2B	A-2C	A-3A	A-3B	A-3C	A-9A	A-9B	A-9C	A-9D	A-9E	A-9F	A-9G	A-9H	2
SiO <sub>2</sub>	28.94	28.9	28.99	29.69	29.83	29.59	31.58	30.85	30.84	30.96	30.17	30.68	30.43	31.27	30.14	30.07
TiO <sub>2</sub>	0.02	0.01	0.01	0.03	0.01	0.02	0.1	0.11	0.06	0.06	0.03	0.02	0.05	0.07	0.01	0.02
Al <sub>2</sub> O <sub>3</sub>	20.64	20.94	20.53	21.08	20.85	21.01	15.87	17.62	17.13	17.23	19.95	18.17	17.6	16.1	18.41	18.22
Cr <sub>2</sub> O <sub>3</sub>	2.49	1.99	2.62	1.62	1.42	2.15	3.63	3.15	3.46	3.84	2.1	3.52	3.52	3.67	1.57	2.31
Fe <sub>2</sub> O <sub>3</sub>	1.08	0.93	0.96	1.18	1.18	1.22	1.15	0.96	0.61	1.26	1.02	1.08	1.39	0.86	0.77	1.16
FeO	4.39	4.53	5.08	2.29	2.17	2.23	0.8	0.99	0.99	0.4	1.3	1.56	0.52	1.03	2.72	1.33
MnO	0.03	0.03	0.04	0	0	0.01	0.04	0.03	0	0	0.01	0.01	0	0.03	0.01	0.03
MgO	28.58	28.82	28.46	30.32	30.39	30.18	32.15	32.18	32.81	31.93	31.46	31.6	31.13	32.5	30.77	30.51
NiO	0	0	0	0	0	0	0	0	0	0	0	0	0	0	0.06	0.04
CaO	0.01	0.02	0.02	0.01	0.01	0	0.04	0.02	0	0.06	0.05	0.01	0.02	0	0	0.03
Na <sub>2</sub> O	0	0	0.02	0	0.01	0	0	0	0.01	0	0.01	0	0	0	0.02	0.05
K <sub>2</sub> O	0.01	0	0.01	0	0	0	0.11	0.04	0.08	0.02	0.02	0	0.02	0.07	0.03	0.03
Cl	0	0	0	0	0	0	0	0.01	0.01	0	0.01	0.01	0.01	0	0	0
H <sub>2</sub> O*	12.38	12.39	12.41	12.56	12.53	12.56	12.44	12.53	12.54	12.5	12.59	12.58	12.34	12.46	12.29	12.23
Total	98.57	98.55	99.15	98.78	98.41	98.98	97.9	98.49	98.55	98.25	98.71	99.25	97.03	98.06	96.8	96.04
Si	5.592	5.58	5.589	5.653	5.693	5.63	6.065	5.887	5.886	5.918	5.731	5.83	5.889	6.003	5.867	5.877
Al <sup>iv</sup>	2.408	2.42	2.411	2.347	2.307	2.37	1.935	2.113	2.114	2.082	2.269	2.17	2.111	1.997	2.133	2.123
Al <sup>vi</sup>	2.308	2.357	2.266	2.398	2.398	2.357	1.67	1.86	1.746	1.813	2.21	1.911	1.917	1.655	2.101	2.089
Ti	0.002	0.001	0.002	0.004	0.002	0.002	0.015	0.015	0.008	0.008	0.005	0.003	0.008	0.01	0.001	0.002
Cr	0.38	0.304	0.399	0.243	0.214	0.323	0.551	0.475	0.522	0.58	0.315	0.529	0.538	0.556	0.242	0.357
Fe <sup>3+</sup>	0.157	0.135	0.14	0.169	0.17	0.174	0.166	0.138	0.088	0.182	0.145	0.155	0.202	0.125	0.112	0.171
Fe <sup>2+</sup>	0.709	0.731	0.818	0.364	0.347	0.355	0.128	0.158	0.158	0.063	0.207	0.248	0.084	0.165	0.443	0.218
Mn	0.005	0.004	0.007	0	0	0.001	0.007	0.004	0	0	0.001	0.002	0	0.005	0.002	0.004

Mg	8.233	8.293	8.177	8.605	8.646	8.561	9.207	9.154	9.334	9.101	8.909	8.95	8.981	9.3	8.929	8.889
Ni	0	0	0	0	0	0	0	0	0	0	0	0	0	0	0.009	0.006
Ca	0.003	0.003	0.003	0.003	0.002	0	0.008	0.005	0	0.012	0.009	0.002	0.004	0	0	0.007
Na	0	0	0.012	0	0.007	0.003	0.002	0.002	0.008	0.003	0.007	0	0	0	0.015	0.039
K	0.006	0	0.004	0	0.001	0.002	0.052	0.02	0.037	0.008	0.011	0	0.008	0.034	0.013	0.017
Cl	0	0	0.001	0	0	0.003	0	0.004	0.007	0.001	0.003	0.004	0.005	0.001	0	0
OH*	16	16	15.999	16	16	15.997	16	15.996	15.993	15.999	15.997	15.996	15.995	15.999	16	16
Total	35.802	35.828	35.828	35.785	35.786	35.779	35.805	35.83	35.902	35.77	35.821	35.8	35.743	35.851	35.866	35.801
Fe/Fe+Mg	0.1	0.09	0.1	0.06	0.06	0.06	0.03	0.03	0.03	0.03	0.04	0.04	0.03	0.03	0.06	0.04

Table 7.S6 (Continued)

Sample No.		PX04										
Analysis No.	6a-25	2	3	16	27	28	29	30	31	8	9	11
SiO <sub>2</sub>	30.68	32.52	33.25	34.07	31.49	31.24	30.99	31.66	30.84	32.75	33.5	33.35
TiO <sub>2</sub>	0.02	0.11	0.11	0.06	0.04	0.06	0.02	0.05	0.05	0.19	0.13	0.03
Al <sub>2</sub> O <sub>3</sub>	19.3	15.89	14.07	12.44	18.91	19.37	19.25	18.26	18.75	16.93	16.48	13.35
Cr <sub>2</sub> O <sub>3</sub>	1.05	1.5	1.19	1.68	0.29	0.32	0.67	0.17	1.11	0.56	0.62	2.31
Fe <sub>2</sub> O <sub>3</sub>	1.21	0.63	1.89	1.11	1.11	0.92	1.11	0.78	0.75	1.47	1.43	1.3
FeO	1.65	1.31	0	1.5	0.95	1.1	0.87	0.96	1.46	1.67	1.29	4.55
MnO	0.01	0.01	0.07	0	0.03	0	0	0.01	0	0.05	0.01	0.06
MgO	30.54	33.26	31.61	33	32.19	32.38	31.83	33.06	32.17	31.93	32.55	30.74
NiO	0.12	0.07	0.21	0.19	0.35	0.29	0.37	0.3	0.35	0.33	0.22	0.25
CaO	0.03	0.03	0.08	0.06	0.01	0.01	0.05	0	0.01	0.01	0.01	0.04
Na <sub>2</sub> O	0.13	0.05	0.06	0.02	0.01	0.03	0	0	0.01	0.01	0	0.02
K <sub>2</sub> O	0.08	0.26	0.04	0.23	0	0.01	0	0	0	0.03	0.25	0.01
Cl	0	0	0	0	0	0	0	0	0	0	0	0
H <sub>2</sub> O*	12.41	12.55	12.16	12.33	12.57	12.62	12.52	12.58	12.53	12.58	12.69	12.34
Total	97.22	98.19	94.75	96.68	97.96	98.35	97.68	97.83	98.02	98.52	99.18	98.35
Si	5.904	6.195	6.524	6.603	5.99	5.921	5.918	6.026	5.892	6.22	6.304	6.461
Al <sup>iv</sup>	2.096	1.805	1.476	1.397	2.01	2.079	2.082	1.974	2.108	1.78	1.696	1.539
Al <sup>vi</sup>	2.3	1.774	1.796	1.457	2.242	2.259	2.264	2.131	2.123	2.025	1.976	1.52
Ti	0.002	0.015	0.017	0.009	0.006	0.009	0.002	0.007	0.007	0.027	0.018	0.004
Cr	0.16	0.226	0.185	0.257	0.043	0.049	0.101	0.026	0.168	0.085	0.093	0.354
Fe <sup>3+</sup>	0.176	0.091	0.279	0.162	0.158	0.131	0.16	0.111	0.108	0.21	0.203	0.19
Fe <sup>2+</sup>	0.265	0.209	0	0.243	0.152	0.174	0.138	0.153	0.233	0.265	0.203	0.737
Mn	0.001	0.001	0.012	0	0.005	0	0	0.001	0	0.008	0.001	0.01

Mg	8.761	9.445	9.245	9.534	9.128	9.148	9.061	9.381	9.162	9.04	9.131	8.877
Ni	0.019	0.01	0.033	0.03	0.053	0.044	0.057	0.046	0.054	0.051	0.033	0.04
Ca	0.005	0.006	0.017	0.012	0.003	0.003	0.009	0	0.003	0.002	0.002	0.008
Na	0.094	0.037	0.047	0.015	0.01	0.024	0.001	0	0.007	0.01	0	0.016
K	0.04	0.127	0.019	0.112	0	0.004	0.001	0	0.002	0.014	0.12	0.003
Cl	0	0	0	0	0	0	0	0	0	0	0	0
OH*	16	16	16	16	16	16	16	16	16	16	16	16
Total	35.824	35.941	35.652	35.832	35.801	35.843	35.796	35.857	35.865	35.738	35.78	35.759

Table 7.S7. Chemical compositions of sulfides and native copper in Zone III

Mineral		Chalcocite														
Sample No	PX05	PX06			PX04											
Analysis No.	11	5	6	7	4	5	6	7	8	9	10	11	12	13	14	15
Au	0.05	0	0	0	0.14	0	0	0	0	0	0	0	0.13	0.1	0	0
Fe	0.03	0.06	0.05	0.05	0	0.01	0.03	0	0.04	0	0	0	0.04	0.03	0	0.02
Pb	0.03	0.01	0.07	0.07	0	0.05	0.13	0.01	0.1	0.06	0.12	0.11	0	0.03	0.17	0.05
As	0.03	0.08	0.04	0	0.03	0.03	0.06	0.04	0.02	0	0	0	0.01	0	0	0
S	20.05	20.66	20.57	21.71	20.32	20.16	20.41	20.32	21.27	20.68	21.1	20.47	20.99	20.59	20.46	20.53
Co	0	0	0	0	0	0	0.02	0	0	0.01	0.01	0	0.04	0.05	0.03	0.01
Cd	0	0	0	0	0.81	0.02	0.05	0.53	0.01	0.01	0	0	0.01	0.03	0.01	0
Sb	0	0	0	0	0.05	0.09	0.06	0	0	0	0	0.04	0	0.04	0.03	0
Ni	0	0.01	0	0.02	0	0	0	0.05	0.05	0	0.01	0	0.04	0	0	0.05
Cu	79.38	79.21	79.03	76.69	79.69	80.61	80.44	79.82	78.65	80.09	80.17	80.39	79.86	80.92	79.69	78.91
Zn	0	0.19	0	0.07	0.03	0.07	0.04	0.03	0	0.09	0.05	0	0	0	0.07	0.04
Total	99.58	100.21	99.76	98.61	101.06	101.04	101.24	100.8	100.14	100.94	101.46	101.01	101.13	101.79	100.45	99.61

Table 7.S7 (Continued)

Mineral	Greenockite						Native copper									
	Sample No			PX05		IRKJPX05				IRKJPX04				IRKJPX06		
Analysis No.	15	16	17	2	3	2	3	4	8	2	3	4	6	1	3	4
Au	0	0.08	0.01	0	0.16	9.19	11.82	0	0.24	0.1	0	0	0.17	0.12	0.26	0
Fe	0.02	0	0	0.14	0.02	0.05	0.02	0.14	0	0.25	0.22	0.19	0.18	0.36	0.05	0.04
Pb	0.05	0.04	0.09	0	0.01	0	0	0	0	0	0.05	0.09	0	0.01	0	0
As	0	0	0	0	0	0.03	0	0.06	0	0	0	0.05	0	0.02	0.11	0
S	20.53	20.62	20.36	21.48	21.54	0	0	0.03	0.03	0	0.03	0.01	0.03	0.01	0	0
Co	0.01	0.01	0	0.05	0	0.02	0	0	0	0	0.02	0.05	0	0.01	0	0
Cd	0	0	0.58	78.11	76.52											
Sb	0	0.03	0	0	0	0	0.05	0.01	0	0.02	0	0.01	0	0	0	0.04
Ni	0.05	0.02	0	0	0	0.34	0.07	0.15	0.06	0.02	0.09	0	0	0	0.08	0
Cu	78.91	79.96	80.6	3.87	6.78	90.54	88.7	99.85	100.78	98.62	99.53	99.44	98.99	98.57	99.6	100.19
Zn	0.04	0	0.06	0.19	0.17	0.02	0.27	0.25	0	0	0	0.05	0.09	0.08	0.03	0
Total	99.61	100.75	101.71	103.83	105.21	100.19	100.93	100.48	101.12	99	99.94	99.88	99.46	99.18	100.12	100.27

## Chapter 9

### 2. References

---

- Abdulzahra, I. K., Hadi, A., Asahara, Y., Azizi, H., & Yamamoto, K. (2018). Petrogenesis and geochronology of Mishao peraluminous I-type granites, Shalair valley area, NE Iraq. *Chemie Der Erde*, 78(2), 215–227. <https://doi.org/10.1016/j.chemer.2018.01.003>
- Abrajano, T. A., Sturchio, N. C., Bohlke, J. K., Lyon, G. L., Poreda, R. J., & Stevens, C. M. (1988). Methane-hydrogen gas seeps, Zambales Ophiolite, Philippines: Deep or shallow origin? *Chemical Geology*, 71(1–3), 211–222. [https://doi.org/10.1016/0009-2541\(88\)90116-7](https://doi.org/10.1016/0009-2541(88)90116-7)
- Abrajano, T. A., & Pasteris, J. D. (1989). Zambales ophiolite, Philippines - II. Sulfide petrology of the critical zone of the Acoje Massif. *Contributions to Mineralogy and Petrology*, 103(1), 64–77. <https://doi.org/10.1007/BF00371365>
- Adabi, M. H., & Ager, D. V. (1997). Late Jurassic brachiopods from north-east Iran. *Palaeontology*, 40(2), 355–362.
- Afshar-Harb, A. (1994). Geology of the Kopet-Dagh, Iran. Geological Survey of Iran, Tehran ([In Persian]).
- Afshar-Harb, A. (1979). The Stratigraphy, Tectonics and Petroleum Geology of the Kopet Dagh Region, Northern Iran. (Doctoral Dissertation). Imperial College London (University of London).
- Agard, P., Omrani, J., Jolivet, L., & Mouthereau, F. (2005). Convergence history across Zagros (Iran): Constraints from collisional and earlier deformation. *International Journal of Earth Sciences*, 94(3), 401–419. <https://doi.org/10.1007/s00531-005-0481-4>.
- Agard, P., Omrani, J., Jolivet, L., Whitechurch, H., Vrielynck, B., Spakman, W., Monié, P., Meyer, B., & Wortel, R. (2011). Zagros orogeny: A subduction-dominated process. *Geological Magazine*, 148(5–6), 692–725. <https://doi.org/10.1017/S001675681100046X>
- Aghanabati, A. (2004). Geology of Iran. Geological survey of Iran publication, 558p.
- Agard, P., Omrani, J., Jolivet, L., Whitechurch, H., Vrielynck, B., Spakman, W., Monié, P., Meyer, B., & Wortel, R. (2011). Zagros orogeny: A subduction-dominated process. *Geological Magazine*, 148(5–6), 692–725. <https://doi.org/10.1017/S001675681100046X>
- Alavi, M. (1991). Tectonic map of the Middle East. Geol. Surv. Iran, Scale 1:5,000,000, Sheet 1.
- Alavi, M. (1994). Tectonics of the Zagros orogenic belt of Iran: new data and interpretations. *Tectonophysics*, 229(3–4), 211–238. [https://doi.org/10.1016/0040-1951\(94\)90030-2](https://doi.org/10.1016/0040-1951(94)90030-2)
- Alavi, M. (1980). Tectonostratigraphic evolution of the Zagrosides of Iran. *Geology*, 8(3), 144–149. [https://doi.org/10.1130/0091-7613\(1980\)8<144:TEOTZO>2.0.CO;2](https://doi.org/10.1130/0091-7613(1980)8<144:TEOTZO>2.0.CO;2)

- Alavi, M. (2007). Structures of the Zagros fold-thrust belt in Iran. *American Journal of Science*, 307(9), 1064–1095. <https://doi.org/10.2475/09.2007.02>
- Ali, S. A., Buckman, S., Aswad, K. J., Jones, B. G., Ismail, S. A., & Nutman, A. P. (2012). Recognition of late cretaceous hasanbag ophiolite-arc rocks in the Kurdistan region of the Iraqi Zagros suture zone: A missing link in the paleogeography of the closing neotethys ocean. *Lithosphere*, 4(5), 395–410. <https://doi.org/10.1130/L207.1>
- Ali, S. A., Buckman, S., Aswad, K. J., Jones, B. G., Ismail, S. A., & Nutman, A. P. (2013). The tectonic evolution of a Neo-Tethyan (Eocene-Oligocene) island-arc (Walash and Naopurdan groups) in the Kurdistan region of the Northeast Iraqi Zagros Suture Zone. *Island Arc*, 22(1), 104–125. <https://doi.org/10.1111/iar.12007>
- Alikhani, M., Sohrabi Mehr, M., Mehrvarz, A., Akhoundi, H., Mehrvarz, A., & Ansari, M. (2019). Geological Map of the Olang-Sir mine. KBC Exploration group, scale 1:25,000.
- Allen, D. E., & Seyfried, W. E. (2003). Compositional controls on vent fluids from ultramafic-hosted hydrothermal systems at mid-ocean ridges: An experimental study at 400°C, 500 bars. *Geochimica et Cosmochimica Acta*, 67(8), 1531–1542. [https://doi.org/10.1016/S0016-7037\(02\)01173-0](https://doi.org/10.1016/S0016-7037(02)01173-0)
- Allen, M. B. (2009). Discussion on the Eocene bimodal Piranshahr massif of the Sanadaj-Sirjan Zone, West Iran: A marker of the end of collision in the Zagros orogen. *Journal of the Geological Society*, 166(5), 981–982. <https://doi.org/10.1144/0016-76492009-020>
- Allen, M. B., & Armstrong, H. A. (2008). Arabia-Eurasia collision and the forcing of mid-Cenozoic global cooling. *Palaeogeography, Palaeoclimatology, Palaeoecology*, 265(1–2), 52–58. <https://doi.org/10.1016/j.palaeo.2008.04.021>
- Allen, M. B., Kheirkhah, M., Emami, M. H., & Jones, S. J. (2011). Right-lateral shear across Iran and kinematic change in the Arabia-Eurasia collision zone. *Geophysical Journal International*, 184(2), 555–574. <https://doi.org/10.1111/j.1365-246X.2010.04874.x>
- Allen, M., Jackson, J., & Walker, R. (2004). Late Cenozoic reorganization of the Arabia-Eurasia collision and the comparison of short-term and long-term deformation rates. *Tectonics*, 23(2). <https://doi.org/10.1029/2003TC001530>
- Alt, J. C., & Shanks, W. C. (1998). Sulfur in serpentinized oceanic peridotites: Serpentinization processes and microbial sulfate reduction. *Journal of Geophysical Research: Solid Earth*, 103(5), 9917–9929. <https://doi.org/10.1029/98jb00576>
- Andreani, M., Escartín, J., Delacour, A., Ildefonse, B., Godard, M., Dyment, J., ... Fouquet, Y. (2014). Tectonic structure, lithology, and hydrothermal signature of the rainbow massif (Mid-Atlantic Ridge 36° 14'N). *Geochemistry, Geophysics, Geosystems*, 15(9), 3543–3571. <https://doi.org/10.1002/2014GC005269>
- Angiboust, S., Agard, P., De Hoog, J. C. M., Omrani, J., & Plunder, A. (2013). Insights on deep, accretionary subduction processes from the Sistan ophiolitic “mélange” (Eastern Iran). *Lithos*, 156–159, 139–158. <https://doi.org/10.1016/j.lithos.2012.11.007>
- Arai, S. (1994). Characterization of spinel peridotites by olivine-spinel compositional relationships: Review and interpretation. *Chemical Geology*, 113(3–4), 191–204. [https://doi.org/10.1016/0009-2541\(94\)90066-3](https://doi.org/10.1016/0009-2541(94)90066-3)

- Arai, S., & Oyama, T. (1981). Unusual olivine in peridotite from Ochiai-Hokubo ultramafic complex, western Japan. *Annual Report of the Institute of Geoscience, University of Tsukuba* 7, 70–73.
- Arai, S. (1980). Dunite - harzburgite - chromitite complexes as refractory residue in the Sangun - Yamaguchi Zone, Western Japan. *Journal of Petrology*, 21(1), 141–165. <https://doi.org/10.1093/petrology/21.1.141>
- Arjmandzadeh, R., & Santos, J. F. (2014). Sr-Nd isotope geochemistry and tectonomagmatic setting of the Dehsalm Cu-Mo porphyry mineralizing intrusives from Lut Block, eastern Iran. *International Journal of Earth Sciences*, 103(1), 123–140. <https://doi.org/10.1007/s00531-013-0959-4>
- Asadi, S., Moore, F., & Zarasvandi, A. (2014). Discriminating productive and barren porphyry copper deposits in the southeastern part of the central Iranian volcano-plutonic belt, Kerman region, Iran: A review. *Earth-Science Reviews*, 138, 25–46. <https://doi.org/10.1016/j.earscirev.2014.08.001>
- Ashley, P. M. (1975). Opaque mineral assemblage formed during serpentinization in the coolac ultramafic belt, New South Wales. *Journal of the Geological Society of Australia*, 22(1), 91–102. <https://doi.org/10.1080/00167617408728877>
- Ashrafi, N., Jahangiri, A., Hasebe, N., & Eby, G. N. (2018). Petrology, geochemistry and geodynamic setting of Eocene-Oligocene alkaline intrusions from the Alborz-Azerbaijan magmatic belt, NW Iran. *Chemie Der Erde*, 78(4), 432–461. <https://doi.org/10.1016/j.chemer.2018.10.004>
- Augé, T. (1987). Chromite deposits in the northern Oman ophiolite: Mineralogical constraints. *Mineralium Deposita*, 22(1), 1–10. <https://doi.org/10.1007/BF00204235>
- Azizi, H., Asahara, Y., Mehrabi, B., & Chung, S. L. (2011). Geochronological and geochemical constraints on the petrogenesis of high-K granite from the Suffi abad area, Sanandaj-Sirjan Zone, NW Iran. *Chemie Der Erde*, 71(4), 363–376. <https://doi.org/10.1016/j.chemer.2011.06.005>
- Azizi, H., & Asahara, Y. (2013). Juvenile granite in the Sanandaj-Sirjan Zone, NW Iran: Late Jurassic-Early Cretaceous arc-continent collision. *International Geology Review*, 55(12), 1523–1540. <https://doi.org/10.1080/00206814.2013.782959>
- Azizi, H., Hadad, S., Stern, R. J., & Asahara, Y. (2019). Age, geochemistry, and emplacement of the ~40-Ma Baneh granite-appinite complex in a transpressional tectonic regime, Zagros suture zone, northwest Iran. *International Geology Review*, 61(2), 195–223. <https://doi.org/10.1080/00206814.2017.1422394>
- Azizi, H., & Jahangiri, A. (2008). Cretaceous subduction-related volcanism in the northern Sanandaj-Sirjan Zone, Iran. *Journal of Geodynamics*, 45(4–5), 178–190. <https://doi.org/10.1016/j.jog.2007.11.001>
- Azizi, H., Kazemi, T., & Asahara, Y. (2017). A-type granitoid in Hasansalaran complex, northwestern Iran: Evidence for extensional tectonic regime in northern Gondwana in the Late Paleozoic. *Journal of Geodynamics*, 108, 56–72. <https://doi.org/10.1016/j.jog.2017.05.003>

- Azizi, H., Lucci, F., Stern, R. J., Hasannejad, S., & Asahara, Y. (2018). The Late Jurassic Panjeh submarine volcano in the northern Sanandaj-Sirjan Zone, northwest Iran: Mantle plume or active margin? *Lithos*, 308–309, 364–380. <https://doi.org/10.1016/j.lithos.2018.03.019>
- Azizi, H., & Stern, R. J. (2019). Jurassic igneous rocks of the central Sanandaj–Sirjan zone (Iran) mark a propagating continental rift, not a magmatic arc. *Terra Nova*, 31(5), 415–423. <https://doi.org/10.1111/ter.12404>
- Babaie, H. A., Babaei, A., Ghazi, A. M., & Arvin, M. (2006). Geochemical,  $^{40}\text{Ar}/^{39}\text{Ar}$  age, and isotopic data for crustal rocks of the Neyriz ophiolite, Iran. *Canadian Journal of Earth Sciences*, 43(1), 57–70. <https://doi.org/10.1139/e05-111>
- Babazadeh, S. A., & De Wever, P. (2004). Radiolarian Cretaceous age of Soulabest radiolarites in ophiolite suite of eastern Iran. *Bulletin de La Société Géologique de France*, 175(2), 121–129. <https://doi.org/10.2113/175.2.121>
- Babazadeh, S. A., & De Wever, P. (2004). Age créacé des radiolarites de Soulabest dans la suite ophiolitique d’Iran oriental. *Bulletin de La Societe Geologique de France*, 175(2), 121–129. <https://doi.org/10.2113/175.2.121>
- Babazadeh, S., Ghorbani, M. R., Bröcker, M., D’Antonio, M., Cottle, J., Gebbing, T., Mazzeo, F.C., & Ahmadi, P. (2017). Late Oligocene–Miocene mantle upwelling and interaction inferred from mantle signatures in gabbroic to granitic rocks from the Urumieh–Dokhtar arc, south Ardestan, Iran. *International Geology Review*, 59(12), 1590–1608. <https://doi.org/10.1080/00206814.2017.1286613>
- Bach, W., & Früh-Green, G. L. (2010). Alteration of the oceanic lithosphere and implications for seafloor processes. *Elements*, 6(3), 173–178. <https://doi.org/10.2113/gselements.6.3.173>
- Bach, W., & Klein, F. (2009). The petrology of seafloor rodingites: Insights from geochemical reaction path modeling. *Lithos*, 112(1–2), 103–117. <https://doi.org/10.1016/j.lithos.2008.10.022>
- Bach, W., Paulick, H., Garrido, C. J., Ildefonse, B., Meurer, W. P., & Humphris, S. E. (2006). Unraveling the sequence of serpentinization reactions: Petrography, mineral chemistry, and petrophysics of serpentinites from MAR 15°N (ODP Leg 209, Site 1274). *Geophysical Research Letters*, 33(13). <https://doi.org/10.1029/2006GL025681>
- Bach, W., Paulick, H., Garrido, C. J., Ildefonse, B., Meurer, W. P., & Humphris, S. E. (2006). Unraveling the sequence of serpentinization reactions: Petrography, mineral chemistry, and petrophysics of serpentinites from MAR 15°N (ODP Leg 209, Site 1274). *Geophysical Research Letters*, 33(13). <https://doi.org/10.1029/2006GL025681>
- Badr, A., Davoudian, A. R., Shabanian, N., Azizi, H., Asahara, Y., Neubauer, F., Dong, Y., & Yamamoto, K. (2018). A- and I-type metagranites from the North Shahrekord Metamorphic Complex, Iran: Evidence for Early Paleozoic post-collisional magmatism. *Lithos*, 300–301, 86–104. <https://doi.org/10.1016/j.lithos.2017.12.008>
- Badr, M. J., Collins, A. S., Masoudi, F., Cox, G., & Mohajjel, M. (2013). The U-Pb age, geochemistry and tectonic significance of granitoids in the Soursat Complex, northwest Iran. *Turkish Journal of Earth Sciences*, 22(1), 1–31. <https://doi.org/10.3906/yer-1001-37>

- Baggio, S. B., Hartmann, L. A., Lazarov, M., Massonne, H. J., Opitz, J., Theye, T., & Viefhaus, T. (2018). Origin of native copper in the Paraná volcanic province, Brazil, integrating Cu stable isotopes in a multi-analytical approach. *Mineralium Deposita*, 53(3), 417–434. <https://doi.org/10.1007/s00126-017-0748-2>
- Bagheri, S., & Gol, S. D. (2020). The eastern Iranian orocline. *Earth-Science Reviews*, 210, 103322. <https://doi.org/10.1016/j.earscirev.2020.103322>
- Bagheri, S., & Stampfli, G. M. (2008). The Anarak, Jandaq and Posht-e-Badam metamorphic complexes in central Iran: New geological data, relationships and tectonic implications. *Tectonophysics*, 451(1–4), 123–155. <https://doi.org/10.1016/j.tecto.2007.11.047>
- Baharifar, A., Moinevaziri, H., Bellon, H., & Piqué, A. (2004). The crystalline complexes of Hamadan (Sanandaj–Sirjan zone, western Iran): metasedimentary Mesozoic sequences affected by Late Cretaceous tectono-metamorphic and plutonic events. *Comptes Rendus Geoscience*, 336(16), 1443–1452. <https://doi.org/10.1016/j.crte.2004.09.014>
- Baharifar, A., Moinevaziri, H., Bellon, H., & Piqué, A. (2004). Les complexes cristallins de Hamadan (zone de Sanandaj-Sirjan, Iran occidentale): Des roches métasédimentaires mésozoïques affectées par un événement tectono-métamorphique et magmatique au Crétacé supérieur. *Comptes Rendus - Geoscience*, 336(16), 1443–1452. <https://doi.org/10.1016/j.crte.2004.09.014>
- Bahrudi, A. (1999). Geological Map of the Forumad Quadrangle: Tehran, Geological Survey of Iran, scale 1:100,000.
- Bahrudi, A., & Omrani, S.J. (1999). Geological Map of the Bashtin Quadrangle: Tehran, Geological Survey of Iran, scale 1:100,000.
- Balaghi Einalou, M., Sadeghian, M., Zhai, M., Ghasemi, H., & Mohajjel, M. (2014). Zircon U-Pb ages, Hf isotopes and geochemistry of the schists, gneisses and granites in Delbar Metamorphic-Igneous Complex, SE of Shahrood (Iran): Implications for Neoproterozoic geodynamic evolutions of Central Iran. *Journal of Asian Earth Sciences*, 92, 92–124. <https://doi.org/10.1016/j.jseaes.2014.06.011>
- Ballhaus, C., Berry, R. F., & Green, D. H. (1991). High pressure experimental calibration of the olivine-orthopyroxene-spinel oxygen geobarometer: implications for the oxidation state of the upper mantle. *Contributions to Mineralogy and Petrology*, 107(1), 27–40. <https://doi.org/10.1007/BF00311183>
- Ballato, P., Uba, C. E., Landgraf, A., Strecker, M. R., Sudo, M., Stockli, D. F., Friedrich, A., & Tabatabaei, S. H. (2011). Arabia-Eurasia continental collision: Insights from late Tertiary foreland-basin evolution in the Alborz Mountains, Northern Iran. *Bulletin of the Geological Society of America*, 123(1–2), 106–131. <https://doi.org/10.1130/B30091.1>
- Barbero, E., Pandolfi, L., Delavari, M., Dolati, A., Saccani, E., Catanzariti, R., Luciani, V., Chiari, M., & Marroni, M. (2021). The western Durkan Complex (Makran Accretionary Prism, SE Iran): A Late Cretaceous tectonically disrupted seamounts chain and its role in controlling deformation style. *Geoscience Frontiers*, 12(3). <https://doi.org/10.1016/j.gsf.2020.12.001>
- Barnes, I., Lamarche, V. C., & Himmelberg, G. (1967). Geochemical evidence of present-day serpentinization. *Science*, 156(3776), 830–832. <https://doi.org/10.1126/science.156.3776.830>

- Barnes, I., Lamarche, V. C., & Himmelberg, G. (1967). Geochemical evidence of present-day serpentinization. *Science*, 156(3776), 830–832. <https://doi.org/10.1126/science.156.3776.830>
- Barnes, I., O'Neil, J. R., & Trescases, J. J. (1978). Present day serpentinization in New Caledonia, Oman and Yugoslavia. *Geochimica et Cosmochimica Acta*, 42(1), 144–145. [https://doi.org/10.1016/0016-7037\(78\)90225-9](https://doi.org/10.1016/0016-7037(78)90225-9)
- Barnes, I., & O'Neil, J. R. (1969). The relationship between fluids in some fresh alpine-type ultramafics and possible modern serpentinization, western United States. *Bulletin of the Geological Society of America*, 80(10), 1947–1960. [https://doi.org/10.1130/0016-7606\(1969\)80\[1947:TRBFIS\]2.0.CO;2](https://doi.org/10.1130/0016-7606(1969)80[1947:TRBFIS]2.0.CO;2)
- Barnes, S. J. (2000). Chromite in komatiites, II. Modification during greenschist to mid-amphibolite facies metamorphism. *Journal of Petrology*, 41(3), 387–409. <https://doi.org/10.1093/petrology/41.3.387>
- Barnes, S. J. (2000). Chromite in komatiites, II. Modification during greenschist to mid-amphibolite facies metamorphism. *Journal of Petrology*, 41(3), 387–409. <https://doi.org/10.1093/petrology/41.3.387>
- Barnes, S. J., & Roeder, P. L. (2001). The range of spinel compositions in terrestrial mafic and ultramafic rocks. *Journal of Petrology*, 42(12), 2279–2302. <https://doi.org/10.1093/petrology/42.12.2279>
- Baroz, F., Macaudière, J., Montigny, R., Noghreyan, M., Ohnenstetter, M., & Rocci, G. (1984). Ophiolites and Related Formations in the Central Part of the Sabzevar Range (Iran) and Possible Geotectonic Reconstructions. *Neues Jahrbuch Für Geologie Und Paläontologie - Abhandlungen*, 168(2–3), 358–388. <https://doi.org/10.1127/njgpa/168/1984/358>
- Barra, F., Gervilla, F., Hernández, E., Reich, M., Padrón-Navarta, J. A., & González-Jiménez, J. M. (2014). Alteration patterns of chromian spinels from La Cabaña peridotite, south-central Chile. *Mineralogy and Petrology*, 108(6), 819–836. <https://doi.org/10.1007/s00710-014-0335-5>
- Barra, F., Gervilla, F., Hernández, E., Reich, M., Padrón-Navarta, J. A., & González-Jiménez, J. M. (2014). Alteration patterns of chromian spinels from La Cabaña peridotite, south-central Chile. *Mineralogy and Petrology*, 108(6), 819–836. <https://doi.org/10.1007/s00710-014-0335-5>
- Barriga, F. J. A. S., Fouquet, Y., Almeida, A., Biscoito, M.J., Charlou, J-L., Costa, R.L.P., Dias, A., Marques, A.M.S.F., Miranda, J.M.A., Olu, K., Porteiro, F., Queiroz, M.G.P.S. (1998). Discovery of the Saldanha hydrothermal field on the Famous segment of the MAR (36°30'N), *Eos Trans. AGU*, 79(45), Fall Meet. Suppl., F67.
- Barth, M. G., Mason, P. R. D., Davies, G. R., & Drury, M. R. (2008). The Othris Ophiolite, Greece: A snapshot of subduction initiation at a mid-ocean ridge. *Lithos*, 100(1–4), 234–254. <https://doi.org/10.1016/j.lithos.2007.06.018>
- Batanova, V. G., Sobolev, A. V., & Magnin, V. (2018). Trace element analysis by EPMA in geosciences: Detection limit, precision and accuracy. In *IOP Conference Series: Materials Science and Engineering*, 304, p. 304(1). <https://doi.org/10.1088/1757-899X/304/1/012001>

- Bayati, M., Esmaeily, D., Maghdour-Mashhour, R., Li, X. H., & Stern, R. J. (2017). Geochemistry and petrogenesis of Kolah-Ghazi granitoids of Iran: Insights into the Jurassic Sanandaj-Sirjan magmatic arc. *Chemie Der Erde*, 77(2), 281–302. <https://doi.org/10.1016/j.chemer.2017.02.003>
- Beard, J. S., Frost, B. R., Fryer, P., McCaig, A., Searle, R., Ildefonse, B., ... Sharma, S. K. (2009). Onset and progression of serpentinization and magnetite formation in Olivine-rich troctolite from IODP hole U1309D. *Journal of Petrology*, 50(3), 387–403. <https://doi.org/10.1093/petrology/egp004>
- Beard, J. S., & Frost, B. R. (2016). The stoichiometric effects of ferric iron substitutions in serpentine from microprobe data. *International Geology Review*, 59(5–6), 541–547. <https://doi.org/10.1080/00206814.2016.1197803>
- Bebout, G. E., & Barton, M. D. (1989). Fluid flow and metasomatism in a subduction zone hydrothermal system: Catalina Schist terrane, California. *Geology*, 17(11), 976–980. [https://doi.org/10.1130/0091-7613\(1989\)017<0976:FFAMIA>2.3.CO;2](https://doi.org/10.1130/0091-7613(1989)017<0976:FFAMIA>2.3.CO;2)
- Beeson, M. H., & Jackson, E. D. (1969). Chemical composition of altered chromites from the Stillwater Complex, Montana. *American Mineralogist*, 54(7–8), 1084–1100.
- Beinlich, A., Klemd, R., John, T., & Gao, J. (2010). Trace-element mobilization during Cametasomatism along a major fluid conduit: Eclogitization of blueschist as a consequence of fluid-rock interaction. *Geochimica et Cosmochimica Acta*, 74(6), 1892–1922. <https://doi.org/10.1016/j.gca.2009.12.011>
- Beinlich, A., von Heydebrand, A., Klemd, R., Martin, L., & Hicks, J. (2020). Desulphurisation, chromite alteration, and bulk rock PGE redistribution in massive chromitite due to hydrothermal overprint of the Panton Intrusion, east Kimberley, Western Australia. *Ore Geology Reviews*, 118, 103288. <https://doi.org/10.1016/j.oregeorev.2019.103288>
- Ben Othman, D., Luck, J. M., Bodinier, J. L., Arndt, N. T., & Albarède, F. (2006). Cu–Zn isotopic variations in the Earth's mantle. *Geochimica et Cosmochimica Acta*, 70(18), A46. <https://doi.org/10.1016/j.gca.2006.06.201>
- Berberian, F., & Berberian, M. (1981). Tectono-plutonic episodes in Iran. In: H.K. Gupta and F.M. Delany (eds.), Zagros-Hindu Kush-Himalaya Geodynamic Evolution, Am. *American Geophysical Union, Washington DC*, 5–32.
- Berberian, F., Muir, I. D., Pankhurst, R. J., & Berberian, M. (1982). Late Cretaceous and early Miocene Andean-type plutonic activity in northern Makran and central Iran. *Journal of the Geological Society*, 139(5), 605–614. <https://doi.org/10.1144/gsjgs.139.5.0605>
- Berberian, M. (1983). The southern Caspian: a compressional depression floored by a trapped, modified oceanic crust. *Canadian Journal of Earth Sciences*, 20(2), 163–183. <https://doi.org/10.1139/e83-015>
- Berberian, M., & King, G. C. P. (1981). Towards a Paleogeography and Tectonic Evolution of Iran. *Canadian Journal of Earth Sciences*, 18(2), 210–265. <https://doi.org/10.1139/e81-019>
- Beydokhti, R. M., Karimpour, M. H., Mazaheri, S. A., Santos, J. F., & Klötzli, U. (2015). U–Pb zircon geochronology, Sr–Nd geochemistry, petrogenesis and tectonic setting of

- Mahoor granitoid rocks (Lut Block, Eastern Iran). *Journal of Asian Earth Sciences*, 111, 192–205. <https://doi.org/10.1016/j.jseaes.2015.07.028>
- Bird, P. (2003). An updated digital model of plate boundaries. *Geochemistry, Geophysics, Geosystems*, 4(3). <https://doi.org/10.1029/2001GC000252>
- Blaauw, C., Stroink, G., Leiper, W., & Zentilli, M. (1979). Moessbauer analysis of some Canadian chrysotiles. *Canadian Mineralogist*, 17, 713–717.
- Blanc, E. J. P., Allen, M. B., Inger, S., & Hassani, H. (2003). Structural styles in the Zagros Simple Folded Zone, Iran. *Journal of the Geological Society*, 160(3), 401–412. <https://doi.org/10.1144/0016-764902-110>
- Bliss, N. W., & MacLean, W. H. (1975). The paragenesis of zoned chromite from central Manitoba. *Geochimica et Cosmochimica Acta*, 39(6–7), 973–990. [https://doi.org/10.1016/0016-7037\(75\)90042-3](https://doi.org/10.1016/0016-7037(75)90042-3)
- Bordage, A., Balan, E., de Villiers, J. P. R., Cromarty, R., Juhin, A., Carvallo, C., Calas, G., Sunder Raju, P.V., & Glatzel, P. (2011). V oxidation state in Fe-Ti oxides by high-energy resolution fluorescence-detected X-ray absorption spectroscopy. *Physics and Chemistry of Minerals*, 38(6), 449–458. <https://doi.org/10.1007/s00269-011-0418-3>
- Borisova, A. Y., Ceuleneer, G., Kamenetsky, V. S., Arai, S., Béjina, F., Abily, B., Bindeman, I.N., Polvé, M., Parseval, P.D., Aigouy, T., & Pokrovski, G. S. (2012). A new view on the petrogenesis of the Oman ophiolite chromitites from microanalyses of chromite-hosted inclusions. *Journal of Petrology*, 53(12), 2411–2440. <https://doi.org/10.1093/petrology/egs054>
- Bornhorst, T. J., & Mathur, R. (2017). Copper isotope constraints on the genesis of the keweenaw peninsula native copper district, Michigan, USA. *Minerals*, 7(10), 185. <https://doi.org/10.3390/min7100185>
- Bostock, M. G., Hyndman, R. D., Rondenay, S., & Peacock, S. M. (2002). An inverted continental moho and serpentinization of the forearc mantle. *Nature*, 417(6888), 536–538. <https://doi.org/10.1038/417536a>
- Bosi, F., Biagioni, C., & Pasero, M. (2019). Nomenclature and classification of the spinel supergroup. *European Journal of Mineralogy*, 31, 183–192. <https://doi.org/10.1127/ejm/2019/0031-2788>
- Boutroy, E., Dare, S. A. S., Beaudoin, G., Barnes, S. J., & Lightfoot, P. C. (2014). Magnetite composition in Ni-Cu-PGE deposits worldwide: Application to mineral exploration. *Journal of Geochemical Exploration*, 145, 64–81. <https://doi.org/10.1016/j.gexplo.2014.05.010>
- Braud, J., & Ricou, L.E. (1971). L'accident du Zagros ou Main Thrust un charriage et un coulissement. *Comptes Rendus Acad Sci*, 272, 203–206.
- Bretis, B., Grasemann, B., & Conradi, F. (2012). An active fault zone in the western Kopet-Dagh (Iran). *Austrian Journal of Earth Sciences*, 105, 95–107.
- Bröcker, M., Fotoohi Rad, G., Burgess, R., Theunissen, S., Paderin, I., Rodionov, N., & Salimi, Z. (2013). New age constraints for the geodynamic evolution of the Sistan Suture Zone, eastern Iran. *Lithos*, 170–171, 17–34. <https://doi.org/10.1016/j.lithos.2013.02.012>

- Brown, J. R., & Karson, J. A. (1988). Variations in axial processes on the Mid-Atlantic Ridge: The median valley of the MARK area. *Marine Geophysical Researches*, 10(1–2), 109–138. <https://doi.org/10.1007/BF02424663>
- Brunet, F. (2019). Hydrothermal production of hopenspiinfspi2closespiinfspi and magnetite from steel slags: A geo-inspired approach based on olivine serpentinization. *Frontiers in Earth Science*, 7, 17. <https://doi.org/10.3389/feart.2019.00017>
- Buddington, A. F., & Lindsley, D. H. (1964). Iron-titanium oxide minerals and synthetic equivalents. *Journal of Petrology*, 5(2), 310–357. <https://doi.org/10.1093/petrology/5.2.310>
- Burkhard, D. J. M. (1993). Accessory chromium spinels: Their coexistence and alteration in serpentinites. *Geochimica et Cosmochimica Acta*, 57(6), 1297–1306. [https://doi.org/10.1016/0016-7037\(93\)90066-6](https://doi.org/10.1016/0016-7037(93)90066-6)
- Bussolesi, M., Grieco, G., Cavallo, A., & Zaccarini, F. (2022). Different tectonic evolution of fast cooling ophiolite mantles recorded by olivine-spinel geothermometry: case studies from Iballe (Albania) and Nea Roda (Greece). *Minerals*, 12, 64. <https://doi.org/10.3390/min12010064>.
- Cabral, A. R., & Beaudoin, G. (2007). Volcanic red-bed copper mineralisation related to submarine basalt alteration, Mont Alexandre, Quebec Appalachians, Canada. *Mineralium Deposita*, 42(8), 901–912. <https://doi.org/10.1007/s00126-007-0141-7>
- Calzolari, G., Della Seta, M., Rossetti, F., Nozaem, R., Vignaroli, G., Cosentino, D., & Faccenna, C. (2016). Geomorphic signal of active faulting at the northern edge of Lut Block: Insights on the kinematic scenario of Central Iran. *Tectonics*, 35(1), 76–102. <https://doi.org/10.1002/2015TC003869>
- Camp, V. E., & Griffis, R. J. (1982). Character, genesis and tectonic setting of igneous rocks in the Sistan suture zone, eastern Iran. *Lithos*, 15(3), 221–239. [https://doi.org/10.1016/0024-4937\(82\)90014-7](https://doi.org/10.1016/0024-4937(82)90014-7)
- Cann, J. R., Blackman, D. K., Smith, D. K., McAllister, E., Janssen, B., Mello, S., Avgerinos, E., Pascoe, A.R., & Escartín, J. (1997). Corrugated slip surfaces formed at ridge–transform intersections on the Mid-Atlantic Ridge. *Nature*, 385(6614), 329–332. <https://doi.org/10.1038/385329a0>
- Cannat, M. (1993). Emplacement of mantle rocks in the seafloor at mid-ocean ridges. *Journal of Geophysical Research*, 98(B3), 4163–4172. <https://doi.org/10.1029/92JB02221>
- Cannat, M., Bideau, D., & Bougault, H. (1992). Serpentinized peridotites and gabbros in the Mid-Atlantic Ridge axial valley at 15°37'N and 16°52'N. *Earth and Planetary Science Letters*, 109(1–2), 87–106. [https://doi.org/10.1016/0012-821X\(92\)90076-8](https://doi.org/10.1016/0012-821X(92)90076-8)
- Cannat, M., Bideau, D., & Bougault, H. (1992). Serpentinized peridotites and gabbros in the Mid-Atlantic Ridge axial valley at 15°37'N and 16°52'N. *Earth and Planetary Science Letters*, 109(1–2), 87–106. [https://doi.org/10.1016/0012-821X\(92\)90076-8](https://doi.org/10.1016/0012-821X(92)90076-8)
- Cannat, M., Fontaine, F., & Escartín, J. (2013). Serpentinization and Associated Hydrogen and Methane Fluxes at Slow Spreading Ridges. In *Diversity of Hydrothermal Systems on Slow Spreading Ocean Ridges* (pp. 241–264). <https://doi.org/10.1029/2008GM000760>

- Carbonin, S., Martin, S., Tumiati, S., & Rossetti, P. (2015). Magnetite from the Cogne serpentinites (Piemonte ophiolite nappe, Italy). Insights into seafloor fluid–rock interaction. *European Journal of Mineralogy*, 27(1), 31–50. <https://doi.org/10.1127/ejm/2014/0026-2410>
- Carlson, R. L., & Jay Miller, D. (1997). A new assessment of the abundance of serpentinite in the oceanic crust. *Geophysical Research Letters*, 24(4), 457–460. <https://doi.org/10.1029/97GL00144>
- Castro, A., Aghazadeh, M., Badrzadeh, Z., & Chichorro, M. (2013). Late Eocene-Oligocene post-collisional monzonitic intrusions from the Alborz magmatic belt, NW Iran. An example of monzonite magma generation from a metasomatized mantle source. *Lithos*, 180–181, 109–127. <https://doi.org/10.1016/j.lithos.2013.08.003>
- Ceuleneer, G., & Nicolas, A. (1985). Structures in podiform chromite from the Maqсад district (Sumail ophiolite, Oman). *Mineralium Deposita*, 20(3), 177–184. <https://doi.org/10.1007/BF00204562>
- Charlou, J. L., Donval, J. P., Fouquet, Y., Jean-Baptiste, P., & Holm, N. (2002). Geochemistry of high H<sub>2</sub> and CH<sub>4</sub> vent fluids issuing from ultramafic rocks at the Rainbow hydrothermal field (36°14'N, MAR). *Chemical Geology*, 191(4), 345–359. [https://doi.org/10.1016/S0009-2541\(02\)00134-1](https://doi.org/10.1016/S0009-2541(02)00134-1)
- Charlou, J. L., Donval, J. P., Konn, C., Ondréas, H., Fouquet, Y., Jean-Baptiste, P., & Fourré, E. (2013). High Production and Fluxes of H<sub>2</sub> and CH<sub>4</sub> and Evidence of Abiotic Hydrocarbon Synthesis by Serpentinization in Ultramafic-Hosted Hydrothermal Systems on the Mid-Atlantic Ridge. In *Diversity of Hydrothermal Systems on Slow Spreading Ocean Ridges* (pp. 265–296). <https://doi.org/10.1029/2008GM000752>
- Charlou, J. L., Donval, J. P., Konn, C., Ondreas, H., Fouquet, Y., Jean-Baptiste, P., & Fourre, E. (2010). High production and fluxes of H<sub>2</sub> and CH<sub>4</sub> and evidence of abiotic hydrocarbon synthesis by serpentinization in ultramafic-hosted hydrothermal systems on the Mid-Atlantic Ridge, in *Diversity of Hydrothermal Systems on Slow Spreading Ocean Ridges*, Geophys. Monogr. Ser., vol. 188, edited by P. A. Rona et al., pp. 321– 367, AGU, Washington, D. C.
- Chen, T., Jin, Z., Shen, A. H., & Li, W. (2016). Altered spinel as a petrotextonic indicator in abyssal peridotite from the easternmost part of Southwest Indian Ridge. *Journal of Earth Science*, 27, 611–622. <https://doi.org/10.1007/s12583-016-0707-3>
- Christensen, N. I. (1972). The abundance of serpentinites in the oceanic crust. *The Journal of Geology*, 80(6), 709–719. <https://doi.org/10.1086/627796>
- Ciobanu, C. L., Verdugo-Ihl, M. R., Slattery, A., Cook, N. J., Ehrig, K., Courtney-Davies, L., & Wade, B. P. (2019). Silician Magnetite: Si–Fe-nanoprecipitates and other mineral inclusions in Magnetite from the Olympic Dam deposit, South Australia. *Minerals*, 9(5), 311. <https://doi.org/10.3390/min9050311>
- Clark, I. D., & Fontes, J. C. (1990). Paleoclimatic reconstruction in northern Oman based on carbonates from hyperalkaline groundwaters. *Quaternary Research*, 33(3), 320–336. [https://doi.org/10.1016/0033-5894\(90\)90059-T](https://doi.org/10.1016/0033-5894(90)90059-T)
- Colás, V., González-Jiménez, J. M., Griffin, W. L., Fanlo, I., Gervilla, F., O'Reilly, S. Y., Pearson, N.J., Kerestedjian, T., & Proenza, J. A. (2014). Fingerprints of metamorphism in

- chromite: New insights from minor and trace elements. *Chemical Geology*, 389, 137-152. <https://doi.org/10.1016/j.chemgeo.2014.10.001>
- Colás, V., Padrón-Navarta, J. A., González-Jiménez, J. M., Fanlo, I., López Sánchez-Vizcaíno, V., Gervilla, F., & Castroviejo, R. (2017). The role of silica in the hydrous metamorphism of chromite. *Ore Geology Reviews*, 90, 274-286. <https://doi.org/10.1016/j.oregeorev.2017.02.025>
- Colás, V., González-Jiménez, J. M., Camprubí, A., Proenza, J. A., Griffin, W. L., Fanlo, I., O'Reilly, S.Y., Gervilla, F., & González-Partida, E. (2019). A reappraisal of the metamorphic history of the Tehuitzingo chromitite, Puebla state, Mexico. *International Geology Review*, 61(14), 1706-1727. <https://doi.org/10.1080/00206814.2018.1542633>
- Coleman, R. G. (1967). Low-temperature reaction zones and alpine ultramafic rocks of California, Oregon, and Washington. *Geological Society Bulletin*. <https://doi.org/10.3133/b1247>
- Connolly, J. A. D. (2005). Computation of phase equilibria by linear programming: A tool for geodynamic modeling and its application to subduction zone decarbonation. *Earth and Planetary Science Letters*, 236(1-2), 524-541. <https://doi.org/10.1016/j.epsl.2005.04.033>
- Coogan, L. A., Saunders, A. D., & Wilson, R. N. (2014). Aluminum-in-olivine thermometry of primitive basalts: Evidence of an anomalously hot mantle source for large igneous provinces. *Chemical Geology*, 368, 1-10. <https://doi.org/10.1016/j.chemgeo.2014.01.004>
- Cornwall, H. R. (1956). A summary of ideas on the origin of native copper deposits. *Economic Geology*, 51(7), 615-631. <https://doi.org/10.2113/gsecongeo.51.7.615>
- Dare, S. A. S., Barnes, S. J., Beaudoin, G., Méric, J., Boutroy, E., & Potvin-Doucet, C. (2014). Trace elements in magnetite as petrogenetic indicators. *Mineralium Deposita*, 49(7), 785-796. <https://doi.org/10.1007/s00126-014-0529-0>
- Dargahi, S., Arvin, M., Pan, Y., & Babaei, A. (2010). Petrogenesis of post-collisional A-type granitoids from the Urumieh-Dokhtar magmatic assemblage, Southwestern Kerman, Iran: Constraints on the Arabian-Eurasian continental collision. *Lithos*, 115(1-4), 190-204. <https://doi.org/10.1016/j.lithos.2009.12.002>
- Davoudian, A. R., Genser, J., Dachs, E., & Shabanian, N. (2008). Petrology of eclogites from north of Shahrekord, Sanandaj-Sirjan Zone, Iran. *Mineralogy and Petrology*, 92(3-4), 393-413. <https://doi.org/10.1007/s00710-007-0204-6>
- Davis, D. W., & Edwards, G. R. (1986). Crustal evolution of Archean rocks in the Kakagi Lake area, Wabigoon Subprovince, Ontario, as interpreted from high-precision U- Pb geochronology. *Canadian Journal of Earth Sciences*, 23(2), 182-192. <https://doi.org/10.1139/e86-021>
- de Martin, B. J., Reves-Sohn, R. A., Canales, J. P., & Humphris, S. E. (2007). Kinematics and geometry of active detachment faulting beneath the Trans-Atlantic geotraverse (TAG) hydrothermal field on the Mid-Atlantic Ridge. *Geology*, 35(8), 711-714. <https://doi.org/10.1130/G23718A.1>
- de Obeso, J. C., & Kelemen, P. B. (2020). Major element mobility during serpentinization, oxidation and weathering of mantle peridotite at low temperatures. *Philosophical*

- Deditius, A. P., Reich, M., Simon, A. C., Suvorova, A., Knipping, J., Roberts, M. P., Rubanov, S., Dodd, A., & Saunders, M. (2018). Nanogeochemistry of hydrothermal magnetite. *Contributions to Mineralogy and Petrology*, 173(6), 6. <https://doi.org/10.1007/s00410-018-1474-1>
- Dekov, V. M., Rouxel, O., Asael, D., Hålenius, U., & Munnik, F. (2013). Native Cu from the oceanic crust: Isotopic insights into native metal origin. *Chemical Geology*, 359, 136–149. <https://doi.org/10.1016/j.chemgeo.2013.10.001>
- Della Giusta, A., Carbonin, S., & Russo, U. (2011). Chromite to magnetite transformation: Compositional variations and cation distributions (southern Aosta Valley, Western Alps, Italy). *Periodico Di Mineralogia*, 80(1 SPEC. ISSUE), 1–17. <https://doi.org/10.2451/2011PM0001>
- deMartin, B. J. (2007). Experimental and seismological constraints on the rheology, evolution, and alteration of the lithosphere at oceanic spreading centers. Experimental and seismological constraints on the rheology, evolution, and alteration of the lithosphere at oceanic spreading centers. PhD thesis, Massachusetts Institute of Technology and Woods Hole Oceanographic Institution. 212 pp. <https://doi.org/10.1575/1912/1686>
- Deschamps, F., Godard, M., Guillot, S., & Hattori, K. (2013). Geochemistry of subduction zone serpentinites: A review. *Lithos*, 178, 96–127. <https://doi.org/10.1016/j.lithos.2013.05.019>
- DeShon, H. R., & Schwartz, S. Y. (2004). Evidence for serpentinization of the forearc mantle wedge along the Nicoya Peninsula, Costa Rica. *Geophysical Research Letters*, 31(21). <https://doi.org/10.1029/2004GL021179>
- Dick, H. J. B., & Bullen, T. (1984). Chromian spinel as a petrogenetic indicator in abyssal and alpine-type peridotites and spatially associated lavas. *Contributions to Mineralogy and Petrology*, 86(1), 54–76. <https://doi.org/10.1007/BF00373711>
- Diener, J. F. A., Powell, R., White, R. W., & Holland, T. J. B. (2007). A new thermodynamic model for clino- and orthoamphiboles in the system Na<sub>2</sub>O-CaO-FeO-MgO-Al<sub>2</sub>O<sub>3</sub>-SiO<sub>2</sub>-H<sub>2</sub>O-O. *Journal of Metamorphic Geology*, 25(6), 631–656. <https://doi.org/10.1111/j.1525-1314.2007.00720.x>
- Dubessy, J., Poty, B., & Ramboz, C. (1989). Advances in C-O-H-N-S fluid geochemistry based on micro-Raman spectrometric analysis of fluid inclusions. *European Journal of Mineralogy*, 1(4), 517–534.
- Dupuis, C., & Beaudoin, G. (2011). Discriminant diagrams for iron oxide trace element fingerprinting of mineral deposit types. *Mineralium Deposita*, 46(4), 319–335. <https://doi.org/10.1007/s00126-011-0334-y>
- Dyment, J., Arkani-Hamed, J., & Ghods, A. (1997). Contribution of serpentinized ultramafics to marine magnetic anomalies at slow and intermediate spreading centres: Insights from the shape of the anomalies. *Geophysical Journal International*, 129(3), 691–701. <https://doi.org/10.1111/j.1365-246X.1997.tb04504.x>

- Eckstrand, O. R. (1975). The dumont serpentinite: A model for control of nickel-iferous opaque mineral assemblages by alteration reactions in ultramafic rocks. *Economic Geology*, 70(1), 183–201. <https://doi.org/10.2113/gsecongeo.70.1.183>
- Edgell, H. S. (1996). Salt tectonism in the Persian Gulf Basin. *Geological Society Special Publication*, 100, 129–151. <https://doi.org/10.1144/GSL.SP.1996.100.01.10>
- Eftekharneshad, J. (1981). Tectonic division of Iran with respect to sedimentary basins [in Persian], *Journal of Iranian Petroleum Society*, 82, 19–28.
- Engi, M. (1984). Equilibria involving Al-Cr spinel; Mg-Fe exchange with olivine; experiments, thermodynamic analysis, and consequences for geothermometry; erratum. *American Journal of Science*, 284(3), 288. <https://doi.org/10.2475/ajs.284.3.288>
- Escartín, J., Hirth, G., & Evans, B. (1997). Effects of serpentinitization on the lithospheric strength and the style of normal faulting at slow-spreading ridges. *Earth and Planetary Science Letters*, 151(3–4), 181–189. [https://doi.org/10.1016/s0012-821x\(97\)81847-x](https://doi.org/10.1016/s0012-821x(97)81847-x)
- Escartín, J., Hirth, G., & Evans, B. (2001). Strength of slightly serpentinitized peridotites: Implications for the tectonics of oceanic lithosphere. *Geology*, 29(11), 1023–1026. [https://doi.org/10.1130/0091-7613\(2001\)029<1023:SOSSPI>2.0.CO;2](https://doi.org/10.1130/0091-7613(2001)029<1023:SOSSPI>2.0.CO;2)
- Escartín, J., Mével, C., MacLeod, C. J., & McCaig, A. M. (2003). Constraints on deformation conditions and the origin of oceanic detachments: The Mid-Atlantic Ridge core complex at 15°45'N. *Geochemistry, Geophysics, Geosystems*, 4(8). <https://doi.org/10.1029/2002GC000472>
- Eslami, A. (2015). Mineralogy, Geochemistry and Genesis of Chromite and Platinum Group Minerals at Cheshmeh-Bid Chromite Deposit, Neyriz Ophiolite. MSc thesis. Tarbiat Modares University.
- Eslami, A., Arai, S., Miura, M., & Mackizadeh, M. A. (2018a). Metallogeny of the peridotite-hosted magnetite ores of the Nain ophiolite, Central Iran: Implications for Fe concentration processes during multi-episodic serpentinitization. *Ore Geology Reviews*, 95, 680–694. <https://doi.org/10.1016/j.oregeorev.2018.03.020>
- Eslami, A., Grieco, G., & Davoudi, M. (2018b). Preliminary geochemical studies of podiform chromitites in the Cheshmeh-Khan Mining District, central sector of Sabzevar ophiolite belt, NE Iran. In: 8th Geochemistry Symposium, Antalya, Turkey
- Eslami, A., Ghaderi, M., Griffin, W. L., Gain, S., Grieco, G., & González-Jiménez, J. M. (2015). Magmatic and post-magmatic signatures of chromian spinels in podiform chromitites from the Cheshmeh-Bid chromitite deposit, Khajeh-Jamali ophiolitic massifs, Iran. *Ophioliti*, 40(2), 91–106. <https://doi.org/10.4454/ofioliti.v40i2.437>
- Eslami, A., Malvoisin, B., Grieco, G., Aradi, L. E., Marchesi, C., Cavallo, A., Montanini, A., Borghini, G., Mathur, R., Ikehata, K., Davis, D.W., Li, C-H., & Szabó, C. (2021). Native copper formation associated with serpentinitization in the Cheshmeh-Bid ophiolite massif (Southern Iran). *Lithos*, 382–383, 105953. <https://doi.org/10.1016/j.lithos.2020.105953>
- Eslami, A., Malvoisin, B., Brunet, F., Kananian, A., Bach, W., Grieco, G., Cavallo, A., & Gatta, G. D. (2021). Podiform magnetite ore(s) in the Sabzevar ophiolite (NE Iran): oceanic hydrothermal alteration of a chromite deposit. *Contributions to Mineralogy and Petrology*, 176(43). <https://doi.org/10.1007/s00410-021-01799-0>

- Esmaeili, R., Ao, S., Shafai Moghadam, H., Zhang, Z., Griffin, W. L., Ebrahimi, M., Xiao, W., Wan, B., & Bhandari, S. (2021). Amphibolites from makran accretionary complex record Permian-Triassic Neo-Tethyan evolution. *International Geology Review*, 1-17. <https://doi.org/10.1080/00206814.2021.1946663>
- Evans, B. W. (1977). Metamorphism of Alpine Peridotite and Serpentinite. *Annual Review of Earth and Planetary Sciences*, 5(1), 397–447. <https://doi.org/10.1146/annurev.ea.05.050177.002145>
- Evans, B. W., Dyar, M. D., & Kuehner, S. M. (2012). Implications of ferrous and ferric iron in antigorite. *American Mineralogist*, 97(1), 184–196. <https://doi.org/10.2138/am.2012.3926>
- Evans, B. W. & Frost, B. R. (1975). Chrome spinel in progressive metamorphism—a preliminary analysis. *Geochimica et Cosmochimica Acta*, 39, 959–972.
- Evans, B. W., Johannes, W., Oterdoom, H., & Trommsdorff, V. (1976). Stability of chrysotile and antigorite in the serpentinite multisystem. *Schweizerische Mineralogische Und Petrographische Mitteilungen*, 56, 79–93.
- Evans, K. A., Powell, R., & Frost, B. R. (2013). Using equilibrium thermodynamics in the study of metasomatic alteration, illustrated by an application to serpentinites. *Lithos*, 168–169, 67–84. <https://doi.org/10.1016/j.lithos.2013.01.016>
- Falcon, N. (1974) Zagros mountains, Mesozoic-Cenozoic orogenic belts (edited by Spencer, A.). *Spec. Pub. Geological Society of London*, 4, 199–211.
- Faramarzi, R., Alikhani, M., Pourfaraj, H., Akhoundi, H., Mehrvarz, A., Sohrabi Mehr, M., & Ansari, M. (2017). Geological Map of the Cheshmeh-Khan, KBC Exploration group, scale 1:25,000.
- Faramarzi, R., Pourfaraj, H., Alikhani, M., Akhoundi, H., Mehrvarz, A., Sohrabi Mehr, M., & Ansari, M. (2018). Geological Map of the Cheshmeh-Palangan, KBC Exploration group, scale 1:25,000.
- Farhoudi, G., & Karig, D. E. (1977). Makran of Iran and Pakistan as an active arc system. *Geology*, 5(11), 664–668. [https://doi.org/10.1130/0091-7613\(1977\)5<664:MOIAPA>2.0.CO;2](https://doi.org/10.1130/0091-7613(1977)5<664:MOIAPA>2.0.CO;2)
- Fleet, M. E., Angeli, N., & Yuanming Pan. (1993). Oriented chlorite lamellae in chromite from the Pedra Branca mafic- ultramafic complex, Ceara, Brazil. *American Mineralogist*, 78(1–2), 68–74.
- Floyd, P. A. (1997). Serpentinites: Records of Tectonic and Petrological History. *Mineralogical Magazine*, 61(408), 742.
- Floyd, P. A. (1997). D.S. O’Hanley Serpentinites: Records of Tectonic and Petrological History, New York and Oxford (Oxford University Press). 1996, xiv + 277 pp. Price £70.00 hardback. ISBN 0-19-508254-0. *Mineralogical Magazine*, 61(408), 742–742. <https://doi.org/10.1180/minmag.1997.061.408.22>
- Förster, H. (1978). Mesozoic-Cenozoic metallogenesis in Iran. *Journal of the Geological Society*, 135(4), 443–455. <https://doi.org/10.1144/gsjgs.135.4.0443>

- Fotoohi Rad, G. R., Droop, G. T. R., & Burgess, R. (2009). Early Cretaceous exhumation of high-pressure metamorphic rocks of the Sistan Suture Zone, eastern Iran. *Geological Journal*, 44(1), 104–116. <https://doi.org/10.1002/gj.1135>
- Fotoohi Rad, G. R., Droop, G. T. R., Amini, S., & Moazzen, M. (2005). Eclogites and blueschists of the Sistan Suture Zone, eastern Iran: A comparison of P-T histories from a subduction mélange. *Lithos*, 84(1–2), 1–24. <https://doi.org/10.1016/j.lithos.2005.01.007>
- Frost, B. R. (1985). On the stability of sulfides, oxides, and native metals in serpentinite. *Journal of Petrology*, 26(1), 31–63. <https://doi.org/10.1093/petrology/26.1.31>
- Frost, B. R., Evans, K. A., Swapp, S. M., Beard, J. S., & Mothersole, F. E. (2013). The process of serpentinization in dunite from New Caledonia. *Lithos*, 178, 24–39. <https://doi.org/10.1016/j.lithos.2013.02.002>
- Frost, R. B., & Beard, J. S. (2007). On silica activity and serpentinization. *Journal of Petrology*, 48(7), 1351–1368. <https://doi.org/10.1093/petrology/egm021>
- Früh-Green, G. L., Weissert, H., & Bernoulli, D. (1990). A multiple fluid history recorded in Alpine ophiolites. *Journal of the Geological Society*, 147(6), 959–970. <https://doi.org/10.1144/gsjgs.147.6.0959>
- Fryer, P., Ambos, E. L., & Hussong, D. M. (1985). Origin and emplacement of Mariana forearc seamounts (Pacific). *Geology*, 13(11), 774–777. [https://doi.org/10.1130/0091-7613\(1985\)13<774:OAEOMF>2.0.CO;2](https://doi.org/10.1130/0091-7613(1985)13<774:OAEOMF>2.0.CO;2)
- Fryer, P. (2002). Recent studies of serpentinite occurrences in the oceans: Mantle-ocean interactions in the plate tectonic cycle. *Chemie Der Erde*, 62(4), 257–302. <https://doi.org/10.1078/0009-2819-00020>
- Fuchs, Y., Linares, J., & Mellini, M. (1998). Mossbauer and infrared spectrometry of lizardite-1T from Monte Fico, Elba. *Physics and Chemistry of Minerals*, 26(2), 111–115. <https://doi.org/10.1007/s002690050167>
- Gahlan, H. A., & Arai, S. (2007). Genesis of peculiarly zoned Co, Zn and Mn-rich chromian spinel in serpentinite of Bou-Azzer ophiolite, Anti-Atlas, Morocco. *Journal of Mineralogical and Petrological Sciences*, 102(2), 69–85. <https://doi.org/10.2465/jmps.060212>
- Gahlan, H. A., Arai, S., Ahmed, A. H., Ishida, Y., Abdel-Aziz, Y. M., & Rahimi, A. (2006). Origin of magnetite veins in serpentinite from the Late Proterozoic Bou-Azzer ophiolite, Anti-Atlas, Morocco: An implication for mobility of iron during serpentinization. *Journal of African Earth Sciences*, 46(4), 318–330. <https://doi.org/10.1016/j.jafrearsci.2006.06.003>
- Galvez, M. E., Connolly, J. A. D., & Manning, C. E. (2016). Implications for metal and volatile cycles from the pH of subduction zone fluids. *Nature*, 539(7629), 420–424. <https://doi.org/10.1038/nature20103>
- Galvez, M. E., Manning, C. E., Connolly, J. A. D., & Rumble, D. (2015). The solubility of rocks in metamorphic fluids: A model for rock-dominated conditions to upper mantle pressure and temperature. *Earth and Planetary Science Letters*, 430, 486–498. <https://doi.org/10.1016/j.epsl.2015.06.019>

- Garzanti, E., & Gaetani, M. (2002). Unroofing history of late Paleozoic magmatic arcs within the “Turan Plate” (Tuarkyr, Turkmenistan). *Sedimentary Geology*, 151(1–2), 67–87. [https://doi.org/10.1016/S0037-0738\(01\)00231-7](https://doi.org/10.1016/S0037-0738(01)00231-7)
- Gauthier, M., Corrivaux, L., Trottier, L. J., Cabri, J., Laflamme, J. H. G., & Bergeron, M. (1990). Chromitites platinifères des complexes ophiolitiques de l’Estrie-Beauce, Appalaches du sud du Québec. *Mineralium Deposita*, 25(3), 169–178. <https://doi.org/10.1007/BF00190378>
- German, C. R., & Seyfried, W. E. (2013). Hydrothermal Processes. In *Treatise on Geochemistry: Second Edition* (pp. 191–233). <https://doi.org/10.1016/B978-0-08-095975-7.00607-0>
- Gervilla, F., Padrón-Navarta, J. A., Kerestedjian, T., Sergeeva, I., González-Jiménez, J. M., & Fanlo, I. (2012). Formation of ferrian chromite in podiform chromitites from the Golyamo Kamenyane serpentinite, Eastern Rhodopes, SE Bulgaria: A two-stage process. *Contributions to Mineralogy and Petrology*, 164(4), 643–657. <https://doi.org/10.1007/s00410-012-0763-3>
- Gervilla, F., Asta, M. P., Fanlo, I., Grolimund, D., Ferreira-Sánchez, D., Samson, V. A., Hunziker, D., Colas, V., González-Jiménez, J., Kerestedjian, T.N., & Sergeeva, I. (2019). Diffusion pathways of Fe<sup>2+</sup> and Fe<sup>3+</sup> during the formation of ferrian chromite: a  $\mu$ XANES study. *Contributions to Mineralogy and Petrology*, 174(8). <https://doi.org/10.1007/s00410-019-1605-3>
- Ghasemi, A., & Talbot, C. J. (2006). A new tectonic scenario for the Sanandaj-Sirjan Zone (Iran). *Journal of Asian Earth Sciences*, 26(6), 683–693. <https://doi.org/10.1016/j.jseaes.2005.01.003>
- Gill, J. B. (1981). Orogenic Andesites and Plate Tectonics. *Orogenic Andesites and Plate Tectonics*. [https://doi.org/10.1016/0377-0273\(82\)90060-9](https://doi.org/10.1016/0377-0273(82)90060-9)
- Gimeno Serrano, M. J., Auqué Sanz, L. F., & Nordstrom, D. K. (2000). REE speciation in low-temperature acidic waters and the competitive effects of aluminum. *Chemical Geology*, 165(3–4), 167–180. [https://doi.org/10.1016/S0009-2541\(99\)00166-7](https://doi.org/10.1016/S0009-2541(99)00166-7)
- González-Jiménez, J. M., Griffin, W. L., Proenza, J. A., Gervilla, F., O’Reilly, S. Y., Akbulut, M., Pearson, N.J., & Arai, S. (2014). Chromitites in ophiolites: How, where, when, why? Part II. The crystallization of chromitites. *Lithos*, 189, 140–158. <https://doi.org/10.1016/j.lithos.2013.09.008>
- González-Jiménez, J. M., Kerestedjian, T., Proenza, J. A., & Gervilla, F. (2009). Metamorphism on chromite ores from the Dobromirski Ultramafic Massif, Rhodope Mountains (SE Bulgaria). *Geologica Acta*, 7(4), 413–429. <https://doi.org/10.1344/104.000001447>
- González-Mancera, G., Ortega-Gutiérrez, F., Nava, N. E., & Arriola, H. S. (2003). Mössbauer Study of Serpentine Minerals in the Ultramafic Body of Tehuitzingo, Southern Mexico. In *Hyperfine Interactions* (pp. 61–71). <https://doi.org/10.1023/B:HYPE.0000003765.32151.3b>
- González-Mancera, G., Ortega-Gutiérrez, F., Nava, N. E., & Arriola, H. S. (2003). Mössbauer Study of Serpentine Minerals in the Ultramafic Body of Tehuitzingo, Southern Mexico. In *Hyperfine Interactions* (Vol. 148–149, pp. 61–71). <https://doi.org/10.1023/B:HYPE.0000003765.32151.3b>

- Govindaraju, K. (1994). 1994 Compilation of Working Values and Sample Description for 383 Geostandards. *Geostandards Newsletter*, 18, 1–158. <https://doi.org/10.1046/j.1365-2494.1998.53202081.x-i1>
- Grant, J. A. (2005). Isocon analysis: A brief review of the method and applications. *Physics and Chemistry of the Earth*, 30(17-18 SPEC. ISS.), 997–1004. <https://doi.org/10.1016/j.pce.2004.11.003>
- Greenbaum, D. (1977). The chromitiferous rocks of the Troodos ophiolite complex, Cyprus. *Economic Geology*, 72(7), 1175–1194. <https://doi.org/10.2113/gsecongeo.72.7.1175>
- Grieco, G., Bussolesi, M., Tzamos, E., Rassios, A. E., & Kapsiotis, A. (2018). Processes of primary and re-equilibration mineralization affecting chromitite ore geochemistry within the Vourinos ultramafic sequence, Vourinos ophiolite (West Macedonia, Greece). *Ore Geology Reviews*, 95, 537-551. <https://doi.org/10.1016/j.oregeorev.2018.03.009>
- Grieco, G., & Merlini, A. (2012). Chromite alteration processes within Vourinos ophiolite. *International Journal of Earth Sciences*, 101(6), 1523–1533. <https://doi.org/10.1007/s00531-011-0693-8>
- Grimes, C. B., John, B. E., Cheadle, M. J., & Wooden, J. L. (2008). Protracted construction of gabbroic crust at a slow spreading ridge: Constraints from  $^{206}\text{Pb}/^{238}\text{U}$  zircon ages from Atlantis Massif and IODP Hole U1309D (30°N, MAR). *Geochemistry, Geophysics, Geosystems*, 9(8). <https://doi.org/10.1029/2008GC002063>
- Guillot, S., Hattori, K. H., & De Sigoyer, J. (2000). Mantle wedge serpentinization and exhumation of eclogites: Insights from eastern Ladakh, northwest Himalaya. *Geology*, 28(3), 199–202. [https://doi.org/10.1130/0091-7613\(2000\)028<0199:mwsaeo>2.3.co;2](https://doi.org/10.1130/0091-7613(2000)028<0199:mwsaeo>2.3.co;2)
- Guillot, S., Hattori, K. H., & De Sigoyer, J. (2000). Mantle wedge serpentinization and exhumation of eclogites: Insights from eastern Ladakh, northwest Himalaya. *Geology*, 28(3), 199–202. [https://doi.org/10.1130/0091-7613\(2000\)028<0199:mwsaeo>2.3.co;2](https://doi.org/10.1130/0091-7613(2000)028<0199:mwsaeo>2.3.co;2)
- Guillot S., Hattori K., Agard P., Schwartz S., Vidal O. (2009) Exhumation Processes in Oceanic and Continental Subduction Contexts: A Review. In: Lallemand S., Funicello F. (eds) Subduction Zone Geodynamics. Frontiers in Earth Sciences. Springer, Berlin, Heidelberg. [https://doi.org/10.1007/978-3-540-87974-9\\_10](https://doi.org/10.1007/978-3-540-87974-9_10)
- Gunia, P. (1986). Native copper from rodingitized gabbroic dykes in serpentinites of the Braszowice-BrzeŹnica massif (Lower Silesia). *Mineralogia Polonica* 17, 63–76.
- Gürbüz, A., & Farzipour Saein, A. (2019). Tectonic Geomorphology of the Zagros Orogen (pp. 131–144). <https://doi.org/10.1016/b978-0-12-815048-1.00008-1>
- Haas, J. R., Shock, E. L., & Sassani, D. C. (1995). Rare earth elements in hydrothermal systems: Estimates of standard partial molal thermodynamic properties of aqueous complexes of the rare earth elements at high pressures and temperatures. *Geochimica et Cosmochimica Acta*, 59(21), 4329–4350. [https://doi.org/10.1016/0016-7037\(95\)00314-P](https://doi.org/10.1016/0016-7037(95)00314-P)
- Hacker, B. R., Peacock, S. M., Abers, G. A., & Holloway, S. D. (2003). Subduction factory 2. Are intermediate-depth earthquakes in subducting slabs linked to metamorphic dehydration reactions? *Journal of Geophysical Research: Solid Earth*, 108(B1). <https://doi.org/10.1029/2001jb001129>

- Hadavi, F., & Khodadadi, L. (2014). Nannostratigraphy and palaeoecology of uppermost Mozduran Formation in the Kopeh-Dagh range (NE Iran). *Arabian Journal of Geosciences*, 7(5), 1879–1889. <https://doi.org/10.1007/s12517-013-0839-z>
- Hafkenscheid, E., Wortel, M. J. R., & Spakman, W. (2006). Subduction history of the Tethyan region derived from seismic tomography and tectonic reconstructions. *Journal of Geophysical Research: Solid Earth*, 111(B8). <https://doi.org/10.1029/2005JB003791>
- Hallam, A. (1976). Geology and plate tectonics interpretation of the sediments of the Mesozoic radiolarite-ophiolite complex in the Neyriz region, southern Iran. *Bulletin of the Geological Society of America*, 87(1), 47–52. [https://doi.org/10.1130/0016-7606\(1976\)87<47:GAPTIO>2.0.CO;2](https://doi.org/10.1130/0016-7606(1976)87<47:GAPTIO>2.0.CO;2)
- Hamilton, W. C. (1958). Neutron diffraction investigation of the 119°K transition in magnetite. *Physical Review*, 110(5), 1050–1057. <https://doi.org/10.1103/PhysRev.110.1050>
- Hasenclever, J., Theissen-Krah, S., Rüpke, L. H., Morgan, J. P., Iyer, K., Petersen, S., & Devey, C. W. (2014). Hybrid shallow on-axis and deep off-axis hydrothermal circulation at fast-spreading ridges. *Nature*, 508(7497), 508–512. <https://doi.org/10.1038/nature13174>
- Haslam, H. W., Harding, R. R., & Tresham, A. E. (1976). Chromite-chlorite intergrowths in peridotite at Chimwadzulu Hill, Malawi. *Mineralogical Magazine*, 40(315), 695–701. <https://doi.org/10.1180/minmag.1976.040.315.03>
- Hassanzadeh, J. (1993) Metallogenic and tectonomagmatic events in the SE sector of the Cenozoic active continental margin of Central Iran (Shahr e Babak area, Kerman Province): Ph.D. dissertation, University of California, Los Angeles, 204 p.
- Hassanzadeh, J., Stockli, D. F., Horton, B. K., Axen, G. J., Stockli, L. D., Grove, M., Schmitt, A.K., & Walker, J. D. (2008). U-Pb zircon geochronology of late Neoproterozoic-Early Cambrian granitoids in Iran: Implications for paleogeography, magmatism, and exhumation history of Iranian basement. *Tectonophysics*, 451(1–4), 71–96. <https://doi.org/10.1016/j.tecto.2007.11.062>
- Hassanzadeh, J., & Wernicke, B. P. (2016). The Neotethyan Sanandaj-Sirjan zone of Iran as an archetype for passive margin-arc transitions. *Tectonics*, 35(3), 586–621. <https://doi.org/10.1002/2015TC003926>
- Hattori, K. H., & Guillot, S. (2003). Volcanic fronts form as a consequence of serpentinite dehydration in the forearc mantle wedge. *Geology*, 31(6), 525–528. [https://doi.org/10.1130/0091-7613\(2003\)031<0525:VFFAAC>2.0.CO;2](https://doi.org/10.1130/0091-7613(2003)031<0525:VFFAAC>2.0.CO;2)
- Hatzipanagiotou, K., & Tsikouras, B. (2001). Rodingite formation from diorite in the Samothraki ophiolite, NE Aegean, Greece. *Geological Journal*, 36(2), 93–109. <https://doi.org/10.1002/gj.887>
- Hessami, K., Koyi, H. A., Talbot, C. J., Tabasi, H., & Shabaniyan, E. (2001). Progressive unconformities within an evolving foreland fold-thrust belt, Zagros Mountains. *Journal of the Geological Society*, 158(6), 969–982. <https://doi.org/10.1144/0016-764901-007>
- Hodel, F., Macouin, M., Triantafyllou, A., Carlut, J., Berger, J., Rouse, S., Ennih, N., & Trindade, R. I. F. (2017). Unusual massive magnetite veins and highly altered Cr-spinels as relics of a Cl-rich acidic hydrothermal event in Neoproterozoic serpentinites (Bou Azzer

- ophiolite, Anti-Atlas, Morocco). *Precambrian Research*, 300, 151–167. <https://doi.org/10.1016/j.precamres.2017.08.005>
- Höhn, S., Frimmel, H. E., Debaille, V., Pašava, J., Kuulmann, L., & Debouge, W. (2017). The case for metamorphic base metal mineralization: pyrite chemical, Cu and S isotope data from the Cu-Zn deposit at Kupferberg in Bavaria, Germany. *Mineralium Deposita*, 52(8), 1145–1156. <https://doi.org/10.1007/s00126-017-0714-z>
- Holland, T. J. B., & Powell, R. (1998). An internally consistent thermodynamic data set for phases of petrological interest. *Journal of Metamorphic Geology*, 16(3), 309–343. <https://doi.org/10.1111/j.1525-1314.1998.00140.x>
- Holland, T. J. B., & Powell, R. (2011). An improved and extended internally consistent thermodynamic dataset for phases of petrological interest, involving a new equation of state for solids. *Journal of Metamorphic Geology*, 29(3), 333–383. <https://doi.org/10.1111/j.1525-1314.2010.00923.x>
- Holland, T., Baker, J., & Powell, R. (1998). Mixing properties and activity-composition relationships of chlorites in the system MgO-FeO-Al<sub>2</sub>O<sub>3</sub>-SiO<sub>2</sub>-H<sub>2</sub>O. *European Journal of Mineralogy*, 10(3), 395–406. <https://doi.org/10.1127/ejm/10/3/0395>
- Holland, T., & Powell, R. (1996). Thermodynamics of order-disorder in minerals: II. Symmetric formalism applied to solid solutions. *American Mineralogist*, 81(11–12), 1425–1437. <https://doi.org/10.2138/am-1996-11-1215>
- Horton, B. K., Hassanzadeh, J., Stockli, D. F., Axen, G. J., Gillis, R. J., Guest, B., Amini, A., Fakhari, M.D., Zamanzadeh, S.M., & Grove, M. (2008). Detrital zircon provenance of Neoproterozoic to Cenozoic deposits in Iran: Implications for chronostratigraphy and collisional tectonics. *Tectonophysics*, 451(1–4), 97–122. <https://doi.org/10.1016/j.tecto.2007.11.063>
- Hosseinyar, G., Moussavi-Harami, R., Abdollahie Fard, I., Mahboubi, A., & Noemani Rad, R. (2019). Seismic geomorphology and stratigraphic trap analyses of the Lower Cretaceous siliciclastic reservoir in the Kopeh Dagh-Amu Darya Basin. *Petroleum Science*, 16(4), 776–793. <https://doi.org/10.1007/s12182-019-0347-1>
- Hosseiniyoon, M., Taheri, J., Azadbakht, S., & Alavinejad, A. (2017). The Jurassic ammonites in the Koppeh Dagh tectono-sedimentary zone (NE Iran) based on paleontological archive center. In: First International Congress on Jurassic of Iran and Neighboring Countries (ICJI). Geological Survey of Iran, Mashhad, p. 8.
- Huang, J., Hao, J., Huang, F., & Sverjensky, D. A. (2019). Mobility of chromium in high temperature crustal and upper mantle fluids. *Geochemical Perspectives Letters*, 12, 1–6. <https://doi.org/10.7185/GEOCHEMLET.1926>
- Huang, R., Lin, C. T., Sun, W., Ding, X., Zhan, W., & Zhu, J. (2017). The production of iron oxide during peridotite serpentinization: Influence of pyroxene. *Geoscience Frontiers*, 8(6), 1311–1321. <https://doi.org/10.1016/j.gsf.2017.01.001>
- Huberty, J. M., Konishi, H., Heck, P. R., Fournelle, J. H., Valley, J. W., & Xu, H. (2012). Silician magnetite from the Dales Gorge Member of the Brockman Iron Formation, Hamersley Group, Western Australia. *American Mineralogist*, 97(1), 26–37. <https://doi.org/10.2138/am.2012.3864>

- Hunziker, D., Burg, J. P., Bouilhol, P., & Von Quadt, A. (2015). Jurassic rifting at the Eurasian Tethys margin: Geochemical and geochronological constraints from granitoids of North Makran, southeastern Iran. *Tectonics*, 34(3), 571–593. <https://doi.org/10.1002/2014TC003768>
- Husseini, M. I., & Hussein, S. I. (1990). Origin of the Infracambrian Salt Basins of the Middle East. *Geological Society Special Publication*, 50, 279–292. <https://doi.org/10.1144/GSL.SP.1990.050.01.14>
- Hyndman, R. D., & Peacock, S. M. (2003). Serpentinization of the forearc mantle. *Earth and Planetary Science Letters*, 212(3–4), 417–432. [https://doi.org/10.1016/S0012-821X\(03\)00263-2](https://doi.org/10.1016/S0012-821X(03)00263-2)
- Ikehata, K., Chida, K., Tsunogae, T., & Bornhorst, T. J. (2016). Hydrothermal native copper in Ocean Island Alkali basalt from the Mineoka Belt, Boso Peninsula, Central Japan. *Economic Geology*, 111(3), 783–794. <https://doi.org/10.2113/econgeo.111.3.783>
- Ikehata, K., & Hirata, T. (2012). Copper isotope characteristics of copper-rich minerals from the horoman peridotite complex, Hokkaido, Northern Japan. *Economic Geology*, 107(7), 1489–1497. <https://doi.org/10.2113/econgeo.107.7.1489>
- Ikehata, K., Notsu, K., & Hirata, T. (2011). Copper isotope characteristics of copper-rich minerals from besshi-type volcanogenic massive sulfide deposits, Japan, determined using a femtosecond LA-MC-ICP-MS. *Economic Geology*, 106(2), 307–316. <https://doi.org/10.2113/econgeo.106.2.307>
- Ilton, E. S., & Eugster, H. P. (1989). Base metal exchange between magnetite and a chloride-rich hydrothermal fluid. *Geochimica et Cosmochimica Acta*, 53(2), 291–301. [https://doi.org/10.1016/0016-7037\(89\)90381-5](https://doi.org/10.1016/0016-7037(89)90381-5)
- Ionov, D. A., Savoyant, L., & Dupuy, C. (1992). Application of the Icp-MS Technique To Trace Element Analysis of Peridotites and Their Minerals. *Geostandards Newsletter*, 16(2), 311–315. <https://doi.org/10.1111/j.1751-908X.1992.tb00494.x>
- Ivandić, M., Grevemeyer, I., Bialas, J., & Petersen, C. J. (2010). Serpentinization in the trench-outer rise region offshore of Nicaragua: Constraints from seismic refraction and wide-angle data. *Geophysical Journal International*, 180(3), 1253–1264. <https://doi.org/10.1111/j.1365-246X.2009.04474.x>
- Iyer, K., Rüpke, L. H., & Morgan, J. P. (2010). Feedbacks between mantle hydration and hydrothermal convection at ocean spreading centers. *Earth and Planetary Science Letters*, 296(1–2), 34–44. <https://doi.org/10.1016/j.epsl.2010.04.037>
- Iyer, K. (2007). Mechanisms of serpentinization and some geochemical effects. Dissertation for Doctoral Degree. Scientiarum: University of Oslo. 42
- Jafari, M. K., Babaie, H. A., & Mirzaie, M. (2013). Geology, petrology and tectonomagmatic evolution of the plutonic crustal rocks of the Sabzevar ophiolite, NE Iran. *Geological Magazine*, 150(5), 862–884. <https://doi.org/10.1017/S0016756812000933>
- Janecky, D. R., & Seyfried, W. E. (1986). Hydrothermal serpentinization of peridotite within the oceanic crust: Experimental investigations of mineralogy and major element chemistry. *Geochimica et Cosmochimica Acta*, 50(7), 1357–1378. [https://doi.org/10.1016/0016-7037\(86\)90311-X](https://doi.org/10.1016/0016-7037(86)90311-X)

- Jennings, E. S., & Holland, T. J. B. (2015). A simple thermodynamic model for melting of peridotite in the system NCFMASOCr. *Journal of Petrology*, 56(5), 869–892. <https://doi.org/10.1093/petrology/egv020>
- Jochum, K. P., Weis, U., Schwager, B., Stoll, B., Wilson, S. A., Haug, G. H., Andreae, M.O., & Enzweiler, J. (2016). Reference Values Following ISO Guidelines for Frequently Requested Rock Reference Materials. *Geostandards and Geoanalytical Research*, 40(3), 333–350. <https://doi.org/10.1111/j.1751-908X.2015.00392.x>
- Johnson, J. W., Oelkers, E. H., & Helgeson, H. C. (1992). SUPCRT92: A software package for calculating the standard molal thermodynamic properties of minerals, gases, aqueous species, and reactions from 1 to 5000 bar and 0 to 1000°C. *Computers and Geosciences*, 18(7), 899–947. [https://doi.org/10.1016/0098-3004\(92\)90029-Q](https://doi.org/10.1016/0098-3004(92)90029-Q)
- Kallikragas, D. T., Plugatyr, A. Y., & Svishchev, I. M. (2014). High temperature diffusion coefficients for O<sub>2</sub>, H<sub>2</sub>, and OH in water, and for pure water. *Journal of Chemical and Engineering Data*, 59(6), 1964–1969. <https://doi.org/10.1021/je500096r>
- Kamiya, S., & Kobayashi, Y. (2000). Seismological evidence for the existence of serpentized wedge mantle. *Geophysical Research Letters*, 27(6), 819–822. <https://doi.org/10.1029/1999GL011080>
- Kaneda, H., Takenouchi, S., & Shoji, T. (1986). Stability of pentlandite in the Fe-Ni-Co-S system. *Mineralium Deposita*, 21(3), 169–180. <https://doi.org/10.1007/BF00199797>
- Kapsiotis, A., Economou-Eliopoulos, M., Zheng, H., Huang, Q., Lenaz, D., Antonelou, A., Velicogna, M., & Xia, B. (2021). Metallogeny of a base metal sulfide-bearing magnetite body from the Eretria mine, East Othris massif, Greece: Insights into an ancient seafloor hydrothermal system. *Journal of Geochemical Exploration*, 221, 106703. <https://doi.org/10.1016/j.gexplo.2020.106703>
- Kapsiotis, A. N. (2015). Alteration of chromitites from the Voidolakkos and Xerolivado mines, Vourinos ophiolite complex, Greece: Implications for deformation-induced metamorphism. *Geological Journal*, 50(6), 739–763. <https://doi.org/10.1002/gj.2590>
- Kargaranbafghi, F., Neubauer, F., & Genser, J. (2015). Rapid Eocene extension in the Chapedony metamorphic core complex, Central Iran: Constraints from <sup>40</sup>Ar/<sup>39</sup>Ar dating. *Journal of Asian Earth Sciences*, 106, 156–168. <https://doi.org/10.1016/j.jseaes.2015.03.010>
- Kargaranbafghi, F., Neubauer, F., Genser, J., Faghih, A., & Kusky, T. (2012). Mesozoic to Eocene ductile deformation of western Central Iran: From Cimmerian collisional orogeny to Eocene exhumation. *Tectonophysics*, 564–565, 83–100. <https://doi.org/10.1016/j.tecto.2012.06.017>
- Karson, J.A. (1990). Seafloor spreading on the Mid-Atlantic Ridge: Implications for the structure of ophiolites and oceanic lithosphere produced in slow-spreading environments, in Malpas, J., et al., eds., *Ophiolites and oceanic crustal analogues: Proceedings of the Symposium “ Troodos 1987”*: Nicosia, Cyprus, Geological Survey Department, p. 125–130.
- Katayama, I., Kurosaki, I., & Hirauchi, K. ichi. (2010). Low silica activity for hydrogen generation during serpentization: An example of natural serpentinites in the Mineoka

- ophiolite complex, central Japan. *Earth and Planetary Science Letters*, 298(1–2), 199–204. <https://doi.org/10.1016/j.epsl.2010.07.045>
- Kavoosi, M. A., Lasemi, Y., Sherkati, S., & Moussavi-Harami, R. (2009). Facies analysis and depositional sequences of the Upper Jurassic Mozduran Formation, a carbonate reservoir in the Kopet Dagh Basin, NE Iran. *Journal of Petroleum Geology*, 32(3), 235–259. <https://doi.org/10.1111/j.1747-5457.2009.00446.x>
- Kazemi, Z., Ghasemi, H., Tilhac, R., Griffin, W., Moghadam, H. S., O'Reilly, S., & Mousivand, F. (2019). Late cretaceous subduction-related magmatism on the southern edge of Sabzevar basin, NE Iran. *Journal of the Geological Society*, 176(3), 530–552. <https://doi.org/10.1144/jgs2018-076>
- Kelemen, P. B., Matter, J., Streit, E. E., Rudge, J. F., Curry, W. B., & Blusztajn, J. (2011). Rates and mechanisms of mineral carbonation in peridotite: Natural processes and recipes for enhanced, in situ CO<sub>2</sub> capture and storage. *Annual Review of Earth and Planetary Sciences*, 39, 545–576. <https://doi.org/10.1146/annurev-earth-092010-152509>
- Kelemen, P. B., & Matter, J. (2008). In situ carbonation of peridotite for CO<sub>2</sub> storage. *Proceedings of the National Academy of Sciences of the United States of America*, 105(45), 17295–17300. <https://doi.org/10.1073/pnas.0805794105>
- Kelley, D. S., Karson, J. A., Blackman, D. K., Früh-Green, G. L., Butterfield, D. A., Lilley, M. D., Olson, E.J., Schrenk, M.O., Roe, K.K., Lebon, G.T., Rivizzigno, P. & the AT3-60 Shipboard Party. (2001). An off-axis hydrothermal vent field near the mid-Atlantic ridge at 30° N. *Nature*, 412(6843), 145–149. <https://doi.org/10.1038/35084000>
- Kelley, D. S., Karson, J. A., Früh-Green, G. L., Yoerger, D. R., Shank, T. M., Butterfield, D. A., Hayes, J.M., Schrenk, M.O., Olson, E.J., Proskurowski, G., Jakuba, M., Bradley, A., Larson, B., Ludwig, K., Glickson, D., Buckman, K., Bradley, A.S., Brazelton, W.J., Roe, K., Elend, M.J., Delacour, A., Bernasconi, S.M., Lilley, M.D., Baross, J.A., Summons, R.E., & Sylva, S. P. (2005). A serpentinite-hosted ecosystem: The Lost City hydrothermal field. *Science*, 307(5714), 1428–1434. <https://doi.org/10.1126/science.1102556>
- Kendelewicz, T., Liu, P., Doyle, C. S., Brown, G. E., Nelson, E. J., & Chambers, S. A. (2000). Reaction of water with the (100) and (111) surfaces of Fe<sub>3</sub>O<sub>4</sub>. *Surface Science*, 453(1–3), 32–46. [https://doi.org/10.1016/S0039-6028\(00\)00305-8](https://doi.org/10.1016/S0039-6028(00)00305-8)
- Khalatbari Jafari, M., Babaie, H. A., & Gani, M. (2013). Geochemical evidence for late Cretaceous marginal arc-to-backarc transition in the Sabzevar ophiolitic extrusive sequence, northeast Iran. *Journal of Asian Earth Sciences*, 70–71, 209–230. <https://doi.org/10.1016/j.jseaes.2013.03.015>
- Khalil, I., & El-Makky, A. M. (2009). Alteration mechanisms of chromian-spinel during serpentinization at wadi sifein area, eastern desert, Egypt. *Resource Geology*, 59(2), 194–211. <https://doi.org/10.1111/j.1751-3928.2009.00090.x>
- Khedr, M. Z., & Arai, S. (2018). Composite origin of magnetite deposits hosted in Oman peridotites: Evidence for iron mobility during serpentinization. *Ore Geology Reviews*, 101, 180–198. <https://doi.org/10.1016/j.oregeorev.2018.07.003>
- Kimball, K. L. (1990). Effects of hydrothermal alteration on the compositions of chromian spinels. *Contributions to Mineralogy and Petrology*, 105(3), 337–346. <https://doi.org/10.1007/BF00306543>

- Klein, F., & Bach, W. (2009). Fe-Ni-Co-O-S phase relations in peridotite-seawater interactions. *Journal of Petrology*, 50(1), 37–59. <https://doi.org/10.1093/petrology/egn071>
- Klein, F., Bach, W., Humphris, S. E., Kahl, W. A., Jöns, N., Moskowitz, B., & Berquó, T. S. (2014). Magnetite in seafloor serpentinite—Some like it hot. *Geology*, 42(2), 135–138. <https://doi.org/10.1130/G35068.1>
- Klein, F., Bach, W., Jöns, N., McCollom, T., Moskowitz, B., & Berquó, T. (2009). Iron partitioning and hydrogen generation during serpentinization of abyssal peridotites from 15°N on the Mid-Atlantic Ridge. *Geochimica et Cosmochimica Acta*, 73(22), 6868–6893. <https://doi.org/10.1016/j.gca.2009.08.021>
- Klein, F., Bach, W., & McCollom, T. M. (2013). Compositional controls on hydrogen generation during serpentinization of ultramafic rocks. *Lithos*, 178, 55–69. <https://doi.org/10.1016/j.lithos.2013.03.008>
- Klemme, S., Ivanic, T. J., Connolly, J. A. D., & Harte, B. (2009). Thermodynamic modelling of Cr-bearing garnets with implications for diamond inclusions and peridotite xenoliths. *Lithos*, 112, 986–991. <https://doi.org/10.1016/j.lithos.2009.05.007>
- Kopp, C., Fruehn, J., Flueh, E. R., Reichert, C., Kukowski, N., Bialas, J., & Klaeschen, D. (2000). Structure of the makran subduction zone from wide-angle and reflection seismic data. *Tectonophysics*, 329(1–4), 171–191. [https://doi.org/10.1016/S0040-1951\(00\)00195-5](https://doi.org/10.1016/S0040-1951(00)00195-5)
- Kyser, T. K., & Kerrich, R. (1991). Retrograde exchange of hydrogen isotopes between hydrous minerals and water at low temperatures. In: Taylor H. P., Jr, O’Neil, J. R. and Kaplan, I. R. (eds.). *Stable Isotope Geochemistry: a tribute to Samuel Epstein*, The Geochemical Society, Special Publication, 3, 409–424.
- Lanphere, M. A., & Pamić, J. (1983).  $^{40}\text{Ar}/^{39}\text{Ar}$  Ages and tectonic setting of ophiolite from the Neyriz area, southeast Zagros Range, Iran. *Tectonophysics*, 96(3–4), 245–256. [https://doi.org/10.1016/0040-1951\(83\)90220-2](https://doi.org/10.1016/0040-1951(83)90220-2)
- Larson, P. B., Maher, K., Ramos, F. C., Chang, Z., Gaspar, M., & Meinert, L. D. (2003). Copper isotope ratios in magmatic and hydrothermal ore-forming environments. *Chemical Geology*, 201(3–4), 337–350. <https://doi.org/10.1016/j.chemgeo.2003.08.006>
- Lensch, G. & Davoudzadeh, M. (1982). Ophiolites in Iran. *Neues Jahrbuch für Geologie und Paläontologie—Monatshefte*, 5, 306–20.
- Lavier, L. L., Buck, W. R., & Poliakov, A. N. B. (1999). Self-consistent rolling-hinge model for the evolution of large-offset low-angle normal faults. *Geology*, 27(12), 1127–1130. [https://doi.org/10.1130/0091-7613\(1999\)027<1127:SCRHMF>2.3.CO;2](https://doi.org/10.1130/0091-7613(1999)027<1127:SCRHMF>2.3.CO;2)
- Lavier, L. L., Buck, W. R., & Poliakov, A. N. B. (2000). Factors controlling normal fault offset in an ideal brittle layer. *Journal of Geophysical Research: Solid Earth*, 105(B10), 23431–23442. <https://doi.org/10.1029/2000jb900108>
- Leach, D. L., Bradley, D. C., Huston, D., Pisarevsky, S. A., Taylor, R. D., & Gardoll, S. J. (2010). Sediment-hosted lead-zinc deposits in earth history. *Economic Geology*, 105(3), 593–625. <https://doi.org/10.2113/gsecongeo.105.3.593>

- Leake, B. E., Woolley, A. R., Arps, C. E. S., Birch, W. D., Gilbert, M. C., Grice, J. D., Hawthorne, F.C., Kato, A., Kisch, H.J., Krivovichev, V.G., Linthout, K., Laird, J., Mandarino, J., Maresch, W.V., Nickel, E.H., Rock, N.M.S., Schumacher, J.C., Smith, D.C., Stephenson, N.C.N., Ungaretti, L., Whittaker, E.J.W., & Youzhi, G. (1997). Nomenclature of amphiboles: Report of the subcommittee on amphiboles of the international mineralogical association, commission on new minerals and mineral names. *American Mineralogist*, 82(9–10), 1019–1037. <https://doi.org/10.1180/minmag.1997.061.405.13>
- Lench, G. (1980). Major element geochemistry of the ophiolites in north-eastern Iran. In: Panayiotou, A. (Ed.). Proceedings to International Ophiolite Symposium. Ministry of Agriculture and Natural Resources, Geological Survey Department, Republic of Cyprus, pp.389-401.
- Li, D. F., Chen, H. Y., Hollings, P., Zhang, L., Sun, X. M., Zheng, Y., Xia, X-P., Xiao, B., Wang, C-M., & Fang, J. (2018). Trace element geochemistry of magnetite: Implications for ore genesis of the Talate skarn Pb-Zn (-Fe) deposit, Altay, NW China. *Ore Geology Reviews*, 100, 471–482. <https://doi.org/10.1016/j.oregeorev.2017.03.015>
- Lindsley, D.H. (1991). Experimental studies of oxide minerals. In: Lindsley DH (ed) Oxide minerals: petrological and magnetic significance. *Mineral Soc America Rev Mineral*, 25, 69–106.
- Liu, S. A., Huang, J., Liu, J., Wörner, G., Yang, W., Tang, Y. J., Chen, Y., Tang, L., Zheng, J., & Li, S. (2015). Copper isotopic composition of the silicate Earth. *Earth and Planetary Science Letters*, 427, 95–103. <https://doi.org/10.1016/j.epsl.2015.06.061>
- Liu, Z. B., Li, J. C., Zhao, T., Song, Y., Yuan, G. L., Lin, Y., & Shao, H. S. (2020). Serpentinisation and magnetite formation in the Angwu ultramafic rocks from the central Bangong–Nujiang suture zone, Tibetan Plateau. *Geological Journal*, 55(2), 1283–1299. <https://doi.org/10.1002/gj.3496>
- Lorand, J. P. (1987). CuFeNiS mineral assemblages in upper-mantle peridotites from the Table Mountain and Blow-Me-Down Mountain ophiolite massifs (Bay of Islands area, Newfoundland): Their relationships with fluids and silicate melts. *Lithos*, 20(1), 59–76. [https://doi.org/10.1016/0024-4937\(87\)90024-7](https://doi.org/10.1016/0024-4937(87)90024-7)
- Lorand, J. P., & Ceuleneer, G. (1989). Silicate and base-metal sulfide inclusions in chromites from the Maqsad area (Oman ophiolite, Gulf of Oman): A model for entrapment. *Lithos*, 22(3), 173–190. [https://doi.org/10.1016/0024-4937\(89\)90054-6](https://doi.org/10.1016/0024-4937(89)90054-6)
- Lorand, J. P., & Grégoire, M. (2006). Petrogenesis of base metal sulphide assemblages of some peridotites from the Kaapvaal craton (South Africa). *Contributions to Mineralogy and Petrology*, 151(5), 521–538. <https://doi.org/10.1007/s00410-006-0074-7>
- Ludwig, K. R. (2003). User's manual for Isoplot 3.00, a geochronological toolkit for Microsoft Excel. Berkeley Geochronology Center special publication no.4. *Components*, (4), 70.
- Lyberis, N., Manby, G., Poli, J.-T., Kalougin, V., Yousouphocaev, H., & Ashirov, T. (1998). Post-triassic evolution of the southern margin of the Turan plate. *Comptes Rendus de l'Académie Des Sciences - Series IIA - Earth and Planetary Science*, 326(2), 137–143. [https://doi.org/10.1016/s1251-8050\(97\)87458-7](https://doi.org/10.1016/s1251-8050(97)87458-7)

- Maanijou, M., Aliani, F., Miri, M., & Lentz, D. R. (2013). Geochemistry and petrology of igneous assemblage in the south of Qorveh area, west Iran. *Chemie Der Erde*, 73(2), 181–196. <https://doi.org/10.1016/j.chemer.2013.04.001>
- MacDonald, A. H., & Fyfe, W. S. (1985). Rate of serpentinization in seafloor environments. *Tectonophysics*, 116(1–2), 123–135. [https://doi.org/10.1016/0040-1951\(85\)90225-2](https://doi.org/10.1016/0040-1951(85)90225-2)
- Maffione, M., Morris, A., Plümper, O., & Van Hinsbergen, D. J. J. (2014). Magnetic properties of variably serpentinized peridotites and their implication for the evolution of oceanic core complexes. *Geochemistry, Geophysics, Geosystems*, 15(4), 923–944. <https://doi.org/10.1002/2013GC004993>
- Mahmoudi, S., Corfu, F., Masoudi, F., Mehrabi, B., & Mohajjel, M. (2011). U-Pb dating and emplacement history of granitoid plutons in the northern Sanandaj-Sirjan Zone, Iran. *Journal of Asian Earth Sciences*, 41(3), 238–249. <https://doi.org/10.1016/j.jseaes.2011.03.006>
- Majidifard, M. R. (2003). Biostratigraphy, Lithostratigraphy, ammonite taxonomy and microfacies analysis of the Middle and Upper Jurassic of northeastern Iran. *Ph. D. Thesis, University of Wuerzburg*.
- Makvandi, S., Ghasemzadeh-Barvarz, M., Beaudoin, G., Grunsky, E. C., McClenaghan, M. B., Duchesne, C., & Boutroy, E. (2016). Partial least squares-discriminant analysis of trace element compositions of magnetite from various VMS deposit subtypes: Application to mineral exploration. *Ore Geology Reviews*, 78, 388–408. <https://doi.org/10.1016/j.oregeorev.2016.04.014>
- Makvandi, S., Beaudoin, G., Beth McClenaghan, M., & Quirt, D. (2017). Geochemistry of magnetite and hematite from unmineralized bedrock and local till at the Kiggavik uranium deposit: Implications for sediment provenance. *Journal of Geochemical Exploration*, 183, 1–21. <https://doi.org/10.1016/j.gexplo.2017.09.010>
- Malvoisin, B., & Brunet, F. (2014). Water diffusion-transport in a synthetic dunite: Consequences for oceanic peridotite serpentinization. *Earth and Planetary Science Letters*, 403, 263–272. <https://doi.org/10.1016/j.epsl.2014.07.004>
- Malvoisin, B., Carlut, J., & Brunet, F. (2012). Serpentinization of oceanic peridotites: 1. A high-sensitivity method to monitor magnetite production in hydrothermal experiments. *Journal of Geophysical Research: Solid Earth*, 117(1). <https://doi.org/10.1029/2011JB008612>
- Malvoisin, B., Zhang, C., Müntener, O., Baumgartner, L. P., & Kelemen, P. B. (2020). Measurement of volume change and mass transfer during serpentinization: insights From the Oman Drilling Project. *Journal of Geophysical Research: Solid Earth*, 125(5). <https://doi.org/10.1029/2019JB018877>
- Marcaillou, C., Muñoz, M., Vidal, O., Parra, T., & Harfouche, M. (2011). Mineralogical evidence for H<sub>2</sub> degassing during serpentinization at 300°C/300bar. *Earth and Planetary Science Letters*, 303(3–4), 281–290. <https://doi.org/10.1016/j.epsl.2011.01.006>
- Markovich, V. V., & Ostrovskaya, R. U. (1977). Inhibitory processes in the cerebral cortex and anticonvulsive action of benzodiazepine derivatives. *Byulleten Eksperimentalnoi Biologii i Meditsiny*, 84(10), 431–433.

- Martin, W., Baross, J., Kelley, D., & Russell, M. J. (2008). Hydrothermal vents and the origin of life. *Nature Reviews Microbiology*, 6, pages 805–814. <https://doi.org/10.1038/nrmicro1991>
- Martin, B., & Fyfe, W. S. (1970). Some experimental and theoretical observations on the kinetics of hydration reactions with particular reference to serpentinization. *Chemical Geology*, 6(C), 185–202. [https://doi.org/10.1016/0009-2541\(70\)90018-5](https://doi.org/10.1016/0009-2541(70)90018-5)
- Mathur, R., Ruiz, J., Titley, S., Liermann, L., Buss, H., & Brantley, S. (2005). Cu isotopic fractionation in the supergene environment with and without bacteria. *Geochimica et Cosmochimica Acta*, 69(22), 5233–5246. <https://doi.org/10.1016/j.gca.2005.06.022>
- Mathur, R., Titley, S., Barra, F., Brantley, S., Wilson, M., Phillips, A., Munizaga, F., Maksaev, V., Vervoort, J., & Hart, G. (2009). Exploration potential of Cu isotope fractionation in porphyry copper deposits. *Journal of Geochemical Exploration*, 102(1), 1–6. <https://doi.org/10.1016/j.gexplo.2008.09.004>
- Mathur, R., Titley, S., Hart, G., Wilson, M., Davignon, M., & Zlatos, C. (2009). The history of the United States cent revealed through copper isotope fractionation. *Journal of Archaeological Science*, 36(2), 430–433. <https://doi.org/10.1016/j.jas.2008.09.029>
- Mathur, R., Wilson, M., & Parra, M. L. (2014). Challenges of using copper isotope ratios to trace the origin of native copper artifacts: An example from the Keweenaw Peninsula. *Annals of Carnegie Museum*, 82(3), 241–245. <https://doi.org/10.2992/007.082.0304>
- Mayhew, L. E., Ellison, E. T., McCollom, T. M., Trainor, T. P., & Templeton, A. S. (2013). Hydrogen generation from low-temperature water-rock reactions. *Nature Geoscience*, 6(6), 478–484. <https://doi.org/10.1038/ngeo1825>
- Mayhew, L. E., Ellison, E. T., Miller, H. M., Kelemen, P. B., & Templeton, A. S. (2018). Iron transformations during low temperature alteration of variably serpentinized rocks from the Samail ophiolite, Oman. *Geochimica et Cosmochimica Acta*, 222, 704–728. <https://doi.org/10.1016/j.gca.2017.11.023>
- Mazhari, S. A., Bea, F., Amini, S., Ghalamghash, J., Molina, J. F., Montero, P., Scarrow, J.H., & Williams, I. S. (2009). The Eocene bimodal Piranshahr massif of the Sanandaj-Sirjan Zone, NW Iran: A marker of the end of the collision in the Zagros orogen. *Journal of the Geological Society*, 166(1), 53–69. <https://doi.org/10.1144/0016-76492008-022>
- McCollom, T. M. (1999). Methanogenesis as a potential source of chemical energy for primary biomass production by autotrophic organisms in hydrothermal systems on Europa. *Journal of Geophysical Research E: Planets*, 104(E12), 30729–30742. <https://doi.org/10.1029/1999JE001126>
- McCollom, T. M. (2016). Abiotic methane formation during experimental serpentinization of olivine. *Proceedings of the National Academy of Sciences of the United States of America*, 113, 13965–13970. <https://doi.org/10.1073/pnas.1611843113>
- McCollom, T. M., & Bach, W. (2009). Thermodynamic constraints on hydrogen generation during serpentinization of ultramafic rocks. *Geochimica et Cosmochimica Acta*, 73(3), 856–875. <https://doi.org/10.1016/j.gca.2008.10.032>
- McQuarrie, N. (2004). Crustal scale geometry of the Zagros fold-thrust belt, Iran. *Journal of Structural Geology*, 26(3), 519–535. <https://doi.org/10.1016/j.jsg.2003.08.009>

- Mehrnoosh, M., & Hamdi, B. (1979). A preliminary study on the Neyriz radiolarian cherts. Geological Survey of Iran, report No. 2/61978 (pp. 6).
- Mellini, M., Rumori, C., & Viti, C. (2005). Hydrothermally reset magmatic spinels in retrograde serpentinites: Formation of “ferritchromit” rims and chlorite aureoles. *Contributions to Mineralogy and Petrology*, 149(3), 266–275. <https://doi.org/10.1007/s00410-005-0654-y>
- Merlini, A., Giovanni, G., & Valeria, D. (2009). Ferritchromite and chromian-chlorite formation in mélangé-hosted Kalkan chromitite (Southern Urals, Russia). *American Mineralogist*, 94(10), 1459–1467. <https://doi.org/10.2138/am.2009.3082>
- Mével, C. (2003). Serpentinization of abyssal peridotites at mid-ocean ridges. *Comptes Rendus Geoscience*, 335(10–11), 825–852.
- Michailidis, K. M. (1990). Zoned chromites with high Mn-contents in the Fe-Ni-Cr-laterite ore deposits from the Edessa area in Northern Greece. *Mineralium Deposita*, 25(3), 190–197. <https://doi.org/10.1007/BF00190380>
- Miller, H. M., Matter, J. M., Kelemen, P., Ellison, E. T., Conrad, M. E., Fierer, N., Ruchala, T., Tominaga, M., & Templeton, A. S. (2016). Modern water/rock reactions in Oman hyperalkaline peridotite aquifers and implications for microbial habitability. *Geochimica et Cosmochimica Acta*, 179, 217–241. <https://doi.org/10.1016/j.gca.2016.01.033>
- Miller, D. J., & Christensen, N.I. (1997). Seismic velocities of lower crustal and upper mantle rocks from the slow-spreading Mid-Atlantic Ridge, south of the Kane transform fault, Proc. Ocean Drill. Program Sci. Results, 153, 437–454.
- Mirnejad, H., Raeisi, D., McFarlane, C., & Sheibi, M. (2019). Tafresh intrusive rocks within the Urumieh-Dokhtar Magmatic Arc: Appraisal of Neo-Tethys subduction. *Geological Journal*, 54(3), 1745–1755. <https://doi.org/10.1002/gj.3266>
- Mitra, S., Pal, T., Maity, P.K., & Moon, H-S. (1992). Ferritchromite and its opto-chemical behaviour. *Mineralogical Journal*, 16 (4), 173-186.
- Mitra, S., Pal, T., & Pal, T. (1991). Petrogenetic implication of the Mössbauer hyperfine parameters of Fe<sup>3+</sup>-chromites from Sukinda (India) ultramafites. *Mineralogical Magazine*, 55(381), 535–542. <https://doi.org/10.1180/minmag.1991.055.381.06>
- Miura, M., & Arai, S. (2014). Platinum-group element and mineral characteristics of sub-arc chromitite xenoliths from the Takashima alkali basalt, Southwest Japan arc. *Canadian Mineralogist*, 52(5), 899–916. <https://doi.org/10.3749/canmin.1300049>
- Miyoshi, A., Kogiso, T., Ishikawa, N., & Mibe, K. (2014). Role of silica for the progress of Serpentinization reactions: Constraints from Successive changes in mineralogical textures of serpentinites from Iwanaidake ultramafic body, Japan. *American Mineralogist*, 99 (5-6), 1035–1044. <https://doi.org/10.2138/am.2014.4748>
- Mohajjel, M., & Fergusson, C. L. (2014). Jurassic to Cenozoic tectonics of the zagros orogen in northwestern Iran. *International Geology Review*, 56(3), 263–287. <https://doi.org/10.1080/00206814.2013.853919>
- Mohajjel, M., Fergusson, C. L., & Sahandi, M. R. (2003). Cretaceous-Tertiary convergence and continental collision, Sanandaj-Sirjan Zone, Western Iran. *Journal of Asian Earth Sciences*, 21(4), 397–412. [https://doi.org/10.1016/S1367-9120\(02\)00035-4](https://doi.org/10.1016/S1367-9120(02)00035-4)

- Mohajjel, M., & Fergusson, C. L. (2000). Dextral transpression in Late Cretaceous continental collision, Sanandaj-Sirjan Zone, western Iran. *Journal of Structural Geology*, 22(8), 1125–1139. [https://doi.org/10.1016/S0191-8141\(00\)00023-7](https://doi.org/10.1016/S0191-8141(00)00023-7)
- Moinevaziri, H., Akbarpour, A., & Azizi, H. (2015). Mesozoic magmatism in the northwestern Sanandaj–Sirjan zone as an evidence for active continental margin. *Arabian Journal of Geosciences*, 8(5), 3077–3088. <https://doi.org/10.1007/s12517-014-1309-y>
- Monnin, C., Chavagnac, V., Boulart, C., Ménez, B., Gérard, M., Gérard, E., Pisapia, C., Quéméneur, M., Erauso, G., Postec, A., Guentas-Dombrowski, L., Payri, C., & Pelletier, B. (2014). Fluid chemistry of the low temperature hyperalkaline hydrothermal system of Prony bay (New Caledonia). *Biogeosciences*, 11, 5687–5706. <https://doi.org/10.5194/bg-11-5687-2014>
- Monsef, I., Monsef, R., Mata, J., Zhang, Z., Pirouz, M., Rezaeian, M., Esmaili, R., & Xiao, W. (2018). Evidence for an early-MORB to fore-arc evolution within the Zagros suture zone: Constraints from zircon U-Pb geochronology and geochemistry of the Neyriz ophiolite (South Iran). *Gondwana Research*, 62, 287–305. <https://doi.org/10.1016/j.gr.2018.03.002>
- Moody, J. B. (1976). An experimental study on the serpentinization of iron-bearing olivines. *Canadian Mineralogist*, 14(4), 462–478.
- Moore, D. E., Lockner, D. A., Ma, S., Summers, R., & Byerlee, J. D. (1997). Strengths of serpentinite gouges at elevated temperatures. *Journal of Geophysical Research: Solid Earth*, 102(B7), 14787–14801. <https://doi.org/10.1029/97jb00995>
- Morley, C. K., Kongwung, B., Julapour, A. A., Abdolghafourian, M., Hajian, M., Waples, D., Warren, J., Otterdoom, H., Srisuriyon, K., & Kazemi, H. (2009). Structural development of a major late Cenozoic basin and transpressional belt in central Iran: The Central Basin in the Qom-Saveh area. *Geosphere*, 5(4), 325–362. <https://doi.org/10.1130/GES00223.1>
- Mottl, M.J. (2009). Highest pH? *Geochemical News*, 141.
- Mottl, M. J., Wheat, C. G., Fryer, P., Gharib, J., & Martin, J. B. (2004). Chemistry of springs across the Mariana forearc shows progressive devolatilization of the subducting plate. *Geochimica et Cosmochimica Acta*, 68(23), 4915–4933. <https://doi.org/10.1016/j.gca.2004.05.037>
- Mottl, M. J., Komor, S. C., Fryer, P., & Moyer, C. L. (2003). Deep-slab fluids fuel extremophilic Archaea on a Mariana forearc serpentinite mud volcano: Ocean drilling program leg 195. *Geochemistry, Geophysics, Geosystems*, 4(11). <https://doi.org/10.1029/2003GC000588>
- Mouthereau, F., Lacombe, O., & Meyer, B. (2006). The Zagros folded belt (Fars, Iran): Constraints from topography and critical wedge modelling. *Geophysical Journal International*, 165(1), 336–356. <https://doi.org/10.1111/j.1365-246X.2006.02855.x>
- Mouthereau, F., Lacombe, O., & Vergés, J. (2012). Building the Zagros collisional orogen: Timing, strain distribution and the dynamics of Arabia/Eurasia plate convergence. *Tectonophysics*, 532-535, 27-60. <https://doi.org/10.1016/j.tecto.2012.01.022>
- Mukherjee, R., Mondal, S. K., Rosing, M. T., & Frei, R. (2010). Compositional variations in the Mesoarchean chromites of the Nuggihalli schist belt, Western Dharwar Craton (India):

- Potential parental melts and implications for tectonic setting. *Contributions to Mineralogy and Petrology*, 160(6), 865–885. <https://doi.org/10.1007/s00410-010-0511-5>
- Nabatian, G., Ghaderi, M., Neubauer, F., Honarmand, M., Liu, X., Dong, Y., Jiang, S-Y., von Quadt, A., & Bernroider, M. (2014). Petrogenesis of Tarom high-potassic granitoids in the Alborz-Azarbaijan belt, Iran: Geochemical, U-Pb zircon and Sr-Nd-Pb isotopic constraints. *Lithos*, 184–187, 324–345. <https://doi.org/10.1016/j.lithos.2013.11.002>
- Nadimi, A., & Konon, A. (2012). Strike-slip faulting in the central part of the Sanandaj-Sirjan Zone, Zagros Orogen, Iran. *Journal of Structural Geology*, 40, 2–16. <https://doi.org/10.1016/j.jsg.2012.04.007>
- Nagle, F., Fink, L. K., Boström, K., & Stipp, J. J. (1973). Copper in pillow basalts from la désirade, Lesser Antilles island arc. *Earth and Planetary Science Letters*, 19(2), 193–197. [https://doi.org/10.1016/0012-821X\(73\)90114-3](https://doi.org/10.1016/0012-821X(73)90114-3)
- Neal, C., & Stanger, G. (1985). Past and present serpentinisation of ultramafic rocks; an example from the Semail ophiolite nappe of northern Oman. *The Chemistry of Weathering*, 249–275. [https://doi.org/10.1007/978-94-009-5333-8\\_15](https://doi.org/10.1007/978-94-009-5333-8_15)
- Neal, C., & Stanger, G. (1983). Hydrogen generation from mantle source rocks in Oman. *Earth and Planetary Science Letters*, 66(C), 315–320. [https://doi.org/10.1016/0012-821X\(83\)90144-9](https://doi.org/10.1016/0012-821X(83)90144-9)
- Neal, C., & Stanger, G. (1984). Calcium and magnesium hydroxide precipitation from alkaline groundwaters in Oman, and their significance to the process of serpentinization. *Mineralogical Magazine*, 48(347), 237–241. <https://doi.org/10.1180/minmag.1984.048.347.07>
- Neuendorf, K.K.E., Mehl J.P., & Jackson, J.A. (2011). Glossary of Geology, p. 457. London: Springer. 5th ed.
- Nielsen, R. L., Forsythe, L. M., Gallahan, W. E., & Fisk, M. R. (1994). Major- and trace-element magnetite-melt equilibria. *Chemical Geology*, 117(1–4), 167–191. [https://doi.org/10.1016/0009-2541\(94\)90127-9](https://doi.org/10.1016/0009-2541(94)90127-9)
- Noghreyan, M. (1982) Evolution géochimique, mineralogique et structurale d'un édifice ophiolitique singulier: le massif de Sabzevar (partie centrale), NE de l'Iran. TheseDoc. d'Etat, Université de Nancy, France, p 239
- Nozaem, R., Mohajjel, M., Rossetti, F., Della Seta, M., Vignaroli, G., Yassaghi, A., Salvini, F., & Eliassi, M. (2013). Post-Neogene right-lateral strike-slip tectonics at the north-western edge of the Lut Block (Kuh-e-Sarhangi Fault), Central Iran. *Tectonophysics*, 589, 220–233. <https://doi.org/10.1016/j.tecto.2013.01.001>
- Oelkers, E. H., & Helgeson, H. C. (1988). Calculation of the thermodynamic and transport properties of aqueous species at high pressures and temperatures: Aqueous tracer diffusion coefficients of ions to 1000°C and 5 kb. *Geochimica et Cosmochimica Acta*, 52(1), 63–85. [https://doi.org/10.1016/0016-7037\(88\)90057-9](https://doi.org/10.1016/0016-7037(88)90057-9)
- Ogasawara, Y., Okamoto, A., Hirano, N., & Tsuchiya, N. (2013). Coupled reactions and silica diffusion during serpentinization. *Geochimica et Cosmochimica Acta*, 119, 212–230. <https://doi.org/10.1016/j.gca.2013.06.001>

- O'Hanley, D. S., & Dyar, M. D. (1993). The composition of lizardite 1T and the formation of magnetite in serpentinites. *American Mineralogist*, 78(3–4), 391–404.
- O'Hanley, D.S. (1996). Serpentinites: records of tectonic and petrological history. Oxford monographs of geology and geophysics, no 34. Oxford University Press, Oxford.
- O'Hanley, D. S., Kyser, T. K., & Stauffer, M. (1993). Provenance, deformation, and alteration history of mafic-ultramafic rocks east of Amisk Lake, and the provenance of the mafic and ultramafic Boundary Intrusions, in the Flin Flon Domain, trans-Hudson Orogen. *Lithoprobe Report*, 34, 190-206.
- Olive, J. A., Behn, M. D., & Tucholke, B. E. (2010). The structure of oceanic core complexes controlled by the depth distribution of magma emplacement. *Nature Geoscience*, 3(7), 491–495. <https://doi.org/10.1038/ngeo888>
- Omrani, H. (2018). Island-arc and Active Continental Margin Adakites from the Sabzevar Zone, Iran. *Petrology*, 26(1), 96–113. <https://doi.org/10.1134/S0869591118010058>
- O'Neill, H. S. C., & Wall, V. J. (1987). The olivine - orthopyroxene - spinel oxygen geobarometer, the nickel precipitation curve, and the oxygen fugacity of the earth's upper mantle. *Journal of Petrology*, 28(6), 1169–1191. <https://doi.org/10.1093/petrology/28.6.1169>
- Onyeagocha, A. C. (1974). Alteration of Chromite from the Twin Sisters Dunite, Washington. *American Mineralogist*, 59(5–6), 608–612.
- Oufi, O. (2002). Magnetic properties of variably serpentinized abyssal peridotites. *Journal of Geophysical Research*, 107(B5). <https://doi.org/10.1029/2001jb000549>
- Oze, C., Fendorf, S., Bird, D. K., & Coleman, R. G. (2004). Chromium geochemistry in serpentinized ultramafic rocks and serpentine soils from the Franciscan complex of California. *American Journal of Science*, 304(1), 67–101. <https://doi.org/10.2475/ajs.304.1.67>
- Padrón-Navarta, J. A., Hermann, J., Garrido, C. J., López Sánchez-Vizcaíno, V., & Gómez-Pugnaire, M. T. (2010). An experimental investigation of antigorite dehydration in natural silica-enriched serpentinite. *Contributions to Mineralogy and Petrology*, 159(1), 25–42. <https://doi.org/10.1007/s00410-009-0414-5>
- Padrón-Navarta, J. A., Sánchez-Vizcaíno, V. L., Hermann, J., Connolly, J. A. D., Garrido, C. J., Gómez-Pugnaire, M. T., & Marchesi, C. (2013). Tschermak's substitution in antigorite and consequences for phase relations and water liberation in high-grade serpentinites. *Lithos*, 178, 186–196. <https://doi.org/10.1016/j.lithos.2013.02.001>
- Pang, K. N., Chung, S. L., Zarrinkoub, M. H., Khatib, M. M., Mohammadi, S. S., Chiu, H. Y., Chu, C-H., Lee, H-Y., & Lo, C. H. (2013). Eocene-Oligocene post-collisional magmatism in the Lut-Sistan region, eastern Iran: Magma genesis and tectonic implications. *Lithos*, 180–181, 234–251. <https://doi.org/10.1016/j.lithos.2013.05.009>
- Pang, K. N., Chung, S. L., Zarrinkoub, M. H., Mohammadi, S. S., Yang, H. M., Chu, C. H., Lee, H-Y., & Lo, C. H. (2012). Age, geochemical characteristics and petrogenesis of Late Cenozoic intraplate alkali basalts in the Lut-Sistan region, eastern Iran. *Chemical Geology*, 306–307, 40–53. <https://doi.org/10.1016/j.chemgeo.2012.02.020>

- Paraskevopoulos, G.M., & Economou, M.I. (1980). Genesis of magnetite ore occurrences by metasomatism of chromite ores in Greece. *Neues Jahrbuch für Mineralogie*, 140, 29–53.
- Parkinson, G. S., Novotný, Z., Jacobson, P., Schmid, M., & Diebold, U. (2011). Room temperature water splitting at the surface of magnetite. *Journal of the American Chemical Society*, 133(32), 12650–12655. <https://doi.org/10.1021/ja203432e>
- Peacock, S. M. (1993). Large-scale hydration of the lithosphere above subducting slabs. *Chemical Geology*, 108(1–4), 49–59. [https://doi.org/10.1016/0009-2541\(93\)90317-C](https://doi.org/10.1016/0009-2541(93)90317-C)
- Peacock, S. M. (1987a). Thermal effects of metamorphic fluids in subduction zones. *Geology*, 15(11), 1057–1060. [https://doi.org/10.1130/0091-7613\(1987\)15<1057:TEOMFI>2.0.CO;2](https://doi.org/10.1130/0091-7613(1987)15<1057:TEOMFI>2.0.CO;2)
- Peacock, S. M. (1987b). Serpentinization and infiltration metasomatism in the Trinity peridotite, Klamath province, northern California: implications for subduction zones. *Contributions to Mineralogy and Petrology*, 95(1), 55–70. <https://doi.org/10.1007/BF00518030>
- Penney, C., Copley, A., & Oveisi, B. (2015). Subduction tractions and vertical axis rotations in the Zagros-Makran transition zone, SE Iran: The 2013 May 11 Mw 6.1 Minab earthquake. *Geophysical Journal International*, 202(2), 1122–1136. <https://doi.org/10.1093/gji/ggv202>
- Pinsent, R. H., & Hirst, D. M. (1977). The metamorphism of the blue river ultramafic body, cassiar, British Columbia, Canada. *Journal of Petrology*, 18(4), 567–594. <https://doi.org/10.1093/petrology/18.4.567>
- Plümper, O., John, T., Podladchikov, Y. Y., Vrijmoed, J. C., & Scambelluri, M. (2017). Fluid escape from subduction zones controlled by channel-forming reactive porosity. *Nature Geoscience*, 10(2), 150–156. <https://doi.org/10.1038/ngeo2865>
- Porkoláb, K., Duretz, T., Yamato, P., Auzemery, A., & Willingshofer, E. (2021). Extrusion of subducted crust explains the emplacement of far-travelled ophiolites. *Nature Communications*, 12(1). <https://doi.org/10.1038/s41467-021-21866-1>
- Prabhakar, N., & Bhattacharya, A. (2013). Origin of zoned spinel by coupled dissolution-precipitation and inter-crystalline diffusion: Evidence from serpentized wehrlite, Bangriposi, Eastern India. *Contributions to Mineralogy and Petrology*, 166(4), 1047–1066. <https://doi.org/10.1007/s00410-013-0909-y>
- Putnis, A. (2002). Mineral replacement reactions: from macroscopic observations to microscopic mechanisms. *Mineralogical Magazine*, 66(5), 689–708. <https://doi.org/10.1180/0026461026650056>
- Putnis, A., & Austrheim, H. (2010). Fluid-induced processes: Metasomatism and metamorphism. *Geofluids*, 10(1–2), 254–269. <https://doi.org/10.1111/j.1468-8123.2010.00285.x>
- Putnis, C. V., Tsukamoto, K., & Nishimura, Y. (2005). Direct observations of pseudomorphism: Compositional and textural evolution at a fluid-solid interface. *American Mineralogist*, 90(11–12), 1909–1912. <https://doi.org/10.2138/am.2005.1990>

- Qiu, T., & Zhu, Y. (2018). Chromian spinels in highly altered ultramafic rocks from the Sartohay ophiolitic mélangé, Xinjiang, NW China. *Journal of Asian Earth Sciences*, 159, 155–184. <https://doi.org/10.1016/j.jseaes.2017.08.011>
- Radfar, J., & Kohansal, R. (2001). Geological Map of the Davarzan Quadrangle: Tehran, Geological Survey of Iran, scale 1:100,000.
- Rahmani, F., Mackizadeh, M. A., Noghreyan, M., Marchesi, C., & Garrido, C. J. (2020). Petrology and geochemistry of mafic and ultramafic cumulate rocks from the eastern part of the Sabzevar ophiolite (NE Iran): Implications for their petrogenesis and tectonic setting. *Geoscience Frontiers*, 11(6), 2347–2364. <https://doi.org/10.1016/j.gsf.2020.02.004>
- Rahmati Ilkhchi, M. (1999). Geological Map of the Joghatay Quadrangle: Tehran, Geological Survey of Iran, scale 1:100,000.
- Rajabzadeh, M.A. (1998). Mineralisation en chromite et éléments du groupe du platine dans les ophiolites d'Assemion et de Neyriz, centrure du Zagros, Iran. Ph.D. Thesis. Institute National Polytechnique de Lorraine, France, p. 358.
- Rajabzadeh, M. A., & Nazari Dehkordi, T. (2013). Investigation on mantle peridotites from Neyriz ophiolite, south of Iran: Geodynamic signals. *Arabian Journal of Geosciences*, 6, 4445–4461. <https://doi.org/10.1007/s12517-012-0687-2>
- Ramdohr, P. (1950). Über Josephinite, Awaruite, Souesite, ihre Eigenschaften, Entstehung und Paragenesis. *Mineralogical Magazine*, 29, 374–394.
- Ramezani, J., & Tucker, R. D. (2003). The Saghand Region, Central Iran: U-Pb geochronology, petrogenesis and implications for Gondwana tectonics. *American Journal of Science*, 303(7), 622–665. <https://doi.org/10.2475/ajs.303.7.622>
- Ranero, C. R., Phipps Morgan, J., McIntosh, K., & Relchert, C. (2003). Bending-related faulting and mantle serpentinization at the Middle America trench. *Nature*, 425(6956), 367–373. <https://doi.org/10.1038/nature01961>
- Rapp, J. F., Klemme, S., Butler, I. B., & Harley, S. L. (2010). Extremely high solubility of rutile in chloride and fluoride-bearing metamorphic fluids: An experimental investigation. *Geology*, 38(4), 323–326. <https://doi.org/10.1130/G30753.1>
- Rassios, A., & Kostopoulos, D. (1990). The geochemistry of dunite and its relation to the position of chromitites in the Vourinos ophiolite complex, Greece, In: Malpas, J., Moores, E., Panayiotou, A. and Xenophontos, C., eds, Ophiolites, Oceanic Crustal Analogues. Proc. Symp. "Troodos 1987", Nicosia, Cyprus, 593-604.
- Raufaste, C., Jamtveit, B., John, T., Meakin, P., & Dysthe, D. K. (2011). The mechanism of porosity formation during solvent-mediated phase transformations. *Proceedings of the Royal Society A: Mathematical, Physical and Engineering Sciences*, 467(2129), 1408–1426. <https://doi.org/10.1098/rspa.2010.0469>
- Rauch, E. F., & Véron, M. (2014). Automated crystal orientation and phase mapping in TEM. *Materials Characterization*, 98, 1-9. <https://doi.org/10.1016/j.matchar.2014.08.010>
- Regard, V., Bellier, O., Thomas, J. C., Bourlès, D., Bonnet, S., Abbassi, M. R., Braucher, R., Mercier, J., Shabanian, E., Soleymani, Sh., & Feghhi, K. (2005). Cumulative right-lateral

- fault slip rate across the Zagros-Makran transfer zone: Role of the Minab-Zendan fault system in accommodating Arabia-Eurasia convergence in southeast Iran. *Geophysical Journal International*, 162(1), 177–203. <https://doi.org/10.1111/j.1365-246X.2005.02558.x>
- Regard, V., Hatzfeld, D., Molinaro, M., Aubourg, C., Bayer, R., Bellier, O., Yamini-Fard, F., Peyret, M., & Abbassi, M. (2010). The transition between Makran subduction and the Zagros collision: Recent advances in its structure and active deformation. *Geological Society Special Publication*, 330, 43–64. <https://doi.org/10.1144/SP330.4>
- Reynard, B. (2013). Serpentine in active subduction zones. *Lithos*, 178, 171–185. <https://doi.org/10.1016/j.lithos.2012.10.012>
- Rezaei, Z., Noghreyan, M., & Saccani, E. (2018). Petrology and geochemistry of sheeted dykes and pillow lavas from the Sabzevar ophiolitic melange (northeast Iran): New constraints for the late cretaceous evolution of the Neo-tethys oceanic basin between the Central Iranian Microcontinent and Eurasia. *Ofioliti*, 43(2), 147–172. <https://doi.org/10.4454/ofioliti.v43i2.461>
- Riaz, M. S., Bin, S., Naeem, S., Kai, W., Xie, Z., Gilani, S. M. M., & Ashraf, U. (2019). Over 100 years of faults interaction, stress accumulation, and creeping implications, on Chaman Fault System, Pakistan. *International Journal of Earth Sciences*, 108(4), 1351–1359. <https://doi.org/10.1007/s00531-019-01710-0>
- Richards, J. P. (2015). Tectonic, magmatic, and metallogenic evolution of the Tethyan orogen: From subduction to collision. *Ore Geology Reviews*, 70, 323–345. <https://doi.org/10.1016/j.oregeorev.2014.11.009>
- Richards, J. P., & Sholeh, A. (2016). The Tethyan Tectonic History and Cu-Au Metallogeny of Iran, SEG Special Publication 19. *Economic Geology Special Publication*, 19, 193–212.
- Ricou, L.E. (1968a). Sur la mise en place au Crétacé supérieur d'importantes nappes a radiolarites et ophiolites dans les monts Zagros (Iran). *Comptes Rendus de l'Académie des Sciences*, 267, 2272–2275.
- Ricou, L. E. (1968b). Une coupe a travers les series a radiolarites des monts Pichakun (Zagros, Iran). *Bulletin de La Société Géologique de France*, S7-X(4), 478–485. <https://doi.org/10.2113/gssgfbull.s7-x.4.478>
- Ricou, L.-E. (1994). Tethys reconstructed : plates, continental fragments and their Boundaries since 260 Ma from Central America to South-eastern Asia. *Geodinamica Acta*, 7(4), 169–218. <https://doi.org/10.1080/09853111.1994.11105266>
- Ricou, L.-E. (1971). Le metamorphisme au contact des peridotites de Neyriz (Zagros interne, Iran); developpement de skarns a pyroxene. *Bulletin de la Societe Geologique de France*, 7, 146–155.
- Ricou, L.E. (1974). L'étude géologique de la région de Neyriz (Zagros iranien) et l'évolution structurale des Zagrides.
- Ricou, L.-E. (1976). Évolution structurale des Zagrides: la région clef de Neyriz (Zagros iranien). Société Géologique de France.

- Robert, A. M. M., Letouzey, J., Kavooosi, M. A., Sherkati, S., Müller, C., Vergés, J., & Aghababaei, A. (2014). Structural evolution of the Kopeh Dagh fold-and-thrust belt (NE Iran) and interactions with the South Caspian Sea Basin and Amu Darya Basin. *Marine and Petroleum Geology*, 57, 68–87. <https://doi.org/10.1016/j.marpetgeo.2014.05.002>
- Roedder, E. (1984). Fluid inclusions. Reviews in Mineralogy 12. Mineralogical Society of America, p. 644.
- Rossetti, F., Nasrabady, M., Vignaroli, G., Theye, T., Gerdes, A., Razavi, M. H., & Vaziri, H. M. (2010). Early Cretaceous migmatitic mafic granulites from the Sabzevar range (NE Iran): Implications for the closure of the Mesozoic peri-Tethyan oceans in central Iran. *Terra Nova*, 22(1), 26–34. <https://doi.org/10.1111/j.1365-3121.2009.00912.x>
- Rossetti, F., Nozaem, R., Lucci, F., Vignaroli, G., Gerdes, A., Nasrabadi, M., & Theye, T. (2015). Tectonic setting and geochronology of the Cadomian (Ediacaran-Cambrian) magmatism in Central Iran, Kuh-e-Sarhangi region (NW Lut Block). *Journal of Asian Earth Sciences*, 102, 24–44. <https://doi.org/10.1016/j.jseaes.2014.07.034>
- Rossetti, P., Gatta, G. D., Diella, V., Carbonin, S., Della Giusta, A., & Ferrario, A. (2009). The magnetite ore districts of the southern Aosta Valley (Western Alps, Italy): a mineralogical study of metasomatized chromite ore. *Mineralogical Magazine*, 73, 737–751. <https://doi.org/10.1180/minmag.2009.073.5.737>
- Rouméjon, S., & Cannat, M. (2014). Serpentinization of mantle-derived peridotites at mid-ocean ridges: Mesh texture development in the context of tectonic exhumation. *Geochemistry, Geophysics, Geosystems*, 15(6), 2354–2379. <https://doi.org/10.1002/2013GC005148>
- Rouméjon, S., Früh-Green, G. L., Orcutt, B. N., & the IODP Expedition 357 Science Party. (2018). Alteration heterogeneities in peridotites exhumed on the southern wall of the Atlantis Massif (IODP Expedition 357). *Journal of Petrology*, 59(7), 1329–1358. <https://doi.org/10.1093/petrology/egy065>
- Rüpke, L. H., Morgan, J. P., Hort, M., & Connolly, J. A. D. (2004). Serpentine and the subduction zone water cycle. *Earth and Planetary Science Letters*, 223(1–2), 17–34. <https://doi.org/10.1016/j.epsl.2004.04.018>
- Russell, M. J., Hall, A. J., & Martin, W. (2010). Serpentinization as a source of energy at the origin of life. *Geobiology*, 8(5), 355–371. <https://doi.org/10.1111/j.1472-4669.2010.00249.x>
- Saccani, E., Delavari, M., Beccaluva, L., & Amini, S. (2010). Petrological and geochemical constraints on the origin of the Nehbandan ophiolitic complex (eastern Iran): Implication for the evolution of the Sistan Ocean. *Lithos*, 117(1–4), 209–228. <https://doi.org/10.1016/j.lithos.2010.02.016>
- Sack, R. O., & Ghiorso, M. S. (1991). Chromian spinels as petrogenetic indicators: thermodynamics and petrological applications. *American Mineralogist*, 76(5–6), 827–847.
- Salvioli-Mariani, E., Boschetti, T., Toscani, L., Montanini, A., Petriglieri, J. R., & Bersani, D. (2020). Multi-stage rodingitization of ophiolitic bodies from Northern Apennines (Italy): Constraints from petrography, geochemistry and thermodynamic modelling. *Geoscience Frontiers*, 11(6), 2103–2125. <https://doi.org/10.1016/j.gsf.2020.04.017>

- Sánchez-Murillo, R., Gazel, E., Schwarzenbach, E. M., Crespo-Medina, M., Schrenk, M. O., Boll, J., & Gill, B. C. (2014). Geochemical evidence for active tropical serpentinization in the Santa Elena Ophiolite, Costa Rica: An analog of a humid early Earth? *Geochemistry, Geophysics, Geosystems*, 15(5), 1783–1800. <https://doi.org/10.1002/2013GC005213>
- Santos, J. S., Doriguetto, A. C., & Fernandes, N. G. (2005). Magnesium aluminium chromite. *Acta Crystallographica Section C: Crystal Structure Communications*, 61(3), i27–i28. <https://doi.org/10.1107/S0108270105000338>
- Satsukawa, T., Piazzolo, S., González-Jiménez, J. M., Colás, V., Griffin, W. L., O'Reilly, S. Y., Gervilla, F., Fanlo, I., & Kerestedjian, T. N. (2015). Fluid-present deformation aids chemical modification of chromite: Insights from chromites from Golyamo Kamenyane, SE Bulgaria. *Lithos*, 228–229, 78–89. <https://doi.org/10.1016/j.lithos.2015.04.020>
- Sauter, D., Cannat, M., Rouméjon, S., Andreani, M., Birot, D., Bronner, A., Bruneli, D., Carlut, J., Delacour, A., Guyder, V., MacLeod, C.J., Manatschal, G., Mendel, V., Ménez, B., Pasini, V., Ruellan, E., & Searle, R. (2013). Continuous exhumation of mantle-derived rocks at the Southwest Indian Ridge for 11 million years. *Nature Geoscience*, 6(4), 314–320. <https://doi.org/10.1038/ngeo1771>
- Savage, P. S., Moynier, F., Chen, H., Shofner, G., Siebert, J., Badro, J., & Puchtel, I. S. (2015). Copper isotope evidence for large-scale sulphide fractionation during Earth's differentiation. *Geochemical Perspectives Letters*, 1, 53–64. <https://doi.org/10.7185/geochemlet.1506>
- Scambelluri, M., & Tonarini, S. (2012). Boron isotope evidence for shallow fluid transfer across subduction zones by serpentinized mantle. *Geology*, 40(10), 907–910. <https://doi.org/10.1130/G33233.1>
- Schwarzenbach, E. M., Vrijmoed, J. C., Engelmann, J. M., Liesegang, M., Wiechert, U., Rohne, R., & Plümper, O. (2021). Sulfide Dissolution and Awaruite Formation in Continental Serpentinization Environments and Its Implications to Supporting Life. *Journal of Geophysical Research: Solid Earth*, 126, e2021JB021758. <https://doi.org/10.1029/2021JB021758>
- Schwarzenbach, E. M., Gazel, E., & Caddick, M. J. (2014). Hydrothermal processes in partially serpentinized peridotites from Costa Rica: evidence from native copper and complex sulfide assemblages. *Contributions to Mineralogy and Petrology*, 168, 1079. <https://doi.org/10.1007/s00410-014-1079-2>
- Schwarzenbach, E. M., & Steele-MacInnis, M. (2020). Fluids in submarine mid-ocean ridge hydrothermal settings. *Elements*, 16(6), 389–394. <https://doi.org/10.2138/GSELEMENTS.16.6.389>
- Şengör, A. M. C. (1984). *The Cimmeride Orogenic System and Tectonics of Eurasia*. Boulder, CO, USA: Geological Society of America.
- Sepahi, A. A., Salami, S., Lentz, D., McFarlane, C., & Maanijou, M. (2018). Petrography, geochemistry, and U–Pb geochronology of pegmatites and aplites associated with the Alvand intrusive complex in the Hamedan region, Sanandaj–Sirjan zone, Zagros orogen (Iran). *International Journal of Earth Sciences*, 107(3), 1059–1096. <https://doi.org/10.1007/s00531-017-1515-4>

- Sepehr, M., & Cosgrove, J. W. (2004). Structural framework of the Zagros Fold-Thrust Belt, Iran. *Marine and Petroleum Geology*, 21(7), 829–843. <https://doi.org/10.1016/j.marpetgeo.2003.07.006>
- Sepidbar, F., Mirnejad, H., Ma, C., & Moghadam, H. S. (2018). Identification of Eocene-Oligocene magmatic pulses associated with flare-up in east Iran: Timing and sources. *Gondwana Research*, 57, 141–156. <https://doi.org/10.1016/j.gr.2018.01.008>
- Sepidbar, F., Shafaii Moghadam, H., Zhang, L., Li, J. W., Ma, J., Stern, R. J., & Lin, C. (2019). Across-arc geochemical variations in the Paleogene magmatic belt of Iran. *Lithos*, 344–345, 280–296. <https://doi.org/10.1016/j.lithos.2019.06.022>
- Sepidbar, F., Moghadam, H. S., Li, C., Stern, R. J., Jiantang, P., & Vesali, Y. (2020). Cadomian Magmatic Rocks from Zarand (SE Iran) Formed in a Retro-Arc Basin. *Lithos*, 366–367, 105569. <https://doi.org/10.1016/j.lithos.2020.105569>
- Seyfried, W. E., Foustoukos, D. I., & Allen, D. E. (2004). Ultramafic-hosted hydrothermal systems at mid-ocean ridges: Chemical and physical controls on pH, redox and carbon reduction reactions. In *Geophysical Monograph Series* (pp. 267–284). <https://doi.org/10.1029/148GM11>
- Seyfried, W. E., Foustoukos, D. I., & Fu, Q. (2007). Redox evolution and mass transfer during serpentinization: An experimental and theoretical study at 200 °C, 500 bar with implications for ultramafic-hosted hydrothermal systems at Mid-Ocean Ridges. *Geochimica et Cosmochimica Acta*, 71(15), 3872–3886. <https://doi.org/10.1016/j.gca.2007.05.015>
- Shafaii Moghadam, H., Li, Q.-L., Stern, R. J., Chiaradia, M., Karsli, O., & Rahimzadeh, B. (2020). The Paleogene ophiolite conundrum of the Iran–Iraq border region. *Journal of the Geological Society*, 177(5), 955–964. <https://doi.org/10.1144/jgs2020-009>
- Shafaii Moghadam, H., Zaki Khedr, M., Arai, S., Stern, R. J., Ghorbani, G., Tamura, A., & Ottley, C. J. (2015). Arc-related harzburgite-dunite-chromitite complexes in the mantle section of the Sabzevar ophiolite, Iran: A model for formation of podiform chromitites. *Gondwana Research*, 27(2), 575–593. <https://doi.org/10.1016/j.gr.2013.09.007>
- Shafaii Moghadam, H., Corfu, F., Chiaradia, M., Stern, R. J., & Ghorbani, G. (2014). Sabzevar Ophiolite, NE Iran: Progress from embryonic oceanic lithosphere into magmatic arc constrained by new isotopic and geochemical data. *Lithos*, 210–211, 224–241. <https://doi.org/10.1016/j.lithos.2014.10.004>
- Shafaii Moghadam, H., Li, X. H., Stern, R. J., Ghorbani, G., & Bakhshizad, F. (2016). Zircon U-Pb ages and Hf-O isotopic composition of migmatites from the Zanjan-Takab complex, NW Iran: Constraints on partial melting of metasediments. *Lithos*, 240–243, 34–48. <https://doi.org/10.1016/j.lithos.2015.11.004>
- Shafaii Moghadam, H., & Stern, R. J. (2015). Ophiolites of Iran: Keys to understanding the tectonic evolution of SW Asia: (II) Mesozoic ophiolites. *Journal of Asian Earth Sciences*, 100, 31–59. <https://doi.org/10.1016/j.jseaes.2014.12.016>
- Shafaii Moghadam, H., & Stern, R. J. (2021). Subduction initiation causes broad upper plate extension: The Late Cretaceous Iran example. *Lithos*, 398–399, 106296. <https://doi.org/10.1016/j.lithos.2021.106296>

- Shahbazi, H., Siebel, W., Pourmoafee, M., Ghorbani, M., Sepahi, A. A., Shang, C. K., & Vousoughi Abedini, M. (2010). Geochemistry and U-Pb zircon geochronology of the Alvand plutonic complex in Sanandaj-Sirjan Zone (Iran): New evidence for Jurassic magmatism. *Journal of Asian Earth Sciences*, 39(6), 668–683. <https://doi.org/10.1016/j.jseaes.2010.04.014>
- Sheikholeslami, M. R. (2015). Deformations of Palaeozoic and Mesozoic rocks in southern Sirjan, Sanandaj-Sirjan Zone, Iran. *Journal of Asian Earth Sciences*, 106, 130–149. <https://doi.org/10.1016/j.jseaes.2015.03.007>
- Shen, P., Hwang, S.-L., Chu, H.-T., & Jeng, R.-C. 1988. STEM study of “ferritchromit” from the Heng-Chun chromitite. *American Mineralogist*, 73 (3-4), 383–388.
- Shojaat, B., Hassanipak, A. A., Mobasher, K., & Ghazi, A. M. (2003). Petrology, geochemistry and tectonics of the Sabzevar ophiolite, North Central Iran. *Journal of Asian Earth Sciences*, 21, 1053–1067. [https://doi.org/10.1016/S1367-9120\(02\)00143-8](https://doi.org/10.1016/S1367-9120(02)00143-8)
- Skomurski, F. N., Kerisit, S., & Rosso, K. M. (2010). Structure, charge distribution, and electron hopping dynamics in magnetite (Fe<sub>3</sub>O<sub>4</sub>) (100) surfaces from first principles. *Geochimica et Cosmochimica Acta*, 74, 4234–4248. <https://doi.org/10.1016/j.gca.2010.04.063>
- Smith, A. G. (2012). A review of the Ediacaran to early Cambrian ('Infra-Cambrian') evaporites and associated sediments of the middle east. *Geological Society Special Publication*, 366(1), 229–250. <https://doi.org/10.1144/SP366.12>
- Smith, D. K., Cann, J. R., & Escartín, J. (2006). Widespread active detachment faulting and core complex formation near 13°N on the Mid-Atlantic Ridge. *Nature*, 442(7101), 440–443. <https://doi.org/10.1038/nature04950>
- Sobolev, A. V, Hofmann, A. W., Kuzmin, D. V, Yaxley, G. M., Arndt, N. T., Chung, S.-L., Danyushevsky, L.V., Elliott, T., Frey, F.A., Garcia, M.O., Gurenko, A.A., Kamenetsky, V.S., Kerr, A.C., Krivolutsкая, N.A., Matvienkov, V.V., Nikogosian, I.K., Rocholl, A., Sigurdsson, I.A., Sushchevskaya, N.M., & Teklay, M. (2007). The amount of recycled crust in sources of mantle-derived melts. *Science*, 316(5823), 412–417. <https://doi.org/10.1126/science.1138113>.
- Spangenberg, K. (1943). Die chromitlaagerstätte von tampedal in Zobten. *Z Prakt Geol* 51, 13–35.
- Stern, R. J., Moghadam, H. S., Pirouz, M., & Mooney, W. (2021). The geodynamic evolution of Iran. *Annual Review of Earth and Planetary Sciences*, 49, 9–36. <https://doi.org/10.1146/annurev-earth-071620-052109>
- Stöcklin, J. (1968). Structural history and tectonics of Iran; a review. *AAPG Bulletin*, 52(7), 1229–1258.
- Stöcklin, J., & Nabavi, M. H. (1973). Tectonic map of Iran, scale 1:250000. Tehran: Geological Survey of Iran.
- Stöcklin, J. (1977) Structural correlation of the Alpine range between Iran and Central Asia. – *Mémoire Hors-Serie, Société Géologique de France*, 8, pp. 333–353.

- Stockli, D. F., Hassanzadeh, J., Stockli, L. D., Axen, G. J., Walker, J. D., Dewane, T. J., & Anonymous. (2004). Structural and geochronological evidence for Oligo-Miocene intra-arc low-angle detachment faulting in the Takab-Zanjan area, NW Iran. *Abstracts with Programs - Geological Society of America*, 36(5), 319.
- Sun, X., Lin, H., Fu, Y., Li, D., Hollings, P., Yang, T., & Liu, Z. (2017). Trace element geochemistry of magnetite from the giant Beiya gold-polymetallic deposit in Yunnan Province, Southwest China and its implications for the ore forming processes. *Ore Geology Reviews*, 91, 477–490. <https://doi.org/10.1016/j.oregeorev.2017.09.007>
- Suzuki, A. M., Yasuda, A., & Ozawa, K. (2008). Cr and Al diffusion in chromite spinel: Experimental determination and its implication for diffusion creep. *Physics and Chemistry of Minerals*, 35(8), 433–445. <https://doi.org/10.1007/s00269-008-0238-2>.
- Sverjensky, D. A., Harrison, B., & Azzolini, D. (2014). Water in the deep Earth: The dielectric constant and the solubilities of quartz and corundum to 60kb and 1200°C. *Geochimica et Cosmochimica Acta*, 129, 125–145. <https://doi.org/10.1016/j.gca.2013.12.019>
- Taheri, J., Fürsich, F. T., & Wilmsen, M. (2009). Stratigraphy depositional environments and geodynamic significance of the Upper Bajocian-Bathonian Kashafrud formation, NE Iran. *Geological Society Special Publication*, 312, 205–218. <https://doi.org/10.1144/SP312.10>
- Tangestani, M. H., Jaffari, L., Vincent, R. K., & Sridhar, B. B. M. (2011). Spectral characterization and ASTER-based lithological mapping of an ophiolite complex: A case study from Neyriz ophiolite, SW Iran. *Remote Sensing of Environment*, 115(9), 2243–2254. <https://doi.org/10.1016/j.rse.2011.04.023>
- Tao, C., Seyfried, W. E., Lowell, R. P., Liu, Y., Liang, J., Guo, Z., Ding, K., Zhang, H., Liu, J., Qiu, L., Egorov, I., Liao, S., Zhao, M., Zhou, J., Deng, X., Li, H., Wang, H., Cai, W., Zhang, G., Zhou, H., Lin, J., & Li, W. (2020). Deep high-temperature hydrothermal circulation in a detachment faulting system on the ultra-slow spreading ridge. *Nature Communications*, 11, 1300. <https://doi.org/10.1038/s41467-020-15062-w>
- Tavakoli, N., Davoudian, A. R., Shabanian, N., Azizi, H., Neubauer, F., Asahara, Y., & Bernroider, M. (2020). Zircon U-Pb dating, mineralogy and geochemical characteristics of the gabbro and gabbro-diorite bodies, Boein–Miandasht, western Iran. *International Geology Review*, 62(13–14), 1658–1676. <https://doi.org/10.1080/00206814.2019.1583139>
- Tirrul, R., Bell, I. R., Griffis, R. J., & Camp, V. E. (1983). The Sistan suture zone of eastern Iran. *Geological Society of America Bulletin*, 94(1), 134–150. [https://doi.org/10.1130/0016-7606\(1983\)94<134:TSSZOE>2.0.CO;2](https://doi.org/10.1130/0016-7606(1983)94<134:TSSZOE>2.0.CO;2)
- Toffolo, L., Nimis, P., Martin, S., Tumiatì, S., & Bach, W. (2017). The Cogne magnetite deposit (Western Alps, Italy): A Late Jurassic seafloor ultramafic-hosted hydrothermal system? *Ore Geology Reviews*, 83, 103–126. <https://doi.org/10.1016/j.oregeorev.2016.11.030>
- Toft, P. B., Arkani-Hamed, J., & Haggerty, S. E. (1990). The effects of serpentinization on density and magnetic susceptibility: a petrophysical model. *Physics of the Earth and Planetary Interiors*, 65(1–2), 137–157. [https://doi.org/10.1016/0031-9201\(90\)90082-9](https://doi.org/10.1016/0031-9201(90)90082-9)
- Toplis, M. J., & Carroll, M. R. (1995). An experimental study of the influence of oxygen fugacity on Fe-Ti oxide stability, phase relations, and mineral-melt equilibria in ferro-

basaltic systems. *Journal of Petrology*, 36(5), 1137–1170.  
<https://doi.org/10.1093/petrology/36.5.1137>

- Toplis, M. J., & Corgne, A. (2002). An experimental study of element partitioning between magnetite, clinopyroxene and iron-bearing silicate liquids with particular emphasis on vanadium. *Contributions to Mineralogy and Petrology*, 144(1), 22–37.  
<https://doi.org/10.1007/s00410-002-0382-5>
- Topuz, G., Candan, O., Zack, T., Chen, F., & Li, Q. L. (2019). Origin and significance of Early Miocene high-potassium I-type granite plutonism in the East Anatolian plateau (the Taşlıçay intrusion). *Lithos*, 348–349, 105210.  
<https://doi.org/10.1016/j.lithos.2019.105210>
- Tucholke, B. E., Lin, J., & Kleinrock, M. C. (1998). Megamullions and mullion structure defining oceanic metamorphic core complexes on the Mid-Atlantic Ridge. *Journal of Geophysical Research: Solid Earth*, 103(5), 9857–9866.  
<https://doi.org/10.1029/98jb00167>
- Ulmer, G. C. (1974). Alteration of chromite during serpentinization in the Pennsylvania-Maryland District. *American Mineralogist*, 59(1969), 1236–1241.
- Ulmer, P. & Trommsdorff, V. (1999). Phase relations of hydrous mantle subducting to 300 km. In: Fei, Y., Bertka, C.M., Mysen, B.O. (Eds.), *Mantle Petrology: Field Observations and High Pressure Experimentation*. Special Publication no. 6. The Geochemical Society, Houston, pp. 259–281.
- Ulmishek, G.F. (2004). Petroleum geology and resources of the Amu-Darya basin, Turkmenistan, Uzbekistan, Afghanistan, and Iran. U.S. Geol. Surv. 2201–H.
- van Aken, D., Becker, H., Walker, R. J., McDonough, W. F., Wombacher, F., Ash, R. D., & Piccoli, P. M. (2010). Formation of pyroxenite layers in the Totalp ultramafic massif (Swiss Alps) - Insights from highly siderophile elements and Os isotopes. *Geochimica et Cosmochimica Acta*, 74, 661–683. <https://doi.org/10.1016/j.gca.2009.10.007>
- Van Baalen, M. R. (1993). Titanium mobility in metamorphic systems: a review. *Chemical Geology*, 110(1–3), 233–249. [https://doi.org/10.1016/0009-2541\(93\)90256-I](https://doi.org/10.1016/0009-2541(93)90256-I)
- Van Den Kerkhof, A. M., & Hein, U. F. (2001). Fluid inclusion petrography. *Lithos*, 55(1–4), 27–47. [https://doi.org/10.1016/S0024-4937\(00\)00037-2](https://doi.org/10.1016/S0024-4937(00)00037-2)
- Van Keken, P. E., Hacker, B. R., Syracuse, E. M., & Abers, G. A. (2011). Subduction factory: 4. Depth-dependent flux of H<sub>2</sub>O from subducting slabs worldwide. *Journal of Geophysical Research: Solid Earth*, 116(1). <https://doi.org/10.1029/2010JB007922>
- Vance, J. A., & Dungan, M. A. (1977). Formation of peridotites by deserpentinization in the Darrington and Sultan areas, Cascade Mountains, Washington. *Bulletin of the Geological Society of America*, 88, 1497–1508. [https://doi.org/10.1130/0016-7606\(1977\)88<1497:FOPBDI>2.0.CO;2](https://doi.org/10.1130/0016-7606(1977)88<1497:FOPBDI>2.0.CO;2)
- Verdel, C., Wernicke, B. P., Hassanzadeh, J., & Guest, B. (2011). A Paleogene extensional arc flare-up in Iran. *Tectonics*, 30(3). <https://doi.org/10.1029/2010TC002809>
- Verlaguet, A., Brunet, F., Goffá, B., & Murphy, W. M. (2006). Experimental study and modeling of fluid reaction paths in the quartz-kyanite ± muscovite-water system at 0.7

GPa in the 350–550 °C range: Implications for Al selective transfer during metamorphism. *Geochimica et Cosmochimica Acta*, 70(7), 1772–1788. <https://doi.org/10.1016/j.gca.2005.12.014>

Vernant, P., Nilforoushan, F., Hatzfeld, D., Abbassi, M. R., Vigny, C., Masson, F., Nankali, H., Martinod, J., Ashtiani, A., Bayer, R., Tavakoli, F., & Chéry, J. (2004). Present-day crustal deformation and plate kinematics in the Middle East constrained by GPS measurements in Iran and northern Oman. *Geophysical Journal International*, 157(1), 381–398. <https://doi.org/10.1111/j.1365-246X.2004.02222.x>

Wakabayashi, J., & Dilek, Y. (2004). What constitutes “emplacement” of an ophiolite?: Mechanisms and relationship to subduction initiation and formation of metamorphic soles. *Geological Society Special Publication*, 218, 427–447. <https://doi.org/10.1144/GSL.SP.2003.218.01.22>

Wall, A. J., Mathur, R., Post, J. E., & Heaney, P. J. (2011). Cu isotope fractionation during bornite dissolution: An in situ X-ray diffraction analysis. *Ore Geology Reviews*, 42(1), 62–70. <https://doi.org/10.1016/j.oregeorev.2011.01.001>

Walpersdorf, A., Manighetti, I., Mousavi, Z., Tavakoli, F., Vergnolle, M., Jadidi, A., Hatzfeld, D., Aghamohammadi, A., Bigot, A., Djamour, Y., Nankali, H., Sedighi, M. (2014). Present-day kinematics and fault slip rates in eastern Iran, derived from 11 years of GPS data. *Journal of Geophysical Research: Solid Earth*, 119(2), 1359–1383. <https://doi.org/10.1002/2013JB010620>

Wang, M., Wang, W., Liu, K., Michalak, P. P., Wei, K., & Hu, M. (2017). In-situ LA-ICP-MS trace elemental analyzes of magnetite: The Tieshan skarn Fe-Cu deposit, Eastern China. *Chemie Der Erde*, 77(1), 169–181. <https://doi.org/10.1016/j.chemer.2016.11.002>

Wang, Y., He, M., Yan, W., Yang, M., & Liu, X. (2020). Jianite: Massive dunite solely made of virtually pure forsterite from Ji'an County, Jilin Province, Northeast China. *Minerals*, 10(3), 220. <https://doi.org/10.3390/min10030220>

Wegner, W. W., & Ernst, W. G. (1983). Experimentally determined hydration and dehydration reaction rates in the system MgO-SiO<sub>2</sub>-H<sub>2</sub>O. *American Journal of Science*, 283(A), 151–180.

White, Powell, Holland, & Worley. (2000). The effect of TiO<sub>2</sub> and Fe<sub>2</sub>O<sub>3</sub> on metapelitic assemblages at greenschist and amphibolite facies conditions: Mineral equilibria calculations in the system K<sub>2</sub>O-FeO-MgO-Al<sub>2</sub>O<sub>3</sub>-SiO<sub>2</sub>-H<sub>2</sub>O-TiO<sub>2</sub>-Fe<sub>2</sub>O<sub>3</sub>. *Journal of Metamorphic Geology*, 18, 497–511. <https://doi.org/10.1046/j.1525-1314.2000.00269.x>

Whitechurch, H., Omrani, J., Agard, P., Humbert, F., Montigny, R., & Jolivet, L. (2013). Evidence for Paleocene-Eocene evolution of the foot of the Eurasian margin (Kermanshah ophiolite, SW Iran) from back-arc to arc: Implications for regional geodynamics and obduction. *Lithos*, 182–183, 11–32. <https://doi.org/10.1016/j.lithos.2013.07.017>

Wylie, A. G., Candela, P. A., & Burke, T. M. (1987). Compositional zoning in unusual Zn-rich chromite from the Sykesville district of Maryland and its bearing on the origin of “ferritchromite”. *American Mineralogist*, 72(3–4), 413–422.

Zarrinkoub, M. H., Pang, K. N., Chung, S. L., Khatib, M. M., Mohammadi, S. S., Chiu, H. Y., & Lee, H. Y. (2012). Zircon U-Pb age and geochemical constraints on the origin of the

Birjand ophiolite, Sistan suture zone, eastern Iran. *Lithos*, 154, 392–405. <https://doi.org/10.1016/j.lithos.2012.08.007>

Zhou, H., Sun, X., Cook, N. J., Lin, H., Fu, Y., Zhong, R., & Brugger, J. (2017). Nano- to micron-scale particulate gold hosted by magnetite: A product of gold scavenging by bismuth melts. *Economic Geology*, 112(4), 993–1010. <https://doi.org/10.2113/econgeo.112.4.993>

Zou, Z., Wang, Z., Li, M., Becker, H., Geng, X., Hu, Z., & Lazarov, M. (2019). Copper isotope variations during magmatic migration in the mantle: insights from mantle pyroxenites in Balmuccia Peridotite Massif. *Journal of Geophysical Research: Solid Earth*, 124(11), 11130–11149. <https://doi.org/10.1029/2019JB017990>